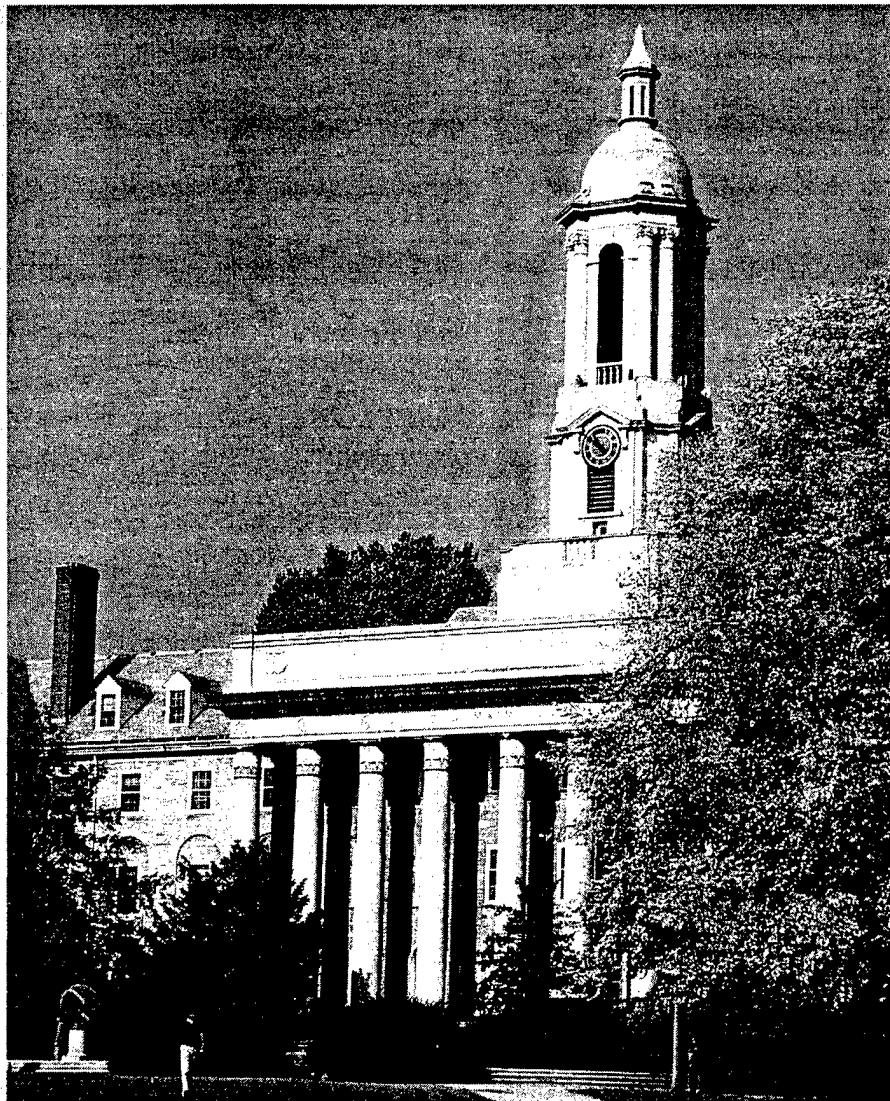


Fourth ARO Workshop on Smart Structures



August 16-18, 1999

Penn State, University Park Campus, Pennsylvania



DTIC QUALITY INSPECTED 4

PENNSSTATE

DISTRIBUTION STATEMENT A
Approved for Public Release
Distribution Unlimited



University
Park

outreach program of the College of Engineering, sponsored by the U.S. Army Research Office

REPORT DOCUMENTATION PAGE

Form Approved
OMB NO. 0704-0188

The Reporting burden for this collection of information is estimated to average 1 hour per response, including the time for reviewing instructions, searching existing data sources, gathering and maintaining the data needed, and completing and reviewing the collection of information. Send comment regarding this burden estimate or any other aspect of this collection of information, including suggestions for reducing this burden, to Washington Headquarters Services, Directorate for Information Operations and Reports, 1215 Jefferson Davis Highway, Suite 1204, Arlington, VA 22202-4302, and to the Office of Management and Budget, Paperwork Reduction Project (0704-0188), Washington, DC 20503.

1. AGENCY USE ONLY (Leave Blank)		2. REPORT DATE September 2000		3. REPORT TYPE AND DATES COVERED Final Report. July 12, 1999 - July 11, 2000.	
4. TITLE AND SUBTITLE Fourth ARO Workshop on Smart Structures				5. FUNDING NUMBERS DAAD19-99-1-0308	
6. AUTHOR(S) Kon-Well Wang					
7. PERFORMING ORGANIZATION NAME(S) AND ADDRESS(ES) Dr. Kon-Well Wang 157B Hammond Building The Pennsylvania State University University Park, PA 16802				8. PERFORMING ORGANIZATION REPORT NUMBER	
9. SPONSORING / MONITORING AGENCY NAME(S) AND ADDRESS(ES) U. S. Army Research Office P.O. Box 12211 Research Triangle Park, NC 27709-2211				10. SPONSORING / MONITORING AGENCY REPORT NUMBER ARO 39165.1-EG-CF	
11. SUPPLEMENTARY NOTES The views, opinions and/or findings contained in this report are those of the author(s) and should not be construed as an official statement of the Army position, policy or decision, unless so designated by the documentation.					
12. DISTRIBUTION / AVAILABILITY STATEMENT Approved for public release; distribution unlimited.				12 b. DISTRIBUTION CODE	
13. ABSTRACT (Maximum 200 words) The objective of this project is to hold a three-day "Workshop on Smart Structures" at the Pennsylvania State University from August 16 through August 18 in 1999. This workshop has achieved the following basic goals: <ul style="list-style-type: none"> To enhance fundamental understanding of the phenomena associated with smart structures technology; Mutual sharing of experience of analysis techniques to solve small-scale and full-scale system problems; Methodology assessment of smart structures and materials; Disseminate new experimental data and results from different organizations; Show technology gaps and suggest new directions for research to meet the future challenge of Army missions and Promote an exchange between the various MURI programs and principal investigators of ARO, industry and Army Labs. Papers have been solicited from all technical areas associated with smart structures and materials. Over 80 papers have been presented (oral and poster sessions) at the workshop. Over 130 people from various army labs, other government labs, universities, and industry attended the workshop and participated in the sessions. Copies of individual abstracts and presentation materials were bound in a volume and provided to all workshop attendees.					
14. SUBJECT TERMS Smart structures				15. NUMBER OF PAGES 4 (including this cover page)	
				16. PRICE CODE	
17. SECURITY CLASSIFICATION OR REPORT UNCLASSIFIED	18. SECURITY CLASSIFICATION ON THIS PAGE UNCLASSIFIED	19. SECURITY CLASSIFICATION OF ABSTRACT UNCLASSIFIED	20. LIMITATION OF ABSTRACT UL		

NSN 7540-01-280-5500

Standard Form 298 (Rev.2-89)

Enclosure 1

The Fourth ARO Workshop on Smart Structures

Description

We have held a three-day "*Workshop on Smart Structures*" at the Pennsylvania State University from August 16 through August 18 in 1999. This workshop has achieved the following basic objectives:

- To enhance fundamental understanding of the phenomena associated with smart structures technology;
- Mutual sharing of experience of analysis techniques to solve small-scale and full-scale system problems;
- Methodology assessment of smart structures and materials;
- Disseminate new experimental data and results from different organizations;
- Show technology gaps and suggest new directions for research to meet the future challenge of Army missions and
- Promote an exchange between the various MURI programs and principal investigators of ARO, industry and Army Labs.

Papers have been solicited from all technical areas associated with smart structures and materials, including smart actuators and sensors, mathematics and control in smart structures, processing and instrumentation, smart materials processing, and theoretical and numerical modeling of smart structures. Over 80 papers have been presented (twelve oral sessions and a poster session) at the workshop. Over 130 people from army labs (e.g., AVRDEC, ARDEC, TACOM-ARDEC, AFDD, ARL, USAANCOM), other government labs (e.g., NASA, Airforce), universities, and industry have attended the workshop and participated in the sessions.

20001010 069

This multidisciplinary forum has focused on theoretical/experimental aspects of intelligent sensing, processing, and actuation, as well as on design/implementation issues.

The sessions and topics included:

- Overviews of Emerging Smart Structures Technology in Army/DoD
- Control Issues
- Actuators and Active Composites
- Health Monitoring and Sensor Research
- Helicopter Applications
- Semi-Active Devices (including ER/MR fluids and shunt piezoelectric networks)
- SMA Research
- Modeling and Characterization Issues
- Damping Treatments
- Transducer Issues: Materials, Device Design and Power
- Active Vibration and Noise Control

The workshop has made a very good assessment on the state-of-the-art on smart structures and materials and its applications to Army systems. It has also created an excellent environment for the army and DoD people to exchange ideas with the university and industrial researchers.

Documentation

Copies of individual abstracts and presentation materials were bound in a volume and provided to all workshop attendees. Authors have also been encouraged to submit their workshop papers to a special issue in *Journal of Intelligent Material Systems and Structures* for subsequent publications.

Special Benefits to the Army Research Office

In addition to the active involvement in a technical workshop of major interest to the U.S. Army, the following special benefits have been provided:

- U.S. Army attendees were waived of registration fee for attending the workshop.
- Six copies of the bound volume are provided to the Army Research Office at no charge (enclosed with this report).



PENNSTATE



Fourth ARO Workshop on Smart Structures

August 16-18, 1999
The Nittany Lion Inn
State College, PA

Sponsored by the U.S. Army Research Office

Hosted by the Pennsylvania State University

Organizing Committee

ARO Program Managers

Dr. Gary L. Anderson
Dr. Devendra Garg
Structural Mechanics Branch
Mechanical and Environmental Sciences Division
U. S. Army Research Office

Workshop Chairman

Professor K. W. Wang
Department of Mechanical & Nuclear Engineering
The Pennsylvania State University

Local Committee Members

Karen Thal, Staff Assistant
Professor Mary Frecker, Department of Mechanical & Nuclear Engineering
Professor Farhan Gandhi, Department of Aerospace Engineering
Professor George Lesieutre, Department of Aerospace Engineering

Penn State Conference Planner

Judy Hall

PROGRAM
FOURTH ARO WORKSHOP ON SMART STRUCTURES
The Pennsylvania State University

Nittany Lion Inn
State College, PA

All Technical Sessions will be Held in
***Ballroom CDE* of the Nittany Lion Inn**

August 15, 1999 (Sunday)

8:00 -10:00 p.m. Registration (Rotunda Lobby of the Nittany Lion Inn)

August 16, 1999 (Monday)

7:00 a.m. - 5:00 p.m. Registration (Atrium Outside of Ballroom)

7:00 - 8:00 a.m. Continental Breakfast (Atrium Outside of Ballroom)

Welcome and Workshop Overview

8:00 – 8:15 a.m. *David Wormley, Dean of Engineering, The Pennsylvania State University*
K. W. Wang, The Pennsylvania State University

Introductory Remarks

8:15 - 8:40 a.m. *Gary Anderson, US Army Research Office*

Session 1: **Overviews of Emerging Smart Structures Technology in Army/DoD**
Session Chair: **Gary Anderson, US Army Research Office**

8:40 a.m. *Robert A. Ormiston, US Army AVRDEC*
 “Smart Materials and Structures for Rotor Dynamics Applications”

9:00 a.m. *Mike Mattice and Robert Testa, US Army ARDEC*
 “Smart Structures and Materials Concepts for Army Weapon Systems”

9:20 a.m. *Eric Kathe, US Army TACOM-ARDEC Benet Labs*
 Roger L. Ellis, Naval Surface Warfare Center
 “Application of Smart Structure Technology to Improve Large Caliber Gun
System Performance”

9:40 a.m. *Ephraim Garcia, DARPA*
 “Future Concepts and Enabled Systems”

10:00 – 10:20 a.m. **BREAK**

Session 2: **Control Issues**
Session Chair: **Devendra Garg, US Army Research Office**

10:20 a.m. *John Baillieul, Boston University*
 “Feedback Designs for Controlling Device Arrays with Communication Bandwidth Constraints”

10:40 a.m. *Eric Justh and P. S. Krishnaprasad, University of Maryland*
 “Pattern Formation for Control of Large Arrays”

11:00 a.m. *Ayman A. El-Badawy and Ali H. Nayfeh, Virginia Polytechnic Institute and State University*
 “Nonlinear Control of a Parametrically Excited Structural Dynamic Model of an F-15 Tail Section”

11:20 a.m. *Sridhar Sana and Vittal S. Rao, University of Missouri-Rolla*
 “Application of Linear Matrix Inequalities in the Control of Smart Structural Systems”

11:40 a.m. *Ralph C. Smith, North Carolina State University*
 M. Dapino and Alison Flatau, Iowa State Univ.
 C. Hom, Lockheed Martin
 Z. Ounaies, ICASE, NASA Langley
 R. Zrostlik, Etrema Products
 “Modeling and Control Issues Concerning Smart Materials with Hysteresis”

12:00 a.m. – 1:00 p.m. **LUNCH (Ballroom AB)**

Session 3: **Actuators and Active Composites**
Session Chair: **Ephraim Garcia, DARPA**

1:00 p.m. *Philippe Bouchilloux, Rensselaer Polytechnic Institute*
 Burhanettin Koc and Kenji Uchino, The Pennsylvania State University
 “Piezoelectric Motion Couplers”

1:20 p.m. *Mary Frecker and Shawn Canfield, The Pennsylvania State University*
 “Systematic Design of Compliant Mechanism Amplifiers for Piezoelectric Actuators”

1:40 p.m. *Taeoh Lee and Inderjit Chopra, University of Maryland*
"Design and Validation of a Multi-Stage Stroke Amplifier for Piezostack-Based Trailing-Edge Flap Actuator"

2:00 p.m. *Q. M. Zhang and A. E. Glazounov, The Pennsylvania State University*
C. Kim, Naval Research Laboratory
"Torsional Actuator and Motor Based on Mechanically Amplified Shear Piezoelectric Response"

2:20 p.m. *Nesbitt W. Hagood, Mauro J. Atalla, Yet-Ming Chiang, Michael J. Cima,*
Steven R. Hall, Harry L. Tuller, Massachusetts Institute of Technology
"Overview of the MIT MURI on Smart Composite Systems"

2:40 – 3:00 p.m. **BREAK**

Session 4: Health Monitoring and Sensor Research
Session Chair: Mark Fulton, US Army AFDD

3:00 p.m. *Fu-Kuo Chang, Stanford University*
"A Built-In Structural Diagnostics for Composite Structures"

3:20 p.m. *P. Frank Pai and Si Jin, University of Missouri-Columbia*
"Boundary Effect Detection Method for Locating Structural Damage"

3:40 p.m. *M. El-Sherif, K. Fidanboyu, Drexel University*
D. El-Sherif, Photonics Lab Inc.,
R. Gafsi, J. Yuan, C. Lee, and J. Fairneny, US Army Natick R&D
"A Novel Fiber Optic System for Measuring the Dynamic Structural Behavior of Parachutes"

4:00 p.m. *J. S. Sirkis, X. D. Jin, T. Rossmanith, M. Rutherford, J. S. Sirkis, A. Dasgupta, D.*
DeVoe, and F. F. Rosenberger, III, University of Maryland
V. S. Venkat and Y. C. Shi, Analytical Service and Materials, Inc.
C. Askins, Naval Research Lab
"Structurally Embedded Multi-Axis Fiber Optic Sensors"

4:20 p.m. *Mahmoud A. El-Sherif and Jianming Yuan, Drexel University*
"Fiber Optic Sensors and Smart Fabrics -- An Overview on the ARO MURI Project: Functionally Tailored Fibers and Fabrics"

4:40 p.m. *Dryver R. Huston, University of Vermont*
"Electromagnetic Interrogation of Structures"

5:00 p.m. *Grant Bourhill, Ian Sage, Rodney Badcock, Lisa Humberstone, Norman Geddes,*
Martin Kemp and Sharon Bishop, Defence Evaluation and Research Agency
"Real-Time Damage Sensors Based on Triboluminescence"

5:20 p.m. *Peng Thian Teo, Vinoy, K.A.Jose, V.K.Varadan, The Penn State University*
Yeow B Gan, DSO National Laboratory, Singapore
"Design of Multi-Layer Smart Ferroelectric Antenna"

5:40 p.m. **ADJOURN**

6:00 –8:00 p.m. **RECEPTION AND POSTER SESSION (Penn State Room and Patio -
will move to Boardroom I & II if weather is not good)**

Poster Session

Mark J. Schulz, Anindya Ghoshal, and Mannur Sundaresan, North Carolina A&T State University

P.F. Pai, University of Missouri-Columbia

Ed Smith, The Pennsylvania State University

"Health Monitoring of Helicopter Rotor Systems"

Mehdi Ahmadian and James C. Poynor, Virginia Polytechnic Institute and State University

"Application of Magneto-Rheological Dampers for Controlling Gun Recoil"

Burhanettin Koc and Kenji Uchino, The Pennsylvania State University

Philippe Bouchilloux, Rensselaer Polytechnic Institute

"Piezoelectric Miniature Motor Using a Radial-Torsional Stator Vibrator"

Farhan Gandhi, The Pennsylvania State University

"On Constrained Layer Damping Treatments – Influence of Nonlinear Viscoelastic Material Characterization"

Xiaojie Wang and Faramarz Gordaninejad, University of Nevada

"Herscel-Bulkley Analysis of Controllable Fluid Dampers in Flow Mode"

Yun-Han Chen and Kenji Uchino, The Pennsylvania State University

Senji Hirose, Yamagata University

Dwight Viehland, Naval Undersea Warfare Center

" $\text{Pb}(\text{Mg}_{1/3}\text{Nb}_{2/3})\text{O}_3$ - PbTiO_3 Ceramics for High Power Transduction Applications"

Ronald Morgan and K.W. Wang, The Pennsylvania State University

"Active Tuning and Coupling Enhancement of Piezoelectric Vibration Absorbers for Variable Frequency Harmonic Excitations in MDOF Mechanical Systems"

Askari Badre-Alam, K.W. Wang, and F. Gandhi, The Pennsylvania State University

"Optimization of Enhanced Active Constrained Layer (EACL) Treatment on Helicopter Flexbeams for Aeromechanical Stability Augmentation"

A. Hood and D.J. Pines, University of Maryland
"Modeling and Testing of a Multifunctional Sensor"

Yanning Liu and K. W. Wang, The Pennsylvania State University
"Surface Damping Treatment with an Active-Passive Hybrid Constraining Layer"

Paul D. Samuel and D. J. Pines, University of Maryland
"Helicopter Transmission Diagnostics"

Jason S. Kiddy and D. J. Pines, University of Maryland
"A Modal-Based Damage Detection Technique for Helicopter Rotor Blades"

George Lesieutre, Gary Koopmann, Jeremy Frank, and Weiching Chen, The Pennsylvania State University
"High Force Piezoelectric Linear Stepping Motors"

E. Luft and B. Balachandran, University of Maryland
"Interior Noise Control Using Smart Materials"

Ramkumar Krishnan, Vijay Madhavan, and Norman Wereley, University of Maryland
"Thermomechanical Modeling of Elastomeric Lag Dampers"

Rebecca Snyder, Gopalakrishna M. Kamath, and Norman Wereley, University of Maryland
"Dynamic Characterization and Analysis of Magnetorheological Damper Behavior"

John Rodgers, Mide
"Active System Solutions"

August 17, 1999 (Tuesday)

7:00 a.m. - 5:00 p.m. Registration (Atrium Outside of Ballroom)

7:00 - 8:00 a.m. Continental Breakfast (Atrium Outside of Ballroom)

Session 5: Helicopter Applications
Session Chair: Yung Yu, NRTC

8:00 a.m. *Nikhil Koratkar and Inderjit Chopra, University of Maryland*
"Hover Testing of a Mach Scaled Rotor with Trailing Edge Flaps"

8:20 a.m. *Greg P. Carman, UCLA*
"Meso-Scale Actuator Devices for Rotorcraft"

- 8:40 a.m. *A. Purekar and D. J. Pines, University of Maryland*
 “A Direct Field Approximation to Infer Damage in Tapered Rotorcraft Flexbeams”
- 9:00 a.m. *Andreas P.F. Bernhard and Inderjit Chopra, University of Maryland*
 “Mach Scale Design of a Helicopter Rotor with Active Blade Tips”
- 9:20 a.m. *Michael G. Spencer, Robert M. Sanner, and Inderjit Chopra, University of Maryland*
 “Active Rotorcraft Vibration Reduction with Real Time Neural Network Controller”
- 9:40 a.m. *Douglas B. Weems and Robert C. Derham, Boeing*
Nesbitt Hagood, MIT
John Rodgers, Mide
 “Structural Modeling of a Rotor Blade Incorporating Active Fiber Composites”

10:00 – 10:20 a.m. **BREAK**

Session 6: Semi-Active Devices

Session Chair: Arthur R. Johnson, Army Research Laboratory NASA Langley

- 10:20 a.m. *Faramarz Gordaninejad and Shawn P. Kelso, University of Nevada*
 “Magneto-Rheological Fluid Shock Absorbers for Off-Highway, High-Payload, Ground Vehicles”
- 10:40 a.m. *Jason E. Lindler and Norman M. Wereley, University of Maryland*
 “Design and Fabrication of an Electrorheological Fluid Automotive Shock Absorber”
- 11:00 a.m. *William W. Clark, University of Pittsburgh*
 “Semi-Active Structural Control”
- 11:20 a.m. *George A. Lesieutre, The Pennsylvania State University*
 “Effective Loss Factors for Switch-Shunted Piezo Materials”
- 11:40 a.m. *Kenneth Cunefare, Nader Sadegh, and Gregg Larson, The Georgia Institute of Technology*
Sergio DeRosa, University of Naples
 “State-Switched Absorber/Damper for Semi-Active Structural Control”

12:00 – 1:00 p.m. **LUNCH (Ballroom AB)**

Session 7: SMA Research
Session Chair: Robert Ormiston, US Army AVRDEC

- 1:00 p.m. *Harsha Prahlad, Inderjit Chopra, and Monica Vohba, University of Maryland*
"Experimental Characterization and Modeling of Ni-Ti Shape Memory Alloy (SMA) Wires"
- 1:20 p.m. *Hugh A. Bruck and Charles L. Moore, University of Maryland*
"Mechanical Characterization of Shape Memory Alloy Composites for Designing Smart Structures"
- 1:40 p.m. *Farhan Gandhi, David Wolons, Brendon Malovrh, and Gautier Chapuis, The Pennsylvania State University*
"Use of Shape Memory Alloy Pseudoelastic Hysteresis for Augmentation of Passive Structural Damping"
- 2:00 p.m. *John A. Shaw, The University of Michigan*
"Thermo-Mechanical Instabilities in Shape Memory Alloys"
- 2:20 p.m. *Travis L. Turner, NASA Langley Research Center*
"Environmentally Activated SMA Hybrid Composites"
- 2:40 p.m. *Jeanette J. Epps and Inderjit Chopra, University of Maryland*
"In-Flight Tracking of Helicopter Rotor Blades Using Shape Memory Alloy Actuators"
- 3:00 p.m. *D.C. Lagoudas, D.A. Miller and L. Rong, Texas A&M University*
"Experiments on the Thermomechanical Fatigue of SMAs"
- 3:20 – 3:40 p.m. **BREAK**

Session 8: Modeling and Characterization Issues
Session Chair: Eric L. Kathe, US Army TACOM- ARDEC Benet Labs

- 3:40 p.m. *Senthil S. Vel and R. C. Batra, Virginia Polytechnic Institute and State University*
"Analytical Solutions for the Cylindrical Bending of Smart Structures: Statics and Vibration"
- 4:00 p.m. *C. T. Sun, Purdue University*
"Fracture and Fatigue of Piezoceramics Under Electrical and Mechanical Loading"
- 4:20 p.m. *M. W. Hyer and A. B. Jilani, Virginia Polytechnic Institute and State University*
"Prediction of the As-Manufactured Shapes of Rectangular and Circular Piezoceramic Benders"

- 4:40 p.m. *Christopher Lynch, The Georgia Institute of Technology*
"Measurement of the Constitutive and Fracture Behavior of PZT"
- 5:00 p.m. *Ken Ho, John Gill, Jenna Favelukis, Peter Jardine, and Greg P. Carman, UCLA*
"Thin Film NiTi Shape Memory Actuators"
- 5:20 p.m. *J. Chroscielewski, Politechnika Gdanska*
R. Schmidt, Institute of General Mechanics, RWTH Aachen
"Nonlinear Static and Transient Response of Smart Beams and Shells with Piezoelectric Layers"
- 5:40 p.m. **ADJOURN**
- 6:30 - 7:00 p.m. **CASH BAR AND SOCIAL HOUR (Atrium Outside of Ballroom)**
- 7:00 - 9:00 p.m. **DINNER (Ballroom AB)**
Banquet Speaker: Robert E. Newnham, The Penn State University
"Ferroic Engineering in Ferroic Valley"

August 18, 1999 (Wednesday)

- 7:00 a.m. - 5:00 p.m. Registration (Atrium Outside of Ballroom)
- 7:00 - 8:00 a.m. Continental Breakfast (Atrium Outside of Ballroom)
- Session 9: Damping Treatments I**
Session Chair: Mike Mattice, US Army ARDEC
- 8:00 a.m. *S. Poh and A. Baz, University of Maryland*
"Impedance Matching Control of Active Constrained Layer Damping"
- 8:20 a.m. *V. Steffen, Jr. and D. J. Inman, Virginia Polytechnic Institute and State University*
"Using Piezoelectric Materials for Vibration Damping in Mechanical Systems"
- 8:40 a.m. *J. Tang and K. W. Wang, The Pennsylvania State University*
"High Authority and Nonlinearity Issues in Active-Passive Hybrid Piezoelectric Networks for Structural Damping"
- 9:00 a.m. *B. Bhattacharya and Geof Tomlinson, University of Sheffield*
"Active Magnetostrictive Free Layer Damping"
- 9:20 a.m. *Arthur R. Johnson, Army Research Lab at NASA Langley Research Center*
"Modeling Issues for Cyclic and Step-Strain Relaxation Deformations of Elastomers"

9:40 – 10:00 a.m. **BREAK**

Session 10: **Transducer Issues: Materials, Device Design and Power**
Session Chair: **Dino Sciulli, Air Force Research Lab**

- 10:00 a.m. *Alison Flatau, Marcelo Dapino, Iowa State University*
 F. Tad Calkins, Boeing
 "An Overview of Magnetostrictive Device Design & Performance"
- 10:20 a.m. *Jayant Sirohi and Inderjit Chopra, University of Maryland*
 "Actuator Power Reduction Using a Tuned L-C Oscillator Circuit"
- 10:40 a.m. *Douglas K. Lindner, Sriram Chandrasarkaren, and Jeffrey Scruggs, Virginia Polytechnic Institute and State University*
 "Controlling Power Flow Through Electronically Integrated Smart Devices"
- 11:00 a.m. *Donald J. Leo, Virginia Polytechnic Institute and State University*
 "Renewable Fuel Cell Power Sources for Active Structures"
- 11:20 a.m. *Reza Kashani and Kevin Hallinan, The University of Dayton*
 "Micro-Scale Electrohydrodynamic Pumped High Performance Actuation"
- 11:40 a.m. *Kenji Uchino, The Pennsylvania State University*
 "Overview of Penn State MURI on Acoustic Transduction: Materials & Devices"

12:00 – 1:00 p.m. **LUNCH (Ballroom AB)**

Session 11: **Damping Treatments II**
Session Chair: **Donald Merkley, US Army USAAMCOM**

- 1:00 p.m. *Jessica M. Yellin, I. Y. Shen, Per G. Reinhall, and Peter Y. H. Huang, University of Washington*
 "An Analytical and Experimental Analysis for a One-Dimensional Passive Stand-Off Layer Damping Treatment"
- 1:20 p.m. *Gang Wang and Norman M. Wereley, University of Maryland*
 "Spectral Element Method for Sandwich Beam with Passively Constrained Viscoelastic Damping Layers"
- 1:40 p.m. *Peter Y. H. Huang, Per G. Reinhall, I. Y. Shen, and Jessica M. Yellin, University of Washington*
 "Thickness Deformation of Constrained Layer Damping: An Experimental Evaluation"
- 2:00 p.m. *V. K. Kinra and R. D. Friend, Texas A&M University*
 "Particle Impact Damping"

2:20 –2:40 p.m. **BREAK**

Session 12: Active Vibration and Noise Control

Session Chair: Richard J. Silcox, NASA Langley Research Center

- 2:40 p.m. *Gary P. Gibbs, NASA Langley Research Center*
Kenneth W. Eure, Naval Surface Warfare Center
John W. Lloyd, Virginia Polytechnic Institute and State University
“Active Control of Turbulent Boundary Layer Induced Sound Radiation from Aircraft Style Panels”
- 3:00 p.m. *W. C. Huang, Aircraft Structure Research Institute*
G. H. Koopmann, W. C. Chen, and Steve Sharp, The Pennsylvania State University
“Enhanced Low Frequency Transmission Loss of Light Weight Trim Panels Using PZT Inertial Actuators”
- 3:20 p.m. *I. Pelinescu, B. Balachandran, and D. Ortel, University of Maryland*
“Active Control of Wave Transmission Through Struts”
- 3:40 p.m. *Uwe Stöbener and Lothar Gaul, University of Stuttgart*
“Modal Vibration Control for PVDF Coated Plates”
- 4:00 p.m. *E.A. Wheeler, A. Ghoshal, C. R. Ashok Kumar, M. J. Sundaresan, M. J. Schultz, and M. Human, North Carolina A&T State University*
P. Frank Pai, University of Missouri-Columbia
“Vibration Suppression Using a Laser Vibrometer and Piezoceramic Patches”
- 4:20 p.m. *S. Hanagud, M. Bayon de Noyer, H. Luo, The Georgia Institute of Technology*
D. Henderson, Air Force Research Lab
K. S. Nagaraja, Rohini International
" Buffet Alleviation: An Adaptive Structures Approach"

Closing Remarks

- 4:40 p.m. *Gary Anderson, US Army Research Office*
K. W. Wang, The Pennsylvania State University

ADJOURN

Welcome to Penn State



PENNSTATE



Conferences & Institutes

General Information

Conferences and Institutes
The Pennsylvania State University
The Penn Stater Conference
Center Hotel
University Park, PA 16802-7002
Phone: (814) 863-5100
Hours: 8:00 a.m.—5:00 p.m.
weekdays

and

Conferences and Institutes
The Pennsylvania State University
118 Keller Building
University Park, PA 16802-1300
Phone: (814) 863-1738
Hours: 8:00 a.m.—5:00 p.m.
weekdays

Facts and Figures

HISTORY

Penn State was founded in 1855 as the Farmer's High School and became Pennsylvania's land-grant college following the passage of the Morrill Act in 1862.

PROGRAMS

Penn State provides opportunities for resident and continuing education. It offers more than 180 baccalaureate, 150 graduate, and 25 associate degree majors through eleven academic units: the Colleges of Agricultural Sciences, Arts and Architecture, Communications, Earth and Mineral Sciences, Education, Engineering, Health and Human Development, and the Liberal Arts; the Eberly College of Science; The Mary Jean and Frank P. Smeal College of Business Administration; and The Graduate School. Twelve Commonwealth College campuses serve the educational needs of Pennsylvania communities. These Colleges provide access to associate degrees, the first two years of baccalaureate study in most curriculums, and baccalaureate degrees in several fields.

Penn State has several special mission campuses: The Pennsylvania College of Technology in Williamsport, The College of Medicine at The Milton S. Hershey Medical Center in Hershey, and The Dickinson School of Law in Carlisle.

ENROLLMENT

Penn State has an enrollment of approximately 80,000, with more than half of those at University Park and the remainder at all other locations.

OPERATIONS

The major source of Penn State's \$1.4 billion total operating budget comes from tuition and fees paid by students, 34.2 percent. Other sources include restricted funds, which include grants and contracts, 23 percent, state appropriations, 20.5 percent, auxiliary enterprises, 12 percent, and 10.3 percent from other sources.

Control of the University is governed by a thirty-two member Board of Trustees.

FACILITIES

The University owns more than 18,000 acres of land throughout Pennsylvania. This includes campuses, recreation areas, farms, agricultural experiment grounds, and forest tracts used for research.

The University Park campus is located near the geographic center of the state. At University Park there are over 400 buildings used for classrooms, offices, laboratories, and residence halls. There are 325 principal buildings located on Penn State's other campuses.

DEGREES

More than 12,000 degrees are granted each year, in addition to associate degrees and medical degrees.

ALUMNI ASSOCIATION

- There are 400,000 living alumni.
- The Alumni Association has 142,000 members, and is the largest in the nation.
- One in every 60 Pennsylvanian's is a Penn State alumnus/a.
- One in every 775 Americans is a Penn State alumnus/a.
- One in every 125 Americans with a college degree is a Penn State graduate.

For information call
1-800-548-5466

Telephone

ON CAMPUS

When calling University numbers from University phones, dial only the last five digits, not the "86." When calling off-campus local numbers from a University telephone, dial "8" plus the listed number. To reach an "800" number, dial 8-1-800-number. For information on University telephone numbers, dial 865-4700. Telephone and student directory information is also available at the registration desk.

RESIDENCE HALL DESKS

East Halls

Findlay 865-0465

North Halls

Warnock 865-9522

Pollock Halls

Pollock 865-8692

South Halls

Redifer 865-5263

MAILING ADDRESS

On campus—University Park
PA 16802

In town—State College PA
16801

EMERGENCY INFORMATION

Police

University Safety, Police Services
863-1111 or 911

State College Borough Police

234-7150 or 911

State Police—Rockview
355-7545

Fire or Accident
863-1111 or 911

MEDICAL SERVICE

University Health Services

For registered conference participants attending meetings on campus, medical attention for acute illness or injury is available through the **University Health Services**. The center is located on campus at the intersection of Pollock and Shortlidge roads.

Urgent Care for illness or injury will be provided by professional staff on a fee-for-services basis. If follow-up care is necessary, patients will be referred to the medical provider of their choice. Payment must be made at the time of service. Hours are Monday, Tuesday, Thursday, and Friday, 8:00 a.m.—5:00 p.m., and Wednesday from 9:00 a.m.—5:00 p.m. Phone: 865-6556

AMBULANCE SERVICE

University Health Services

operates its own ambulance on campus for emergency transportation. Call 911.

Other ambulance service is provided by the **Alpha Fire Company** by calling 237-8163 or 911.

Centre Community Hospital handles serious medical or surgical emergencies, 231-7000.



Transportation

AIRLINES

State College Airport
US Airways Express

237-1774
(800) 428-4322

United Express

237-1714
(800) 241-6522

Northwest Airlin

(800) 225-2525

AIRPORT TRANSPORTATION

Taxi by Handy Delivery
353-6001

Fullington Airport Limo

237-4211

LOCAL BUS SERVICE

Centre Area Transportation
Authority (CATA)

Consult conference receptionist
for schedule.

BUS TERMINAL

Greyhound

238-7971

Fullington Trailways

238-1100

RAILWAY SCHEDULES

AMTRACK

Consult the yellow pages under
railroads for ticket agents.

Shopping

ON CAMPUS

Penn State Bookstore,
863-0205

Adjacent to Hetzel Union Building
(HUB)

8:00 a.m.—8:00 p.m. Mon-Thu

8:00 a.m.—5:00 p.m. Fri

9:00 a.m.—5:00 p.m. Sat

noon—4:00 p.m. Sun

Penn State Shop, East Halls,
5-9411

7:00 a.m.—8:00 p.m. Mon-Thurs

9:00 a.m.—7:00 p.m. Friday

11:00 a.m.—4:00 p.m. Sat & Sun

Penn State Shop,

The Nittany Lion Inn,
863-8474

7:00 a.m.—8:00 p.m. M-Sat

7:00 a.m.—6:00 p.m. Sun

Penn State Shop, Penn Stater

Conference Center Hotel, Lobby,
863-8436

8:00 a.m.—7:00 p.m. M-F

9:00 a.m.—4:00 p.m. Sat & Sun

OFF CAMPUS

Generally, downtown stores are
open weekdays from 10:00 a.m.
to 5:30 p.m. and Thursday
evenings until 8:00 p.m. Weekend
hours are Saturday from 10:00
a.m. to 5:30 p.m. and Sunday
from noon to 4:00 p.m.

Lodging

THE NITTANY LION INN

(237 guest rooms)

1-800-233-7505

On Campus

THE PENN STATER

CONFERENCE CENTER HOTEL

(150 guest rooms)

1-800-233-7505

Penn State Research Park

Food

In addition to numerous
restaurants in and near State
College, the following facilities on
campus offer food.

CREAMERY ICE CREAM

865-7535

7:00 a.m.—10:00 p.m. M-Thu

7:00 a.m.—11:00 p.m. Fri

8:00 a.m.—11:00 p.m. Sat

9:00 a.m.—10:00 p.m. Sun

HETZEL UNION BUILDING

865-7623

The Bean Machine

7:30 a.m.—2:00 p.m. M-F

The Cellar

11:00 a.m.—10:00 p.m. M-Thu

11:00 a.m.—7:30 p.m. Fri, Sat, Sun

Coaly's Cafe

11:00 a.m.—2:00 p.m. M-F

Chat's

7:30 a.m.—2:00 a.m. M-F

7:00 p.m.—2:00 a.m. Sat, Sun

Union Street Burger Company

7:30 a.m.—3:00 p.m. M-F

Food Court

Piccalilli's

11:00 a.m.—6:30 p.m. M-Thu

11:00 a.m.—5:00 p.m. Fri

Casa Ortega

11:00 a.m.—3:00 p.m. M-F

Chik-fil-A

10:00 a.m.—6:30 p.m. M-F

KERN GRADUATE BUILDING

Otto's 865-6886

7:00 a.m.—6:30 p.m. weekdays

MATEER BUILDING

Cafe Laura 865-1851

8:30 a.m.—11:00 a.m. Cafecart

11:30 a.m.—1:30 p.m. weekdays

THE NITTANY LION INN

865-8500

The Dining Room

Breakfast, 6:45—11:00 a.m.

Lunch, 11:30 a.m.—2:00 p.m.

Dinner, 5:30—9:00 p.m.

Whisker Lounge

Monday—Saturday,

11:30 a.m.—1:00 a.m.

Sunday, 11:30 a.m.—11:00 p.m.

THE PENN STATER

CONFERENCE HOTEL

The Gardens Restaurant

863-5090

Breakfast, 7:00—9:00 a.m.

Lunch, 11:30 a.m.—2:00 p.m.

Dinner, 5:30 p.m.—9:00 p.m.

Sunday Brunch, 10:00—2:00 p.m.

Legends Lounge

11:30 a.m.—11:30 p.m.

seven days a week

Services

AREA INFORMATION

Centre County Convention

and Visitors Bureau

1-800-358-5466

Chamber of Business and
Industry of Centre County

237-7644

BANKING

Banking is available on campus at
the Penn State Credit Union
located in the Penn State
Bookstore. Automatic teller
machines (ATMs) linked to
national systems are located near
the bookstore.

CHURCH/SYNAGOGUE

SERVICES

Information for services on
campus is available at Eisenhower
Chapel, 865-6548. For State
College services, consult phone
book yellow pages.

CLUBS

Consult receptionist about service
and private clubs.

Recreation

ON CAMPUS

Special rates are available for
conference participants.

Golf

Two eighteen-hole University golf
courses are located west of the
main campus. Call 865-4653 or
865-1833 for green fees,
equipment rental rates, and other
information.

Handball/Racquetball and

Squash

Handball/racquetball and squash
courts are available in the
Recreation and Intramural
buildings. Courts are available to
conference participants whenever
University classes are not using
them. Players must supply their
own equipment.

Ice Skating

Two indoor, climate-controlled
ice-skating rinks are open year-
round at Greensburg Sports
Complex. Call 865-4102 for
equipment rental rates and public
skating hours.

Swimming

The Natatorium has three indoor pools and an Olympic-size outdoor pool. It is located at the center of Bigler and Curtain roads.

White Building also has public swimming; information is available through the Natatorium. Recreation swim times and fees are announced at the beginning of each semester (fees include towel and locker). Consult the receptionist, or call 865-1432.

Tennis

See campus map for court locations. There is no charge for the use of outdoor courts located across campus. Four indoor courts at the Penn State Tennis Center are available for an hourly charge and may be reserved by calling 865-1381.

Earth and Mineral Sciences Museum

865-6427

The College of Earth and Mineral Sciences maintains an outstanding collection of minerals and related items in the Steidle Building. Exhibits demonstrate magnetic, optical, luminescent, and other properties of minerals, and a collection of paintings depicts the mineral industries. Open 9:30 a.m.–5:00 p.m., weekdays, admission is free.

Matson Museum of Anthropology

865-3853

The Matson Museum of Anthropology in the Carpenter Building maintains a collection that illustrates the range of human cultural and biological diversity. It is a center for displaying often irreplaceable specimens while augmenting departmental teaching and research programs. The displayed materials represents only a fraction of museum's holdings. Open to the public when the University is in session: 9:00 a.m.–4:00 p.m. M-F 10:00 a.m.–1:00 p.m. Sat Call for special group tours.

Palmer Museum of Art

865-7672

Dedicated to the appreciation of the visual arts, the Palmer Museum of Art is a place of discovery, learning, and contemplation. As the major art museum between Philadelphia and Pittsburgh, the museum features works from its permanent collection as well as traveling exhibitions. The Museum Store has treasures from around the world. Hours are 10:00 a.m.–4:30 p.m. Tues-Sat Noon–4:00 p.m. Sun

The Bryce Jordan Center

863-5500

The Bryce Jordan Center, located on Penn State's University Park campus, is the only entertainment facility of its size in the region. The 16,000-seat Jordan Center hosts circuses, ice show, sports exhibitions, family shows, commencements, lectures, and Big Ten Basketball, as well as some of the top-name performers in the music entertainment industry.

The Center for the Performing Arts

The Center for the Performing Arts is dedicated to bringing the highest quality professional theatre, dance, and music events to central Pennsylvania. Talented artists and companies travel from around the world to perform throughout the fall, winter, and spring seasons. Current program and ticket information may be obtained by calling 863-0255, 8:30 a.m.–4:30 p.m., weekdays.

Music at Penn's Woods

Musicians from around the world join the Penn State School of Music faculty during June, and July in outstanding performances of the classics of orchestral and chamber music. For program information and tickets, call 863-0255 or 863-1118.

Pennsylvania Centre Stage
Pennsylvania Centre Stage brings professional directors, actors,

designers, and technicians to Penn State from mid-June to early August to produce entertaining musicals, drama, and comedy. For information and tickets, call 863-0255, 8:30 a.m.–4:30 p.m., weekdays.

University Resident Theatre Company

Students and faculty from Penn State's Department of Theatre Arts, as well as visiting guest artists, produce four or five plays and musicals during the academic year. Costumes, lighting, set design and casting are developed on campus. For information and tickets, call 863-0255, 8:30 a.m.–4:30 p.m., weekdays.

OFF CAMPUS

Centre Region Parks and Recreation Office

For information about community recreation programs or other available recreation activities, call 231-3071.

Fishing and Hunting

Centre County and surrounding areas feature some of the best fishing waters and hunting terrain in the Commonwealth. Pennsylvania licenses are required.

Golf

Two off-campus, public golf courses are within ten miles of University Park.

Toftrees Hotel Resort and Conference Center, 238-7600

Tussey Mountain Par Three Golf Course, 466-6810

Skiing

Tussey Mountain, located off Route 322 in Boalsburg, is open daily during the ski season. Call 466-6810 for hours and rates.

State Parks

Whipple Dam

Swimming and picnic area located on U.S. Route 26 about twelve miles from State College.

Greenwood Furnace State Park

Swimming, picnic area, and camping sites located on Route 305 about eighteen miles from State College.

Black Moshannon State Park

Swimming, picnic area, fishing, and camping sites located in Route 504 about twenty miles from State College.

Stone Valley Recreation Area

863-0762

Penn State operates the Stone Valley Recreation Area, which includes Shaver's Creek Environmental Center (description follows), a seventy-two acre lake, ten rental cabins, a picnic area and pavilion, fishing, and boat rental facilities. Stone Valley is located about fourteen miles from campus via U.S. Route 26. A parking fee is charged.

Shaver's Creek Environmental Center

863-2000

Shaver's Creek Environmental Center, operated by Penn State, provides environmental education programs for all ages, including training for future and current environmental educators and school-day, residential, team-building, and other public programs. Shaver's Creek also has a Raptor Center for in-depth learning about owls, eagles, hawks, and falcons.

For more information, visit:

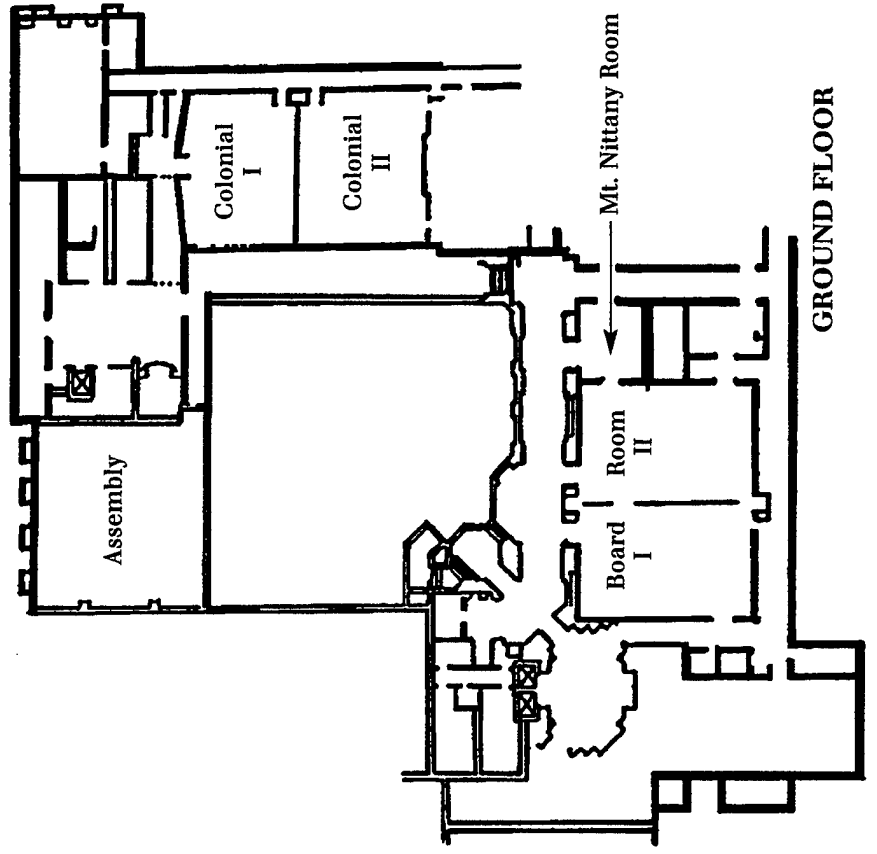
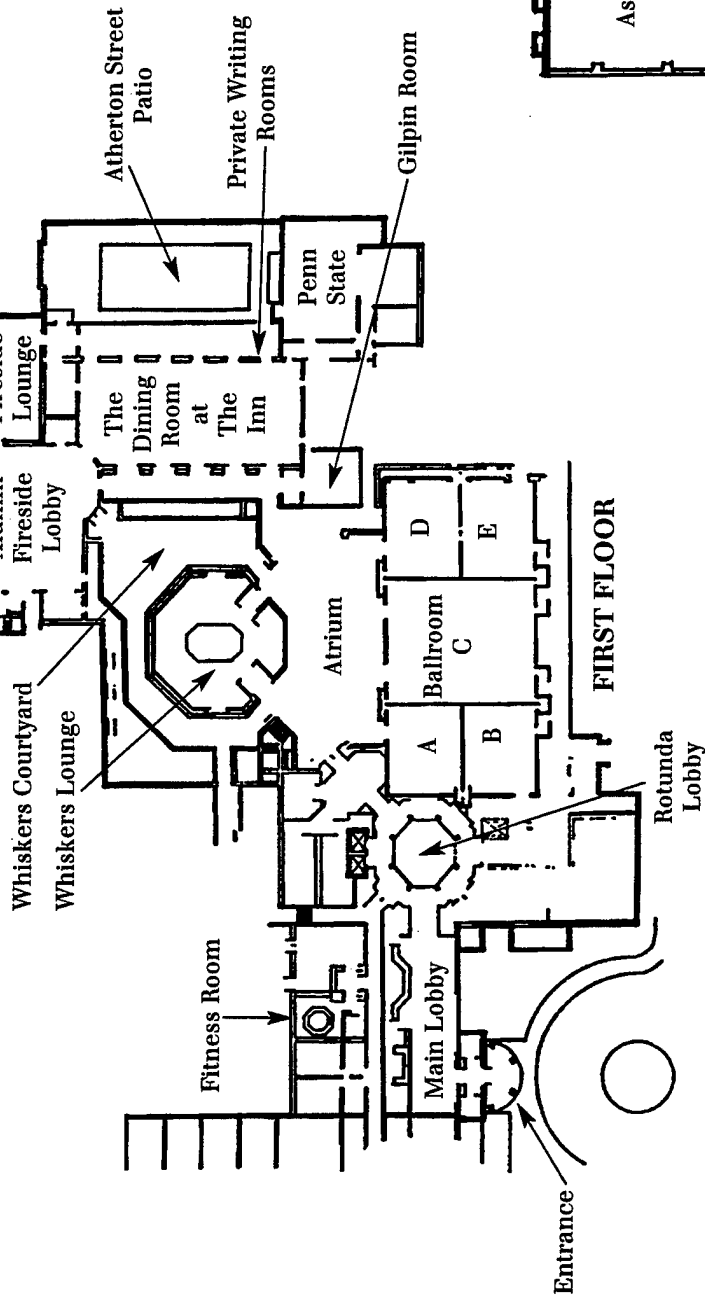
<http://www.cde.psu.edu/>

This publication is available in alternative media on request.

Penn State is committed to affirmative action, equal opportunity, and the diversity of its workforce.

DS23401as 2/7/99

Produced by Outreach Marketing Communications



CONFERENCE ROOM LAYOUT

THE
NITTANY LION
INN
PENNSTATE





GENERAL INFORMATION

Welcome to Penn State and the ARO Workshop on Smart Structures

MEETING ROOMS: Meeting room locations are listed on your conference program.

PARKING: Complimentary parking is available at The Nittany Lion Inn. If you need to park in the parking garage that is adjacent to the NLI, the front desk staff will provide you with a ticket or validate the parking garage ticket.

MESSAGES: The NLI staff will interrupt meeting sessions **ONLY** for emergencies, not for business calls. Messages will be posted on the ARO Message Board located outside of the ballroom.

IMPORTANT TELEPHONE NUMBERS: You may wish to advise your family and associates of the following numbers and the name of the program that you attending:

Nittany Lion Inn	(814) 865-8500	(Front Desk)
Police Services	(814) 863-1111	(24 hours a day)

PERSONAL BELONGINGS: Meeting rooms will be refreshed during breaks and lunches, so we ask that you keep your personal belongings with you at all times. Penn State and/or NLI are not responsible for lost items.

BREAK SERVICES: Break service will be served in the morning and afternoon outside of the ballroom.

RESTROOMS & TELEPHONES: They are located on each floor of the Nittany Lion Inn.

Enjoy your visit at Penn State!

Smart Materials and Structures for Rotor Dynamics Applications

**Robert A. Ormiston
Chief Scientist, Aeromechanics Branch**

**Army/NASA Rotorcraft Division
NASA Ames Research Center
and
Aeroflightdynamics Directorate
US Army Aviation RD&E Center (AMCOM)
Moffett Field, California**

**Fourth ARO Workshop on Smart Structures
The Pennsylvania State University, State College, PA
August 16-18, 1999**

Outline

- **Overview**
- **AFDD Experimental Research**
- **AFDD SBIR Projects**
- **AFDD/NASA Ames Projects**
- **ARL VTC/NASA Langley ATR**
- **Concluding Remarks**

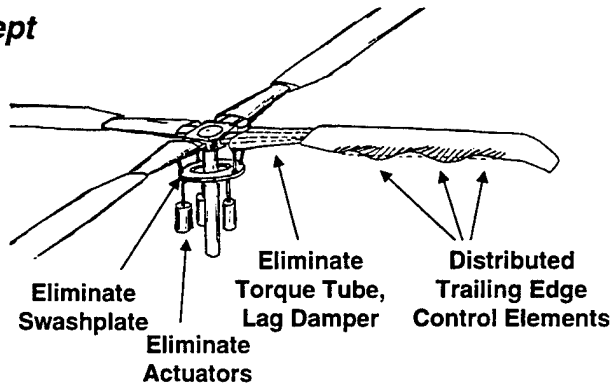
Revolutionary Potential for Smart Structure Active Rotor Technology

Develop on-blade active control to improve...



Blade Vibratory Loads
Vehicle Vibration
Blade-Vortex-Interaction Noise
Aero Performance
Flight Control

Notional Concept

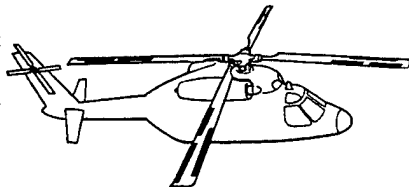


Payoff for Mission Range Performance System Upgrade - UH-60 Baseline

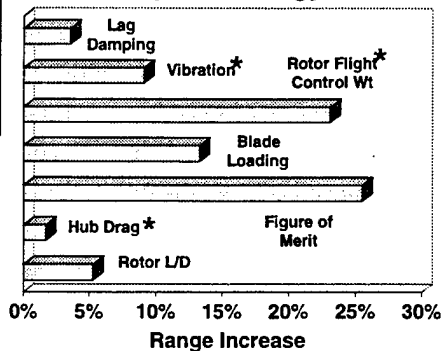
Advanced Rotor & Controls Technology

Total Range Increase (baseline payload)

Rotor Technologies + On-Blade Flight Control (Swashplateless Rotor)	85%
Rotor Technologies Alone	63%



Range Increase Breakdown by Technology



* Based primarily on smart materials & structures

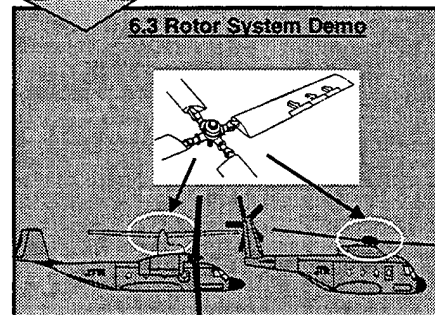
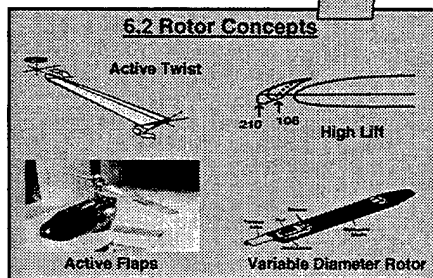
Variable Geometry Advanced Rotor Technology (VGART)

Objective

Develop the technology to understand how to APPLY and TRANSITION advanced concepts such as Active Flaps, Variable Diameter Rotor, High Lift, and Active Twist to the JTR Rotor System Demo FY02-05

• Army
• DARPA
• Industry
• DUS&T

Affordable
Reliable
Scalable



Rotor Technology Impact is 25% of JTR / AAN Technology

Spectrum of Rotor Smart Material and Structure Applications

Application

Approach

Pros and Cons

• Blade Tracking
1/Rev Vibration

• Smart Tab

Slow response materials suffice

• Blade Vibratory Loads
• Vehicle Vibration
• Blade Vortex Interaction
Noise

• Blade Root HHC/IBC

Proven effective
Mechanical complexity, high power

• Active Twist Rotor
(Active Fiber Composite)

Structurally integral, low aero drag
Limited spanwise control modes
High voltage, material integrity

• Flight Control
(Swasplateless Rotor)

• On-Blade Elevon

Multiple elevons-spanwise control modes
Low voltage
Mechanical complexity, aero drag

• Integral Elevon

Simplicity
Limited concepts available

• Aeromechanical
Stability

• Smart Damping

Simplicity
Effectiveness, practicality

• Aeroperformance

• Variable Twist (Tilt Rotor)

Significant performance benefit
Slow response materials suffice
Mechanical complexity

• Variable Geometry Airfoils
Deformable Leading Edge
Oscillatory Blowing/Virtual Jets
Modulated LE Slot
BLC

High payoff
Basic concepts unproven
Mechanical complexity
Multiple implementation issues

Smart Structure Active Rotor Technology Involves Broad Scope of Disciplines

- **Aeroelasticity/Structural Dynamics**
Control effectiveness, dynamic response
Optimization - mode shapes, control surface placement, stability
- **Actuation/Actuators**
Smart material force capability, stroke, frequency, weight, power, volume
- **Structural Design**
Discrete/integral control surfaces, integral twist, structural integrity
- **Controllers /Sensors**
Algorithms, transient response, maneuvers, robustness, flight control integration
- **Safety/Reliability/Maintainability/Cost**

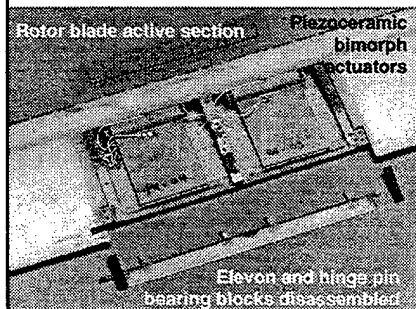
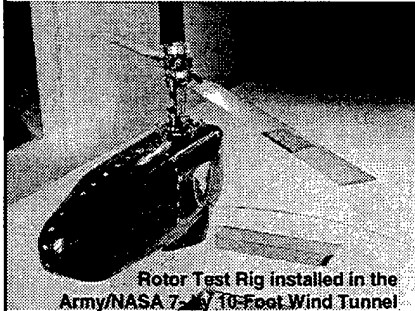
AFDD Small-Scale Model Rotor Experiments

- **Exploratory feasibility investigations of 7.5-ft rotor with on-blade elevons and smart structure actuators to reduce rotor blade vibratory loads in forward flight**
 - 1996-97 - Hover Testing
 - 1998 - Forward Flight Testing , 7-by 10-ft AFDD/Ames Wind Tunnel
- **Actuator achieved design goal of $\pm 5^\circ$ at 760 RPM**
- **Demonstrated significant vibratory flap moment reduction**
- **Illuminated strong influence of structural dynamics on elevon effectiveness**

Related Publications

1. Fulton, M.V., and Ormiston, R.A., "Hover Testing of a Small-Scale Rotor with On-Blade Elevons," *Proceedings of the 53rd Annual Forum of the American Helicopter Society*, Virginia Beach, Virginia, April 29-May 1, 1997.
2. Fulton, M.V., and Ormiston, R.A., "Small-Scale Rotor Experiments with On-Blade Elevons to Reduce Blade Vibratory Loads in Forward Flight," *Proceedings of the 54th Annual Forum of the American Helicopter Society*, Washington, DC, May 20-22, 1998.
3. Ormiston, Robert A. and Fulton, Mark V., "Aeroelastic and Dynamic Rotor Response with On-Blade Elevon Control," *Proceedings of the 24th European Rotorcraft Forum*, Marseilles, France, September 15-17, 1998.

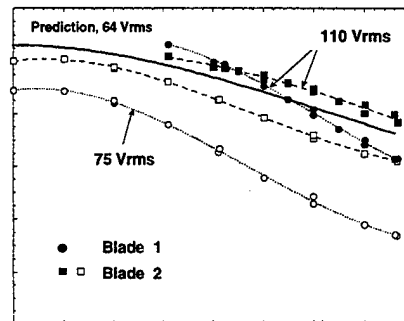
AFDD Small-Scale Model Rotor Experiments



Two-Blade Hingeless Rotor

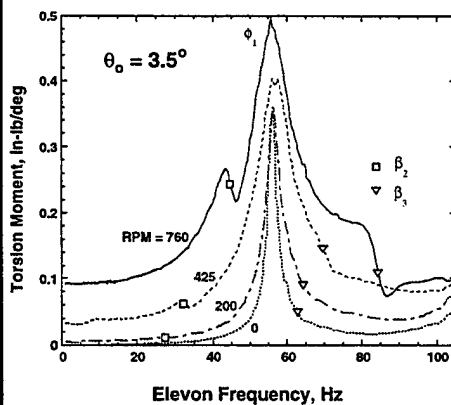
Diameter	7.5 ft
Blade chord	3.4 in
Elevon Chord	0.34 in, 10% c
Elevon span	5.5 in, 12% R
Elevon radial location	75% R
Tip speed (760 RPM)	298 ft/sec
Tip Reynolds No.	5.4×10^5
Airfoil section	NACA 0012

Elevon Deflection $> \pm 5^\circ$ @ 760 RPM

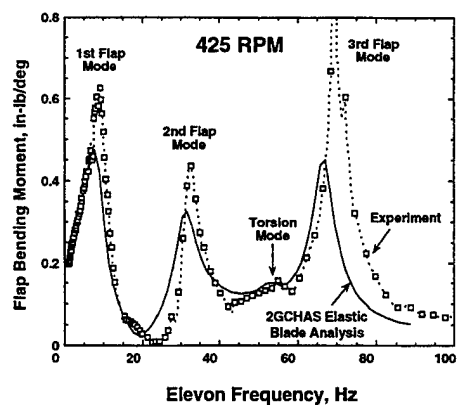


Rotor Blade Frequency Response to Elevon Excitation in Hover

Blade Root Torsion Moment



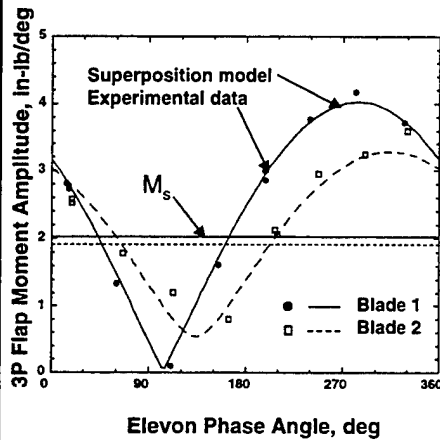
Blade Root Flap Bending Moment



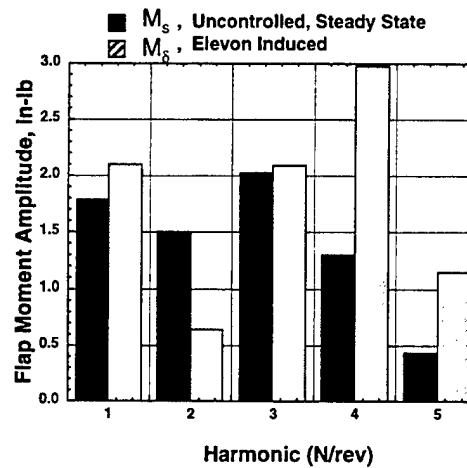
Blade Loads Reduction in Forward Flight

760 RPM, $\theta_0 = 4^\circ$, $\mu = 0.2$

3P Bending Moment
Variation with Elevon Phase

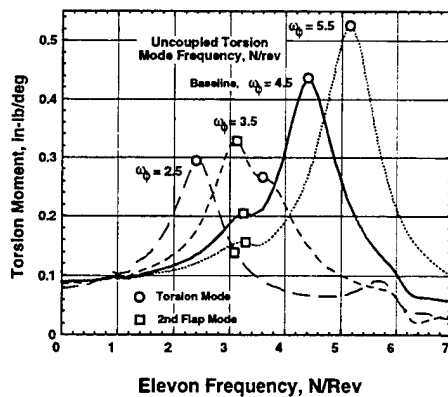


Elevon Control Authority Sufficient to Null
Vibratory Blade Loads (3P-5P)

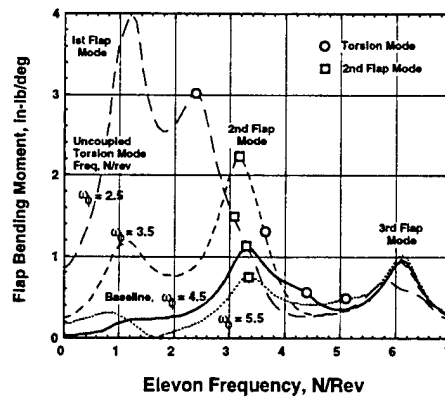


Elevon Effectiveness Optimized to Reduce Vibratory Loads by Tailoring Blade Torsion Stiffness

Torsion Moment Freq Response



Flap Bending Moment Freq Response



AFDD Small-Scale Model Rotor Experiments Future Plan Options

- **Experimental Investigations**
 - Develop Mach-Scaled Active Elevon Rotor (AER) experimental demonstrator
 - Investigate closed-loop active control capability, transient response, stall and compressibility effects
 - Further explore dynamics and aeroelastic mechanisms of hub and blade vibratory loads, and rotor performance
- **Comprehensive Analysis**
 - Refine and validate analytical methods
 - Studies to optimize elevon/rotor aeroelastic design
- **Improve S&T readiness for 6.2 VGART & 6.3 VGARD Advanced Tech Demonstrator**

SBIR - Integral Airfoil Actuation Concepts For On-Blade Active Control

Domzalski Machine, Gilbert, AZ, Deformable Trailing Edges and Smart Material Actuation of Active Control of Rotor Blades, March 1999 - June 2001

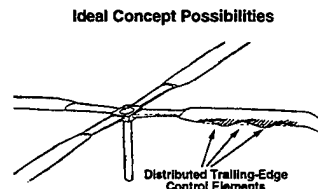
OBJECTIVE

- Develop design concepts to integrate the actuation and rotor blade structural functions
- Provide continuous system rather than discrete components



APPROACH

- Integral actuator and airfoil structure
- Continuous airfoil/structure deformation



PAYOFF

- Reduced complexity, parts count, maintenance cost
- Improved reliability, availability

SBIR - Coaxial Optimal Electric Servo Actuator For On-Blade Control of Active Rotor

Diversified Technologies, Inc., Bedford,
MA, March 1997 - November 1998

OBJECTIVE

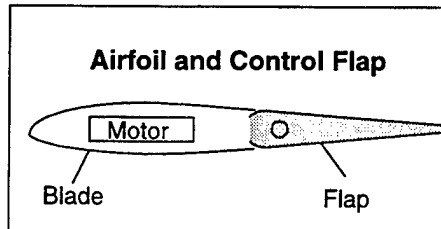
- Alternative high force and displacement actuator for helicopter on-blade control applications

APPROACH

- Apply linear electric motor technology to develop on-blade actuator
- Demonstrate feasibility on bench and in rotating environment

RESULTS

- Whirl testing on OH-58 rotor to 81% Nr
- +/- 8 degrees deflection
- Simple, no moving parts



OH-58 Rotor Whirl Test Rig



SBIR - Individual Blade Control for Helicopter Rotor Blade One/Rev Vibration Reduction

Continuum Dynamics, Inc., Princeton, NJ; Individual Blade Control for One/Rev
Vibration Reduction, September 1997 - September 1999

OBJECTIVE

- Practical rotor blade tracking system for reducing 1/rev vibration

APPROACH

- Apply smart materials for actuation with simple sensors and an active controller for in-flight adjustment
- Demonstrate feasibility on bench and in large-scale whirl test environment

PAYOFF

- Phase 1 bench-top testing of SMA to refine actuator concepts
- Overall concept demonstrated to be feasible

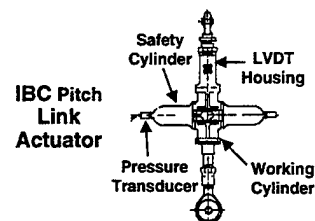
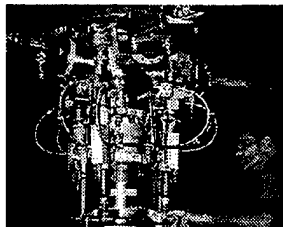
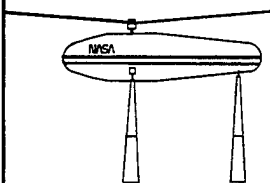
Joint NASA & ARMY Active Control Programs

DARPA/Boeing Smart Rotor

- Objectives
 - Flight test helicopter with smart material actuators and on-blade controls
 - Wind tunnel tests for evaluation of noise, vibration, and performance benefits
 - Demonstrate applications of smart materials to rotorcraft
- Approach
 - DARPA funded Boeing Mesa/Phil, MIT,UM, NASA & Army participation
 - Test full-scale SMART Rotor (MD-900 Explorer) with piezoelectric actuated flaps in NASA Ames NFAC 80x120 Wind Tunnel
 - Conduct both open and closed loop tests
- Accomplishments
 - Determined wind tunnel requirements with Boeing Mesa
 - Completed fatigue test and spin test of smart material actuated flaps
- Plans
 - Integrate smart flaps on MD-900 blades
 - Prepare for DARPA SMART Rotor entry in Q2 FY00

Joint NASA & ARMY Active Control Programs

Rotorcraft Algorithm Development & Integrated Control Laws (RADICL)



Demo Individual Blade Control (IBC) on full-scale UH-60 rotor (Blade root pitch)

- Reduce BVI noise (up to 12 dB)
- Reduce vibration simultaneously (85-90%)
- Maintain performance while at reduced tip speeds
- Improve performance (5%) or delay stall above cruise speed

NASA Ames NFAC Wind tunnel and simulation work to support flight test

- IBC checkout, system risk reduction, in 80 x 120 Wind Tunnel (FY00)
- Test IBC on UH-60/LRTA rotor in 40 x 80 Wind Tunnel (FY01)

UH-60 IBC Flight Test

- ZFL to design flight-worthy actuators

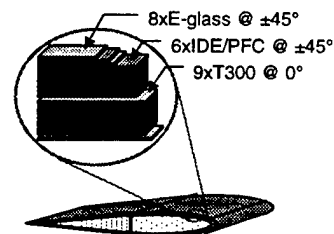


Active Twist Rotor Program

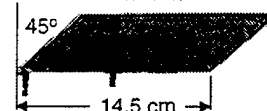


- Develop helicopter rotor blade aeroelasticity analysis methods suitable for active twist rotor preliminary design, control studies, and detailed design evaluation - PETRA
- Evaluate potential of advanced piezoelectric twist actuation strategies
 - embedded piezoelectric fiber composite laminae (PFC)
 - interdigitated electrode technology (IDE)
- Assess benefits of Active Twist Rotor technology when applied to significant rotor vibration problems
 - e.g., high-speed forward flight dynamic stall
- Compute vibration reduction with CAMRAD-II
- Demonstrate Active Twist Rotor concept in 'realistically' scaled Transonic Dynamics Tunnel tests - open loop
- Pursue control strategies for vibration reduction (closed loop) and extend concept to address issues in noise/performance

Conceptual ATR Piezoelectric-fiber-composite blade structure



MIT developed PFC patch with IDE

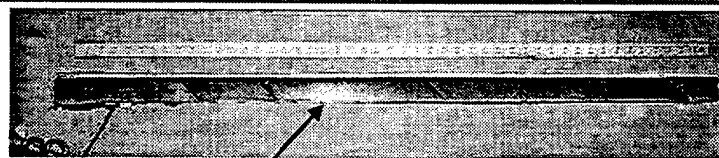


Active Twist Rotor Schedule

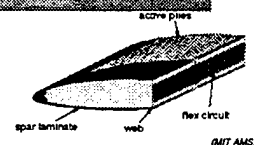


- PETRA / Advanced Actuator
- CAMRAD- II
- Prototype Blade
- Rotor System construction
- Hover tests
- TDT tests
- Correlation with Analyses

FY96 FY97 FY98 FY99 FY00 FY01 FY02



- Structural 'pull test' blade delivered for wind tunnel certification tests
- Prototype blade delivered 3-19 for bench and hover tests
 - 6 of 24 packs inoperative
 - Twist authority still impressive in hover tests (5-99)
 - Manufacturing errors identified, five blade set initiated
- TDT wind tunnel tests scheduled for July 2000



Blade Spar Construction

Current Technology Assessment

Discipline	Importance	Current Emphasis	Technology Readiness	Future Emphasis
Aero, dynamics, aeroelastics	High	Moderate	Ready	Continue
Control theory - architecture, algorithms	High	Moderate	Ready	Continue
Materials - strain, force	Very high	Low	Not ready	Much more
System integration	High	Low	Not ready	More

Concluding Remarks

- **Revolutionary potential for future rotorcraft**
- **Cost is paramount - if smart structures increases cost or maintenance then technology won't fly**
- **Helicopters are already too complicated - active control smart structures must get simpler**
- **Active control must be reliable before industry will buy it**
- **Smart material actuation limitations persist**

Abstract
TACOM-ARDEC
Advanced Drives and Weapon Stabilization (ADAWS) Lab
Smart Structures and Materials

Research in Smart Structures and Materials is one of the most challenging and exciting areas to be involved in today. The highly interdisciplinary nature of this field of endeavor, located at the intersection of a number of different technical disciplines, has room for significant contributions at all levels of development. The search to create new structures and materials that cost less than their passive counterparts and yet perform better, offers excellent opportunities to improve the warfighting and cost effectiveness of today's Army and the Army After Next (AAN).

The significance of this area to the future of Army effectiveness has not been lost on DoD and Department of the Army (DA) upper management. Smart Materials and Structures has been identified as a DoD Strategic Research Objective (SRO) and a Technology Thrust Area within the Engineering and Environmental Sciences Division at the Army Research Office (ARO).

The Army Tank Automotive and armaments Command, Armament Research Development and Engineering Center (TACOM-ARDEC) Advanced Drives and Weapon Stabilization (ADAWS) Lab located at Picatinny Arsenal NJ., has been responsible for identifying and developing new technologies to improve the accuracy, lethality and cost effectiveness of Army weapon systems. These technologies initially encompassed advanced gearless drives and robust digital control systems which did improve performance but in of themselves were limited in their ability to drastically reduce the muzzle pointing error and improve the accuracy of gun systems. This is a prime objective of the ADAWS Lab; reducing the muzzle pointing error which has the greatest effect on first round hit probability and probability of kill. To realize these types of improvements requires both an accurate sensing of the muzzle angle due to terrain, platform or firing disturbances and actuator authority co-located near the muzzle to reject and correct for these disturbances.

To address this objective, the ADAWS team began investigating the use of optical fiber sensors with Dr. Sircus for measuring the muzzle angle and the use of stacked piezo translators as actuators located externally along the gun barrel. These devices were first successfully demonstrated in the ADAWS Lab on an Apache 30mm chain gun and designs were developed to transition and demonstrate these technologies on the 120mm smooth bore tank gun. While this work was progressing other technologies were offering opportunities to improve weapon systems and potentially to improve commercial products and civil systems or structures. For example, the use of MR/ER fluids for robust "smart" dampers or actuators was studied in our work with Dr. Wereley, piezo based Surface Acoustic Wave (SAW) devices for remote sensors were investigated through our exposure and relationship with Dr.'s Varidan, Vibration Control and Confinement (VCC) techniques are being applied to weapon platforms with Dr. Allaei at QRDC and Active/Semi Active Structural Control techniques are being studied and developed with Dr. Clark.

These efforts, while just an example, demonstrate the successful teaming of the Advanced Drives and Weapon Stabilization Team with Universities, Industries and ARO. The support of TACOM-ARDEC management and their FY99 investment has enabled the ADAWS team to continue the research and development of smart materials and structures for military applications. This commitment will enable a continuation of our partnering and teaming and our continued participation in technical conferences and symposia critical for the development of new ideas and concepts for Smart Materials and Structures for military applications.

Application of Smart Structure Technology to Improve Large Caliber Gun System Performance

Eric Kathe
US Army, TACOM-ARDEC Benet Laboratories
Watervliet Arsenal
Watervliet, NY 12189-4050

Roger L Ellis
Naval Surface Warfare Center - Dahlgren Division
Attention G-32
17320 Dahlgren Rd.
Dahlgren, VA 22448

ABSTRACT

The engineering of large caliber gun systems is upon the threshold of a new era of improved performance enabled by the application of robust smart structure technology. The vision of the army after next is placing extreme emphasis upon reduced gun system weight, means to mitigate the effects of recoil upon future lightweight fighting vehicles, and system accuracy. This is also true for the Navy's advanced gun systems with additional emphasis on extended range guided munitions and high volume of fire. Additionally, such systems are being required to radically adapt system parameters to effectively launch a wide variety of ordnance with dramatically different ballistic properties from round to round. (E.g., armor piercing projectiles, extended range rocket assist munitions, and mortar bombs). In this presentation, potential areas for the inclusion of smart structure technology will be outlined, and recent applications of non-traditional cannon design will be highlighted.



Fourth ARO Smart Structures Workshop

August 16-18, 1999 Penn State



Application of Smart Structure Technology to Improve Large Caliber Gun System Performance

Eric Kathe

US Army TACOM-ARDEC Benet Labs
AMSTA-AR-CCB-TC, Building 115
Watervliet, NY 12189-4050
ekathe@PICA.ARMY.MIL

Roger Ellis

US Naval Surface Warfare Center
Dahlgren Division, G-32
17320 Dahlgren Rd.
Dahlgren, VA 22448
EllisRL@NSWC.NAVY.MIL



Abstract



The engineering of large caliber gun systems is upon the threshold of a new era of improved performance enabled by the application of robust smart structure technology. The vision of the army after next is placing extreme emphasis upon reduced gun system weight, means to mitigate the effects of recoil upon future lightweight fighting vehicles, and system accuracy. This is also true for the Navy's advanced gun systems with additional emphasis on extended range guided munitions and high volume of fire. Additionally, such systems are being required to radically adapt system parameters to effectively launch a wide variety of ordnance with dramatically different ballistic properties from round to round. (E.g., armor piercing projectiles, extended range rocket assist munitions, and mortar bombs). In this presentation, potential areas for the inclusion of smart structure technology will be outlined, and recent applications of non-traditional cannon design will be highlighted.





Army Gun Technology Needs



Recoil Mitigation

- Direct Fire Out Of Battery
- EM Augmented Recoil
- Adaptive Muzzle Brakes
- Active Recoil Mitigation Suspension
- Inertial Breech Containment
- Recoilless Revisited For UAV's & Robotic
- Double Action Recoil
- Traveling Charge

Performance Enhancement

- Composite Cannon
- Swing Chamber Autoloader Interface
- Integral Barrel Cooling
- Smart Structure Technology
- Controlled Kick-Off
- ETC Integration
- Two Stage Cannon
- Two Round Salvo Gun
- EM/Gas Hybrid Cannon
- Signature Management

Multi Role Cannon

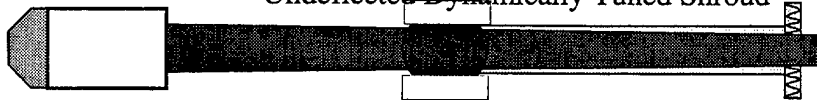
- Adaptive Recoil
- Adaptive Bore-Evacuation
- Adaptive Muzzle Brakes
- Adaptive Expansion Ratio / Chamber Volume
- Full Elevation Envelope for Direct Fire Gun
- Prismatic Bore



A Gun Barrel Vibration Absorber for Increased Accuracy



Undelected Dynamically Tuned Shroud



Deflected Dynamically Tuned Shroud

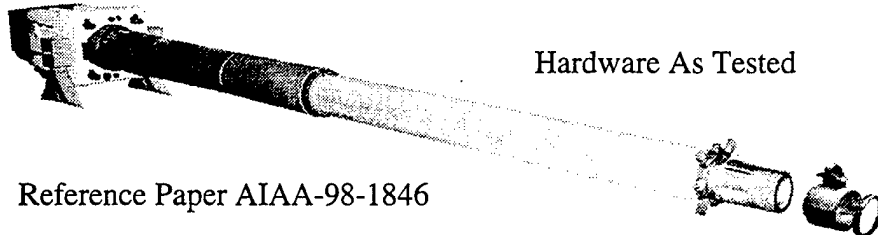


Patent Pending Serial # 09/215,000
07 December 1998





A Gun Barrel Vibration Absorber for Increased Accuracy

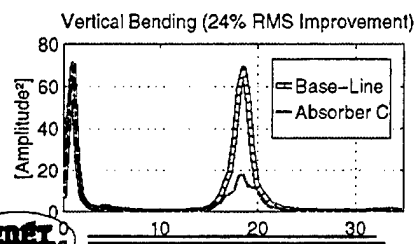


Hardware As Tested

Reference Paper AIAA-98-1846



Results



A Two Pronged Approach to Recoil Mitigation

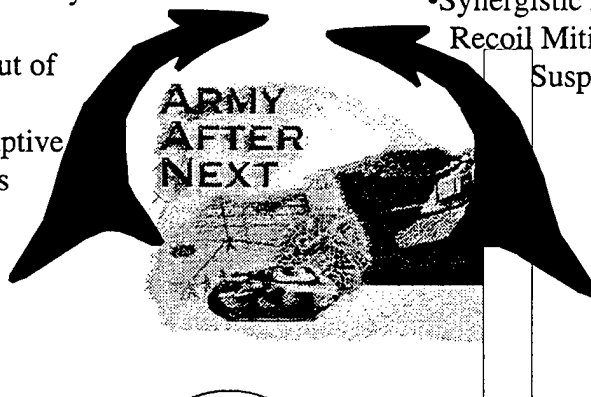


Gun System Approaches:

- Electromagnetically Controlled Recoil
- Active Fire out of Battery
- Novel & Adaptive Muzzle Brakes
- Efficient Recoilless

Vehicle Approach:

- Synergistic Active Recoil Mitigation Suspension



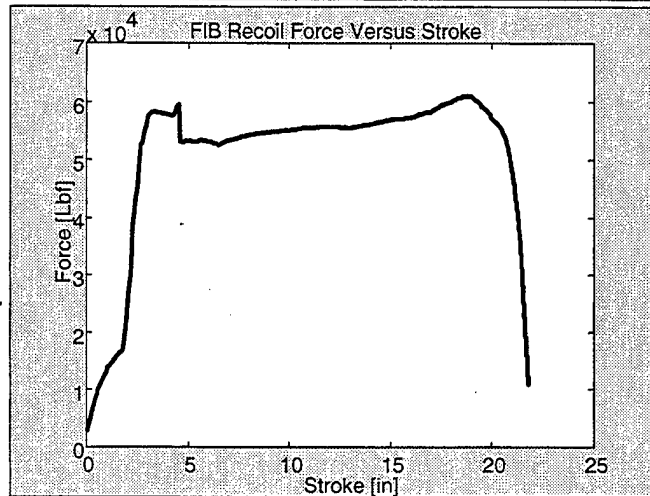


Fire out of Battery M35



Fire In Battery
(FIB) Recoil
Force
Versus Stroke.

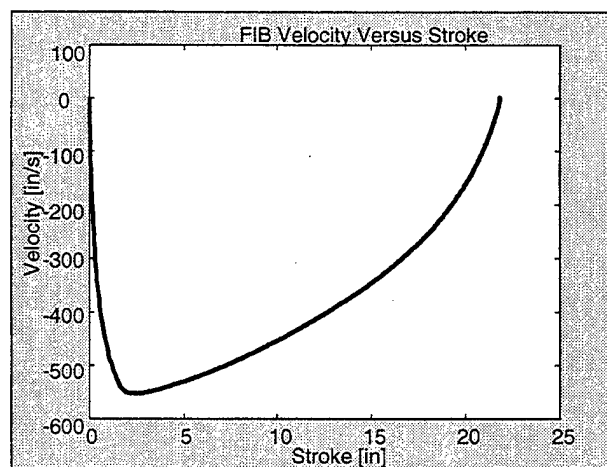
Note: it is as flat as possible. This is achieved via variable orifice hydraulic brake.



Fire out of Battery M35



Fire In Battery
(FIB) Recoil
Velocity
Versus Stroke.



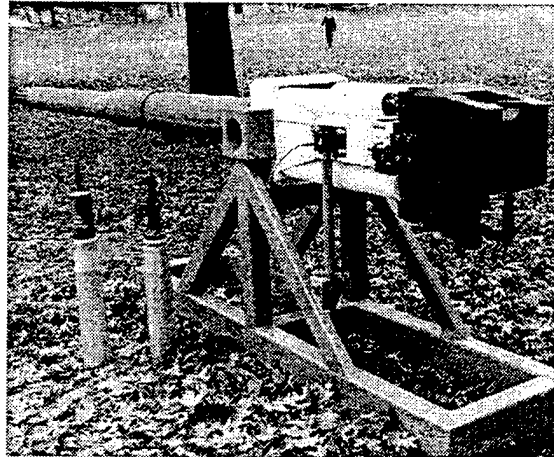


Fire out of Battery M35



The M35 105mm Tank Gun

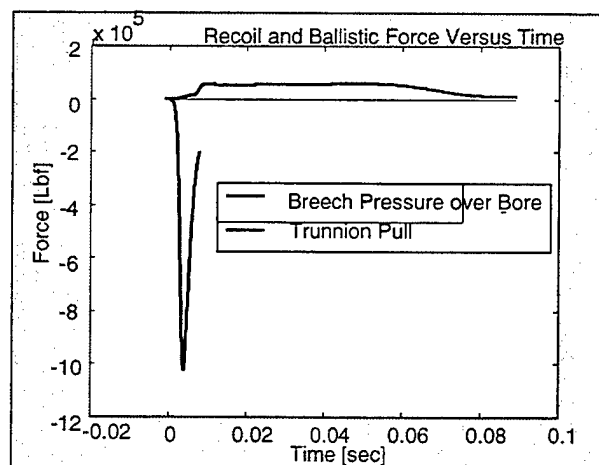
- An image of the EX35, with muzzle brake.
- The recoil system consists of four cylinders. Two hydraulic brakes (upper left and lower right) and two recuperators.



Fire out of Battery M35



Fire In Battery (FIB) Ballistic and Recoil Force Versus Time



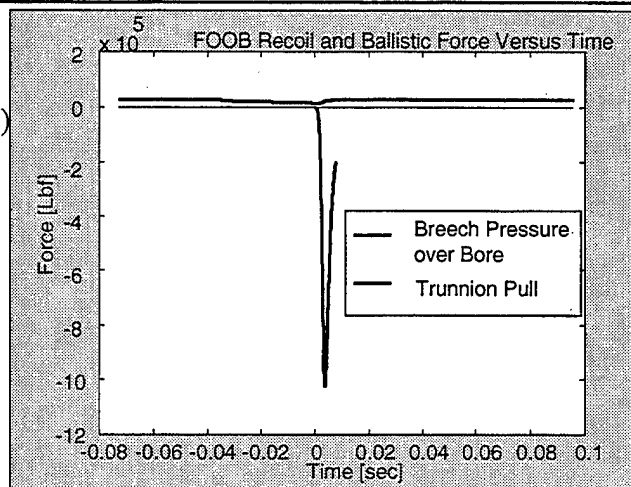


Fire out of Battery M35



Fire Out Of
Battery (FOOB)
Ballistic and
Recoil Force
Versus Time.

*Note: The gun is
pre-accelerated
forward.*



BENET
Labs



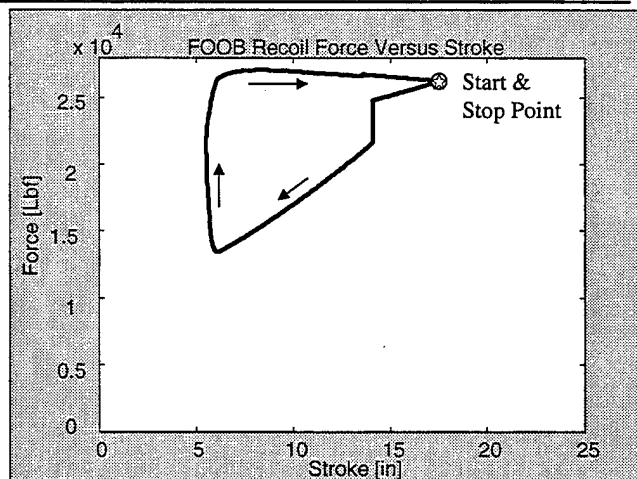
Fire out of Battery M35



Fire Out Of
Battery (FOOB)
Recoil Force
Versus Stroke.

*Note: The hysteresis
and linear ramp are
caused by undesirable
damping and spring
rate effects
respectively.*

*Also, recoil stroke is
lost at both ends for
misfire and hang-fire
handling.*



BENET
Labs

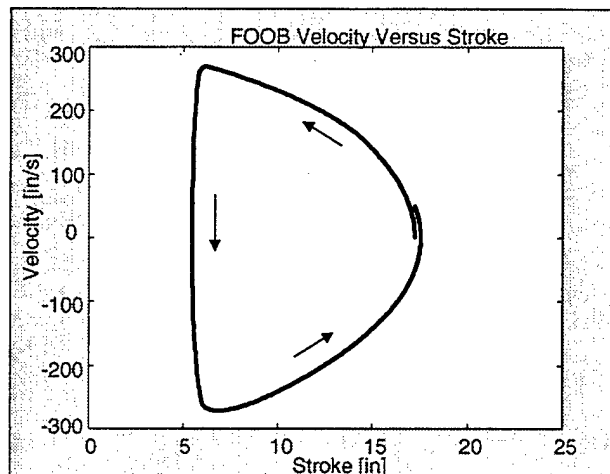


Fire out of Battery M35



Fire Out Of Battery (FOOB) Recoil Velocity Versus Stroke.

Note: It comes back with slightly higher speed to accommodate frictional losses and to ensure that it recoils beyond the catch and release latch.



BENET
Labs



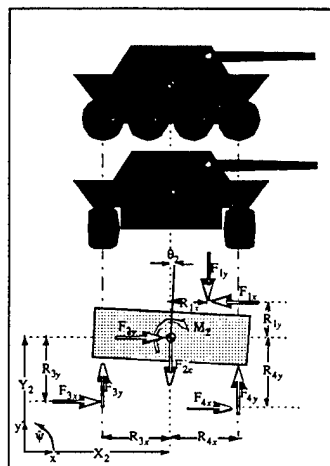
Active Recoil Mitigation Suspension



- Future active suspensions may enable the vehicle to tolerate higher launch momentum.

- Active suspensions enable some portion of the recoil impulse to be directly coupled to earth in real time.

I.e., they may intentionally couple the hull to ground as opposed to decoupling it.



BENET
Labs



Army Conclusions



New technology is required to:

- Mitigate the effects of recoil
- Lighten future gun systems
- Improve reliability
- Increase/maintain accuracy
- Increase firing rate
- Enable radical gun system parametric adaptation for a wide variety of firing missions
- Provide robust obturation seal for sliding breech or chamber



*Naval Surface Warfare Center
Virginia Tech*

MR Gun Recoil Demonstration

Roger Ellis - NSWC

*Mehdi Ahmadian - Virginia Tech
Senior Design Team - Virginia Tech*



NAVAL SEA SYSTEMS COMMAND



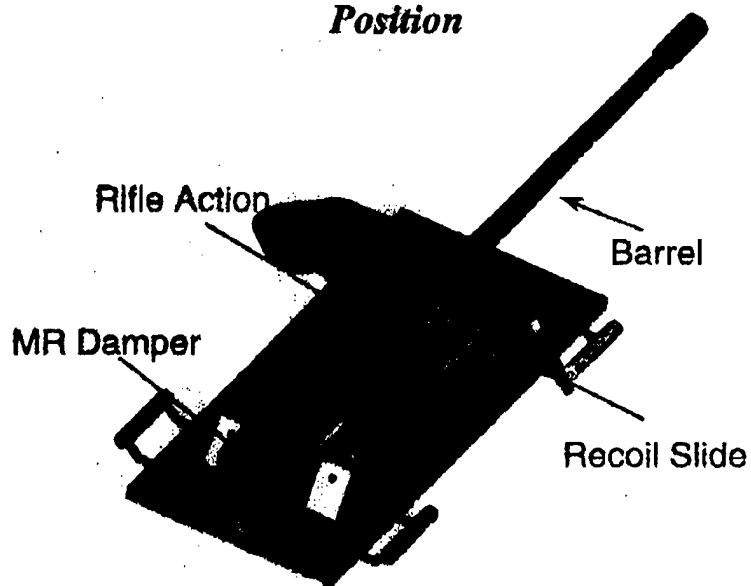
Panama City

Dahlgren

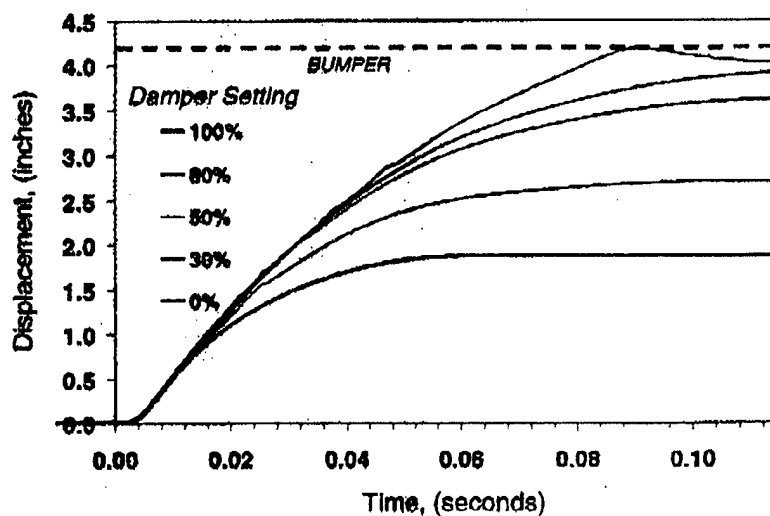
APPROACH

- Evaluated maximum recoil force and velocity requirements for a large caliber gun (150,000 lbf, 10 ft/sec)
- Chose a 50 caliber BMG demonstrator
 - live ammunition
 - reasonable recoil energy (force/velocity)
 - readily available
- Demonstrate ability to vary recoil distance with MR fluids.

Recoil Demonstrator Shown in Battery Position



Recoil Displacement Profile



Next Steps

- Characterize MR fluid in large caliber gun recoil environment
- Demonstrate active recoil control
- Demonstrate in a large caliber gun system



Laboratory for Intelligent
Mechatronic Systems

Feedback Designs for Controlling Device Arrays with Communication Bandwidth Constraints

John Baillieul
Boston University
johnb@bu.edu

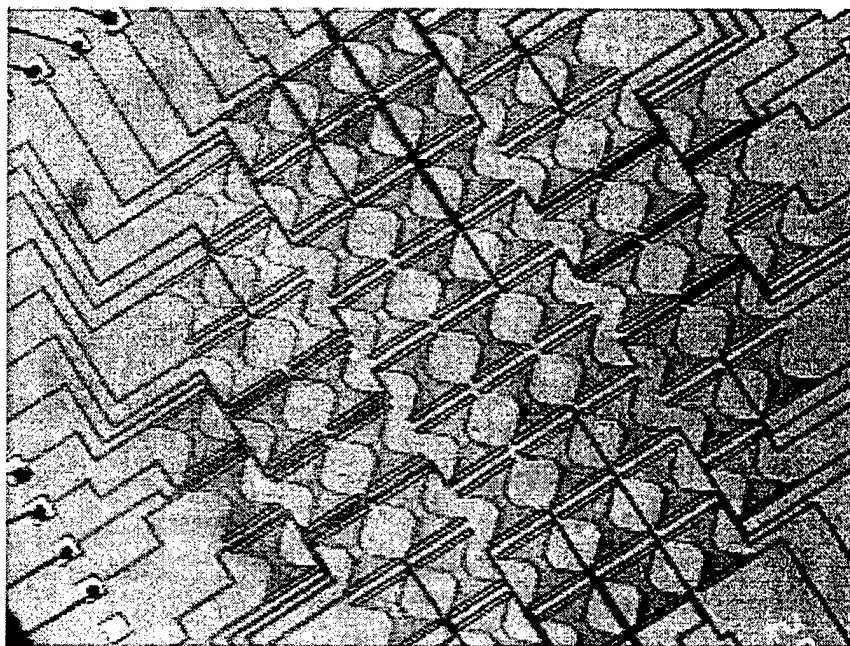
August 16, 1999



Laboratory for Intelligent Mechatronic Systems

Controlling Device Arrays with Communications Bandwidth Constraints

The arrays of MEMS devices currently being fabricated at Boston University are becoming more densely packed, and as the numbers of devices on each chip increase to over 1000, it will be unlikely that individual devices will have dedicated link connecting them to a central real time control computer. The next generation of arrays---such as the valve array below---will have shared communication links and will be addressable. The attached note summarizes some results of recent work concerned with communication issues in the real time control of large scale device arrays.



Feedback Designs for Controlling Device Arrays with Communication Channel Bandwidth Constraints

J. Baillieul*

July 23, 1999

Abstract

This paper reports a tight bound on the data capacity a feedback channel must provide in order to stabilize a right half-plane pole.

1 Introduction

Device arrays of MEMS actuators such as micro-pistons and micro-valves comprise a “smart structures” technology which is both interesting and challenging. Current designs are quickly moving beyond the “proof-of-concept” stage in which relatively small arrays, with between four and twenty actuators on a single chip, have been tested with each device in the array having direct communication by means of “wires” for both control and sensing. We have recently fabricated arrays with between 50 and 100 devices on a single chip, and these designs seem to have achieved more or less the maximum possible device density in which direct addressing of each actuator is feasible. In the next generation of device arrays, which will feature as many as 10,000 actuators on a single chip, it will be necessary to close feedback control loops using communication channels shared by multiple device elements. Work is only just now beginning on the switching and encoding strategies that will be needed to produce stable closed-loop dynamics across a broad spectrum of applications. We are finding that many of the bandwidth assignment issues that are predominant in managing the traffic in modern communications networks are also present in some form in networked actuator arrays.

This note presents recent results on the effects of communications bandwidth constraints in feedback control designs. The main results involve a novel interplay between control and information theory. From one viewpoint, the theory of control using bandwidth-constrained feedback channels may be thought of as an enriched version of classical digital control theory. Indeed, bandwidth constraints in feedback control raise interesting quantization issues in which there is a trade-off between the coarseness of control and observation data and the time required to send data over the link. High performance in many applications calls for finely quantized data and a correspondingly large set of codewords used to describe the system’s inputs and outputs. It has been shown that fine data quantization requires either a larger channel capacity or longer periods allocated to data transmission. The relationship between the control system structure and the channel capacity is central to understanding the design of feedback control laws which are capable of providing high-quality regulation of the system’s performance.

An interesting concept which has emerged in this research is that of “required attention”—a term which is intended to serve as both a descriptive characteristic of dynamical systems in general and a figure of merit for closed-loop feedback designs. In Brockett ([1]), this latter notion of “required attention” is developed, and in the case of linear systems having no right half-plane poles, the term is given a precise quantitative meaning in terms of something called an “attention functional”. For linear systems having no right half-plane poles, Brockett has solved the “minimum attention” problem using a variational argument. In the present

note, we shall present a slightly different perspective in which the notion of “required attention” is captured by the amount of channel capacity (in bits per second) which is required to implement a stable feedback law. One intuitively appealing result is that by our measure, the required attention for a stable feedback law increases as a function of how far open-loop poles extend into the right half-plane. This definition of “required attention” provides the first instance of which we are aware of a characterization of a system’s complexity in terms of how much information must be transmitted in order to control it. It is expected that this measure will play a role in developing channel allocation strategies for controlling large scale device arrays.

Classical feedback control theory is aimed at understanding design principles for integrating sensors and actuators for controlling a physical system in a way that it will perform its prescribed tasks efficiently and reliably. The basic principles are very simple as illustrated in Figure 1. Information about the state of the system of interest (called the plant G) is provided by output sensor data. The control system (represented by the box labeled H together with the dotted interconnection) processes signals from sensor outputs, compares the state of the system with specified operating goals, and “closes the loop” by sending appropriate actuator signals to keep the system operating as near as possible to its operating goals. There is today a vast array of mathematically sophisticated tools for design and analysis of the controller H .

The tools apply to both continuous and discrete-time systems, and for many applications, they have become an essential aid for implementations of feedback control mediated by digital microprocessors. As we shall indicate below, however, many feedback control laws cannot be implemented in a satisfactory way if the links between the plant (G) and the controller (H) do not have adequate information carrying capacity. The paper is organized as follows. In the next section, a bound is established on the capacity required on the channel between G and H in order to stabilize a right half-plane pole in G . The bound is tight and the result has been proved for the case of first order systems. Section 3 discusses extensions to higher order systems.

2 Digital control of first order systems with uniform sampling rate

We consider controlling a first-order plant, as depicted in Figure 1, $G(s) = b/(s - a)$. The cases of greatest interest are those in which $a > 0$, since the controller H must be designed to stabilize the plant. Classical control theory (e.g. [2]) provides many approaches to designing H , and implementations mediated by digital microprocessors can be carried out by selecting the appropriate discrete-time tools. We wish to understand how these results are affected if there are bandwidth constraints or limitations on the feedback links connecting G and H .

The case we shall treat here involves digital control with a uniform sampling interval h . We assume control actuation is of the sample-and-hold type, so that control inputs to the system are constant over each sampling interval. The state of the plant evolves in discrete time according to

$$x(k+1) = \alpha x(k) + \beta u(k), \quad (1)$$

where

$$\alpha = e^{ah}, \quad \text{and} \quad \beta = \frac{b}{a}(e^{ah} - 1).$$

If a digital computer is used to implement feedback control, a sensor reading of the (typically analog) value $x(k)$ is digitized and stored in a computer register. Using whatever control algorithm has been implemented, the computer determines a value of the control input $u(k)$ (from a finite set U of admissible control values), and this in turn is converted to an analog value (e.g. a voltage or a current) which is then fed back to the plant.

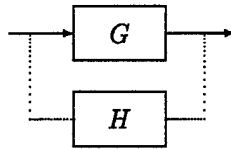


Figure 1:

For many applications, eight or fewer bits suffice to specify the values of the control function $u(\cdot)$, and hence the cardinality of the set U of admissible control values is typically ≤ 256 . Whatever the cardinality, $|U|$, of the set of admissible controls, the number N of bits needed to uniquely encode each control value is such that $|U| \leq 2^N$. The inequality may be strict since some encoding schemes will use a certain number of bits for purposes other than identifying control values.

Our interest in the present note is in the case in which the communication channels between the control computer and the plant have a low data rate—say R bits per second. This situation would arise, for instance, if a single computer were controlling many plants connected serially by a single communication link. In this setting, a number of interesting nonclassical issues arise.

- There is a trade-off between the cardinality of the set of admissible control values (or levels) $u(k)$ and amount of time required on average to transmit digitally encoded data from the control computer to the plant. This problem is discussed in Wong and Brockett, [3], where both controller and sensor data are assumed to be encoded using *prefix codes*. Using known bounds on the average length of codewords in prefix codes, bounds are given on the minimum sampling interval, h , required to permit the transmission of control data between the sensors and actuators and the control computer.
- Some systems are intrinsically more complex than others in the sense that a finer quantization of control levels is required to guarantee stable performance. The main results of the present note are that (i) the number K of distinct possible control values or levels must be greater than or equal to e^{ah} in order to implement stable feedback control, and (ii) the channel capacity R must exceed $a \log_2 e$. Stated in less precise but more suggestive language, the greater the degree of instability of the open-loop system, the finer the quantization of control values and the more information there is which must be communicated between the controller and plant in each time interval.

Classical notions of asymptotic stability must be modified in order to discuss control designs with quantized control values.

Definition 1 (Wong & Brockett, [3]) A linear control system is said to be *containable* if for any open set S containing the origin, there is a corresponding open set M containing the origin and an encoding of a feedback control law such that any trajectory started in M remains in S for all time.

Definition 2 A linear control system (1) with admissible control set U is *boundable* if there exists a compact set S such that for each $x_0 \in S$ there is a control sequence $\mathcal{U} = \{u(k) \in U : k = 1, 2, \dots\}$ such that the trajectory defined by (1) with $x(0) = x_0$ and control input sequence \mathcal{U} remains in S for all time.

Containability is a property the discrete-time control system (1) must possess in order for there to exist a finite set U of control values which can be used to implement an (approximately) asymptotically stabilizing control law. Boundability assumes that a finite set U of control values has been chosen together with a

systematic way of encoding and transmitting these values from the controller to the plant. Containability is stronger than boundability, and any system which is not boundable cannot be containable.

Example 1 *The case of binary control.* Suppose the set U of admissible control values has two elements. These correspond to what we assume are precisely two different possible actuator commands. While these values might be different voltages or currents or other physical quantities of constant magnitudes, there is no loss of generality in the model in assuming that $U = \{-1, 1\}$, since this may always be brought about for a system of the form (1) by an affine change of coordinates. To make the discussion of boundability interesting, we assume that (1) is open-loop unstable: i.e. $\alpha > 1$. In this case, it is not difficult to see that implementing any stabilizing feedback law results in closed loop dynamics given explicitly by

$$x(k+1) = \begin{cases} \alpha x(k) + \beta & x(k) \leq 0 \\ \alpha x(k) - \beta & x(k) > 0 \end{cases} \quad (2)$$

Fact *The closed loop system (2) admits an invariant interval if and only if $\alpha < 2$.*

Proof There are two fixed points of the mapping (2): $-\beta/(\alpha-1), \beta/(\alpha-1)$. In studying the closed loop mapping (2), it is important to note that $\alpha < 2$ if and only if $\beta < \beta/(\alpha-1)$. If $\alpha < 2$, an easy calculation shows that the interval $[-\beta/(\alpha-1), \beta/(\alpha-1)]$ is invariant. (There are other invariant intervals too in this case.) Suppose on the other hand that there is an invariant interval. This can only happen if $\beta \leq \beta/(\alpha-1)$, because otherwise there is a subinterval of points containing the origin (specifically

$$\left(\frac{-\beta}{\alpha-1} \left(1 - \frac{2}{\alpha}\right), \frac{\beta}{\alpha-1} \left(1 - \frac{2}{\alpha}\right) \right)$$

such that no bounded trajectory of (2) can enter the interval. But the set of points in $(-\beta/(\alpha-1), \beta/(\alpha-1))$ which are initial points of trajectories entering this neighborhood can be shown to be dense. On the other hand, any trajectory started outside $[-\beta/(\alpha-1), \beta/(\alpha-1)]$ is clearly unbounded. This proves our statement. \square

This result that (1) is boundable using a two-element control set $U = \{-1, 1\}$ if and only if $\alpha < 2$ is a special case of our more general result. Specifically the inequalities $\alpha < 2$ and $ah \log_2 e < 1$ are equivalent. The second more clearly expresses the bound which the product of the (right half-plane) pole magnitude and the sampling interval must satisfy in order for the system to be boundable using binary control. The main result of the section is the following:

Theorem 1 *Consider a first order system $G(s) = \frac{b}{s-a}$ whose sampled realization is given by (1). If the channel capacity R is greater than $a \log_2 e$, then we may choose a sampling interval h and a set U of admissible control values such that $|U| > e^{ah}$ and such that the resulting feedback control implementation is boundable.*

Remark 1 *Control information versus control authority.* An interesting aspect of the example and the main theorem is that the conditions for boundability and the existence of invariant intervals do not depend on β . They depend only on the amount of information that can be communicated between the controller and plant in one unit of time.

Remark 2 *Remarks on the channel capacity conditions.* (i) The proof of this theorem involves the explicit construction of the set U of control values together with a feedback law which renders a compact interval invariant under motions of the system (1). As indicated in the above example, the condition $a \log_2 e < R$ is also essentially necessary because the cardinality of the set U must be larger than e^{ah} in order to guarantee bounded motions of (1). The channel capacity R must in turn be large enough to transmit enough bits of data to uniquely identify control values in each time interval h . (ii) The theorem actually represents a

crude lower bound on the amount of channel capacity one would like to have to implement feedback control of a physical system. It provides only a condition for the existence of a bounded response. To address the myriad standard control design issues such as rise time, gain and phase margins, etc., we shall need to have the capacity to transmit a great deal more data through the channel.

Remark 3 *Design of the control value set.*

1. *Magnitude and spacing of the control values.* In our general formulation of the problem of quantized feedback control, we have assumed the set of admissible control values is symmetric about the origin: $U = \{-d_n, -d_{n-1}, \dots, -d_1, d_1, \dots, d_n\}$ (where the elements are listed in order of increasing magnitude). In real-time digital control implementations, an interesting design question is whether the control levels d_i should be evenly spaced. (This question comes up, for instance, in choosing whether to use integer [evenly spaced] or floating point arithmetic [logarithms of floating point numbers are evenly spaced].) Suppose we focus the discussion on the case in which a standard constant gain feedback design, $u = u(x) = -kx$ is being implemented in terms of our quantized finite set of control values. If we choose a control set U corresponding to the bounding case in which $|U| \sim e^{ah}$ in Theorem 1, one is then forced to take the control values to be more or less evenly spaced. Stable control with logarithmic spacing of the control values will thus require higher channel capacity in the feedback loops.

The magnitude of the control values in the finite set U is a design parameter whose value may be chosen without regard to the channel capacity (assuming it takes no more bits to transmit a large value than to transmit a small value provided the cardinality of the set U itself is fixed). There is, however, the following consideration.

2. *Switching thresholds.* Suppose we again choose to implement a constant gain feedback control law $u = -kx$. The following are important considerations:

- (a) For each sampled value of the state $x(j)$, one should choose a control value $d_i \in U$ such that

$$|d_i + kx(j)| = \min_{d \in U} \{|d + kx(j)|\},$$

and the algorithm should switch control levels at each sampling time as needed so as to ensure this choice of control level is applied.

- (b) While the question of whether it is ever useful to consider sets U of unevenly spaced control values remains open, it appears that unevenly spaced switching thresholds tend to make the dynamics of (1) relatively erratic.
- (c) For sets of evenly spaced control values $U = \{-d_n, -d_{n-1}, \dots, -d_1, d_1, \dots, d_n\}$, where $d_j = jd$ for a *fundamental control value* d , it is important to choose $d \sim k$. Not doing so can also result in relatively erratic dynamic behavior of (1)

These observations will be amplified and illustrated by simulation experiments to be reported elsewhere.

3 The case of higher order and multivariable systems

We have remarked that the channel capacity bound of Theorem 1 provides a crude lower bound guaranteeing the existence of bounded motions in the idealized case of first order systems. For higher order systems, the requirements on channel capacity are more severe if there is more than one right half-plane pole in the open loop (uncontrolled) system. The following result presents conditions under which bounded motions are assured for a system evolving in \mathbb{R}^n .

Theorem 2 Consider the constant coefficient linear control system

$$\dot{x}(t) = Ax(t) + bu(t) \quad (3)$$

where A is an $n \times n$ matrix and b is $n \times 1$. (Thus u is a scalar input.) Assume A has distinct real eigenvalues and (A, b) is a controllable pair. Let

$$\tau = e^{\lambda(A)_{\max} h},$$

where $\lambda(A)_{\max}$ is the largest eigenvalue of A . Then if

$$\log_2 \tau < 1/n,$$

there is a finite set U of control values such that the sampled version of (3) is boundable.

Proof The sampled system corresponding to (3) is

$$x(k+1) = Fx(k) + \Gamma u(k),$$

where $F = e^{Ah}$ and $\Gamma = A^{-1}(e^{Ah} - I)b$. Let U be a (finite) set of control values. A set K is invariant if for any $x \in K$, there is a control sequence $u_1, \dots, u_m \in U$ such that

$$F^m x + F^{m-1} \Gamma u_1 + \dots + \Gamma u_m \in K.$$

This is equivalent to

$$x \in F^{-m}(K - F^{m-1} \Gamma u_1 - \dots - \Gamma u_m),$$

for some m ; $u_1, \dots, u_m \in U$, or

$$K \subseteq \bigcup_{m \geq 1} \bigcup_{u_1, \dots, u_m \in U} [F^{-m} K - F^{-1} \Gamma u_1 - \dots - F^{-(m-1)} \Gamma u_m]. \quad (4)$$

Under the hypothesis of the theorem, it is not difficult to show that the unit hypercube, $K = [0, 1]^n$, can be made to be invariant by proper choice of control set U . Since $\lambda_{\max}(F) < 2^{1/n}$, $\lambda_{\min}(F^{-1}) > 2^{-1/n}$. From this it follows that

$$\text{vol}(F^{-n}(K)) > \frac{1}{2^n} \text{vol}(K).$$

(Since both K and $F^{-n}(K)$ are rectangular, and the length of a side of $F^{-n}(K)$ $> 1/2$ the length of a side of K , the result is straightforward.) From this, it follows that we may chose 2^n control values such that equation (4) is satisfied. This proves the theorem. \square

Remark 4 *Remarks on quantized control of higher order systems.* The first order quantized control systems considered in the previous section are of some importance for device arrays of MEMS actuators, since individual device elements are frequently modeled by such low order systems. Nevertheless, the theory of higher order systems is also important, although at present it is somewhat less developed. If a system has two or more unstable open loop poles, for instance, we do not have a tight bound on the smallest possible channel capacity needed to implement a stable (or at least bounded) feedback law. Theorem 2 provides sufficient conditions for implementing a control law with a bounded response, but the minimum possible size of the control set U (together with corresponding channel capacity requirements) is not specified.

Example 2 *The inverted micropendulum.* For control systems with only a single unstable pole, the results of the previous section apply. An interesting example is provided by a slight modification of the classical inverted pendulum example. Recently, using fundamentally nonlinear methods, we have stably balanced some very small ($\frac{1}{8}$ -inch) pendulums. It is interesting to think about trying to balance pendulums of this size using digital implementations of classical feedback methods. Recall that for the inverted pendulum there is one right half-plane pole whose magnitude is roughly $\sqrt{g/\ell}$. Taking $g = 10$ (meters/sec.²) and $\ell = 0.001$ (meters), we can use the bound of Theorem 1 to estimate the minimum channel capacity needed to implement this control. In this case $a = \sqrt{g/\ell} = 100$, and thus the minimum channel capacity required is $100 \log_2 e = 144.2695041\dots$ bits per second. As remarked in the previous section, this is a tight bound, but it is one which gives only a conservative estimate of the data capacity that is needed to support a moderately sophisticated control law (as prescribed by standard LQR or H^∞ techniques). Moreover, if sophisticated data encoding is used in the communications link between the plant and controller, the required channel capacity will be even higher. While a data rate of even 1000 bits/second is well within the bounds of even the slowest telephone modems, it suggests that there could be limits in trying to multiplex a large number of devices using a noisy channel such as might be encountered in a MEMS array.

4 Conclusion

This short note has raised the question of what is the minimum data capacity needed in the communication link between a controller and plant in order to stabilize a system with right half-plane poles. For systems with a single real right half-plane pole a , the requirement on the channel capacity R is that

$$R > a \log_2 e.$$

References

- [1] R.W. BROCKETT, 1997. "Minimum Attention Control," 36-th IEEE Conference on Decision and Control, San Diego, CA, December 10-12, 1997, pp. 2628-2632.
- [2] B. FRIEDLAND, 1986. *Control System Design: An Introduction to State-Space Methods*, McGraw-Hill, New York.
- [3] W.S. WONG & R.W. BROCKETT, 1999. "Systems with Finite Communications Bandwidth Constraints II: Stabilization with Limited Information Feedback," Preprint.

PATTERN FORMATION FOR CONTROL OF LARGE ARRAYS

Eric Justh and P.S. Krishnaprasad

Electrical & Computer Engineering Department
& Institute for Systems Research

University of Maryland, College Park
College Park, Maryland 20742

justh@isr.umd.edu, krishna@isr.umd.edu

Fourth ARO Smart Structures Workshop
Pennsylvania State University, August 16-18, 1999

This research was supported in part by grants from the National Science Foundation's Engineering Research Centers Program: NSF DCR 8803012; and by the Army Research Office under the ODDR&E MURI97 Program Grant No. DAAG55-97-1-0114 to the **Center for Dynamics and Control of Smart Structures** (through Harvard University).

ABSTRACT

With the advent of technological accomplishments such as the Texas Instruments Digital Micromirror Device (DMD), we are in an era where it is possible to envision arrays of as many as 500,000 actuators. Component actuators in such arrays could serve to manipulate meso-scale particles, pump/meter/mix fluids, interact with coherent structures in fluids, modulate acoustic radiation, etc. Such functionality would typically depend on coordinated action of segments of the array at hand. This leads naturally to a challenging problem of coordinated control of large arrays of actuators.

In our joint work, we have proposed a pattern formation approach to coordinated actuation of arrays. Specifically, the approach consists of creating (in software or in analog/digital circuitry) "interconnection templates," which in the passage to continuum limit, lead to dynamical systems that support interesting spatio-temporal patterns. Diffusive couplings and reactive growth and decay fall into this category. The spatio-temporal patterns determine the actuation patterns. Generating such spatio-temporal patterns typically involves "stressing" the interconnection by raising or lowering a parameter resulting in crossing of stability thresholds. The possibility of making such parametric adjustments via feedback on a slower time scale offers a solution to the problem of communicating effectively with a large array - the communication is achieved through the interconnection template.

The mathematics behind the above idea leads us into the rich domain of nonlinear partial differential equations with spatio-temporal pattern solutions. We have investigated certain classes of equations - the activator inhibitor equations - and explored their mathematical structure and implications for model problems involving arrays of actuators. In this talk, we will present an overview of this research, discuss illustrative examples, and present recent numerical results related to these examples.

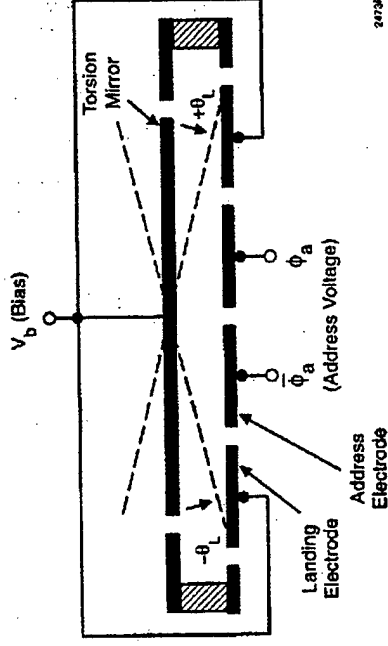
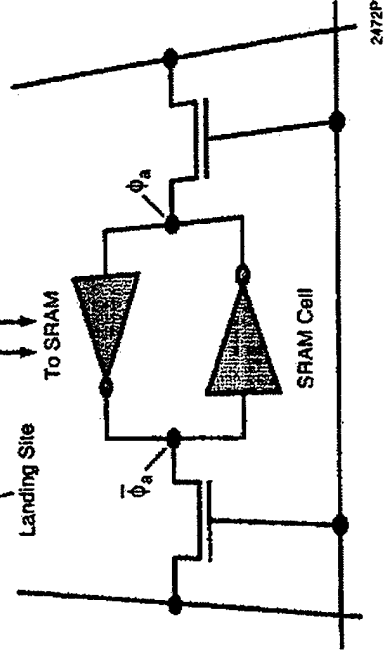
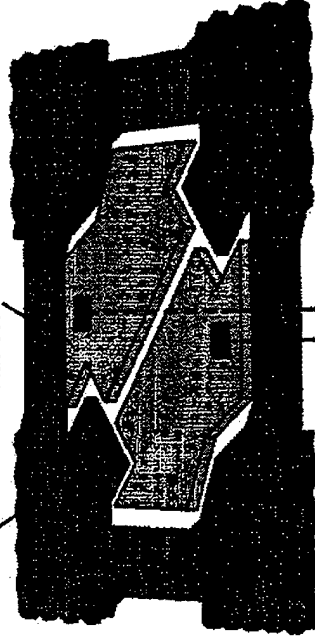
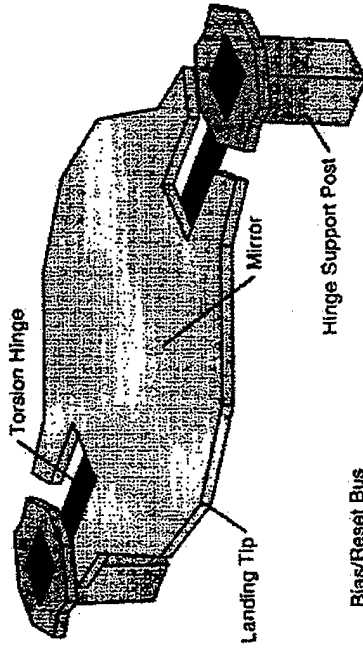
PATTERN-FORMING SYSTEMS

- Pattern-forming systems are systems of differential equations having the property that as a bifurcation (or control) parameter passes through a critical value, a stable spatially uniform state gives way to a stable pattern state, which may have spatial variation, time variation, or both.
- Pattern-forming systems arise in many diverse physical contexts.
 - Biology: population dynamics; animal coloration patterns; nervous systems, e.g., visual hallucination patterns.
 - Chemistry: certain catalyzed reactions, including catalytic converters for converting CO to CO₂.
 - Physics: shaken collections of particles, gas discharge tubes, semiconductor electron-hole plasmas, Josephson-junction arrays.
- Pattern-forming systems have been studied extensively (both theoretically and experimentally) for many years.
- The philosophy behind the study of pattern-forming systems is that certain basic features of pattern-forming behavior are universal; i.e., independent of the details of the particular physical models.
- Therefore, the standard approach to studying patterns is to write down simplified model equations which can be shown analytically to give rise to the patterns under study.
- Only recently are these systems starting to receive attention in a controls context.

ACTUATOR ARRAYS

- With recent advances in MEMS technology, it is now possible to build two-dimensional actuator arrays containing millions of simple actuators.
- **Potential applications** for large two-dimensional arrays of small actuators include
 - Adaptive optics (in particular, micro-mirror arrays),
 - Control of flow separation,
 - Micro-positioning small parts,
 - Manipulating small quantities of chemical reactants.
- As the number of actuators increases, so does the bandwidth required to command each actuator individually.
- **Goals of using pattern-forming systems for large actuator arrays** are to
 - Enable the external control inputs to be lower-bandwidth; for example, by having the same control input influence many actuators, or by having the control input set quasistatic parameters which determine how the (much faster) pattern-forming system dynamics evolve;
 - Allow the actuator control signals to be computed in parallel at each actuator site using mostly local information;
 - Permit large arrays to be treated mathematically using nonlinear dynamical systems theory so that control schemes can be developed.

MEMS ACTUATOR ARRAY EXAMPLE: TEXAS INSTRUMENTS MICROMIRROR ARRAY CHIP



- An example of a two-dimensional array of torsional microflaps.
- Built using silicon CMOS MEMS technology.
- The Texas Instruments chip is $21 \times 25 \text{ mm}^2$ with 1280×1024 mirrors on a $17 \mu\text{m}$ pitch (for HDTV applications).
- (Figures from Larry Hornbeck of Texas Instruments.)

CUBIC NONLINEARITY ACTIVATOR-INHIBITOR MODEL DYNAMICS

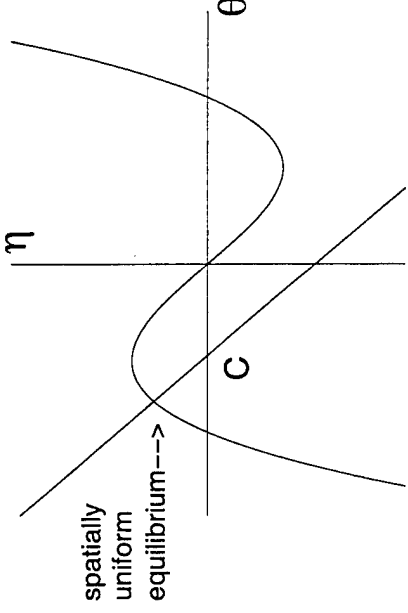
- System of two coupled parabolic PDEs:

$$\tau_\theta \frac{\partial \theta}{\partial t} = l^2 \Delta \theta - \theta^3 + \theta + \eta,$$

$$\tau_\eta \frac{\partial \eta}{\partial t} = L^2 \Delta \eta - \eta - \theta + C,$$

where Δ is the Laplacian operator, θ is the activator, η is the inhibitor, τ_θ and τ_η are time constants, l and L are diffusion lengths, and C is the control (or bifurcation) parameter. We also define $\alpha = \tau_\theta/\tau_\eta$ and $\beta = l/L$.

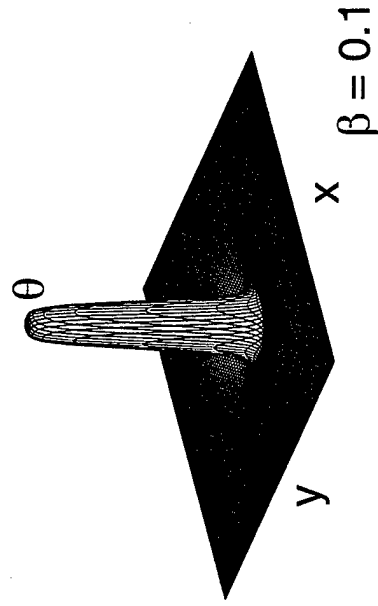
- A spatially uniform equilibrium solution is given by the intersection of the curve $\eta = \theta^3 - \theta$ with the line $\eta = -\theta + C$ (shown below for $C = -\frac{2\sqrt{2}}{3\sqrt{3}}$):



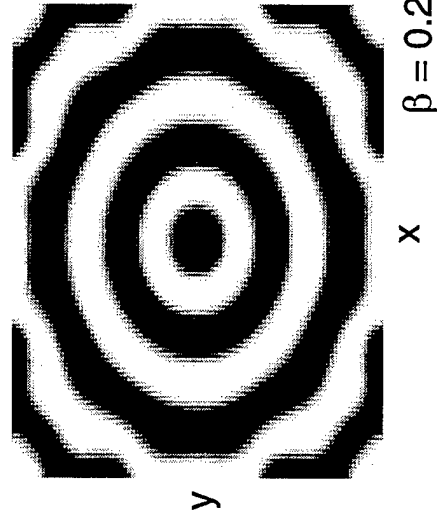
- We consider the case $\beta = l/L < 1$, in which case the spatially uniform equilibrium solution is stable for $|C| > \frac{1}{3\sqrt{3}}$. When the spatially uniform equilibrium solution is unstable, a pattern solution is stable. When $\alpha = \tau_\theta/\tau_\eta > 1$ and the spatially uniform equilibrium solution is stable, other interesting equilibria may also be stable.

TWO-DIMENSIONAL CUBIC NONLINEARITY MODEL EQUILIBRIA

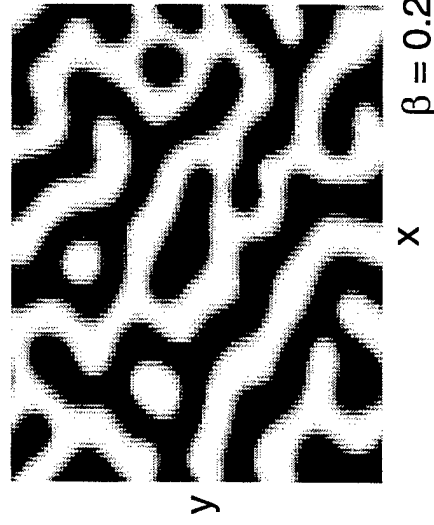
- Two-dimensional spike equilibrium ($C = -\frac{2\sqrt{2}}{3\sqrt{3}}$):



- Two-dimensional pattern equilibria ($C = 0$):



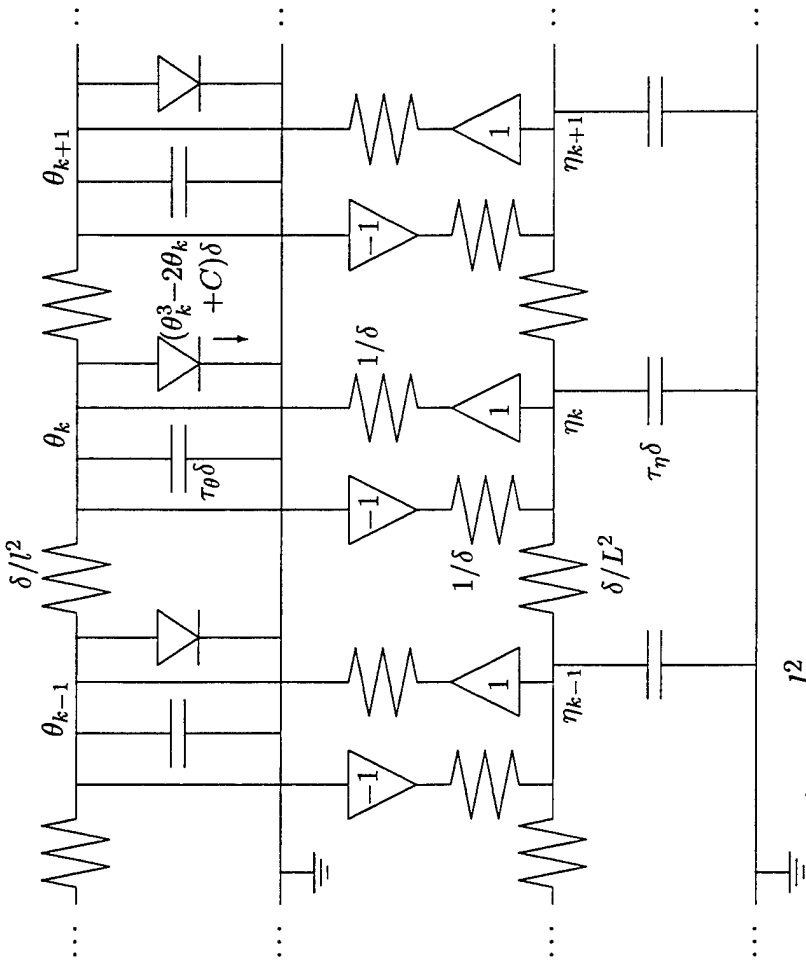
A symmetric pattern



An irregular pattern

ELECTRONIC CIRCUIT REALIZATION OF THE DYNAMICS

- A VLSI realization of the (spatially discretized) real activator-inhibitor dynamics could be collocated with a MEMS actuator array:



$$\begin{aligned}\tau_\theta \dot{\theta}_k &= \frac{l^2}{\delta^2}(\theta_{k+1} - 2\theta_k + \theta_{k-1}) - \theta_k^3 + \theta_k + \eta_k - C, \\ \tau_\eta \dot{\eta}_k &= \frac{L^2}{\delta^2}(\eta_{k+1} - 2\eta_k + \eta_{k-1}) - \eta_k - \theta_k.\end{aligned}$$

- The voltages θ_k could be used to drive, for example, electrostatic piston actuators.

BRAYTON-MOSER TECHNIQUE YIELDS A LYAPUNOV FUNCTION

- The dynamics (of the circuit realization) are (indefinite) gradient dynamics with respect to the energy function

$$V = \frac{l^2}{\delta^2} \left(\sum_k \theta_k^2 - \sum_k \theta_k \theta_{k+1} \right) + \frac{1}{4} \sum_k \theta_k^4 - \frac{1}{2} \sum_k \theta_k^2 - \sum_k \theta_k \eta_k - \frac{L^2}{\delta^2} \left(\sum_k \eta_k^2 - \sum_k \eta_k \eta_{k+1} \right) - \frac{1}{2} \sum_k \eta_k^2 + C \sum_k \eta_k.$$

- The matrix of second partial derivatives is

$$D^2V = \begin{bmatrix} P & -I \\ -I & Q \end{bmatrix}, \quad Q = -I + \frac{L^2}{\delta^2} \begin{bmatrix} -2 & 1 & 0 & \cdots & 1 \\ 1 & -2 & 1 & 0 & \vdots \\ 0 & 1 & -2 & 1 & 0 \\ \vdots & 0 & \ddots & \ddots & 1 \\ 1 & \cdots & 0 & 1 & -2 \end{bmatrix}.$$

- The Lyapunov function (when $\alpha > 1$) is

$$V^* = \frac{l^2}{\delta^2} \left(\sum_k \theta_k^2 - \sum_k \theta_k \theta_{k+1} \right) + \frac{1}{4} \sum_k \theta_k^4 - \frac{1}{2} \sum_k \theta_k^2 + \frac{L^2}{\delta^2} \left(\sum_k \eta_k^2 - \sum_k \eta_k \eta_{k+1} \right) + \frac{1}{2} \sum_k \eta_k^2 - C \sum_k \eta_k + \sum_k \theta_k \eta_k - (\theta - C\gamma)^T Q^{-1} (\theta - C\gamma),$$

where $\gamma = [1 \ 1 \ \cdots \ 1]^T$ (and Q is invertible).

- V^* is radially unbounded (implying global convergence).

SELECTED REFERENCES

- E.W. Justh and P.S. Krishnaprasad, "Analysis of a complex activator-inhibitor equation," *Proceedings of the American Control Conference*, pp. 1613-1617, 1999 (also ISR TR 99-13).
- E.W. Justh and P.S. Krishnaprasad, "A Lyapunov functional for the cubic nonlinearity activator-inhibitor model equation," *Proceedings of the IEEE Conference on Decision and Control*, pp. 1404-1409, 1998 (also ISR TR 98-36).
- E.W. Justh, "Control of Large Actuator Arrays using Pattern-Forming Systems," ISR Ph.D. Thesis Report 98-6, 1998.
- R.K. Brayton, J.K. Moser, "A Theory of Nonlinear Networks - I," *Quarterly of Applied Mathematics*, Vol. XXII, No. 1, pp. 1-33, 1964.
- B.S. Kerner, V.V. Osipov. *Autosolitons*. Kluwer Academic Publishers: Boston, 1994.
- Roger Temam. *Infinite-Dimensional Dynamical Systems in Mechanics and Physics*, 2nd Ed. Springer-Verlag, 1997.
- Lawrence Evans. *Partial Differential Equations*. Berkeley Mathematics Lecture Notes, 1994.

Nonlinear Control of a Parametrically Excited Structural Dynamic Model of an F-15 Tail Section

By
Ayman A. El-Badawy
Ali. H. Nayfeh

OUTLINE

- Introduction
- Model and experimental setup
- Mathematical model
- Control Law Development
 - Theoretical and Experimental Frequency-Response Curves
 - Theoretical and Experimental Force-Response Curves
 - Effect of Varying Gain on Transient Response
- Comments and Conclusions

INTRODUCTION



Buffet problem:

- Present aircraft require agility and high maneuvering at high AOA
- Induced buffeting flows occur when the airflow on the upper wing surface becomes detached
- This flow will induce high-frequency oscillations of the twin vertical tails in fighter aircraft
- In these flow situations, buffet of the tail surface occurs with a potential for fatigue induced structural failure

8/16/99

El-Badawy/Nayfeh

3

INTRODUCTION



The two most notable cases are the F-18 and F-15:

F-18:

- The flow field is dominated by strong vortices generated over the wing LEX
- These vortices undergo a rapid expansion and violent breakdown at certain flight conditions
- The tails are engulfed in intense broadband turbulent velocity fluctuations

8/16/99

El-Badawy/Nayfeh

4

INTRODUCTION



F-15: In the flow field

- No strong LEX vortex present
- The vortex motion present is referred to as wake-like
- Nearly periodic velocity fluctuations are present
- Their frequencies vary with AOA and velocity and “tune” to the tail structural modes

8/16/99

El-Badawy/Nayfeh

5

COEXISTING MULTIPLE RESPONSES



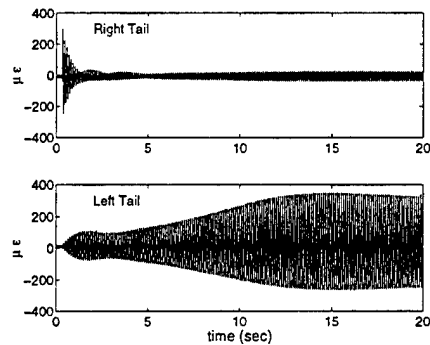
- Very small-amplitude motions of both tails
- Response of right tail > Response of left tail
- Response of left tail > Response of right tail
- In-phase response
- Out-of-phase response

8/16/99

El-Badawy/Nayfeh

6

ENERGY TRANSFER MECHANISM



8/16/99

El-Badawy/Nayfeh

7

Model



- The tail section used is a 1/16 dynamically scaled model of the F-15 tail assembly.
- Constructed by Professor S. Hanagud
- Dimensions: 0.355 m long, 0.28 m tall, and 0.482 m wide
- Constructed from a series of aluminum channels, brass rings, composite plates, metal masses,...

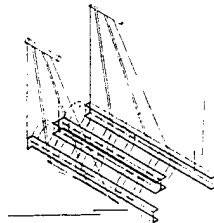


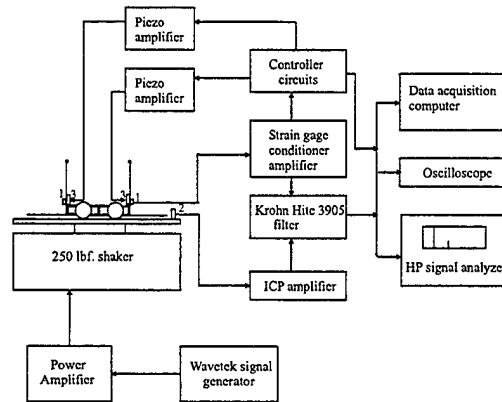
Figure 1: (i) Three-dimensional view of the twin-tail assembly

8/16/99

El-Badawy/Nayfeh

8

Experimental setup



1: MicroMeasurements strain gage CEA 06 125 UW 350
 2: Accelerometer PCB 303A02
 3: Piezo Systems PZT single sheet Part number : T107-H4E-602

8/16/99

El-Badawy/Nayfeh

9

MATHEMATICAL FORMULATION



$$\ddot{u}_1 + \omega_1^2 u_1 + 2\mu_1 \dot{u}_1 + \alpha_1 u_1^3 + \mu_3 \dot{u}_1 |\dot{u}_1| - \eta_1 k(u_2 - u_1) - u_1 \eta_1 F \cos(\Omega t + \tau_1) - T_1 = 0$$

$$\ddot{u}_2 + \omega_2^2 u_2 + 2\mu_2 \dot{u}_2 + \alpha_2 u_2^3 + \mu_4 \dot{u}_2 |\dot{u}_2| - \eta_2 k(u_1 - u_2) - u_2 \eta_2 F \cos(\Omega t + \tau_2) - T_2 = 0$$

where :

u_1, u_2 : modal coordinates (micro strains (μs))
 ω_1, ω_2 : natural frequencies (radian / s)
 μ_1, μ_2 : linear damping coefficients (radian / s)
 μ_3, μ_4 : aerodynamic damping coefficients. ($1/\mu s$)
 α_1, α_2 : coefficients of cubic nonlinearity ($1/\mu s^2 * s^2$)
 η_1, η_2 : transmissibility terms ($1/g * s^2$)
 k : coupling term. ($1/s^2$)
 T_1, T_2 : control forces

8/16/99

El-Badawy/Nayfeh

10

Development:

We used a control law given by cubic velocity feedback:

$$T_1 = -G_1 \dot{u}_1^3 \quad \& \quad T_2 = -G_2 \dot{u}_2^3$$

Performance:

- Calculate the equilibrium solutions of the modulation equations
- Examine their stability as a function of the parameters

F, σ and G

8/16/99

El-Badawy/Nayfeh

11

Theoretical Frequency-Response Curves

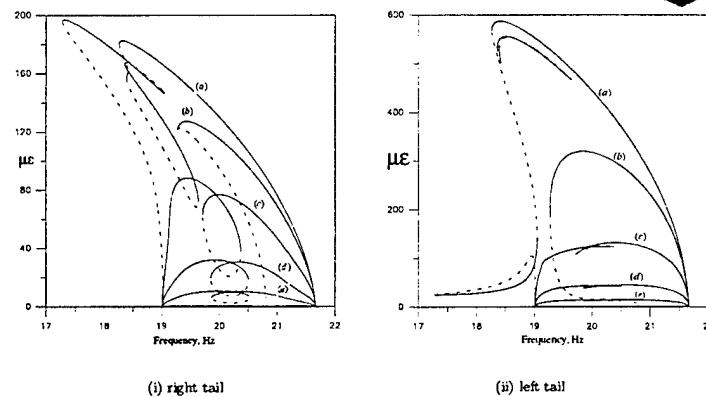


Figure 6: Effect of varying the feedback gain on the frequency-response curves of the specified tail ($F=3.2$ gs): a) $G=0$, b) $G=0.01$, c) $G=0.1$, d) $G=1$, e) $G=10$

8/16/99

El-Badawy/Nayfeh

12

Theoretical Force-Response Curves

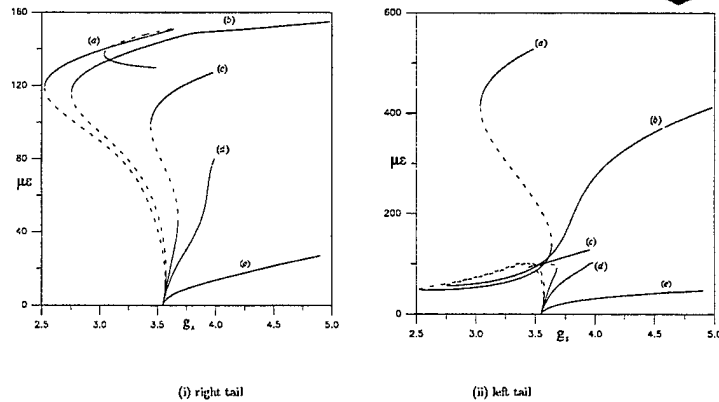


Figure 7: Effect of varying the feedback gain on the force-response curves of the specified tail (freq=18 Hz): a) $G=0$, b) $G=0.01$, c) $G=0.05$, d) $G=0.1$, e) $G=1$

8/16/99

El-Badawy/Nayfeh

13

Experimental Frequency-Response Curves

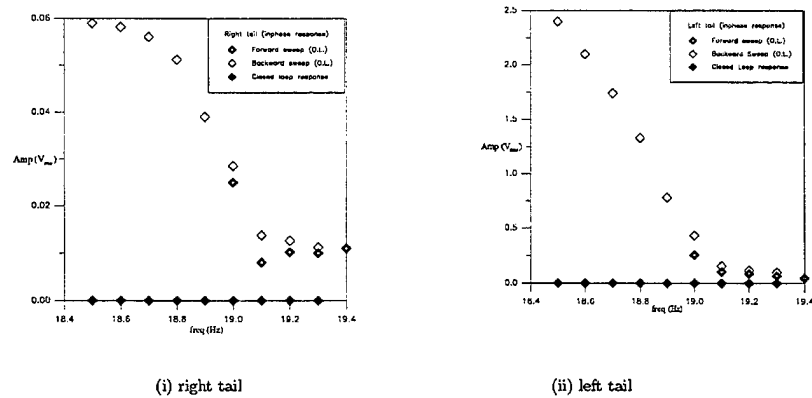


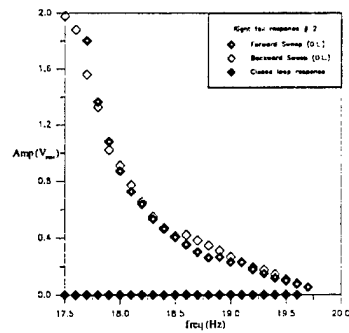
Figure 8: Frequency-response curves of the in-phase responses before and after control

8/16/99

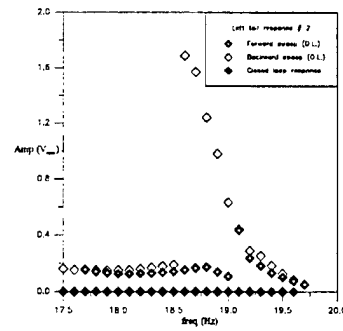
El-Badawy/Nayfeh

14

Experimental FRC continued



(i) right tail



(ii) left tail

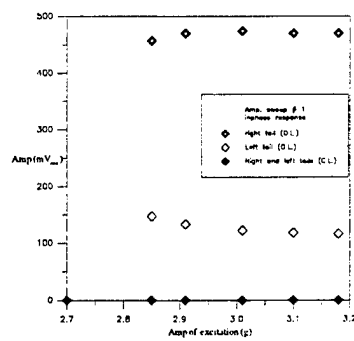
Figure 9: Frequency-response curves of the out-of-phase responses before and after control

8/16/99

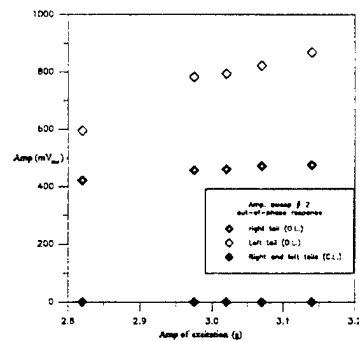
El-Badawy/Nayfeh

15

Experimental Force-Response Curves



(i) in-phase responses



(ii) out-of-phase responses

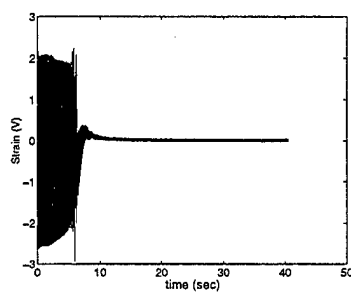
Figure 10: Force-response curves of the tails before and after control

8/16/99

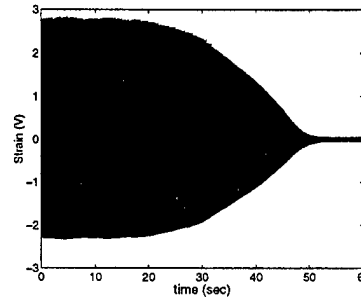
El-Badawy/Nayfeh

16

Effect of Varying the Gain on Transient Response



(i) right tail



(ii) left tail

Figure 11: Time histories of the responses of the tails before and after applying control for different control gains (a) $K_2 = 5K_1$, (b) $K_1 = 1$

8/16/99

El-Badawy/Nayfeh

17

CONCLUSIONS



- Described the problem and justified the need for nonlinear analysis.
- Developed a mathematical model of an 1/16 structural dynamic scale model of the F-15 aircraft.
- Implemented a cubic velocity feedback control law to suppress the vibrations of the scale model under principal parametric excitation.

8/16/99

El-Badawy/Nayfeh

18

Application of Linear Matrix Inequalities in the Control of Smart Structural Systems

Sridhar Sana and Vittal S. Rao

Electrical and Computer Engineering Department and Intelligent System Center
University of Missouri-Rolla, Rolla, MO 65401

Abstract

Smart structures have emerged as a result of effective integration of sensors, actuators and controller and signal processing with the structural systems. The smart structural systems found many applications in areas like aerospace, automotive and civil engineering. These structural systems need to consume less power, require less controller hardware and be robust to the system uncertainties. These constraints limit the complexity of the controller that can be integrated with the structures. The unmodeled dynamics resulting from truncating the plant model can some times lead to spill over problems. Additional uncertainties can also result from the parameter variations due to the environmental changes, operating conditions or aging of the structures. These unmodeled dynamics, structural parameter variations and limits on the control effort result in degradation in closed loop performance and some times cause instability. Hence, we need to design controllers using multi-objective design methodologies for guaranteed stability and maximum possible performance in the presence of the uncertainties.

In recent years, the concept of Linear Matrix Inequalities (LMIs) has been applied to several multi-objective controller design problems. We present a procedure for the formulation and design of controllers for smart structural systems using LMIs. Specifically, we consider the design of output feedback robust controllers with actuator limits and structured/unstructured uncertainties. The structured and unstructured uncertainties result from the parameter variations and the unmodeled dynamics in structural systems respectively. For ensuring the performance requirements, we select the appropriate locations for the closed loop poles. All these requirements on the controller design are formulated as a solution of a set of matrix inequalities in the design parameters. Some of these matrix inequalities are bilinear in the design variables and hence can not be solved using convex optimization techniques. Hence, we make use of a parameterization of the design parameters and change of variables to transform the set of bilinear matrix inequalities (BLMIs) into a set of LMIs. The controller parameters are recovered from the LMI solutions. The proposed controller design procedure is used for designing a robust controller for an experimental cantilever beam smart structure. This structure uses Lead Zirconite Titanate (PZT) patches for actuation and sensing. These actuators have limited amount of control effort. The designed controllers are tested and the results are presented.



Application of Linear Matrix Inequalities in the Control of Smart Structural Systems

Sridhar Sana and Vittal S. Rao

Department of Electrical and Computer Engineering

Intelligent Systems Center

University of Missouri-Rolla, Rolla, MO 65409

Fourth ARO Workshop on Smart Structures

August 16-18, 1999

Penn State, University Park Campus, Pennsylvania



Outline

- Introduction
- Multi Objective Design - Linear Matrix Inequalities (LMIs)
- Output Feedback Robust Controller Design
 - Parametric Uncertainties
 - Unmodeled Dynamics
 - Control Input Constraints
- Experimental Results
 - Robust Stability
 - Robust Performance
- Conclusions and Future work



Introduction

- Smart Structures involve integration of sensors, actuators and control systems into structural systems
- Objectives of the Control System:
 - Robustness to parametric uncertainty / unmodeled dynamics (spill-over effects)
 - Performance (Vibration Suppression)
 - Control input to be within limits for the specified set of disturbances and uncertainties.
- Design using Multi-Objective optimization:
 - Linear Matrix Inequalities (LMIs) are utilized to design an output feedback robust controllers
 - Feasible solution using all the objective functions.



- Parametric Uncertainties in Smart Structural Systems
 - Natural frequency variations
 - Damping factors
 - Normalized linear fractional representation
- Unmodeled Dynamics
 - High frequency dynamics
 - Treated as additive uncertainty
- Control input constraints
 - Saturation Limits
 - Constraints on every input of multi-input system

Linear Matrix Inequalities (LMIs)

- An Linear Matrix Inequality (LMI) is a constraint of the form

$$L(x) < 0 \quad \text{---(L.1)}$$

$$L_0 + L_1 x_1 + \dots + L_p x_p < 0 \quad \text{---(L.2)}$$

where $L(x)$ is a symmetric matrix and depends *affinely* on the vector $x \in R^p$

- Several LMIs in the same decision variable can be combined to form a single LMI.
- Solving an LMI implies finding a *feasible* vector x
- The solution set is convex and *convex optimization* algorithms like *interior point methods* can be applied
- LMI-Software:
 - LMITool-2.0: Front end for LMI optimization (Semidefinite Programming)
 - LMI Toolbox from Mathworks



Useful lemmas for LMI manipulation

- Schur's complement Lemma:

For any symmetric matrix Φ partitioned as Φ_{11} , Φ_{12} and Φ_{22} , the following are equivalent.

$$(1) \begin{bmatrix} \Phi_{11} & \Phi_{12} \\ \Phi_{12}^T & \Phi_{22} \end{bmatrix} > 0 \quad (2) \Phi_{11} > 0, \Phi_{22} > \Phi_{12}^T \Phi_{11}^{-1} \Phi_{12} \quad (3) \Phi_{22} > 0, \Phi_{11} > \Phi_{12} \Phi_{22}^{-1} \Phi_{12}^T$$

- Elimination Lemma:

For a real matrices G , U and V the following are equivalent

$$(1) G + V X^T U^T + U X V^T < 0 \text{ holds for some real matrix } X \quad (2) V^T G V < 0 \text{ and } U^T G U < 0$$

- S-procedure:

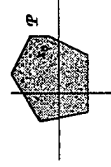
For real symmetric square matrices T_0, T_1, \dots, T_p , the condition,

$$x^T T_0 x > 0 \text{ holds for all } x \neq 0 \text{ such that } x^T T_i x \geq 0, i = 1, \dots, p$$

if there exist $\tau_1 \geq 0, \dots, \tau_p \geq 0$ such that $T_0 - \sum_{i=1}^p \tau_i T_i > 0$

Design Specifications

- A polytope \mathcal{P} of initial conditions is considered.



- $X(x_0)$: family of closed loop trajectories of the uncertain system in response to any given $x_0 \in \mathcal{P}$
- Specifications:
 - Maximum possible decay rate α and maximum possible damping for every trajectory in $X(x_0)$, that is

$$\lim_{t \rightarrow \infty} e^{-\alpha t} \bar{x}(t) = 0 \text{ where } \bar{x}(t) \text{ is a closed loop trajectory in } X(x_0)$$
 - For every trajectory in $X(x_0)$, each of the command inputs u_i satisfies for all $|u_i(t)| \leq u_{max}$ for all $t \geq 0$



Robust control in the presence of parametric uncertainties

- The identified model considered in the design:

$$\dot{x}_i = A_i x_i + B_i u$$

$$y = C_i x_i + D_i u$$

- Parameter Variation:

$$\omega_i^{min} \leq \omega_i \leq \omega_i^{max}$$

$$\zeta_i^{min} \leq \zeta_i \leq \zeta_i^{max}$$

- Normalized Linear Fractional Representation:

$$\dot{x} = Ax + B_u u + B_w w$$

$$y = C_x x + D_{yu} u + D_{yw} w$$

$$z_i = C_{zi} x + D_{zi} u + D_{zi} w$$

$$w = \Delta(\delta)z \text{ with } \|\Delta(\delta)\|_\infty \leq 1 \text{ and } \delta = (\delta_1, \delta_2, \dots)$$



Normalized Linear Fractional Representation

• Step 1: Transformation into Block Companion Form

$$\dot{x}_T = A_T x_T + B_T u$$

$$y = C_T x_T + D_T u$$

where,

$$A_T = \begin{bmatrix} p_1 & & & & & 0 \\ & \ddots & & & & \\ & & p_r & & & \\ & & 0 & -\omega_{s_1}^2 & & \\ & & 1 & -2\zeta_{s_1}\omega_{s_1} & & \\ & & & & \ddots & \\ 0 & & & & & -\omega_{s_m}^2 \\ & & & & & 1 & -2\zeta_{s_m}\omega_{s_m} \end{bmatrix}$$

r : number of simple poles

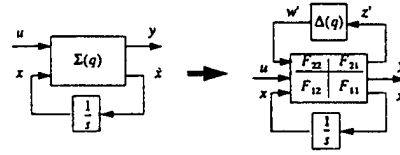
m : number of modes



• Step 2: Linear Fractional Representation

Uncertain State Space System:

$$\begin{pmatrix} \dot{x} \\ y \end{pmatrix} = \begin{bmatrix} D_T & C_T \\ B_T & A_T(q) \end{bmatrix} \begin{pmatrix} u \\ x \end{pmatrix} = \Sigma(q) \begin{pmatrix} u \\ x \end{pmatrix}$$



Structured Tree Decomposition:

$$\Sigma(q) = E + \sum_{i=1}^m U_i L_{i1}(q) L_{i2}(q) V_i \quad \text{with} \quad L_{i1}(q) = \begin{bmatrix} -\omega_{s_i} \\ -2\zeta_{s_i} \end{bmatrix}, L_{i2}(q) = \begin{bmatrix} \omega_{s_i} \end{bmatrix}$$

$$L_{i1}(q) L_{i2}(q) = L_{i2} + L_{i1} \Delta_i(q) (I - L_{i1} \Delta_i(q))^{-1} L_{i2} \quad \text{and} \quad \Delta_i(q) = \text{diag}(\omega_{s_i}, \omega_{s_i}, \zeta_{s_i})$$

$$\Sigma(q) = L(\Delta(q), F) = F_{22} + F_{21} \Delta(q) (I - F_{11} \Delta(q))^{-1} F_{12}$$

$$F_{22} = E + \sum_{i=1}^m U_i L_{i2} V_i, F_{21} = \begin{bmatrix} U_1 & U_2 & \dots & U_m \end{bmatrix} L_{21}, \quad F_{12} = L_{12} \begin{bmatrix} V_1 \\ \vdots \\ V_m \end{bmatrix}$$

$$F_{11} = \text{diag}(L_{11}, L_{11}, \dots, L_{11})$$

$$\Delta(q) = \text{diag}(\omega_{s_1}, \omega_{s_1}, \zeta_{s_1}, \omega_{s_2}, \omega_{s_2}, \zeta_{s_2}, \dots, \omega_{s_m}, \omega_{s_m}, \zeta_{s_m})$$



• Step 3: Normalization

$$q_i = a_i + b_i \delta_i$$

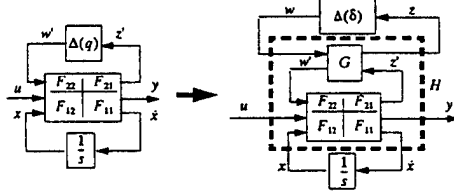
$$|\delta_i| \leq 1, a_i = \frac{1}{2}(q_i^+ + q_i^-) \quad \text{and} \quad b_i = \frac{1}{2}(q_i^+ - q_i^-)$$

$$\Delta(q) = L(\Delta(\delta), G)$$

$$G_{11} = 0, G_{12} = I, G_{21} = \text{diag}\{b_1, b_2, \dots, b_m\} \quad \text{and}$$

$$G_{22} = \text{diag}\{a_1, a_2, \dots, a_m\}$$

Normalized Linear Fractional Representation:



$$\Sigma(\delta) = L(L(\Delta(\delta), G), F) = L(\Delta(\delta), H)$$

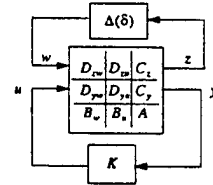
$$\begin{bmatrix} z \\ y \\ x \end{bmatrix} = \begin{bmatrix} H \end{bmatrix} \begin{bmatrix} w \\ u \\ x \end{bmatrix}$$

where $w = \Delta(\delta)z$ and H can be partitioned as

$$H = \begin{bmatrix} D_{1w} & D_{1z} & C_1 \\ D_{2w} & D_{2z} & C_2 \\ B_w & B_z & A \end{bmatrix}$$



Closed Loop System



• Controller K :

$$\dot{x}_c = A_c x_c + B_c y$$

$$u = C_c x_c$$

• Closed-loop Plant:

$$\dot{\bar{x}} = \bar{A} \bar{x} + \bar{B}_w w$$

$$z = \bar{C} \bar{x} + \bar{D}_w w$$

$$w = \Delta(\delta)z \quad \text{i.e.} \quad w_i^2 \leq z_i^2, i = 1, 2, \dots, n_p$$

where,

$$\bar{x} = \begin{bmatrix} x \\ x_c \end{bmatrix}, \bar{A} = \begin{bmatrix} A & B_c C_c \\ B_c C_c & A_c + B_c D_{22} C_c \end{bmatrix}, \bar{B}_w = \begin{bmatrix} B_w \\ B_c D_{22} \end{bmatrix}$$

$$\bar{C} = \begin{bmatrix} C & D_{22} C_c \end{bmatrix}, \bar{D}_w = D_{1w} \quad \text{and} \quad \bar{C}_c = \begin{bmatrix} 0 & C_c \end{bmatrix}$$

Matrix Inequality Formulation

- Robust α -stability:

Considering the Lyapunov Function $V(\bar{x}) = \bar{x}^T \bar{P} \bar{x}$.

$\exists \bar{P} > 0$ and $S = \text{diag}(\tau_1, \tau_2, \dots, \tau_s) > 0$ such that,

$$\begin{bmatrix} \bar{A}_0^T \bar{P} + \bar{P} \bar{A}_0 + \alpha \bar{P} + \bar{C}_i^T S \bar{C}_i & \text{sym} \\ \bar{B}_i^T \bar{P} + D_{i0}^T S \bar{C}_i & -S + D_{i0}^T S D_{i0} \end{bmatrix} < 0 \quad \text{--- (R)}$$

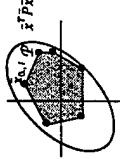
- Control Input Constraints:

$$\bar{x}_{a,i}^T \bar{P} \bar{x}_{a,i} \leq 1 \text{ for all vertices of the polytope } \mathcal{P} \quad \text{--- (C1)}$$

$$\text{and } \bar{x}^T(t) \begin{bmatrix} 0 \\ C_{i,j} \end{bmatrix} \bar{x}(t) < u_{a,i}^2, i \geq 0 \text{ for each control input } \quad \text{--- (C2)}$$

Upon ensuring the robust stability condition we have $\bar{x}^T \bar{P} \bar{x} < 1$, the (C1) constraint

becomes, $[0 \ C_{i,j}] \bar{P}^{-1} \begin{bmatrix} 0 \\ C_{i,j} \end{bmatrix} < u_{a,i}^2$ for each control input $\quad \text{--- (C2)}$



Elimination of controller variables

- Parameterizations:

$$\bar{P} = \begin{bmatrix} P & M \\ M^T & \bar{P} \end{bmatrix} \quad \bar{Q} = \begin{bmatrix} Q & N \\ N^T & \bar{Q} \end{bmatrix}$$

with $\bar{Q} = \bar{P}^{-1}$, $N = (I - QP)M^T$, $\bar{P} = M^T(P - Q^{-1})^{-1}M$ and $\bar{Q} = N^T(Q - P^{-1})^{-1}N$

- Definitions: $Y = C_i N^T$; $Z = M B_i$

- Elimination of A_i from Robust Stability Condition:

$$G(\bar{P}, S) + U(\bar{P}) A_i V^T + V A_i^T U(\bar{P})^T < 0 \quad \text{--- (R)}$$

where,

$$G(\bar{P}, S) = \begin{bmatrix} \bar{A}_0^T \bar{P} + \bar{P} \bar{A}_0 + \alpha \bar{P} + \bar{C}_i^T S \bar{C}_i & \text{sym} \\ \bar{B}_i^T \bar{P} + D_{i0}^T S \bar{C}_i & -S + D_{i0}^T S D_{i0} \end{bmatrix}, \bar{A}_0 = \begin{bmatrix} A & B_i C_i \\ B_i C_i & B_i D_{i0} C_i \end{bmatrix}, j = \begin{bmatrix} 0 \\ j \end{bmatrix}, U(\bar{P}) = \begin{bmatrix} \bar{P} \\ 0 \end{bmatrix}$$

and $V = \begin{bmatrix} j \\ 0 \end{bmatrix}$

LMI problem for Robust Stability

The closed loop system is robustly α -stable if $\exists \bar{P}, Q > 0, S, T \in D(n_i), \forall i \in R^{+*}$ and $Z \in R^{+*}$, such that

$$\begin{bmatrix} P & I \\ I & Q \end{bmatrix} \geq 0 \quad \text{--- (R1)}$$

$$\begin{bmatrix} A_i^T P + P A_i + \alpha P + Z C_i + C_i^T Z^T + \bar{C}_i^T S \bar{C}_i & \text{sym} \\ B_i^T P + D_{i0}^T S \bar{C}_i + D_{i0}^T S \bar{C}_i & -S \end{bmatrix} < 0 \quad \text{--- (R2)}$$

$$\begin{bmatrix} Q A_i^T + A_i Q + \alpha Q + B_i Y + Y^T B_i^T + B_i T B_i^T & \text{sym} \\ C_i Q + D_{i0} Y + D_{i0} T B_i^T & D_{i0} T D_{i0}^T - I \end{bmatrix} < 0 \quad \text{--- (R3)}$$

$$S T = I \quad \text{--- (R4)}$$

where

$$D(n) = \{\text{diag}(\tau_1, \tau_2, \dots, \tau_n), \tau_i > 0, i = 1, 2, \dots, n\}$$

LMI conditions for control input constraints

With the use of parameterizations and $x_i = 0$ the LMI problem for satisfying $|u_i(t)| < u_{a,i}$ for all $t \geq 0$ for each of the control inputs is

Find P, Q and Y

$$x_{a,i}^T P x_{a,i} \leq 1 \text{ for every initial condition } x_0 \text{ in polytope } \mathcal{P} \quad \text{--- (C1)}$$

and

$$\begin{bmatrix} 0 & C_{i,j} \end{bmatrix} \begin{bmatrix} Q & N \\ N^T & Q - P^{-1} \end{bmatrix} \begin{bmatrix} 0 \\ C_{i,j} \end{bmatrix} < u_{a,i}^2 \quad \text{--- (C2)}$$

or equivalently with the use of Schur complement Lemma

$$\begin{bmatrix} u_{a,i}^2 & Y_i & 0 \\ Y_i^T & Q & I \\ 0 & I & P \end{bmatrix} \geq 0 \text{ where } Y_i = C_{i,j} N^T \quad \text{--- (C2)}$$

for each control input i

Solution of the controller design problem

- Cone complementarity Linearization Algorithm: (El Ghaoui et. al)

minimize $\text{Tr}(S^T)$ subject to

$$\begin{bmatrix} S & I \\ I & T \end{bmatrix} \geq 0 \quad \text{---(E)}$$

along with the robust stability(R1,R2,R3) and control input conditions(C1,C2)

- Solution of the optimization problem

(1) Find s, τ that satisfy the LMIs E,R1,R2,R3,C1,C2. If the problem is infeasible, stop.

Otherwise, set $k = 1$

(2) Find s_k, τ_k which solve the LMI optimization problem,

minimize $\text{Tr}(s_{k-1}T_k + s_kT_{k-1})$ subject to the LMIs E,R1,R2,R3,C1,C2

(3) If the objective $\text{Tr}(s_{k-1}T_k + s_kT_{k-1})$ has reached a stationary point, stop. Otherwise, set $k = k + 1$ and go to step(2).

Reconstruction of the controller

- Select an invertible matrix for M

- Find $N = (I - QP)M^T$

- Find C_c and B_c from

$$Y = C_c N^T \text{ and } Z = MB_c$$

- Form \tilde{P} as

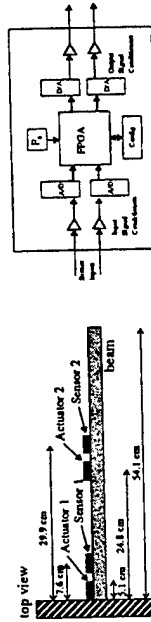
$$\tilde{P} = \begin{bmatrix} P & M \\ M^T & \tilde{P} \end{bmatrix}$$

- Solve the following inequality for A_c in the robust stability condition (R)

$$\begin{bmatrix} A & B_c C_c \\ B_c C_c A + B_c D_{cc} C_c \end{bmatrix}^T \tilde{P} + \tilde{P} \begin{bmatrix} A & B_c C_c \\ B_c C_c A + B_c D_{cc} C_c \end{bmatrix} + \alpha \tilde{P} + \tilde{C}_c^T \tilde{C}_c \quad \text{sym} \quad < 0 \quad \text{---(R)}$$

$$\tilde{B}_c^T \tilde{P} + D_{cc}^T \tilde{S} \tilde{C}_c \quad \text{---} S + D_{cc}^T \tilde{S} D_{cc}$$

Experimental Setup



Test Structure

Controller Board

- Lead Zirconite Titanate (PZT) patches are used as actuators and sensors
- First two modes are at 8.73 Hz and 52.74 Hz with damping of 1%
- Control Input Limit: $\pm 5v$
- Field Programmable Gate Array (FPGA) based controller board is used
- The controller board is stand alone and is reconfigurable

Parametric Uncertainty representation

- Uncertainty: $\pm 5\%$ in natural frequencies and $\pm 10\%$ in damping ratios

- Normalized Linear Fractional Representation:

$$A = \begin{bmatrix} -0.5628 & -54.8213 & -0.1055 & -0.0990 \\ -54.8214 & -0.5337 & -0.1034 & -0.0971 \\ -0.0006 & 0.0009 & -3.4936 & -3.313468 \\ 0.0008 & -0.0005 & 3.113468 & -3.1337 \end{bmatrix}, B_u = \begin{bmatrix} 0.1627 \\ -0.1603 \\ 2.4139 \\ -2.2635 \end{bmatrix}, B_w = \begin{bmatrix} 0.4419 & -24.7094 & 0.0088 \\ -0.4435 & 23.8232 & 0.0089 \\ 0 & 0.0001 & 0 \\ 0 & 0.0001 & 0 \end{bmatrix}$$

$$C_y^T = \begin{bmatrix} -23.7202 & -22.8029 & -2.4139 & -2.2635 \\ -3.1024 & 0.0566 & -6.2048 & -3.0916 & 0.0564 & -6.1833 \\ 0.0019 & 0 & 0.0038 & -0.0020 & 0 & 0.0040 \end{bmatrix}, D_{yu} = \begin{bmatrix} 0 & 0 & 0 \end{bmatrix}, D_{yw} = \begin{bmatrix} 0 & 0 & 0 \end{bmatrix}$$

$$D_{yu} = [0.17], D_{yw} = [0 \ 0 \ 0]$$

$$D_{yu} = \begin{bmatrix} 0 & -2.7412 & 0 \\ 0 & -5.4824 & 0 \\ 0 & 0 & 0 \end{bmatrix} \text{ and } D_{yw} = \begin{bmatrix} 0 & -2.7412 & 0 \\ 0 & -5.4824 & 0 \\ 0 & 0 & 0 \end{bmatrix}$$

**Controller Design (Parametric Uncertainties)**

- Vertices for the initial condition set are chosen such that they result in a sensor output of $\pm 3v$ for each mode.
- A decay rate α of 3.3 is achieved upon specifying an α of 0.1.
- Controller Matrices:

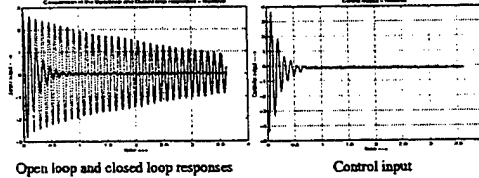
$$A_c = \begin{bmatrix} -33.522 & 24.7 & -20.036 & 35747 \\ -24.7 & -34.463 & 315.95 & -1.0802e5 \\ -20.036 & -315.95 & -42.317 & 1.4438e5 \\ -35747 & -1.0803e5 & -1.4438e5 & -3.0614e9 \end{bmatrix}$$

$$B_c = \begin{bmatrix} -9.4009 \\ -3.0977 \\ -3.0426 \\ -4997 \end{bmatrix} \text{ and } C_c^T = \begin{bmatrix} 9.4009 \\ -3.0977 \\ 3.0426 \\ -4997 \end{bmatrix}$$

- μ stability tests resulted in a $\mu^{-1} = 9.797$ which shows robust stability to the uncertainty.

**Experimental Results**

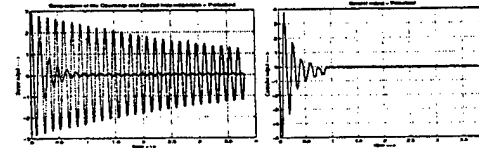
- Responses for the Nominal Plant



Open loop and closed loop responses

Control input

- Responses for the Perturbed Plant (First Mode changed from 8.73 hz to 6.82 hz)



Open loop and closed loop responses

Control input

**Robust control in the presence of Unmodeled dynamics**

- The unmodeled dynamics is considered as additive uncertainty

$$G_{\text{actual}} = G_{\text{nom}} + \Delta_{\text{additive}}$$

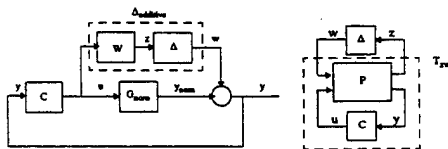


Figure 1. Additive Uncertainty Representation

$$\Delta_{\text{additive}} = W\Delta \text{ such that } \|\Delta\|_{\infty} < 1$$

- The generalized plant P is given by,

$$\dot{x} = Ax + B_p u + B_w w$$

$$y = C_p x + D_{pw} u + D_{yw} w$$

$$z = C_z x + D_{zw} u + D_{zw} w$$

$$z = \Delta w$$

- Controller C is given by,

$$\dot{\hat{x}}_c = A_c \hat{x}_c + B_c y$$

$$u = C_c \hat{x}_c$$



- Closed loop system is given by

$$\dot{\tilde{x}} = \tilde{A}\tilde{x} + \tilde{B}_w w$$

$$z = \tilde{C}_z \tilde{x} + D_{zw} w$$

$$u = \tilde{C}_u \tilde{x} \text{ and}$$

$$z = \Delta w \text{ with } \|\Delta\|_{\infty} \leq 1$$

where

$$\tilde{A} = \begin{bmatrix} A & B_w C_c \\ B_c C_p & A_c + B_c D_{pw} C_p \end{bmatrix}, \tilde{B}_w = \begin{bmatrix} B_w \\ B_c D_{pw} \end{bmatrix}, \tilde{C}_z^T = \begin{bmatrix} C_z^T \\ C_c^T D_{zw}^T \end{bmatrix}, \tilde{C}_u^T = \begin{bmatrix} 0 \\ C_c^T \end{bmatrix} \text{ and}$$

$$\tilde{x} = \begin{bmatrix} x \\ \hat{x}_c \end{bmatrix}$$

- Condition for Robust Stability (Small Gain Theorem):

$$\|T_{zw}\|_{\infty} \|\Delta\|_{\infty} < 1 \text{ implies } \|T_{zw}\|_{\infty} < 1 \text{ or equivalently } \|z\|_2 < \|w\|_2$$

- Lyapunov formulation of Robust Stability with $v(\tilde{x}) = \tilde{x}^T X \tilde{x}$:

$$\exists X_{\infty} = X_{\infty}^T > 0 \text{ such that } \dot{v}(\tilde{x}) + (z^T z - w^T w) < 0$$

- LMI formulation:

$$\exists X_{\infty} = X_{\infty}^T > 0 \text{ such that, } \begin{bmatrix} \tilde{A} X_{\infty} + X_{\infty} \tilde{A}^T & X_{\infty} \tilde{B}_w & \tilde{C}_z^T \\ \tilde{B}_w^T X_{\infty} & -I & D_{zw}^T \\ \tilde{C}_z & D_{zw} & -I \end{bmatrix} < 0$$



Specifications on closed loop pole locations

- Performance is specified in terms of constraints on the closed-loop pole locations in the complex plane C
- LMI-region (Chilali et al, 1997): Subset D of the complex plane, given by

$$D = \{z \in C: f(z) < 0\} \text{ with } f(z) = L + zM + z^*M^T$$

where L and M are real matrices such that $L^T = L$

- Examples of LMI regions:

 1. half-plane $\text{Re}(z) < -\alpha$: $f_D(z) = z + \bar{z} + 2\alpha < 0$, $L = 2\alpha$ and $M = 1$
 2. conic-sector with apex at the origin and inner angle 2θ :

$$f_D(z) = \begin{bmatrix} \sin\theta(z + \bar{z}) & \cos\theta(z - \bar{z}) \\ -\cos\theta(z - \bar{z}) & \sin\theta(z + \bar{z}) \end{bmatrix}, L = \begin{bmatrix} 0 & 0 \\ 0 & 0 \end{bmatrix} \text{ and } M = \begin{bmatrix} \sin\theta & \cos\theta \\ -\cos\theta & \sin\theta \end{bmatrix}$$

- Intersection of LMI-regions is also an LMI-region
- Arbitrary regions symmetric with respect to real-axis can be approximated by LMI-regions
- LMI Formulation: For each LMI-region with L_i and M_i ,

$$\exists X_c = X_c^T > 0 \text{ such that } L_i \otimes X + M_i \otimes (X, \bar{A}) + M_i^T (\bar{A}^T X_c) < 0$$



Control Input Constraints

- The control input constraints are defined on a set of initial conditions defined by an ellipsoid E :

$$\bar{x}_0^T X_c \bar{x}_0 < 1 \text{ where } X_c > 0$$

- Any polytope P of initial conditions can be covered by the ellipsoid by satisfying
$$\exists X_c = X_c^T > 0 \text{ such that } \bar{x}_0^T X_c \bar{x}_0 < 1 \text{ for each vertex } \bar{x}_0 \text{ of } P$$
- $S(\bar{x}_0)$ is the family of closed loop state trajectories for all \bar{x}_0 in P
- By satisfying the stability requirements with the Lyapunov function $V(\bar{x}) = \bar{x}^T X_c \bar{x} > 0$ we have,

$$\bar{x}^T X_c \bar{x} < 1 \text{ for all } S(\bar{x}_0)$$

- The constraint on each control input is given by,

$$u_i^2 < u_{max,i}^2 \text{ for all } S(\bar{x}_0)$$

$$\bar{x}^T \bar{C}_{u,i}^T (u_{max,i}^{-2}) \bar{C}_{u,i} \bar{x} < 1 \text{ for all } S(\bar{x}_0)$$

- The inequality condition on each control input:

$$\exists X_c = X_c^T > 0 \text{ such that } \bar{C}_{u,i}^T (u_{max,i}^{-2}) \bar{C}_{u,i} < X_c$$



Controller Synthesis

- Multi Objective Design:

Find $X = X^T > 0$, A_c , B_c and C_c such that the closed loop system satisfies the conditions robust stability, regional pole placement and control input constraints with $X = X_c = X_c^T$,

- This problem is not an LMI feasibility problem in X , A_c , B_c and C_c , since the variables appear bilinearly.

- With the use of the parametrizations (C. Scherer et al, 1997)

$$X = \begin{bmatrix} R & N \\ N^T & U \end{bmatrix} \text{ and } X^{-1} = \begin{bmatrix} S & M \\ M^T & V \end{bmatrix}$$

where $R = R^T > 0$ and $S = S^T > 0$ and $NM^T = I - RS$ and the change of variables,

$$A_K = RAS + RB_c C_K + B_K C_c S + NA_c M^T + B_K D_{KK} C_K$$

$$B_K = NB_c \text{ and } C_K = C_c M^T$$

the matrix inequalities are transformed into LMIs in the variables R , S , A_K , B_K and C_K .



- Robust Stability:

$$\begin{bmatrix} \Phi_{11} + \Phi_{11}^T & \Phi_{12} & \Phi_{13} \\ \Phi_{12}^T & -I & D_{12}^T \\ \Phi_{13}^T & D_{12} & -I \end{bmatrix} < 0$$

- Regional Pole Placement:

$$L_i \otimes \begin{bmatrix} S & I \\ I & R \end{bmatrix} + M_i \otimes \Phi_{11} + M_i^T \otimes \Phi_{11}^T < 0 \text{ for } i = 1, 2, \dots, n_r$$

- Control input Constraint:

$$\begin{bmatrix} u_{max,i}^2 & C_{K,i} & 0 \\ C_{K,i}^T & S & I \\ 0 & I & R \end{bmatrix} > 0 \text{ for each } i = 1, 2, \dots, n_u$$

and with $x_{0,i} = 0$, $\bar{x}_{0,i}^T R \bar{x}_{0,i} < 1$ for all $\bar{x}_{0,i}$

$$\text{where, } \Phi_{11} = \begin{bmatrix} AS + B_c C_K & A \\ A_K & RA + B_K C_K \end{bmatrix}, \Phi_{12} = \begin{bmatrix} B_c \\ RB_c + B_K D_{KK} \end{bmatrix},$$

$$\Phi_{13} = \begin{bmatrix} SC_c^T + C_K^T D_{KK}^T \\ C_c^T \end{bmatrix}$$

- The controller variables, A_c , B_c and C_c are calculated back from the solution R , S , A_K , B_K and C_K .



Specifications

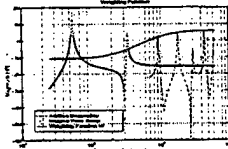


Figure 2a: Weighting function

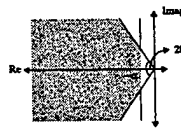


Figure 2b: LMI-region specification

- Robust Stability:

$$\|T_{\text{out}}\|_{\infty} \|W\|_{\infty} < 1 \text{ with } W(s) = \frac{2(s+300)(s+300)}{(s+700)(s+900)}$$

- Robust Regional Pole Placement:

Maximum possible decay rate α and minimum possible θ

- Control input Constraint:

Vertices for the initial condition set:

$$x_{0,1} = [-1.1038 \ -0.0094 \ 0.0048 \ 0.0043 \ 0 \ 0]^T$$

$$x_{0,2} = [-0.0053 \ -0.0055 \ -0.5214 \ 0.7629 \ 0 \ 0]^T$$

$$u_{\text{max}} = 5v$$



Results

- A 6th order controller was designed.
- A feasible solution was obtained for $\alpha = 2.5$ and $\theta = \frac{79\pi}{160}$
- Closed loop Damping:
 - First mode: 6.27%
 - Second mode: 2.2%



Figure 3a: Open-loop and Closed-loop pole locations

- Responses for the First Mode:

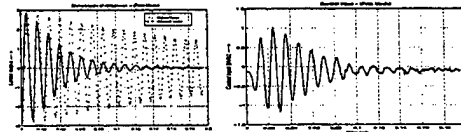


Figure 4: Controller Performance (First Mode)



Robustness tests

- Robust Stability: $\|T_{\text{out}}\|_{\infty} < 1 \Leftrightarrow |T_{\text{out}}(\omega)|^{-1} > |W(\omega)|$ for all ω

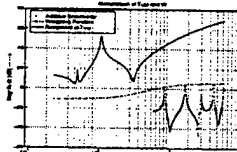


Figure 5b: Robustness Analysis

- The closed loop system with an 8th order model had a minimum decay rate of 3.35 and minimum global damping of 2.17%
- Experimental Test:

The third mode (147.2 Hz) was excited to $\pm 1v$ and the first mode is excited to an additional $\pm 3v$

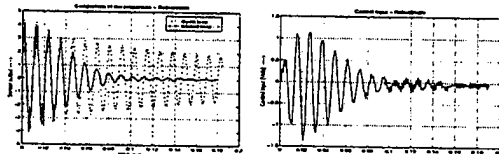


Figure 6: Robustness Verification



Conclusions and Future Work

- Linear Matrix Inequalities (LMIs) are used to design output feedback robust controllers for structural systems with control input limits in the presence of parametric uncertainties and unmodeled dynamics. Both the designs are experimentally tested.
- This approach allows the designer to concentrate on the performance requirements without worrying about the robustness or control input violations.
- Both the designs resulted in conservative controllers.
- Output feedback robust controller in the presence of both parametric uncertainty and unmodeled dynamics will be investigated.
- Better analysis tools for robust stability like Popov stability criteria or some relaxation approaches will be used to reduce conservatism.
- Reduced order controller design.

MODELING AND CONTROL ISSUES CONCERNING SMART MATERIALS WITH HYSTERESIS

Ralph C. Smith

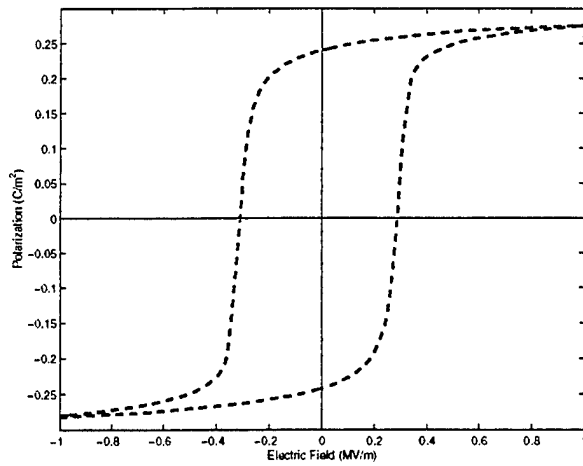
Center for Research in Scientific Computation

Department of Mathematics

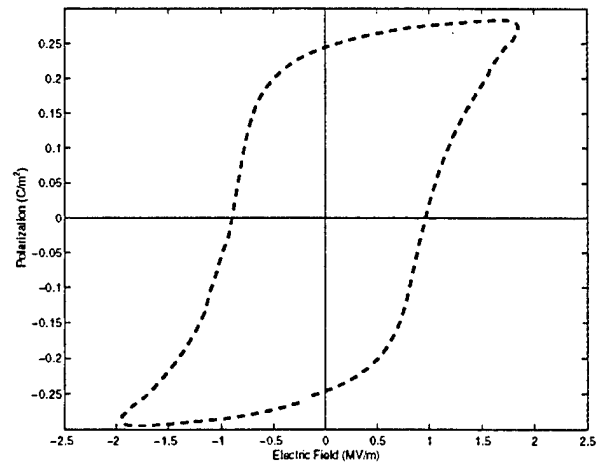
North Carolina State University

- Marcelo Dapino, Iowa State University
- Alison Flatau, Iowa State University
- Craig Hom, Lockheed Martin
- Zoubeida Ounaies, ICASE, NASA Langley Research Center
- Rick Zrostlik, Etrema Products

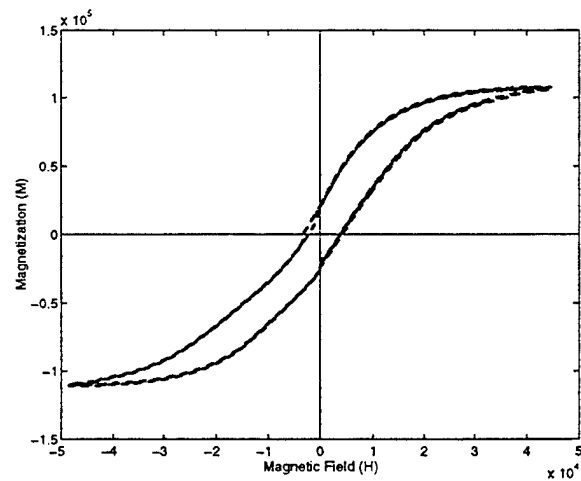
MODEL CRITERIA



Relaxor Ferroelectric Data



Piezoceramic Data



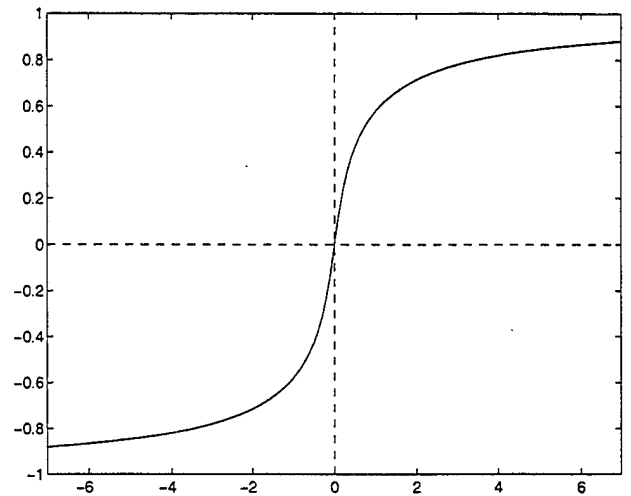
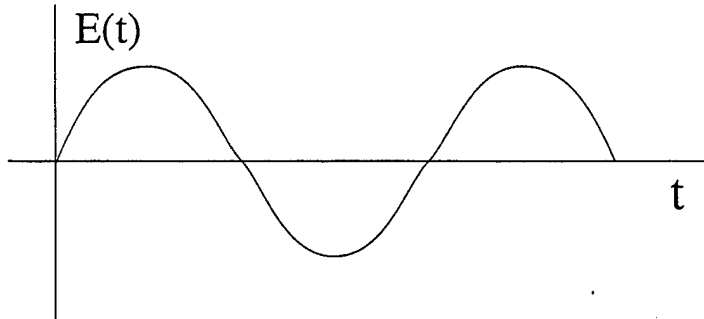
Magnetostrictive Data

Goals:

- Develop models which encompass both ferroelectric and ferromagnetic materials
- Models should be amenable to control design (small number of parameters)

ANHYSTERETIC POLARIZATION

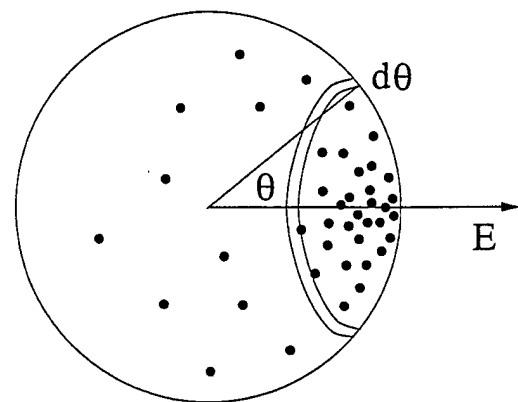
Note: In materials free from defects, polarization exhibits no hysteresis.



Modeling Approach: Employ Boltzmann statistics to determine the probability

$$\mu(\mathcal{E}) = C e^{-\mathcal{E}/K_B T}$$

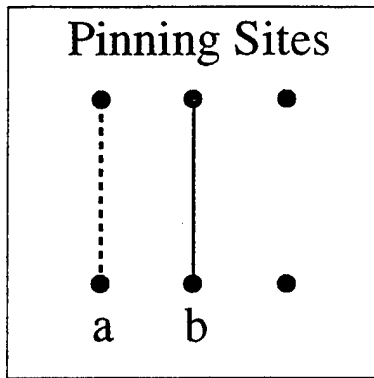
that a dipole occupies the energy state $\mathcal{E} = -p_0 E \cos \theta$.



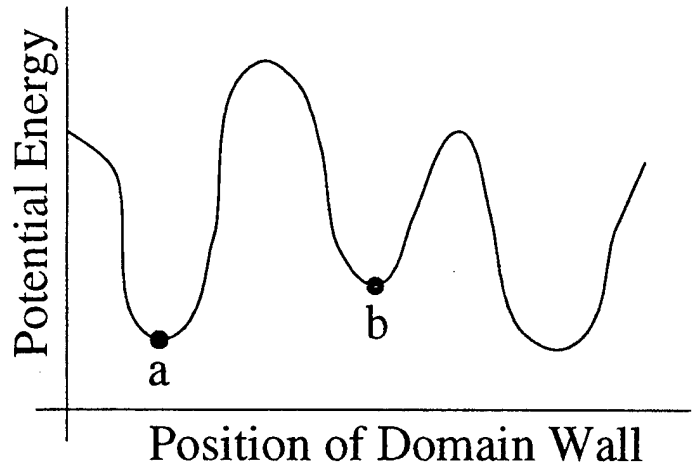
Langevin Model: Assuming that cells can orient in any direction yields

$$P_{an} = P_s [\coth(E_e/a) - (a/E_e)]$$

IRREVERSIBLE POLARIZATION



Domain Wall Translation



Pinning Energy: The energy required to break pinning sites can be expressed as

$$\mathcal{E}_{pin}(P) = -k \int_0^P dP$$

where $k = \frac{n \langle \varepsilon_\pi \rangle}{2p}$.

Work in Polarization Process:

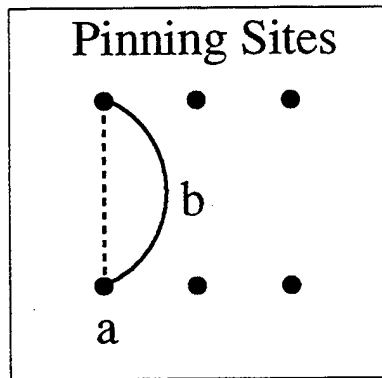
Energy Supplied = Change in Electrostatic Energy + Hysteresis Loss

$$\frac{1}{\epsilon_0} \int_0^{D_e} P_{irr}(E_e) dD_e = \frac{1}{\epsilon_0} \int_0^{D_e} P_{an}(E_e) dD_e - \int_0^{D_e} k \frac{dP_{irr}}{dD_e} dD_e$$

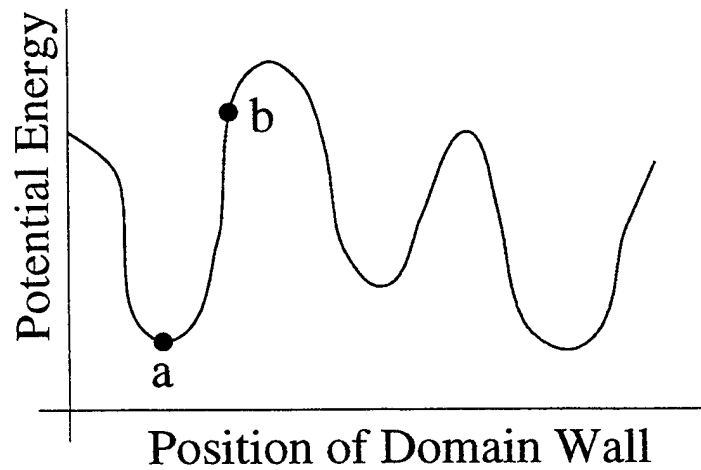
$$\Rightarrow P_{irr} = P_{an} - \delta \epsilon_0 k \frac{dP_{irr}}{dD_e}$$

$$\Rightarrow \frac{dP_{irr}}{dE} = \frac{P_{an} - P_{irr}}{\delta k - \alpha(P_{an} - P_{irr})}$$

REVERSIBLE POLARIZATION



Domain Wall Bending



Strategy:

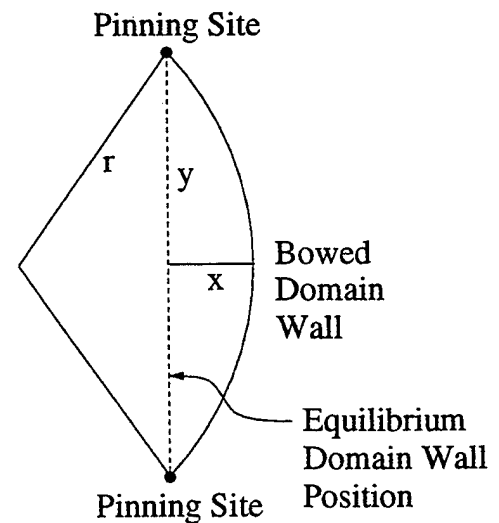
- (1) Energy balancing provides the relation

$$F = k(P_{an} - P)$$

for the force on the domain wall.

- (2) Computation of the displaced volume and resulting polarization yields the reversible component

$$P_{rev} = c(P_{an} - P).$$



ALTERNATIVE FORMULATION AND MODEL INVERSE

Model: For the Ising spin model, the polarization is given by

$$\frac{dP}{dE} = \mathcal{F}(E, P)$$

$$P(E_0) = P_0$$

where

$$\mathcal{F}(E, P) = \frac{1}{1 - \frac{cP_s\alpha}{a}\text{sech}^2\left(\frac{E+\alpha P}{a}\right)} \cdot \left\{ \frac{\tilde{\delta} \left[P_s \tanh\left(\frac{E+\alpha P}{a}\right) - P \right]}{k\delta - \tilde{\alpha} \left[P_s \tanh\left(\frac{E+\alpha P}{a}\right) - P \right]} + \frac{cP_s}{a}\text{sech}^2\left(\frac{E+\alpha P}{a}\right) \right\}.$$

Inverse Model: The inverse is then computed via

$$\frac{dP^{-1}}{dE} = \frac{1}{\mathcal{F}(P^{-1}, E)}$$

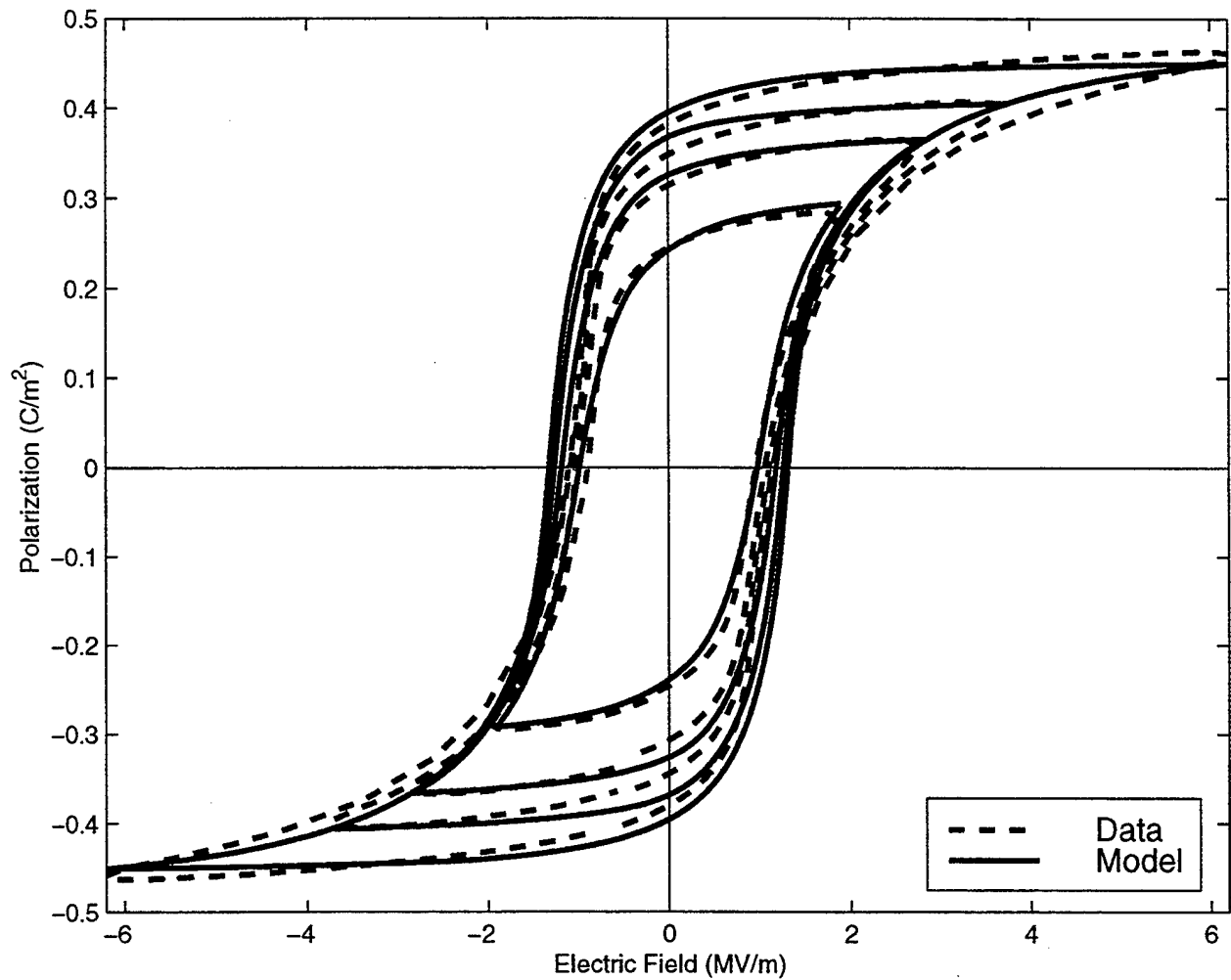
$$P^{-1}(E_0) = P_0^{-1}$$

Control Design:

- Filter the control signal through the inverse before inputting it to the actuator.
- The inverse compensates for the nonlinearities and hysteresis and permits linear control design.

EXPERIMENTAL VALIDATION

Piezoceramic (PZT-5A):



Experimental Conditions:

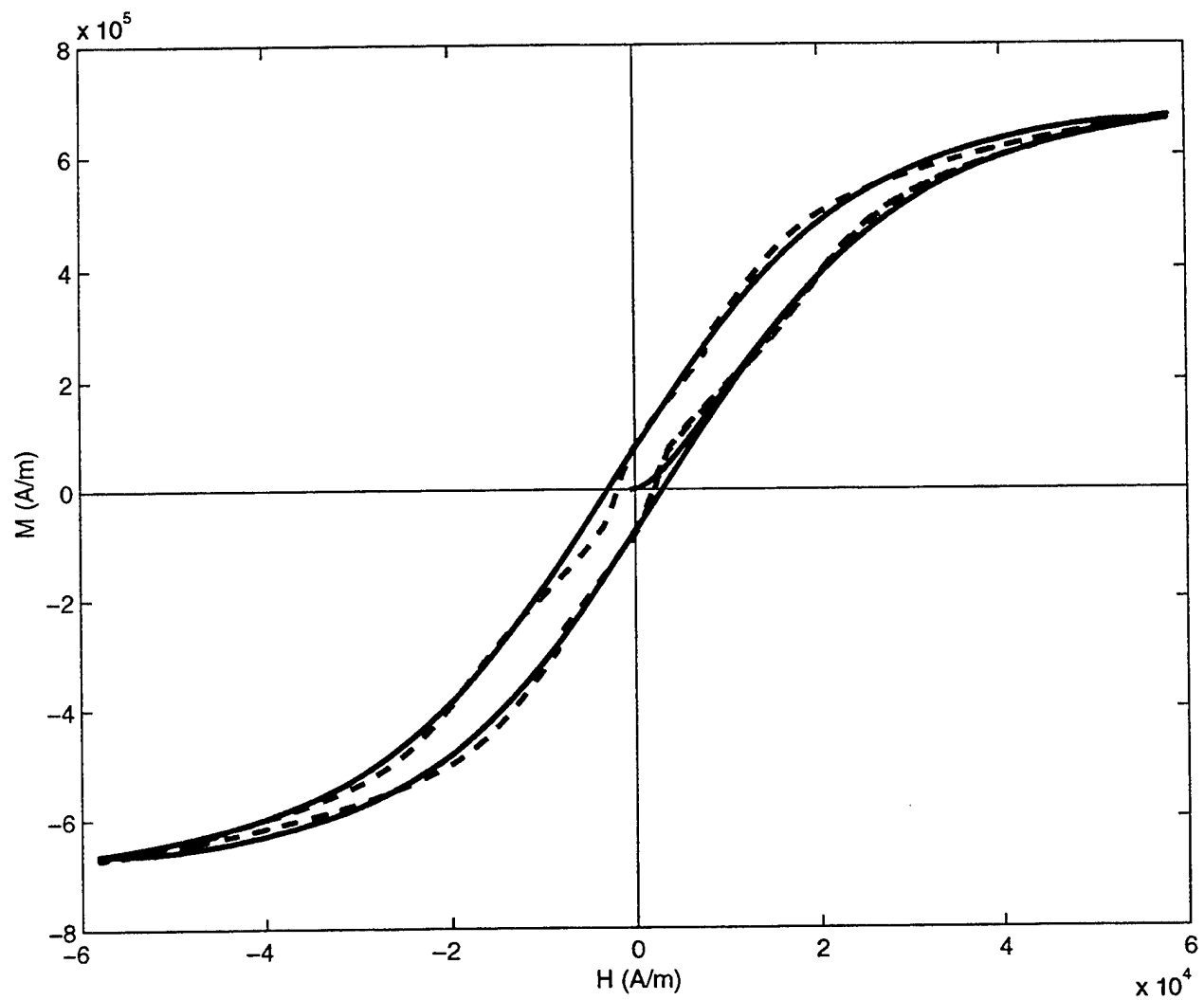
- Data collected by Zoubeida Ounaies, ICASE, NASA LaRC
- Quasistatic operation (0.2 Hz)
- Maximum inputs of 600 V, 800 V, 1000 V, 1600 V

Note:

- One set of parameters α, a, c, k, P_s for all four cases.

EXPERIMENTAL VALIDATION

(2) Magnetostrictive Materials: (Terfenol-D)

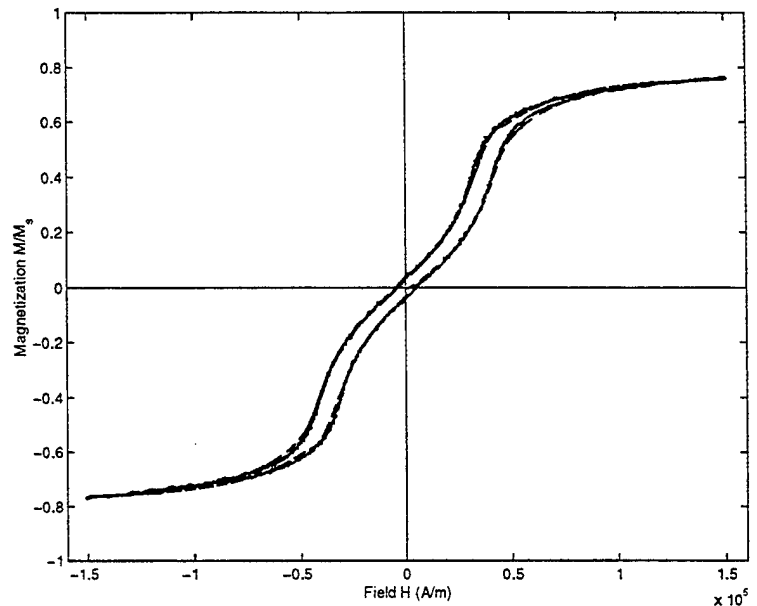


- [Dapino, Smith, Flatau, 1998]

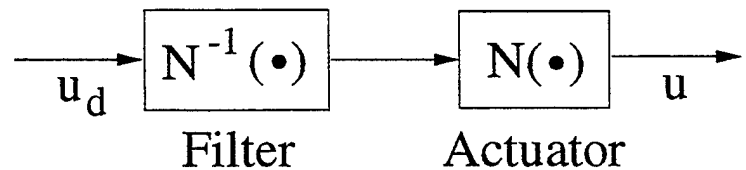
EXPERIMENTAL VALIDATION

(1) Model Validation:

- Model
- - - Experimental Data
(Rick Zrostlik, Etrema
Products, Inc.)

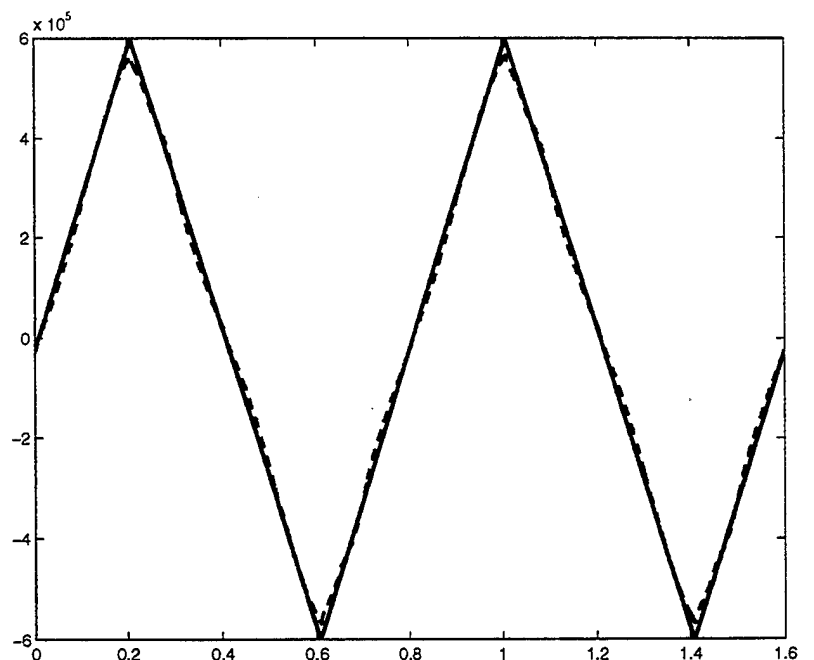


(2) Inverse Compensator:



- Treat inverse $N^{-1}(\cdot)$ as a filter before actuator.

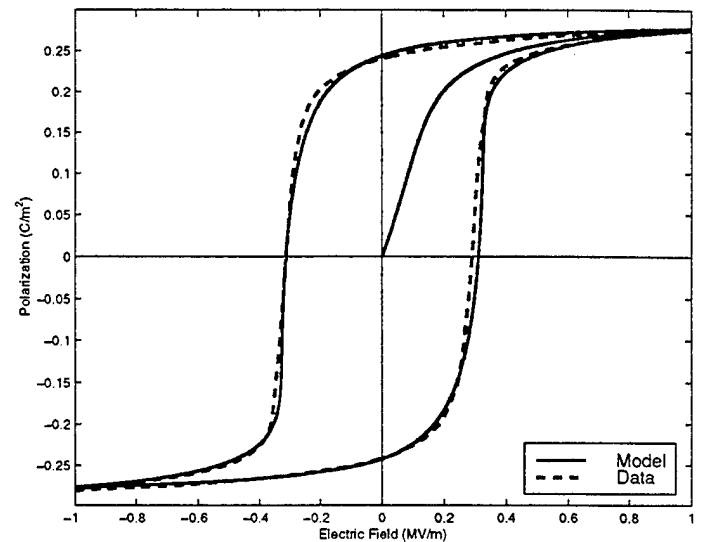
- Desired Input u_d
- - - Experimental Input u



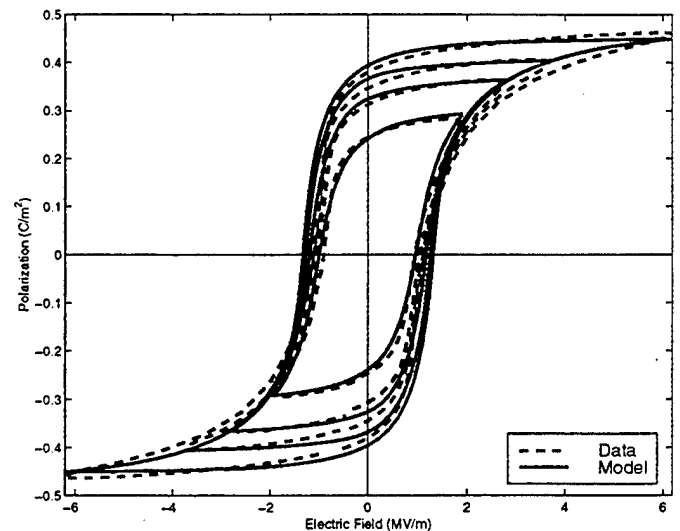
CONCLUDING REMARKS

Model Capabilities:

- (1) At low frequencies, both major and minor loops are characterized by the domain wall model.
- (2) Low number (five) and physical nature of parameters facilitates parameter estimation and control implementation (e.g., P_s is often known *a priori*).
- (3) The technique provides a unified framework for modeling hysteresis in ferroelectric and ferromagnetic materials.
- (4) The model is amenable to inversion which promotes linear control design.
- (5) Current Investigations
 - Thermal Effects
 - Frequency Dependence



PMN-PT-BT



PZT-5A

Piezoelectric Motion Couplers

Philippe Bouchilloux^(a), Burhanettin Koc^(b), Kenji Uchino^(b)

^(a) Active Materials and Smart Structures Laboratory

Department of Mechanical Engineering, Aeronautical Engineering and Mechanics
Rensselaer Polytechnic Institute, Troy, NY 12180-3590, USA

^(b) International Center for Actuators and Transducers

Materials Research Laboratory

The Pennsylvania State University, University Park, PA 16802, USA

This paper presents two original piezoelectric motors for application in space and robotics. These motors are named 'motion couplers' because they use two friction surfaces to transmit motion. Two versions of these motors are presented: one for rotary motion and one for linear motion.

These devices offer the usual characteristics found in piezoelectric motors: large torque or force to weight ratio, high holding torque or force, high positioning resolution, short response time, low input voltage, operation independent of the magnetic environment, and compact and gearless design.

The first part of the paper describes the concept underlying the design of the motion couplers: the rotary piezoelectric motion coupler consists of a ring-shaped vibrator excited in a non-axisymmetrical mode; the linear version of the coupler is based on a longitudinal vibrator using a L1B4 excitation. Both couplers are bi-directional and use a double friction surface.

The second part of the paper gives experimental results obtained with the rotary motion coupler in terms of speed and torque.

The motion couplers are being developed for applications in space and robotics. The last part of the paper explains how the piezoelectric motion couplers can be implemented in adaptive truss members and used to deploy geometry variable structures in space.

Contact information:

Philippe Bouchilloux
Magsoft Corporation
1223 Peoples Ave.
Troy, NY 12180
Tel: (518) 271-1352
Fax: (518) 276-6380
Email: pb@magsoft-flux.com



New Ultrasonic Motors for Variable Geometry Structures

Philippe Bouchilloux


Burhanettin Koc

Kenji Uchino

Kevin Craig



Outline

- Introduction
 - Two classical ultrasonic motor designs
 - New ultrasonic motors
 - Finite element analysis
 - Construction & Measurement
 - Discussion and future work
 - Conclusion
- 

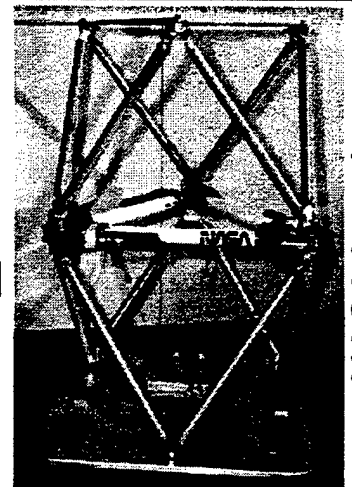
Introduction

- Characteristics of ultrasonic motors:
 - Compact
 - Position locking with no power
 - Large force to weight ratio
 - Low power consumption
 - No magnetic interference
- These properties make USMs good candidates to replace the electromagnetic stepper motors commonly used in truss structures



Introduction

- Variable geometry structures:
 - Mostly used in space
 - Passive and active applications:
 - Passive: to deploy antennas, orbital station units, etc.
 - Active: to obtain large actuators such as the crane used to launch satellites from the space shuttle (the active truss members deploy and actuate the crane structure)



NASA Langley

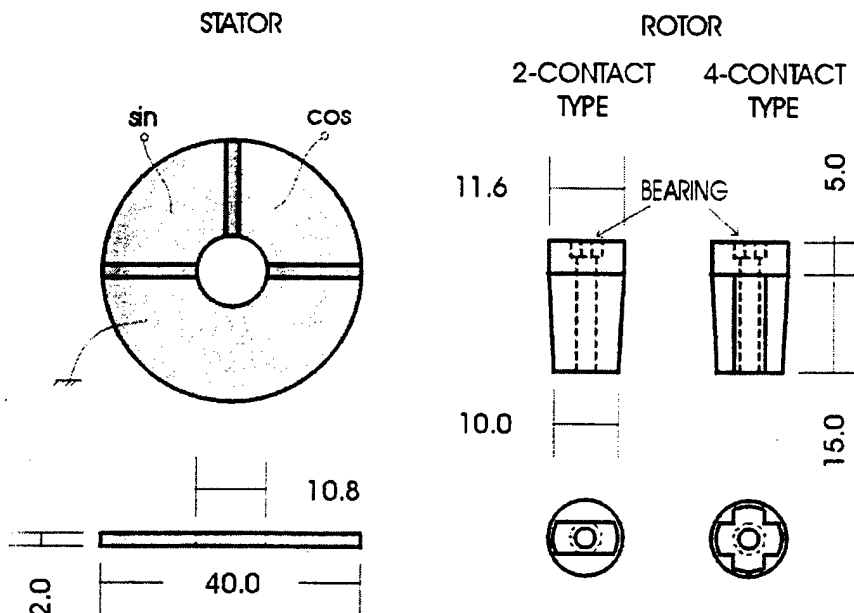


Classical Ultrasonic Motors

- We focus our interest on two ultrasonic motor designs:
 - A rotary USM: the 'hula-hoop' motor
 - A linear USM: the LIB4 motor

Classical USM: The 'hula-hoop' Motor

- Design of a hula-hoop motor:



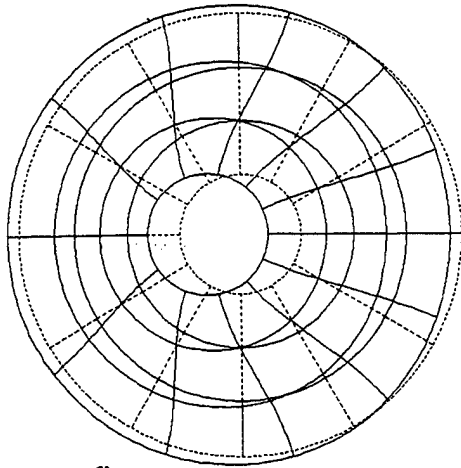
Classical USM: The 'hula-hoop' Motor

■ Operating principle:

- The ((1,1)) non axisymmetrical mode

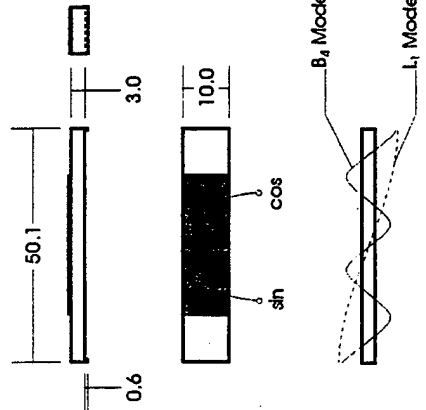
Resonance frequency:

$$f_r = \frac{\alpha_{n,m}}{2\pi a} \sqrt{\frac{E}{\rho(1-\sigma^2)}}$$



Classical USM: The LIB4 Motor

■ Design of a LIB4 motor:



$$f_{L1} = \frac{1}{2l} \sqrt{\frac{E}{\rho}}$$

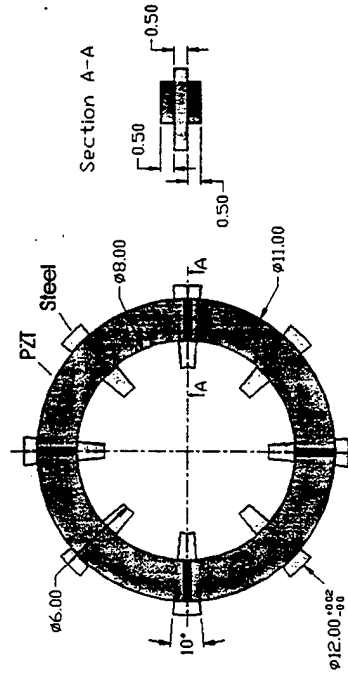
$$f_{Bn} = \frac{\alpha_n^2 t}{4\pi \sqrt{3} l^2} \sqrt{\frac{E}{\rho}} \alpha_n$$

$$f_{Bn} \approx \frac{2n+1}{2} \pi, \quad n = 4-8$$



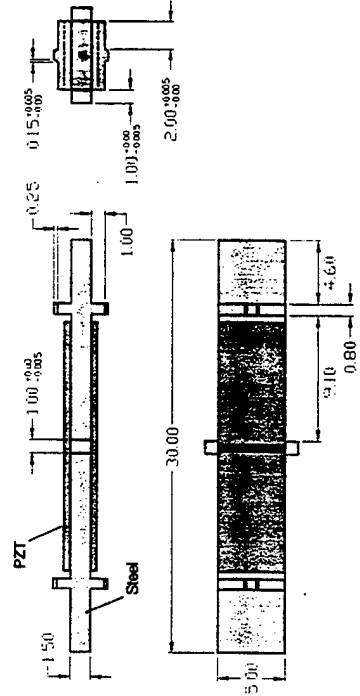
New Ultrasonic Motors

■ Design of the stator for the rotary motor:



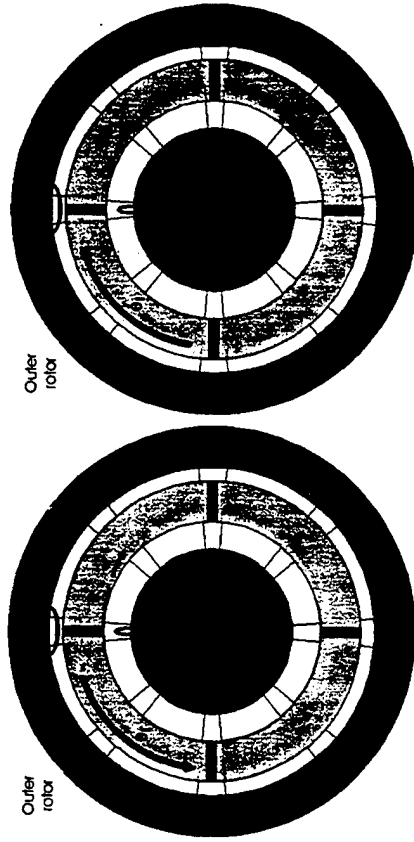
New Ultrasonic Motors

■ Design of the stator for the linear motor:

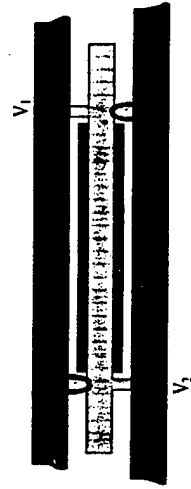


New Ultrasonic Motors

$$\dot{\theta}_{total} = \dot{\theta}_1 + \dot{\theta}_2$$



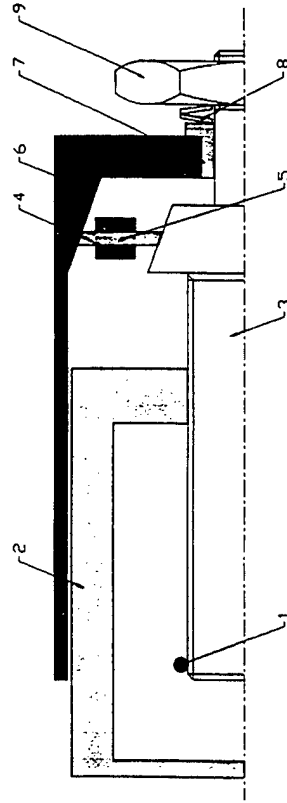
New Ultrasonic Motors



$$V_{total} = V_1 + V_2$$

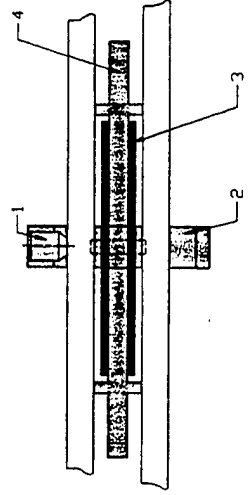
Variable Geometry Structures

- With the rotary motor, a screw can be used to transform rotary motion into linear motion. This roto-linear converter can achieve the desired extension requirement.



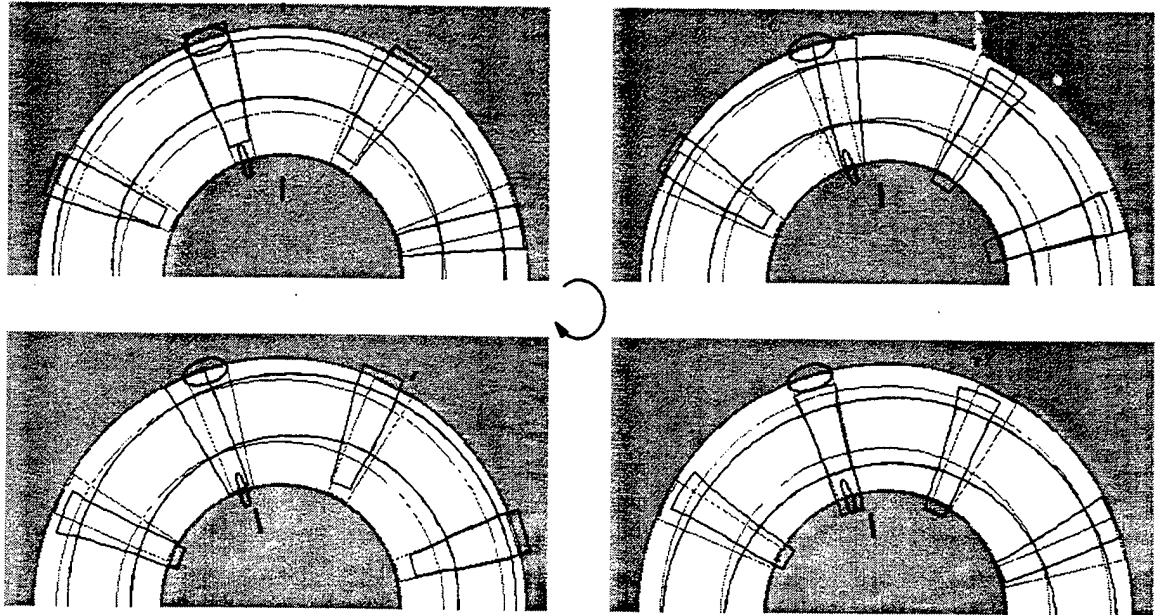
Variable Geometry Structures

- Using the linear motor with two rails (rotors), it is possible to achieve $\sqrt{2}$ elongation as long as each rail is at least $1 + \sqrt{2}/2$ times longer than the length of the stator:



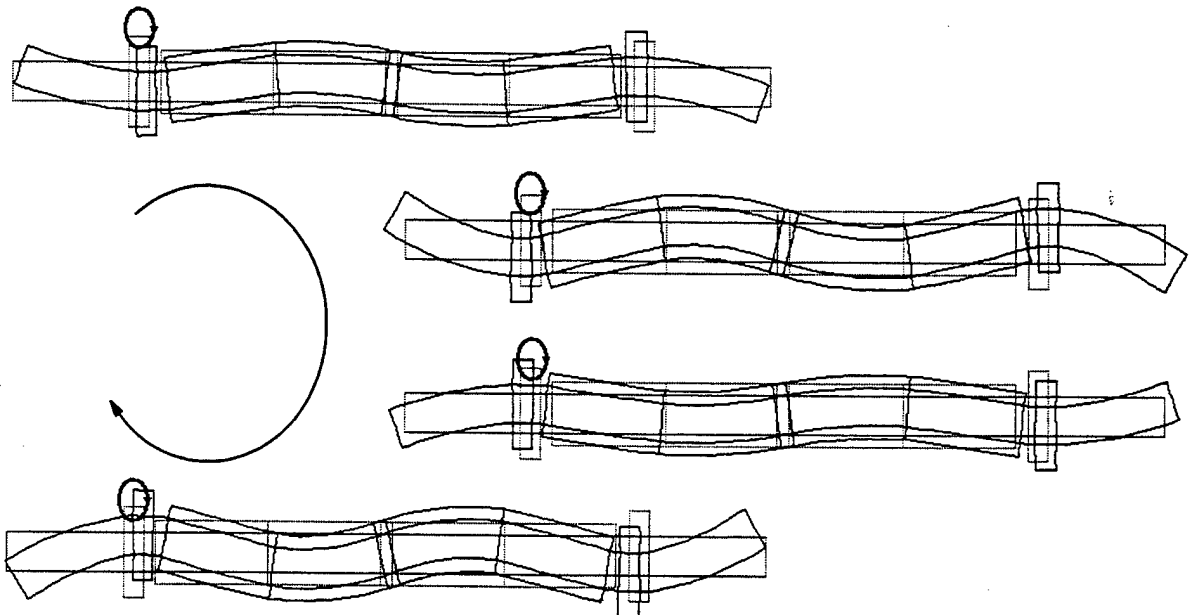
Design Using FEA

■ One cycle of the motion: rotary case



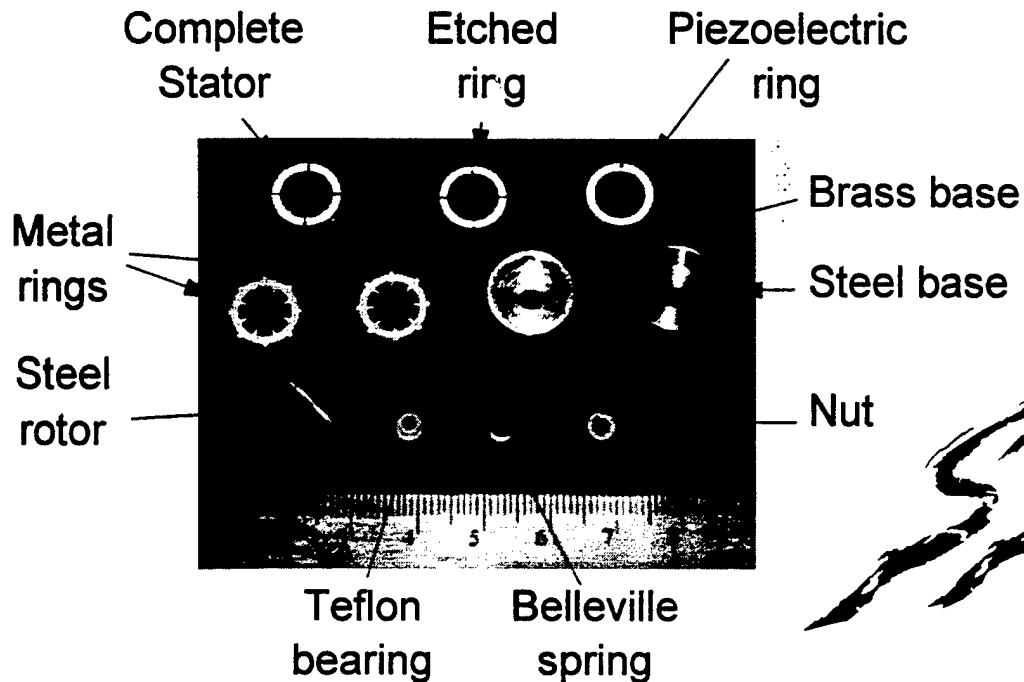
Design Using FEA

■ One cycle of the motion: linear case



Experimental Results

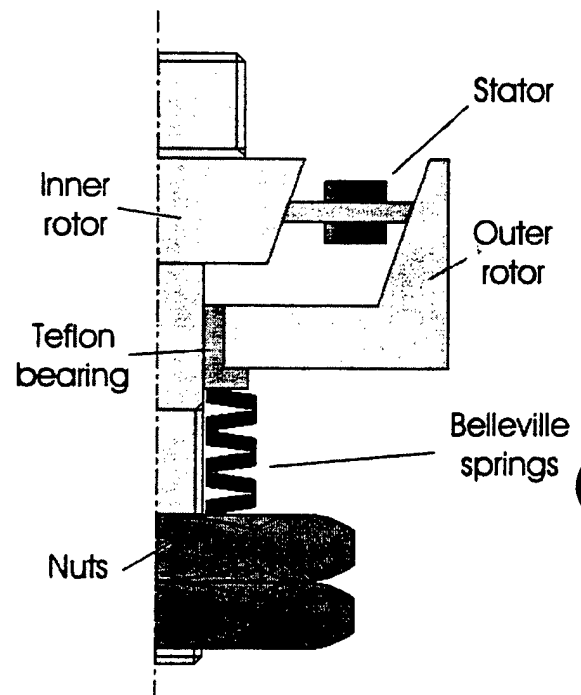
■ Parts for the rotary motor prototype



Experimental Results

- The static prestress is determined by the Belleville springs
- Since both inner and outer peripheries are used for friction, brushes must be implemented in the complete motor

Assembled prototype:

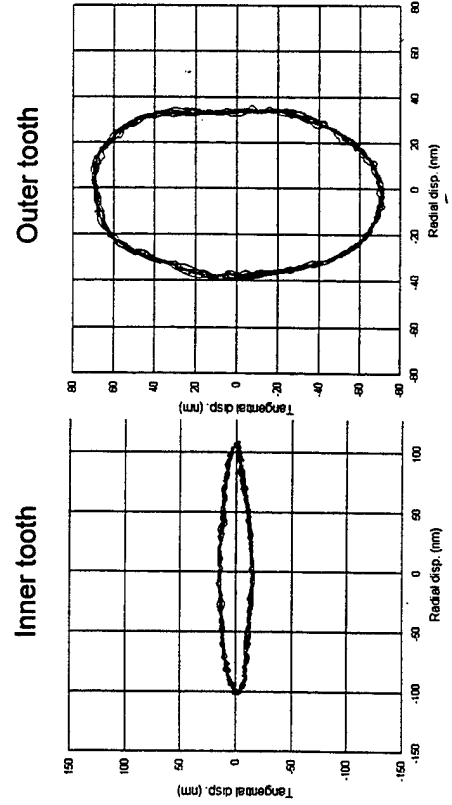


Experimental Results

- Laser interferometry is used to measure the displacement at the tip of the teeth (use of mirrors)
- The shape of the ellipses found confirms the FEA
- Experimental conditions:
 - Unloaded motor
 - $f = 173.9 \text{ kHz}$
 - $V_{p-p} = 35 \text{ V}$

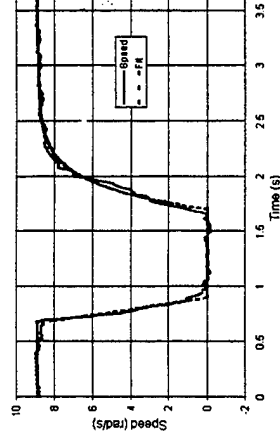


Experimental Results



Experimental Results

- The transient speed is as follows:

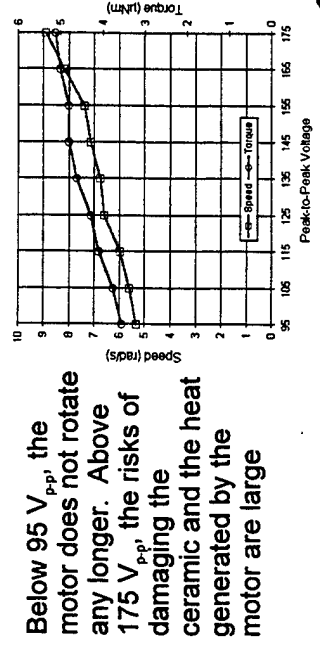


The steady-state speed is very slow: 85 rpm



Experimental Results

- The load characteristic of the motor is obtained from the transient speed curve:



Below 95 V_{p-p} , the motor does not rotate any longer. Above 175 V_{p-p} , the risks of damaging the ceramic and the heat generated by the motor are large



Discussion

- Preliminary results for the new rotary ultrasonic motor have been obtained
- They confirm the validity of the concept: motion can be generated at the same time at the inner and at the outer peripheries of the stator

■ These results also show the problems of the prototype and give useful guidelines for the future of this project



Discussion

- More tests are necessary to understand what happens when the two friction surfaces are used at the same time. It seems obvious that algebraic speeds will add up, and that the minimum torque obtained (either at the inner or outer surface) will represent the torque value of the motor:

$$\begin{aligned}\dot{\theta}_{total} &= \dot{\theta}_1 + \dot{\theta}_2 \\ T_{total} &= \min(T_1, T_2)\end{aligned}$$



Discussion

- Problem of contact between the stator and rotors
 - The metal rings were fabricated by EDM which did not allow for making conformal surfaces
 - Application of the prestress could not be verified
 - Friction mechanism could not be investigated
- Problem of wiring a small two-phase motor
 - Excessive soldering
 - Extremely difficult to connect brushes



Conclusions

- We presented new rotary and linear USM concepts:
 - Double friction surface to eliminate the elastic mount
- We are developing specific design rules and optimization procedures using FEA
- Future work will focus on the implementation of USMs into a variable geometry structure
 - Evaluation of the performance
 - Specification of USM requirements



Systematic Design of Compliant Mechanism Amplifiers for Piezoelectric Actuators

Mary Frecker, Assistant Professor
Shawn Canfield, Graduate Student Research Assistant

The Pennsylvania State University
Department of Mechanical and Nuclear Engineering
233 Reber Bldg.
University Park, PA 16803
(814) 865-1617 phone, (814) 863-4848 fax
e-mail: mxf36@psu.edu

Abstract

Compliant mechanisms are defined as single-piece flexible structures which achieve force and motion transmission via elastic deformation rather than through rigid links and joints. Because compliant mechanisms can be designed as monolithic entities without hinges, they offer the benefits of single piece construction and lack of joint clearances over their rigid-link mechanism counterparts. One application of compliant mechanisms are as coupling structures with piezoelectric actuator materials, where the compliant mechanism is designed to provide mechanical amplification for the PZT actuator. This research focuses on developing systematic methods to design such monolithic devices for integration with piezoceramic stack actuators. This work addresses the need in the field of smart structures for actuators with improved output stroke capability.

A systematic design method has been developed using concepts of structural topology optimization. Two different optimal design formulations have been developed, one where the geometric advantage (GA) of the coupling structure is maximized, and one where the mechanical efficiency (ME) of the coupling structure is maximized. The GA formulation maximizes the overall stroke amplification of the coupling structure, whereas the ME formulation minimizes the elastic losses. These formulations are implemented using two different solution methods, sequential linear programming (SLP), and an optimality criteria (OC) method. Details of the underlying mathematical theory of the optimal design formulations will be discussed, as well as details of the computational solution techniques and implementation. The procedure predicts an optimal compliant mechanism topology based on the user-specified inputs of applied voltage to a piezoceramic stack, and a desired force-deflection relationship between the actuator material and surrounding structure. Results show good algorithm convergence for both solution procedures, with the OC method providing significantly less computation time than the SLP method. The main advantages of using this systematic method is that reliance on ad-hoc or intuitive design methods is eliminated, and coupling structures with any direction of force and motion transmission can be designed. Such structures differ from flextensional amplifiers, which are limited to only a 90 degree transmission of force and motion.

An automated procedure has also been developed to aid the designer in interpretation of the topology design results. Typically the process of converting the topology design results to a detailed solid model is a somewhat qualitative one done using the designer's own interpretation. Using the results of the topology optimization routine in Matlab, knowledge of the material layout is converted to a neutral data file containing 3-D geometry which is universal to most CAD, FEA, and CAM programs. This converter can identify extraneous members of the optimal topology which do not contribute to the overall motion of the compliant mechanism, and automatically remove them. Information based on connectivity of the elements used in the optimization routine is translated into surfaces and curves and written to a program-independent geometry file. This information is then imported into I-DEAS as solid geometry.

Both the topology design and solid model generation methods will be illustrated with design examples, and physical prototypes have been fabricated as proof of concept.

SYSTEMATIC DESIGN OF COMPLIANT MECHANISM AMPLIFIERS FOR PIEZOELECTRIC ACTUATORS

Mary Frecker

Assistant Professor

Shawn Canfield

Graduate Student

Department of Mechanical & Nuclear Engineering
Penn State University
University Park



APD Workshop on Smart Structures

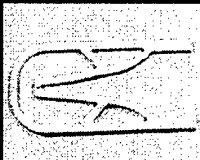
Outline

- I. Introduction
- II. Topology Optimization Formulation
- III. Design Examples
- IV. Conclusions and Future Work

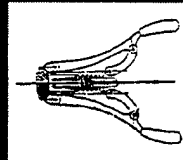
APD Workshop on Smart Structures

Compliant Mechanisms

jointless devices where elastic deformation is intended as a source for motion



Single-piece compliant crimping mechanism



Conventional rigid link crimping mechanism with six moving parts and a spring

APD Workshop on Smart Structures

Compliant Mechanisms

- **Benefits:**

- single-piece construction => no assembly
- no joint clearances or backlash
- well-suited for small range of motion

- **Applications**

- MEMS
- smart structures and actuators
- hand-held tools and surgical instruments

Research in CM Design

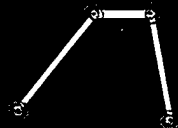
- **Topology Design Approach**

- based on structural optimization



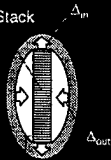
- **Pseudo Rigid Body Model Approach**

- based on kinematics

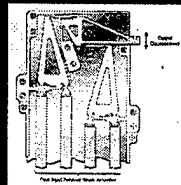


Compliant Mechanism Amplifiers

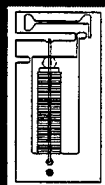
PZT Stack



Flextensional Amplifier



Long Stroke Precision PZT Actuator
Bamford et al., 1995



Flat Plate Actuator
Samuelson et al., 1997

- Designed using intuitive methods and/or kinematic models

Research Objectives

- development of a *systematic* design method using a topology optimization approach
 - eliminates reliance on ad-hoc methods
 - allows any direction of force and motion transmission
- development of detailed solid models
- prototype fabrication and experimental validation

-
-
-
-
-
-

Topology Design Approach

Resisting Load

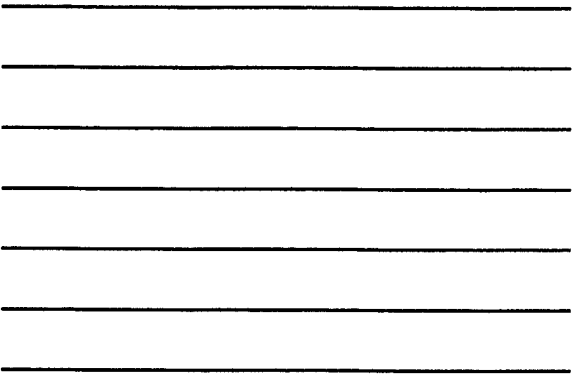
Compliant Amplifier

PZT Stack

DESIGN DOMAIN

OUTPUT DISPLACEMENT

ACTUATOR INPUT DISPLACEMENT



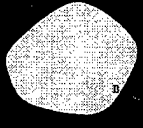
Problem Formulations

- Geometric Advantage
$$\max(GA) = \frac{\text{output displacement}}{\text{input displacement}}$$
- Mechanical Efficiency
$$\max(ME) = \frac{\text{output displacement} \bullet \text{output force}}{\text{input displacement} \bullet \text{input force}}$$

-
-
-
-
-
-

$$\max(ME) = \frac{\text{output displacement} \cdot \text{output force}}{\text{input displacement} \cdot \text{input force}}$$

Geometric Advantage



f_a, Δ_{in}

f_b, Δ_{out}

f_b = unit load based on specified voltage input to piezoceramic stack
 Δ_{out} = output displacement of compliant amplifier

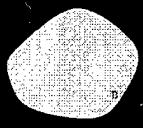
Δ_{out} = Mutual Potential Energy
 $= MPE = v_b^T K u_a$

$\Delta_{in} = f_a^T \Delta_{out} = u_a^T K u_a$

$\max(GA) = \frac{v_b^T K u_a}{u_a^T K u_a}$

s.t. $f_a = K u_a$
 $f_b = K v_b$
 $Volume \leq V_0$
 bounds on design variables

Mechanical Efficiency



f_a, Δ_{in}

f_b, Δ_{out}

k_b

k_b = stiffness of linear spring representing output loading

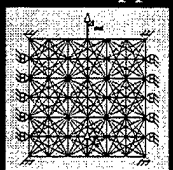
$\max(ME) = \frac{\frac{1}{2} k_b MPE^2 \text{sgn}(MPE)}{f_a^T \Delta_{in}} = \frac{\frac{1}{2} k_b (v_b^T K u_a)^2 \text{sgn}(v_b^T K u_a)}{u_a^T K u_a}$

s.t. $f_a = K u_a$
 $f_b = K v_b$
 $Volume \leq V_0$
 bounds on design variables

$\max(ME) = \frac{\frac{1}{2} k_b MPE^2 \text{sgn}(MPE)}{f_a^T \Delta_{in}} = \frac{\frac{1}{2} k_b (v_b^T K u_a)^2 \text{sgn}(v_b^T K u_a)}{u_a^T K u_a}$

s.t. $f_a = K u_a$
 $f_b = K v_b$
 $Volume \leq V_0$
 bounds on design variables

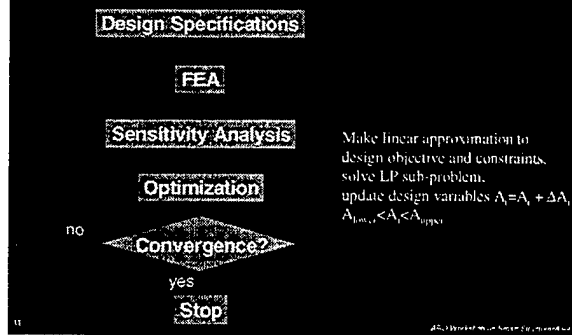
Implementation: Ground Structure Approach



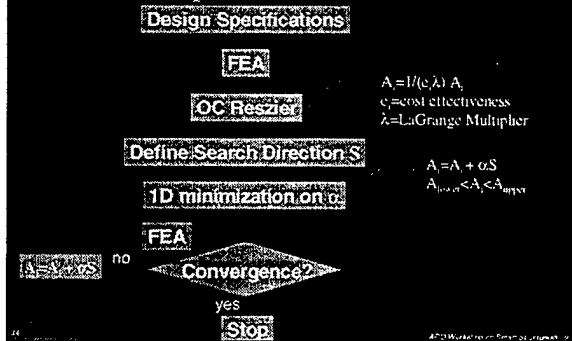
- linear elastic material behavior assumed
- design variables A_i

$A_{lower} < A_i < A_{upper}$

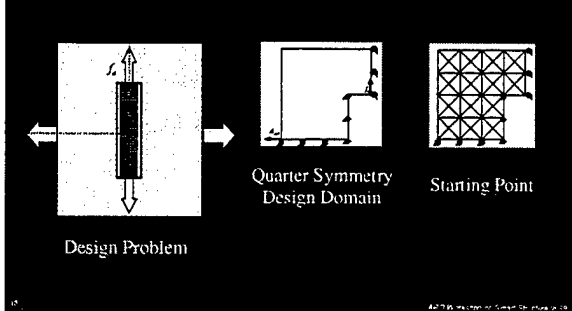
Basic Computational Procedure: SLP

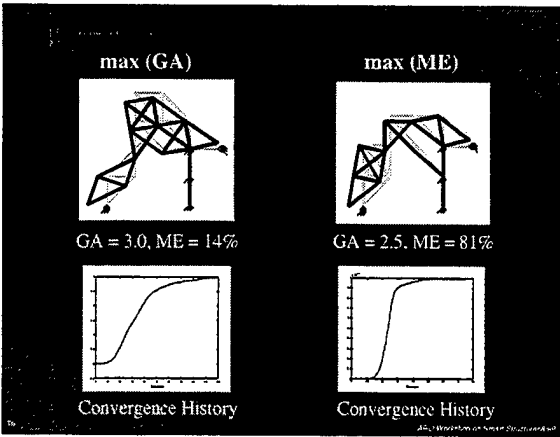


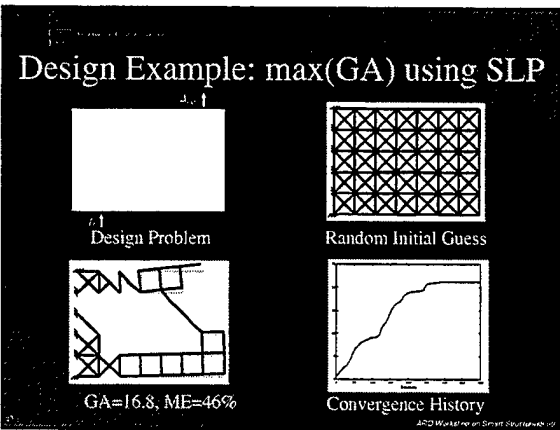
Basic Computational Procedure: OC

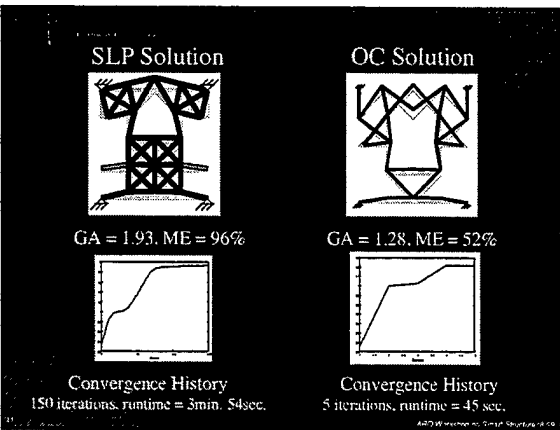


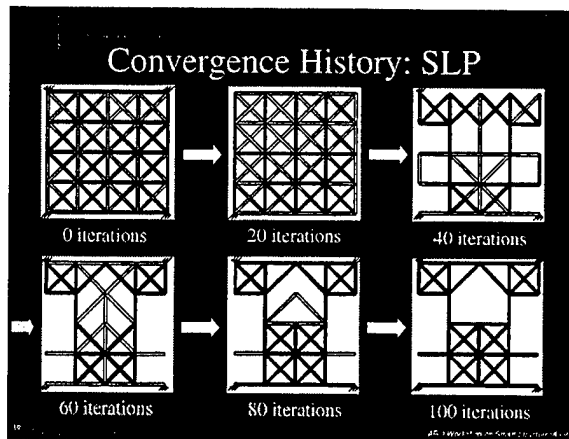
Design Example (Opposite Motion to Flextensional)

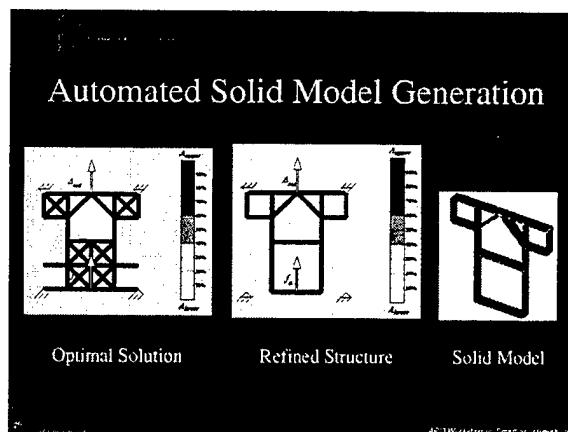


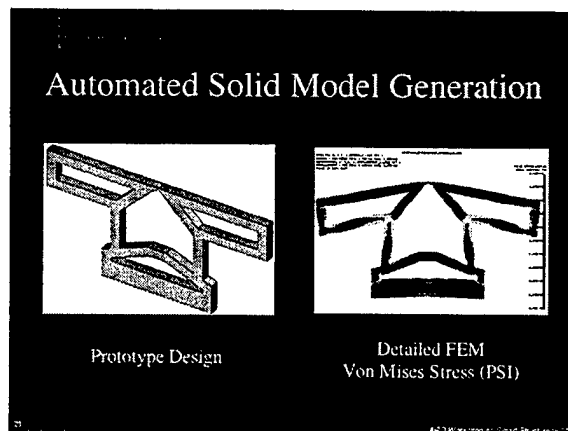










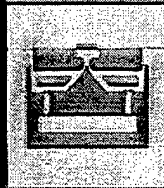


Conclusions

- New topologies with high amplification can be generated
- Need to design for stiffness matching with PZT actuator
- Dynamic case has yet to be studied

Ongoing Research

- Prototype fabrication and experimental validation
- Design for stiffness matching via 2nd stage size optimization
- Dynamic modeling



Acknowledgements

- NSF Division of Design, Manufacturing, and Industrial Innovation DMI 98-70527

Design and Validation of a Multi-Stage Stroke Amplifier for Piezostack-Based Trailing-Edge Flap Actuator

Taeoh Lee*

Inderjit Chopra†

Alfred Gessow Rotorcraft Center
Department of Aerospace Engineering
University of Maryland, College Park, MD 20742

Helicopters are susceptible to high vibration because of the unsteady and complex aerodynamic environment in which the main rotor operates. These high vibratory loads result in low fatigue life of structural components, poor ride quality, high maintenance cost and poor system reliability/performance. To reduce these problems, numerous passive and active devices are adopted with resultant weight penalties and reduced payloads. Recently, with the emergence of the smart material actuators such as piezoceramic and magnetostrictive actuators, active vibration control schemes show the potential of effectively controlling the vibratory forces.

Smart structures have great potential for use in helicopters because they have mechanical simplicity, lightweight, high bandwidth, and low power consumption. With enhanced actuation force capability, the piezostacks are considered feasible to actuate the full-scale blade trailing edge flap using effective stroke amplification mechanism. The present authors developed a mechanical amplification concept called double-lever (L-L) amplification mechanism that has a high amplification capability. The bench-top test results of the prototype L-L actuator showed an overall amplification factor of 19.4 and a feasible operating range of the actuation frequency for up to 8/rev. In vacuum spin test, the L-L actuator showed no major degradation in performance for the centrifugal loading up to 600g. It was shown that the L-L actuator has good potential for the full-scale rotorcraft application. The design refinement issues for L-L amplification and flap-linkage mechanisms are investigated to reduce/eliminate the losses observed in prototype testing, and thereby to improve the performance of the actuator. The primary concern focuses on minimizing the losses due to the elastic deformation, such as contact losses at the interface, elastic bending deformation of Inner-/Outer-lever and the hinge housing. It was finalized with the size of 7-3/16 inch width, 2-13/16 inch depth and 3/4 inch height, and its overall weight is approximately 2 pounds. A blade section model of 12 inch span and 12 inch chord was fabricated to mount the L-L actuator for open-jet wind tunnel testing. To evaluate the performance of the trailing edge flap actuator under different test conditions and to validate the analytic model, the blade section model is tested on bench-top, and then, investigations is conducted in vacuum chamber, and in an open-jet wind tunnel. The performance of the flap is evaluated at different actuation frequency, angles of attack, and rotational speed. This study will help the development of a full-scale rotor blade with trailing edge flap actuated using piezostacks.

* Graduate Research Assistant

† Alfred Gessow Rotorcraft Professor and Director



ALFRED GESSOW ROTORCRAFT CENTER
UNIVERSITY OF MARYLAND



Design and Validation of a Multi-Stage Stroke Amplifier for Piezostack-Based Trailing-Edge Flap Actuator

Taeoh Lee

Graduate Research Assistant

Inderjit Chopra

Alfred Gessow Rotorcraft Professor and Director

Presented at the 4th ARO Workshop on Smart Structures
University Park, PA, August 16-18, 1999



Motivation



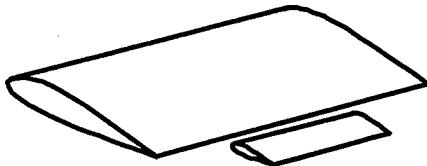
- **Multicyclic Control (HHC)**
 - potential for vibration reduction
 - swashplate control → limited excitation frequency
- **Individual Blade Control (IBC)**
 - excitation at all frequencies → needs hydraulic slip ring
- **Trailing edge flaps**
 - controllable lift and twist inputs
 - compatible with smart structure actuators
 - minimal impact on control system loads
 - offer potential for effective, lightweight vibration reduction system



Flap Configurations

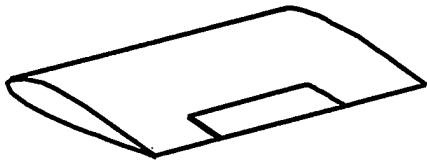


UNIVERSITY OF MARYLAND



- **Servo Flap**

- Large pitching moments
- Reduced effectiveness due to hinge gaps



- **Plain Flap**

- Modifies lift and pitching moment
- Internally mounted actuator and linkage
- Easier sealing of hinge gaps
- Attractive for smart actuation



Smart Material Actuators



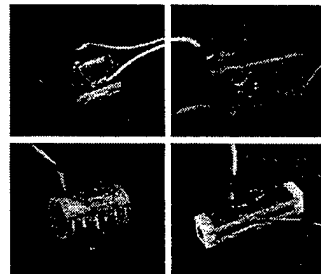
UNIVERSITY OF MARYLAND

- **Smart Material Actuators**

- Piezoelectric Bender
- Piezoelectric material + Coupling mechanism:
- Electrostrictive material
- Piezoelectric Stack
- Shape Memory Alloy

- **Piezoelectric Stack**

- low strain/high force
- potential for full-scale rotorcraft application with stroke amplification mechanism





Objective



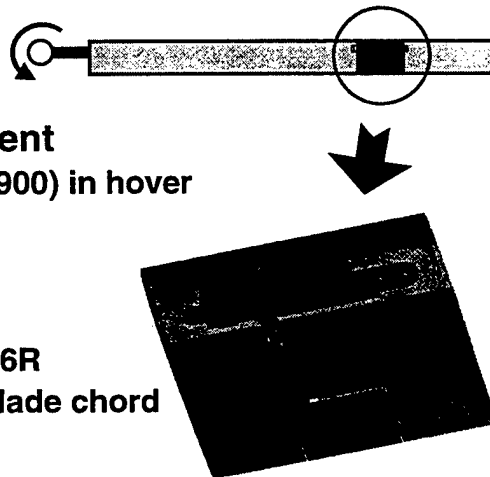
To systematically investigate the feasibility of the trailing edge flap operating in rotating environment using piezostack device in conjunction with refined stroke amplification mechanism



Smart Trailing Edge Flap



- **Design Goal:**
 - flap amplitude of $\pm 5^\circ$
- **Operational Environment**
 - Boeing MD Explorer (MD900) in hover
- **Main Rotor**
 - diameter: 34 feet
 - trailing edge flap
 - ♦ location: $0.78R \sim 0.96R$
 - ♦ flap chord: 25% of blade chord
- **Blade Section Model**
 - 12 inch chord and 12 inch span



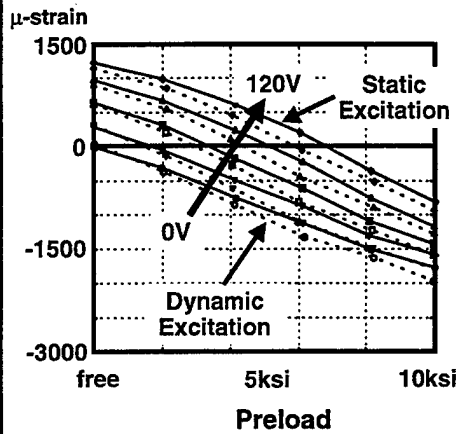


Piezostack

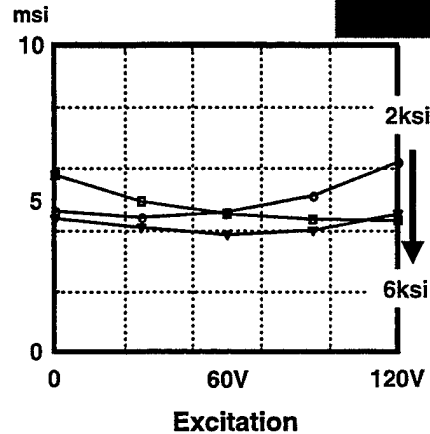
Physik Instrumente P-804.10



Strain vs. Force

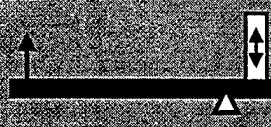
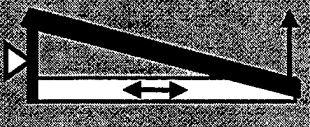


Elastic Modulus



Mechanical Stroke Amplification Concepts



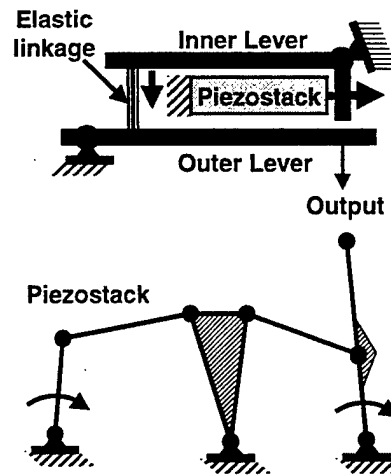
Amplification Mechanism		
Main Idea	Lever-Fulcrum	Triangle frame w/ shallow angle
Amplification Factor	< 10	< 10
Existing Actuator	PI, Bi-axial(Boeing)	Pyramid (SatCon), X-Frame (MIT)
Scale-up	Constant Ratio of Lever Distances	Constant Angles of the frames
Advantage	Design Flexibility	Small chordwise size
Potential Disadvantage	Loss due to elastic deformation	Supporting flexure



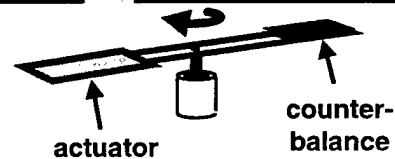
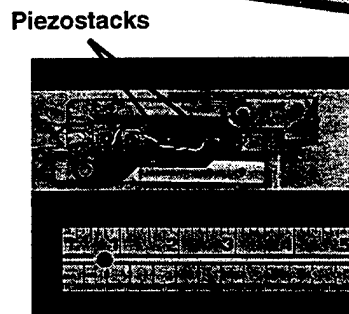
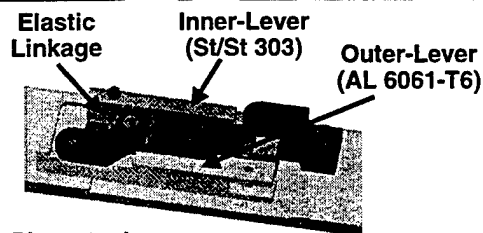
L-L Amplification Mechanism



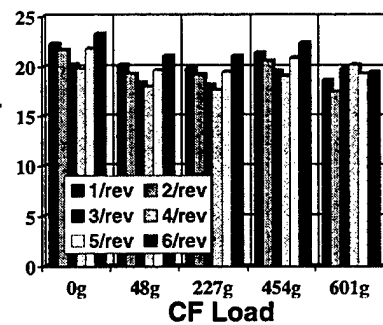
- Two-stage lever-fulcrum mechanism connected through a elastic linkage
- Planar structure
- Higher amplification factor (> 20)
- Embedded supplementary preload mechanism
- Design flexibility



Prototype L-L Actuator



Actuator Stroke (mil)



Full-scale CF loading



Design Refinement Issues



UNIVERSITY OF MARYLAND

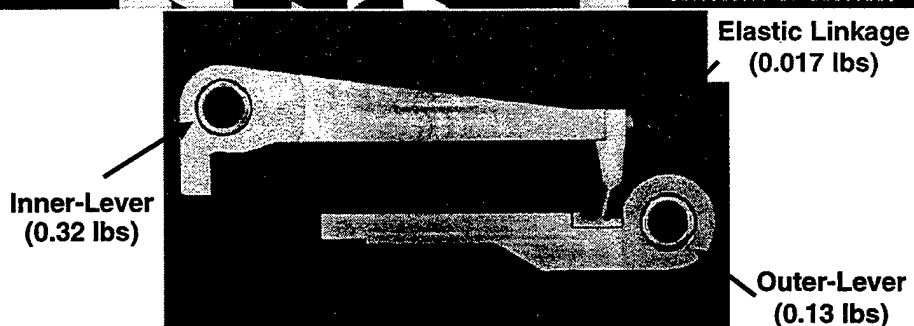
- **Flap Actuator**
 - Actuator housing / Piezostack mounting
 - Interface between piezostack and Inner-Lever
 - Position/Size of elastic linkage
 - Actuator CG location
- **Blade Section Model**
 - Push-rod / Flap hinge mechanism
 - Flap hinge



Levers & Elastic Linkage



UNIVERSITY OF MARYLAND



- **Amplification Factor (ideal)**
 - Inner-Lever: 6
 - Outer-Lever: 5
- **Elastic Linkage located to maximize the load transfer ratio**



Piezostack/Inner-Lever Interface

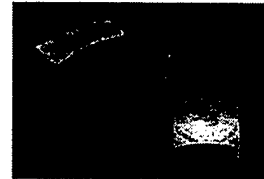
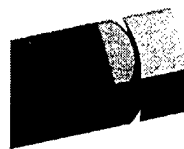


UNIVERSITY OF MARYLAND

OLD
Cylinder/Flat Plate



NEW
Sphere/Spherical Recess



- **Advantages**

- increase the contact area
- reduce the change in contact stress
- obtain good alignment of the components



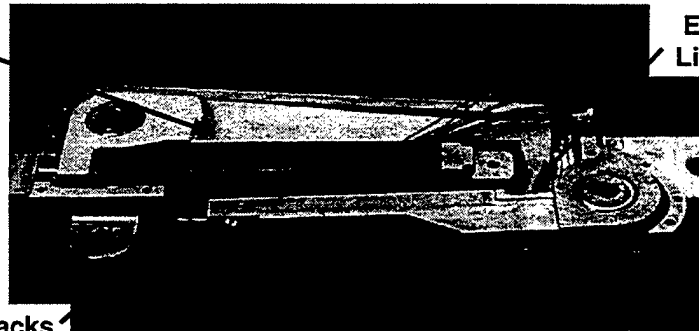
Final Design



UNIVERSITY OF MARYLAND

Inner
Lever

Elastic
Linkage



Piezostacks

Outer Lever

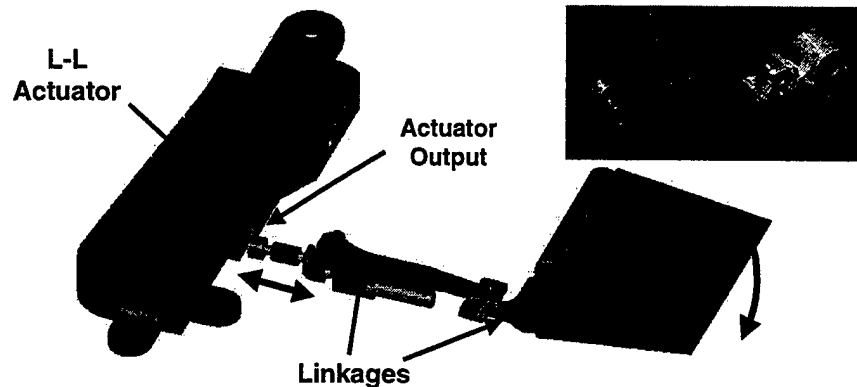
- **Dimensions**

- Piezostack: 0.3937 inch square X 3.9185 inch length w/ end-caps
- Actuator: 7-3/16 inch width X 2-13/16 inch depth X 3/4 inch height

- **Weight: 2.1 lbs**



Push-rod / Flap Mechanism



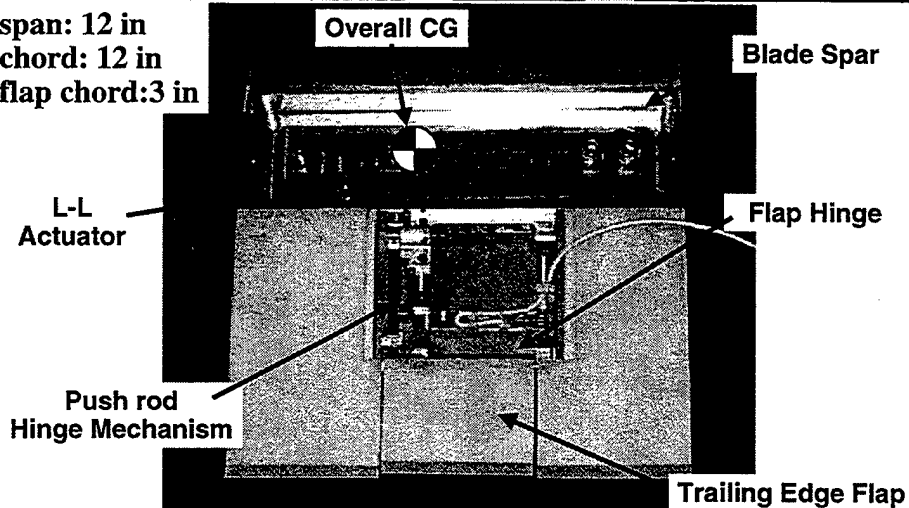
- Linkage mechanism used for transferring linear actuator output to rotary flap deflection



Blade Section Model



span: 12 in
chord: 12 in
flap chord: 3 in





L-L Actuator Testing



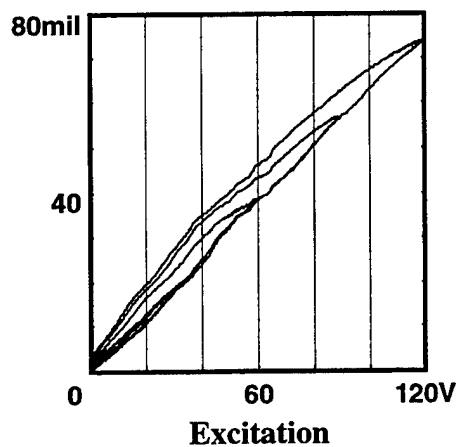
- On Bench-Top
 - Load-free condition
 - with dead weight
 - with spring-load
- In Vacuum Chamber
 - simulate the full-scale centrifugal force condition
- In Open-jet Wind Tunnel
 - flap performance with aerodynamic force



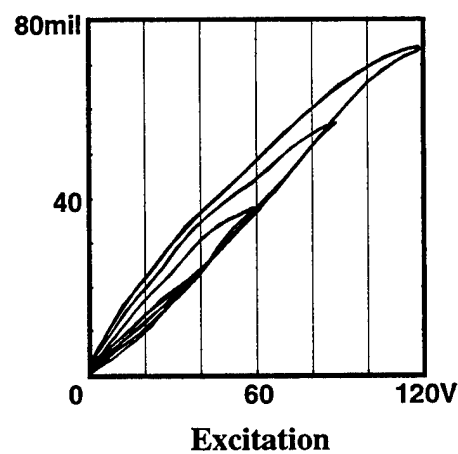
Bench-top Testing (Load-free condition)



Displacement @ 1Hz



Displacement @ 39.2Hz



Torsional actuator and motor based on mechanically amplified shear piezoelectric response

Q. M. Zhang and A. E. Glazounov

Materials Research Laboratory, The Pennsylvania State University

C. Kim

Naval Research Laboratory, Washington DC

This work was supported by the DARPA

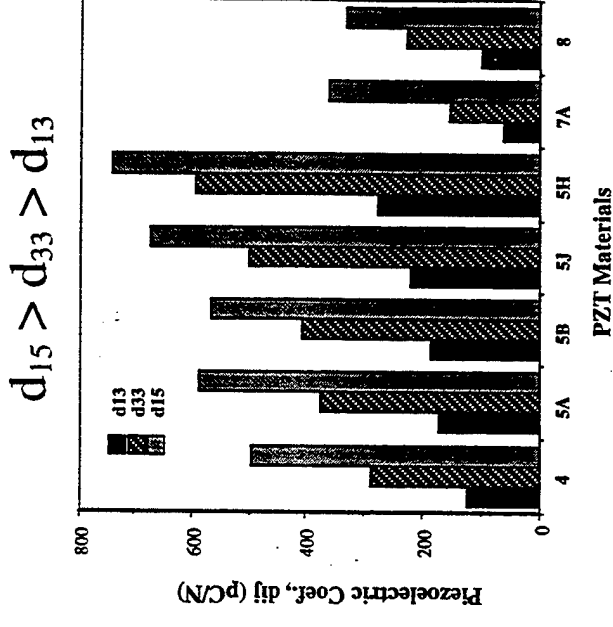
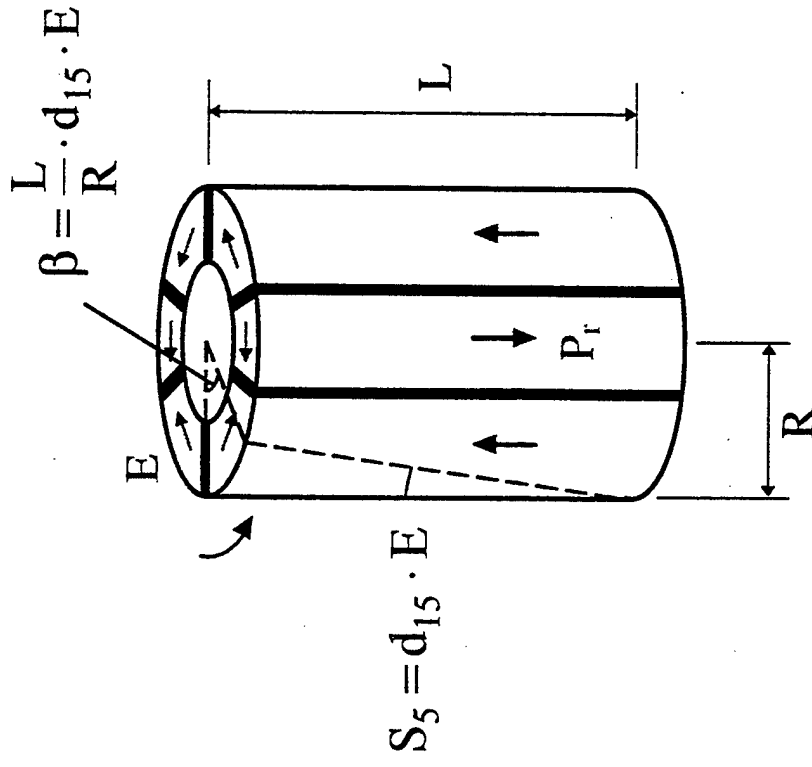
Challenge

How to convert small linear piezoelectric strain
into large torsional motion

Present work: two approaches

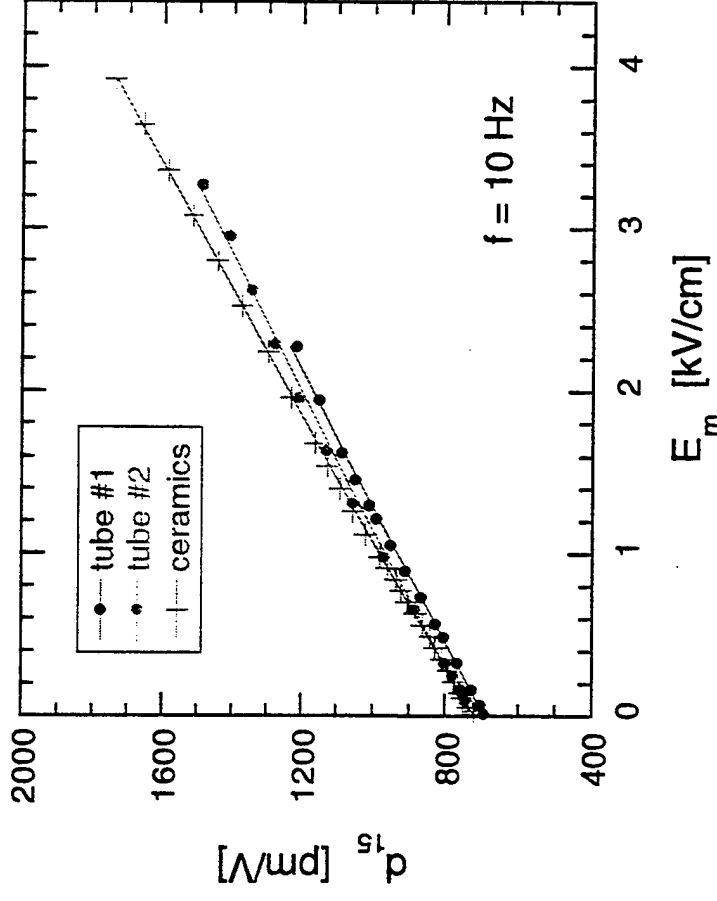
- Angular amplification to achieve large displacement:
torsional actuator
- Make use of high power density of piezoelectric materials and
use rectification mechanism to achieve continuous or stepwise
motion: torsional stepper motor

Torsional actuator



- **Concept:** use mechanical amplification, L/R , of shear strain, $d_{15}E$, to generate large angular displacement, β
- **Merits:**
 - direct conversion of displacement
 - d_{15} is the highest in PZT materials

Proof of torsional actuator concept



We compare

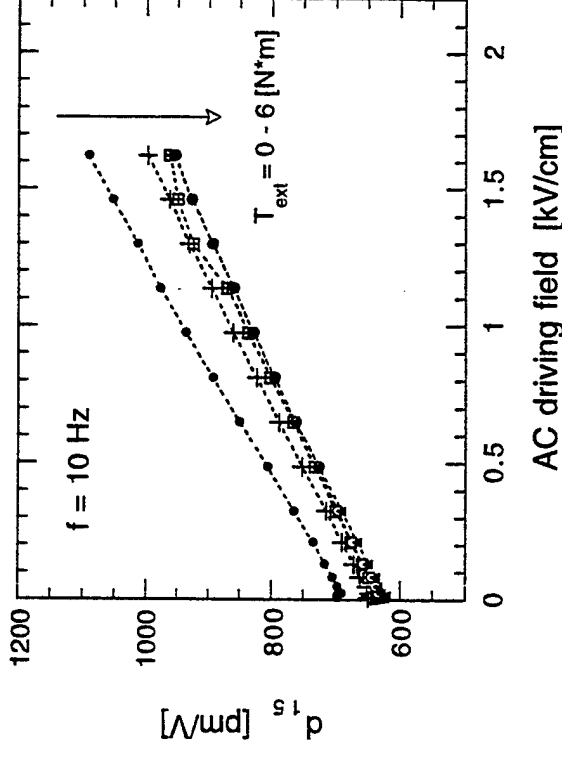
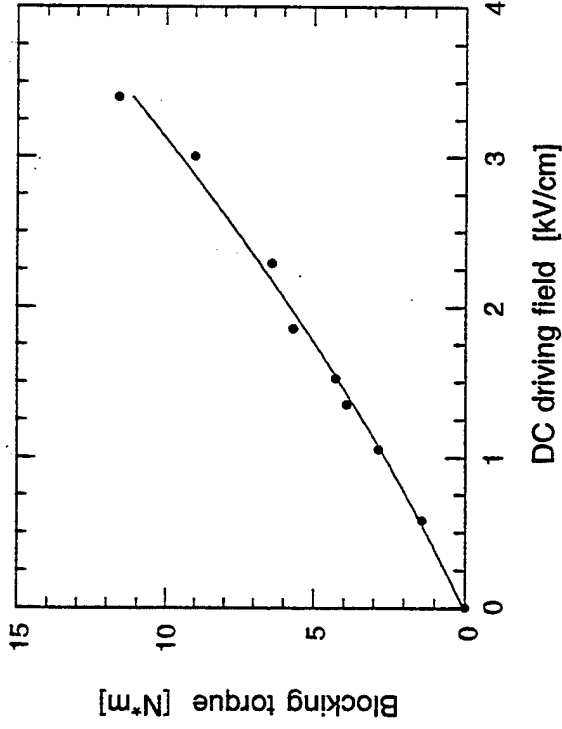
$$d_{15} = \frac{R}{L} \cdot \frac{\beta}{E_m}$$

(tube with $R=0.5''$, $L=2.5''$)
with direct measurement of d_{15} of the
same ceramic composition

- Only a small difference, possibly due to aging or loss of strain in tube joints

Conclusion: Concept works

Actuator response under torque load



- Blocking torque is large, and determined only by material response
- $$T_{bl} = \frac{\pi(R_{out}^4 - R_{in}^4)}{2s_{44}^E R_{out}} \cdot d_{15} \cdot E$$
- Sensitivity, effective $d_{15} \sim \beta/E$, remains nearly constant under static load
 - Conclusion: no effect of torque load was observed for $T_{\text{ext}} < 14 \text{ N·m}$

Piezomotors - conventional approach

displacement (travelling wave) --> friction force coupling --> rotor



Shortcomings:

- **Torque is limited by friction force**
- **Cannot achieve precise control of angular positioning of the rotor**
- **Limited lifetime (wear / friction)**

Present work - new approach

displacement (shear piezoeffect) --> direct coupling via clutch --> rotor

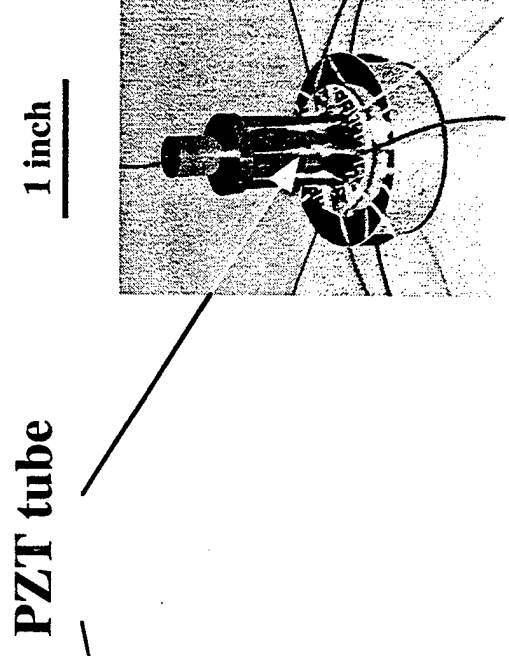
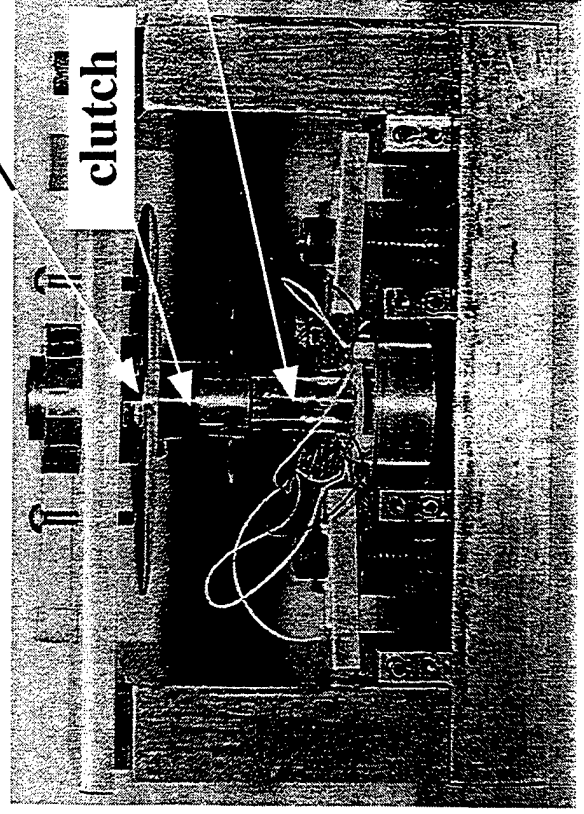
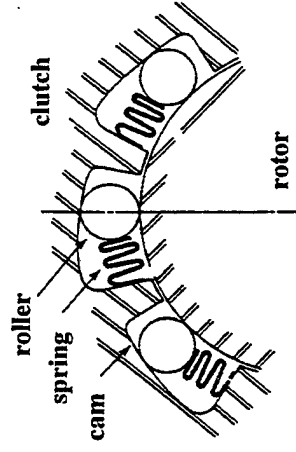
Advantages:

- **Large torque limited only by material response**
- **Can combine precise control of angular positioning with continuous motion of the rotor**



Prototype torsional stepper motor

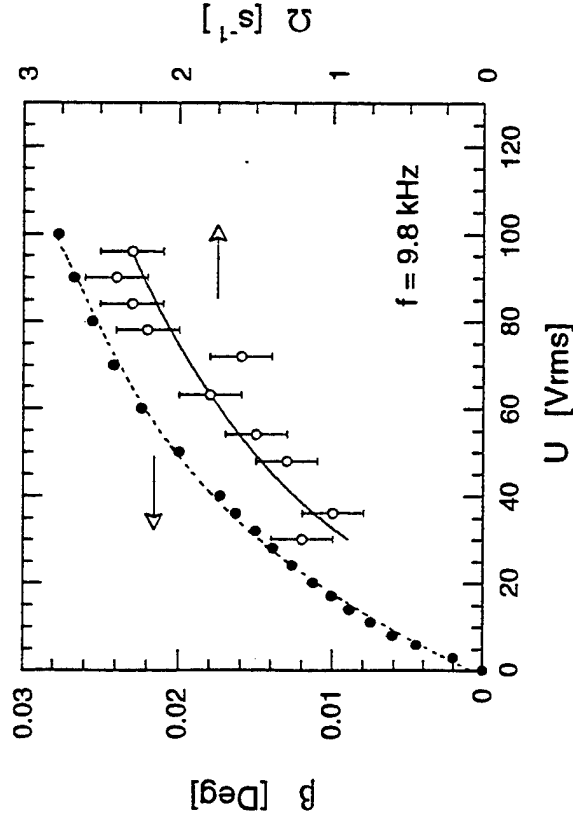
- PZT tube generates angular displacement from shear strain at resonance
- Clutch accumulates the displacement in one direction



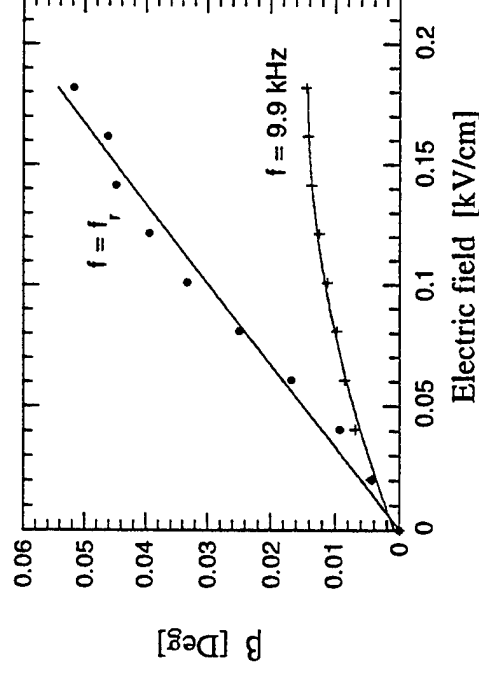
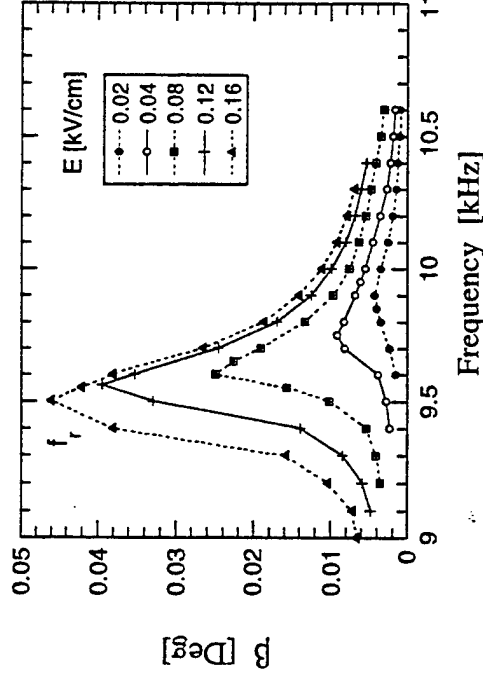
Torsional stepper motor: continuous rotation

Revolution speed Ω and amplitude β of torsional vibrations

Saturation in Ω and β is due to non-linear response of PZT at resonance



$$\Omega = \frac{2 \cdot f}{360^\circ} \cdot \beta$$



Comparison with other designs of piezomotors

Parameter	Present work (direct coupling)	Glenn & Hagood (friction coupl.)	Satonobu et al. (friction coupl.)
Radius [mm]	7	38	7
Rev. speed [rpm]	1200	40	6
Stall torque [N·mm]	600	1700 ⁽ⁱ⁾	150
Torque load limit	fracture of PZT, 8000 N·mm	friction, close to 1700 N·mm	friction, close to 150 N·mm

(i) Torque \propto (Radius)³

(ii) For friction coupling, friction from preload limits both torque and speed

(iii) Comparison is done for the same driving field, $E = 1.5$ kV/cm

(iv) Glenn & Hagood, SPIE, v.3041, p.326 (1997);

Satonobu et al., Jpn. J. Appl. Phys., v.35, p.5038 (1996).

Conclusions

- Tubular/polygonal torsional actuator:
 - uses built-in mechanical amplification of piezoelectric shear strain;
 - can generate large blocking torque;
 - allows control of amplification without loss in the blocking torque.
- Torsional stepper motor:
 - uses high power density of PZT at resonance and direct coupling via clutch;
 - can produce continuous and stepwise motion with precise control of displacement;
 - due to direct coupling, performance (revolution speed and torque) is limited only by material response.

A Built-in Structural Diagnostics for Composite Structures

Fu-Kuo Chang
Dept. of Aeronautics and Astronautics
Stanford University
Stanford, CA 94305

SUMMARY

This research focuses on two major areas: (1) developing an efficient and economical technique for manufacturing composite structures with built-in diagnostics, and (2) developing built-in diagnostic techniques for monitoring and detecting damage in the structures.

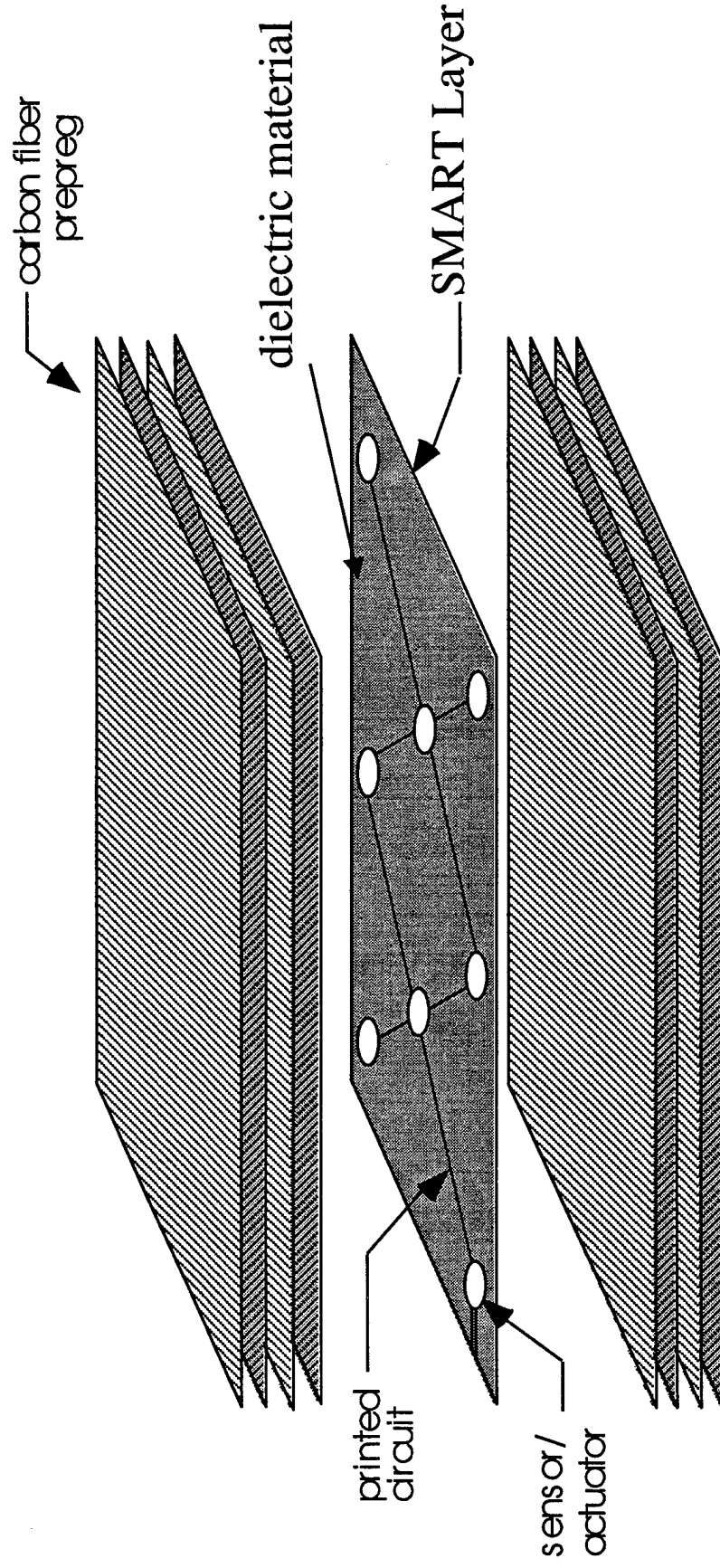
A SMART layer which contains an embedded network of distributed piezoelectric materials has been developed based on a circuit printing technique that is commonly used in the electronics industry. The layer can be laid down between plies or on the surface of the composite laminates during manufacturing. Mechanical and electrical tests showed that no or limited mechanical degradation appeared in the composites due to the presence of the layer and that sensors and actuators provided uniform responses within the network.

By integrating appropriate diagnostic techniques, the layer can be used to monitor the curing process of composites, to identify impact load, and to assess damage resulting from service loads. Based on the SMART layer, diagnostic techniques are being developed and implemented in a PC for identifying in real time the impact force on composite structures and for detecting the extent and size of the impact damage.

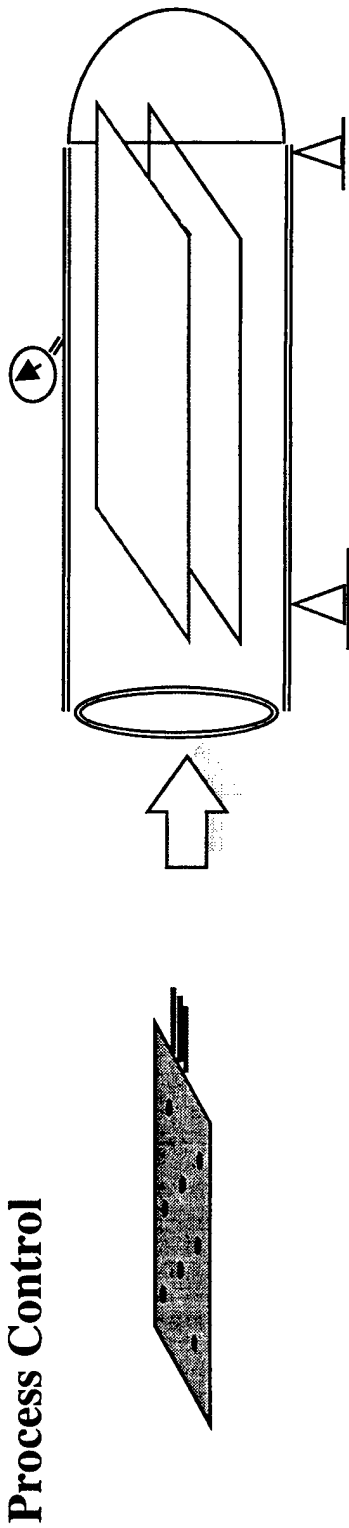
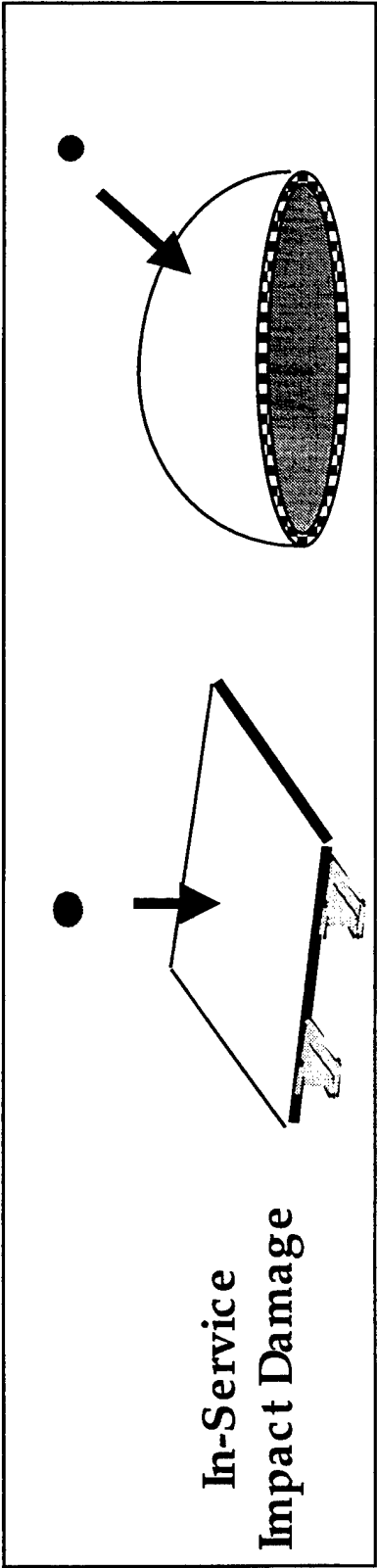
HARDWARE

SMART (Stanford Multi-Actuator Receiver Transduction) Layer

□ FLEXIBLE PRINTED-CIRCUIT BOARD TECHNIQUE



STRUCTURAL HEALTH MONITORING



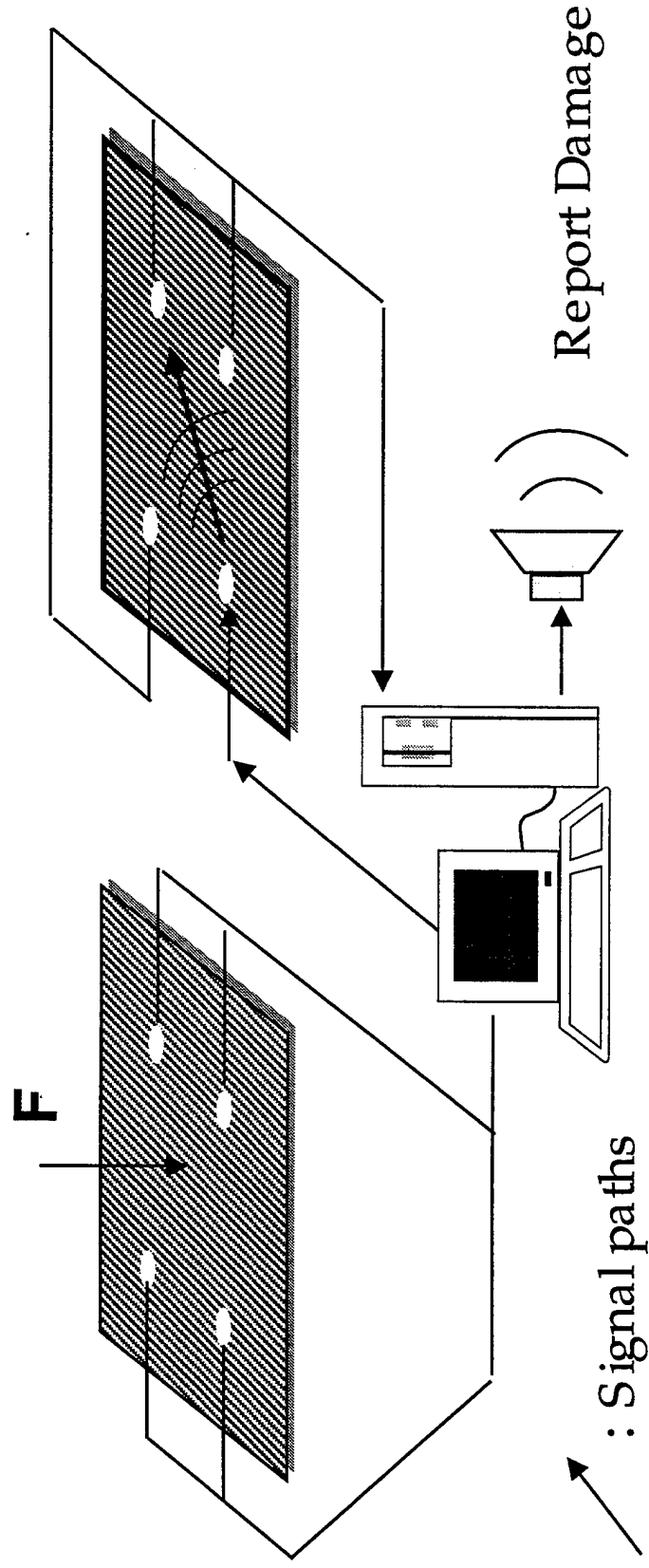
IMPACT DAMAGE IDENTIFICATION

Passive Sensing Diagnostics

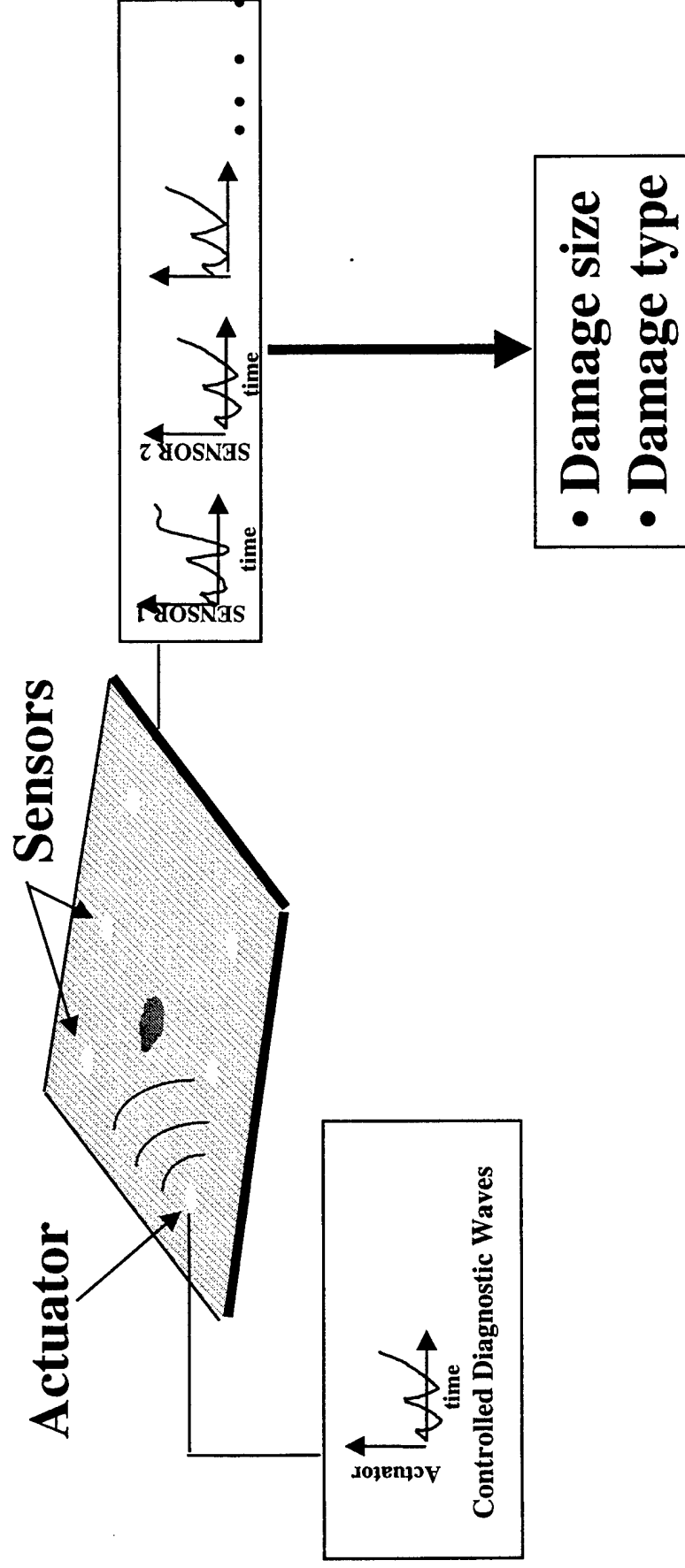
Based on sensor signal only.

Active Sensing Diagnostics

Based on actuators and sensors.



IMPACT DAMAGE ESTIMATION

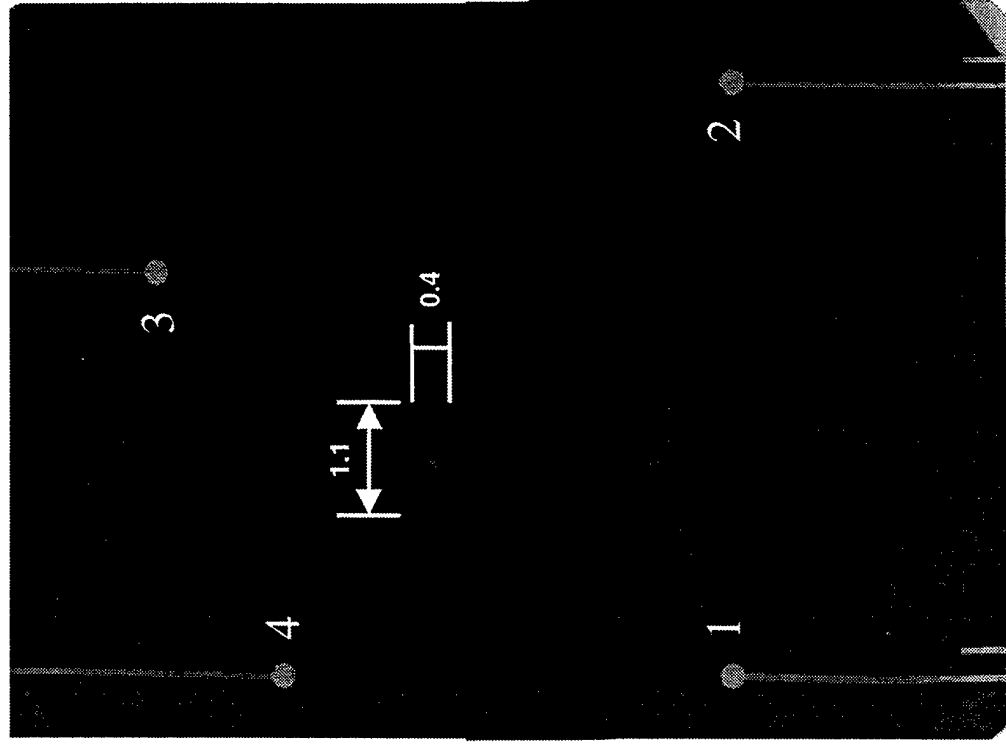
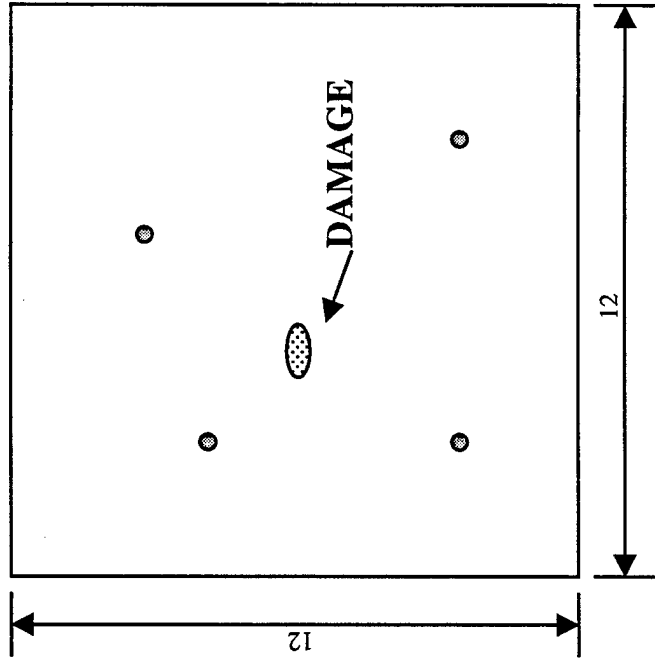


COMPOSITE PLATE WITH IMPACT DAMAGE

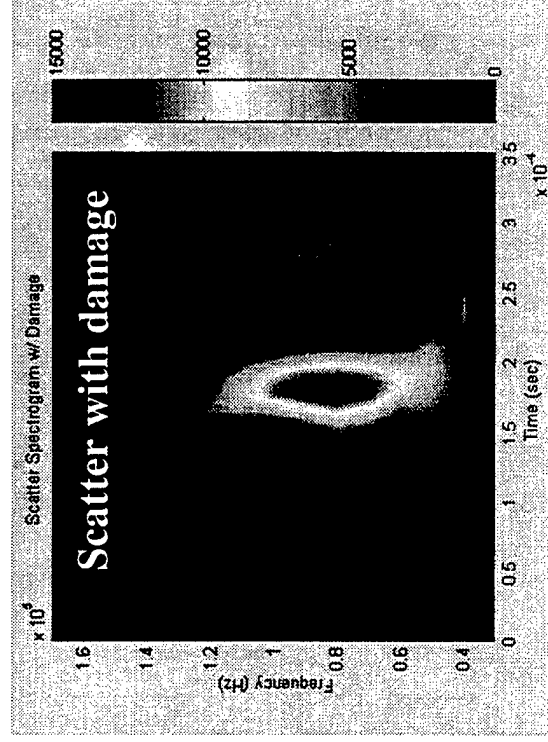
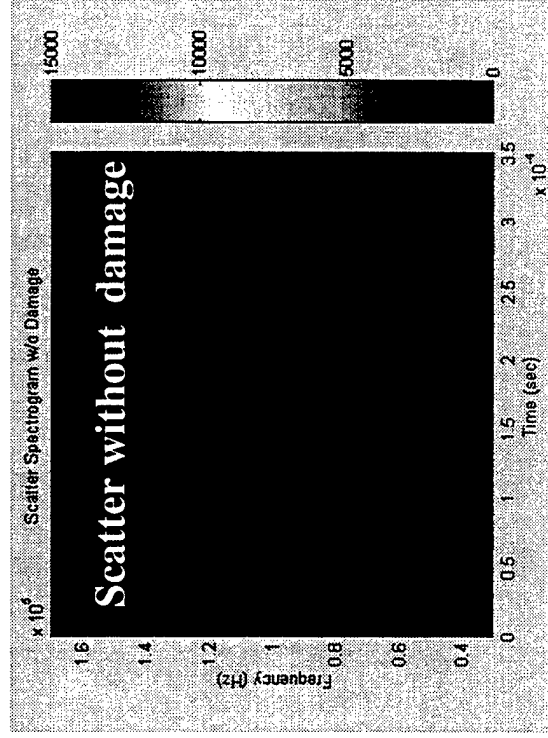
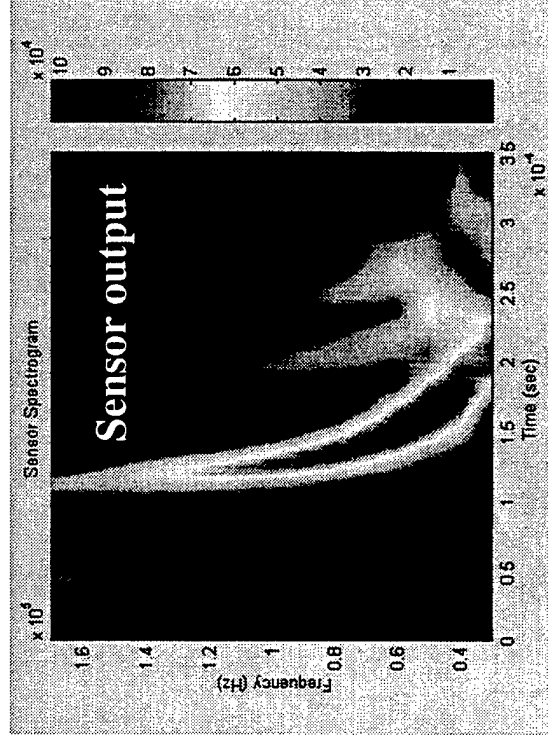
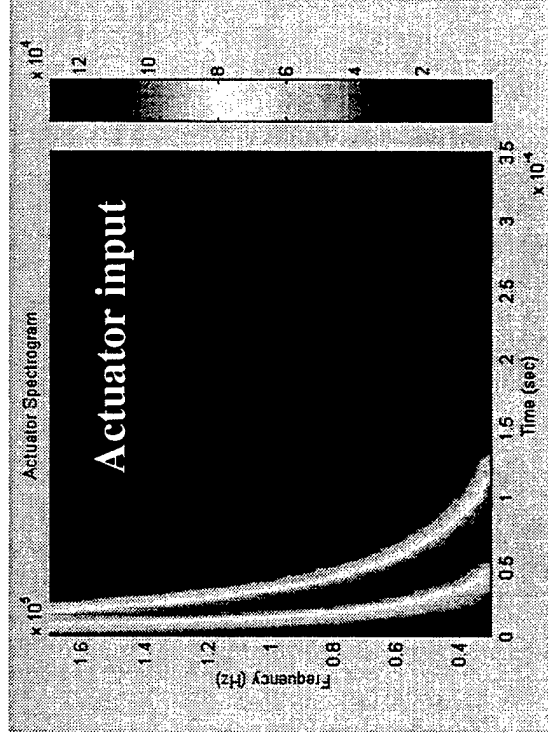
SENSOR



Unit : inch



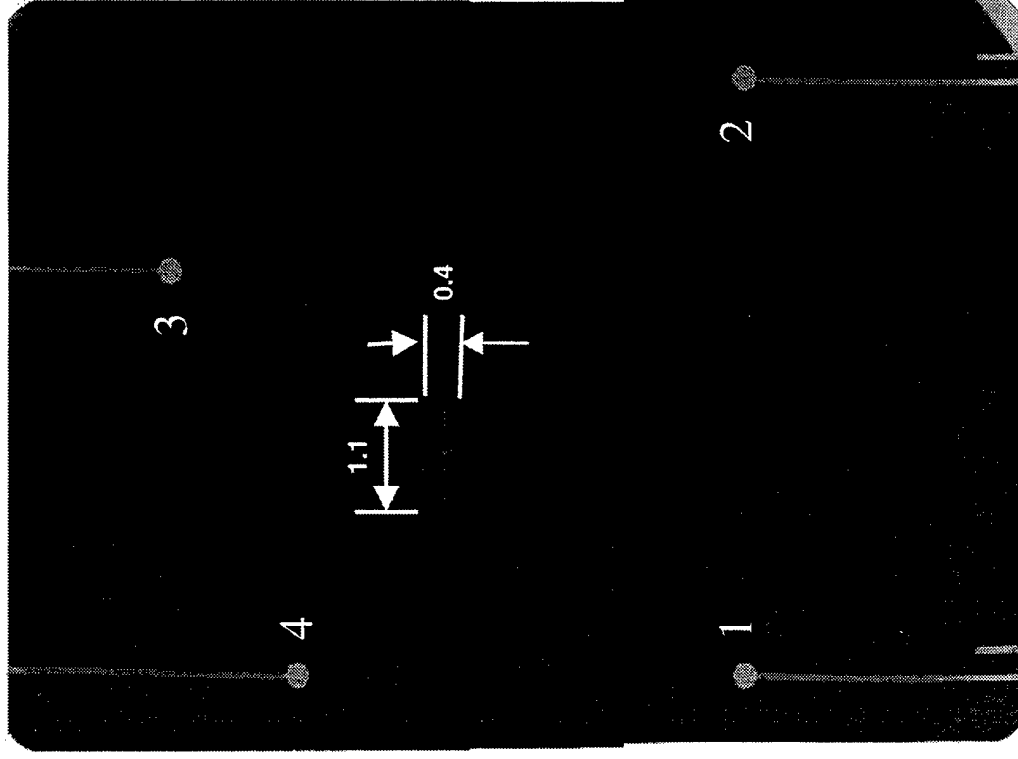
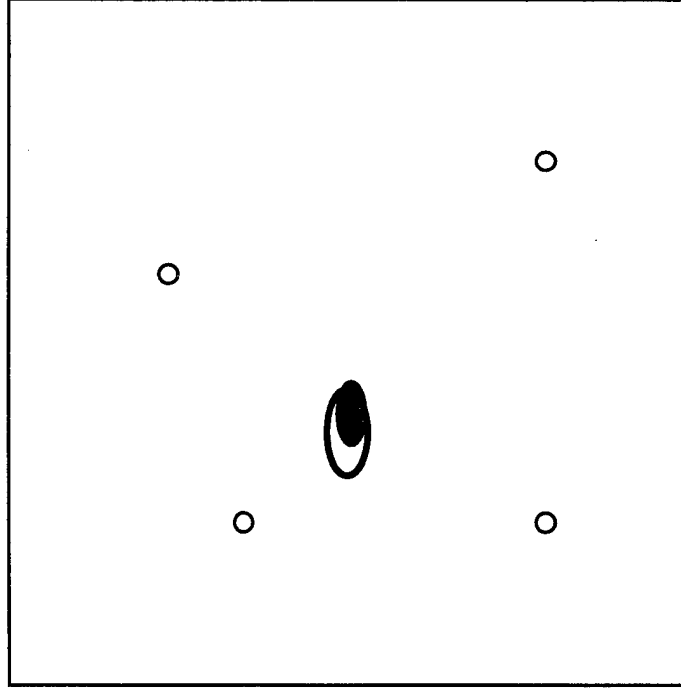
SPECTROGRAM for Path 2 → 3



MODEL VERIFICATION

Layout : $[0_4/90_4]_s$

○ Estimated ● Real Damage



BOUNDARY EFFECT DETECTION METHOD FOR LOCATING STRUCTURAL DAMAGE

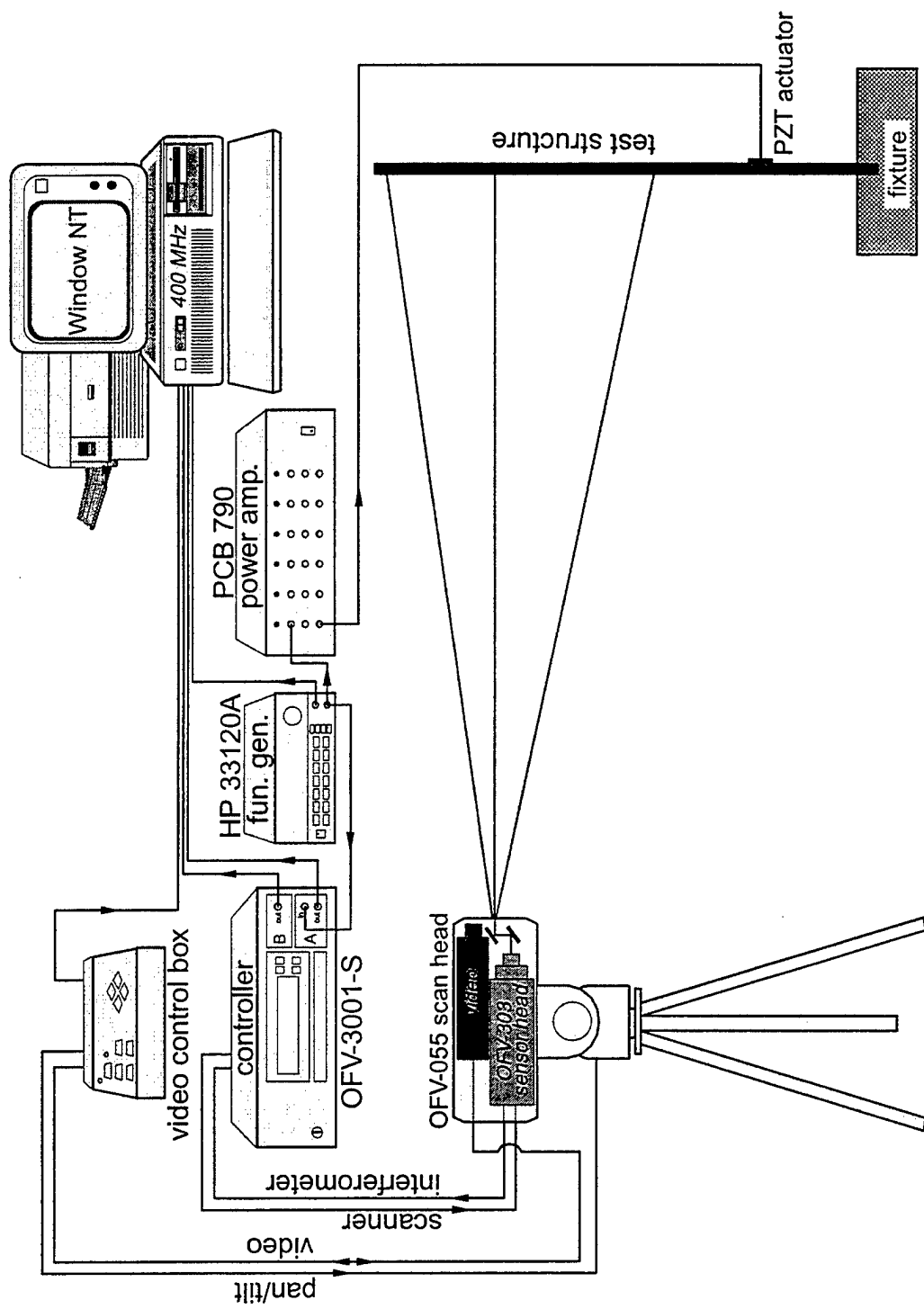
P. Frank Pai and Si Jin

Department of Mechanical and Aerospace Engineering

University of Missouri-Columbia

Columbia, MO 65211

Summary— This paper presents a method of pinpointing structural damage locations using Operational Deflection Shapes (ODSs) measured by a scanning laser vibrometer. The method assumes the form $C_1 \cos \beta x + C_2 \sin \beta x + C_3 \cosh \beta x + C_4 \sinh \beta x$ for an ODS to match with its experimental data using a sliding-window least-squares method to determine the four coefficients C_i . It is shown that C_1 represents the central solution of displacement, C_3 represents the boundary-layer solution of displacement caused by boundary constraints, $C_2 \beta$ represents the central solution of slope, and $C_4 \beta$ represents the boundary-layer solution of slope. Moreover, $C_1 * C_3$ is proportional to the difference of kinetic and elastic energy densities, $C_3 - C_1$ is proportional to the curvature, and $C_4 - C_2$ is proportional to the spatial derivative of the curvature. Because cracks on a structure introduce new boundaries to the structure and these coefficients change significantly at boundaries, crack locations are clearly revealed by the peaks on the $C_1 * C_3$ curve, sign change of C_4 , peaks on the fitting error curve, and sudden changes of $C_3 - C_1$ and $C_4 - C_2$. Moreover, numerical and experimental results show that each of these coefficients requires a different length of data points for curve fitting in order to smooth the curve. Based on this different data length requirement and the peaks and sign change of these coefficients we derive a Boundary Effect Detection (BED) method for finding damage locations. A nonlinear sliding-window least-squares fitting technique is also derived for estimating the extent of structural damage. Moreover, locating structural damage using torsional ODSs is also studied. Numerical and experimental studies on beams with different damages have been performed to prove the accuracy and reliability of this BED method.

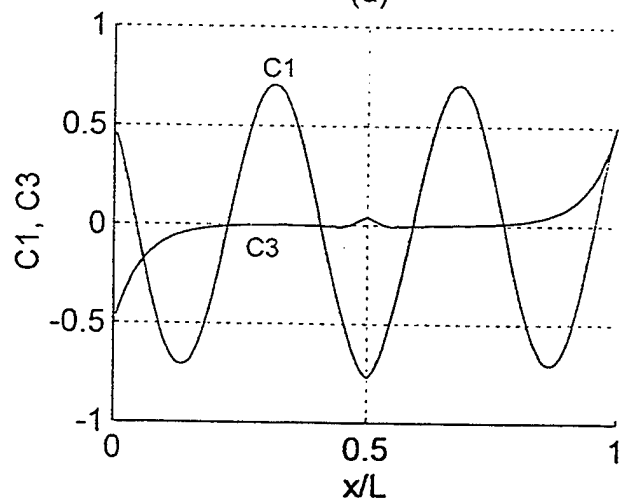
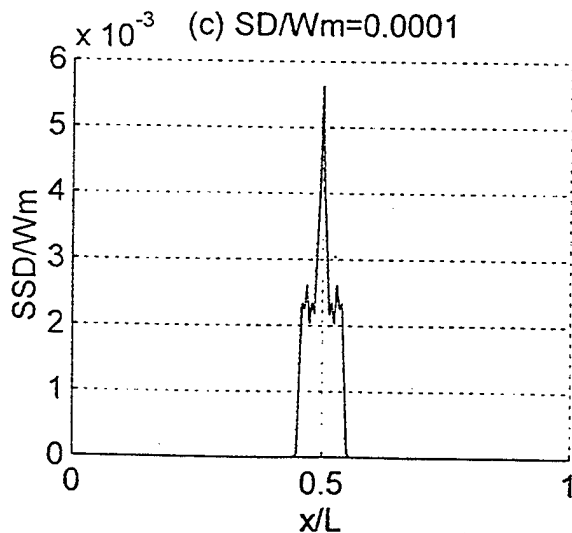
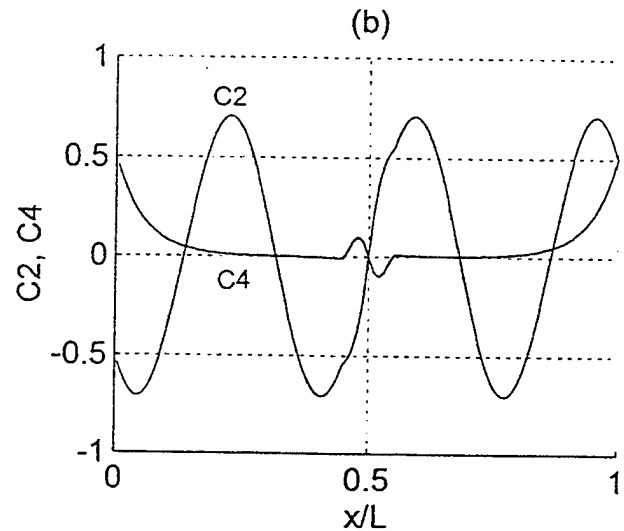
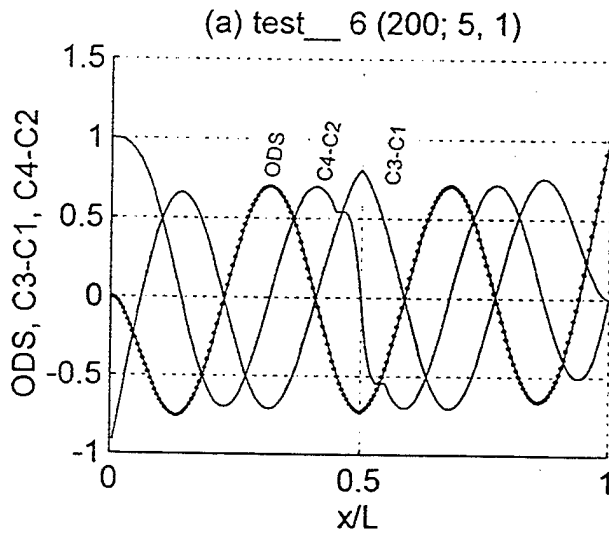
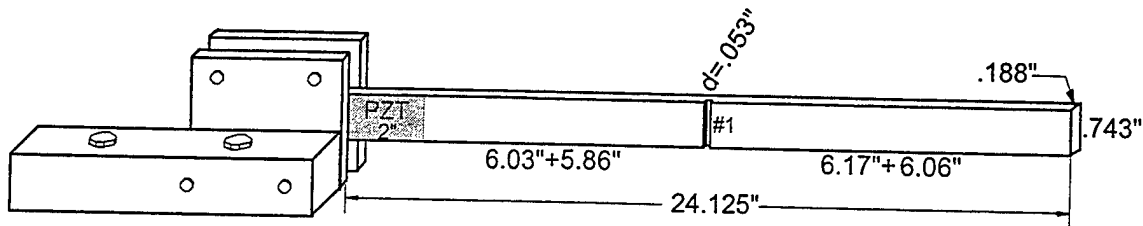


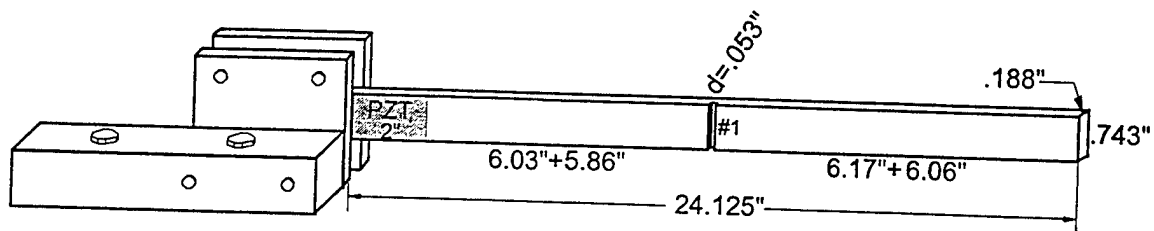
Structural vibration testing using the Polytec PSV-200 scanning laser vibrometer.

Boundary Effect Detection (BED):

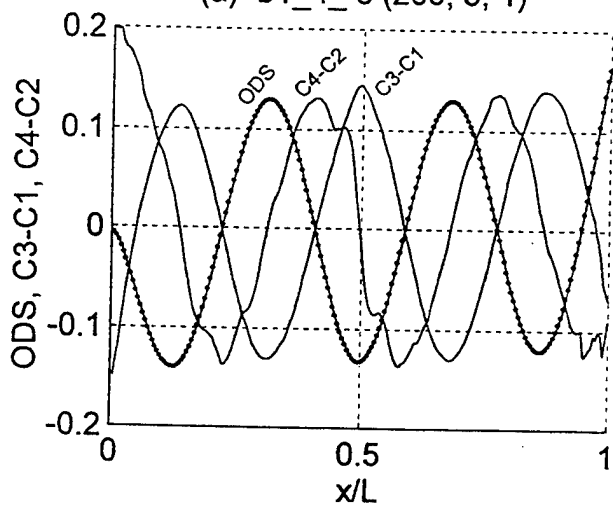
$$W(\bar{x}) = C_1 \cos(\beta \bar{x}) + C_2 \sin(\beta \bar{x}) + C_3 \cosh(\beta \bar{x}) + C_4 \sinh(\beta \bar{x})$$

$$E_{error} = \sum_{i=-N}^N \alpha_i (W_i - Y_i)^2$$

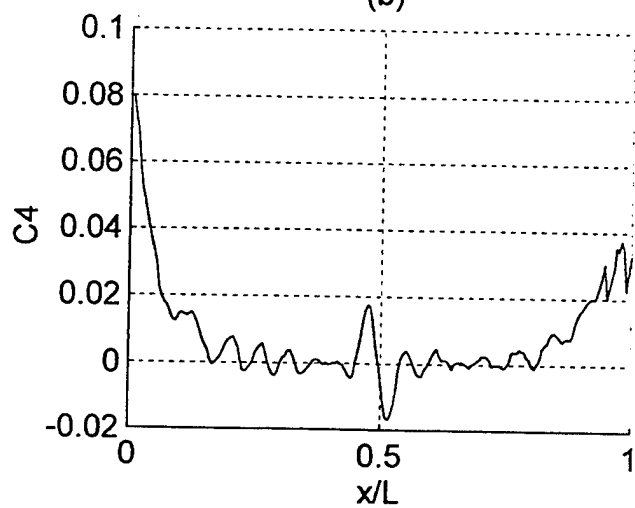




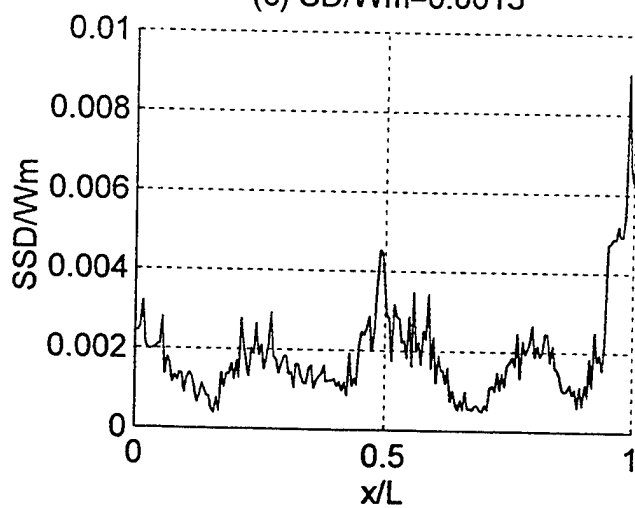
(a) b1_4_6 (200; 5, 1)



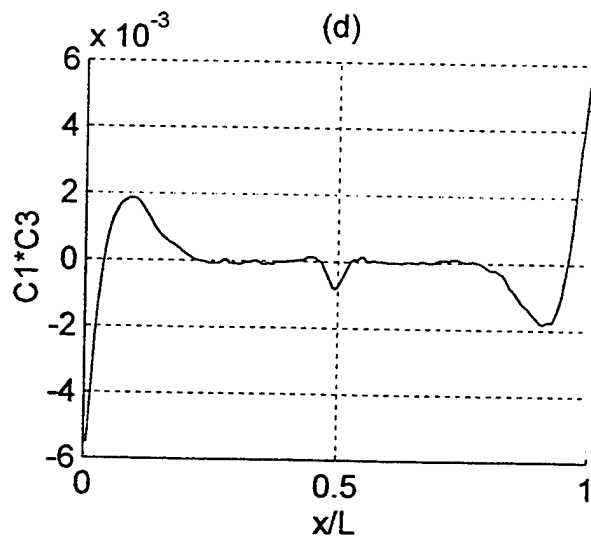
(b)

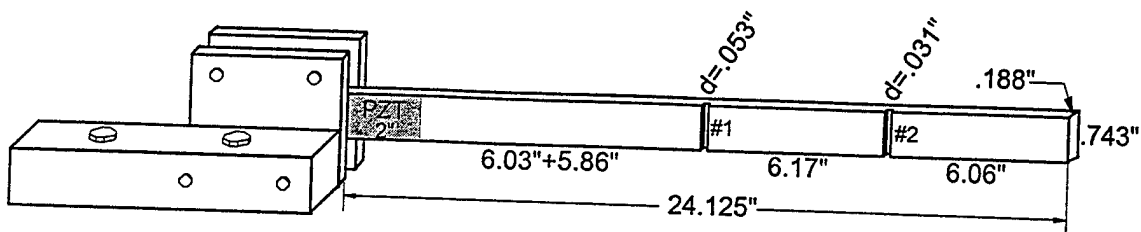


(c) $SD/Wm = 0.0013$

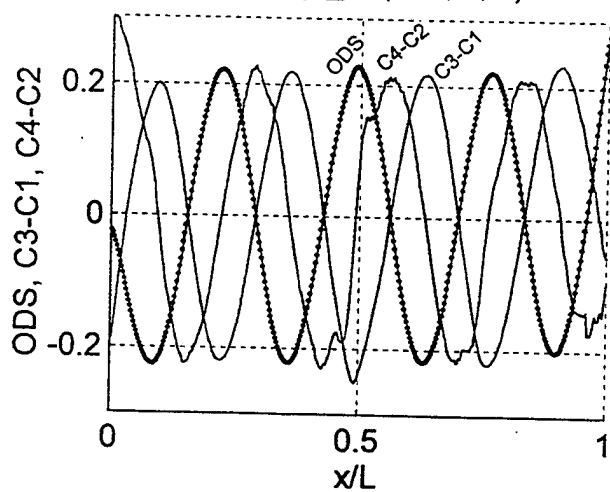


(d)

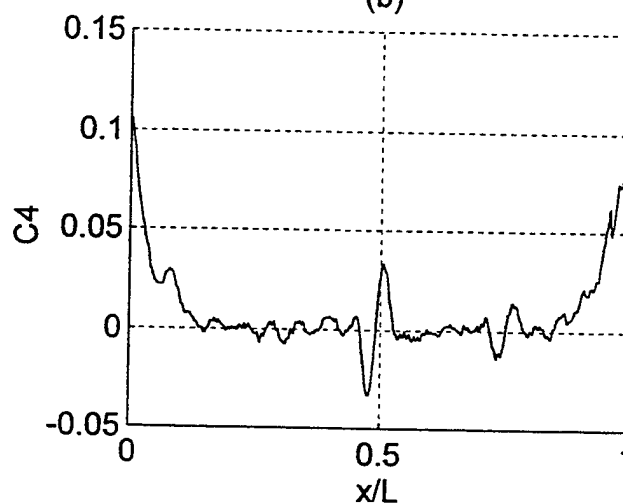




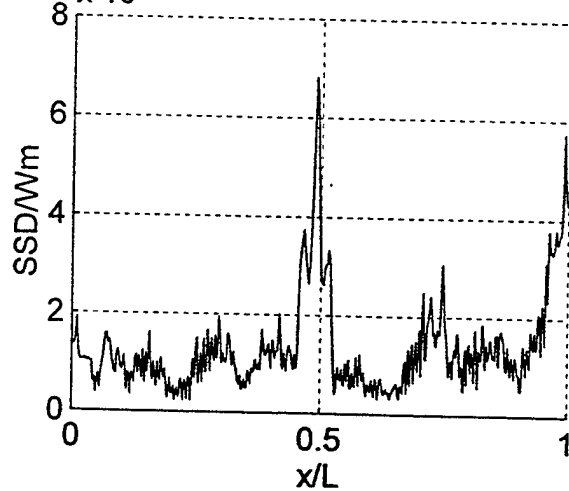
(a) b1_5_8 (400; 5, 2)



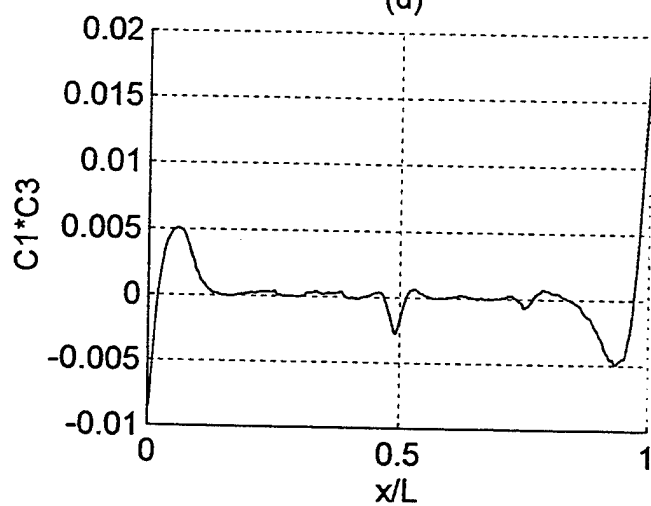
(b)

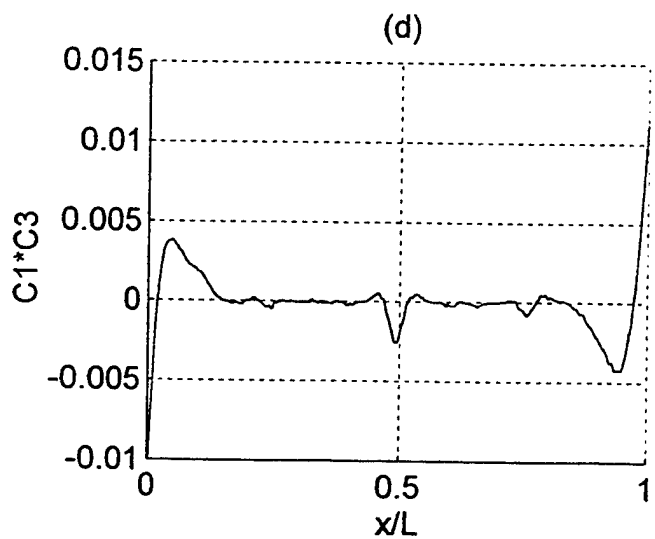
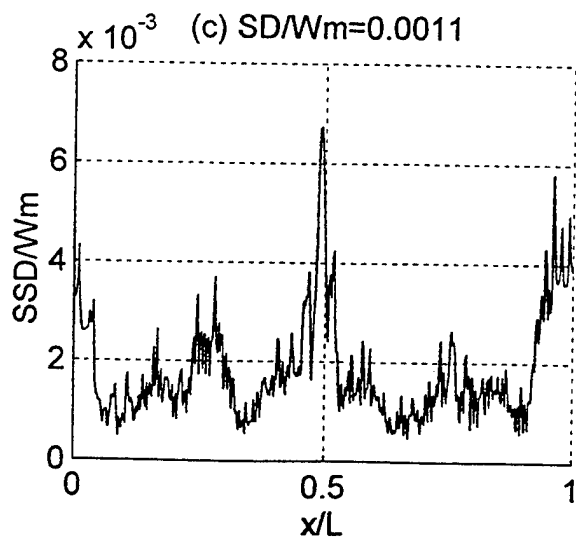
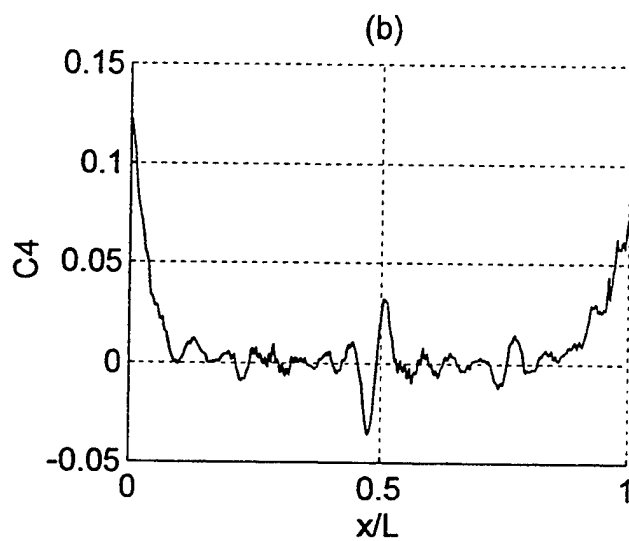
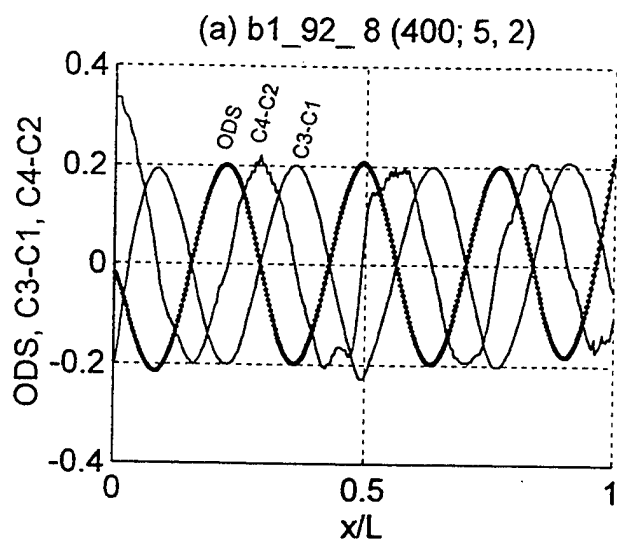
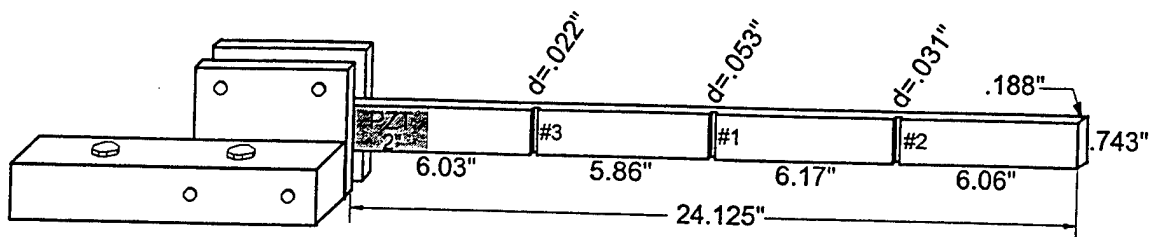


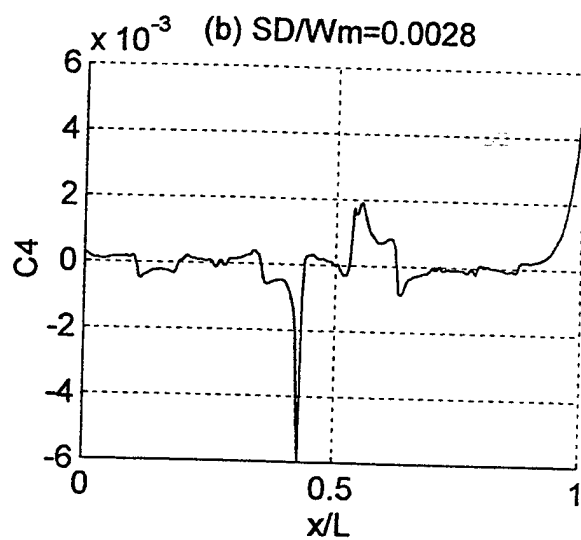
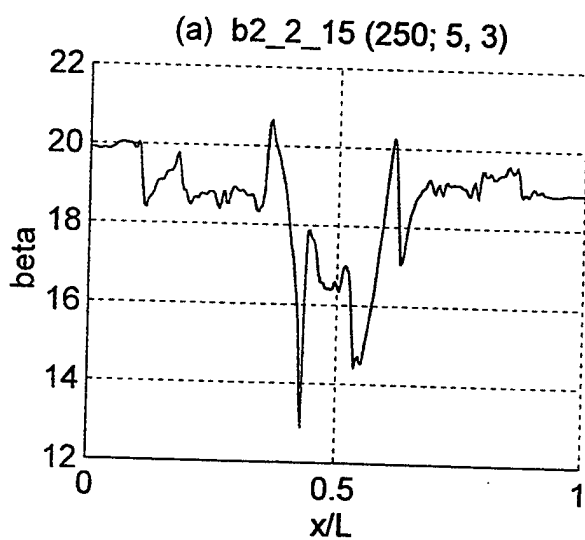
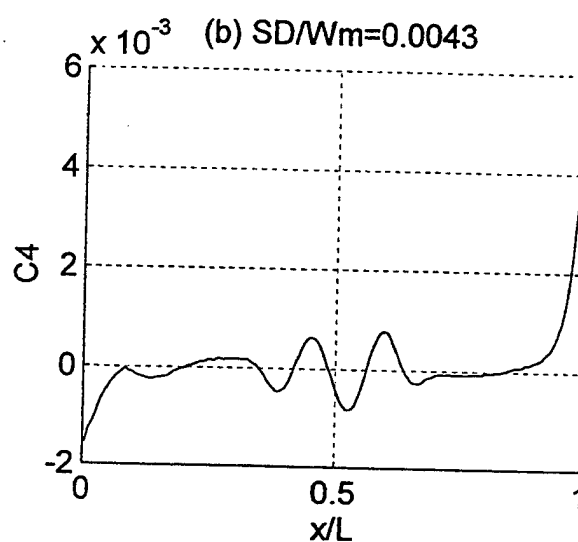
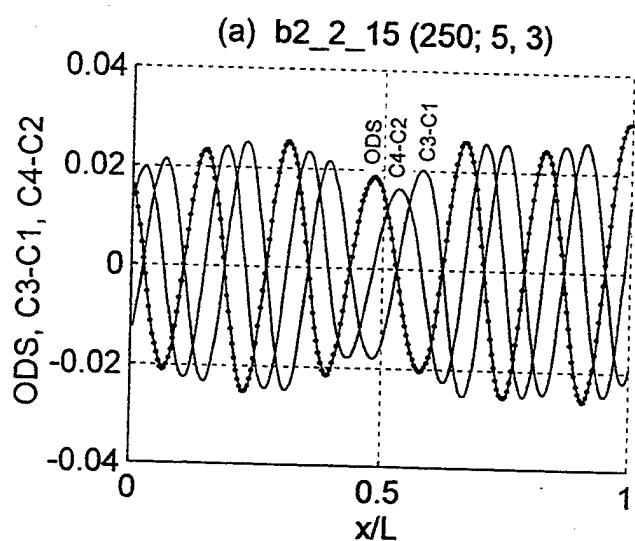
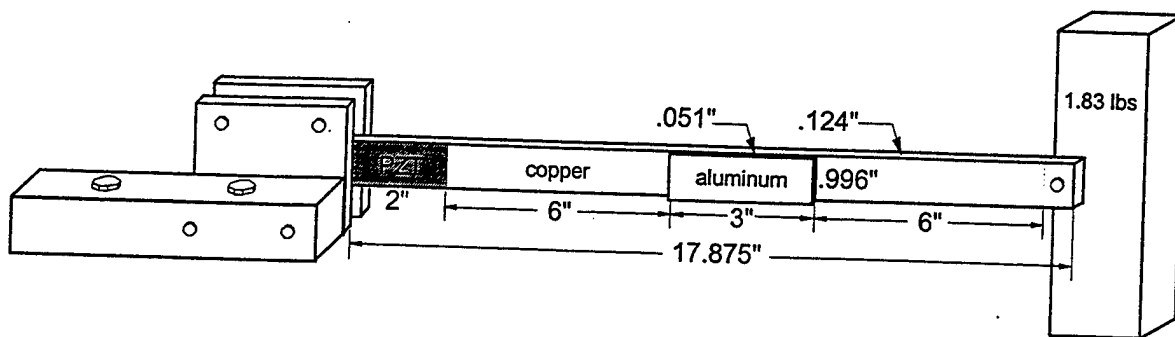
(c) $SD/Wm = 0.0009$

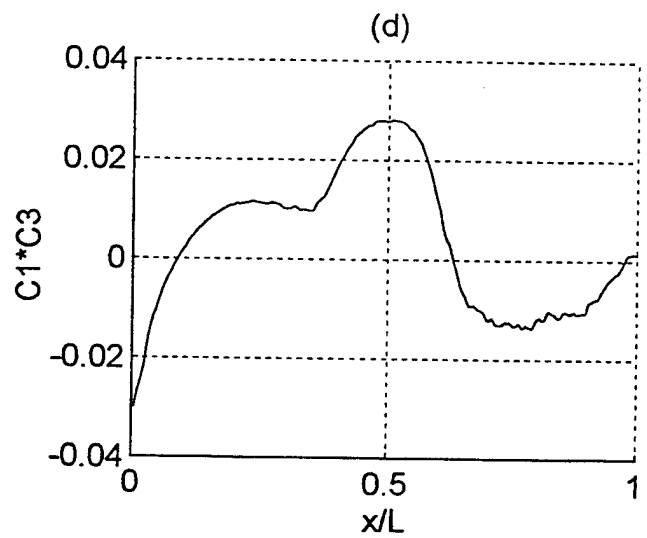
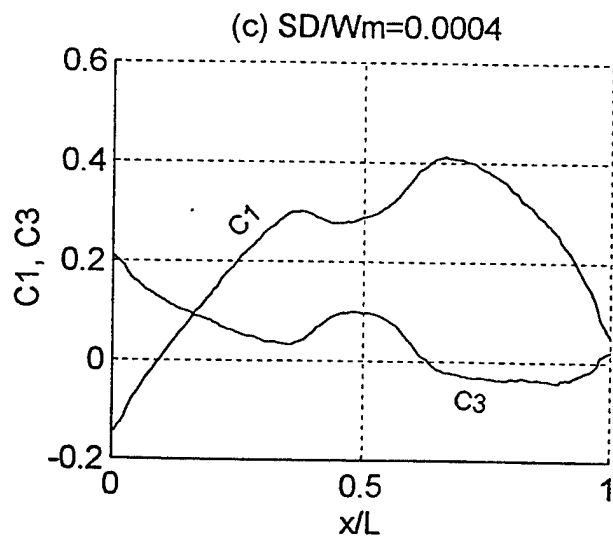
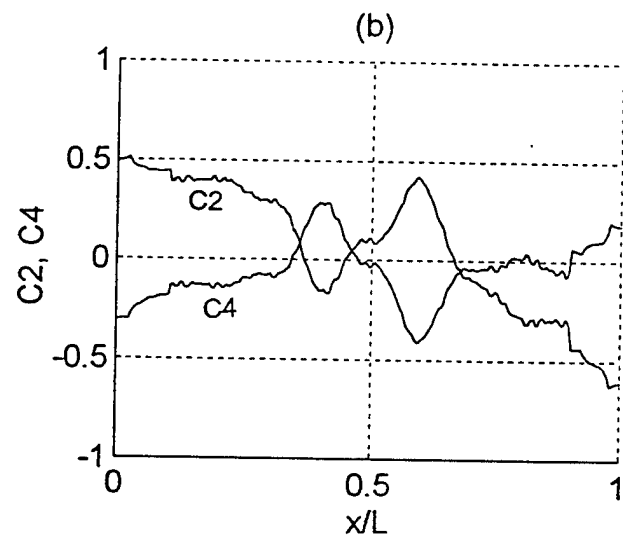
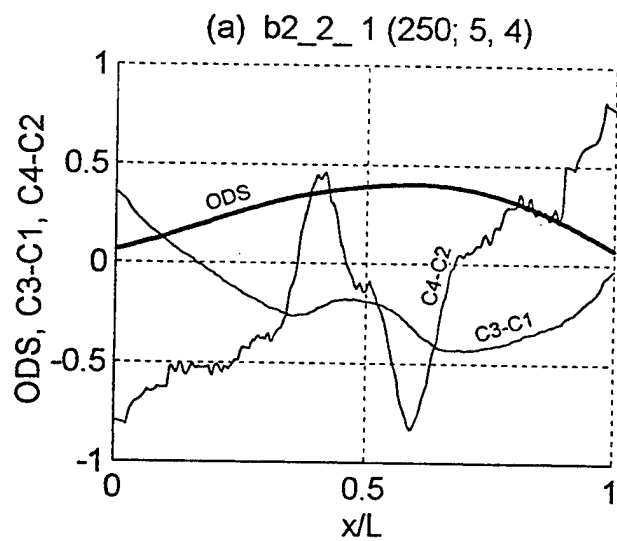
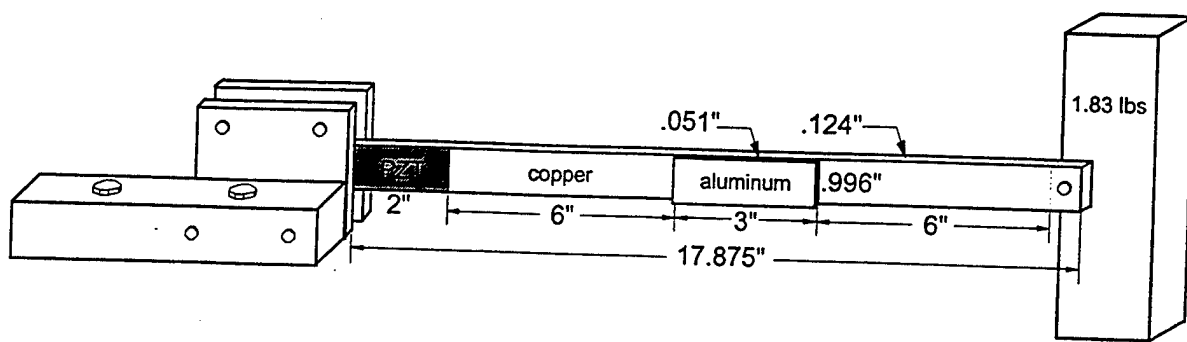


(d)

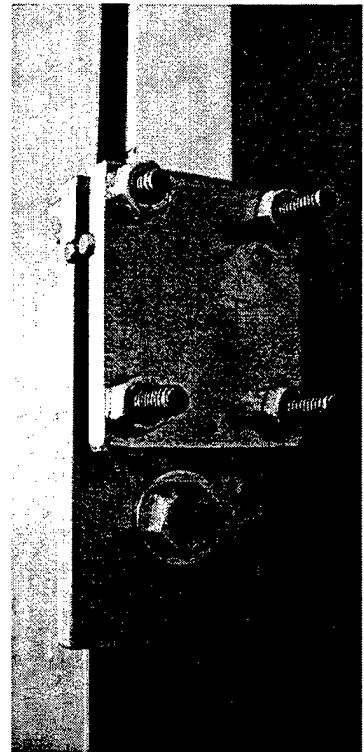
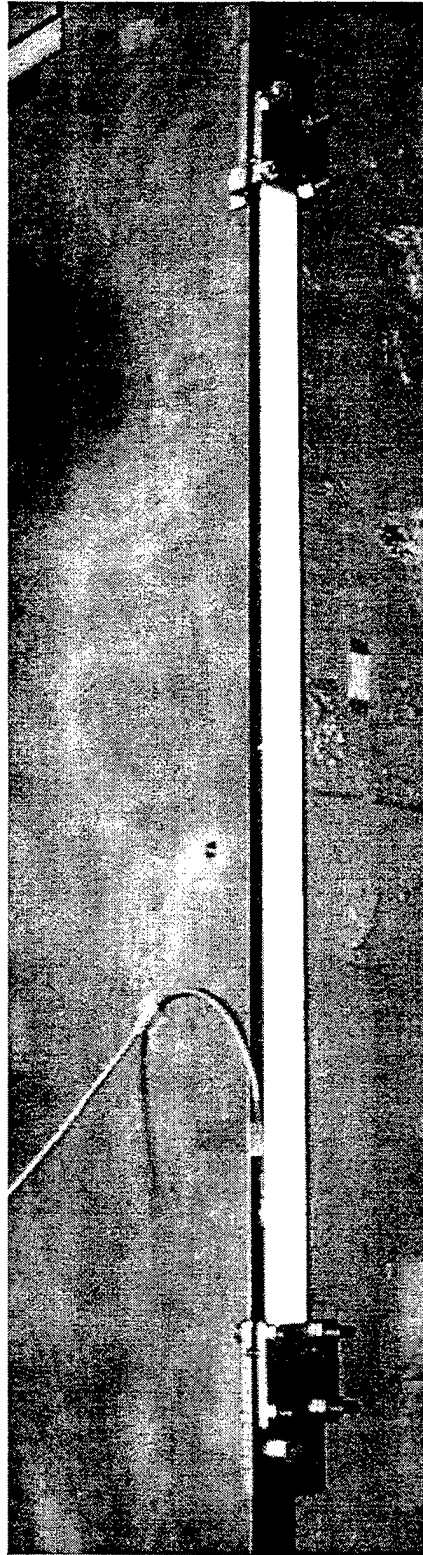
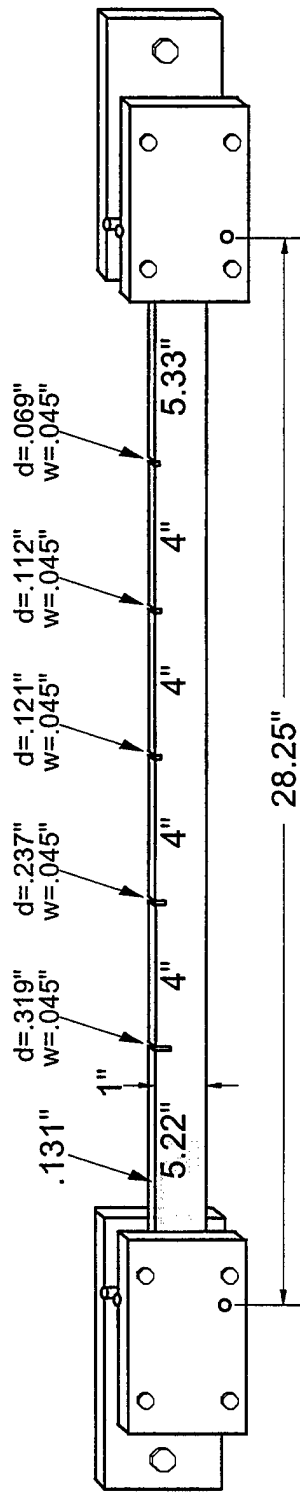




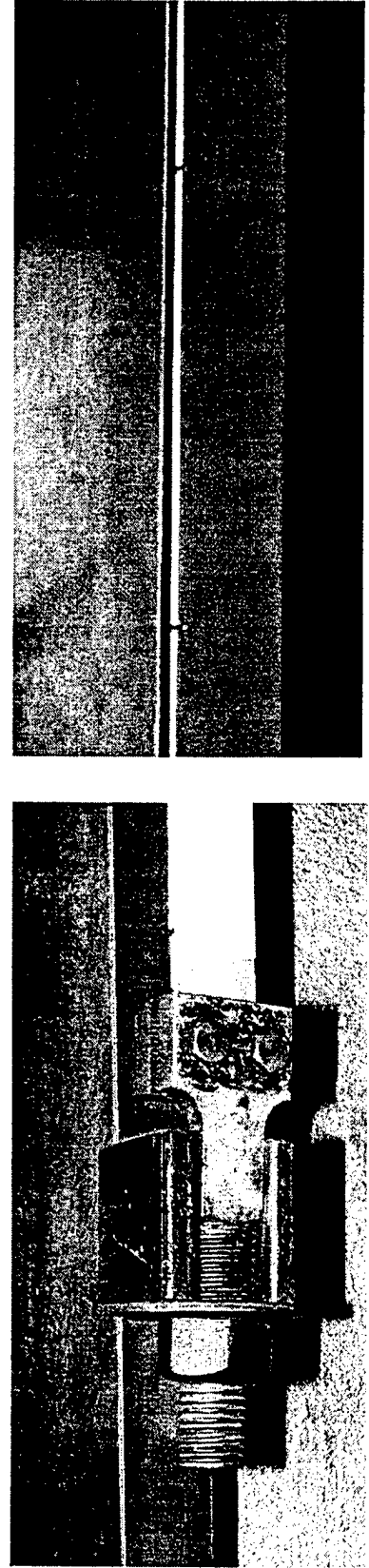
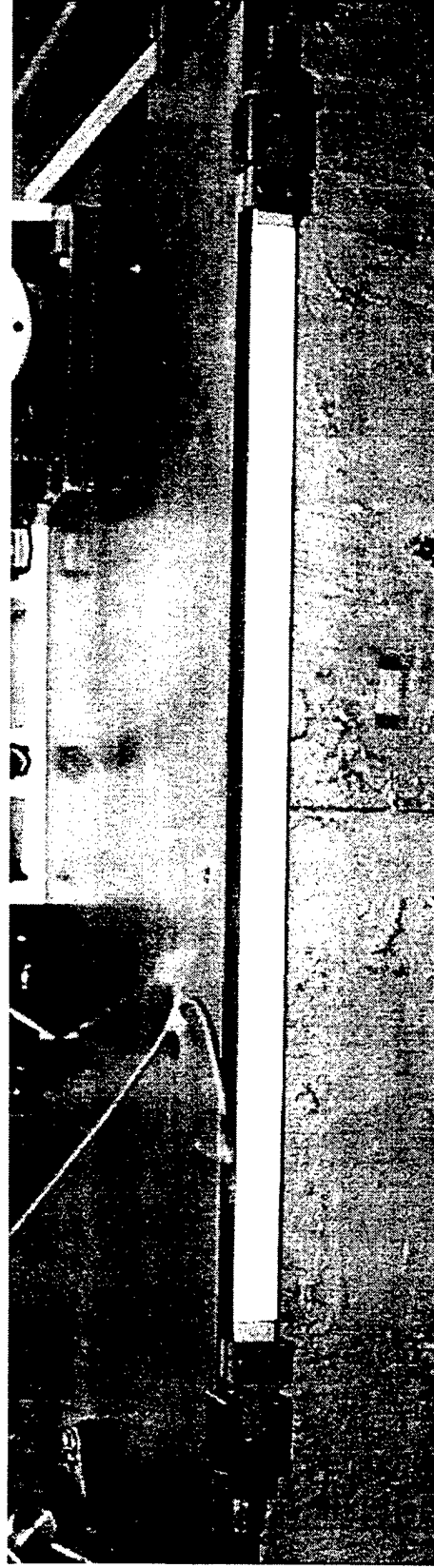
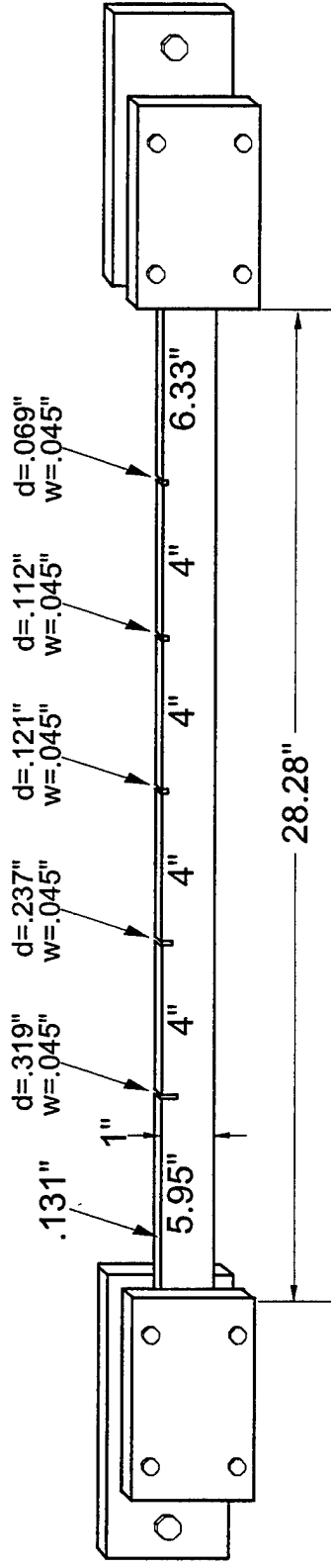




Damage Detection of a Simply Supported Beam:



Damage Detection of a Clamped-Clamped Beam with Pretension:



A Novel Fiber Optic System for Measuring the Dynamic Structural Behavior of Parachutes

M. El-Sherif, K. Fidanboyu, D. El-Sherif*, R. Gafsi, J. Yuan, C. Lee, and J. Fairney****

**Fiber Optics and Photonics Manufacturing Engineering Center
College of Engineering, Drexel University
Philadelphia, PA 19104**

Tel:(215)895-2324, Fax:(215)895-6684

E-mail: elsherif@ece.drexel.edu, Website: <http://coe.drexel.edu/FOPMEC>

*** Photonics Laboratories, Inc., Philadelphia, PA (215-387-9970)**

****US Army Natick RD&E Center, Natick, MA 01760-5019**

SUMMARY

For optimal design of the personnel parachute, the ability to predict the opening forces during an airdrop is crucial. Figure 1 shows the general force-time relation for an airdrop Model. Solving this challenging technical problem will permit better design for both military and civilian parachutes in terms of structural parameters and selection of materials. As a cost-effective solution to the current practice of over-designing parachutes, a novel methodology is presented for real-time characterization of the structural behavior of parachutes during inflation is presented. This method is based on the integration of fiber optic sensors into the parachute fabrics and suspension lines. These embedded sensors are used for stress measurements in real-time.

Two types of fiber optic sensors are used to measure axial, bi-axial, and transverse deformation of a parachute canopy and suspension lines. An optical fiber Bragg grating (FBG) type sensor is used as a short strain gauge for axial strain measurements. The second type of fiber optic sensors is based on the Modal Power Distribution (MPD) technique, developed by M. El-Sherif through several Army and DoD projects. Acting as a long length strain gauge, this is also the only sensor type that can be used in measuring transverse stresses. The integration of these two types form a novel sensory system capable of measuring the dynamic structural behavior of a parachute during inflation. Axial, bi-axial, and drop lab tests were conducted to demonstrate the concept of the proposed methodology.

Three different types of experimental tests were carried out to fulfill the goals of this project. These were broken down into three main components.

- 1) Mechanical testing of parachute fabric.
- 2) Parachute fabric and suspension line testing with optical fiber using the MPD technique.
- 3) Parachute fabric testing with optical fiber using the FBG technique.

Mechanical Testing of Parachute Fabric

With the end goal of fully integrating optical fibers to be used as strain sensors in the canopy material of a parachute, mechanical testing of parachute canopy was essential to establish the required properties of the optical fiber selection. A number of uniaxial tensile tests were performed on rip-stop nylon fabric. This testing was done in both the fill and warp directions to determine the maximum stress, strain, and the Young's modulus of the woven fabric shown in Figure 2. Tensile samples were prepared and tested using a 5000 lb. load cell. Data was obtained by using a Lab View 4.1 interface. Results showed that the warp direction exhibited an average modulus of 228 ksi, while the fill direction had an average modulus of 182 ksi (see Figures 3&4). The fill direction also had two separate regions that were significantly linear. These regions were treated individually. The warp direction did not have two distinctive linear regions. The average stress and strain at failure were also found for both the warp and fill specimens. The warp's average stress and strain at failure was 35 ksi and 25 percent respectively. The fill specimens average stress and strain at failure was 32 ksi and 28 percent respectively.

Testing Parachute Materials Using the MPD Technique

The MPD technique is used with multimode optical fibers for real-time characterization of canopy fabrics and suspension lines. In order to monitor the state of the material, the variation of the modal power within multimode optical fibers in response to external loads is used. The light in multimode optical fibers propagates in a finite number of guided modes forming a set modal patterns. In the presence of an external load applied to a multimode optical fiber, the boundary conditions at the core-cladding interface will change. Changing the boundary conditions will lead to a redistribution of the modal power. This redistribution will be detected at the fiber output end. The modal power redistribution (MPR) measurements will lead to the information on the external disturbance applied to the embedded fiber. By scanning the far-field pattern at the fiber end using a CCD camera or array of photodetectors, the measurements of the distribution and subsequent redistribution of the modal power can be continuously recorded.

Experiment I: Fabric Testing with: (a) CCD Camera and (b) Photo-detector

A strand of optical fiber was stitched and embedded along a square piece of nylon fabric. This nylon fabric was mounted on a Biaxial Tensile Tester. The schematic test set-up is shown in figure 5. The optical fiber was then connected to a light emitting diode (LED) from one end and a CCD camera at the other. The switches on the control panel of the tensile tester allow one to pull the fabric in two directions: in an X-direction or in a Y-direction, or even both. The fabric being tested had the optical fiber running along the X-direction and pulling was performed along the Y-direction only or in both. The control panels display the amount of displacement occurring in the fabric along with the load in kilograms pulling the fabric.

The test was carried out in a uniform systematic way. The tensile tester would pull the fabric a certain amount, then the result (the far-field ring pattern) was captured by the CCD camera and frame grabber and saved in the computer memory. Several readings were taken for loading and

unloading the fabric. The images of the far-field ring patterns were processed and the intensity profile of each image was developed and plotted. These profiles present the light intensity distribution within the multimode fiber at a certain loading condition, as shown in Figure 6. Each curve represents the light intensity profile at a certain loading condition. Each of these profiles is taken at a line passing through the center of the far-field ring pattern.

Figure 6 shows that the fiber was very sensitive to each load applied to the fabric. The figure shows the values of the output scanning angle in degrees, versus the normalized output intensity of the far field pattern at the fiber end. The loads applied to the fabric varied from 0.00 to 21.96 pounds. With no load, the normalized output intensity was approximately 1 at the angle 10.7 degrees, this value decreased as the number of loads increased. We can see that the distribution of light has been changed under various loading conditions. The light shifts partially from higher order modes to lower order modes. As a result, the value of the light intensity at the peak location was gradually decreased. At the same time, the intensity of light at the lower order modes (represented by the lower angles) is increased. The value of intensity at 10.7 degrees was approximately 0.5 when the maximum load 21.96 pounds was applied. In case of replacing the CCD camera with a photo-detector positioned at 10.7 degrees, the photo-detector will show the variation of light at this specific location. The expected output of this photo-detector is presented by the points on the curves which are located at 10.7 degrees, as shown in Figure 7. As the loads decreases, the percent change also decreases.

The results achieved for this part of the project were very positive and very encouraging. Since using a CCD camera for real-time measurements within the parachute is not realistic, the CCD camera was replaced by a photo-detector. In this case, the test set-up was modified to a simple and sensitive set-up.

There are several reasons for replacing the CCD camera with a photo-detector. Planning for the actual experimental set-up for real-time characterization of the parachute during inflation time requires special type of components that are very rigid light and small. The same experiment processed with a CCD camera was repeated with a photo-detector replacing the CCD camera. At each incremental force applied, the induced change in the sensor output as well as the displacement was measured (induced strain was recorded). The results will be presented in the Fourth ARO Workshop.

Experiment II: Rope Testing Using the CCD Camera and Photo-detector

The rope material used in this part of the experiment is the same material being used for the parachute suspension lines. The rope had the optical fiber stitched along its length. The suspension rope had the fiber stitched on its surface in a straight line parallel to the rope axis. The optical fiber was stitched only in the center part of the rope for approximately 4 inches. Therefore, the two ends of the parachute rope (about 4 inches) were free from the optical fiber. This method of stitching was used to insure the fibers' protection against damage when the rope was placed into the biaxial tensile tester.

The experimental set-up is identical to the set-up used for the fabric. Here, the parachute rope was placed along the longitudinal (Y) axis of the biaxial machine. Each end of the rope is

wrapped around one of the center pins along the Y-axis of the machine. One end of the fiber was placed close to the CCD camera while the other was placed off axis to the LED. The rope was tested during loading and unloading. Experimental results are encouraging, and will be presented in the workshop meeting.

As before for testing the parachute fabric materials using the CCD camera and the photo-detector set-ups, in the rope experimental test, the CCD camera was replaced by a photo-detector, as shown in figure 8. As mentioned before, the photo-detector will satisfy the requirements for real-time air drop tests. The results record the relation between the applied force and sensor output as well as the displacement (strain) and the sensor output. Again, very nice accurate uniform relationships were developed correlating axial forces (or strain) applied to the rope to the sensor output. The results will be presented at the meeting.

Testing Canopy Fabrics Using the FBG Technique

Sample Preparation and Experimental Set-Up for Testing a Canopy Nylon Fabric

The grating region of an optical fiber Bragg grating (FBG) was bonded on the surface of a piece of canopy rip-stop nylon fabric, at its central part. This fabric, which integrates the optical fiber Bragg grating, was placed in the biaxial tensile tester. The used optical fiber Bragg grating has a reflection wavelength is $\lambda_{B,0}=1299.97$ nm. The optical fiber was connected to the opto-electronic devices and components. The experimental set-up for the FBG test is shown in Figure 9.

Experimental Work

The optical source is a broadband InGaAs light emitting diode with a central wavelength 1300 nm and a band width equal to 65 nm. The Y optical fiber coupler is a bidirectional 3dB coupler. The optical spectrum analyzer (OSA) is from ANDO Corporation (Model AD-6310B) with a wavelength resolution of 0.1 nm, dynamic range from -80 dBm to +10 dBm and wavelength accuracy of ± 5 nm.

Before starting the test, a strong reflection spectrum of the optical fiber, at the Bragg wavelength was observed. The fabric was placed in the tensile tester and the load was applied. The tests were carried out during loading and unloading conditions. The correlation between the loading and unloading curves confirms the reversibility of the response of the optical Bragg grating fiber to the tensile condition. A sample of the results of the Bragg reflection wavelength versus applied tensile stress (force) is shown in Figure 10. The results reveal good correlation and good reproducibility of the sensors response. The results also showed that the Bragg fibers can be used with textile structures as strain gauge or strain sensor.

Conclusion

Based on the successful achievement on the feasibility study performed throughout this project, the developed methodology will open the doors for many applications. More work is needed for full scale testing of parachutes in real-time. The developed technology will pave the way for future development of smart fabrics for military applications, such as clothing and tentage. In

the commercial market, this technology will be useful for parafoils for sport jumping, canopy and suspension line design for fire fighters and rescue workers, and any flexible network structure.

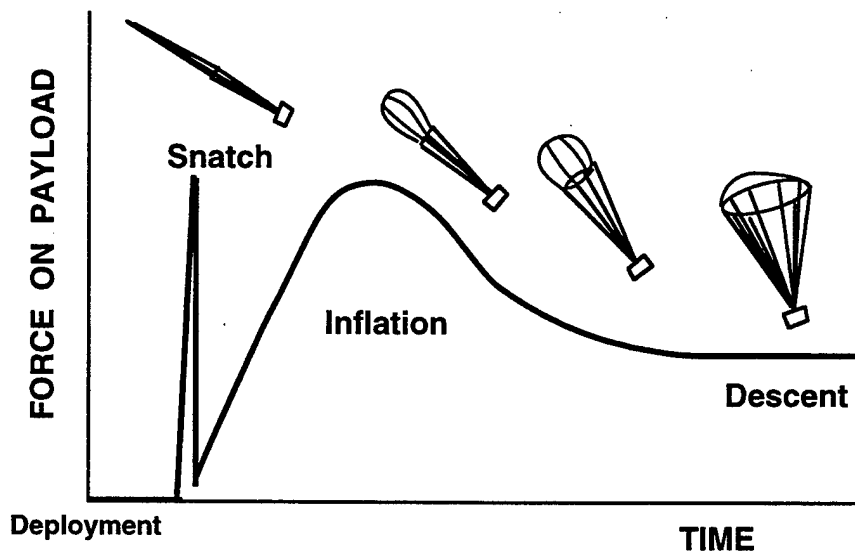


Figure 1. Payload force versus time for a typical circular parachute drop.

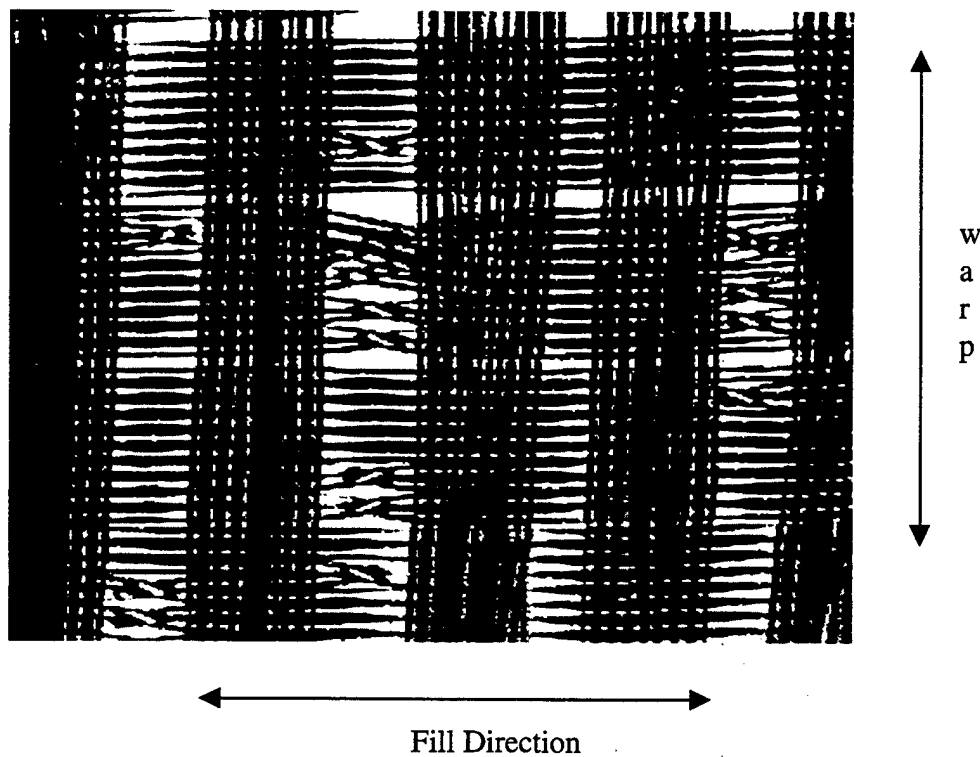
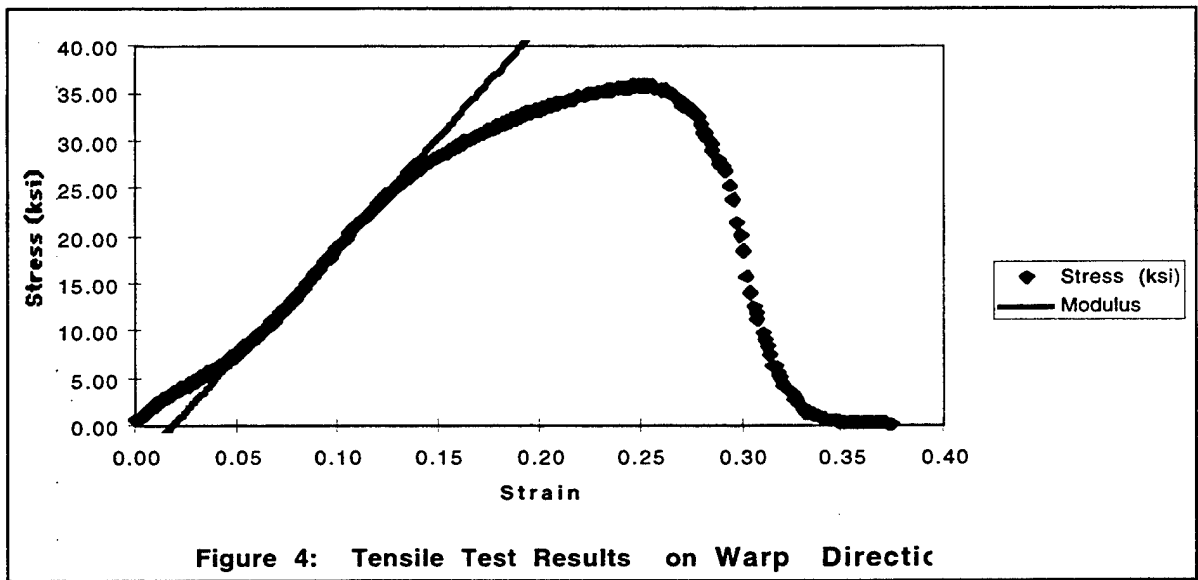
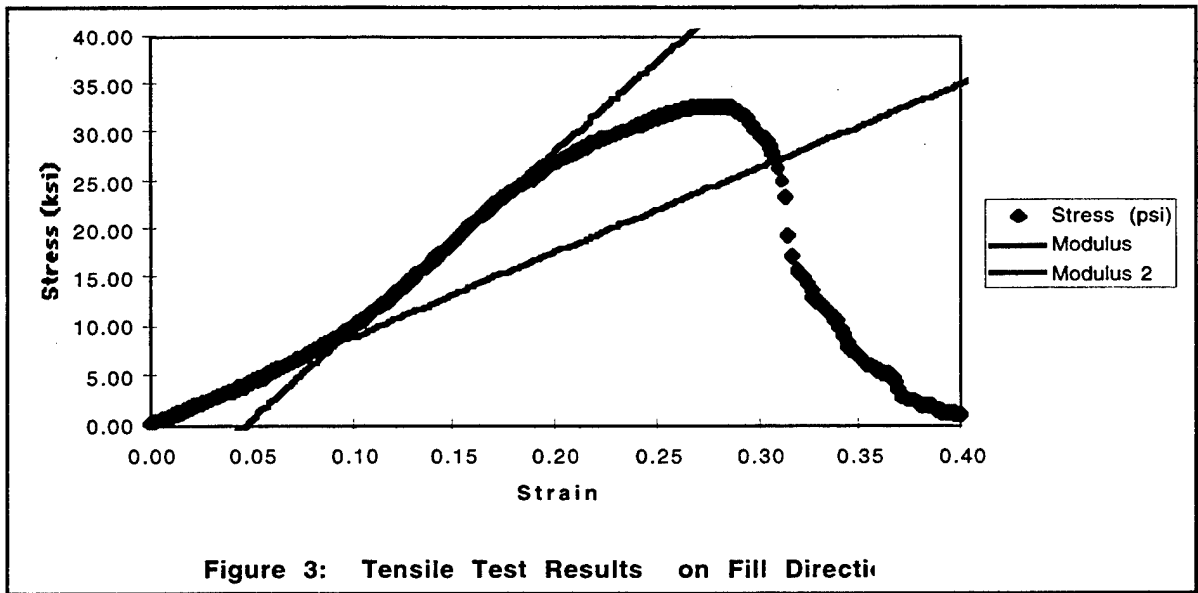


Figure 2 Photomicrograph of a parachute rip-stop nylon fabric.



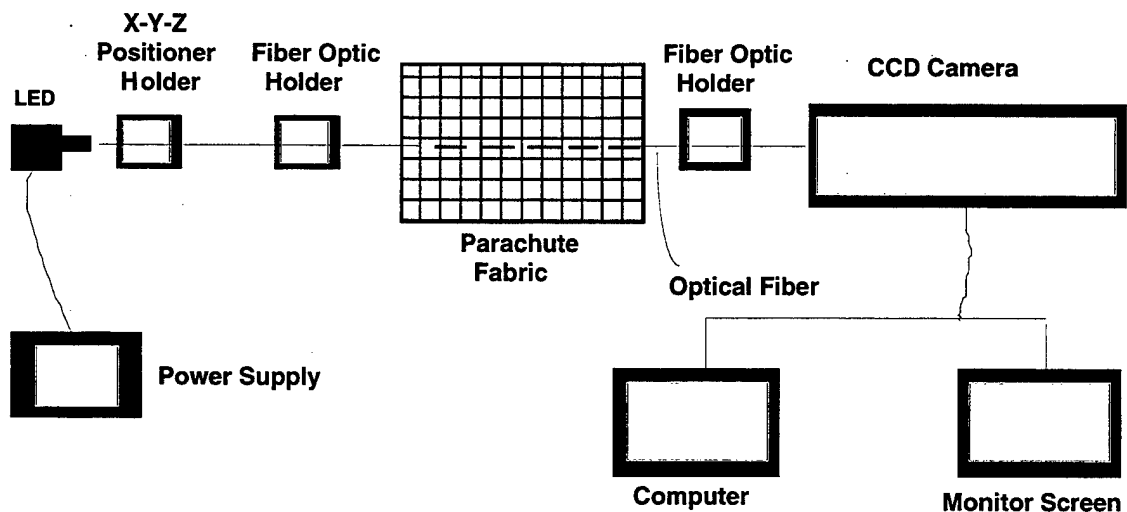


Figure 5 Experimental set-up for testing parachute fabrics using a modal power distribution (MPD) technique with a CCD camera.

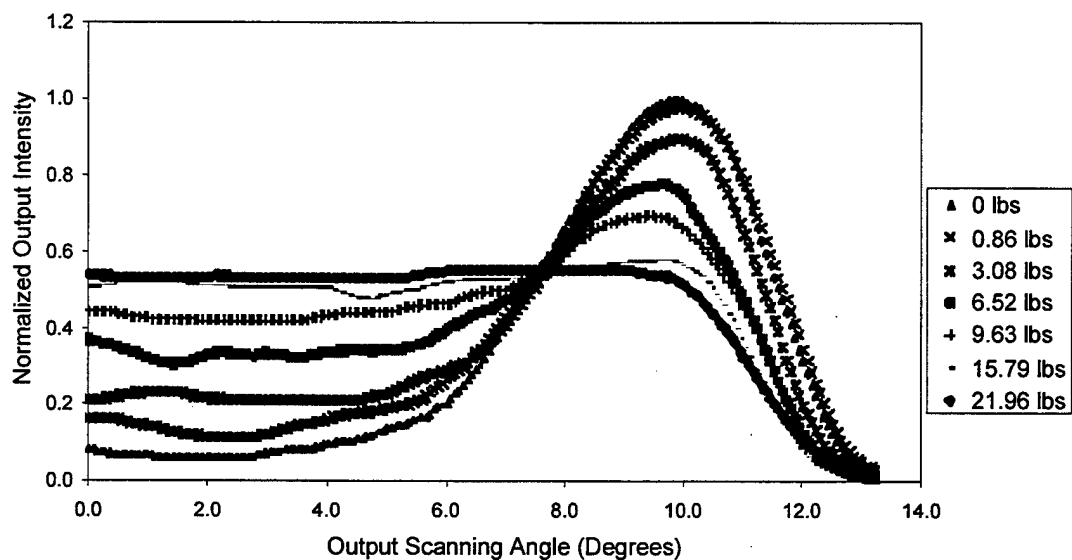
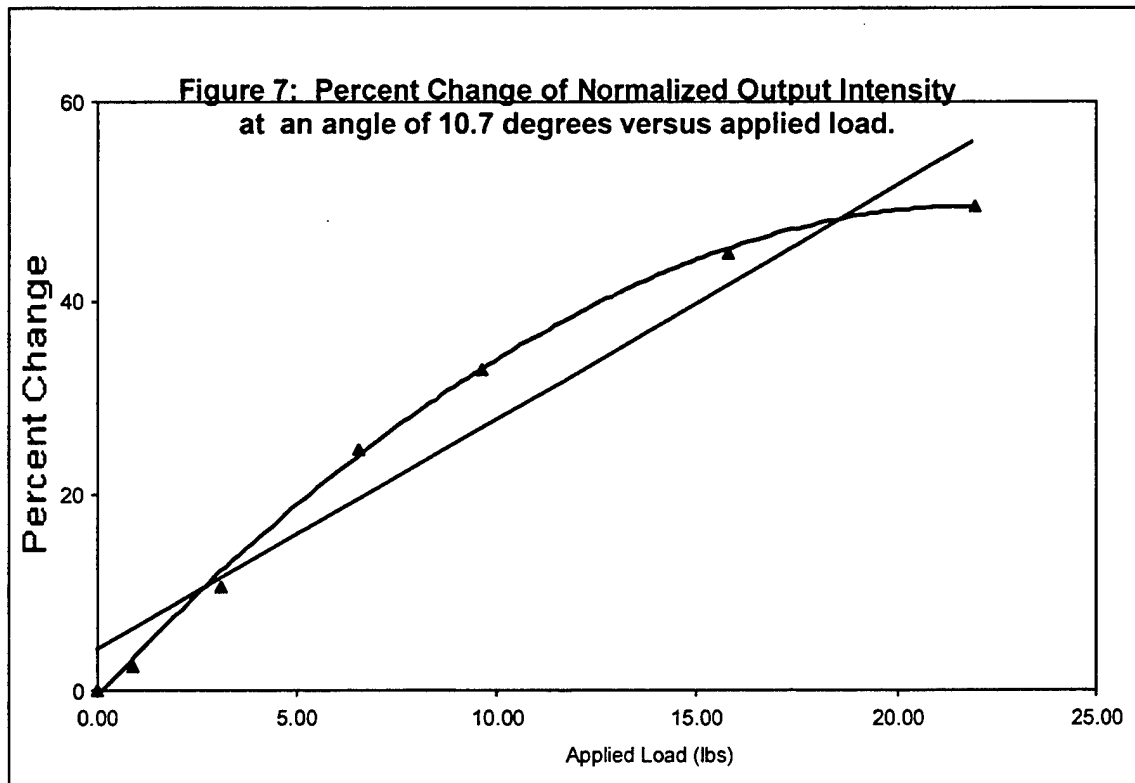


Figure 6 Normalized Output Intensity versus Output Scanning Angle for Different Transverse Axial Load



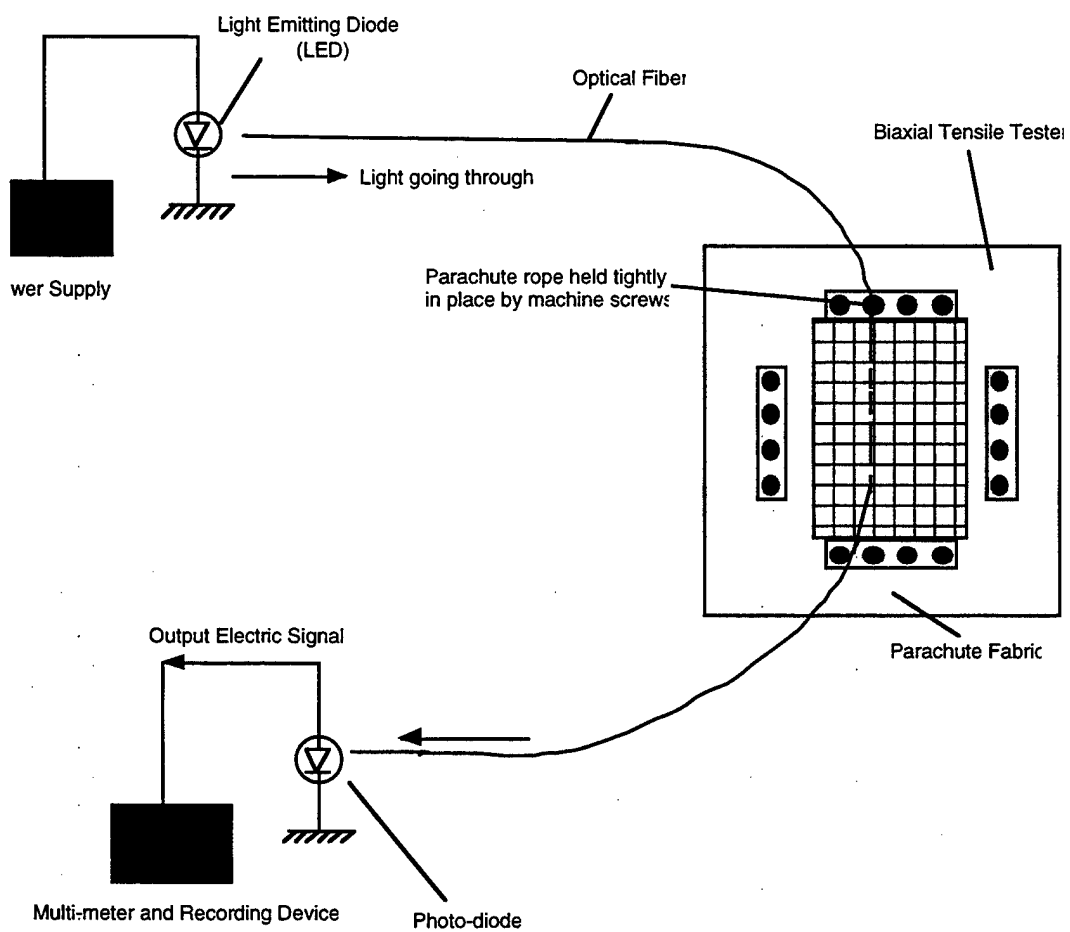


Figure 8 Schematic diagram of fabric testing with photo-detector.

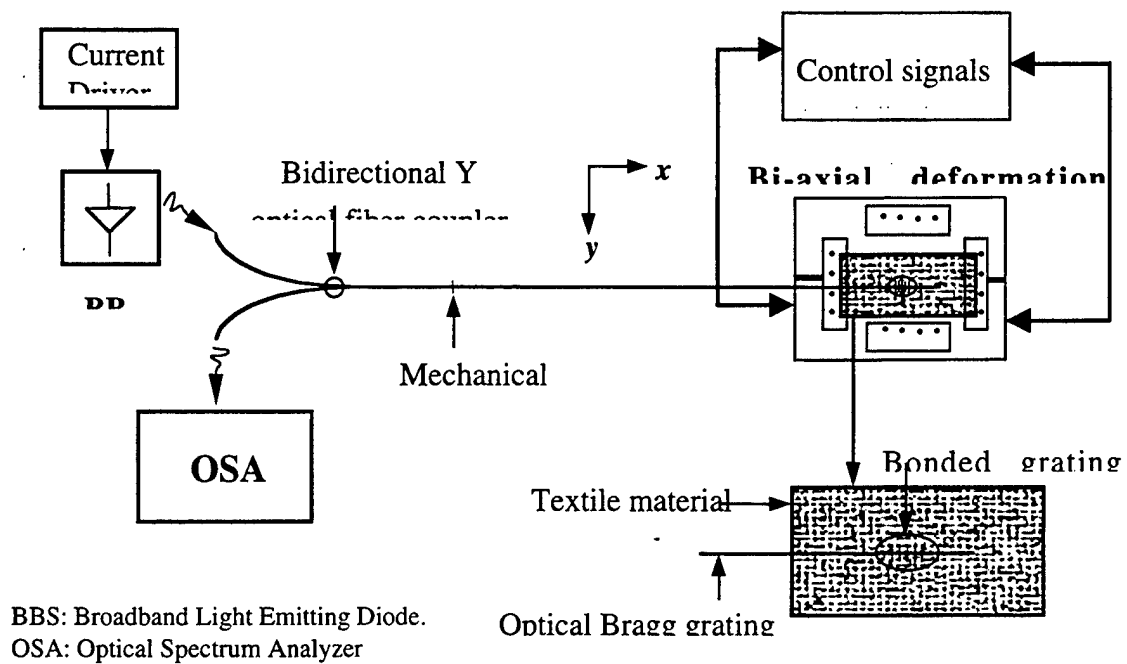


Figure 9 Experimental setup for tensile testing of a nylon canopy fabric, using an optical fiber Bragg grating strain gauge.

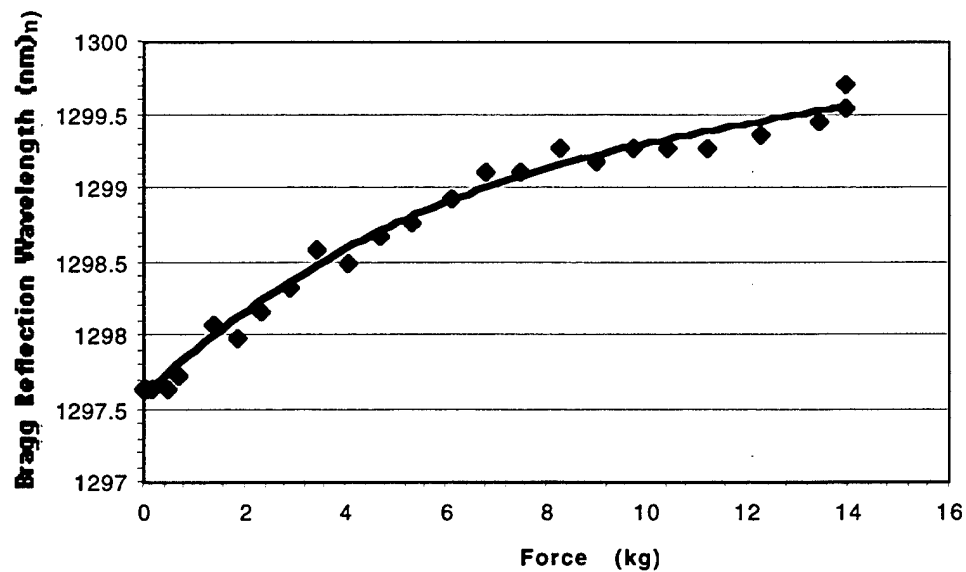


Figure 10 Bragg Reflection versus Applied Forces.

Structurally Embedded Multi-Axis Fiber Optic Sensors

**J. S. Sirkis, X. D. Jin, T. Rossmanith, M. Rutherford, J. S. Sirkis, A. Dasgupta,
D. DeVoe, F. F. Rosenberger, III**

Small Smart Systems Center

University of Maryland at College Park, College Park, MD 20742

V. S. Venkat, Y. C. Shi

Analytical Service & Materials, Inc.

107 Research Drive, Hampton, VA 23666

C. Askins

Naval Research lab.

4555 Overlook Ave., Washington D. C., DC 20375

Embedding optical fiber sensors to provide a measure of the internal strain state is a concept that has recently seen extensive research. However, uniquely relating the change in optical properties to internal strain components, even axial strain, has been much more difficult than first imagined. The difficulties are many fold, but the most important is that all intrinsic fiber optic sensor configurations produce an optical response that is functionally dependent on three orthogonal strain components, rather than a single strain component.

This paper describes a single micro-optical fiber sensor capable of simultaneously measuring four key elements of the complete strain state at one point in composite material. The strain components include the normal strain parallel to the optical fiber axis, the secondary principal strains in the plane perpendicular to the optical fiber axis, and the orientation of the secondary principal plane. This single transducer is based on cascading four micro Fabry-Pérot cavities to measure three normal strains and one shear strain in the plane of the optical fiber cross-section. . The Fabry-Perot cavities are produced from hollow core fiber, circular core fiber, and two sections of side-hole fibers, which are rotated at an angle of 45° relative to each other. These types of fiber are selected because each has a completely different optical response to strain, therefore enabling four independent optical measurements to be used to solve for the three normal strains and one in-plane shear strain.

The hollow core Fabry-Pérot (ILFE) sensor is sensitive only to axial strain, so its optical signal directly provides the axial strain. The LoBi fiber Fabry-Pérot sensor has an isotropic sensitivity to transverse strain, while the side-hole fiber Fabry-Pérot sensors have an anisotropic sensitivity to strain. The two side-hole cavities are oriented a 45° relative to each other so that the stress state in the core of the two cavities would be different in response to the same strain state in the composite host. Using the ILFE sensor to provide direct information about the axial strain has the important advantage of potentially reducing the requisite micromechanics to a two-dimensional analysis. This considerably reduces the complexity of the micromechanics analysis required to determine the strains in the composite structures from sensor readings. As a result, the optical signals from the LoBi and the side-hole fiber sensors lead to the two transverse strains and one in-plane shear strain.

Developing demodulation techniques capable of accommodating the strain rates and ranges generated by ballistic impact is another challenging aspect of the present program. Demodulation is the electro-optic system required to convert the intensity signal recorded by photodetectors to

unambiguous phase change signals. The difficulties primarily arise from the frequency response limitations of many of the electro-optic devices used for phase-modulation. As a result, passive quadrature demodulation techniques will be used. The demodulation scheme used path matched differential interferometry (PMDI) to yield two quadrature shifted intensity signals. Algorithms that allowed the extraction of the strain-induced phase change from these two signals take advantage of the inverse tangent function.

The strain is determined from the strain-induced phase change using the phase-strain model for the sensor. Using PMDI-based coherence division multiplexing to access each of the four cascaded Fabry-Pérot sensors combined with the passive demodulation requires eight read-out interferometers to simultaneously interrogate the four cavity sensors. To reduce the size and cost of the optical system, all read-out interferometers are being fabricated using MEMS (Micro-Electro Mechanical System) technology. Manufacturing all of the read-out interferometers using MEMS technology allows us to reduce an entire array of bulk interferometers to fit on a single chip.

Micromechanics analysis has been applied to the multi-strain sensor to help design the transducer, and to develop a relationship between the strains in the fiber sensor and the far-field strains in the host material. The fact, that the IFP sensors manufactured from non-standard fibers produce complex stress distributions in the core, which even may be discontinuous at the interfaces between Fabry-Pérot cavities, suggests that a three dimensional analysis is required. On the other hand, the geometry of optical fiber sensor, its small cross-section compared with sensor length, and the fact that the ILFE sensor gives direct information about the external strain suggests that 2D models might provide desired results with a much smaller computational penalty. A comparison of the 2D finite element analysis of the strains and the average strains produced by the 3D model shows general agreement to within 5% except for the shear strain in the 45° side-hole fiber for the in-plane shear loading. In this case, there is a 12.8% discrepancy. These comparisons confirm the adequacy of using 2D analysis to examine the strain state in the multi-axis sensor. These results show that the transverse strains in the IFP sensors can be evaluated with reasonable accuracy using 2D methods and are used to find the transformations between the measured strains in the fiber sensor and average strains far away from the embedded sensor. The resulting transformation matrix is combined with the relations between the measured phase change and the principal strains in optical fiber sensors, to develop a nonlinear transformation between the measured phase change and the far-field strains in the composite structure. It can be shown that, which will simplify the nonlinear equations to three linear equations that can be used to find ϵ_x^c , ϵ_y^c and ϵ_{xy}^c if $\Delta\phi^L$, $\Delta\phi^0$ and $\Delta\phi^{45}$ are measured.

This paper has presented the progress made towards an orthogonal strain sensor based on optical fiber technology. The optical arrangement of the three-strain sensor system, including the technical approach, fabrication of the micro-cavity sensors, and MEMS design for read-out interferometers, have been discussed in detail. The finite element method has been applied to the multi-strain sensor to develop a relationship between the strains in the fiber sensor and the far-field strains in the host material. The 2D finite element analysis model results showed that with different loading cases the strains in the side-hole fiber indicated significant core strain and was used to design the placement and diameters of the side holes to maximize transverse strain sensitivity. The results of comparison of 2D and 3D FEM models show that the replacing of 3D model with 2D models gives accurate in-plane strains. Finally a linear solution method was introduced to find the far-field host strains in terms of the measured optical phase changes.

Structurally Embedded Multi-Axis Fiber Optic Sensors

Goal:

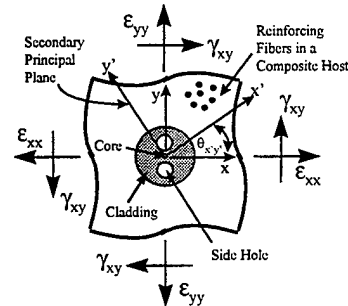
Developing a single micro-optical fiber sensor capable of simultaneously measuring four key elements of the complete strain state at one point in composite material.

Measure multi-axis strain:

- Strain parallel to the optical fiber axis
- Secondary principal strains in the plane perpendicular to the optical fiber axis
- Sensor fabrication

Ballistic impact

- High-speed signal processing techniques



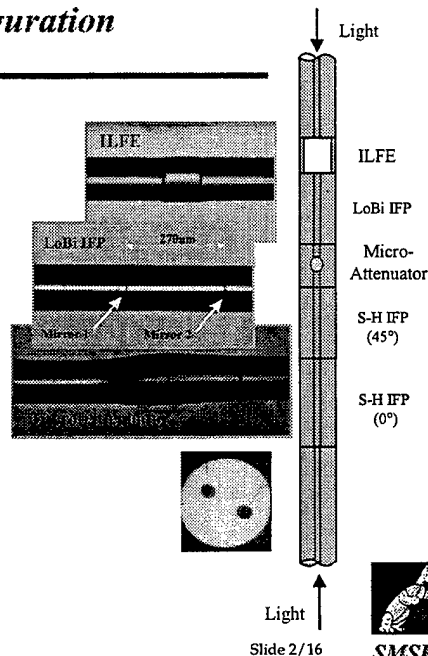
AS&M

Slide 1/16



Sensor Configuration

- **In-Line Fiber Etalon (ILFE):** Is sensitive only to axial strain.
- **Standard Intrinsic Fabry-Perot (IFP):** This sensor has an isotropic sensitivity to transverse strain.
- **Side-Hole Cavities (S-H IFP (0°) and (45°)):** The two side-hole cavities are oriented at 45° relative to each other, therefore exhibiting a different response to the same far-field strain state in the composite host.
- **Micro-Attenuator:** The micro attenuator prevents the two counter-propagating electric fields from interacting with the wrong Fabry-Perot cavities.



AS&M

Slide 2/16



Demodulation technique

$$\Delta\phi = \frac{4\pi n}{\lambda_0} L \varepsilon_z$$

Strain-induced phase change.

$$I_1 = A_1 + B_1 \cos(\Delta\phi)$$

$$I_2 = A_2 + B_2 \sin(\Delta\phi)$$

The two quadrature-shifted intensity signals, I_1 and I_2 , produced by the passive demodulation.

$$\varepsilon_z = \frac{\lambda_0}{4\pi n L} \tan^{-1} \left(\frac{I_2}{I_1} \right)$$

The strain can be determined using the arctangent.

$$\varepsilon_z = \frac{\lambda_0}{4\pi n L} \left[\tan^{-1} \left(\frac{I_2}{I_1} \right) + \text{unwrap} \cdot \pi \right]$$

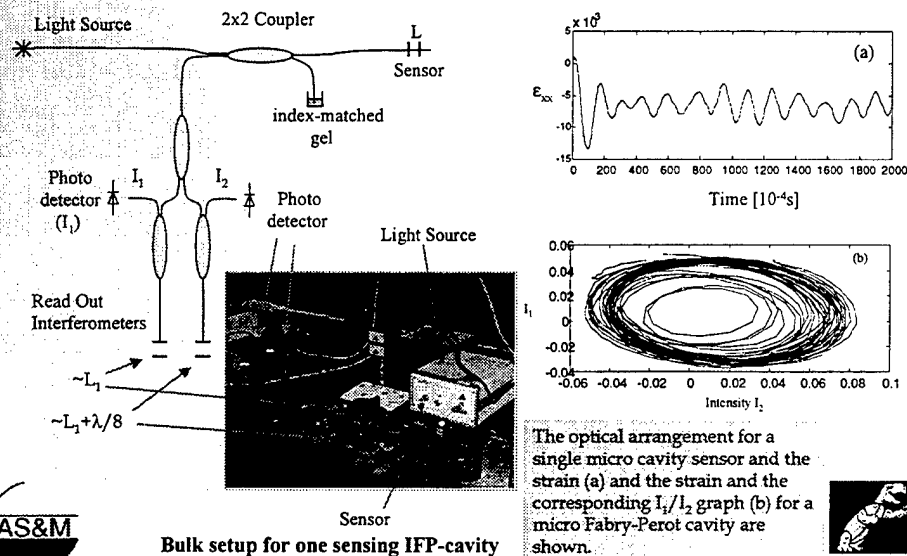
The arctangent is restricted to values between $\pi/2$ and $-\pi/2$, phase, therefore "unwrapping" is used.



Slide 3/16



Optical arrangement for a single micro cavity sensor

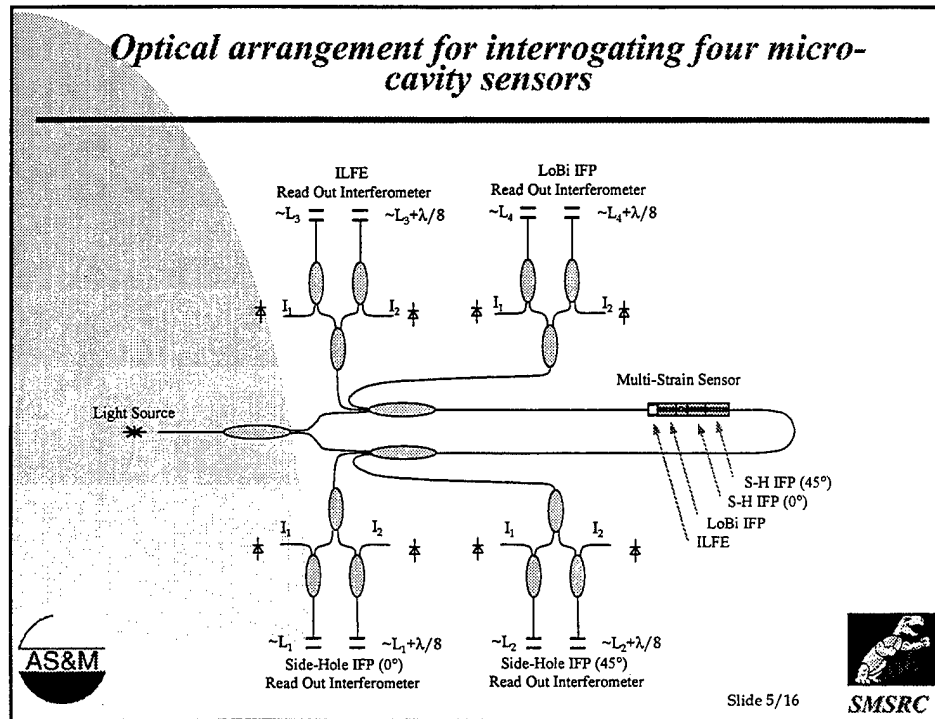


Bulk setup for one sensing IFP-cavity

Slide 4/16



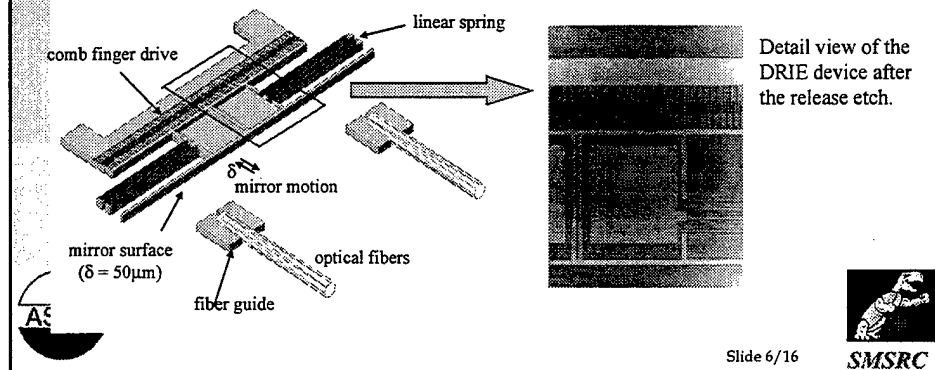
Optical arrangement for interrogating four micro-cavity sensors



MEMS design for read-out interferometers deep reactive-ion etching (DRIE)

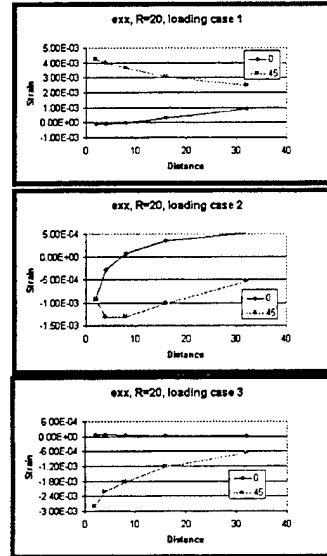
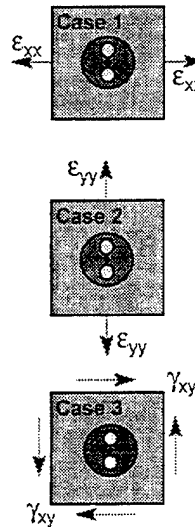
The read-out interferometers using DRIE-MEMS technology consists of a mirror mounted to a folded-flexure spring, and is actuated using a comb finger capacitive drive.

- Using deep reactive-ion etching (DRIE) of single crystal silicon to form mirror, spring, and comb fingers.
- DC voltage across the comb finger actuator tunes the read-out interferometer to match that of the optical sensor cavity length, thereby giving optimal performance.
- The MEMS device allows for greater resolution over the bulk interferometer.



Side-hole fiber design

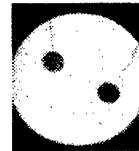
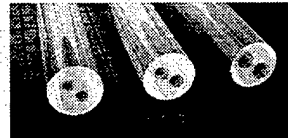
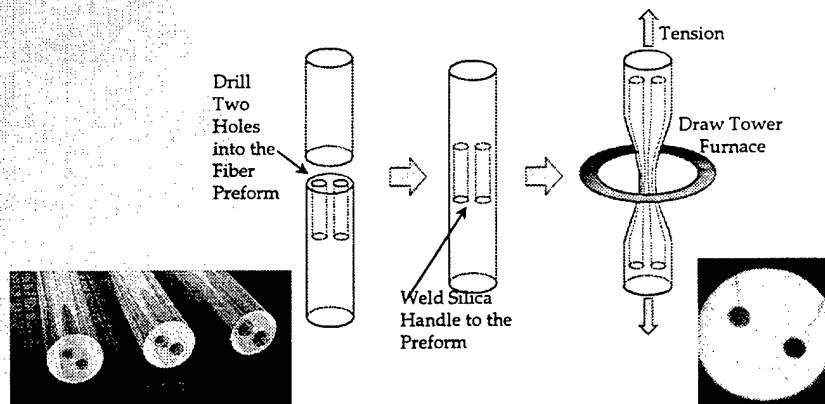
- 2D finite element analysis was conducted with side-hole fibers to determine the maximum transverse strain difference.
- The strains in the core of two fibers oriented at 0° and 45° will have significant difference.
- Radius of the side-holes has to be larger than $10\mu\text{m}$, and the distance to the core has to be less than $20\mu\text{m}$.



Slide 7/16

SMSRC

Manufacturing Side-Hole Fiber



The side-hole preform dimensions are selected so that the resulting optical fibers will have $125\mu\text{m}$ outer diameter with holes of $40\mu\text{m}$, $27\mu\text{m}$ and $34\mu\text{m}$ in diameter each, $10\mu\text{m}$ away from core.

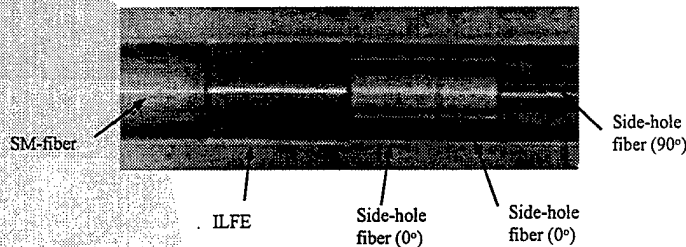


Slide 8/16



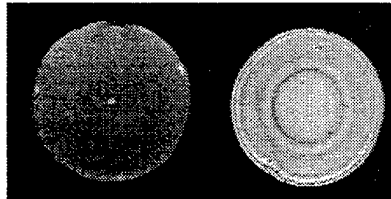
Sensor splicing experiment:

Using the Ericcson fusion splicer to splice sections of different optical fibers together:



Sol-gel process was developed to apply TiO_2 onto:

- Core mirrors (left)
- fully coated end faces (right)

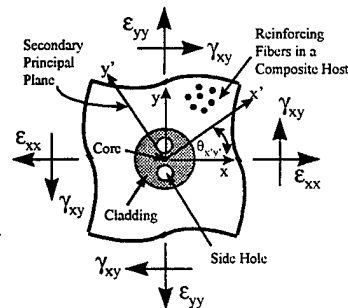


Slide 9/16



Data interpretation

- We want to measure the strains in the host composite structure.
- Host strains do not equal the fiber strains.
- Fiber cores respond to only secondary principal strains.
- We need enough optical measurement in the optical fiber to determine axial strain, two transverse secondary principal strains and secondary principal directions in the host.



Slide 10/16



From optical phase change to far-field strains

Relationship between measured phase change and core strains.

ε_1 Axial strain
 k_{ij} Strain coefficient
 $\varepsilon_2, \varepsilon_3$ Secondary principal strains in fiber cores

$$\begin{aligned}\Delta\phi^{ILFE} &= k_{11}\varepsilon_1 \\ \Delta\phi^L &= k_{21}\varepsilon_1 + k_{22}\varepsilon_2^L + k_{23}\varepsilon_3^L \\ \Delta\phi^0 &= k_{31}\varepsilon_1 + k_{32}\varepsilon_2^0 + k_{33}\varepsilon_3^0 \\ \Delta\phi^{45} &= k_{41}\varepsilon_1 + k_{42}\varepsilon_2^{45} + k_{43}\varepsilon_3^{45}\end{aligned}$$

Four Optical Phase Change Measurements

Strain State in the Core

Model

Far-Field Strain in Host

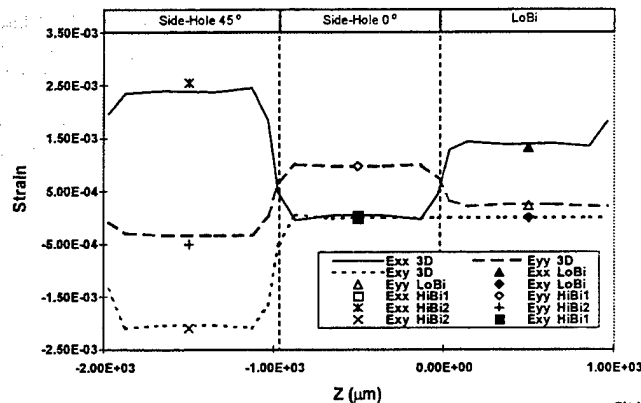


Slide 11/16



3D results of in-plane strain distributions in the sensor core

- 3D simulation of sensor subjected to a uniform tension in x-direction, y-direction and shear in xy-plane.
- 2D strains and the average strains produced by 3D model show general agreement to within 5%
- 2D FEM analysis is used to determine transformation matrix



Slide 12/16



Transformation between measured strains in the core and strains in the far-field host material

Side hole fiber (0°):
Developed using
2D FEM

$$\begin{matrix} \text{Strains in} \\ \text{the sensor} \end{matrix} \begin{Bmatrix} \varepsilon_x \\ \varepsilon_y \\ \varepsilon_{xy} \end{Bmatrix}_{\text{fiber}} = \begin{bmatrix} t_{11} & t_{21} & t_{31} \\ t_{12} & t_{22} & t_{32} \\ t_{13} & t_{23} & t_{33} \end{bmatrix} \begin{matrix} \text{Strains in} \\ \text{the far field} \end{matrix} \begin{Bmatrix} \varepsilon_x \\ \varepsilon_y \\ \varepsilon_{xy} \end{Bmatrix}_{\text{composite}}$$

Transformation Matrix $[T]^0$

Side hole fiber (45°):

Core strains in local
coordinates

$$\{\varepsilon\}_{lf2} = [T]^0 ([D(\alpha)] \{\varepsilon\}_{gc})$$

Far field strains in
global coordinates.

Core strains in global
coordinates

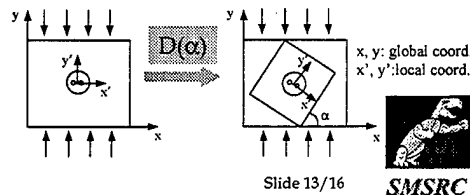
$$\{\varepsilon\}_{gf2} = [D(-\alpha)] [T]^0 [D(\alpha)] \{\varepsilon\}_{gc}$$

$[T]^{45}$

$D(\alpha)$: Local-global
strain transformation

$$[T]^{45} = \begin{bmatrix} 0.255 \cdot 10^{-2} & -0.501 \cdot 10^{-3} & -0.209 \cdot 10^{-2} \\ 0 & 0.264 \cdot 10^{-2} & -0.206 \cdot 10^{-2} \\ -0.114 \cdot 10^{-2} & -0.117 \cdot 10^{-2} & 0.217 \cdot 10^{-2} \end{bmatrix}$$

$$[T]^0 = \begin{bmatrix} -3.953 \cdot 10^{-3} & 7.665 \cdot 10^{-3} & 5.550 \cdot 10^{-3} \\ 1.542 \cdot 10^{-1} & 5.137 \cdot 10^{-1} & 2.709 \cdot 10^{-3} \\ 3.084 \cdot 10^{-3} & 8.647 \cdot 10^{-3} & 4.935 \cdot 10^{-1} \end{bmatrix}$$



AS&M

Slide 13/16

SMSRC

Transformation from phase change to strains in far-field host material.

$$\varepsilon_{2,3} = \frac{\varepsilon_x + \varepsilon_y}{2} \pm \sqrt{\left(\frac{\varepsilon_x - \varepsilon_y}{2}\right)^2 + (\varepsilon_{xy})^2}$$

Secondary principal strains in
terms of the strain state in x/y
plane:

$$\begin{matrix} \varepsilon_2^{45}, \varepsilon_3^{45} \\ \varepsilon_2^0, \varepsilon_3^0 \\ \varepsilon_2^L, \varepsilon_3^L \end{matrix}$$

Three pairs of secondary
principal strains from the
three IFP cavities.

Relationship between far
field strains and strains
in the fiber cores:

$$\{\varepsilon\}^L = [T]^L \{\varepsilon\}_c$$

$$\{\varepsilon\}^0 = [T]^0 \{\varepsilon\}_c$$

$$\{\varepsilon\}^{45} = [T]^{45} \{\varepsilon\}_c$$

$$\Delta\phi^{ILFE} = k_{11}\varepsilon_1$$

$$\Delta\phi^L = k_{21}\varepsilon_1 + k_{22}\varepsilon_2^L + k_{23}\varepsilon_3^L$$

$$\Delta\phi^0 = k_{31}\varepsilon_1 + k_{32}\varepsilon_2^0 + k_{33}\varepsilon_3^0$$

$$\Delta\phi^{45} = k_{41}\varepsilon_1 + k_{42}\varepsilon_2^{45} + k_{43}\varepsilon_3^{45}$$

This leads to a set of
three nonlinear
equations that can be
used to find $\varepsilon_x^c, \varepsilon_y^c$
and ε_{xy}^c if $\Delta\phi^L, \Delta\phi^0$
and $\Delta\phi^{45}$ are
measured.

AS&M

Slide 14/16

SMSRC

Three linear equations to calculate ε_x^c , ε_y^c and ε_{xy}^c

It can be shown that $k_{i,2} = k_{i,3}$, which will simplify the nonlinear equations to three linear equations that can be used to find ε_x^c , ε_y^c and ε_{xy}^c if $\Delta\phi^L$, $\Delta\phi^0$ and $\Delta\phi^{45}$ are measured:

$$\Delta\phi^L = k_{21}\varepsilon_1 + k_{22}(t_{x,j}^L\varepsilon_j^c + t_{y,j}^L\varepsilon_j^c)$$

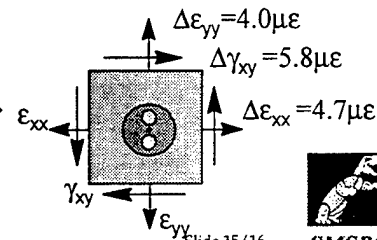
$$\Delta\phi^0 = k_{31}\varepsilon_1 + k_{32}(t_{x,j}^0\varepsilon_j^c + t_{y,j}^0\varepsilon_j^c)$$

$$\Delta\phi^{45} = k_{41}\varepsilon_1 + k_{42}(t_{x,j}^{45}\varepsilon_j^c + t_{y,j}^{45}\varepsilon_j^c)$$

Where t_{ij}^L , t_{ij}^0 and t_{ij}^{45} are the elements of the matrices $[T]^L$, $[T]^0$ and $[T]^{45}$.

Wavelength of $\lambda=1.3\mu\text{m}$,
and cavity lengths of
100 μm will lead to a
minimum detectable
phase of 10^{-3} radian.

Error of the three
far-field strains



Slide 15/16



Summary

- Optical arrangement of the three-strain sensor system
- Fabrication of the micro-cavity sensors
- MEMS design for read-out interferometers
- The 2D finite element analysis showed that the strains in the core of two side-hole fibers oriented at 0° and 45° will have significant difference.
- FEM simulation to develop a relationship between the strains in the fiber sensor and the far-field strains in the host material.
- The comparison of the 2D and 3D FEM models justify the replacing of 3D model with 2D models to derive the transformation matrices.
- Finally linear equations are introduced to find the far-field host strains in terms of the measured optical phase changes.
- Future work includes the manufacturing of the complete sensor and its read-out system and adaptation to ballistic impact.



Slide 16/16



Fiber Optic Sensors and Smart Fabrics

An Overview on the ARO MURI Project: Functionally Tailored Fibers and Fabrics

Mahmoud A. El-Sherif and Jianming Yuan

Fiber Optics and Photonics Manufacturing Engineering Center

College of Engineering, Drexel University

Philadelphia, PA 19104

Tel: (215)895-2324, Fax: (215)-6684

elsherif@ece.drexel.edu, <http://coe.drexel.edu/FOPMEC>

SUMMARY

The Soldier Integrated Protective Ensemble (SIPE) has proven to be an ambitious and farsighted Army program. It is based on a modular system approach which paves the way toward the development of a head-to-toe integrated fighting system for a soldier uniform. This goal requires the design and integration of a micro-system that will provide protection and advance warning. In accordance with the goals of the program, this project presents a novel approach based on the development of fiber optic micro-sensors and on the integration of these sensors into the soldier's uniform. These fiber optic sensors can be used to sense in real-time various battlefield hazards such as chemical and biological warfare threats, above-normal field temperatures, electromagnetic fields, and other applications. The smart uniform will provide protection and early warning to the soldier against multiple battlefield threats.

Feasibility studies are in progress and encouraging results have been achieved toward developing such micro-sensors and integrating them into soldiers' uniforms. Drexel University, in collaboration with the University of Akron (UA), the University of Pennsylvania (U of P), and North Carolina State University (NCSU), has been working on the development of the smart fabrics. Specially, Drexel has developed a fiber optic sensor using multifunctional materials as modified cladding materials of the sensing optical fibers for sensing various environmental conditions. It is known that the light propagation characteristics in optical fibers are strongly influenced by the refractive index of the cladding materials. Thus, the idea of the developed sensors is based on replacing the passive optical fiber cladding by active or sensitive materials.

Two types of materials: segmented polyurethane-diacetylene copolymer (SPU) [synthesized at the University of Akron (UA)] and polyaniline [from at the University of Pennsylvania (U of P)] have been successfully used in the feasibility study to prove the concept of the design and development of the optical fiber sensors. Segmented polyurethane-diacetylene copolymer was selected as the thermochromic material for temperature sensor application. Polyaniline was chosen as a photochemical polymer for chemical sensor application. The developed methodology for building the sensors included modifying the regular optical fibers, applying those sensitive materials to the modified optical fibers, and integrating and characterizing the sensor system. The progress has also been achieved on the integration of the sensory system into textile structures, in collaborating with NCSU's College of Textiles.

The recent research focused on the design and development of the electronic components for improving the sensor system. For each of these components, an in-depth study and research are required to identify the design parameters and required specifications. For example, it is known that the refractive index of a material is a function of light wavelength. Therefore, light sources at different wavelength were used for polyaniline cladding optical fibers to find the most sensitive light signals. This study provided the required information regarding the light source. In addition, to improve the sensitivity of the detection, the Modal Power Distribution Technique was applied to enhance the output signal modulation. A brief summary on R & D accomplished so far is presented in this paper.

Sensor Design

The principle of the on-fiber sensor developed was based on the optical intensity modulation. One of the way to induce the optical intensity modulation was by changing the refractive index of the cladding material. Therefore, in our optical fiber sensor, the original cladding material was replaced by a chemical agent or an environmental sensitive material on a small section of a piece of fiber. The refractive index of the sensitive material changed when the material exposed to different chemicals or environments. Altering the refractive index of the cladding material results in the change of the transmitted light intensity.

A modified optical fiber structure, known as an on-fiber sensor, is shown in Figure 1. In a small section of a piece of fiber, a sensitive material was coated around the fiber core after the fiber jacket and cladding were removed in the section.

A complete sensor system generally includes four major components: (a) light source and power supply, (b) sensing element, (c) detection device, and (d) signal processing and indicator/display. An in-depth study for each elements is required for improving the sensitivity and the dynamic range of the sensor system.

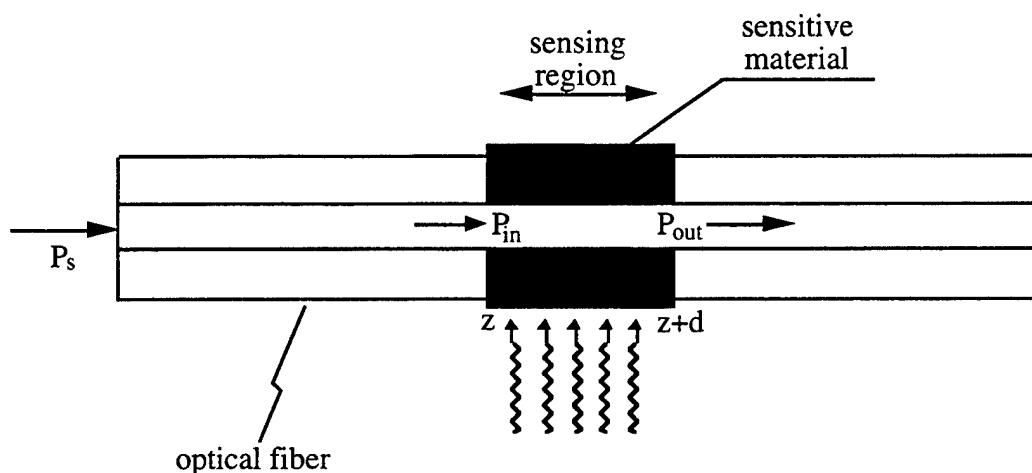


Figure 1 Structure of the modified optical fiber for the on-fiber sensor.

Experimental Work

The experimental work generally followed these steps: (1) characterization of the sensitive materials applied on the optical fiber, (2) preparation of the optical fiber sensing elements, and (3) characterization of the sensory components and (4) integration the sensor system into textile materials.

Spectral characterization of the polymer films

There were two types of polymers used in the research: (1) segmented polyurethane-diacetylene block copolymer (SPU) and (2) polyaniline. A solution of 17% by weight of as-synthesized segmented polyurethane-diacetylene copolymer dissolved in the tetrahydrofuran (THF). Then, thin film samples were cast on glass substrates for testing of photochromic and thermochromic behaviors of the polymer. A 0.3% (w/v) polyaniline solution was made by dissolving 0.3 gram of polyaniline (emeraldine base) powder slowly in 10 ml N-methylpyrrolidinone (NMP) solvent with magnetic stirring for 20 hrs. Polyaniline thin films were made using electronic spinning method on glass substrates. A broad band spectrophotometer (UV/visible/NIR) was used to obtain the light absorption spectra of these films after they were treated by heat and cooling for SPU films or exposed to HCl and NH_4OH chemical vapors for polyaniline films.

Preparation of optical fiber sensing elements

Multi-mode silica optical fiber with dimensions of 100/140/250 μm in diameter for core/cladding/jacket was used to make the sensing element. After the jacket was stripped from a small section of a piece of optical fiber, the silica cladding layer was removed in a hydrofluoric acid (HF) solution (50% HF : H_2O = 2:1 in volume). An experimental set-up, as shown in Figure 2, was used to control and monitor the etching process. Then, segmented polyurethane-diacetylene (SPU) polymer or polyaniline was coated on the fiber core in the modified area as a new sensitive cladding by either of casting or spinning methods. The sensing element was ready for testing and integration into the sensor system.

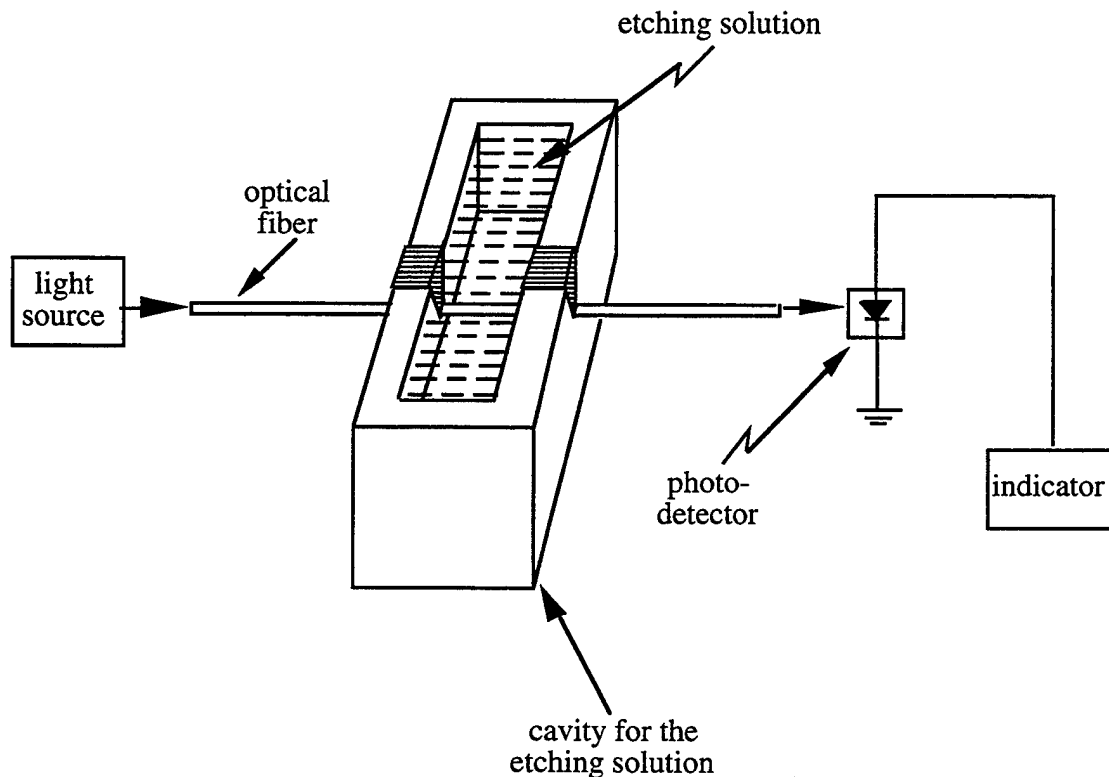


Figure 2 Experimental set-up for monitoring the cladding etching process in HF solution.

Sensor Characterization

The sensor system was built by integrating the sensing element, light source, photodetector and other electronic equipment. The schematic diagram of the fiber optic sensor system is shown in Figure 3. Light sources with different wavelength (630 nm, 830 nm, and 1300 nm) were used in the experiment. Model Power Distribution (MPD) technique was applied, using CCD camera and other electronics, for improving the sensitivity of the sensor system as shown in Figure 4.

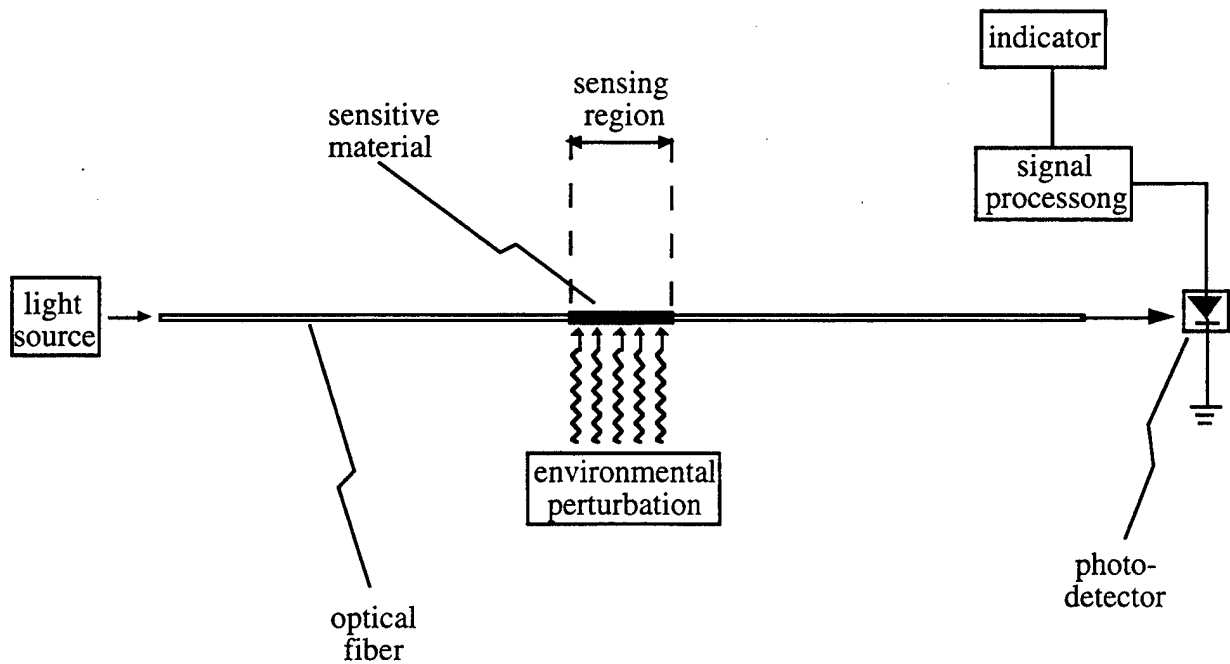


Figure 3 Schematic diagram of the on-fiber optic sensor showing the modified region and required components for characterization.

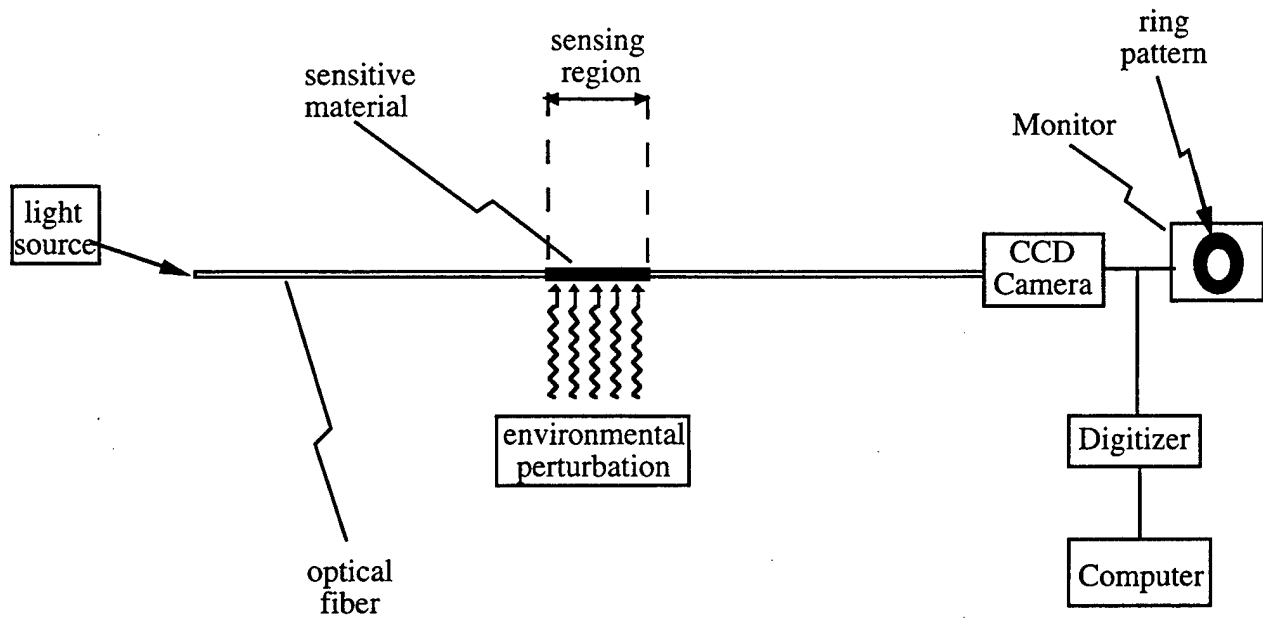


Figure 4 Experimental set-up for the application of the Modal Power Distribution (MPD) technique.

Integration optical fiber into textile material

To develop the process for integration of optical fibers to uniform garments, samples of a single optical fiber integrated with textile structures were developed in collaboration with NCSU. Ultrasonic energy were used for bonding optical fibers to textile fabrics. An experiment set-up was developed at Drexel for characterization of these fiber/textile structures as shown in the Figure 5.

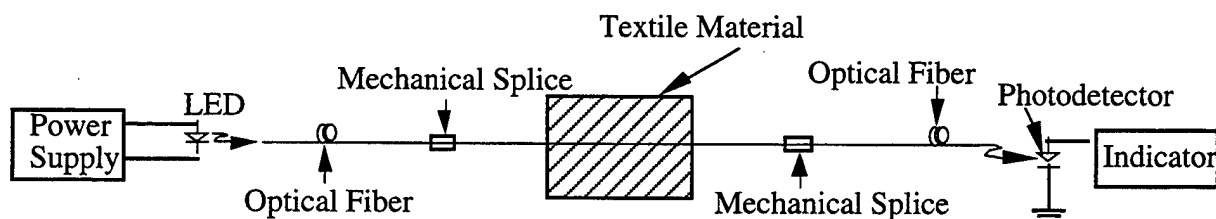
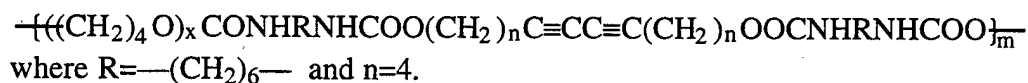


Figure 5 Experimental set-up for characterization of optical fibers integrated in textile materials.

Results and Discussion

Characterization of SPU copolymer films

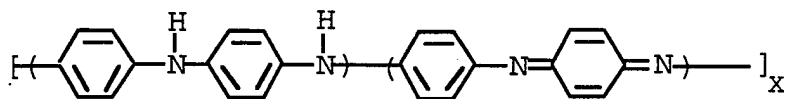
The segmented polyurethane-diacetylene block copolymers were prepared by the Department of Polymer Science, Akron University. The general composition is shown below:



It was observed that films of segmented polyurethane-diacetylene copolymers turned to blue-purple upon exposure to UV light. A typical example of the light absorption spectra is shown in Figure 6 (a). The uv-exposed films were heated from room temperature to 110°C on a hot plate. Thermochromic behavior of the films were observed and their color changes. The light absorbance spectra are shown in Figure 6 (b) for a sample after heated to different temperature and cooled down to the room temperature.

Characterization of polyaniline films

Polyaniline (emeraldine base) has the following composition and consists of alternating reduced and oxidized repeat units.



When the polyaniline films were exposed to HCl vapor, they were doped and turned green. When the doped polyaniline films were exposed to NH_4OH , they were de-doped and returned to blue color. Light absorption spectra shown in Figure 7 were obtained by UV/vis/NIR photospectrometer for one of the polyaniline films after it was exposed to chemical vapors HCl and NH_4OH . The light absorption spectra was measured after the film exposed to HCl vapor for the first time (B) and second time (D), and to NH_4OH vapor for the first time (C) and second time (E).

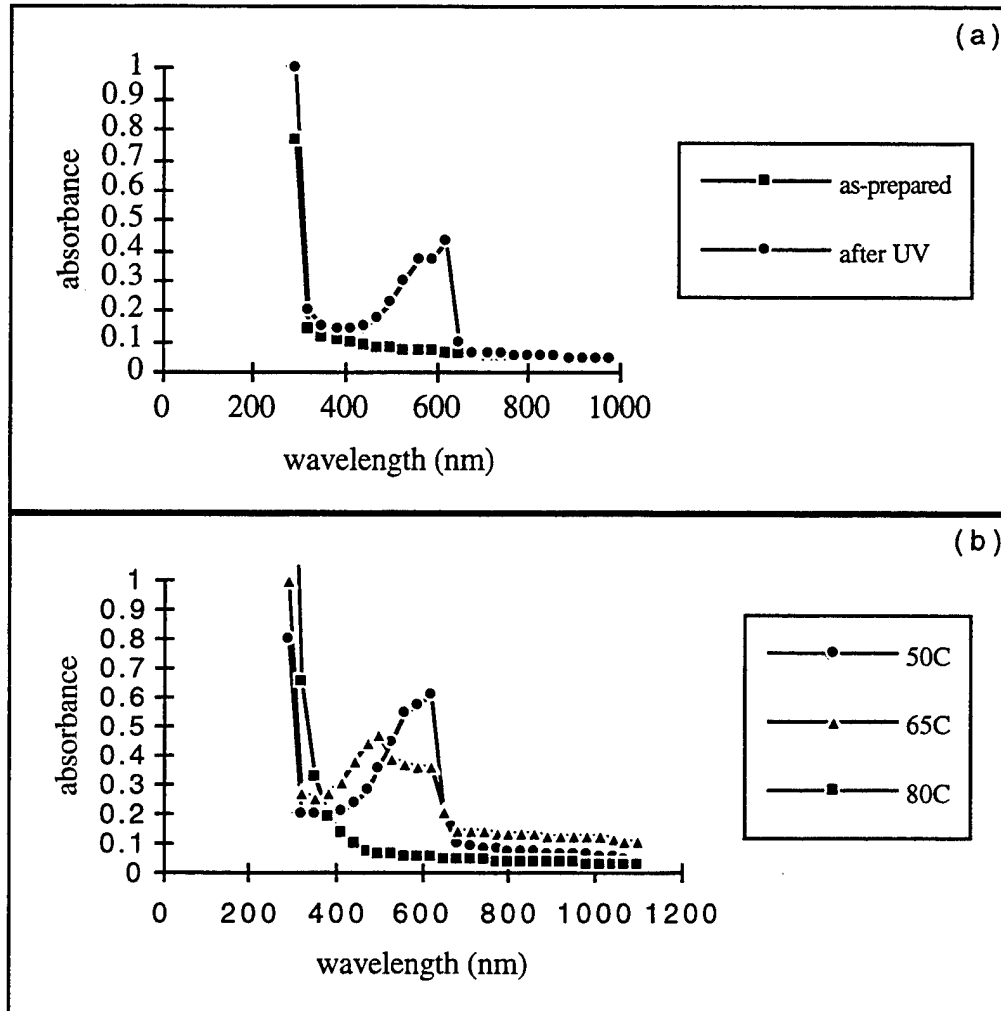


Figure 6 Light absorption spectra of the SPU film (a) before and after UV exposure and (b) after UV exposure then heated to different temperature and cooled down.

Cladding modification

A uniform and clean surface of the fiber core was observed after etching the passive cladding layer, by means of optical microscopy as shown in Figure 8. A uniform layer of the polyaniline material, shown in Figure 9, was coated surrounding the optical fiber core as the modified cladding layer for chemical sensor applications.

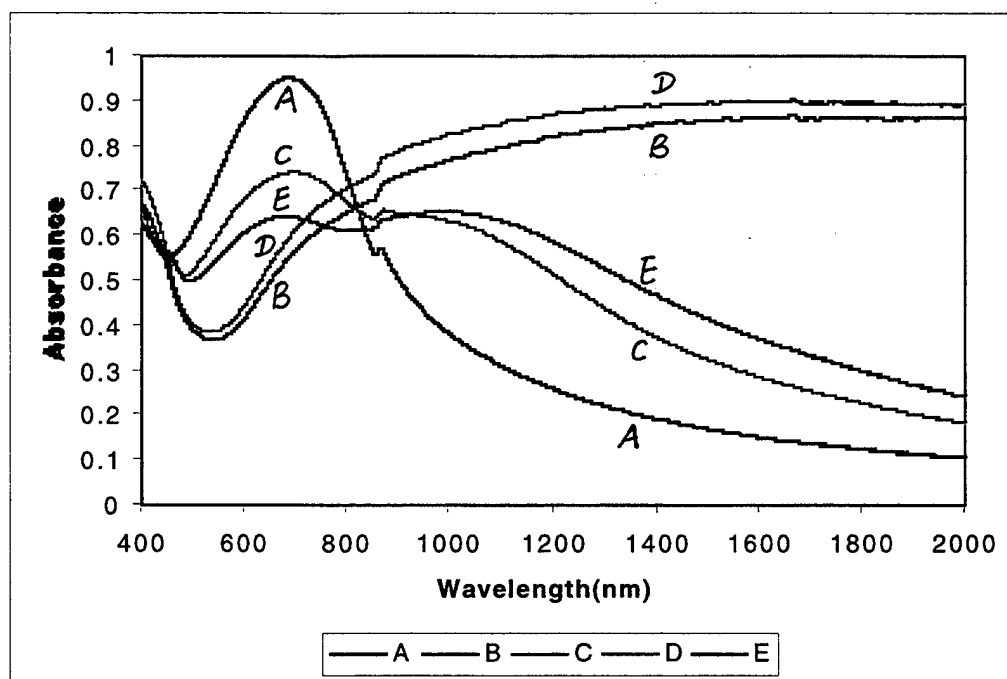


Figure 7 Light absorption spectra of a polyaniline film after exposed to chemical vapors HCl and NH_4OH .

Testing for temperature sensor applications

The segmented polyurethane-diacetylene copolymer was used as a thermochromic cladding material. After the UV exposure, the copolymer showed thermochromic behavior when it was heated to higher temperature. Figure 10 displays the power change of a sensor during heating and cooling in the temperature range from 20°C to 120°C . During heating there were two abrupt changes, starting at 50°C and 95°C . The color of the modified cladding changed from purple to red-purple, orange, yellow and brown with the temperature increase. Figure 10 (a) indicated that during the first heating-cooling cycle, what was occurring was an irreversible thermochromic process. It was noted that, however, a reversible process of heating and cooling occurred when the sensor was heated again and again as shown in Figure 10 (b).

Teating for chemical vapor sensor applications

Polyaniline was used as the replaced cladding material for chemical vapor sensors. When the polymer was exposed to different chemical vapors: HCl and NH_4OH , its color changed. Three light sources, with wavelength 630 nm, 830 nm, and 1300 nm, were applied individually for three sensing elements in the experiments. The normalized output power of each sensor was calculated by dividing the output power by the maximum output power for each light source. The change of the normalized output power, after a sensor was exposed to HCl and then to NH_4OH chemical vapors, is shown in Figure 11. Experimental results showed that when the sensing fiber exposed to different chemical vapors, the change of the normalized output power depended on the wavelength of the light sources used. The maximum change (26%) happened when the 630 nm light source was used. The least change (7%) was when the 1300 nm light source was applied.

The modal power distribution (MPD) technique uses the intensity information in 2-D, which can enhance the signal detection sensitivity and resolution. It was observed that the ring looked more

brighter when the sensing optical fiber exposed to HCl vapor [Figure 12(left)]. The whole ring became darker suddenly when the sensing region exposed to NH_4OH vapor [Figure 12(right)]. The normalized intensity profiles of the ring patterns are shown in Figure 13.

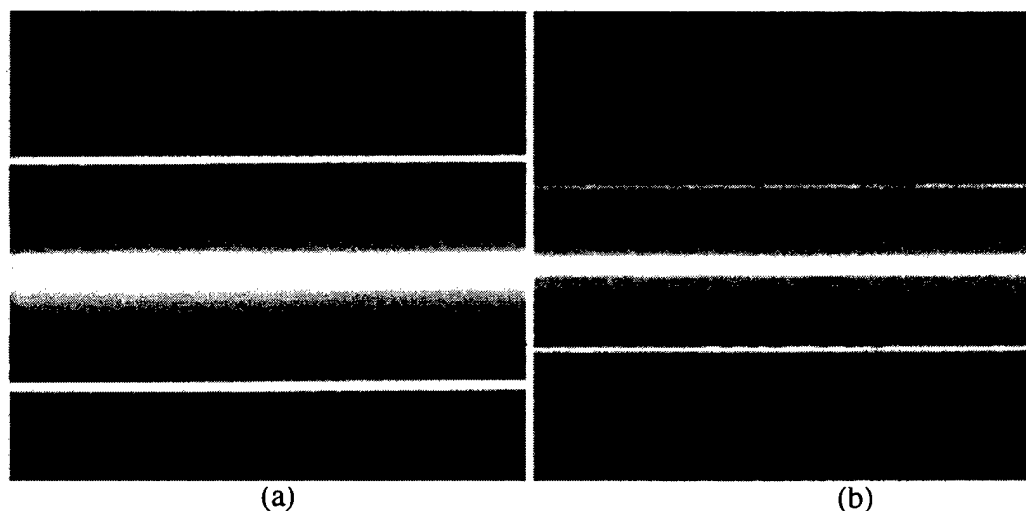


Figure 8. Micro-graphs of an optical fiber with magnification of 200 X
(a) before cladding etched ($140\ \mu\text{m}$ in diameter) and (b) after cladding etched ($100\ \mu\text{m}$ in diameter).

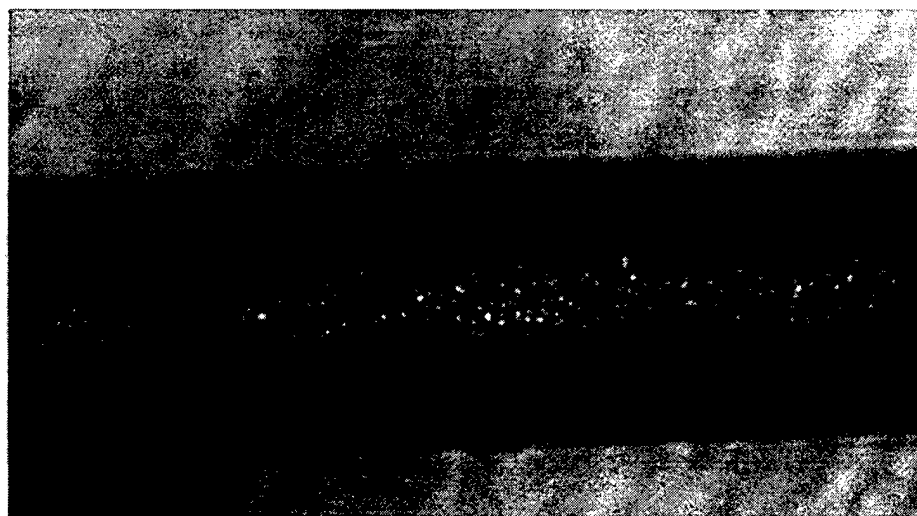


Figure 9. Micro-graphs of a polyaniline coated optical fiber core using electronic spinning with the diameter of $105\ \mu\text{m}$.

Conclusions and Recommendations

A novel on-fiber sensor was developed by using the multifunctional materials as the modified cladding materials. The main sensing mechanism is that the transmitted light intensity is adjusted by the change of the refractive index of the cladding materials. That change is altered by the environmental conditions such as temperature and chemicals. This methodology offers potential applications involving different types of on-fiber sensors such as temperature and chemical sensors. Segmented polyurethane-diacetylene (SPU) copolymer was studied for its chromogenic properties and used to build thermochromic temperature sensors. Conducting polymer - polyaniline was applied to construct

chemical vapor sensors. The sensitivity of the sensors is strongly influenced by the wavelength of the light source used. Modal Power Distribution method shows potential ability to improve the detection technique. Preliminary study on the investigation of these micro-sensors in soldiers' uniforms is encouraging. An in-depth study will be continued on design and development of electronic components for improving the sensor system.

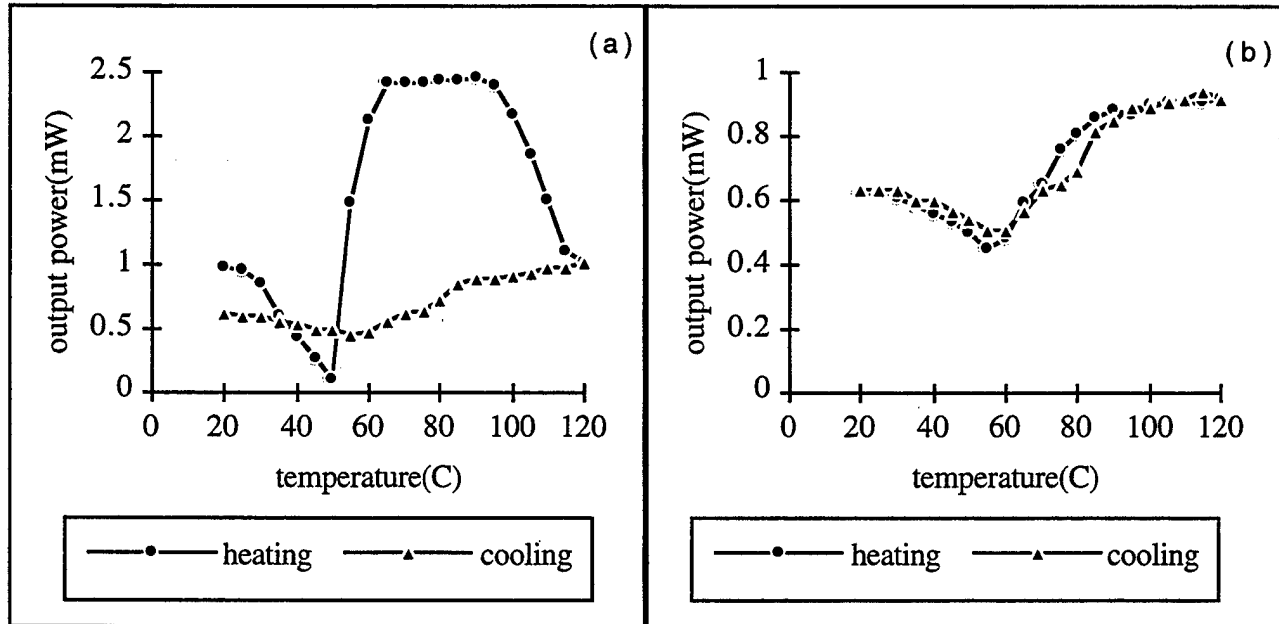


Figure 10. Transmitted output power of a sensor during heat treatment (a) first heating-cooling cycle and (b) second heating-cooling cycle.

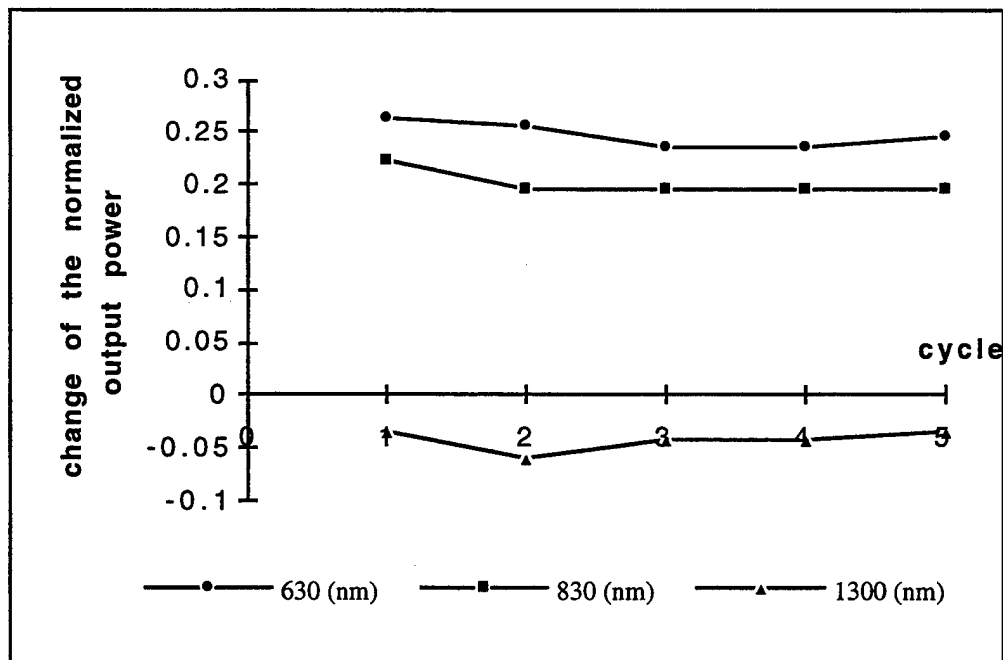


Figure 11. Change of the normalized output power after a sensor exposed to HCl and then to NH_4OH chemical vapors for each light source.

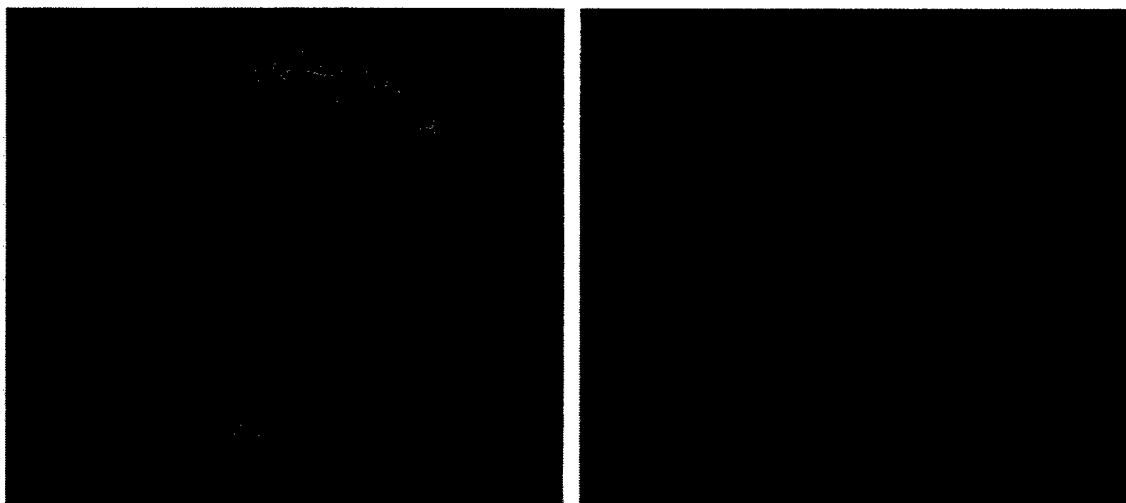


Figure 12. Far-field ring pattern of MPD: left - after sensor exposed to HCl and right - after sensor exposed to NH_4OH .

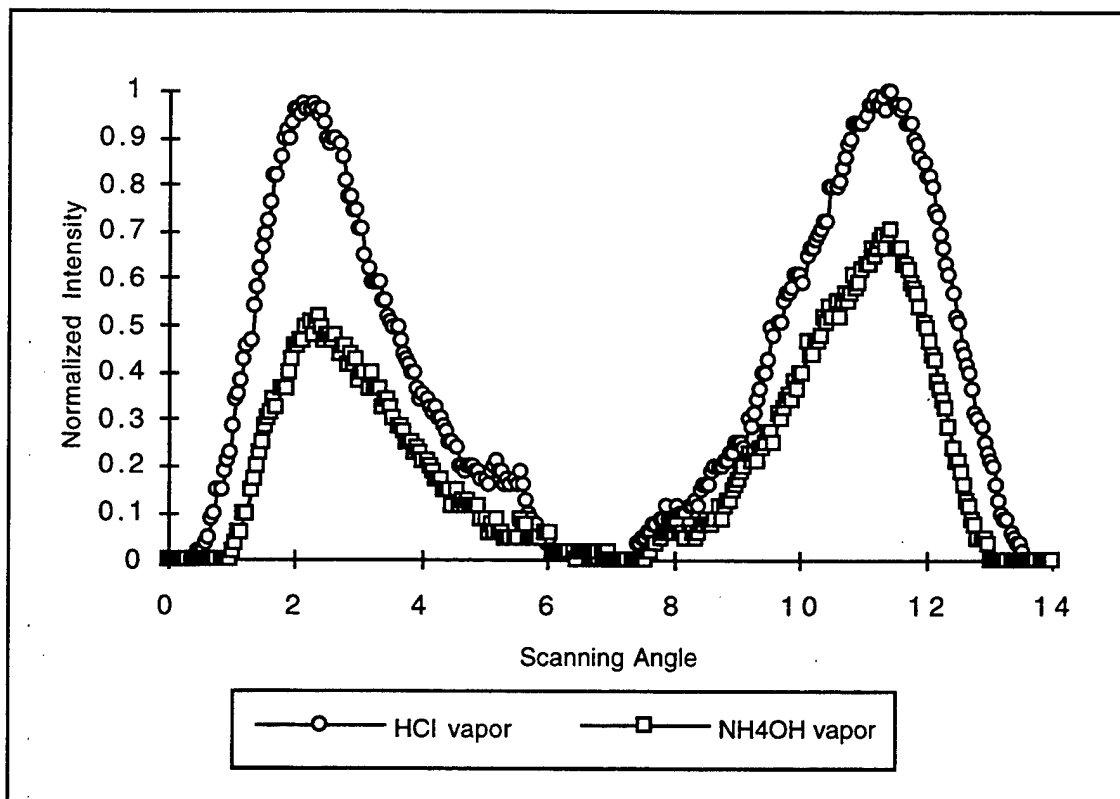


Figure 13. Normalized intensity profiles of the 2-D ring pattern (Figure 12).

Acknowledge

The authors would like to acknowledge the US. Army Research Office through Contract/Grant No. DAAH04-96-1-0018, for its financial support and technical collaboration. The authors would like to thank Dr. R. P. Quirk and Dr. Z. Zhuo, Dept. of Polymer Science, Akron University and Dr. A. G. MacDiarmid and his team, Dept. of Chemistry, University of Pennsylvania for their collaboration.

Electromagnetic Interrogation of Structures

Dryver Huston
Department of Mechanical Engineering
University of Vermont

Monitoring and assessing the health of structural systems remains an important issue, particularly in light of the increasingly aging infrastructures that are in use. The use of electromagnetic effects as an aid in assessing structural health appears to be a promising set of technologies. A primary advantage of the electromagnetic methods is that the structure can be interrogated with noncontacting instruments that can be rapidly slewed across a structure. Two different electromagnetic interrogation methods will be discussed. The first method (often referred to as ground penetrating radar) is where the structure passively interacts with incoming electromagnetic waves by reflecting and scattering off of internal features. High-frequency (0.5 up to 20 GHz) waves are used. The method is particularly well suited for concrete and certain geotechnical structures. The application of modern synthetic aperture radar techniques offers the promise of building a simple hand held unit that can be passed over a structure. This can be particularly useful for the rapid condition assessment of structures following natural and manmade disasters.

The second electromagnetic interrogation technique (investigated as part of a joint project with Microstrain Inc., Burlington VT) is where the structure interacts in an active manner with electromagnetic radiation to measure and transmit physical parameters that are relevant to the state of the structure. A receiver on the structure inductively converts the electromagnetic waves into rectified power for internal microprocessor-driven electronics that interact with transducers, such as strain gages that are embedded in the structure. Signals from the microprocessor are then transmitted back to the sending unit for logging and analysis. A principal advantage of the inductive coupling technique is that the sensors can be positioned at remote sections of a structure that do not need power lines or long term power supplies. This can be quite important for large structures. A disadvantage of the technique is that it for modest power levels, it requires the remote transmitter and receiver to be close to one another. The feasibility of using the inductively powered electronics technique along with a robot to crawl out and position the two antennas close to one another is investigated.

Ground Penetrating Radar

Features

1. Can be conducted at fairly high speeds (moving vehicle inspection of pavement)
2. Internal features can be identified.
3. Good for concrete or other structures with dielectric properties. Not effective for steel structures.
4. Requires complex signal processing techniques.
5. Microwave electronics are expensive.
6. Air-filled delaminations are difficult to identify.
7. Moisture in the concrete can make it highly absorbtive.
8. Small features require high frequency for resolution. High frequencies are absorbed quicker.

Basic Technique

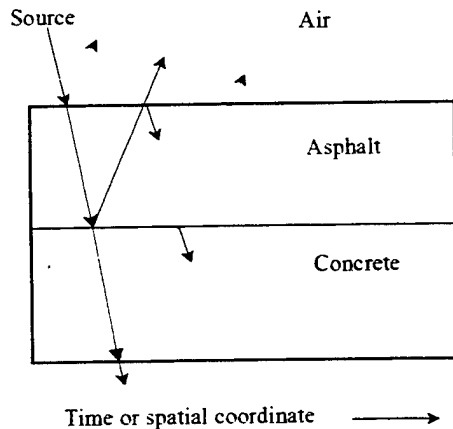
1. Oscillating EM wave (0.5 – 20 GHz) is launched from an antenna at the structure in question.
2. EM waves interact with the structure by reflecting off of, transmitting through, and being absorbed by features such as cracks, delaminations, material property changes, reinforcing bars, moisture and chloride ions.
3. The reflected EM waves are received by an antenna, processed and interpreted.
4. The launch and receive antenna are slewed across the structure to obtain spatial information.

Frequency (GHz)	Wavelength (m)			
	Air $\epsilon_r = 1.0$ Velocity = $3E+8$	Asphalt $\epsilon_r = 5.0$ velocity = $1.34E+8$	Concrete $\epsilon_r = 7.5$ velocity = $1.09E+8$	Water $\epsilon_r = 78.0$ velocity = $3.39E+7$
0.5	0.600	0.268	0.218	0.068
1	0.300	0.134	0.109	0.034
2	0.150	0.067	0.055	0.017
3	0.100	0.045	0.036	0.011
4	0.075	0.034	0.027	0.008
5	0.060	0.027	0.022	0.007
6	0.050	0.022	0.018	0.006

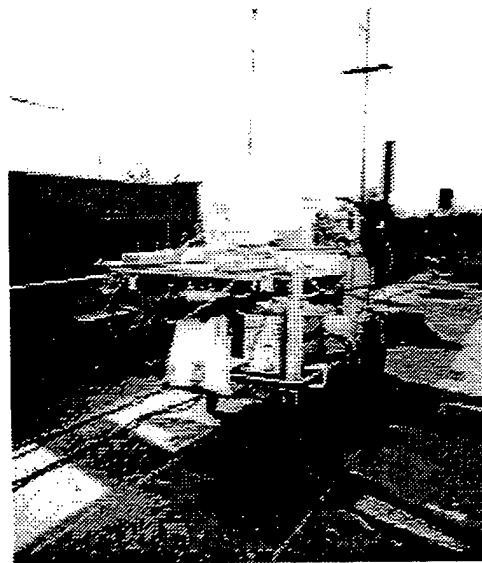
TABLE 1 - Electromagnetic wavelengths as a function of frequency for different media.

GPR SYSTEM COMPONENTS

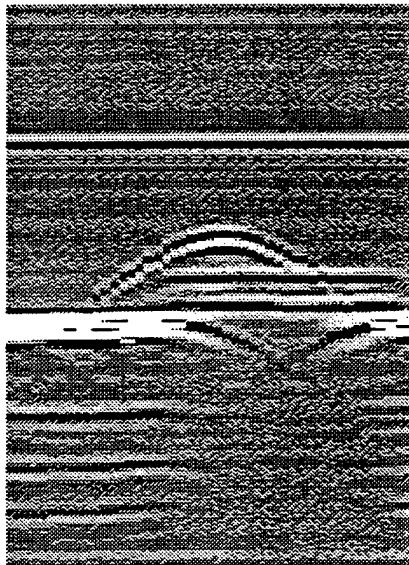
1. Signal generator - step-frequency or pulse generator (*0.5 – 6 GHZ step-frequency system – HP8753D Network Analyzer*)
2. High-fidelity cable – phase angle fidelity under bending
3. Source Antenna – low loss, impedance matching, and small size (*custom antenna – GIMA*)
4. Structure under test
5. Receiving antenna and high-fidelity cable – may be the same as Source Antenna
6. Signal acquisition – high-speed electronics (*HP8753D Network Analyzer*)
7. Signal processing and interpretation – simple to complex, but powerful algorithms
8. Slewing system – move antenna and system, indicate spatial position and synchronize with or trigger system (*measuring wheel with optical encoder*)



Interaction of EM wave with layered medium.



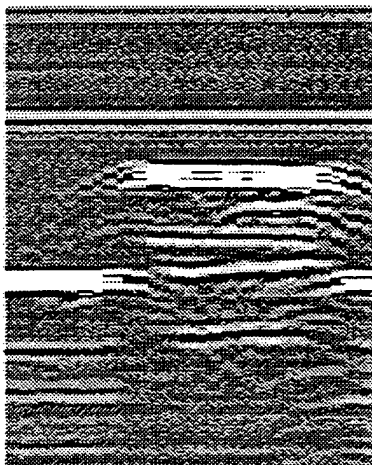
Ground penetrating radar system.



Reflection off a rebar

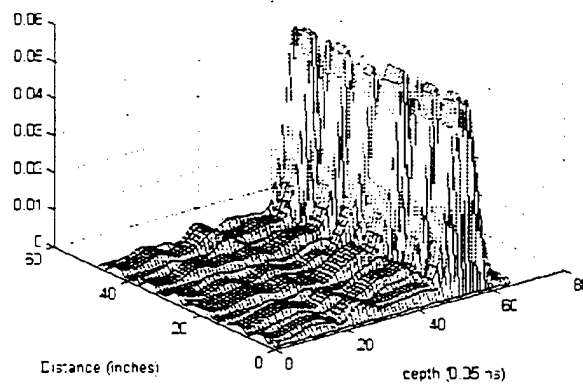


Bostwick bridge, Shelburne, VT



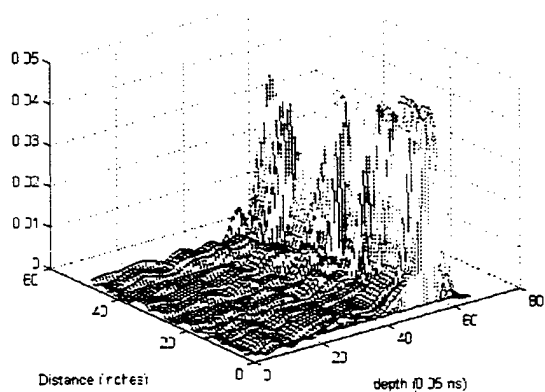
Scan of slab.

GIMA1, the first test, the first line 24 to 26 feet, Bostwick bridge, Shelburne, Vermont

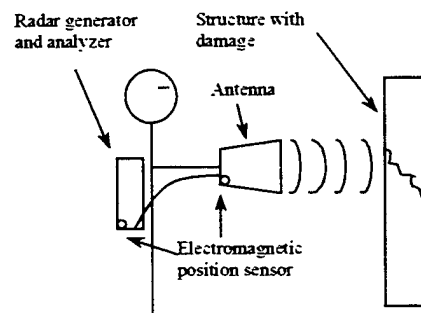


Scan of undamaged Bostwick Bridge section.

GMAT, the first test, the first line 3 to 12 feet, Bostwick bridge, Shelburne Vermont



Scan of damaged section of Bostwick Bridge



Handheld radar unit.

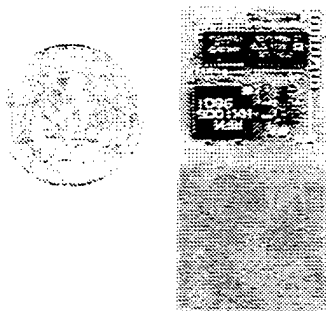
Active Electromagnetic Interrogation of Structures

Joint project with Microstrain of Burlington, VT and University of Vermont.

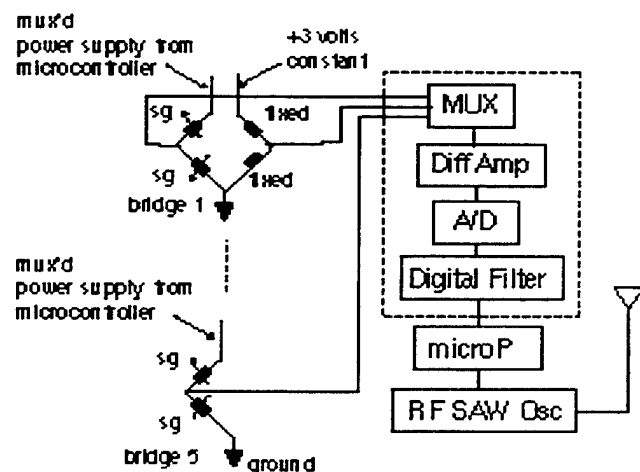
- Microminiature, multichannel, wireless, programmable Addressable Sensing Modules (ASM's)
- Inductively powered nodes will not require batteries or interconnecting lead wires.
- Greatly enhances their reliability and lowers costs.
- Autonomous robotic sensor inspection system capable of remote powering and data collection from a network of embedded sensing nodes.
- Networks of sensing nodes can be embedded, interrogated, and remotely accessed in applications where visual inspection by people is not practical due to: physical space constraints, remote geographic locations, high inspection costs, and high risks involved for those performing the inspections.
- Sensors of peak displacement, peak strain, corrosion, temperature, inclination, and other microelectromechanical sensors (MEMS), are now capable of embeddment in structures, and are compatible with our ASM's.

Inductively Powered ASM

- Developed entirely from off-the-shelf surface mount IC's.
- Inductive power reception coil is printed on the kapton flex board below the component area.
- Bridge signal conditioning, multiplexer, A/D converter, and programmable gain and filter functions are combined on a single chip.
- Microprocessor allows the AD7714 to be reprogrammed through the serial port of a personal computer (PC).
- Pulse code modulation (PCM) of a surface acoustic wave (SAW) radio frequency (RF) oscillator (RF Monolithics, Dallas, TX).



ASM node



Remote powering block diagram

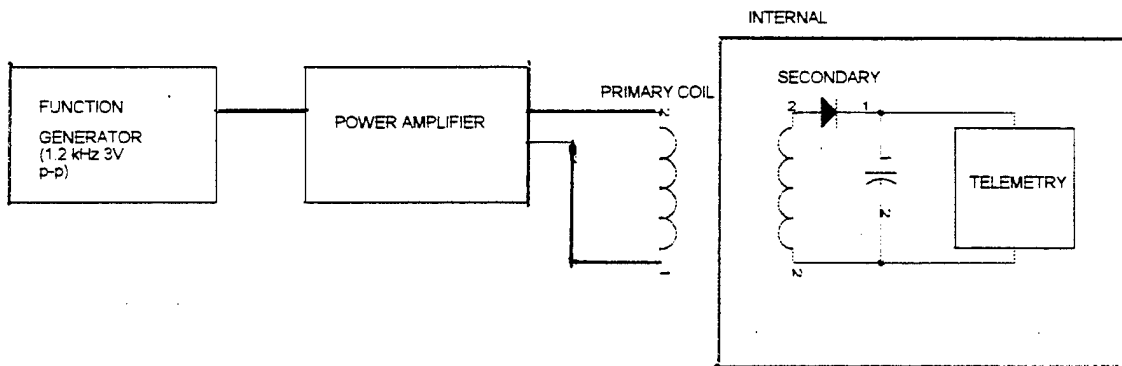


TABLE I. Sensors that are compatible with ASM microtransmitters

PARAMETER/ SENSOR - TYPE	Typical Sensor Power Consumption	Typical gain range requirement	DC Node	AC Node
TEMPERATURE <i>Thermocouple</i>	0	128	YES	NO
TEMPERATURE <i>Thermistor</i>	5 mW	32-64	YES	NO
TEMPERATURE <i>RTD</i>	5 mW	32-64	YES	NO
STRAIN <i>Foil Strain Gauge Bridge</i>	10 mW-30mW	128 Minimum	YES	NO
STRAIN <i>Semiconductor Strain Gauge Bridge</i>	0.5 mW- 5 mW	32-128	YES	NO
STRAIN <i>Capacitive Strain Gauge</i>	<5 mW	128	NO	YES
FORCE <i>Force Sensing Resistor</i>	<1 mW	1	YES	NO
FORCE <i>Foil Strain Gauge</i>	10mW - 30mW	128 Minimum	YES	NO
PRESSURE <i>MEMS Piezoresistive Pressure Sensor</i>	0.5 mW- 5 mW	32-128	YES	NO
ACCELERATION <i>Piezoelectric Accelerometer</i>	0	64 - 128	YES	NO
ACCELERATION <i>MEMS Piezoresistive Accelerometer</i>	0.5 mW- 5 mW	32-128	YES	NO
MAGNETIC FIELD <i>Magnetoresistance</i>	1mW-25 mW	32-128	YES	NO
MAGNETIC	10 mW - 25 mW	16-64	YES	NO

<i>FIELD Hall Effect</i>				
<i>ROTARY Potentiometer</i>	<1 mW	1	YES	NO
<i>HUMIDITY Capacitive</i>	<10mW	64-128	NO	YES
<i>CRACK PROPAGATION Resistive</i>	<10mW	16-64	YES	NO
<i>DISPLACEMENT DIRT LIDT</i>	10mW-25mW	128	NO	YES
<i>DISPLACEMENT Potentiometer</i>	<1mW	1	YES	NO
<i>DISPLACEMENT Non-Contact Inductive</i>	10 mW-25 mW	128	NO	YES
<i>LIGHT INTENSITY Silicon Photodetector</i>	<1mW	64-128	YES	NO
<i>VELOCITY- DIRT</i>	0 mW	64-128	YES	NO

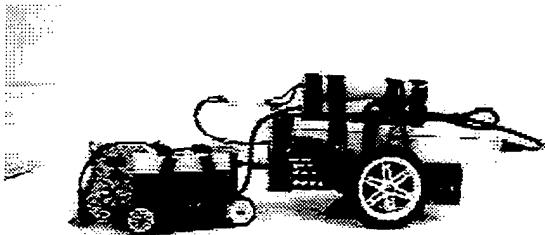
Table II. Sensor Electronics Specifications

Description	Specification
Amplifier gain	1-128: programmable
Filter	Low pass 1-250 Hz: programmable
Sensor inputs	5 pseudo differential: 3 full differential
RF Transmission Frequency	916.5 MHz
A/D resolution	10-16 bits (inversely proportional to low pass filter setting)
Output data rate	80 Hz for 5 channels of data: 220 Hz for 1 channel of data
Bit error rate	10 ppm at 1meter range with error checking
DC power required	9 mW typical
Temperature stability	10 ppm/C offset 100ppm/C gain

Build and test prototype systems with these capabilities using simple robots designed to operate on I-beams used in bridge construction.

Test task set:

- a) depart from its base station at regularly scheduled, and remotely programmable time intervals
- b) follow a predetermined path using magnetic markers and/or a dark stripe painted on the beam
- c) stop at predetermined interrogation points (where ASM's are embedded) along the path, using magnetic markers and/or touch probes for detection of the stopping point
- d) provide power to the embedded nodes
- e) perform data collection from the nodes
- f) acquire digital images at each node location, and save these images for remote downloading (optional for Phase I, required for Phase II)
- g) complete its journey along the path, interrogating each node on the path, until each embedded node has been successfully interrogated (unless a problem with node power up or data recovery is detected by the robot, in which case the robot will move on to interrogate another node)
- h) return to base station for recharging and FTP data downloading for internet data access



Real-time damage sensors based on triboluminescence

Grant Bourhill,^a Ian Sage,^a Rodney Badcock,^b Lisa Humberstone,^b Norman Geddes,^a Martin Kemp^b and Sharon Bishop.^b

a. Defence Evaluation and Research Agency, St. Andrews Rd., Malvern, WR14 3PS, U.K.

b. Defence Evaluation and Research Agency, Farnborough, Hampshire GU14 6TD, U.K.

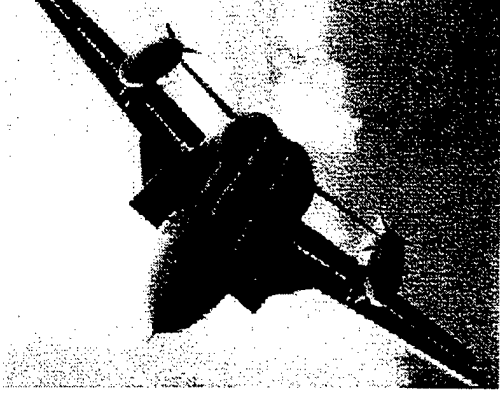
Tel: 44-1684-89-5398

Fax: 44-1684-89-6940

email: gbourhill@dera.gov.uk

Abstract: Triboluminescence is the name given to the light generated by certain materials when they are stressed to the point of fracture. Although this phenomenon has been known for over 400 years, it has only been in the last 40 years that high intensity triboluminescent materials have been reported. However, the majority of work in this area has aimed at detailing the mechanism behind the light emission rather than trying to exploit the triboluminescence itself. In this talk, we shall detail the principle behind using high-efficiency triboluminescent materials as smart optical damage sensors for use in modern composite structures. The triboluminescent materials being examined will be detailed along with the results of impact and tensile tests on resins incorporating a triboluminescent damage sensor. We will demonstrate that triboluminescent damage sensors show significant promise in providing real-time damage severity and location monitoring.

- sensors required to monitor impact severity and location



Primary requirement:

- sensors required to monitor impact severity and location

Secondary requirements:

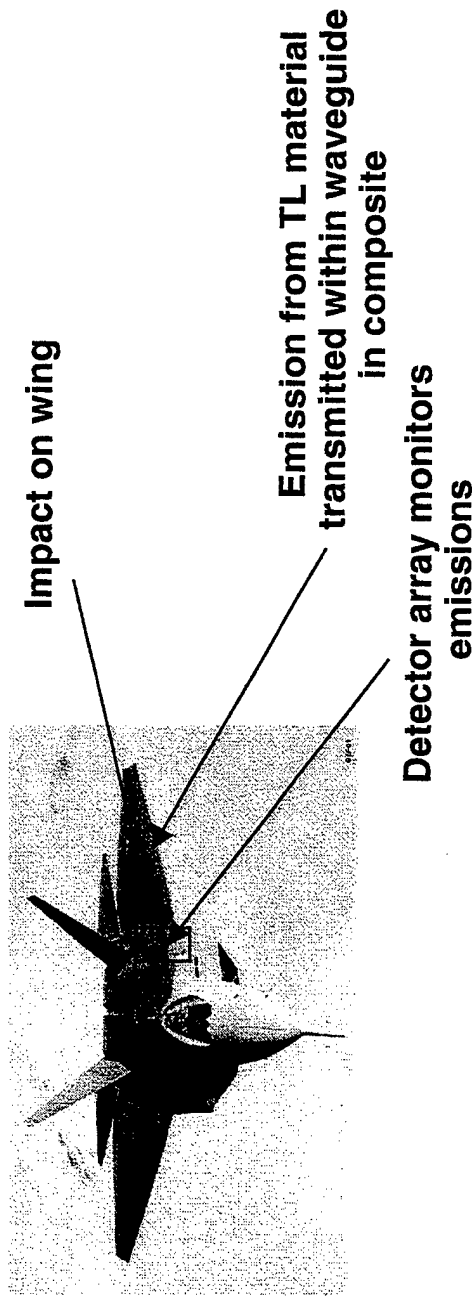
- provide real-time information
- provide ease of analysis
- exhibit minimal parasitic weight
- exhibit minimal deleterious effect on mechanical integrity
- exhibit minimal number of false alarms
- exhibit minimal vulnerability to electromagnetic interference
- inexpensive

- Triboluminescent sensors may address all these requirements

DERA

- impact severity related to triboluminescent intensity

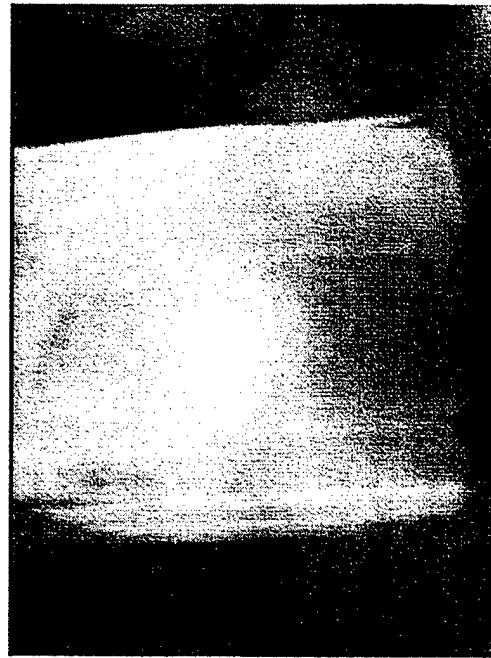
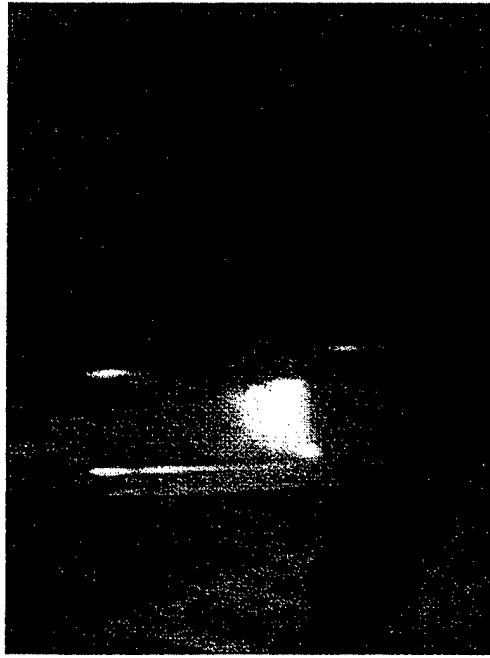
- impact location monitored by: - triboluminescent wavelength



Materials constraints:

- High triboluminescence intensity
- Discrete triboluminescent wavelength
- Discrete triboluminescent lifetime
- Chemically compatible with composite
- High melting point ($>140^{\circ}\text{C}$)
- Inexpensive

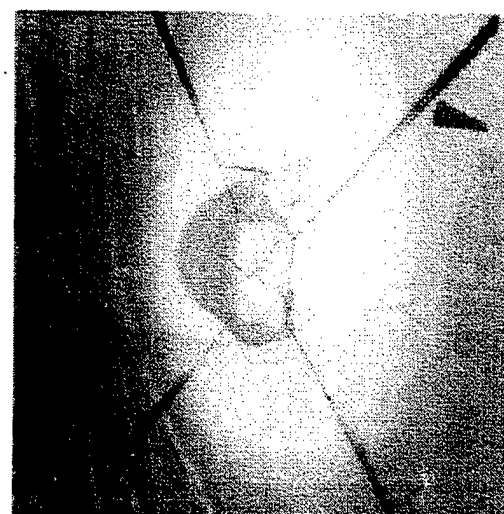
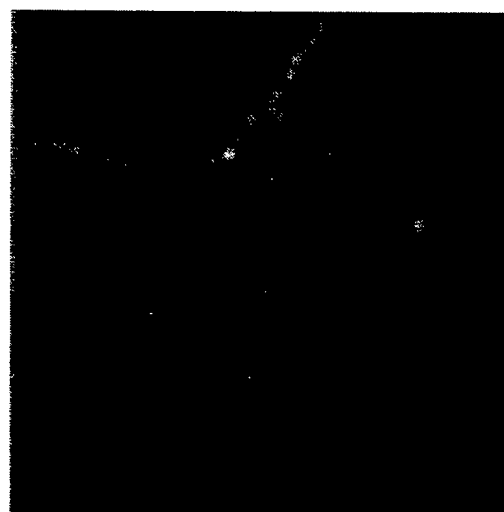
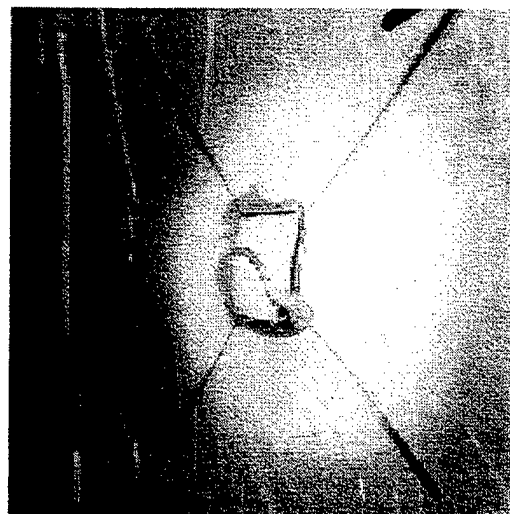
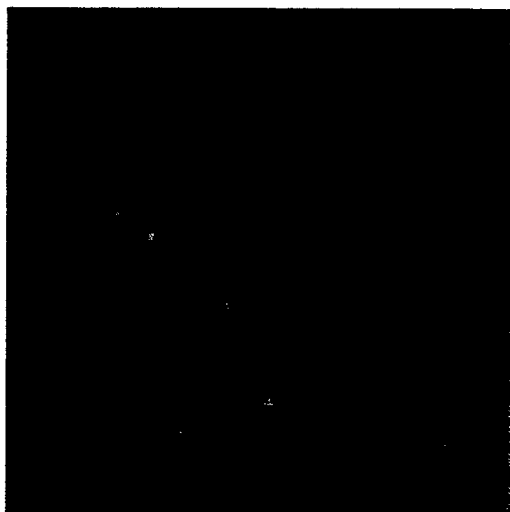
- High triboluminescence intensity



DERA

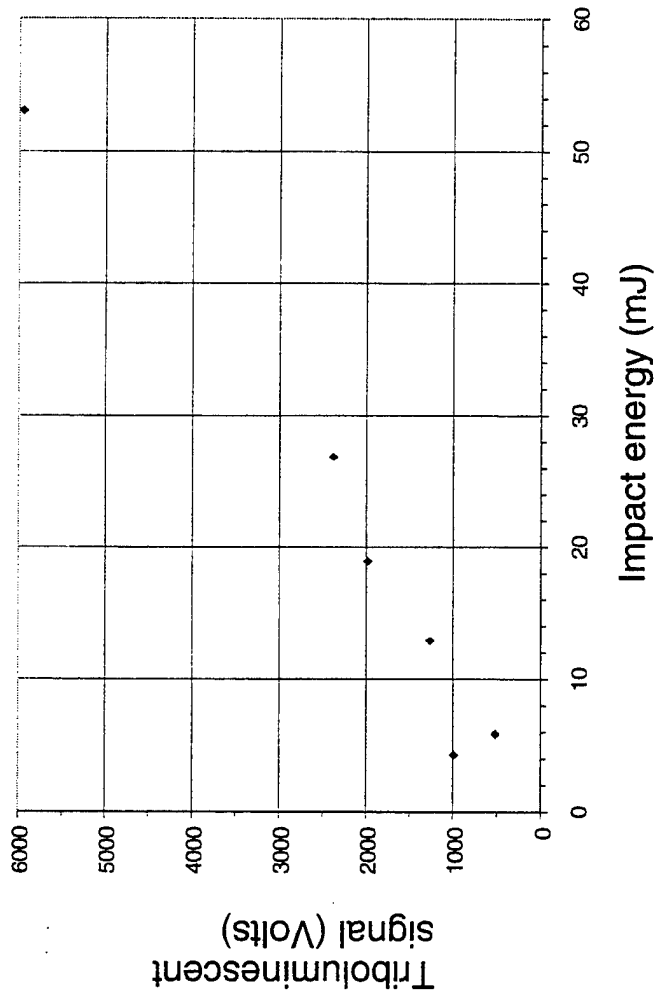
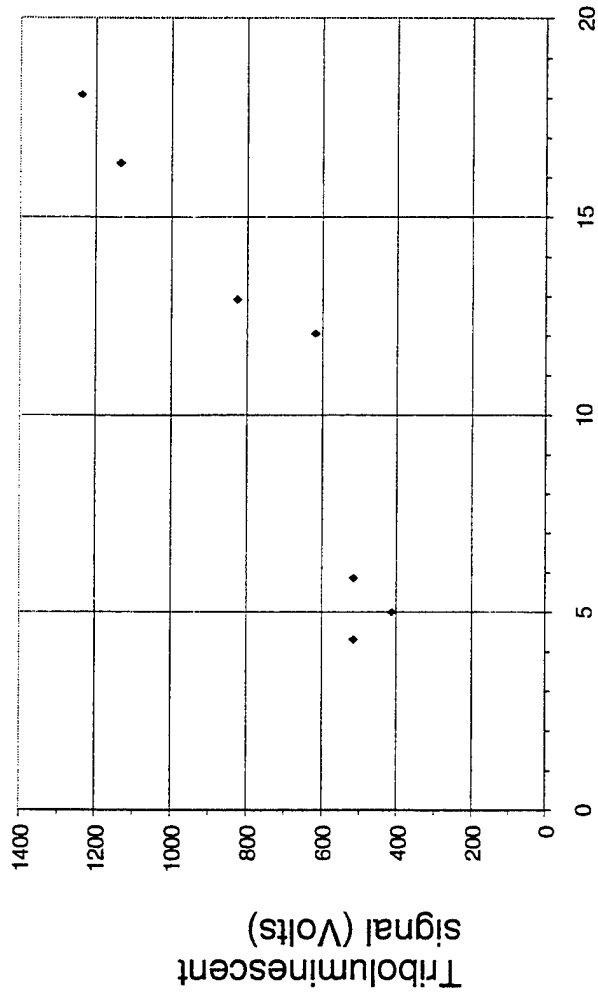


- light emission corresponds to fracture sights



DERA

- Towards obtaining damage severity information:



Summary

- A. Triboluminescence may act as impact severity/location sensor
- B. Triboluminescent mechanism requires further investigation
- C. Proof-of-principle demonstrated
 - **Light intensity related to force**
 - **Location monitoring**
 - **Coupling into optical fibre**

Future work

1. Demonstrate impact severity and location monitoring in composite

Acknowledgement:

The authors are grateful to the UK MoD Corporate Research Programme Technology Group 4 (Materials and Structures) for funding this work

<p>© British Crown Copyright 1999/DERA Published with permission of the Controller of Her Britannic Majesty's Stationary Office</p>

DERA

DESIGN OF MULTI-LAYER SMART FERROELECTRIC ANTENNA

Peng Thian Teo, Vinoy, K.A.Jose, V.K.Varadan
Center for the Engineering of Electronic and Acoustic Materials
The Pennsylvania State University

Yeow B Gan
DSO National Laboratory, Singapore

Abstract

In the Operation Desert Storm, single patch antenna with high dielectric material is utilized for portable GPS receivers. In this paper, we present the design of a multi-layered smart skin antenna structure utilizing ferroelectric materials for tunable multi-frequency and multi-functional performance.

1. Introduction

There is considerable demand for antennas to have a dual band performance and a tunable capability for operating in different frequency bands. In tactical military communications, frequency switching is often employed to prevent tracking and jamming in a battle field communication network. More recently, dual band multi-functional antennas are used with GPS communication and navigational operations [1][2]. In the Operation Desert Storm, single patch antenna with high dielectric material is utilized for portable GPS receivers [3]. Its great success has since triggered intense research on microstrip antennas printed on high dielectric substrates with multi frequency and multi-functional smart operations [4]. Due to its planar and lightweight characteristics, these printed antennas could be mounted conformally onto any aerodynamic flying object, performing various tasks at different frequency bands. Such applications give rise to the design of smart skin antennas whereby thin layers of electromagnetic radiators and avionics circuitry are embedded within the airframe surface [5] [6]. Tunable smart layered antennas utilizing piezoelectric RAINBOW wafers [7] and polyvinylidene films (PVDF) [8] have recently been studied. Tuning is achieved via adaptive mechanical adjustments of the antenna structure. Tunable BST (Barium Strontium Titanate) ferroelectric antenna [9], [10] on the other hand, achieved its tuning via variation of the antenna's equivalent electrical dimension.

2. Design considerations for antennas with smart materials

In this paper, the $\text{Ba}_x\text{Sr}_{1-x}\text{TiO}_3$ series of ferroelectric materials are used for the microwave antenna. The dielectric constant of these materials could change by more than 50%, depending on the applied bias voltage and the BST composition. [11][12]. The BST powder is prepared by the sol-gel method. This process enables dopants to be uniformly distributed throughout the entire BST ceramic, as compared to a rather non-uniform distribution prepared by the conventional methods. Inclusion of graphite to the powder, followed by a firing of the mixture results in a highly porous BST substrate, with the included graphite being burned off eventually. By controlling the amount of graphite added, the desired porosity could be achieved. This enables a low bulk dielectric constant to be obtained for the substrate material. Inorganic filler is then added to the fired substrate to enhance its physical rigidity.

However, it should be noted that fabrication of such ferroelectric materials to meet a high dielectric constant specification is in fact less demanding than to produce one with a low dielectric constant and at the same time maintaining the good tunable characteristics of the material. The challenges and difficulties to produce a low dielectric constant material with good electrical properties for antenna applications have also been highlighted recently by Rao et. al.[13] In trying to produce a low dielectric substrate, electrical inhomogeneity, low tunability and poor loss tangent performance are the commonly associated drawbacks. As a result, most of these ferroelectric antennas are realized on substrates with a relatively higher dielectric constant as compared to the dielectric substrate available commercially. On the other hand, it is well known that microstrip antennas on high permittivity substrates suffer from narrow bandwidth and poor efficiency that is due to the energy loss associated with the excitation of surface waves modes [14]. The stacking of antenna elements could provide a solution to enhance the gain, bandwidth and introduce dual band performance [15]. However, most of these designs are optimized at fixed design frequencies only.

3. Single layer BST ferroelectric antenna

The gain is computed for a single layer BST antenna whose properties are similar to that reported in [14]. With a relative permittivity (ϵ_r) of around 26, loss tangent of 0.0238 and thickness of 2.28mm, the maximum gain obtained using the ENSEMBLETM simulation tool [16] is given as -6dB at a resonance frequency of 0.85GHz. The realized gain G (in dB) can be defined here as:

$$G(\text{dB}) = 10 \log \left(\frac{\text{Power Output}}{\text{Power Input}} \right) \quad (1)$$

Losses in the feed line were taken into account for this gain computation. A negative gain value obtained for the model implies that the power radiated is smaller than the input

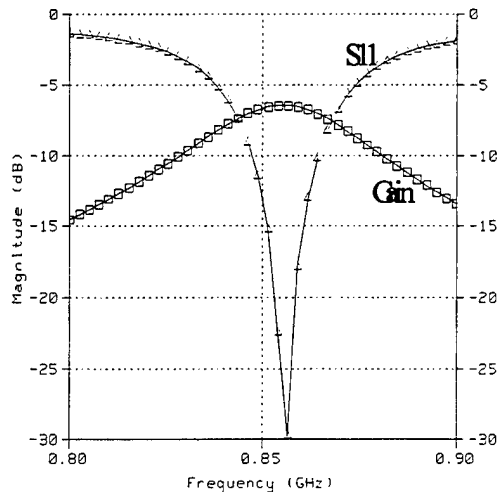


Figure 1a

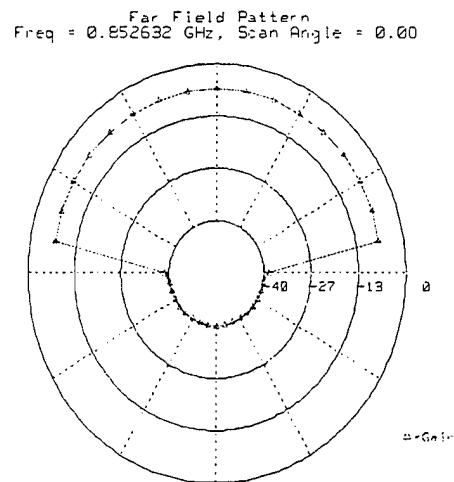


Figure 1b Radiation performance of BST antenna.

power, making such high dielectric antenna rather inefficient. Losses are incurred in the dielectric as well as in the excitation of surface waves at an unusually much lower

frequency [17] [18]. The simulated input reflection and radiation performances are shown in figure 1.

4. Design of tunable air-gap coupled antenna

The multi-layer structure shown in figure 2 consists of a feeder resonator at the bottom and a parasitic radiator at the top. The two layers are separated by an air gap. The feeder element studied in this new investigation is designed at a center frequency of 0.915GHz, with the ferroelectric substrate having a thickness h of 1.5mm, dielectric constant of 16 and loss tangent of 0.0495 [19]. The resonance phenomenon is characterized by a minimal reflection at the input port ($S_{11} = -44\text{dB}$) and a VSWR of less than 1.5 at the design frequency.

The radiating parasitic element, which is electromagnetically coupled to the feeder resonator, is etched on a substrate with a thickness h of 1.6mm, dielectric constant of 120

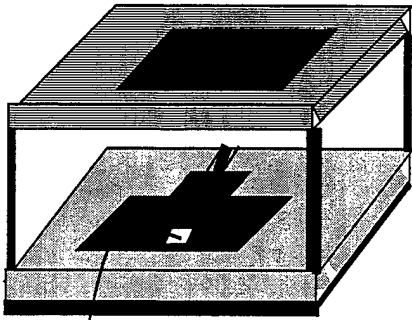


Fig 2 Layered antenna structure with the DC bias

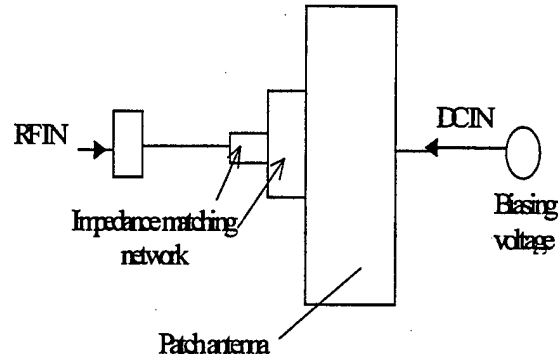


Figure 3 Novel tunable impedance matching

and loss tangent of 0.0066. The air gap spacing is given as 7mm. A variable voltage source is being used to apply a bias voltage across the ferroelectric substrate, thereby changing the dielectric constant and the resonating frequency of the entire antenna device. Tunability may then be defined to be the derivative of the new resonating frequency and the designed center frequency, with the antenna performance being constant or kept to a slight variation. To refine the performance, a pair of tunable cascaded matching network is implemented at the input port of the feeder patch (figure 3). This provides a continuous adaptive impedance matching to the tunable antenna.

The resonance phenomenon for the multi-layer structure is shown in figure 4a and figure 5a with $S_{11} = -18\text{dB}$ and a maximum gain of 3.1dB at around 850MHz respectively. The stacking of the parasitic patch has caused the resonance frequency to shift downwards as compared to that of a single layer antenna. For the antenna to resonate at a different frequency, say 825MHz, an applied voltage of around 1.46kV is required to produce a variation of 0.1 % in the dielectric constant. With a dielectric constant of around 17.6 and loss tangent of 0.047, a resonance phenomenon could be established at 825MHz. The resonance phenomenon obtained after the tuning is shown in figure 4b and figure 5b. The variation in the input impedance is compared in figure 6a and figure 6b

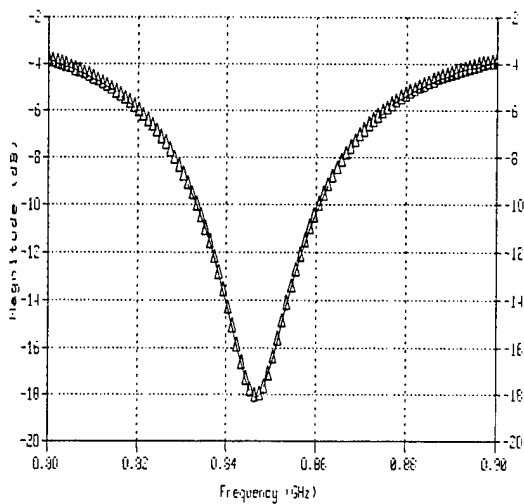


Figure 4a Input reflection coefficient (S11) prior to tuning

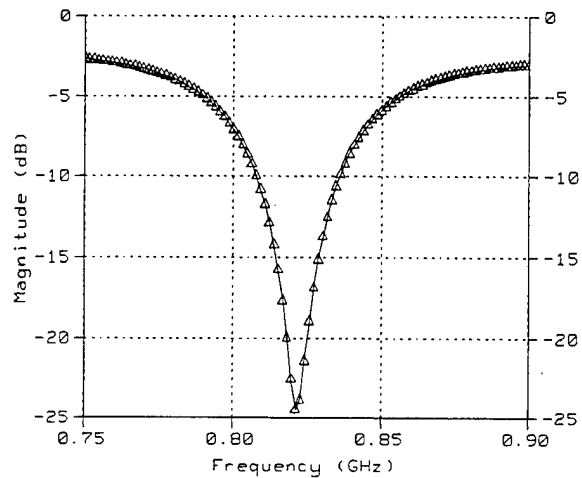


Figure 4b Input reflection coefficient (S11) with biasing voltage tuning

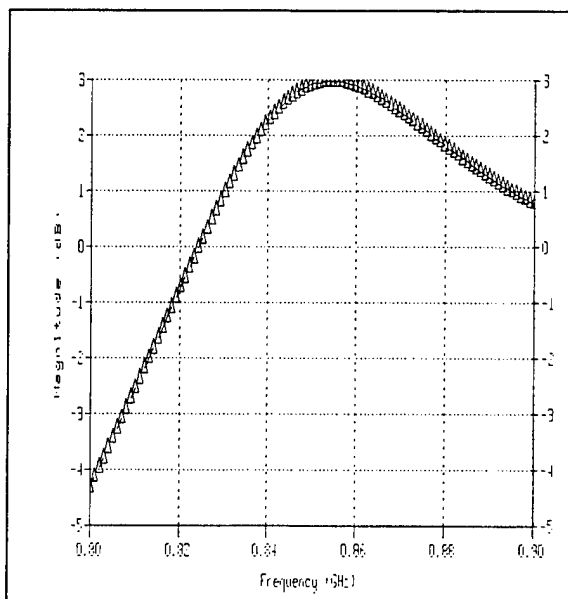


Figure 5a Gain performance for 850MHz-antenna prior to tuning

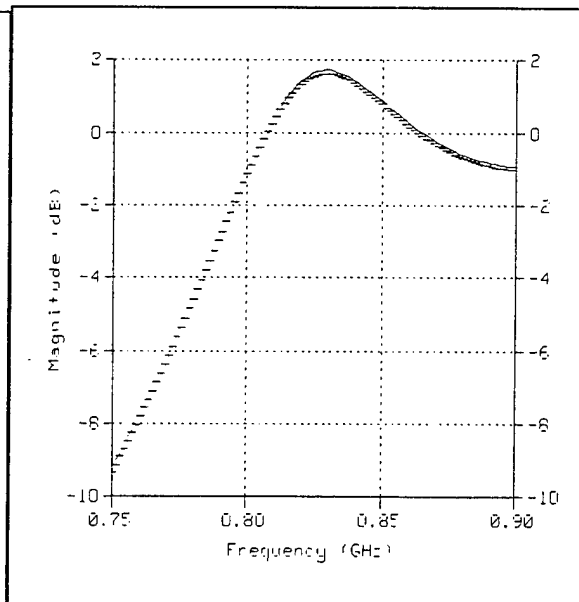


Figure 5b Gain performance peaks at 825MHz with biasing voltage

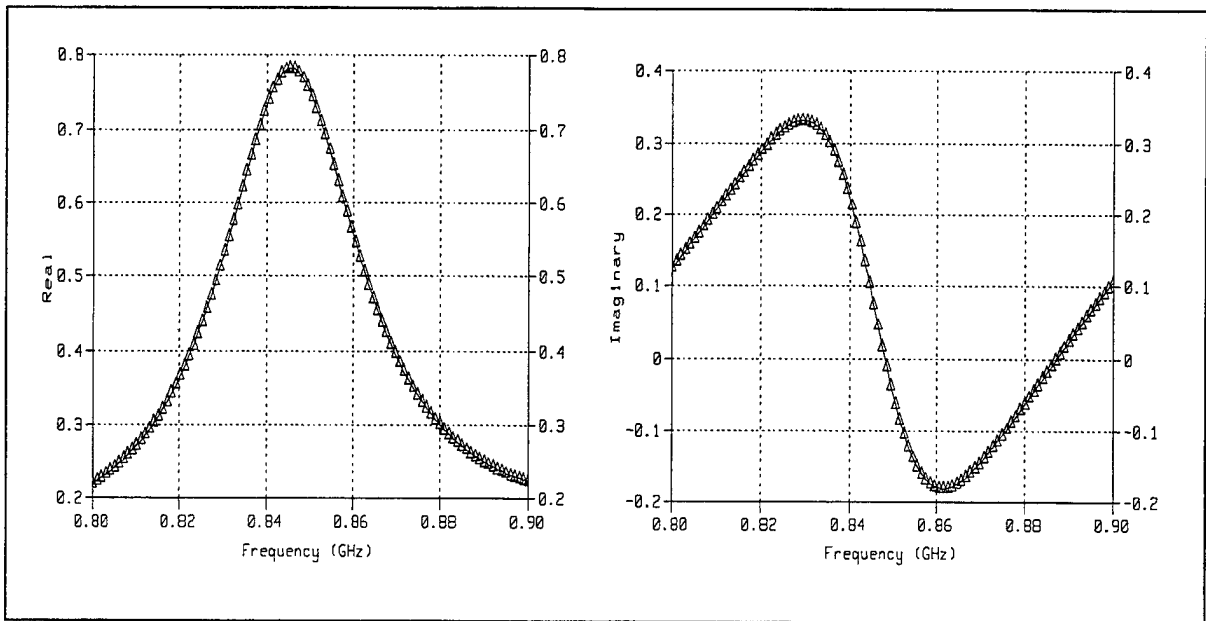


Figure 6a Impedance performance for design frequency of 850MHz prior to tuning:

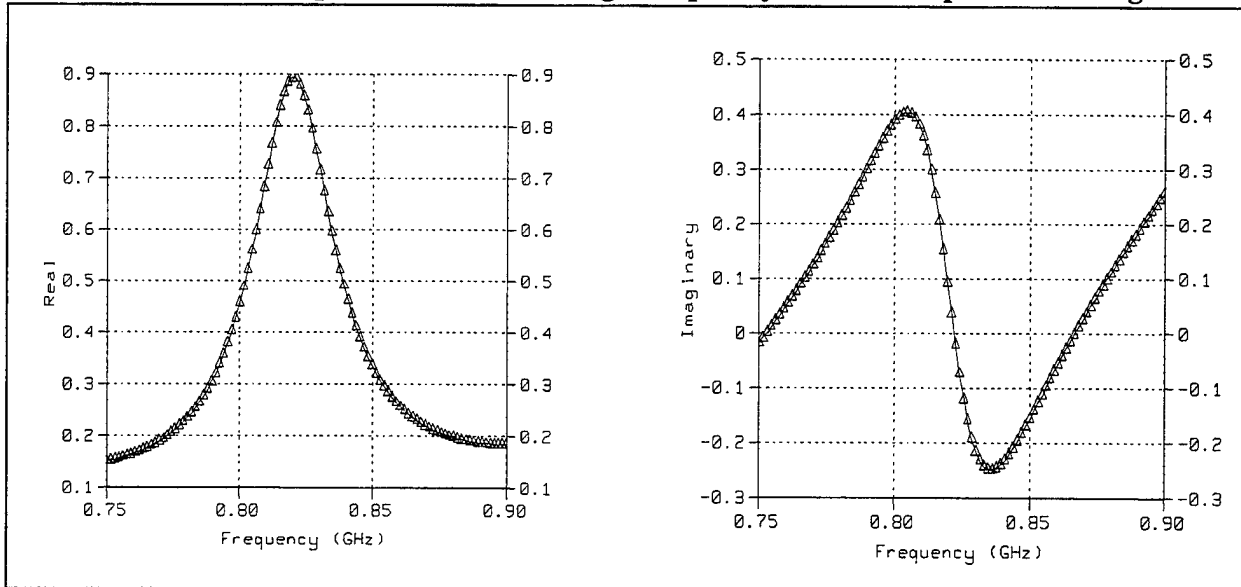


Figure 6b Impedance performance showing resonance at 825MHz with biasing voltage

5. Design of tunable dual-band antenna

This structure is composed of a microstrip patch antenna coupled with a director having a different size but same shape and same axes of symmetry. The bottom microstrip patch, being the feeder element, is printed on a substrate with dielectric constant of around 3. This is a normal dielectric material available from Rogers Corporation. As shown in figure 7, a

ferroelectric material with a patch printed on its upper surface is placed directly on top of the feeder patch.

The bottom substrate layer has a permittivity value much lower than that of the ferroelectric substrate layer. In addition, the bottom feeder-radiator is designed for resonance at 2.45GHz. This is much lower when compared to the resonance frequency (3.0GHz) for the upper director. As a result, the feeder-radiator has a relatively larger radiating surface area. This allows the upper substrate layer to be positioned well within the large surface area of feeder-radiator. The resonance characteristics for the feeder-resonator alone are showed in figure 8. The bottom substrate layer has a dielectric constant =3.0, loss tangent=0.0013 and thickness=1.52mm. The ferroelectric substrate on top has an unbiased dielectric constant = 79.8, loss tangent =0.00777 and thickness = 8mm. The parasitic patch is designed with a dimension of 26mm (H plane) by 19.13mm (E plane) while the feeder is 44.1mm (H plane) by 34.48mm (E plane).

The feeder-radiator serves two purposes; (1) to excite electromagnetic energy for the director element; and (2) to serve as ground plane for the ferroelectric substrate layer. A DC biasing voltage could then be applied across the ferroelectric substrate, causing a tunable performance. The stacking of the different layers enhanced the gain of the otherwise inefficient resonating director fabricated on the ferroelectric substrate. A dual-band performance is also achieved through the stacking structure.

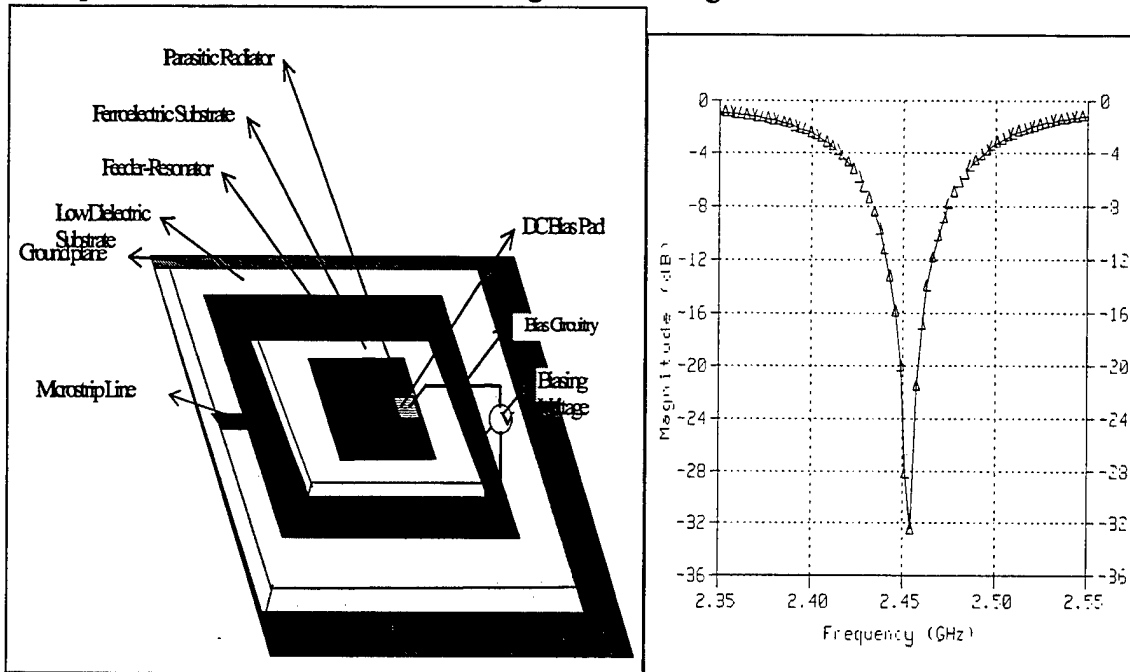


Figure 7 Layered Dual Band Antenna Structure Figure 8 Input reflection coefficient

The dual band S11 performance prior to any applied bias voltages is illustrated in figure 9a. Resonance behavior with $S_{11} < -9\text{dB}$, occurs at around 3.08GHz and 3.838GHz. This is compared with figure 9b, whereby a biased voltage is applied to produce a shift in both the resonance frequencies. With a dielectric constant of 86 and loss tangent of 0.0072, the new resonance frequencies occur at around 2.7GHz and 3.4GHz. A tunable performance is obtained with the ferroelectric substrate. The shift in the antenna gain

performance is illustrated in figure 10a and figure 10b. The radiation patterns for both the upper and lower resonance frequencies prior to any applied bias voltage are shown in figure 11, with an estimated 3dB-beamwidth of $\pm 8^\circ$ at the upper resonance frequency. With the change in the dielectric constant, the radiation patterns for both the upper and lower resonance frequencies are shown in figure 12. It has a 3dB-beamwidth of $\pm 14^\circ$ at the upper resonance frequency. The beamwidth performance at the lower frequency band for both the biased and unbiased structure is narrower compared with those at the upper resonance frequency. From figure 10b, it has also been observed that a radiation null has been tuned into the frequency at which the antenna is previously exhibiting a radiation characteristic. At the particular frequency, this radiation null corresponds to minimal antenna sensitivity in the normal incidence direction. Such feature provides the antenna a means to reject interference or jamming signal targeted at the previous operating frequency and/or coming from the normal incidence direction.

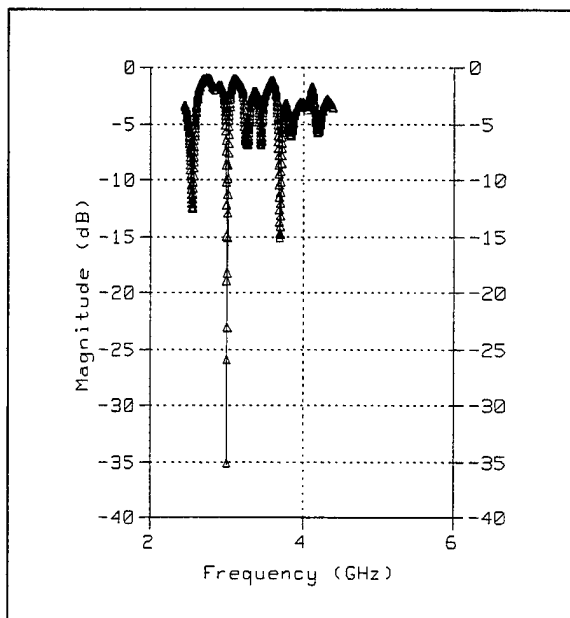


Figure 9a Input reflection coefficient performance for a dual band unbiased antenna

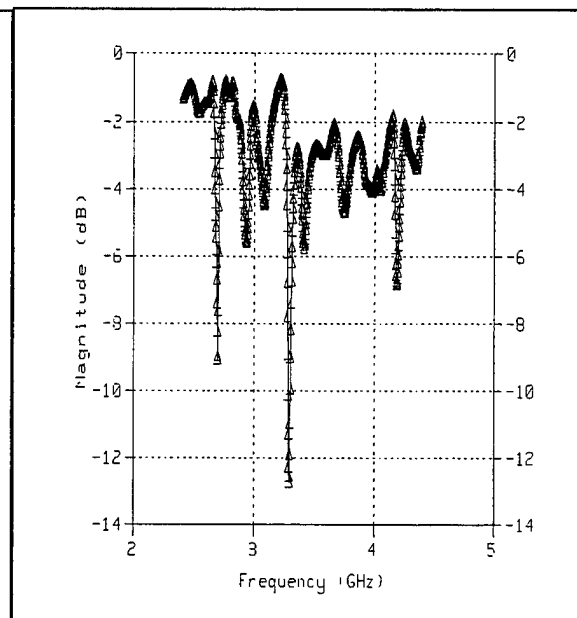


Figure 9b Input reflection coefficient performance for a dual band biased antenna antenna

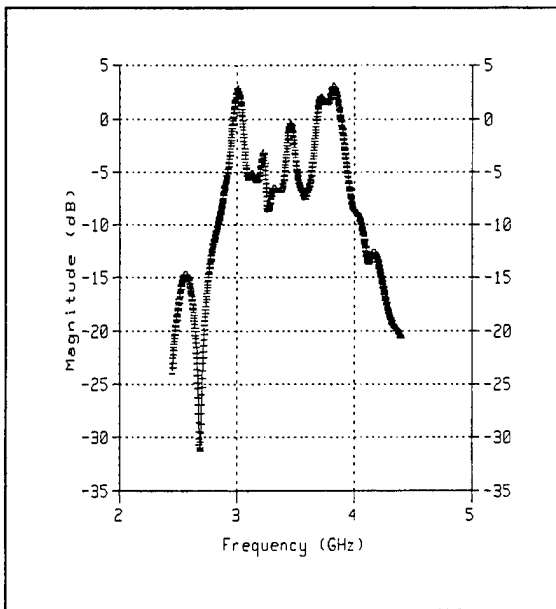


Figure 10a Gain performance for a dual band unbiased antenna

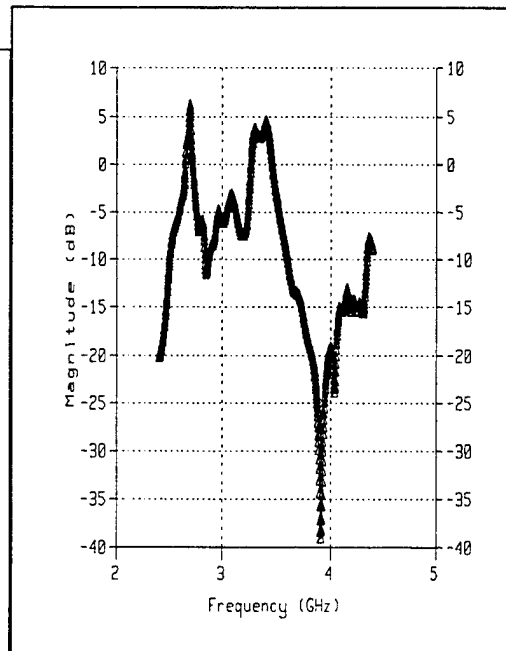


Figure 10b Shift in gain performance with an applied biased voltage

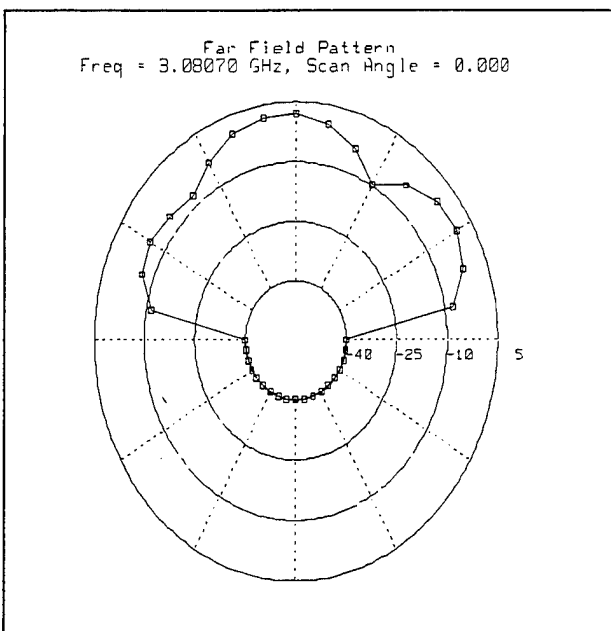


Figure 11a Radiation pattern at the lower resonant frequency (3.08GHz) for the unbiased structure.

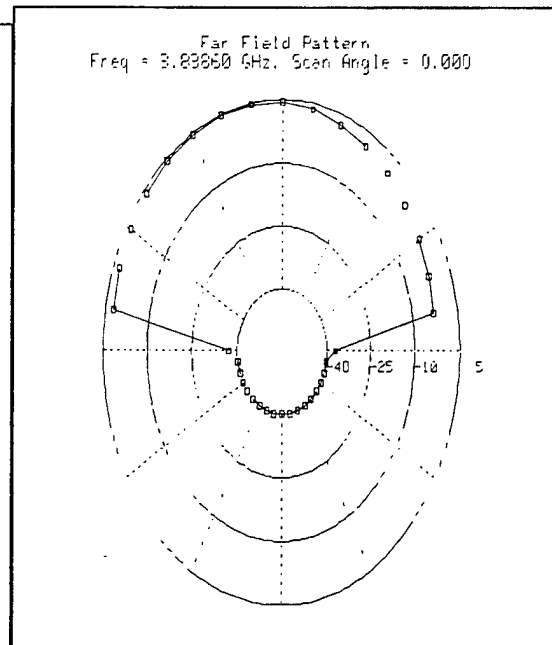


Figure 11b Radiation pattern at the upper resonance frequency (3.838GHz) for the unbiased antenna

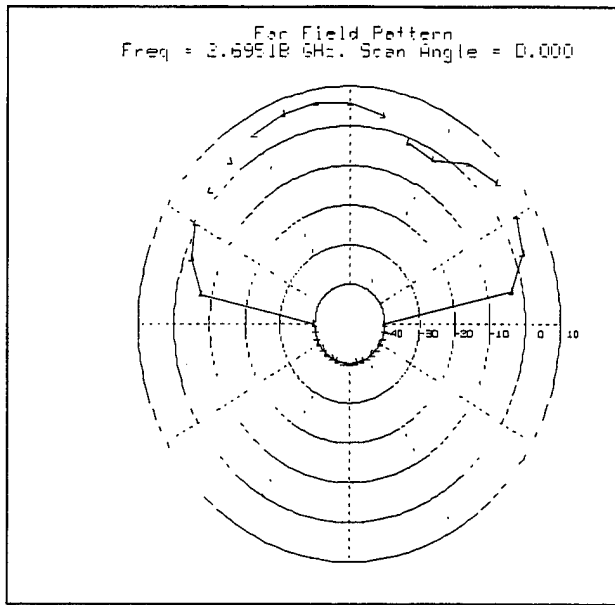


Figure 12a Radiation pattern at the lower resonance frequency (2.7GHz) upon applying a biased voltage

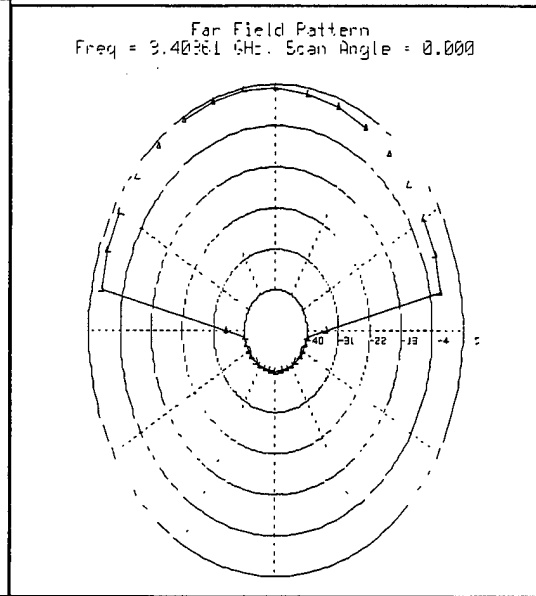


Figure 12b Radiation pattern at the upper resonance frequency (3.40GHz) upon applying a biased voltage

6. Conclusions:

It is found that a properly designed multi-layered ferroelectric antenna could provide higher gain and frequency agile operations. A further improvement of this work will be to consider the effect of the finite substrate size on the radiation characteristics. The multi-layered structure has a further advantage of serving as a protective shield for the inner antenna and its circuitry. Besides, these ferroelectric materials could withstand higher temperatures than most of the dielectrics substrates available in the market, rendering it possible for applications in rugged and hostile environment.

The antenna described in this paper will also be useful for several new generation communications standards that are currently being studied by the ITU. This includes the fixed service wireless network standard [20] and the radiodetermination systems [21]. Most of these systems that are being studied involve the possibility of utilizing the frequency band ranging from 2.7GHz- 3.8GHz, which are being catered in our designs. As been predicted [20], most of these next generation communications systems will command operations in intra, inter-regional, global and multi-services applications. These could find a solution in our multi-layered frequency smart antenna system.

Acknowledgements

This work is supported by a research contract from DRD, Singapore. The authors would like to thank Mr. Quek Gim Pew and Mr. Lee Kim Seng for their support throughout this research.

References:

- [1] Moore S.A.W. and Moore A.R. 1997 Dual frequency multi-function radar antenna research *Tenth International Conference on Antennas and Propagation* **436** 522 – 526
- [2] Pozar D.M. and Duffy S.M. 1997 A dual-band circularly polarized aperture-coupled stacked microstrip antenna for global positioning satellite *IEEE Trans. Antennas Propagation* **45** 1618 - 1625
- [3] Scott W B 1991 Small ceramic microstrip antenna central to surge in new GPS uses *Aviation Week and Space Technology* 55
- [4] Varadan V K and Varadan VV 1996 Design and development of smart skin conformal antenna with MEMS structural sensors and actuators *Proc.SPIE* **3046** 94
- [5] Lockyer A J, Kudva J N and Alt K H 1995 Development of a conformal load-carrying smart skin antenna for military aircraft *Proc. SPIE* **2448** 53-62
- [6] Alt K H, Lockyer A J, Martin C A and Kudva J N 1995 Application for smart skin technologies to the development of a conformal antenna installation in the vertical tail of a military aircraft *Proc. SPIE* **2448** 42-52
- [7] Kiely E, Washington G N and Bernhard J 1998 Design and development of smart microstrip patch antennas *Smart Mater Struct* **7** 792-800
- [8] Washington G N 1996 Smart aperture antennas *Smart Mater Struct* **5** 801-805
- [9] Varadan V K, Jose K A and Varadan V V 1998 Design and development of electronically tunable microstrip antennas *Smart Mater Struct* **8** 238-242
- [10] Jose K A, Varadan V K and Varadan V V 1999 Experimental investigations on electronically tunable microstrip antennas *Microwave and Optical Technology Letters* **20** 166-169
- [11] Varadan V K, Ghodgaonkar, Varadan V V, Kelly J F and Glikerdas P 1992 Ceramic phase shifters for electronically steerable antenna systems *Microwave Journal*. **34** 116-125
- [12] Babit R W Koscia T E Drach W C 1992 Planar electro-optic phase shifters *Microwave Journal* **35** 63-79
- [13] Rao J B L, Patel D P, Sengupta L C and Synowczynski J 1997 Ferroelectric Materials For Phased Array Applications *Proc. IEEE AP-S Int. Symp.* 2284-2287
- [14] Kathei P B and Alexopoulos N G 1983 On the effect of substrate thickness and permittivity on printed circuit dipole properties *IEEE Trans. Antennas Propagation* **31** 34–39
- [15] James J R and Hall P S 1989 *Handbook of microstrip antennas* 1 (London: Peter Peregrinus)
- [16] ENSEMBLE planar electromagnetic field simulator ver 5 product of Ansoft Corporation.
- [17] Schaubert D H and Yngvesson K S 1986 Experimental study of a microstrip array on high permittivity substrate *IEEE Trans. Antennas Propagation* **34** 92–96
- [18] Pozar D M 1983 Considerations for millimeter wave printed antennas *IEEE Trans. Antennas Propagation* **31** 740–747.
- [19] Varadan et al. 1996 US Patent 5557286
- [20] Nortel (Europe) 1998 Spectrum aspects of fixed wireless access(FWA) including the ETSI BRAN project *ITU document 8A-9B/58-E*
- [21] Principal Rapporteur (Working Party 8A) 1998 Technical characteristics of radiodetermination systems operating in the band 3.4 –3.7GHz *ITU document 8A-9B/51-E*

Development of a Smart Rotor with Piezoelectric Bender Actuated Trailing Edge Flaps

Nikhil Koratkar and Inderjit Chopra

Alfred Gessow Rotorcraft Center
Department of Aerospace Engineering
University of Maryland, College Park, MD 20742

Research Objective

Development of an intelligent rotor with piezoelectric-bender actuated trailing-edge flaps for active vibration control of rotorcraft.

Motivation

One of the major current rotorcraft challenges is vibration and noise reduction. The application of smart structures to rotorcraft for this purpose has become increasingly attractive with the development of compact, light-weight and high bandwidth solid state induced strain actuators. The advent of smart structures and materials opens up a hitherto unavailable domain for vibration control, aeromechanical stability augmentation, handling qualities enhancement, stall alleviation and acoustic suppression.

Concept

It is proposed to use trailing-edge flaps for individual blade control. The flap motion will generate new unsteady aerodynamic airloads, that correctly phased, will reduce fixed frame vibration by directly altering the airloads in the rotating frame. For the present research the trailing-edge flap is actuated using a solid state piezoelectric bender.

Approach

Analytic models will be developed for smart rotors with piezoelectric-bender actuation. In order to validate the analysis and demonstrate the concept feasibility, Froude and Mach scaled models with piezo-bender actuated trailing-edge flaps will be designed, fabricated and tested in the vacuum chamber, on the hover stand and in the wind tunnel.

Accomplishments

An analytic model is developed for the coupled bender-flap elastic rotor system in hover flight condition. The rotor blades are modeled as elastic beams capable of coupled flap-wise bending and torsional deformations. The actuator beam is modeled as a elastic beam undergoing elastic flat-wise deformations due to piezoelectric excitation. A time domain unsteady aerodynamic model for compressible, subsonic flow (Leishman & Hariharan) is used to model the unsteady airloads due to flap motion. The actuator and rotor blade equations of motion are coupled via aerodynamic and inertial coupling terms. These coupled set of equations are solved using a Finite Element in time method after the non-linear blade and actuator equations are transformed into normal mode form.

To validate the analytic model and demonstrate the feasibility of Piezo-Bender actuation, two operational (1/8 scale), proof of concept Froude scaled blades were designed and fabricated, in-house. These blades were tested in hover at the Univ. of Maryland bearingless rotor test facility. Flap deflections ± 4 to ± 8 degrees were obtained in the 1-4/rev frequency range at the Froude scaled operating speed of 900 RPM. The trailing-edge flap motion resulted in a 10 % variation in the rotor thrust and torque levels, thus demonstrating the effectiveness of piezo-bender actuation. The analytic model showed good correlation with hover test data over a wide range of rotor speeds and collective settings. Subsequently, two Mach scaled rotor blades were designed and fabricated, in-house. The blades were tested at the Mach scaled operating speed of 1800 RPM on the hover stand using a Bell-412 Mach-scaled rotor hub. Flap deflections of ± 9 degrees were achieved at 1800 RPM, thus demonstrating the ability of the actuator to overcome the centrifugal and frictional hinge moments at Mach scale.

Future Work

- Forward flight tests in the Glen L. Martin wind tunnel at Mach scaled operating conditions
- Extension of the analytic model to Forward Flight and validation with Mach scale test data



ALFRED GESSOW ROTORCRAFT CENTER

Hover Testing of a Mach Scaled Rotor with Trailing-Edge Flaps

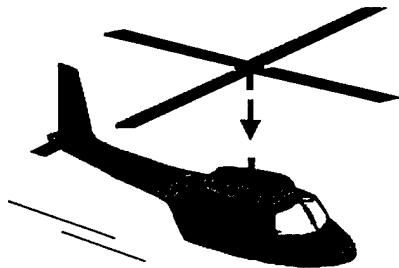
Nikhil A. Koratkar
Minta Martin Fellow

Inderjit Chopra
Alfred Gessow Professor and Director

Fourth ARO Workshop On Smart Structures, Aug. 16-18 1999



Goal : Active Vibration Control



Helicopter Vibration

For an N-Bladed Rotor,

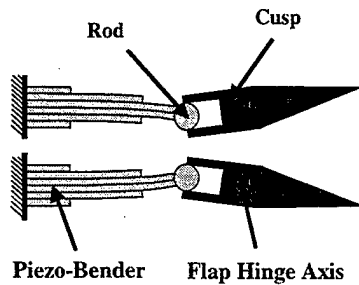
- N/rev and $N \pm 1/\text{rev}$ blade loads
- Transmitted to fuselage via Hub as N/rev forcing

Trailing-Edge Flap used for Individual Blade Control (IBC)

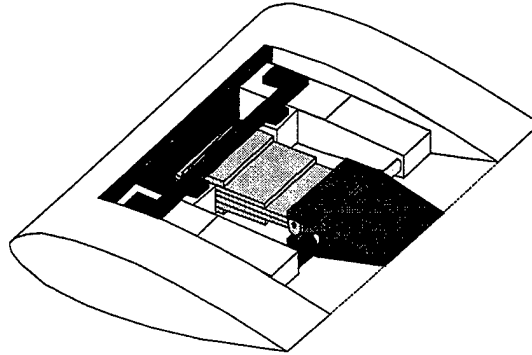
Flap motion causes new unsteady aerodynamic forces. Correctly phased this activation can reduce the vibratory hub loads



Piezoelectric Bender Actuation



Actuator Stroke Amplification



Actuator-Flap Assembly



Research Objectives

- Experimental work with Piezoelectric Benders limited to Froude scaled models : Koratkar & Chopra (SPIE-97), Fulton & Ormiston (AHS-98)
Objective : Carry our Proof-Of-Concept work at Mach Scale
- Available rotor codes with flaps (UMARC, CAMRAD-JA), neglect the actuator dynamics and hence prescribe the flap motion
Objective : Integrate Actuator Model into Rotor Analysis



Analysis

The analysis is developed as follows :

- Implementation of unsteady aerodynamic model
- Actuator model
- Elastic rotor model
- Actuator-Rotor coupling
- Coupled response : FEM in space and time



Analysis - Continued

Aerodynamic Model : Hariharan and Leishman (1995)

- Flapped airfoil in compressible, subsonic flow
- Time Domain Formulation (Indicial Methods)
- Model is implemented using recursively updated deficiency functions applied to quasisteady airloads

Cn (Lift)
Ch (Hinge Moment)
Cm (Pitching Moment)



Actuator Model : (Korathkar & Chopra : SPIE-98)

- Actuator is modeled as elastic beam (Flat-wise Bending only)
- Finite Element Formulation
- Actuator strain energy is modified to account for "PZT induced strain" and "centrifugal loading effects"
- Flap hinge moment (included in actuator load matrix)



Analysis - Continued

Rotor Structural Model

- Rotor Blade : Elastic Beam undergoing coupled Flat-wise Bending and Torsion.
- FEM Formulation (7 DOF Beam Elements)



- Cubic variation in bending deflection and quadratic variation in elastic twist.
- Formulation covers chord-wise offsets of blade center of gravity and aerodynamic center from the elastic axis.



Coupled Response

Coupled Actuator-Flap equations of motion

Actuator

$$\begin{bmatrix} M_a & M_{coupling} \\ 0 & M_b \end{bmatrix} \begin{Bmatrix} \ddot{p} \\ \ddot{u} \end{Bmatrix} + \begin{bmatrix} C_a & C_{coupling} \\ 0 & C_b \end{bmatrix} \begin{Bmatrix} \dot{p} \\ \dot{u} \end{Bmatrix} + \begin{bmatrix} K_a & K_{coupling} \\ 0 & K_b \end{bmatrix} \begin{Bmatrix} p \\ u \end{Bmatrix} = \begin{Bmatrix} Q + H(p, p) \\ F_b + L(p, p) + M(p, p) \end{Bmatrix}$$

Rotor Blades

- **Modal reduction : coupled rotating modes**
- **Periodic response : Finite element in time method**
- **8 equally sized time elements**
- **5th order Lagrange polynomials as time basis functions**



Mach Scaled Model

Requirement

- Mach scaled models are more representative
- Tip Mach number is simulated

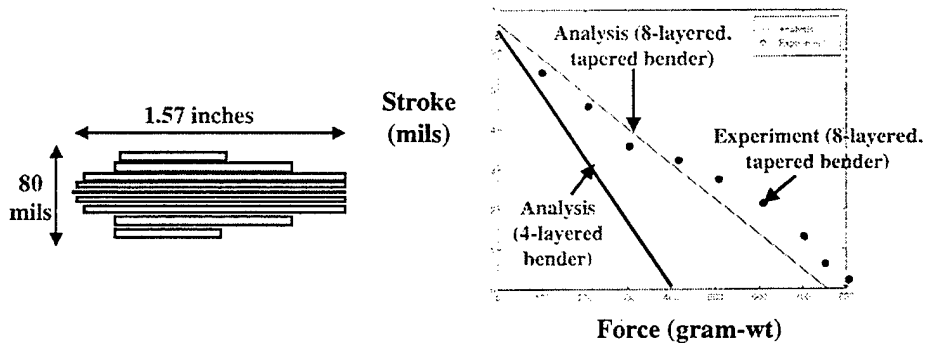
Challenges

- Operating speed is nearly 2.5 times Froude scaled speed (2000 RPM)
- Aerodynamic hinge moments are 6 times Froude Scaled values
- Centrifugal loads are heavily over-scaled : $(\Omega^2 R)_{MACH} = 6.25 \times (\Omega^2 R)_{FROUDE} = 6.3 \times (\Omega^2 R)_{FULL-SCALE}$
- Actuation bandwidth is much larger
 - Mach Scale : (1/rev-5/rev \rightarrow 33 Hz - 165 Hz)
 - Froude Scale : (1/rev-5/rev \rightarrow 15 Hz - 75 Hz)
 - Full Scale : (1/rev -5/rev \rightarrow 5 Hz - 25 Hz)
- High frequency of excitation means large inertial loads on actuator and blade
- Increased bandwidth also means greater actuation power requirements



Actuator Design

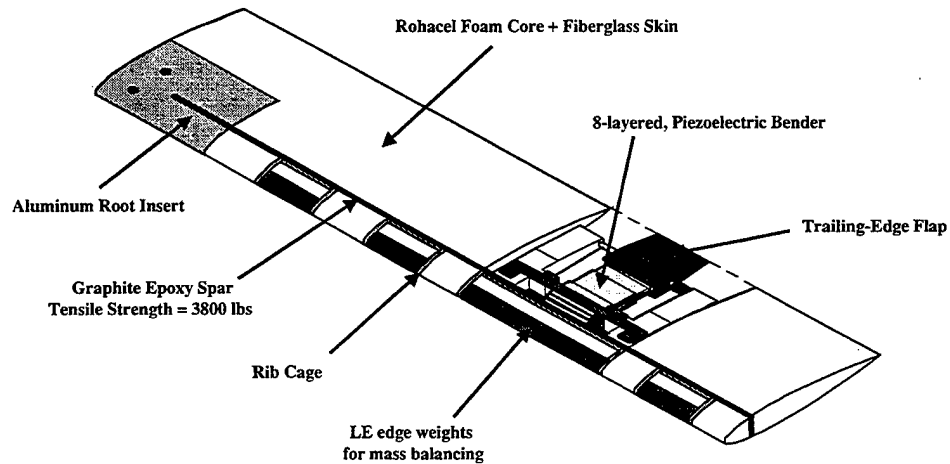
- 8-layered, Tapered Benders were Designed and Fabricated.



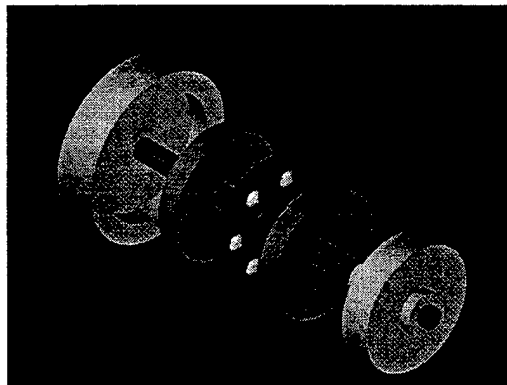
Actuator, Force-Stroke Characteristics



Rotor Blade Fabrication



Thrust Bearing (Minimize Frictional Losses)

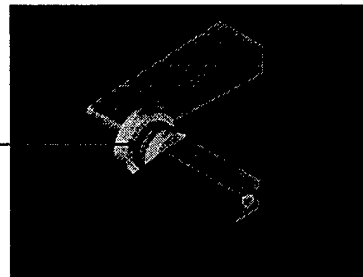


F2-6 Thrust Ball Bearing

Outer radius - 3 mm

Bore radius - 1 mm

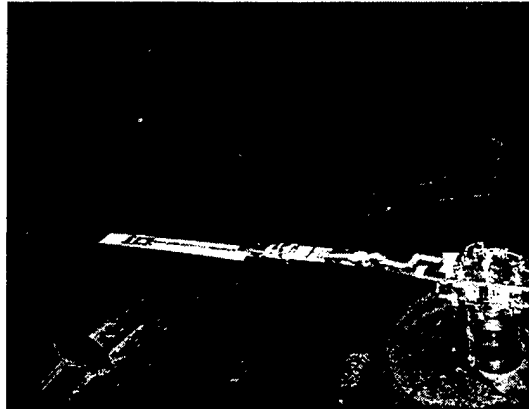
Dynamic Load Capacity - 26.44 Lbs



Exploded View of Thrust Bearing Assembly



Vacuum Chamber Testing

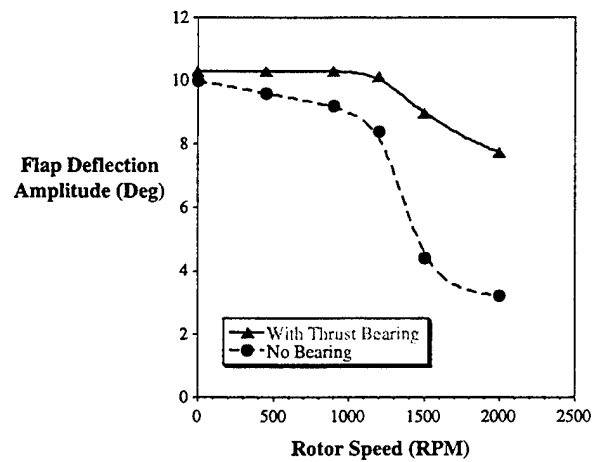


Mach scaled model inside Vacuum Chamber



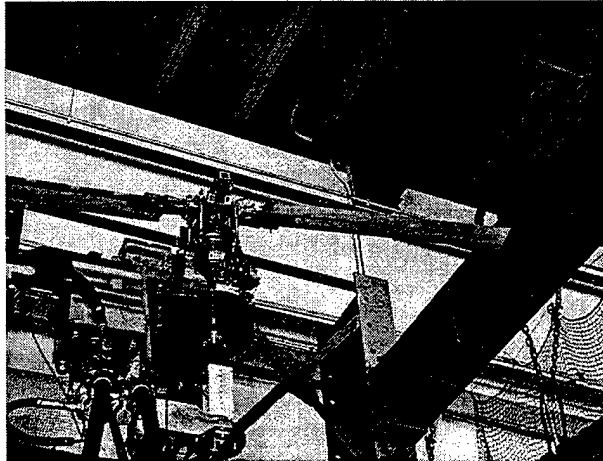
Vacuum Chamber Test (RPM Sweep, Flap excited at 10 Hz)

Bender Excitation : 90 Vrms with 3:1 Bias @ 10 Hz





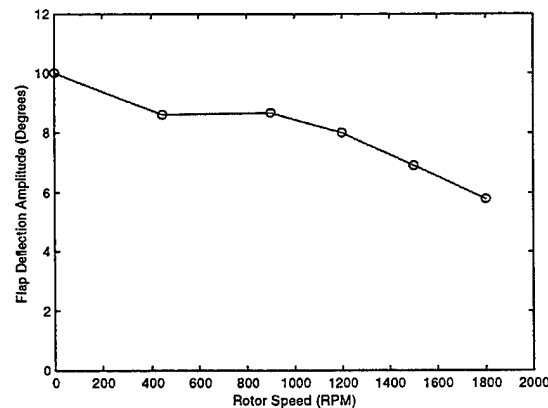
Mach Scaled Model Hover Testing



- Bell-412 Mach Scaled Rotor Hub
- 1/8 Scale Model
- 2-Bladed Rotor (only one blade is active)
- Actuator : 8-layered tapered bender
 - 5 % Span
 - 75% of Rotor Radius
- Trailing-Edge Flap
 - 5 % Span
 - 75% of Rotor Radius



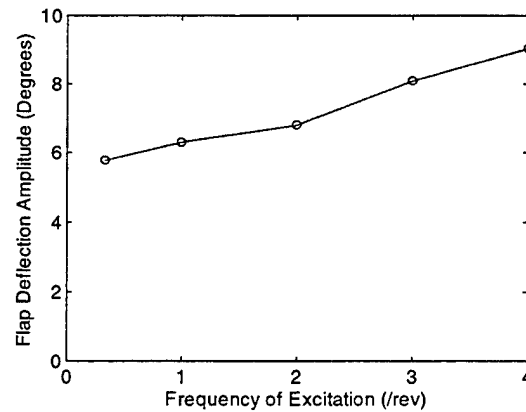
Hover Test : RPM Sweep



Bender excited at 90 Vrms with 3:1 AC bias, excitation frequency = 10 Hz



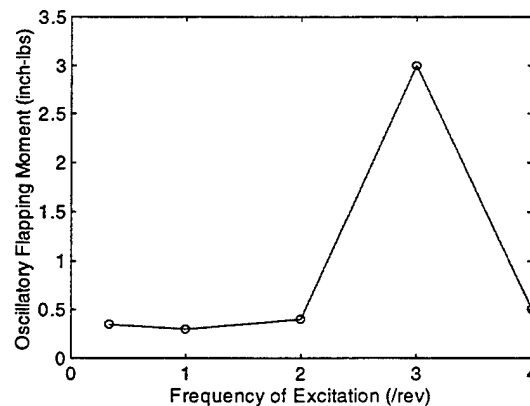
Hover Test : Frequency Sweep



Bender excited at 90 Vrms with 3:1 AC bias, Rotor Speed = 1800 RPM



Hover Test Oscillatory Flapping Moment



Bender excited at 90 Vrms with 3:1 AC bias, Rotor speed = 1800 RPM



Summary

- **Developed analytic model for coupled actuator-flap-rotor system**
- **Validated model with Froude scaled hover test data**
- **Designed and fabricated Mach scaled model**
- **Achieved ± 9 degrees of flap deflection in hover at 1800 RPM**

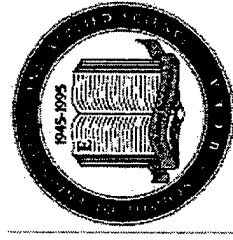


Future Work

- **Fabrication of a matched set of 4 Mach scaled blades**
- **Forward Flight Tests : Glen L. Martin Wind Tunnel**
- **Extension of the coupled analysis for forward flight**

Meso-Scale Actuator Devices For Rotorcraft

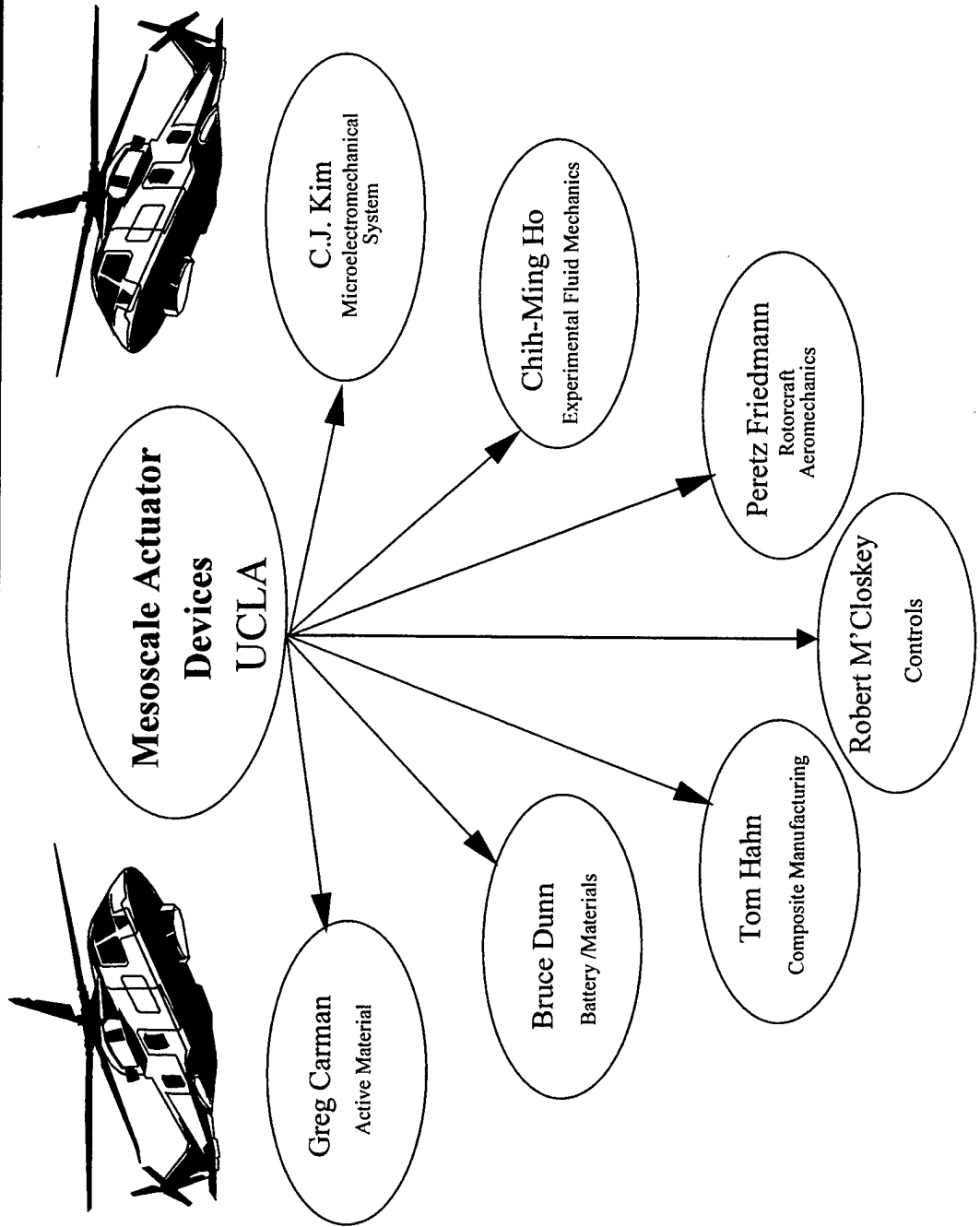
University of California, Los Angeles
<http://aml.seas.ucla.edu>



*Supported by the Army Research Office under contract
DAAH04-95-1-0095. Contract monitor: John Prater*



UCLA Principal Investigators



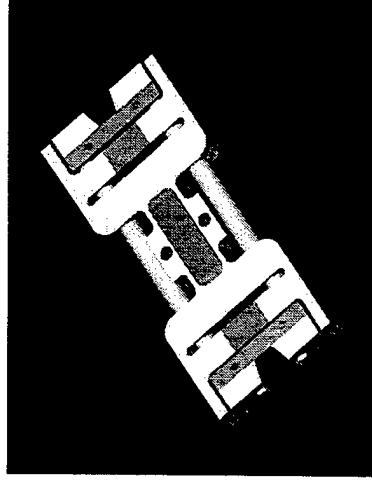
Multidisciplinary Program

Rotorcraft - vibration & stall

Fluids + Aeromechanics

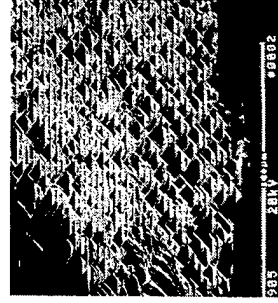


Device design
Mechanical + MEMS



Experimental characterization

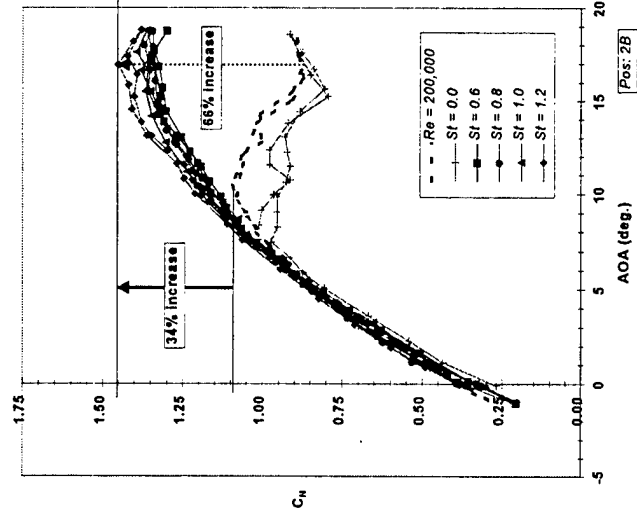
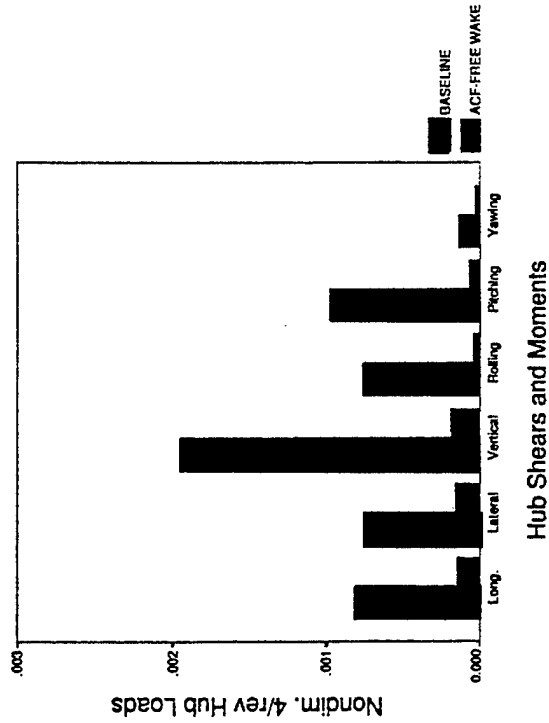
Mechanics + Materials



Active Control Rotorcraft -Application



- Static stall delayed with small perturbation near leading edge (tests)
- Dynamic stall alleviated with small perturbations near leading edge (tests)
- Vibrations reduced due to forward flight 90% with trailing edge flap (theory)
- BVI induced vibrations reduced by 80% with trailing edge flap(theory)



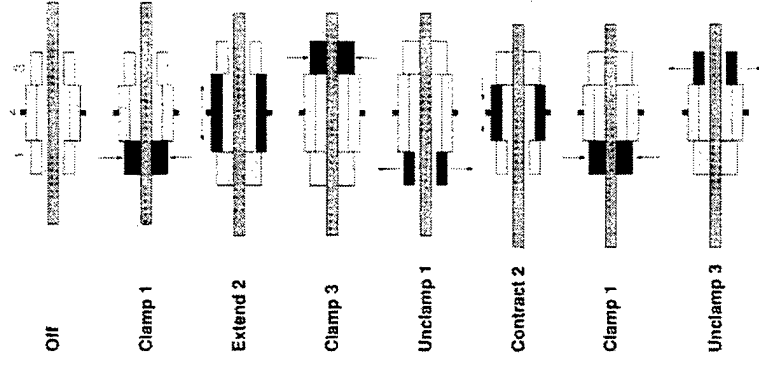
100%

Solution (Frequency Rectification)

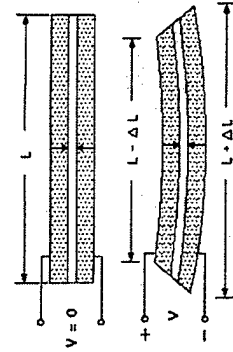
Objective - Combine piezoelectric with MEMS technology to develop a large-force and large-displacement actuator for structural applications

Material/Device	Stress MPa	Strain	Energy kJ/m ³	Power/stack power @30Hz
PZT	40	0.2%	80	1
PZT-(MAD)	40	Unlimited		5(1kHz) ;50(10kHz)

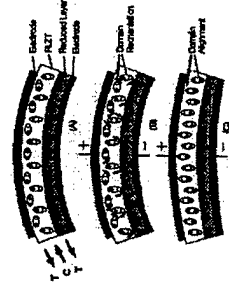
Inchworm motor



Other displacement amplification approaches



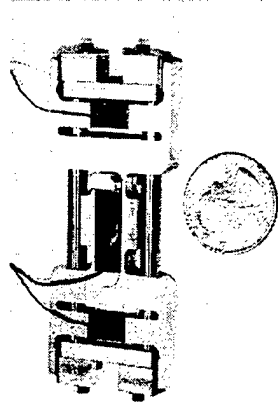
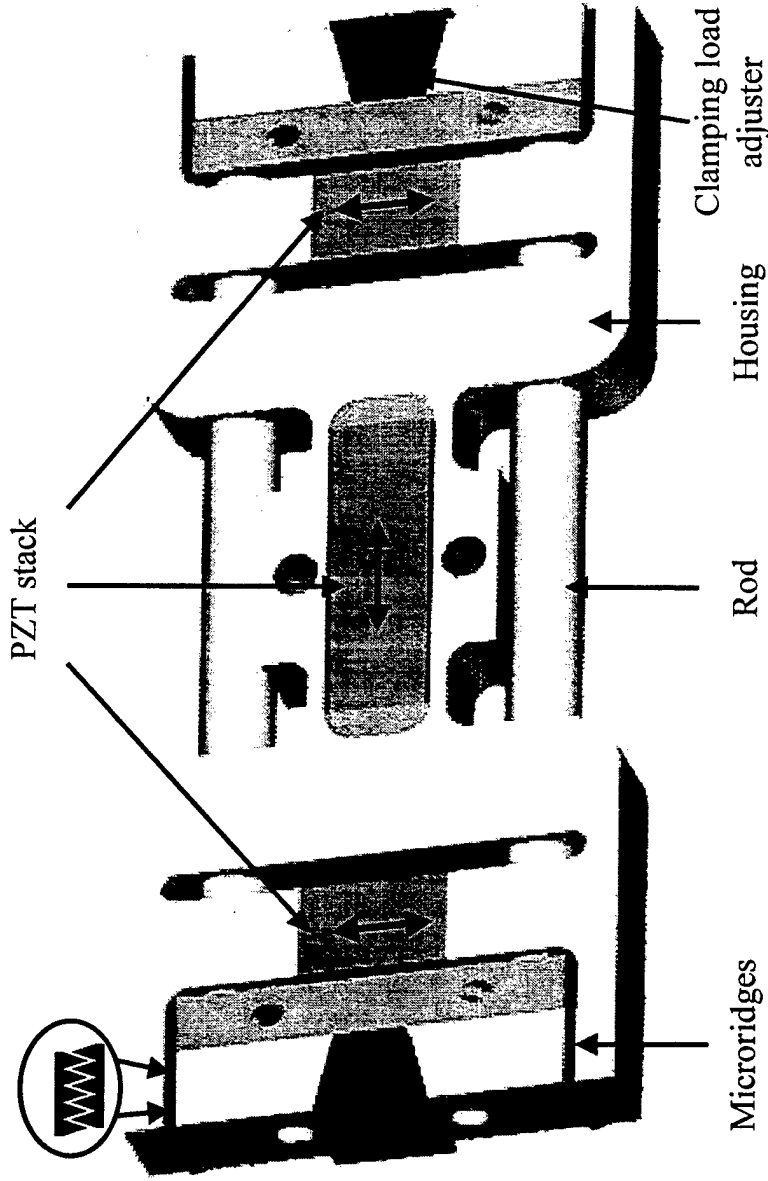
bimorph



rainbow



Compact Device (5th generation)

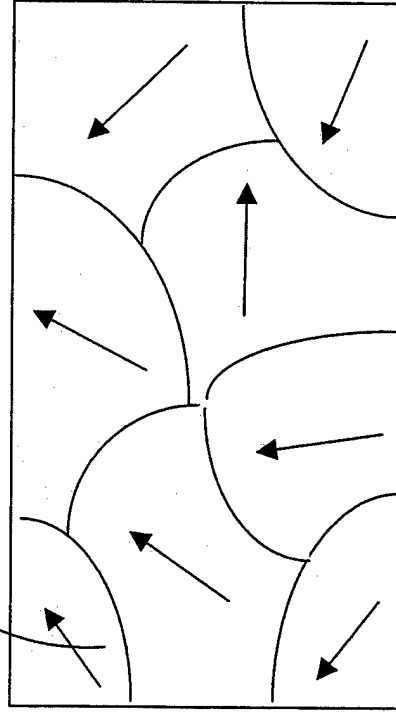


System designed to be compact and produce 500 N
at speeds up to 10mm/s



Piezoceramic Modeling

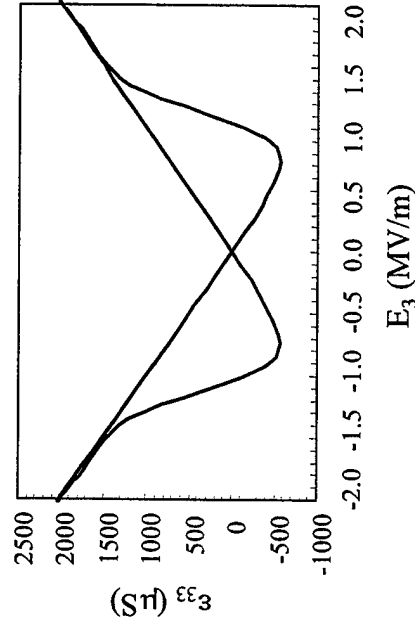
$$\begin{bmatrix} K_{11} & K_{12} \\ K_{21} & K_{22} \end{bmatrix} \begin{Bmatrix} \underline{u} \\ \underline{\phi} \end{Bmatrix} = \begin{Bmatrix} F_1 \\ F_2 \end{Bmatrix}$$



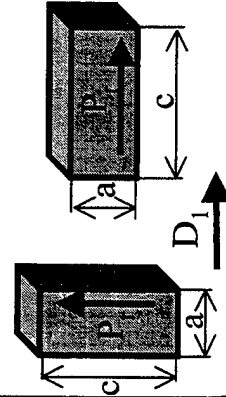
The local matrices are rotated to global coordinates

$$\begin{cases} \mathbf{c}' = \mathbf{L} \mathbf{c} \mathbf{L}^{-1} \\ \mathbf{g}' = \mathbf{L} \mathbf{g} \mathbf{R}^{-1} \\ \mathbf{e}' = \mathbf{R} \mathbf{e} \mathbf{R}^T \end{cases}$$

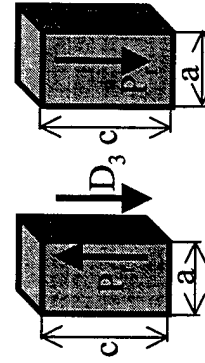
Butterfly Loop



if ($D_1 \geq D_{cr}^{90}$)

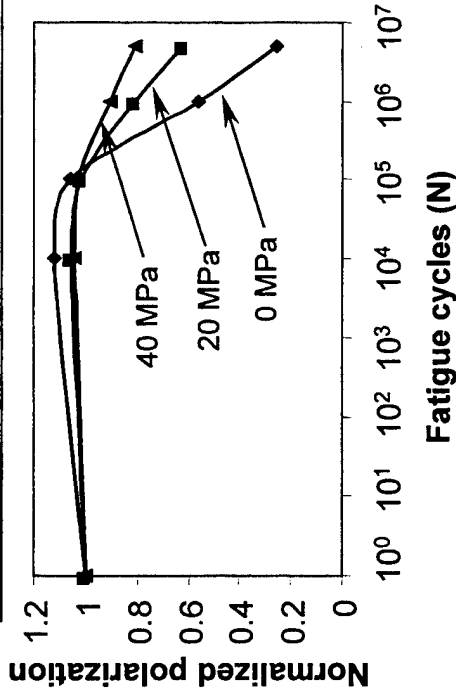


if ($D_3 \geq D_{cr}^{180}$)



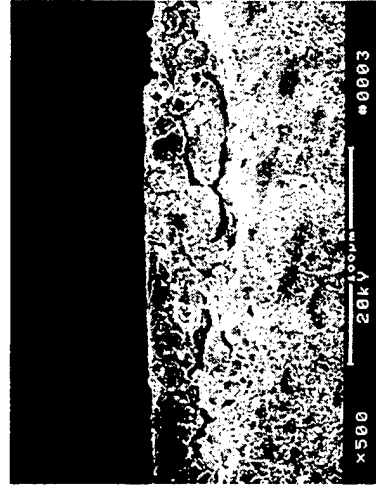
Fatigue Degradation Under Load

Material Fatigue of PZT-5H Under Load



- Mechanical preload decreases fatigue degradation
- SEM pictures reveal that preload eliminates crack from forming
- Switching is believed to initiate at electrodes and grow into the material
- Cracks arise subsurface due to critical stress state reached at a specified depth, shear lag theory

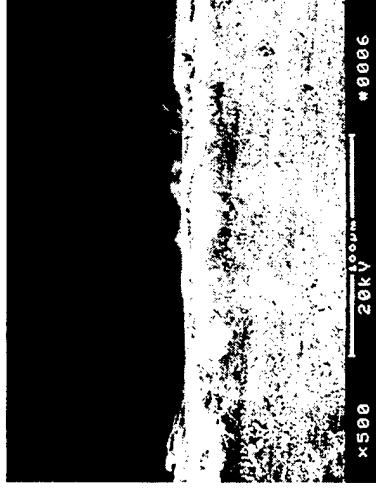
SEM of PZT specimens after 5 million cycles



Preload: 0 MPa



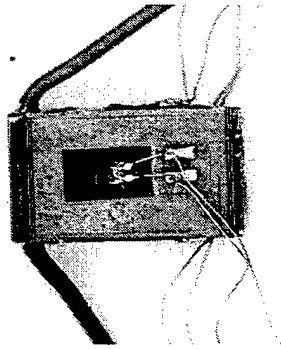
Preload: 20 MPa



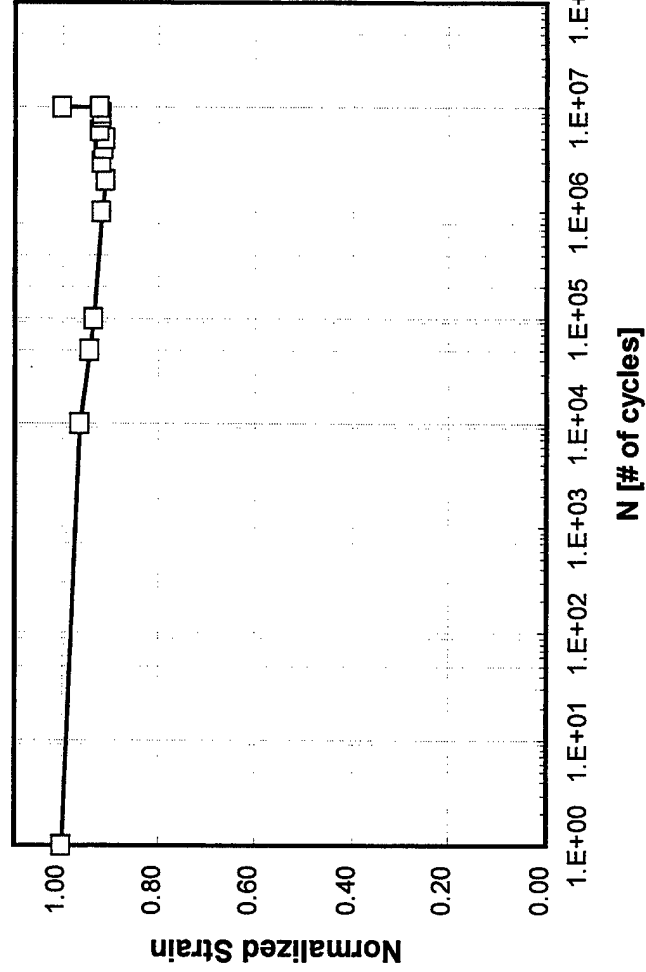
Preload: 40 MPa

Active Materials Lab

Stack Fatigue



- Mechanical preload increases strain output
- Fatigue without mechanical load displays no degradation after 10^7 cycles
- Fatigue under mechanical load currently being conducted

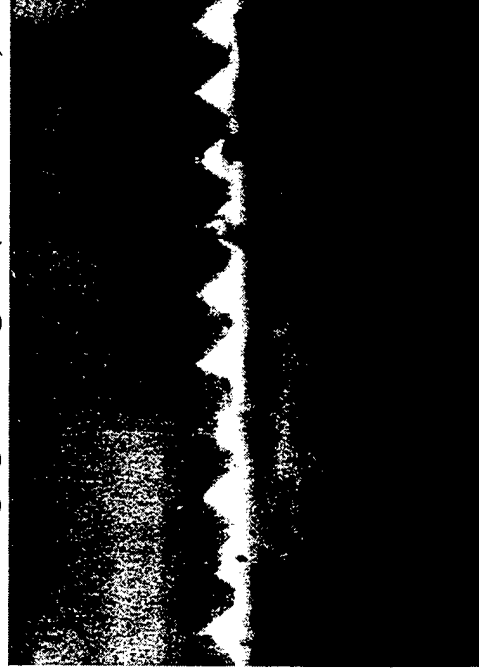
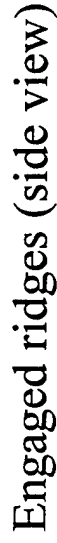


N	Strain [ms]	Strain	Temp
1	1380	1.00	25
10000	1332	0.97	50
50000	1304	0.94	57
100000	1289	0.93	60
1000000	1270	0.92	
2000000	1256	0.91	61
3000000	1270	0.92	
4000000	1261	0.91	61
5000000	1256	0.91	
6000000	1277	0.93	60
8000000	1267	0.92	
9000000	1267	0.92	
10000000	1277	0.93	60
100000000	1380	1.00	25



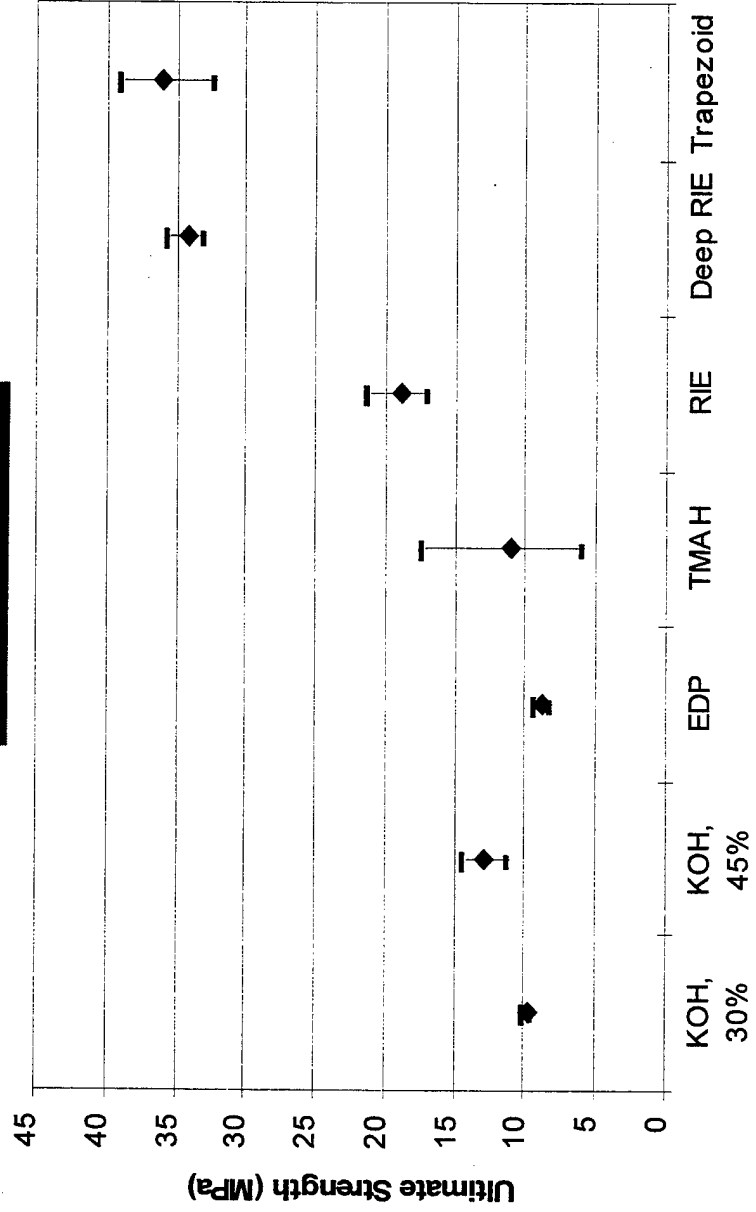
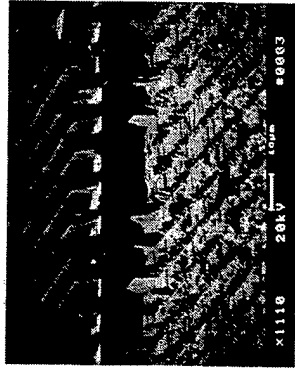
Active Materials Lab

Trapezoid shape ridges (top view)



1. Alumina - 1000 A/min etch rate Davydov et al.
2. Yttria stabilized zirconia
3. Steel - EDM

Macro-Force Transfer Across Micro-ridge



Summary Technical Highlights

- Vibration loads due to forward flight reduced 90% and those due to BVI reduced 80%
- Electro-thermo-mechanical testing and modeling of piezoelectric materials underway
- Fatigue life of piezoceramics long if designed and operated appropriately
- Microcomponents support macroscopic loads and operated at frequencies approaching 1kHz
- Compact hybrid actuator device designed and fabricated to produce larger power output than stack

10/1/00



*University of Maryland
Alfred Gessow
Rotorcraft Center*



A Direct Field Approximation to Infer Damage in Tapered Rotorcraft Flexbeams

Ashish S. Purekar

Graduate Research Assist.

Darryll J. Pines

Assistant Professor

**Army Research Office
4th Workshop on Smart Structures
The Pennsylvania State University
University Park, Pa
August 16-18 1999**



Outline



- **Objective**
- **Motivation**
- **Reverberated (RTF) and Dereverberated (DTF)
Transfer Function Responses**
- **Phase Effects from Damage**
- **Experimental Results and Analysis**
- **Conclusions and Future Work**



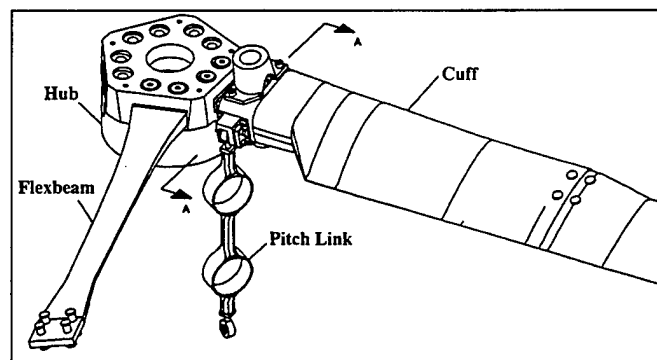
Objective



- Extract DTF response from RTF information.
- Identify presence, location, and extent of damage in flexbeams.
- Develop a qualitative and quantitative damage detection methodology using the direct field response.



Motivation



Comanche Rotor Blade Housing
(Adapted from Panda and Mychalowycz.
Journal of the American Helicopter Society. 1997)



Contributions of this Work



- Use a RTF to obtain an approximation to the DTF.
- Compare analytical and experimental results for undamaged and damaged non-uniform beams.



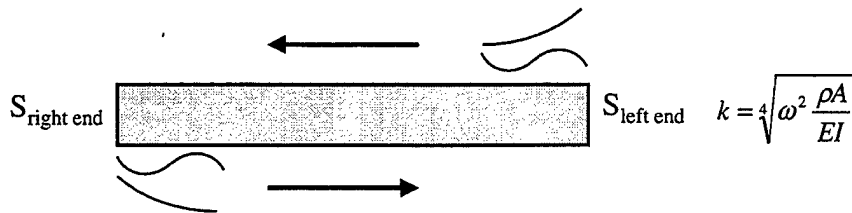
Structural Waves in Beams



Uniform beam dynamics are described by leftward and rightward, propagating and evanescent waves.

$$EI \frac{\partial^4 w(x,t)}{\partial x^4} + \rho A \frac{\partial^2 w(x,t)}{\partial t^2} = 0 \quad \rightarrow \quad EI \frac{\partial^4 w(x,\omega)}{\partial x^4} - \rho A \omega^2 \frac{\partial^2 w(x,\omega)}{\partial t^2} = 0$$

$$w(x,\omega) = w_{rp} e^{-ikx} + w_{re} e^{-kx} + w_{lp} e^{-ik(L-x)} + w_{le} e^{-k(L-x)}$$

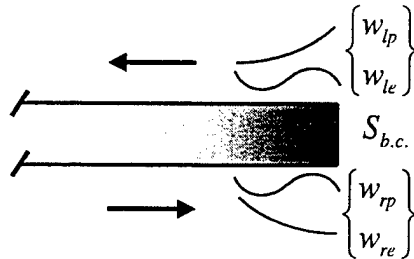




Directional Components are Coupled



$$\begin{Bmatrix} w_{lp} \\ w_{le} \end{Bmatrix} = S_{b.c.} \begin{Bmatrix} w_{rp} \\ w_{re} \end{Bmatrix}$$



$$S_{fixed} = \begin{bmatrix} -i & -1-i \\ -1+i & i \end{bmatrix}$$

$$S_{free} = \begin{bmatrix} -i & 1+i \\ 1-i & i \end{bmatrix}$$

$$S_{pinned} = \begin{bmatrix} -1 & 0 \\ 0 & -1 \end{bmatrix}$$

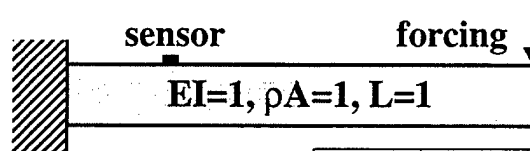
$$S_{no\ reflection.s} = \begin{bmatrix} 0 & 0 \\ 0 & 0 \end{bmatrix}$$



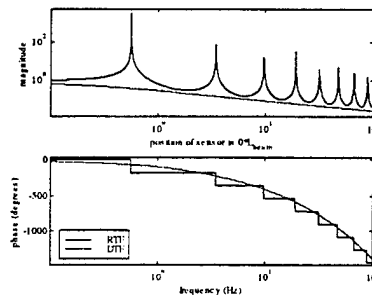
Reverberated vs. Dereverberated TF



DTFs remove the reflections from boundary conditions

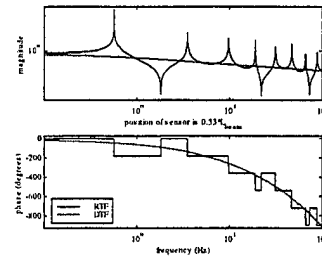
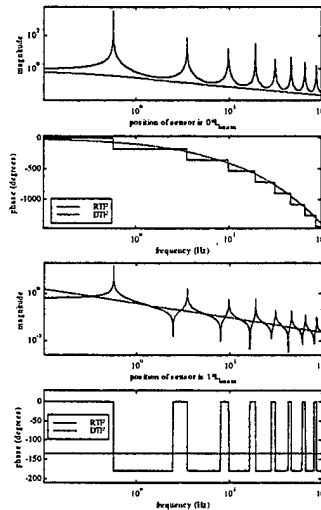


Phase of the DTF
response follows the
phase of the RTF





Zeros Shape the Phase of the Transfer Functions.



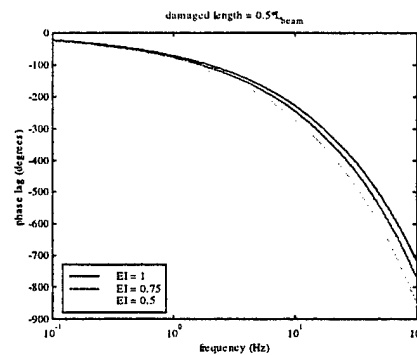
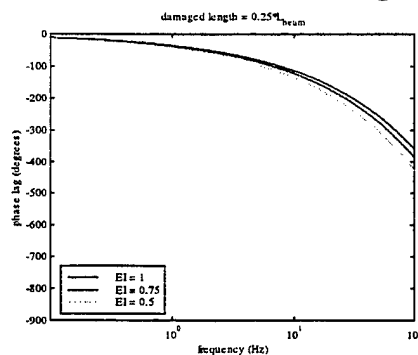
More zeros appear as sensor moves closer to excitation. This shifts the phase up.



Damage Effects on Phase



Length and amount of damage affects the phase of a wave travelling from one end to the other.



Structural waves travel slower in regions of damage.



Tapered Beams



Can be described by solutions analogous to uniform beam wavetypes.

$$\frac{\partial^2}{\partial x^2} \left(EI(x) \frac{\partial^2 w}{\partial x^2} \right) + \rho A(x) \frac{\partial^2 w}{\partial t^2} = 0$$

$$\bar{t} = \frac{t_1 - t_0}{t_0} \quad \bar{b} = \frac{b_1 - b_0}{b_0}$$

For linear taper, exact solution is a set of power series.

$$w = \sum_{n=0}^{\infty} a_n x^n$$

Can choose a_n
corresponding to the
expansion of e^c

w_1



$$e^{ikx}$$

w_2



$$e^{-ikx}$$

w_3



$$e^{kx}$$

w_4



$$e^{-kx}$$

For no thickness or width taper



Finding DTF of non-uniform beams



• Problems

- Cannot construct closed form spatial transition matrices for non-uniform beams.
- Use of spectral elements.
- Incorporation of scattering matrices in spectral elements difficult.

• Possibilities

- Can use controllers to remove reflected components to obtain the direct field response.
- Approximations to the DTF.

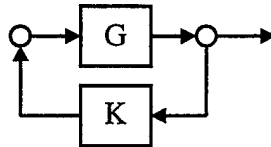


Approximations to DTF

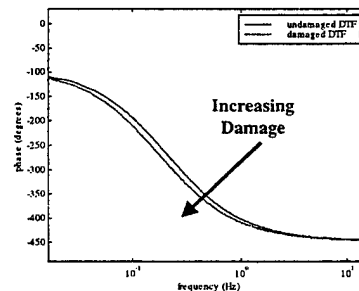
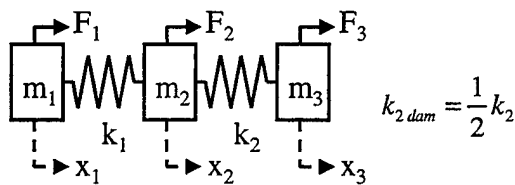
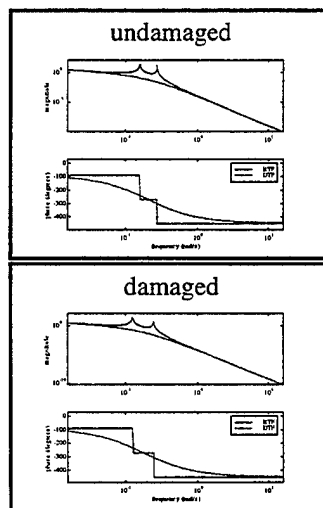


- Approximations involve finding the “average” of the response:
 - mean value method (Skudrzyk 1980)
 - cepstrum of impulse response
 - critically damp poles and zeros (Betros 1993)

→ This is the method chosen.



Mass/Spring Model with and without Damage





Continuous and Discrete Systems



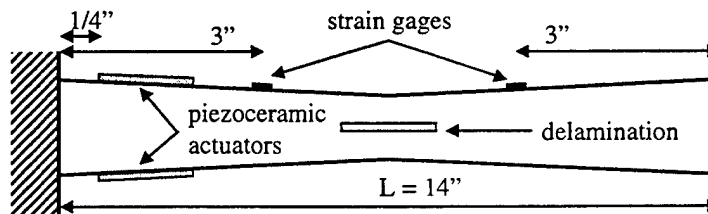
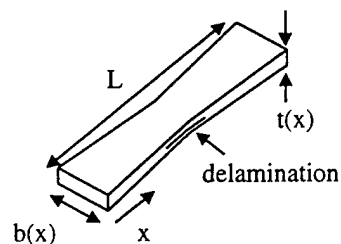
- **Discrete systems**
 - have finite number of modes
 - phase response levels off after last mode
- **Continuous Systems**
 - have infinite number of modes
 - phase response is constantly changing
- **By critically damping the response, treating the system as a discrete system.**
 - no information known about modes beyond the frequency range



Experimental Setup



Properties of Experimental Aluminum Beams					
$E = 70 \text{ GPa}$, $\rho = 2800 \text{ kg/m}^3$					
Case	Length (in.)	Max Width (in.)	Min Width (in.)	Max Thick. (in.)	Min Thick. (in.)
Width Taper	14	1.5	1	1/8	1/8
Thick. Taper	14	1	1	1/8	1/16
Thick./ Width Taper	14	1.5	1	18	1/16



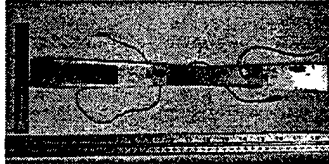


Experimental Beams

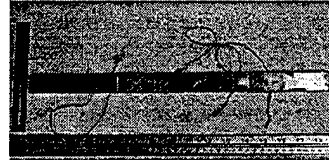


UNIVERSITY OF MARYLAND

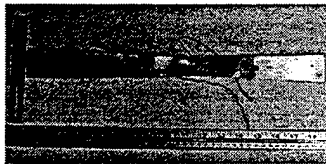
Width tapered



Thickness tapered



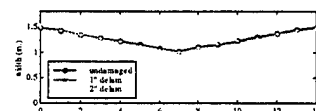
Thickness/Width tapered



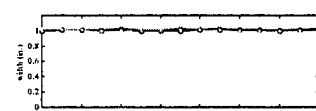
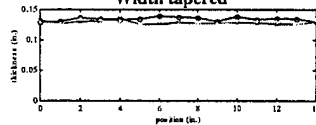
Actual beam dimensions



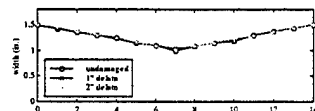
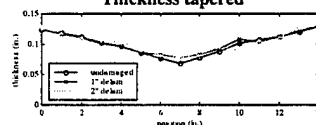
UNIVERSITY OF MARYLAND



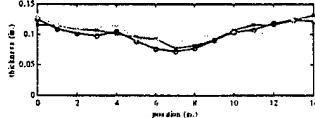
Width tapered



Thickness tapered



Thickness/Width tapered

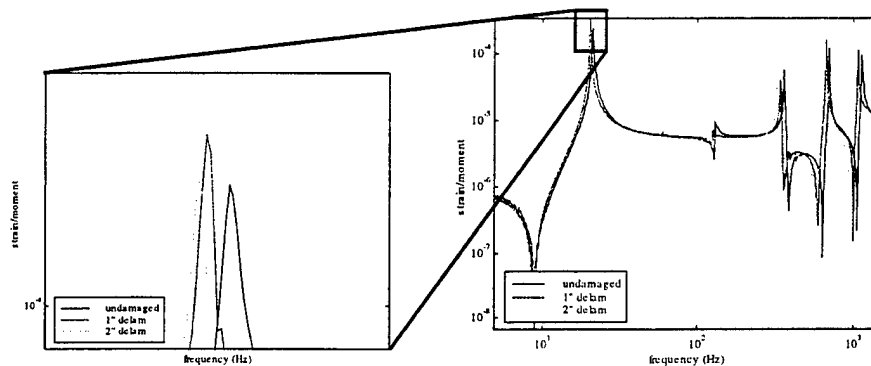




Experimental Results - Width Tapered Beams



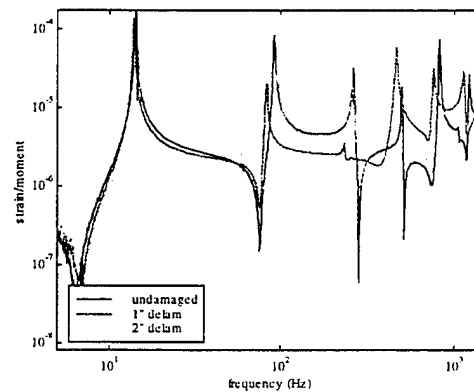
Natural frequencies decrease as the length of delamination increases.



Experimental Results - Thickness Tapered Beams

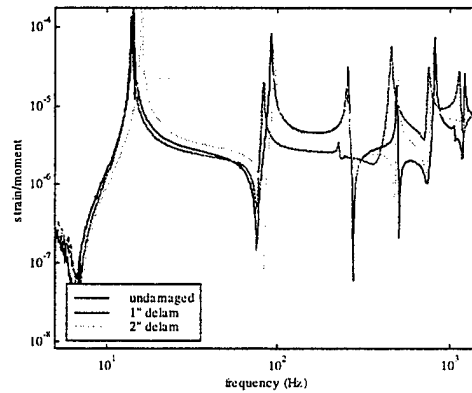


Modes do not shift leftward with increasing damage.





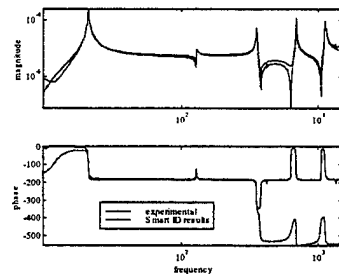
Experimental Results - Thickness/Width Tapered



System Identification



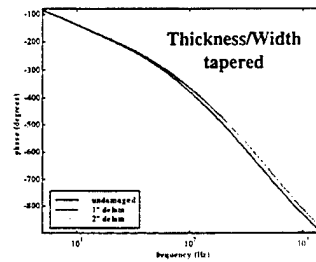
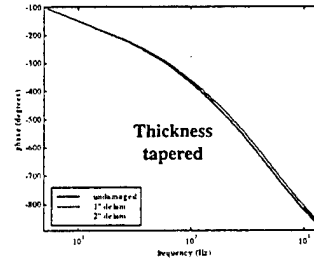
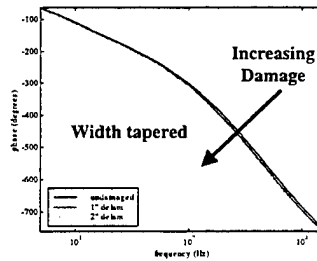
- In order to critically damp the system, need a model of the dynamics.
- Used the SmartID software to obtain a pole/zero representation of the system.



**Matches magnitude and
phase well.**



Phase of tip/root response



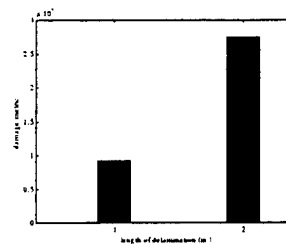
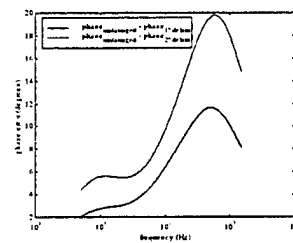
Damage Metric



Look at differences
between undamaged and
damaged phase.

Damage metric:

$$m = \int_{\omega_1}^{\omega_2} |\phi_{und} - \phi_{dam}|^2 d\omega$$





Conclusions and Results



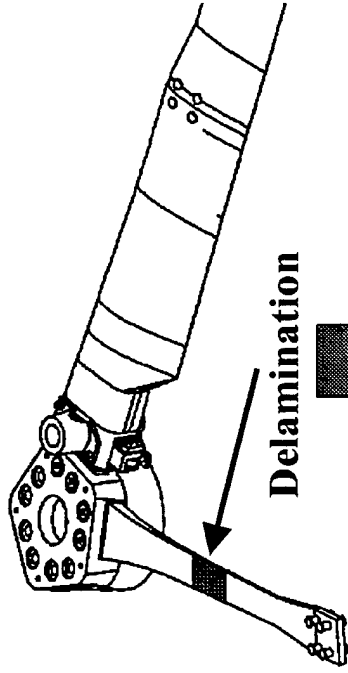
- **Approximate DTF is promising for use in damage detection.**
- **Change in phase of DTF leads to qualitative measure of damage.**
- **Manufacturing defects affect results significantly.**
 - **In real applications, the flexbeam dimensions will remain unchanged.**
 - **Progressive delamination damage should lead to increasing phase and magnitude errors in the DTF response.**



Summary

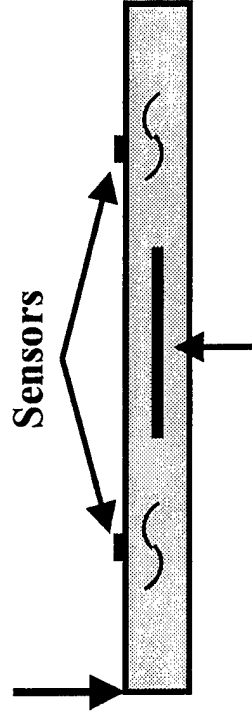
UNIVERSITY OF MARYLAND

Presence and Identification of Damage



Look at Only at Direct
Field Components

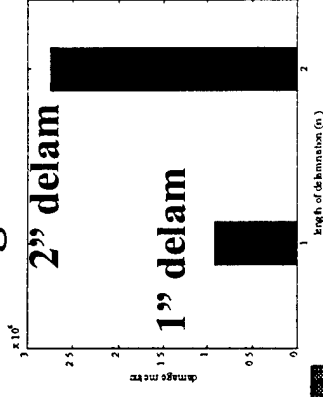
Actuation



Delamination

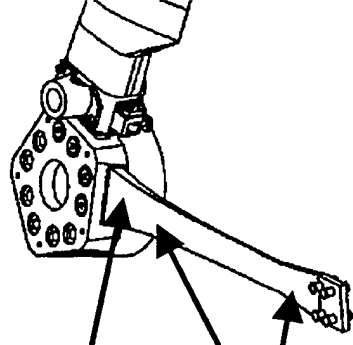
Phase Lag of Direct Field Affected by Damage

Metric gives
qualitative measure of
amount of damage.



Possibility of an Online
Damage Detection Scheme

Actuation
Ability to detect damage
between sensors.



ACTIVE VIBRATION CONTROL USING SMART ROTOR TIPS

Alfred Gessow Rotorcraft Center, University of Maryland
Andreas P.F. Bernhard¹ Inderjit Chopra²

RESEARCH OBJECTIVE

The objective is to develop and test a Mach scale rotor model with active blade tips, activated via a piezo-induced bending-torsion coupled beam. The primary research motivation is helicopter vibration reduction.

CONCEPT

The Smart Active Blade Tips (SABT) are used as an on-blade vibration reduction mechanism. In actively pitching the tips, new unsteady airloads are generated. Correctly phased these can cancel, or at least reduce, the original unsteady blade loads.

RESULTS AND ACCOMPLISHMENTS

- **Analytic Model:** a coupled rotorblade and actuator beam finite element model has been developed to predict the performance of the active blade tip. In particular, the focus at present is on the open-loop dynamic pitch deflection of the SABT and the associated changes in the rotor hub loads. The model incorporates a bearingless hub with elastic rotor blade, integrated actuator beam and active blade tip. The analysis is based on linear elasticity and linear two-dimensional unsteady aerodynamics in conjunction with a linear inflow model.
- **Validation Study:** this is based on the reduced tip speed hover tests (tip Mach = 0.25) conducted in 1997. The analytic results capture the trends of the tip pitch deflection and resultant blade vertical root shear.
- **Mach Scale Design:** the Mach scale rotor blades are designed to be tested on a bearingless 0.15 scale Bell 412 hub. The design is based on the prior Froude-scale design, although several design modifications have been implemented. First, the actuator beam graphite substructure has been thickened by 35% to 2.7mm to ensure that the natural frequency of the tip is located beyond the 5/rev activation frequency and to meet centrifugal strength criteria. Second the attachment points of the actuator beam have been redesigned to overcome boundary condition flexibility encountered in the Froude scale blades. Figure 5 shows a close up the tip assembly.
- **Mach Scale Performance:** the analysis indicates that the improved Mach scale design will achieve tip pitch deflections of 2-4 deg (half peak-to-peak) over the range of 2-5/rev excitation. The resultant dynamic vertical root shear control authority is in excess of 25% of the nominal blade lift. The Mach scale performance analysis was used to define strict excitation voltage and frequency limitations to prevent exceeding the flexbeam flap bending moment and vertical shear limits (see Figure 6)

STATUS

- **Work in Progress:** the Mach scale actuator beams and blades are presently being fabricated. The actuator beams have been tested under mechanical tip torque loads and low frequency excitation. Tip twist amplitudes of 1.8 deg were achieved at 125 Vrms and 15 Hz (non-rotating).
- **Future Work:** Mach scale hover test to demonstrate system integrity, open loop control authority and validate the analytic model (completion projected end August 99), overall concept assesment and review (September 99).
- **Follow Up Work:** integration of the active blade tip with an adaptive control algorithm into a comprehensive rotor code for detailed performance evaluation, open and closed loop aeroelastic stability investigation of the Mach scale blades, wind tunnel entry

RECENT PUBLICATIONS

- Bernhard, A.P. and Chopra, I., "Mach-scale design of a rotor model with active blade tips," in *Proceedings of the 55th American Helicopter Society Forum*, Montreal, Canada, May 1999
- Bernhard, A.P. and Chopra, I., "Hover testing of active rotor blade tips using a piezo-induced bending-torsion coupled beam," *Journal of Intelligent Material Systems and Structures*, accepted for publication May 1999
- Bernhard, A.P. and Chopra, I., "Trailing edge flap activated by a piezo-induced bending-torsion coupled beam," *Journal of the American Helicopter Society*, Vol.44, No. 1, January 1999, pp.3--15.
- Bernhard, A.P. and Chopra, I., "Hover testing of an active rotor blade tip and structural analysis of the actuator beam," in *Proceedings of the 39th AIAA/ASME/ASCE/AHS/ASC Structures, Structural Dynamics and Materials Conference and AIAA/ASME/AHS Adaptive Structures Forum*, Longbeach CA, April 1998.

¹ Gustave J. Hokenson Fellow, email: bernhard@eng.umd.edu

² Professor & Director



ALFRED GESSOW ROTOCRAFT CENTER

UNIVERSITY OF MARYLAND

MACH SCALE DESIGN OF A HELICOPTER ROTOR WITH ACTIVE BLADE TIPS

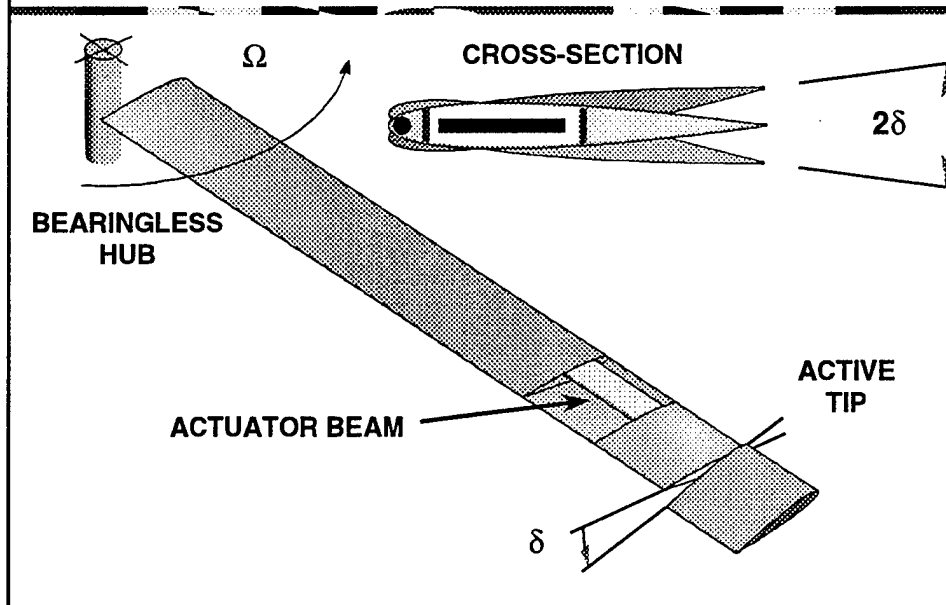
Andy Bernhard

Inderjit Chopra

4th ARO Workshop on Smart Structures

Penn State, August 1999

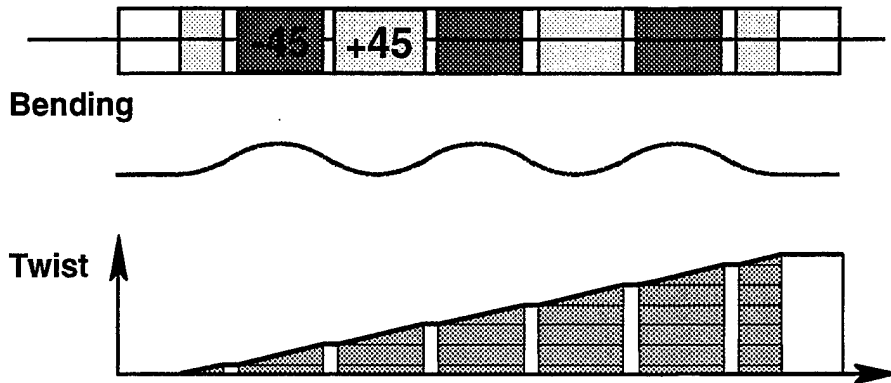
Concept Schematic



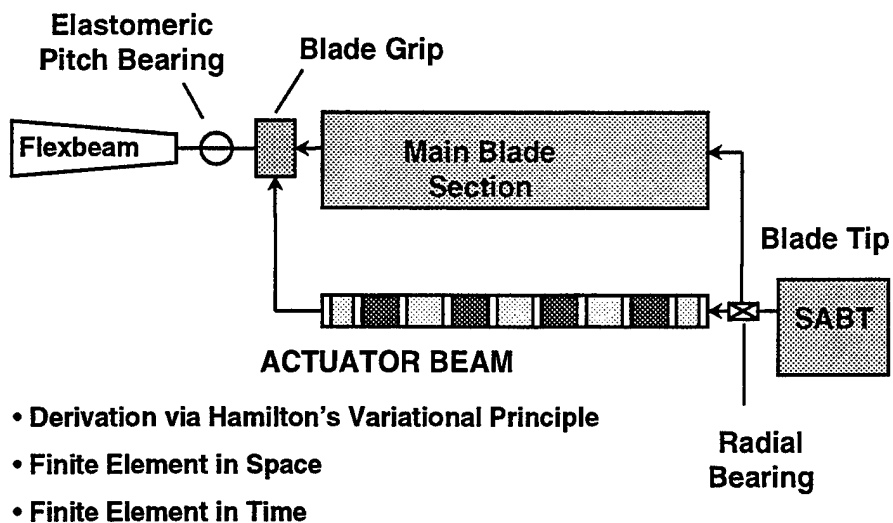
Actuator Beam

Graphite Epoxy Beam with surface bonded PIEZO-elements

- flip-flopping bending-torsion coupling
- flip-flopping bending actuation



Rotor Finite Element Model



Mach Scale Design

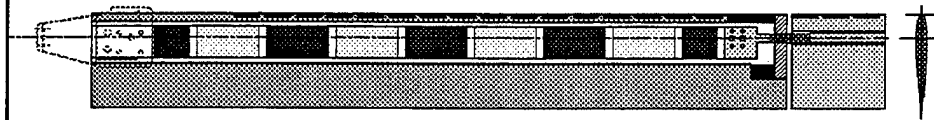
- **Based on the Froude-scale design**
 - Tip Mach = 0.25 design
 - successfully tested in 1997
 - Tip deflection of 2-2.5 deg
 - Oscillatory thrust amplitudes of 5-10% (per blade tip)
- **Redesign of Components**
 - Actuator beam (frequency placement, strength)
 - Tips
 - Actuator/Tip adapter
 - Shaft and bearing assembly
 - Actuator anchor in the blade root
- **Bell 412 bearingless hub design limits**
- **Instrumentation limits**

Tip Mach = 0.5
Speed = 2000 rpm
⇒ 3400 g

Mach Scale Test Facility: Upgrades

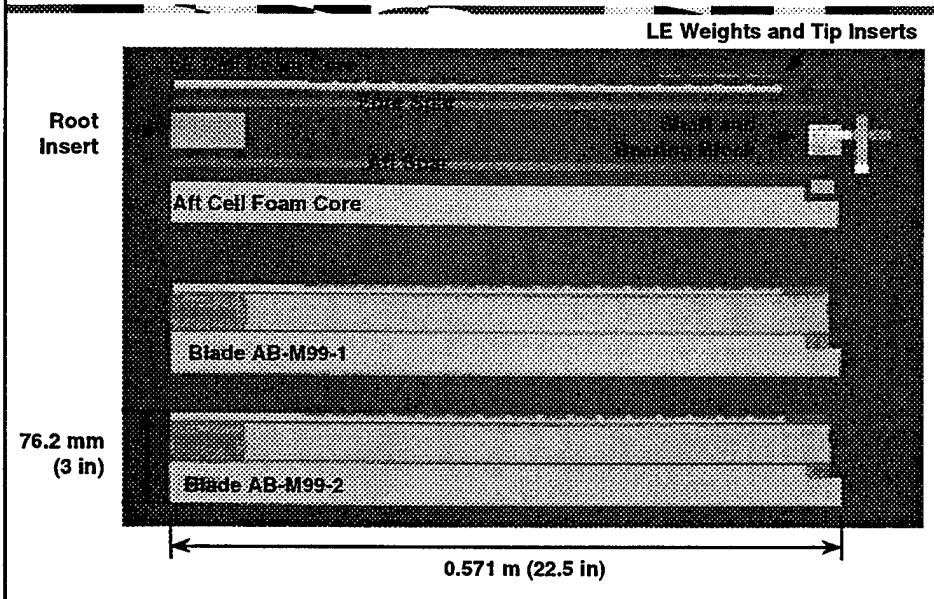
- **12 ft Hover stand with 6 component fixed frame balance**
- **Bell 412 Mach-Scale bearingless hub**
 - Nominal blades: 7ft, tip Mach 0.7
 - Fully instrumented flexbeam yokes
- **50 hp hydraulic motor**
- **Slipring upgrade:**
 - 8 dual-line power channels (250 Vrms, 0.5Amax)
 - 16 quad-line sensor channels
 - Negligible cross-talk has been demonstrated

Active Tip Blades



BLADE		ACTUATOR	BEAM	SABT TIP
Chord	76.2 mm	Length	550 mm	Span 10 %
Radius	762 mm	Active Units	8	δ 3 deg
Profile	NACA 0012	Thickness	2.7 mm	

Fabricated Main Blade Components



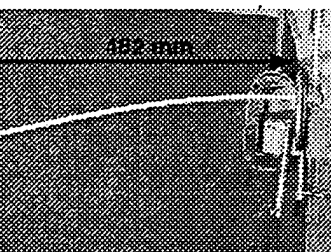
Blade Tip Detail

A 3D exploded view diagram of a blade tip assembly. The components are labeled as follows:

- Main Blade
- Aft Spar
- Actuator Beam Grip
- LE Insert
- Bearing Block
- LE Weights
- Spars
- Aft Insert
- Shaft
- SABL

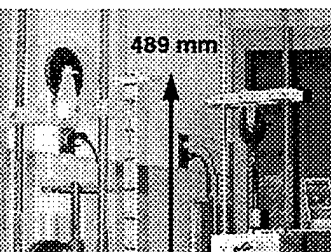
Blade and Actuator Characterization

Blade Bending Moment Test



A black and white photograph showing a long, thin blade being bent by a weight. A horizontal dimension line at the top indicates a length of 482 mm. A label in the lower left corner shows a weight of 24.5 N.

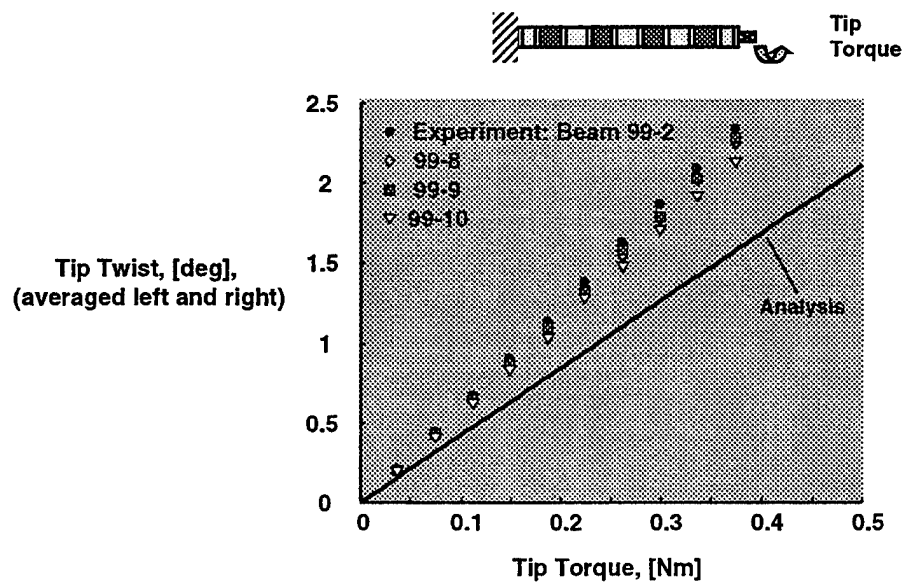
Actuator Beam Tests



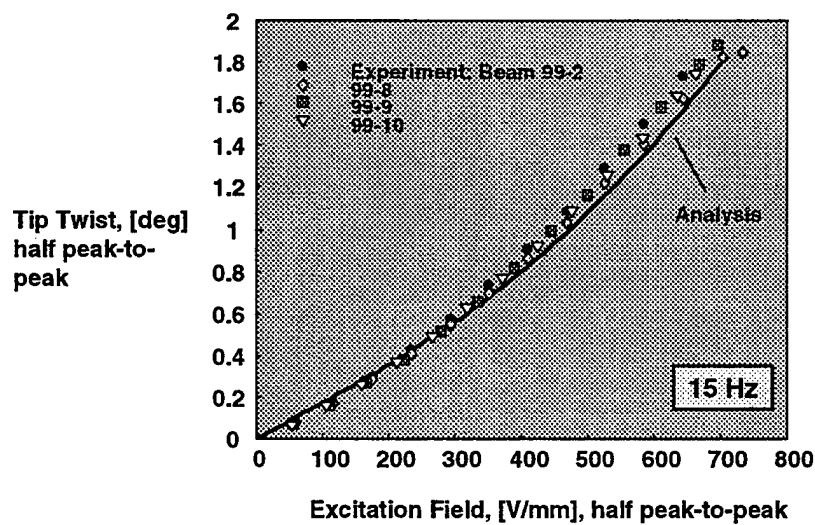
A black and white photograph of a mechanical test setup. A vertical arrow indicates an upward displacement of 489 mm. The setup includes various mechanical components and a weight.

- Static tip torque tests
- Low frequency actuation tests

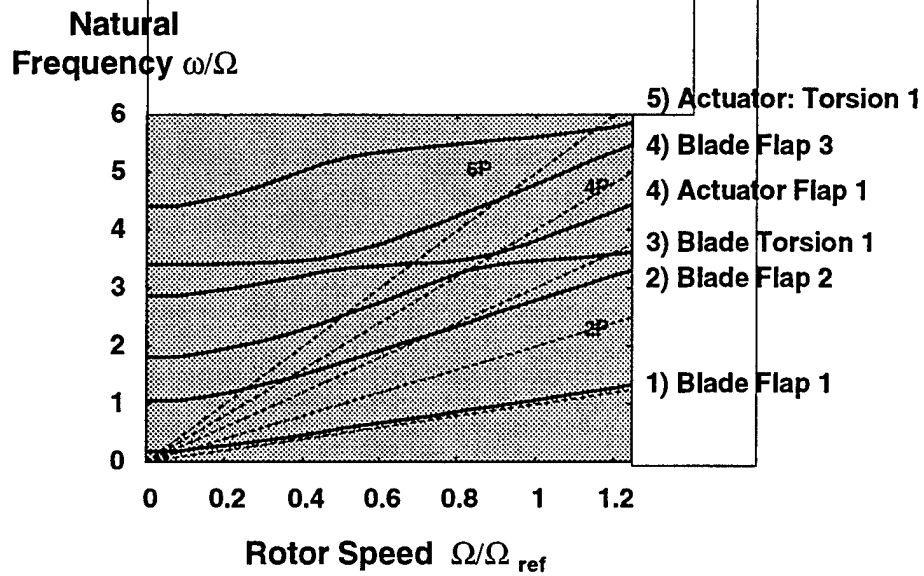
Static Tip Torque Tests



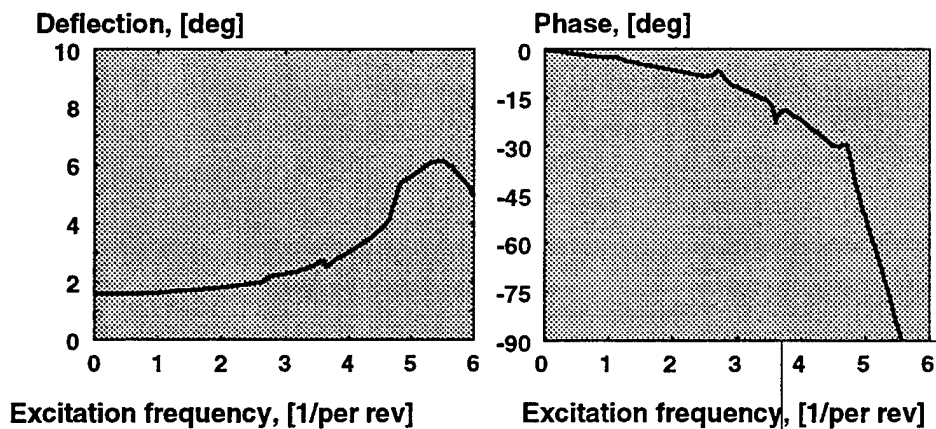
Actuator Beam Low Frequency Test



Rotor Fan Plot



SABT Pitch Deflection

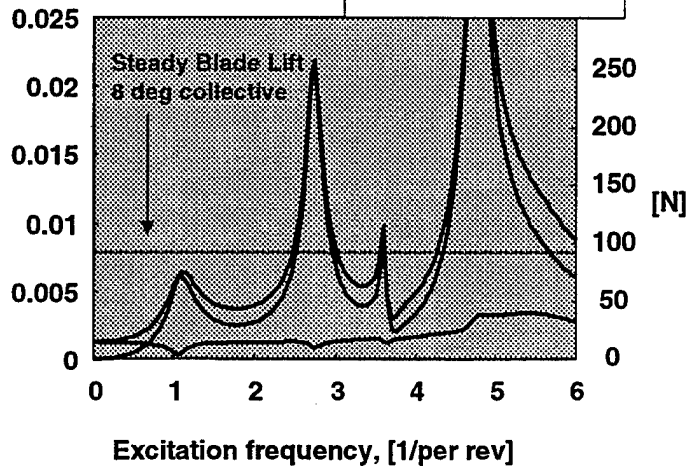


330 μ strain, 2000 rpm

Blade Vertical Root Shear

Magnitude: F_z
(non-dimensional)

330 μ strain, 2000 rpm



AERO

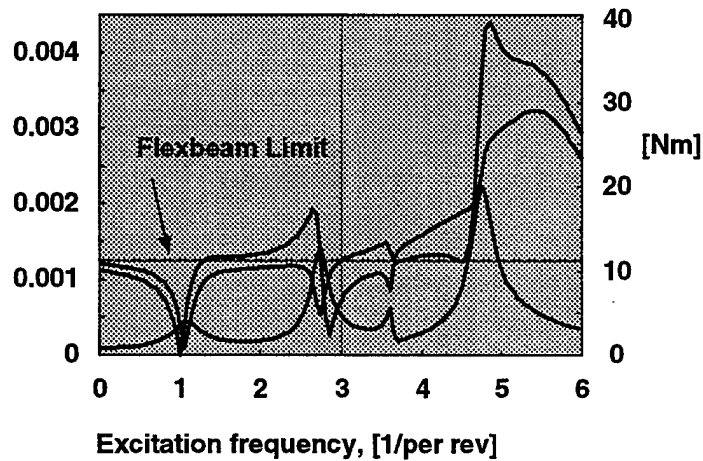
Inertial

Total

Blade Root Flap Moment

Magnitude: M_y
(non-dimensional)

330 μ strain, 2000 rpm



AERO

Inertial

Total

Summary and Conclusions

- Mach Scale design: 2000 rpm, Mach = 0.5
- Mach Scale design of rotor blade is complete
- 2-4 deg SABT pitch deflection is predicted at 3-5/rev
- Fabrication is in progress
- Actuator beam achieves 1.8 deg twist amplitude at 125 Vrms /15 Hz
- Mach Scale hover test planned for late Summer 99

Future Work: Summer 99

- Complete Actuator and Blade Fabrication: end July 99
- Open loop Mach scale hover test: end August 99
- Closed loop hover test: beginning September 99
- Active Blade Tip concept assessment: September 99

Follow Up Work

- Integration of Active Blade Tip model and control algorithm (higher harmonic or neural network) into a comprehensive rotor code
- Forward flight performance evaluation and stability analysis
- Wind tunnel entry (Glenn L. Martin wind tunnel)

ACTIVE ROTORCRAFT VIBRATION REDUCTION WITH REAL TIME NEURAL NETWORK CONTROLLER

Michael G. Spencer
Graduate Research Assistant

Robert M. Sanner
Assistant Professor

Inderjit Chopra
Professor

Alfred Gessow Rotorcraft Center
University of Maryland

My research has been to develop a new, robust individual blade control (IBC) methodology for vibration suppression using a trailing edge flap. The controller uses a neural network, learning in real time, to adaptively cancel the effects of periodic aerodynamic loads on the blades, greatly attenuating the resulting vibrations

Recent analysis of vibration control for rotor blades with trailing edge flaps has been based on a higher harmonic type algorithm. These methods use a linear sensitivity matrix that relates the higher harmonics of the flap input to the harmonics of the vibratory hub loads. Although tests have demonstrated the ability to reduce hub vibrations, the performance may be poor if significant nonlinearities exist or if the operating condition differs significantly from that at which the sensitivity matrix was determined.

The control method proposed employs a neural network to learn to actuate the trailing edge flap to adaptively suppress hub vibrations. In this application, no off-line training is performed. Instead, a neural network is used, in real time, to adaptively command the trailing edge flap deflections that reduce or eliminates hub vibrations. The neurocontrol algorithm is developed by formulating the problem into a discrete, time-periodic framework. The time period of interest is segmented into a set of points at which a neural network is to approximate the flap inputs that would cancel the vibratory forces. This ideal input is not known a priori, and thus must be estimated on-line by the neural network. By explicitly relating the neural network coefficients to the expected samples of the blade vibration, I've shown how a modified extended Kalman filtering algorithm may be used as the basis of a new adaptation algorithm for the ideal network weights. This new discrete time approach appears to have overcome the difficulties of the previous continuous time algorithm, reliably enabling the neural network to learn in real time the necessary trailing edge flap command profile to counter the vibrations arising from an arbitrary periodic disturbance.

Numerical simulations of this discrete time controller have been conducted using UMARC (University of Maryland Advanced Rotor Code) with a model of the Boeing MD-900 rotor in forward flight ($\mu = 0.3$) with a trailing edge flap. The neurocontroller has been developed to simultaneously control any desired combination of hub shears and moments through the appropriate weighting of the respective loads in the combined cost function. This cost function is composed of the weighted sum of the squared vibratory loads as well as the squared flap angles and rates over a single rev. The neurocontroller learns the required set of trailing edge flap inputs necessary to minimize the cost function. The results from the neurocontroller have been compared to a similarly weighted higher harmonic control approach to show that the neurocontroller can provide a greater total vibration reduction.



ALFRED GESSOW ROTORCRAFT CENTER

Active Rotorcraft Vibration Reduction with Real Time Neural Network Controller

Michael G. Spencer
Graduate Research Assistant

Robert M. Sanner
Assistant Professor

Inderjit Chopra
Alfred Gessow Professor and Director

ARO Review, 17 August 1999
Pennsylvania State University



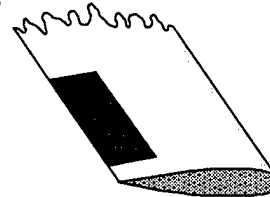
Objective

- Develop and validate by experiment a real time feedback control system that adaptively activates smart material actuators for vibration reduction
- Make the controller robust to uncertainties in blade parameters or the structure of the external disturbances
- Other possible applications
 - Noise suppression
 - Blade load reduction



Active Vibration Control of Rotor

- Smart Structure technologies used to individually control rotor blades
- Analysis (Milgram, 1997) and scale rotor tests (Korotkar & Chopra, 1997) have shown trailing edge flap devices can effectively alter blade aerodynamics
- Excitation of flap generates new aerodynamic forces which can be used to reduce blade loads and resultant vibrations
- Typical control approach has been Higher Harmonic Control



Trailing edge flaps with piezoactuators



Higher Harmonic Control

- HHC uses a “linearized”, frequency domain approach to control hub vibrations

$$\mathbf{Z} = \mathbf{Z}_o + \mathbf{T}\boldsymbol{\theta} + \mathbf{v}$$

- \mathbf{Z} consists of sine & cosine components of N/rev force and moments in the fixed hub frame
- \mathbf{Z}_o is uncontrolled harmonic response of system
- Input vector $\boldsymbol{\theta}$ consists of sine & cosine components of the higher harmonic trailing edge flap deflections

$$\delta(t) = \sum_{k=2}^{N_z} \{ \theta_{k,c} \cos(k\psi) + \theta_{k,s} \sin(k\psi) \}$$

- Transfer matrix \mathbf{T} depends on flight condition (μ , C_T)
- Measurement noise \mathbf{v} is assumed random



HHC Optimal Control

- The optimal control input at a given flight condition is based on the minimization of the performance index

$$J = Z^T W_z Z + \theta^T W_\theta \theta$$

- If T and Z_o are known perfectly, then the optimal input is

$$\theta_{opt} = -[T^T W_z T + W_\theta]^{-1} (T^T W_z Z_o)$$

- But uncertainties due to noise and nonlinearities can lead to errors in the elements of T and Z_o
- Adaptive methods are often used in practice



Time Domain Neural Network Control

- Using a neural network to provide a time domain trailing edge flap input
- A single hidden layer neural network

$$\delta(t) = \sum_{k=0}^{N_{NN}-1} \gamma_k g_k(\tau(t))$$

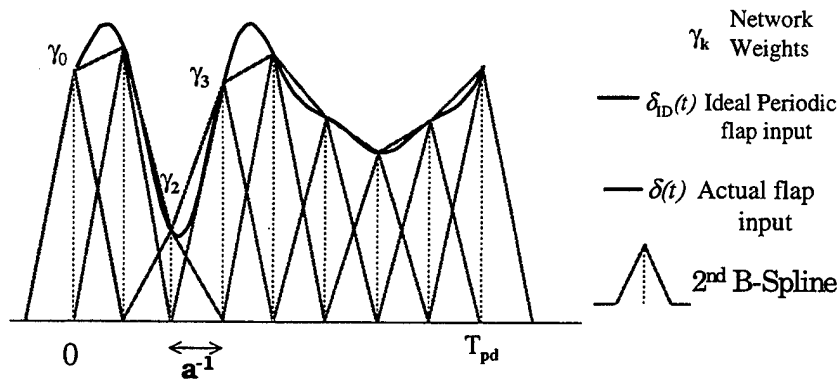
$$\tau(t) = t \bmod T$$

g_k is the computational element

γ_k is the corresponding output weight



Neural Network Example



- Network used as a curve fitting tool
- Example of a 2nd order B-spline “tent” function as the computing element, g



Neural Network Control

- Neural Network Controller assumes a linearized time domain global model of the form

$$y = y_o + H\gamma + v$$
- First consider a single hub load
- y is evenly spaced samples of the rate of change of the hub load
- y_o is the samples of the uncontrolled hub load rate of change
- γ is vector of γ_k coefficients of neural network
- Columns of H represent the components of the neural response due to each basis function g_k
- v assumed random noise



Optimal Neural Input

- The optimal control input at a given flight condition is based on the minimization of the performance index

$$J = y^T W_y y + \gamma^T W_\gamma \gamma$$

$W_y = c[I]$ and c is a constant weighting factor

$W_\gamma = ([I] + D^T D)$ where D determines the finite difference

- If H and y_o are known perfectly, then the optimal input is

$$\gamma_{opt} = -[H^T W_y H + W_\gamma]^{-1} H^T W_y y_o$$

- Assume no knowledge of blade properties so the response transformation H and y_o are unknown a priori
- Adaptive method needed for real-time use, (Kalman Filter)



Circulant Matrix

- Choose a radial basis network with evenly spaced nodes
 - $g_k(t) = \phi(a(t-k))$ $a = NT$ ϕ is a 2nd Order B-Spline
- For the hover condition, the columns of H are shifted versions of the first column
- Then $H \Rightarrow C(h)$ where $C(h)$ is a circulant matrix of the column vectors, h

$$H \equiv C(h) = \begin{bmatrix} h_0 & h_{N-1} & \cdots & h_1 \\ h_1 & h_0 & & h_2 \\ \vdots & & \ddots & \vdots \\ h_{N-1} & h_{N-2} & \cdots & h_0 \end{bmatrix}$$

- The total response of the blade to the neural input is a weighted sum of the individual neural responses: $y_{NN} = H\gamma$ where γ are the weights
- Kalman Filter states are reduced to single vector of \hat{h} and \hat{y}_o



Multiple Hub Loads

- For simultaneous control of multiple hub loads, the network states represent a set of parameters for a single blade in the rotating frame
 - radial, chord and vertical directions
- Hub loads are determined by forming the identity, sine and cosine shift matrices that depend on the number of blades, $[Shi]$, $[Shc]$ & $[Shs]$
- Hub Loads: (Shears and moments have same form)

$$\begin{aligned} F_x &= [Shc]\{y_{or} + H_r\gamma\} + [Shs]\{y_{oc} + H_c\gamma\} \\ F_y &= [Shs]\{y_{or} + H_r\gamma\} - [Shc]\{y_{oc} + H_c\gamma\} \\ F_z &= [Shi]\{y_{ov} + H_v\gamma\} \end{aligned}$$



Multiple Load Cost Function

- The neural cost function for minimizing 3 hub shears and 2 hub moments

$$J = \{y_x^T W_x y_x + y_y^T W_y y_y + y_z^T W_z y_z + y_{Mx}^T W_{Mx} y_{Mx} + y_{My}^T W_{My} y_{My} + \gamma^T W_\gamma \gamma\}$$

- W are weighting matrices for each hub load
- Weights are used for relative importance in minimization
 - y_x is rate of change of longitudinal hub shear
 - y_y is rate of change of lateral hub shear
 - y_z is rate of change of vertical hub shear
 - y_{Mx} is rate of change of hub roll moment
 - y_{My} is rate of change of hub pitch moment

- Optimal network weights, γ_{opt} determined from $\frac{\partial J}{\partial \gamma} = 0$

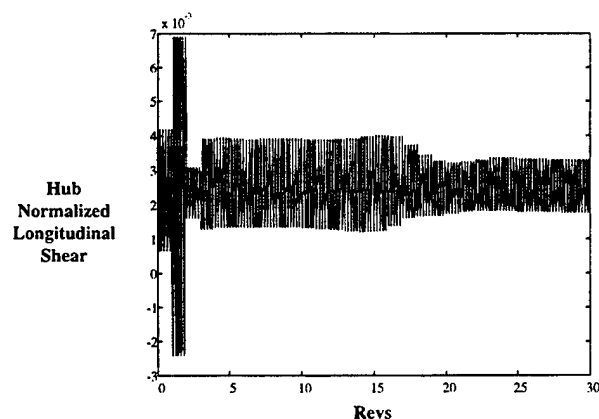


Simulation Results Multi-load Neural Network

- UMARC simulation of 5-bladed MD 900 rotor with trailing edge flap of length 18" centered at 0.75 R
- Forward Flight condition $\mu = 0.3$
- Equal weights for 5 hub loads ($W's = [I]$)
- Normalized loads by max uncontrolled y_z
- Normalized W_y by max flap angle
- 50 neurons per rev



Multi-Load Control UMARC Simulation of Hub F_x Vibration Suppression

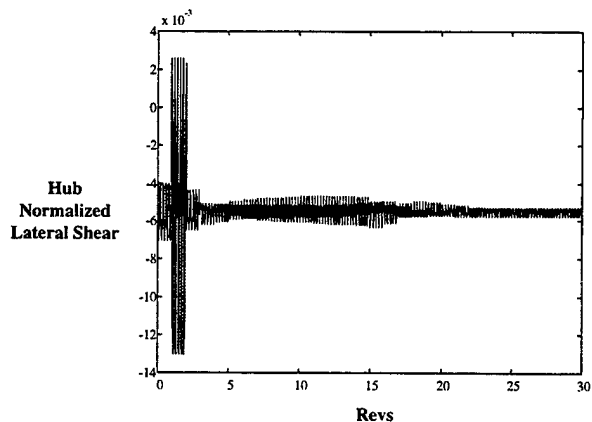


- Five bladed rotor in forward flight $\mu = 0.3$
- Network minimizes hub shear vibration
- Learns network coefficients on-line



Multi-Load Control

UMARC Simulation of Hub F_y Vibration Suppression

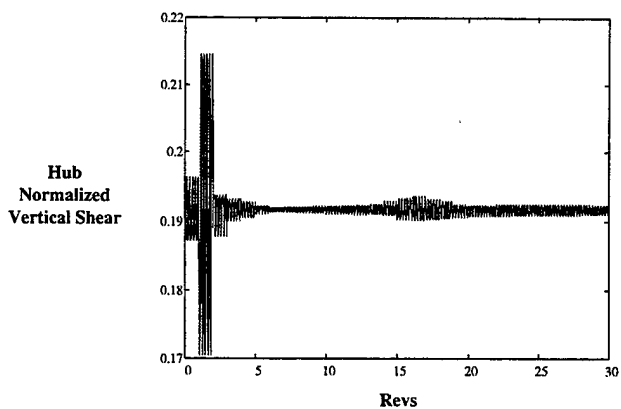


- Five bladed rotor in forward flight $\mu = 0.3$
- Network minimizes hub shear vibration
- Learns network coefficients on-line



Multi-Load Control

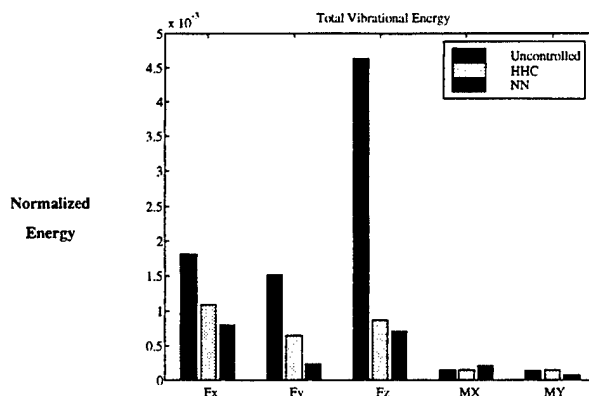
UMARC Simulation of Hub F_z Vibration Suppression



- Five bladed rotor in forward flight $\mu = 0.3$
- Network minimizes hub shear vibration
- Learns network coefficients on-line



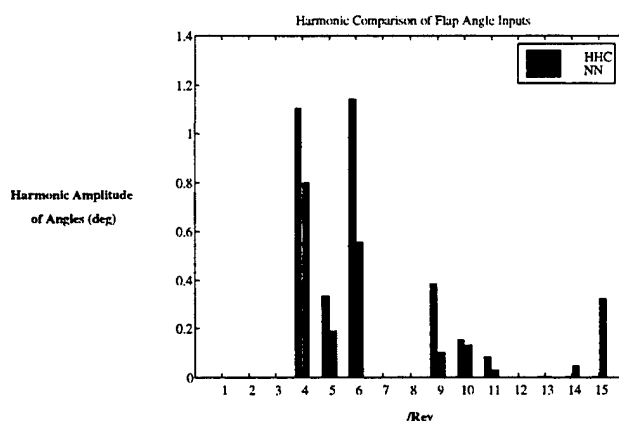
Comparison Vibration Energy Reduction



Comparison of total hub vibrational energy reduction between the HHC and neurocontroller methods
(2-norm of 5P & 10P Vibrations)



Flap Angle Input Harmonic Comparison



Comparison between HHC and neurocontroller trailing edge flap deflections

Structural Modeling of a Rotor Blade Incorporating Active Fiber Composites

Doug Weems, Bob Derham (Boeing), Nesbitt Hagood (MIT), and John Rodgers (Mide)

The Smart Materials and Structures Demonstration Consortium (SMSDC) and its predecessor, the Smart Materials for Rotorcraft Consortium (SSRC), have been working for over 4 years on rotorcraft applications for smart structures. A major part of this ongoing effort has been the design, fabrication, and testing of a rotor blade which incorporates integral Active Fiber Composite (AFC) actuators to achieve higher-harmonic blade twist. The main participants in this task are Boeing Philadelphia and the Active Materials and Structures Lab (AMSL) at MIT. This presentation discusses some of the modeling techniques utilized by Boeing Philadelphia to analyze an active rotor blade.

The specific topic of this presentation is the modeling of composite structure incorporating Active Fiber Composites. On the laminate level, the AFC packs are represented as individual homogenous layers in a composite layup. A modified version of Classic Laminated Plate Theory (CLPT) with terms for linear piezoelectric actuation is presented. The form of these actuation terms is similar to terms for thermal expansion. The resulting equations can be used to calculate laminate and lamina stresses and strains under an arbitrary combination of actuation and mechanical loading.

On the component level, quasi-static actuation is modeled using an off-the-shelf finite element (FE) code in which the linear piezoelectric effect is represented by thermal loading of laminates. An FE model of the subject rotor blade application is shown and the input properties used to model piezoelectric actuation discussed. The linear twist rate predicted by the FE model is then used to calculate an effective torsion moment which can then be used to represent blade actuation in rotor aeroelastic codes. Although the specific example here is the twist of a rotor blade, this approach is suitable for quasi-static actuation in any composite structure containing embedded actuators.

Predictions and measurements are compared to two sets of test data: linear extension of a flat fiberglass laminate containing an AFC actuator, and twist actuation of a 1/6th-scale CH-47D rotor blade. It is concluded that this approach provides a flexible and accurate model for predicting the response of general composite structures to AFC actuation.

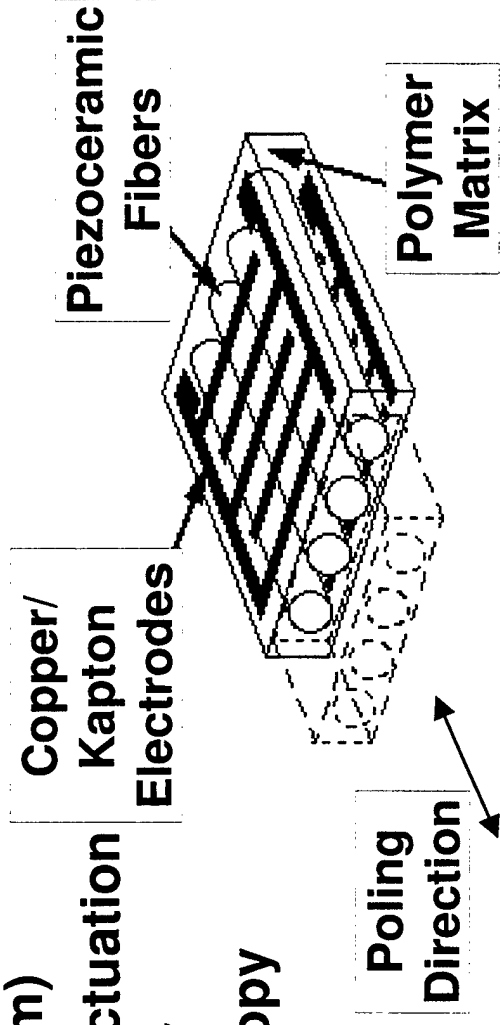
Corresponding Author:

Douglas B. Weems
Boeing Philadelphia
PO Box 16858 M/S P38-13
Philadelphia PA 19142
Phone: 610-591-4242
FAX: 610-591-4948
E-mail: douglas.b.weems@boeing.com

Active Fiber Composites

SMSDC

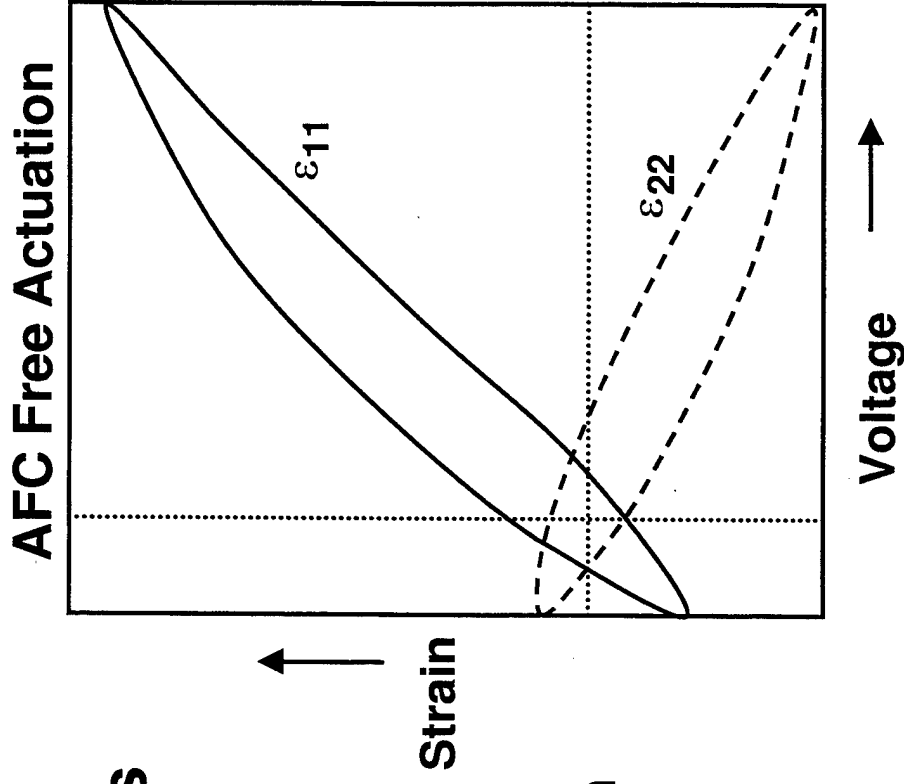
- **AFC Components**
 - Piezoelectric Fibers
 - Polymer Resin
 - Interdigitated Electrodes (Copper/Kapton)
- **Key AFC Characteristics**
 - Thin layer (~0.2 mm)
 - 33 Piezoelectric Actuation
 - Elastic Anisotropy
 - Actuation Anisotropy



*Weems, Derham, Hagood, & Rodgers
Structural Modeling of a Rotor Blade Incorporating Active Fiber Composites*

AFC Characterization

- Lamina Thickness
- In-Plane Elastic Properties
 - Longitudinal Modulus E_x
 - Transverse Modulus E_y
 - Shear Modulus G_{xy}
 - Poisson's Ratio ν_{xy}
- Actuation Level
 - Free strain in Fiber Direction
 - Transverse Actuation Ratio



Active Laminate Model

SMSDC

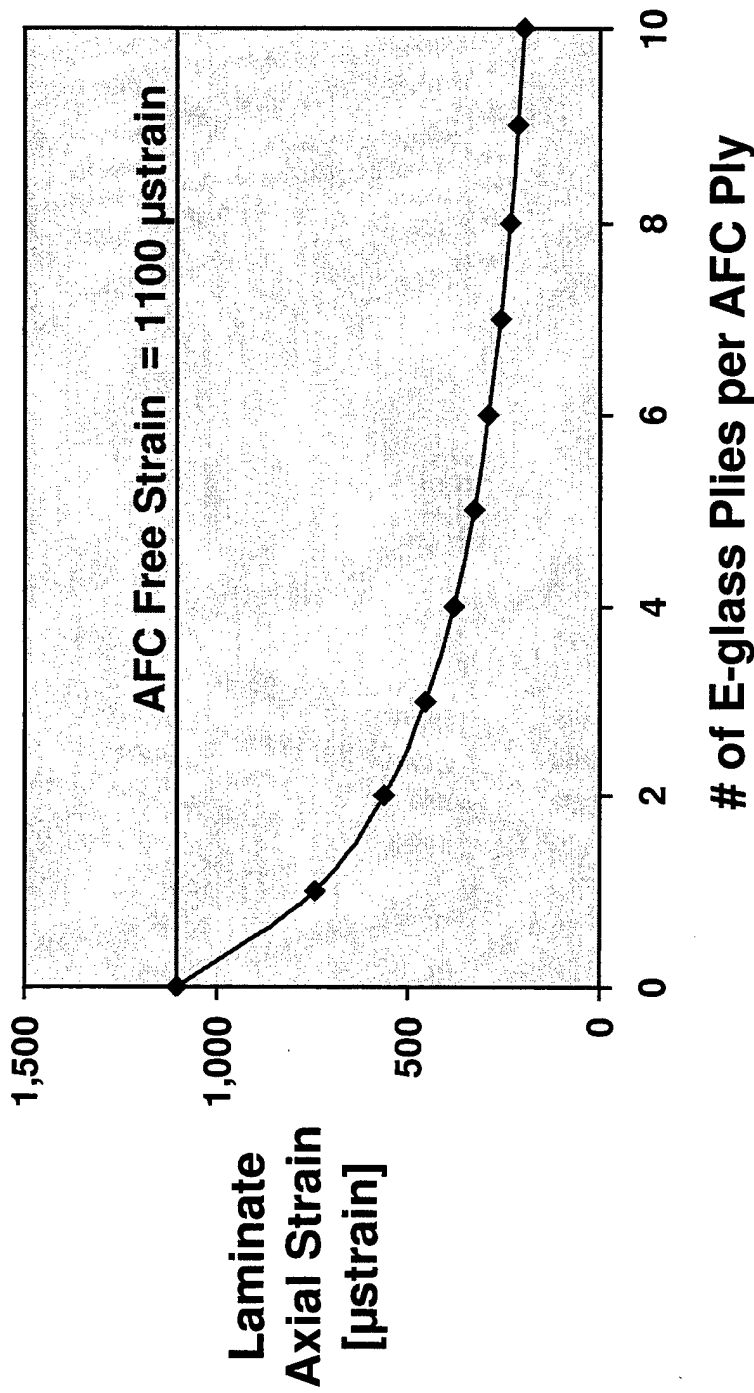
- **Incorporate Active Materials in Classic Laminated Plate Theory (CLPT)**
 - Homogenous but Anisotropic Lamina
 - Mix Active and Passive Lamina
 - Perfect Bonding between Lamina (No Shear Lag)
- **Piezoelectric Effect Like Thermal Expansion**
 - Assume Voltage Applied in One Direction
 - Assume Voltage-Controlled Operation
 - Define Actuation Variable for Entire Laminate (ΔT)
 - Define Actuation Coefficients for Each Lamina (α_{ij})

Active Laminate Example



SMSDC

- Linear Extension of an AFC Embedded in Fiberglass Laminate

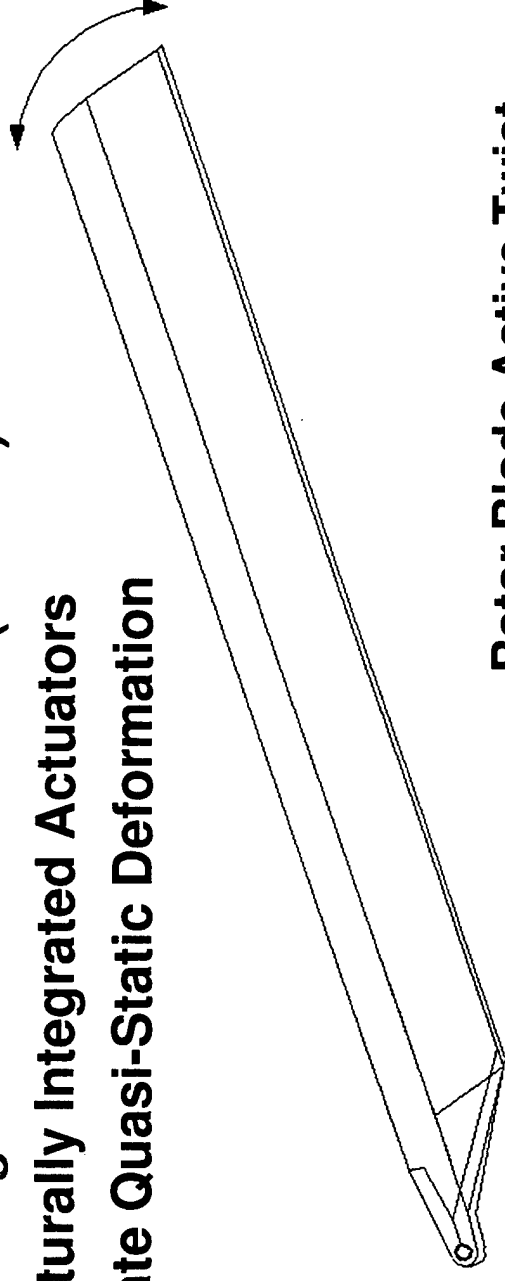


Weems, Derham, Hagood, & Rodgers
Structural Modeling of a Rotor Blade Incorporating Active Fiber Composites

Rotor Blade Application

SMSDC

- **Goals**
 - Reduce Vibration in High-Speed Flight
 - Reduce BVI Noise Reduction
- **Approach**
 - Induce Higher-Harmonic Twist ($> 1/\text{rev}$)
 - Structurally Integrated Actuators
 - Actuate Quasi-Static Deformation



Rotor Blade Active Twist

*Weems, Derham, Hagood, & Rodgers
Structural Modeling of a Rotor Blade Incorporating Active Fiber Composites*

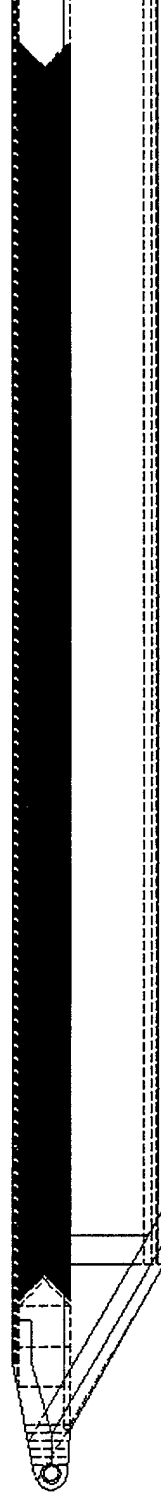


Active Rotor Blade Design



SMSDC

- Active Blade Designed and Built in SSRC Phase I
- 1/6th Scale CH-47 Blade (1.5m Radius, 14cm Chord)
- Six AFC Layers in Spar (Forty-Two AFC Packs)
- All AFC fibers oriented at $+45^\circ$ or -45°



Weems, Derham, Hagood, & Rodgers
Structural Modeling of a Rotor Blade Incorporating Active Fiber Composites

AFC Actuation in FE Model

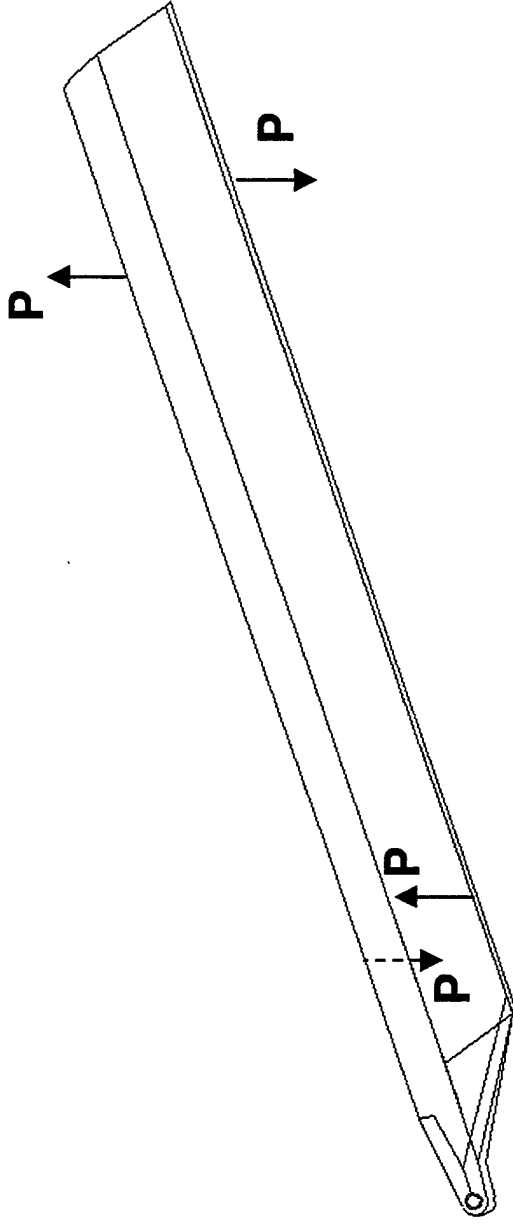
SMSDC

- **Define Lamina Properties and Construct Laminates within MSC/Patran**
 - Zero CTE for Passive Composites
 - Non-zero CTE for AFC
 - » Opposite signs for +45 and -45
- **Model Half of Symmetric Actuation Cycle**
 - Apply Temperature equal to Half AFC Free Strain
 - Set Reference (Stress-Free) Temperature to Zero

Active Rotor Modeling

SMSDC

- **Model Actuation in Rotor Analysis Codes**
 - Calculate Effective Actuation Torque
 - Apply Torque over Active Region of Blade as External Couples



Weems, Derham, Hagood, & Rodgers
Structural Modeling of a Rotor Blade Incorporating Active Fiber Composites

Experimental Results

SMSDC

- **Laminated AFC Actuation**
 - 0° AFC Embedded in 0° E-glass Laminate
 - Actuate AFC with Low-Frequency (1 Hz) Sine
 - Measure Strain in Unconstrained Laminate
- **Quasi-Static Blade Twist**
 - Bench Test - Clamped at Root End
 - Actuate with Low-Frequency (1 Hz) Sine
 - Measure Twist using Laser Interferometry

*Weems, Derham, Hagood, & Rodgers
Structural Modeling of a Rotor Blade Incorporating Active Fiber Composites*

Magneto-Rheological Fluid Shock Absorbers for Off-Highway, High-Payload, Ground Vehicles

Faramarz Gordaninejad¹ and Shawn P. Kelso²

Department of Mechanical Engineering, University of Nevada, Reno, NV 89557

Phone: 775-784-6990, Fax: 775-784-1701, E-mail: faramarz@unr.edu

This work presents the development and evaluation of a controllable, semi-active magneto-rheological (MR) fluid shock absorber. Theoretical as well as experimental studies are conducted. This is a new design that is tailored for ground vehicles which undergo a wide range of dynamic loading including the capability for passive, load-specific, individual rebound and compression characteristics. The specific application for testing and proof-of-concept is the High Mobility, Multipurpose Wheeled Vehicle (HMMWV). The new MR shock absorber emulates stock, original equipment manufacturer (OEM) shock absorber behavior in passive mode (i.e., zero-field) and provides a wide range of controllable damping force above (and below, if needed) zero-field damping levels.

As a component of a semi-active suspension system, the role of the controllable shock is to have the capacity to produce variable damping proportionally reactive to the input, which is often random excitation. The ability to vary damping for a wide range of inputs is the main feature of semi-active suspension systems. Other features include control of body roll during turning, control of vehicle pitch during braking and acceleration and accommodation for a variable vehicle mass (i.e., empty or full payloads). In comparison to typical, passive suspension systems, semi-active technology allows for softer damping when needed in addition to harder damping for situations that demand it. The main benefits of this technology for ground vehicles are: improved vibration isolation for sensitive payloads, an increased level of operator control over vehicle due to a lower disturbance input, and faster operational speeds (over similar terrain).

The objective of this work is to develop theoretical and experimental components of the proof-of-concept effort. The parametric theoretical model has the ability to predict damping behavior by varying physical parameters, while the experimental component aids in the determination of viability of this course of research (i.e., the new design). To validate the model, theoretical and experimental results are compared. This paper focuses on the experimental component of this research.

An experimental, proof-of-concept MR fluid damper was developed and tested for implementation into high-payload, off-highway ground vehicles. The U.S. Army is interested in this technology for a semi-active, controllable HMMWV. This new damper design provides a wide controllable range of damping force that can utilize the on-board power supply of the vehicle. A new method for achieving controllable damping via manipulation of MR passage geometry allows for fine-tuning of passive and semi-active damping behavior. The new damper design also has the capacity of effectively utilize existing ground vehicle shock absorber technology in the arenas of by-pass valves and over-travel protection. Two OEM shock absorbers were tested for a range of frequencies and peak-to-peak displacements to establish a criterion for passive damping of the new MR damper design.

Figure 1 compares the preliminary theoretical model results to the experimental results. The theoretical model employs the Bingham plastic model to provide a term for apparent viscosity as a function of current. Figure 2 illustrate the force envelope of the MR damper prototype as a function of frequency for peak-to-peak displacements of 1.5cm. Also, shown for comparison are the fixed-force results of the OEM shock absorber. The benefit of controllable damping presented in this technology is made evident by these results; a range of damping force (with the MR prototype damper) versus a

¹ Professor

² Graduate Research Assistant

fixed force amount (with the OEM unit). As energy inputs vary to the vehicle, the MR damper has the capability to the rate of energy absorption accordingly.

ACKNOWLEDGEMENTS

This study is funded by the Army Research Office Grant Number DAAG55-97-1-0077. The authors are thankful for the encouragement by Dr. Gary Anderson, the Program Director.

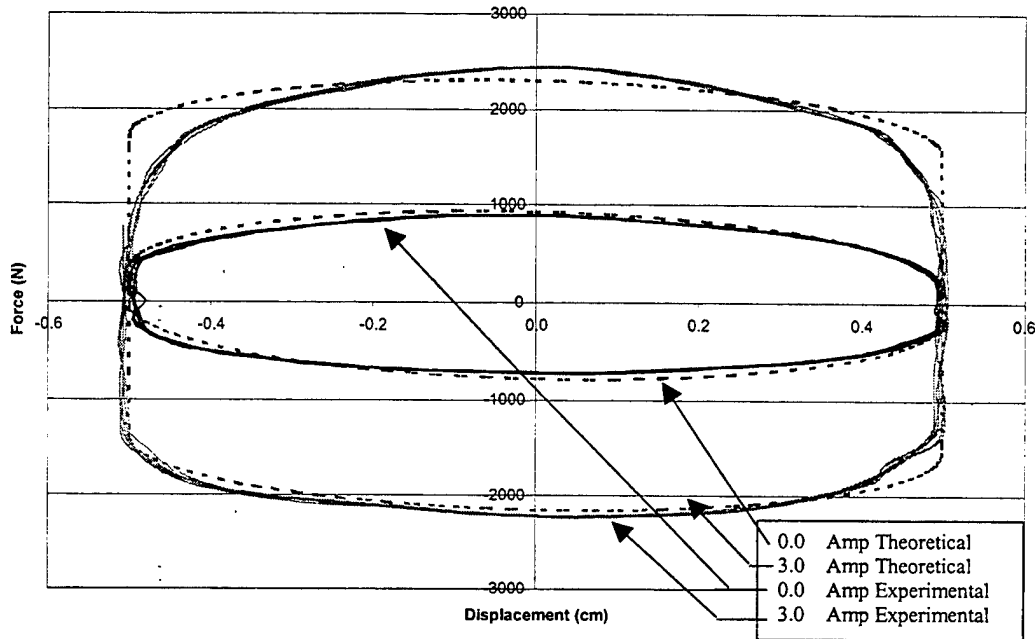


Figure 1. Comparisons between theoretical and experimental force-displacement results of the an UNR MR fluid damper (at 2Hz, 1.0cm P-T-P, for 0.0 and 3.0Amps).

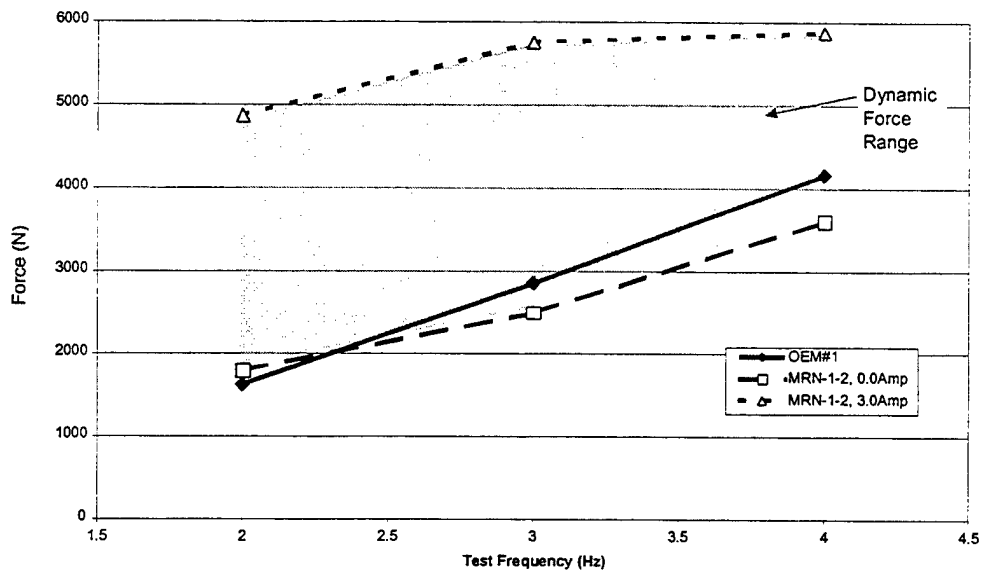
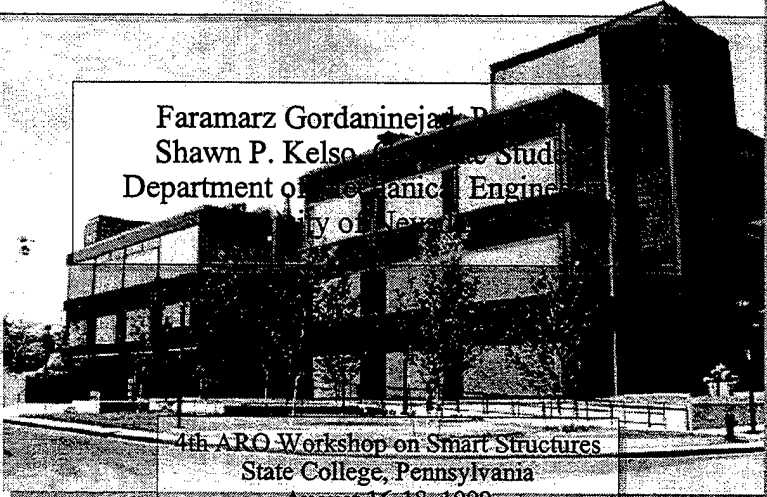


Figure 2. Comparison between peak-to-peak force as a function of frequency for an UNR MR fluid damper and an OEM damper at 1.5cm peak-to-peak displacement.

Magneto-Rheological Controllable Shock Absorbers for Off-Highway, High-Payload Ground Vehicles



Faramarz Gordaninejad, Ph.D.
Shawn P. Kelso, Ph.D.
Department of Mechanical Engineering
University of Delaware

4th ARO Workshop on Smart Structures
State College, Pennsylvania
August 16-18, 1999

Overview of Presentation

- Background of Research
- Experimental Study
- Theoretical Model
- Results and Comparisons

 Composite and Intelligent Materials Laboratory

Background

- Semi-active dampers
- MR/ER fluid dampers
- Use of Semi-active shock absorbers in HMMWV

 Composite and Intelligent Materials Laboratory

Research Objectives

- Research: To investigate the feasibility of implementing controllable, magnetorheological (MR) fluid shock absorbers for off-highway, high-payload ground vehicles
- Target Vehicle: HMMWV - High Mobility Multi-Wheeled Vehicle
- Initial investigation into direction-specific control - (individual rebound and compression damping)
- Passive capabilities emulation of original equipment shock behavior in the absence of a magnetic field

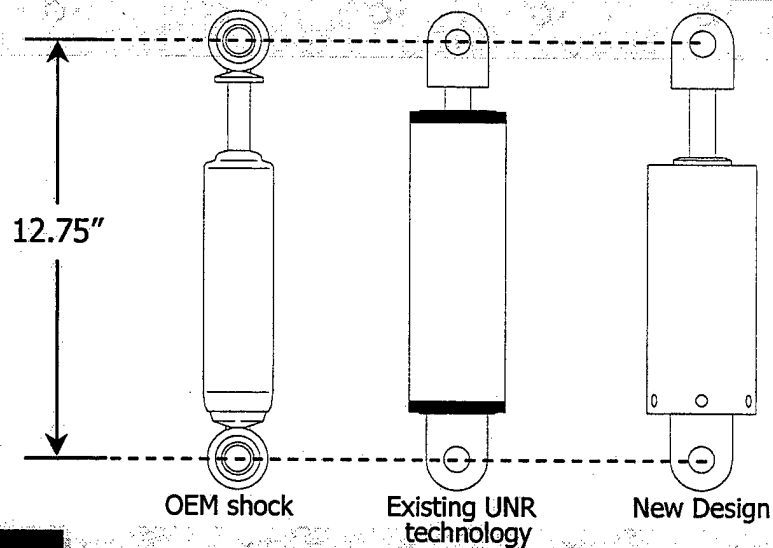
 Composite and Intelligent Materials Laboratory

Experimental Study

- Two Original Equipment Manufacture (OEM) Shocks were characterized to set a standard for damping behavior
- Parameters Explored:
 - Frequency
 - Peak-to-peak displacement
- A damper was designed and tested using existing technology
- A brand new design was explored in detail
 - Frequency
 - Peak-to-peak Displacement
 - Electric current input
 - Number of MRF valves
 - Size of MRF valve
 - Effects of length of MRF valve

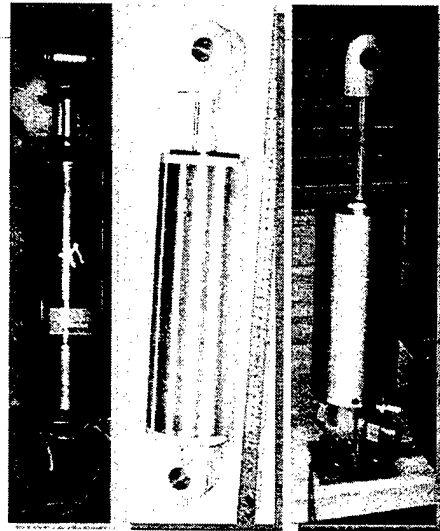
Composite and Intelligent Materials Laboratory

Experimental Study - Damper Comparison



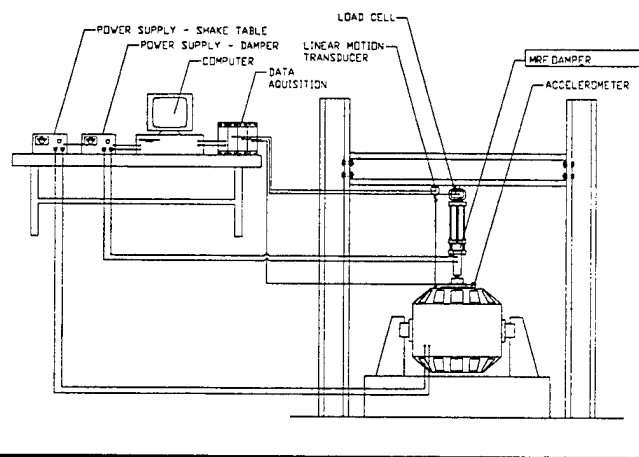
Composite and Intelligent Materials Laboratory

Experimental Study - Dampers



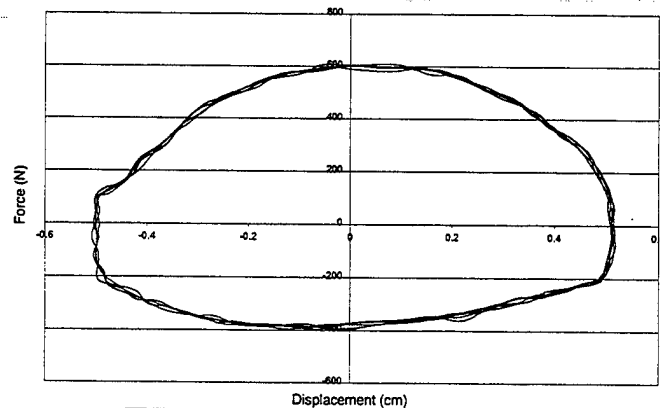
Composite and Intelligent Materials Laboratory

Experimental Study - Experimental Setup



Composite and Intelligent Materials Laboratory

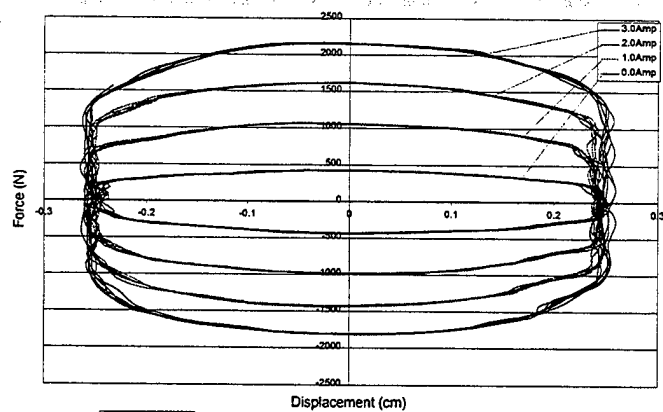
Characterization Results - OEM



Force vs displacement for OEM#1 at 2Hz, 1.0cm p-t-p.

Composite and Intelligent Materials Laboratory

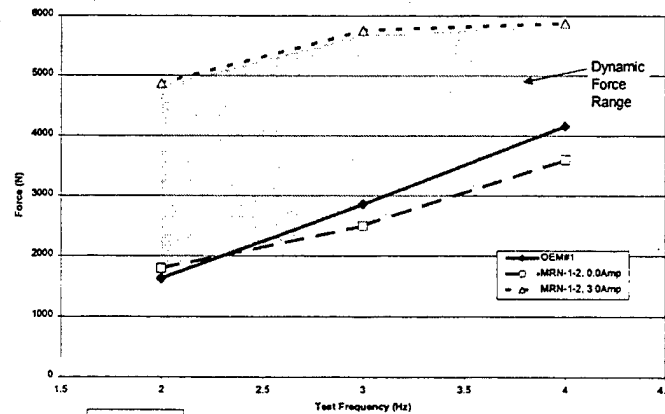
Characterization Results - MRN-Series



Force vs displacement for MRN-2-4 at 2Hz, 0.5cm p-t-p, for various amperages.

Composite and Intelligent Materials Laboratory

Results - OEM and 2nd Generation MRN-Series



Comparison of peak-to-peak force as function of testing frequency for MRN-1-2 and OEM#1 at 1.5cm peak-to-peak displacement.

Composite and Intelligent Materials Laboratory

Theoretical Model

Damping Force Equation

$$F_{DAMPER} = [\Delta P_{MHL} A] + [C_{SF}] + [\Delta P_{INERTIA} A] + F_{POISSEUILLE}$$

Minor head losses

Coulomb Seal Friction

Fluid inertia across piston

Viscous damping

where

$$F_{POISSEUILLE} = [P_0 A] + [K_S \underline{X}_P] + [\Delta P_{VA} A] + [\Delta P_{VP} A] + [\Delta P_{MR} A]$$

Pressure force of accumulator

Spring term of accumulator

Viscous damping of accumulator

Viscous damping across piston

MRP-effect

Composite and Intelligent Materials Laboratory

Bingham Plastic Model

$$\tau = \tau_Y + \mu_0 \dot{\gamma}$$

$$\tau_{\text{Newtonian}} = \mu_0 \dot{\gamma}$$

$$\mu_0 = \frac{\tau_{\text{Newtonian}}}{\dot{\gamma}}$$

$$\mu_{\text{APP}} = \frac{\tau_Y + \mu_0 \dot{\gamma}}{\dot{\gamma}} = \frac{\tau_Y}{\dot{\gamma}} + \mu_0$$

Composite and Intelligent Materials Laboratory

Poiseuille Flow - Major Head Loss

$$\Delta P_{\text{CHC}} = \frac{32 \mu L V}{d^2} = \frac{32 \mu_{\text{APP}} L_{\text{CH}} V_{\text{CHC}}}{D_{\text{eff}}^2}$$

$$\Delta P_A = \frac{32 L_{\text{CH}} V_{\text{CHC}}}{D_{\text{eff}}^2} \left(\mu_0 + \frac{\tau_Y}{\dot{\gamma}} \right)$$

$$\frac{\tau_Y}{\dot{\gamma}} = \frac{K I^\delta}{2 V_{\text{CHC}}} D_{\text{eff}}$$

Composite and Intelligent Materials Laboratory

Poisseuille Flow - Major Head Loss

$$\Delta P_{CH} = \frac{32\mu_0 L_{CH}}{D_{eff}^2} \left(\frac{A_1}{NA_{CH} + \beta MA_B \phi} \right) \dot{X}_P + \frac{32L_{MR} K I^\delta}{D_{eff}}$$

$$\phi = \left(\frac{D_B^2}{D_{eff}^2} \right) \left[1 + \frac{\tau_Y / \dot{\gamma}}{\mu_0} + \frac{L_{MR}}{L_P} + \frac{(\tau_Y / \dot{\gamma}) L_{MR}}{\mu_0 L_P} \right]$$

β = percent opening of valve

M = number of channels that open for compression

N = number of MR fluid channels

 Composite and Intelligent Materials Laboratory

Theoretical Force in Compression

$$F_{PC} = \left[\left(\frac{D_S^2}{D_L^2} K_A + \left(\frac{A_1 \dot{X}_P}{NA_{CH} + \beta MA_B \phi} \right)^2 (NK_P + \beta MK_B \phi) \right) \frac{\rho}{2} \dot{X}_P \right] A_P + C_{SF}$$

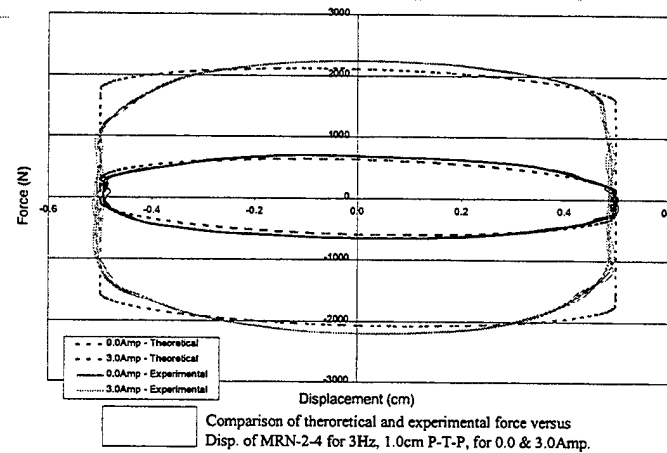
$$+ \rho N L_{CH} \ddot{X}_P A_P + \left[P_0 + \gamma P_0 \left(\frac{D_A^2}{D_S^2} \right) \left[\left(\frac{H_0}{H_0 - \left(\frac{D_S^2}{D_A^2} \dot{X}_P \right)} \right)^{\gamma} - 1 \right] + \frac{128\mu_0 L_L A_S}{\pi D_A^4} \dot{X}_P \right] A_S$$

$$+ \left[\frac{32\mu_0 L_{CH}}{D_{eff}^2} \left(\frac{A_1}{NA_{CH} + \beta MA_B \phi} \right) \dot{X}_P + \frac{16L_{CH} K I^\delta}{D_{eff}} \right] A_{IC}$$

$$\phi = \left(\frac{D_B^2}{D_{eff}^2} \right) \left[1 + \frac{\tau_Y / \dot{\gamma}}{\mu_0} + \frac{L_{MR}}{L_P} + \frac{(\tau_Y / \dot{\gamma}) L_{MR}}{\mu_0 L_P} \right]$$

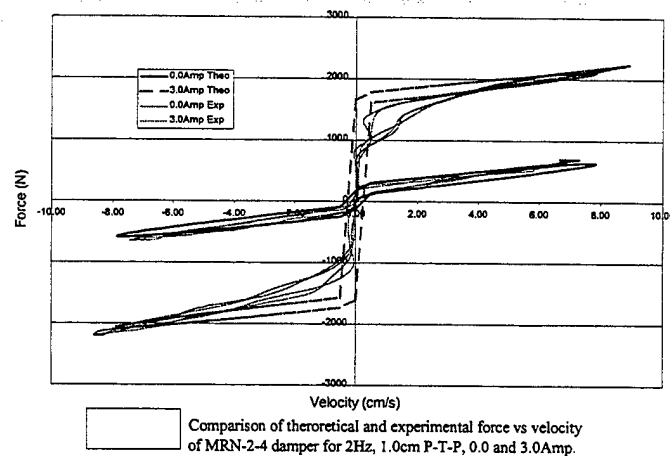
 Composite and Intelligent Materials Laboratory

Comparison of Theoretical and Experimental



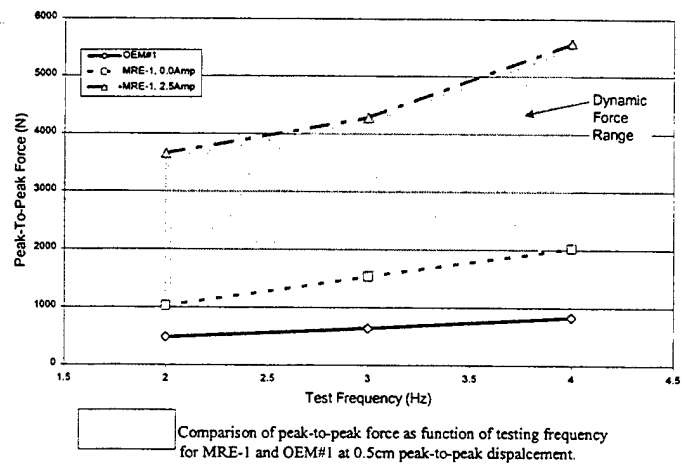
Composite and Intelligent Materials Laboratory

Comparison of Theoretical and Experimental



Composite and Intelligent Materials Laboratory

Results - OEM and MRE-1



Composite and Intelligent Materials Laboratory

Conclusions

- New MRF Damper Design Emerged
- Experimental Results Support Theoretical Predictions

Composite and Intelligent Materials Laboratory

Design and Fabrication of an Electrorheological Fluid Automotive Shock Absorber

Jason Lindler
Research Assistant

Norman Wereley
Associate Professor

Many automotive shocks achieve damping from the pressure required to force a hydraulic fluid through a needle valve. Unfortunately, passive automotive shocks make compromises between a vehicle's ride and handling characteristics. To allow for optimal performance, the needles in many racing shocks can move to adjust the size of the valve opening and vary the amount of damping. However, manual adjustment of the shock often requires time consuming disassembly of the device. In contrast to needle valves, electrorheological fluids (ER), whose yield stress can be controlled with the application of an electric field, can vary their amount of damping without disassembly of the device. The goal of the research is to design and fabricate an electrorheological fluid shock absorber that achieves a double adjustable shock's variable damping requirements.

Due to its adjustable performance, this research utilizes an 8100 series Penske double adjustable shock as the baseline design criterion for the performance of a semi-active automotive shock absorber. Force vs. velocity hysteresis cycles of many shocks may be separated into four distinct regions: low-speed compression, high-speed compression, low-speed rebound and high-speed rebound. A unique damping coefficient characterizes each region, and a distinct yield force divides the low and high-speed regions. Mechanical mechanisms on the main piston head and in the pneumatic reservoir allow for independent control of yield force and damping coefficient during the compression and rebound strokes.

To emulate the performance of a conventional double adjustable shock absorber, an electrorheological (ER) automotive shock absorber was designed and fabricated at the University of Maryland. The shock absorber, composed of hydraulic and pneumatic reservoirs separated by a floating piston, incorporates a monotube, single rod design. Inside the hydraulic cylinder, the piston rod attaches to a piston head containing two cylindrical electrodes. During piston rod motion, ER fluid flows through the piston head in a gap between the cylinder electrodes.

To achieve semi-active properties, the hydraulic cylinder is filled with Bayer Rheobay 3565 electrorheological fluid. An electrical voltage potential between the cylinders creates an electric field in the gap perpendicular to the ER fluid flow direction. The electric field increases the yield stress of the ER fluid between the cylinders. This increase in yield stress alters the velocity profile of the fluid in the gap and raises the pressure required for a given flow rate.

Both the experimental data and the derived equations demonstrate that increasing the voltage across the concentric cylinder annulus controls the yield force of the device. Furthermore, both the experimental data and the derived equations show little change in the post yield damping coefficient in the force vs. velocity cycle. However, many existing passive adjustable shocks can alter the post-yield damping coefficient in addition to the yield force.

One such feasible design to alter the post-yield damping would be to create an eccentricity between the two cylinders. Modifying the shape of the gap between the cylinders creates an increase in the post-yield damping coefficient without great variation in the yield stress. From the fluid properties, the yield stress does not increase with the electric field until a threshold value. As a result, part of the gap on one side of the annulus is large enough not to incur a yield stress and allow fluid motion without a yield stress. Then, as the flow rate increases, the yield stress increases the required pressure and altering the post-yield damping coefficient.

Force measurements from sinusoidal displacement cycles, recorded on a 5HP mechanical dynamometer, validate the performance of the concentric and eccentric cylinders.

Research supported under the Army Young Investigator Program
(Contract N DAAG-5598-10339)
with Dr. Gary Anderson as technical monitor.



**University of Maryland, College Park
Smart Structures Laboratory**

**Design and Testing of an
Electrorheological Fluid
Automotive Shock Absorber**

Jason E. Lindler

Graduate Research Assistant

Norman M. Wereley

Associate Professor

Fourth ARO Workshop on Smart Structures
Penn State, University Park Campus, Pennsylvania.
August 16-18, 1999



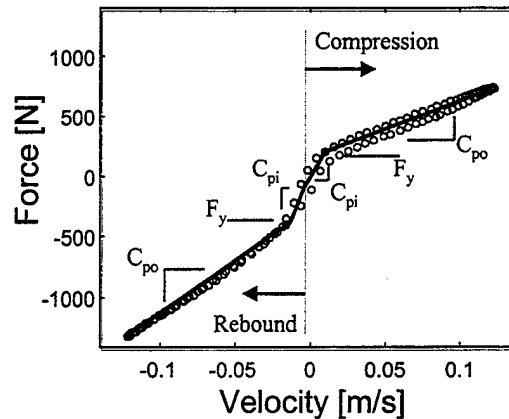
Presentation Overview

- Performance and design of a conventional double adjustable shock absorber
- Motivation, objectives and design approach for an electrorheological automotive damper
- Electrorheological fluid properties and behavior
- Design, modeling and testing of an electrorheological fluid automotive shock
- Conclusions and future work



Performance Metrics (Conventional Double Adjustable Shock Absorber)

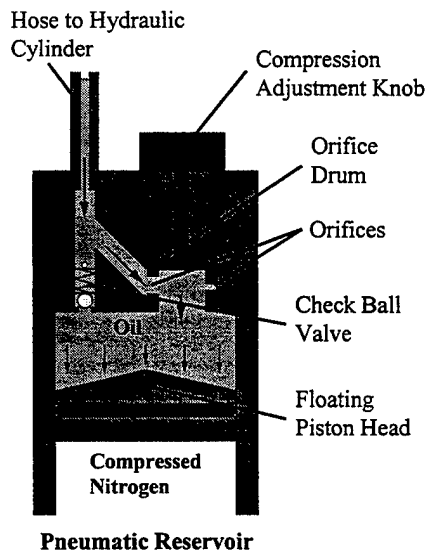
- Penske 8100 series double adjustable shock absorber
- Force vs. velocity graph is composed of four distinct regions
 - Low speed compression, high speed compression, low speed rebound, high speed rebound
 - Unique damping coefficient, C_{po} and C_{pi} , characterizes each region
 - Yield Force, F_y , separates the low and high-speed regions
- Mechanical devices allow for adjustment of the parameters



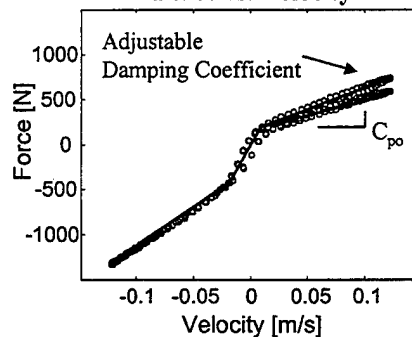
F_y = Yield force
 C_{pi} = Pre-yield damping coefficient
 C_{po} = Post-yield damping coefficient



Adjusting Post-Yield Damping (Conventional Double Adjustable Shock Absorber)



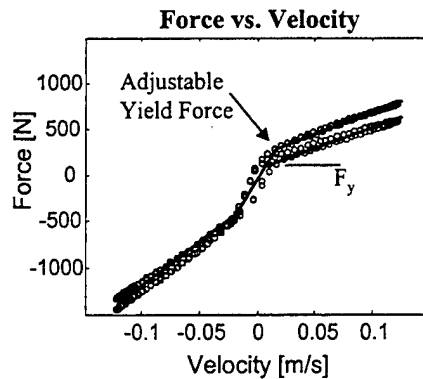
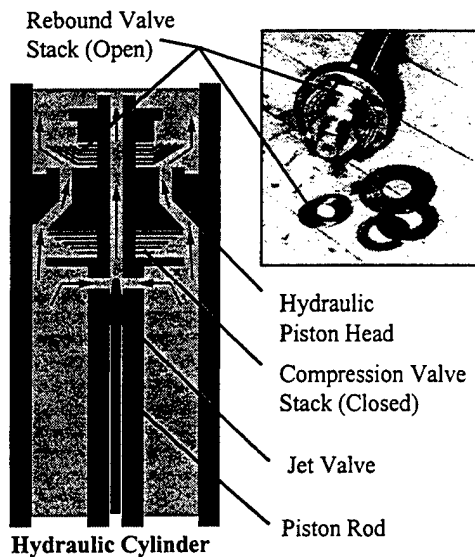
Force vs. Velocity



- Orifice Drum Design
 - Compression adjustment knob turns the orifice drum
 - Turning drum alters orifice size and adjusts the damping coefficient



Adjusting the Yield Force (Conventional Double Adjustable Shock Absorber)



- Valve Stack Design
 - Thin circular steel shims
 - Preloaded spring performance
 - Changing the thickness of the steel shims adjusts the yield force



Motivation

- Electrorheological fluids reduce the number of parts required for semi-active devices
 - Conventional adjustable shocks require different thickness shims
 - Conventional shocks contain multiple orifice adjustment parts
 - ER fluids yield stress, controlled by an applied electric field, alters the level of damping
- Conventional double adjustable shock absorbers requires disassembly to adjust the yield force
 - ER shock absorbers allow for remote control of damper performance
 - ER shock absorbers save time in suspension set-up
 - Multiple control schemes are possible with ER devices





Research Objectives

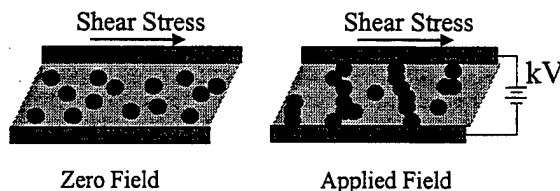
- Design and fabricate an ER fluid shock absorber with dimensions similar to a conventional double adjustable shock absorber
 - Incorporate ER fluid device into the piston head of the shock absorber
 - Shock dimensions comparable to many automotive shocks
 - Spring mounted in parallel with the damper for suspension applications
- Model and fabricated an ER fluid shock absorber to meet similar performance requirements of an conventional adjustable shock
 - Adjustable yield force
 - Adjustable post-yield damping coefficient
 - One electrode gap is design to adjust the yield force
 - Another electrode gap is design to allow adjustment of damping coefficient



Electrorheological Fluids (Bingham Plastic Model)

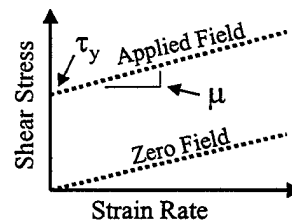
- Bingham plastic ER fluid behavior
 - Newtonian under zero field conditions
 - Bingham plastic under an applied electric field
- Viscosity (μ) is independent of the applied electric field
- Yield Stress (τ_y) is a quadratic function of the applied electric field

Parallel Plate Example



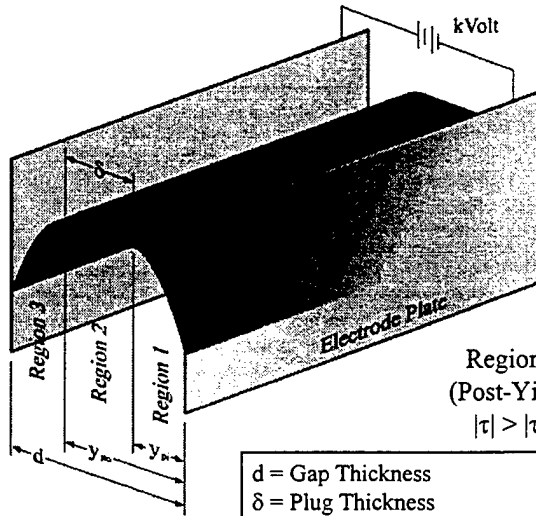
Bingham Plastic

$$\tau = \tau_y + \mu \frac{du}{dy}$$





Velocity Profile of ER Fluid (Between Parallel Plates due to a Pressure Gradient)



- Similar to the parabolic Newtonian velocity profile
- Yield Stress, (τ_y), caused by an applied electric field, creates a plug region of thickness δ
- The plug region alters the pressure drop, ΔP , required to achieve a given flow rate

Region 1
(Post-Yield)
 $|\tau| > |\tau_y|$

Region 2
(Pre-Yield)
 $|\tau| < |\tau_y|$

Region 3
(Post-Yield)
 $|\tau| > |\tau_y|$

d = Gap Thickness
 δ = Plug Thickness
 $\bar{\delta}$ = Non-dimensional Plug Thickness
 L = Length of Electrode Plate

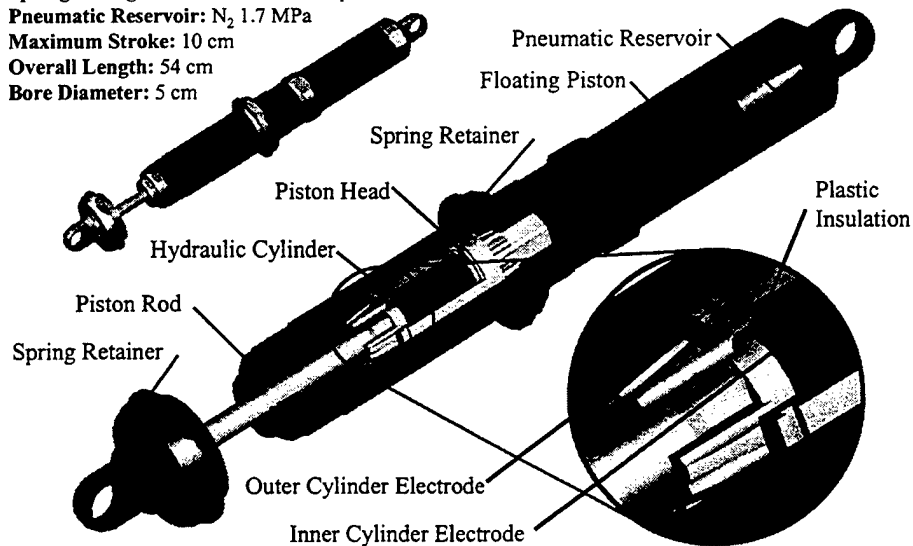
From shear stress profile

$$\bar{\delta} = \frac{\delta}{d} = \frac{2L\tau_y}{d\Delta P}$$



ER Fluid Shock Absorber

Spring Configuration: Coil-over damper
Pneumatic Reservoir: N_2 1.7 MPa
Maximum Stroke: 10 cm
Overall Length: 54 cm
Bore Diameter: 5 cm

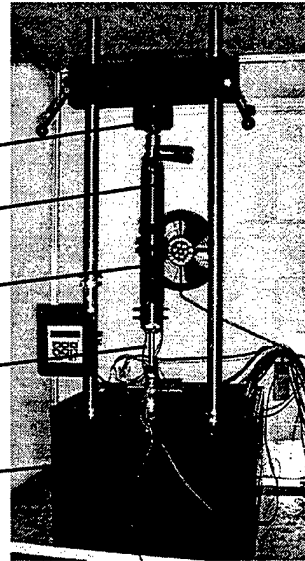




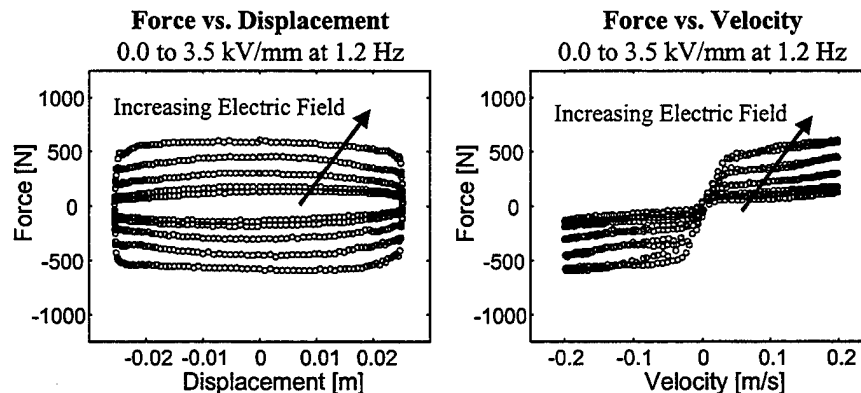
Experimental Testing (Shock Dynamometer)

- Provides a smooth sinusoidal displacement input
 - Displacement created by a cam shaft connected to an electric motor
- Easy recording and viewing of data
 - Turnkey damper testing system
 - Designed for use by racing teams for fast recording of a damper's performance
 - Built-in LVDT and Load Cell
 - Includes computer and data acquisition card

Load cell
Pneumatic cylinder
Main ER fluid cylinder
Piston rod
Location of cam shaft and LVDT



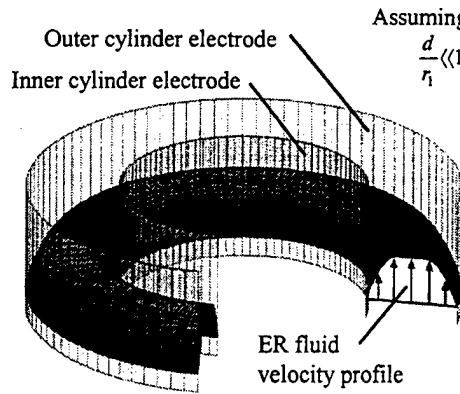
Typical Experimental Data (Electrorheological Fluid Shock Absorber)



- Test Matrix
 - Fixed stroke of 5 cm with frequencies ranging from 0.3 to 1.2 Hz
- With an increasing electric field
 - Area within the force vs. displacement hysteresis, amount of damping, increases.
 - Force vs. displacement is dominated by Coulomb damping mechanism



Flow in the Piston Head (Between Concentric Cylinder Electrodes)



Assuming that $\frac{d}{r_1} \ll 1$

The shear stress profile determines the non-dimensional plug thickness, $\bar{\delta}$

$$\bar{\delta} = \frac{\delta}{d} = \frac{2L\tau_y}{d\Delta P}$$

Integrating the parallel plate velocity profile gives the flow rate per unit width, q

$$q = q_1 + q_2 + q_3 = \frac{d^3\Delta P}{12\mu L} \left((1-\bar{\delta})^2 \left(1 + \frac{\bar{\delta}}{2} \right) \right)$$

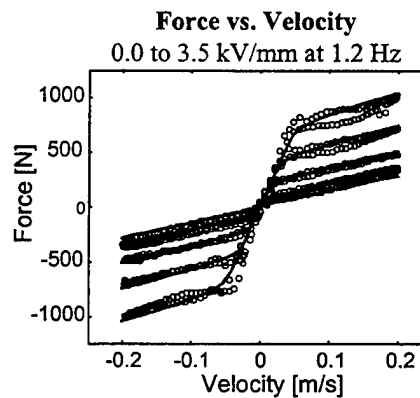
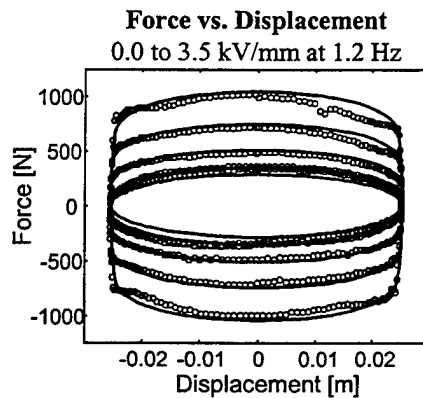
Integrating the flow rate per unit width around the inner cylinder circumference finds the flow rate, Q_c , for a given pressure

$$Q_c = \int_0^{2\pi} q db = 2\pi r_1 \frac{d^3\Delta P}{12\mu L} \left((1-\bar{\delta})^2 \left(1 + \frac{\bar{\delta}}{2} \right) \right)$$

μ = Viscosity δ = Plug Thickness
 τ_y = Yield Stress r_1 = Inner cylinder radius
 d = Gap Thickness L = Inner cylinder length
 ΔP = Pressure Drop Q = flow rate
 b = Distance around the inner cylinder



Experimental Results (Concentric Cylinders - 0.60mm Gap)



Flow through the piston head, Q_c

$$Q_c = 2\pi r_1 \frac{d^3\Delta P}{12\mu L} \left((1-\bar{\delta})^2 \left(1 + \frac{\bar{\delta}}{2} \right) \right)$$

Piston rod force, F

$$F = \Delta P A_p$$

ΔP = Pressure drop
 A_p = Piston head area

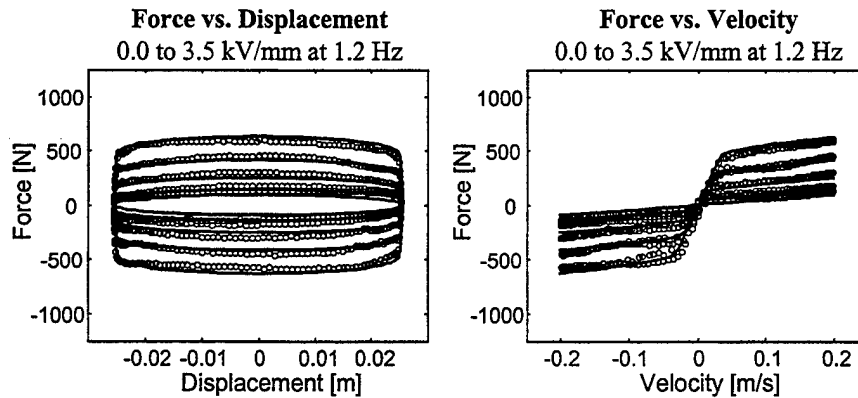
Piston rod velocity, v_o

$$v_o = \frac{Q_c}{A_p}$$



Experimental Results

(Concentric Cylinders - 0.90mm Gap)



Flow through the
piston head, Q_c

$$Q_c = 2\pi r_1 \frac{d^3 \Delta P}{12 \mu L} \left(1 - \bar{\delta}\right)^2 \left(1 + \frac{\bar{\delta}}{2}\right)$$

Piston rod force, F

$$F = \Delta P A_p$$

ΔP = Pressure drop
 A_p = Piston head area

Piston rod velocity, v_o

$$v_o = \frac{Q_c}{A_p}$$



Adjusting Damping Coefficient

(Parallel Cylinders Gaps)

Bingham Plastic Behavior of
Concentric Gaps

$$\Delta P_1 = C_1 Q_1 + F_1$$

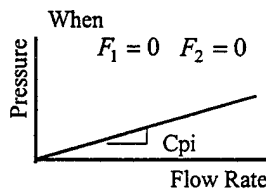
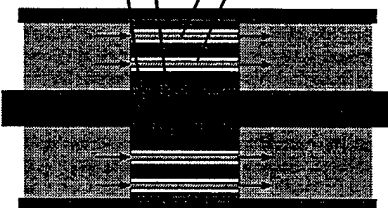
$$\Delta P_2 = C_2 Q_2 + F_2$$

Parallel Flow

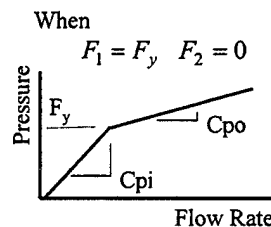
$$Q_t = Q_1 + Q_2$$

$$\Delta P_t = \Delta P_1 = \Delta P_2$$

Piston Head
Piston Rod
Outer Gap
Inner Gap



$$C_{pi} = \frac{1}{\frac{1}{C_1} + \frac{1}{C_2}}$$



$$C_{pi} = C_2$$

$$C_{po} = \frac{1}{\frac{1}{C_1} + \frac{1}{C_2}}$$

When F_1 increases to F_y
 C_{pi} increase to C_2



Flow in the Piston Head (Between Eccentric Cylinder Electrodes)

Based on a two electrode gap piston head, there is a postyield region and a preyield region

Assuming that

$$\frac{d}{r_1} \ll 1$$

Geometry of the cylinders

$$x^2 + y^2 = r_1^2$$

$$(x-e)^2 + y^2 = r_2^2$$

$$d(b) = e \cos\left(\frac{b}{r_1}\right) + \sqrt{e^2 \cos^2\left(\frac{b}{r_1}\right) - e^2 + r_2^2} - r_1$$

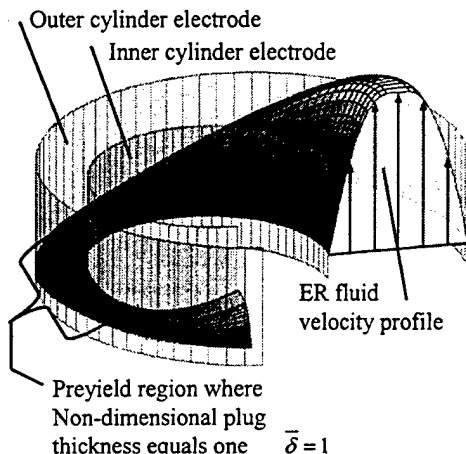
Solve for the limits of the integration, b_y

$$\bar{\delta} = 1 = \frac{2L\tau_y}{d\Delta P}$$

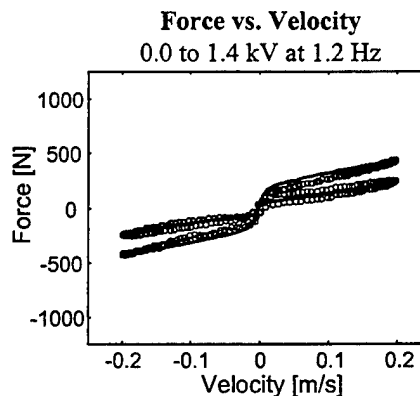
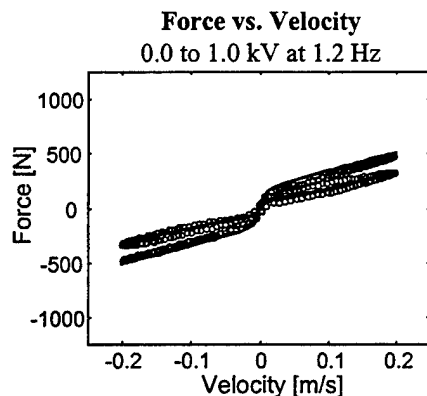
Integrating the velocity profile around the inner cylinder circumference, between $-b_y$ and b_y , finds the flow rate, Q_e , for a given pressure

$$Q_e = \int_{-b_y}^{b_y} q db = \int_{-b_y}^{b_y} \frac{d^3 \Delta P}{12 \mu L} \left(1 - \bar{\delta}\right)^2 \left(1 + \frac{\bar{\delta}}{2}\right) db$$

$$\bar{\delta}(b_y) = f(b, \Delta P) \quad d(b_y) = f(b_y)$$



Experimental Results (Eccentric Cylinders)



Flow through the piston head, Q_e

$$Q_e = \int_{-b_y}^{b_y} q db = \int_{-b_y}^{b_y} \frac{d^3 \Delta P}{12 \mu L} \left(1 - \bar{\delta}\right)^2 \left(1 + \frac{\bar{\delta}}{2}\right) db$$

Piston rod force, F

$$F = \Delta P A_p$$

ΔP = Pressure drop
 A_p = Piston head area

Piston rod velocity, v_o

$$v_o = \frac{Q_e}{A_p}$$



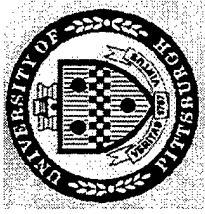
Conclusions

- Adjusting yield force
 - Increasing electric field across concentric cylinder electrodes raises the yield force of device with small effect on the post-yield damping coefficient
- Adjusting the post-yield damping
 - Increasing the electric field across eccentric cylinders raises post yield damping coefficient while incurring a small increase in the yield force



Future Work

- Combine both type of geometries in one damper
 - Place concentric and eccentric cylinders in series for independent control of yield force and the damping coefficient
- Improve performance of eccentric cylinders
 - Increase range of damping coefficient
 - Consider complex gap geometries
- Extend work into Magnetorheological devices



Semi-Active Structural Control

Fourth ARO Workshop on Smart Structures

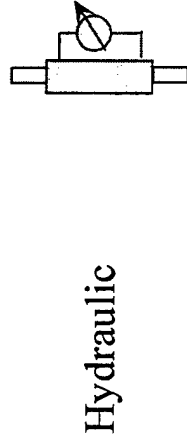
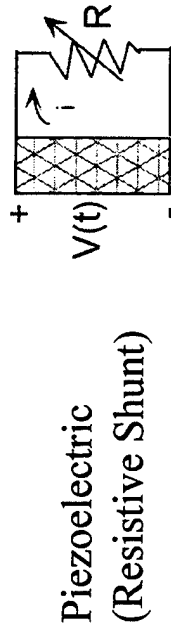
Penn State, University Park Campus, Pennsylvania
August 16-18, 1999

—

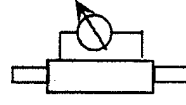
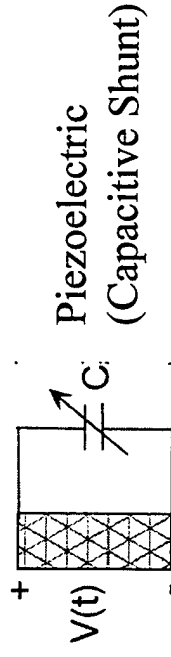
William W. Clark
Vibration and Control Laboratory
Mechanical Engineering Department
University of Pittsburgh

Semi-Active Control with Variable Stiffness vs. Variable Damping

Variable Damping

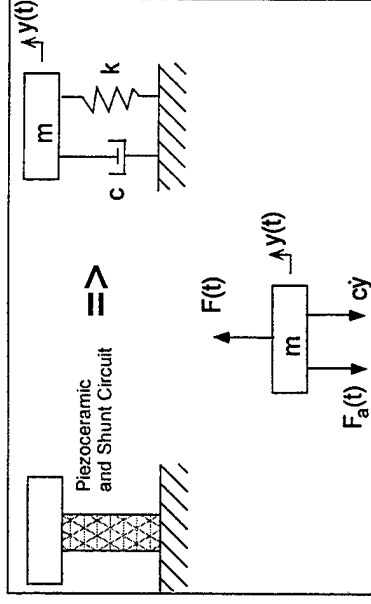


Variable Stiffness



Example System: Piezoelectric

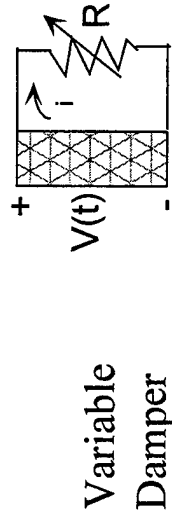
Single degree-of-freedom system with piezoelectric stiffness element:



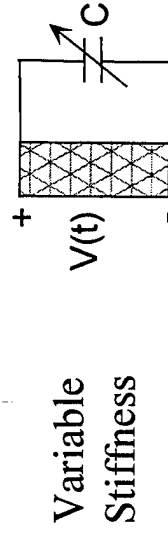
Governing Equation for SDOF System:

$$ms^2Y(s) + \frac{A}{L} \left[s^{SU} \right]^{-1} Y(s) = 0$$

s^{SU} = Mechanical Compliance



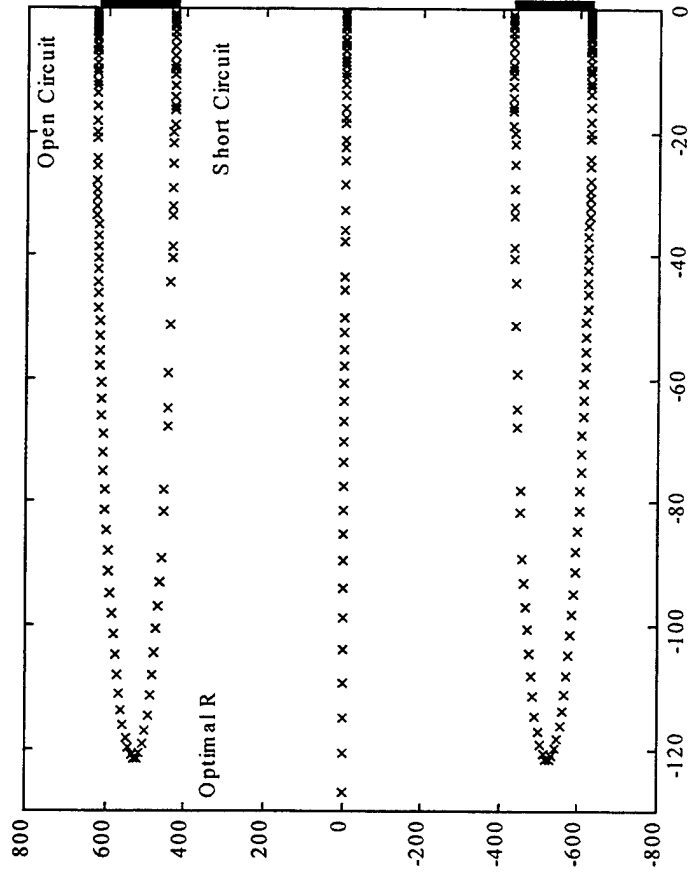
$$s^{SU} = s_{33}^E - \frac{d_{33}^2}{L} As \left(\frac{A\varepsilon_3^T}{L} + \frac{1}{R} \right)^{-1}$$



$$s^{SU} = s_{33}^E - \frac{d_{33}^2}{L} As (sC_{p3}^T + sC)^{-1}$$

Example System: Piezoelectric

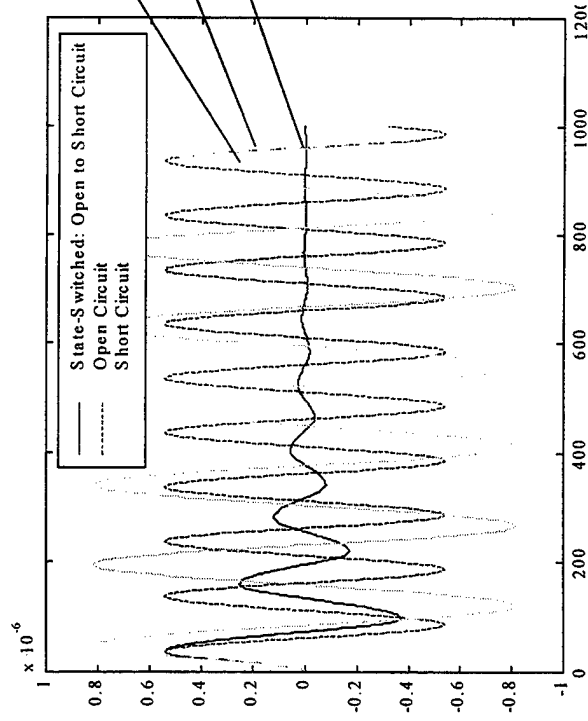
Root Locus Plots for varying R and C



xxxxx Poles for resistive system
 — Poles for capacitive system

- Adaptive-passively tuning R can optimize damping
- Adaptively-passively tuning C can not change damping
- Semi-actively changing C can provide vibration suppression

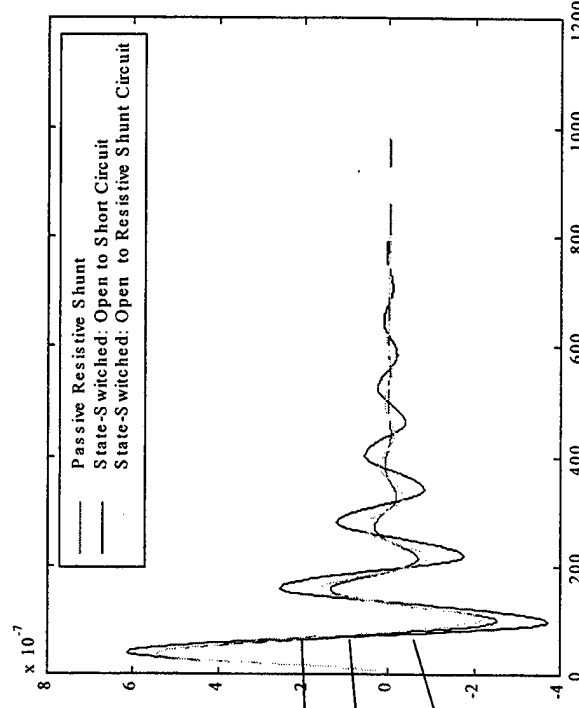
Example System: Piezoelectric



Open circuit (no damping)

Short circuit (no damping)

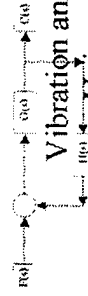
Bi-state semi-active control
(switching between open and short)



Optimal Resistive circuit

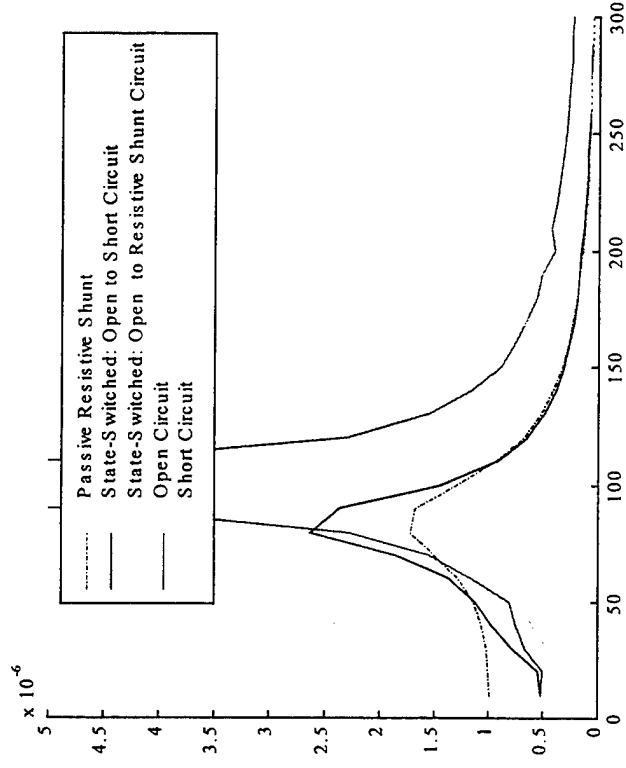
Bi-state semi-active control (switching
between open and short)

Bi-state semi-active control (switching
between open and resistive)



Example System: Piezoelectric

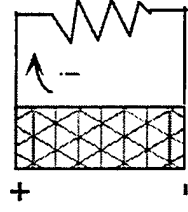
Response to harmonic excitation



Open circuit (no damping)
 Short circuit (no damping)
 Optimal Resistive circuit
 Bi-state semi-active control
 (switching between open and short)
 Bi-state semi-active control
 (switching between open and resistive)

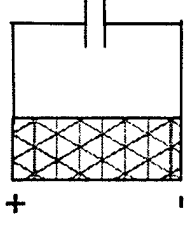
Energy Dissipation

Compare viscous damping to state-switched damping



Viscous Damping

$$V_{diss} = \pi c \omega X^2$$



State-Switched Stiffness

$$V_{diss} \cong \frac{E_{LOW} A}{l} X^2 \delta \cdot 2$$

Equivalent damping? : Viscous = 0.22

State-switched (all capacitive) = 0.12

State-switched (using resistive shunt) = 0.19

Conclusions

- In some applications, tuned variable dampers may provide the best dissipation (i.e. semi-active control is not needed except for secondary reasons such as energy savings)
- For a variable or bi-state stiffness actuator, semi-active control is necessary for dissipation, and can provide performance equal to or perhaps better than equivalent tuned damper

PENNS^TATE



EFFECTIVE LOSS FACTORS FOR SWITCH-SHUNTED PIEZO MATERIALS

George A. Lesieutre

17 August 1999

**ARO Smart Structures Workshop
State College, PA**

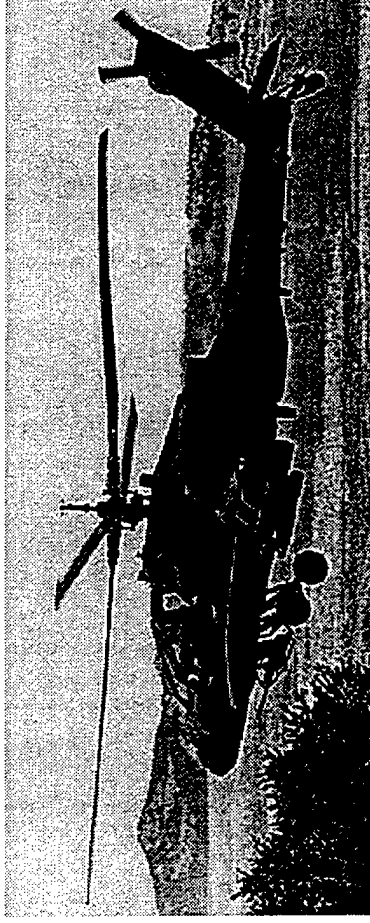
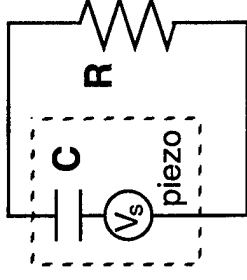
Department of Aerospace Engineering

Center for Acoustics and Vibration

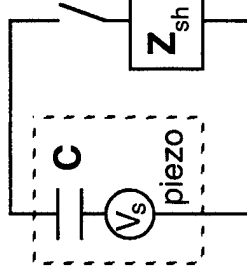
Motivation

- **Passive damping using shunted piezos**

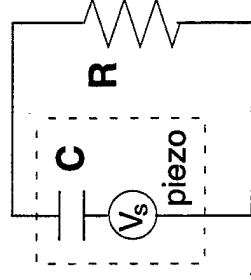
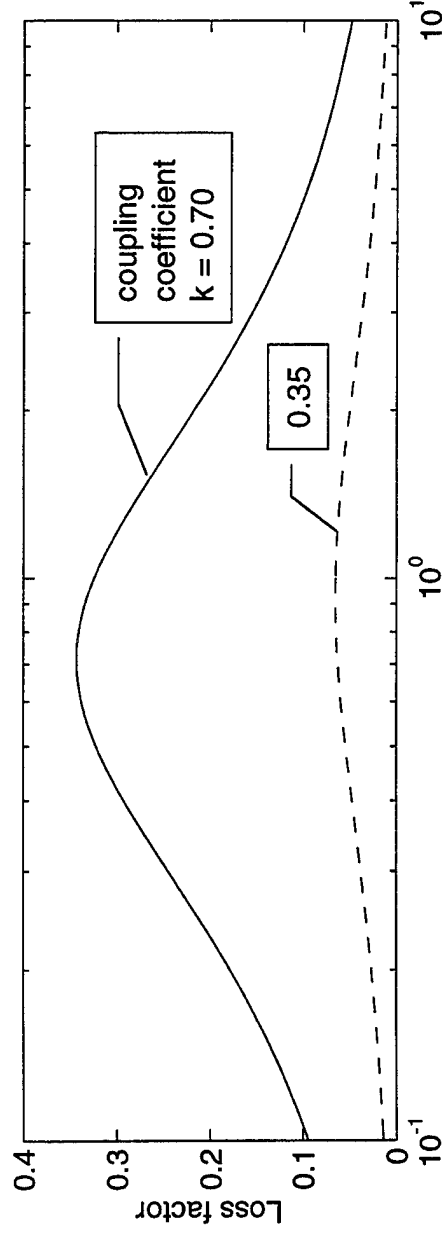
- Resistive shunting yields frequency-dependent damping



- Switch-shunting could provide broadband damping



Resistively-Shunted Damping



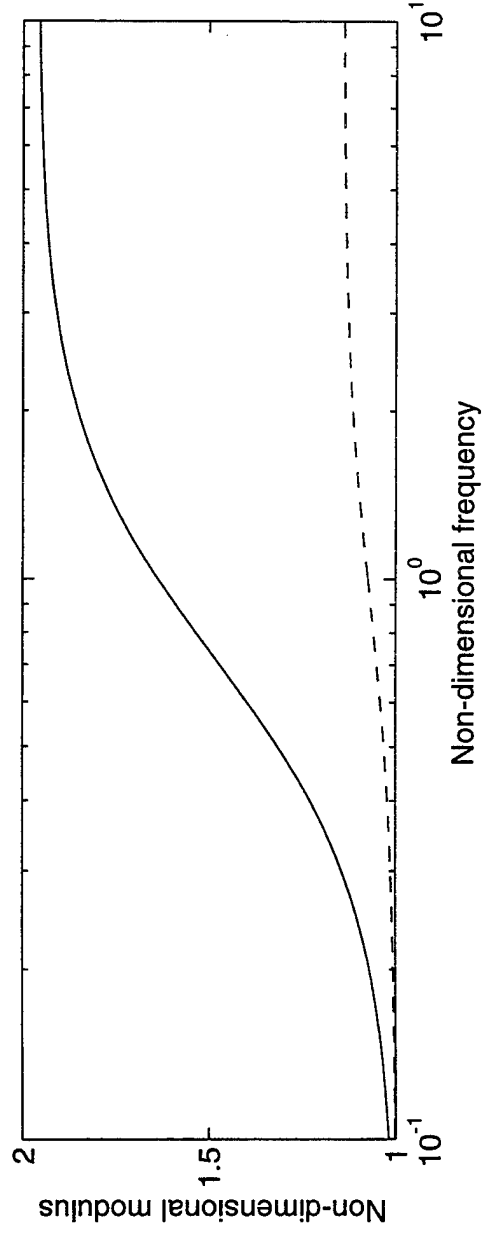
Loss factor

$$\eta(\omega) = \eta_{\max} \frac{2(\omega\tilde{\tau})}{1 + (\omega\tilde{\tau})^2}$$

$$\eta_{\max} = \frac{k^2}{2\sqrt{1-k^2}}$$

$$k = 0.35 \quad \eta = 0.070$$

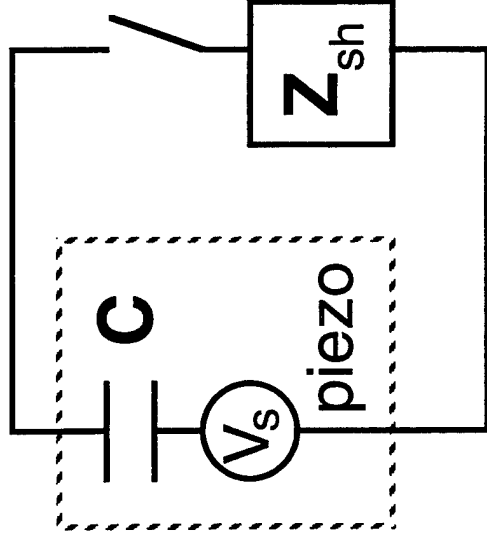
$$k = 0.70 \quad \eta = 0.343$$



Switch-Shunted Damping

- **CONCEPT:**

- Active switching between open-circuit and short-circuit condition

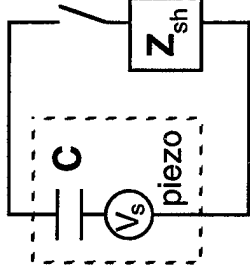


Related work:

- (1) "Semi-Passive Damping using Continuous Switching of a Piezo Device," Richard, Guyomar, Audigier, Ching, SPIE SS&M, 1999.
- (2) "Semi-Active Vibration Control with Piezoelectric Materials as Variable Stiffness Actuators," W.W. Clark, SPIE SS&M, 1999.
- (3) "State- Switching," G.D. Larson.
- (4) "Tunable Vibration Absorber using Capacitive Shunting," Lesieutre & Davis.

Switch-Shunted Damping

- HOW IT WORKS:
 - Switch is open; piezo is open-circuit
 - As piezo is strained, charge / voltage / electrical energy increases
 - When low-R switch is closed, electrical energy is dissipated
 - Non-zero shunt resistance
 - Impulsive force on structure
- ISSUE:
 - Switching strategy

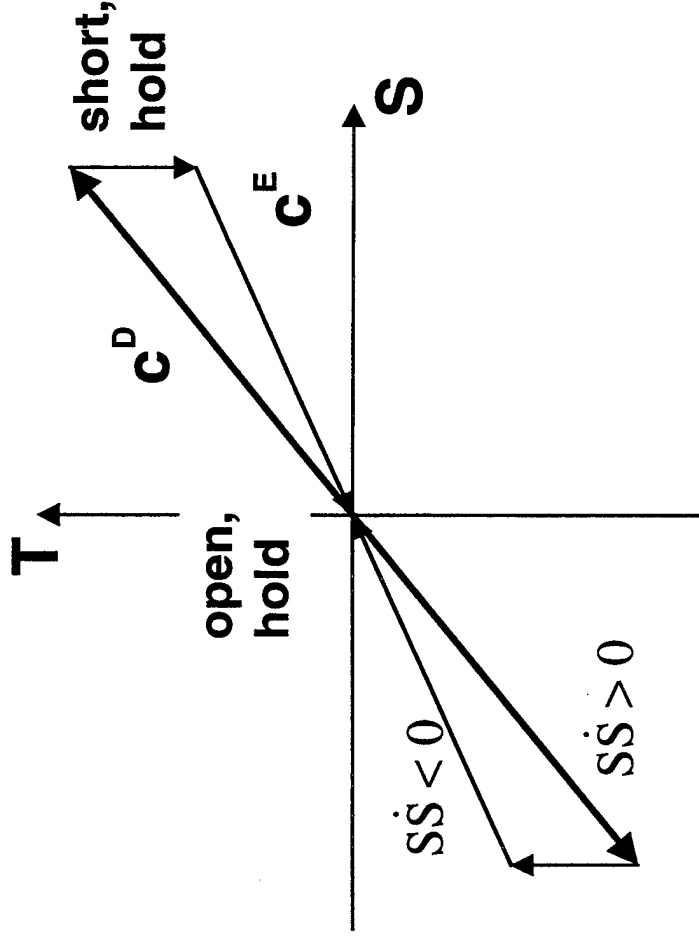


Approach

- **Consider energy dissipated in complete stress-strain cycle**
- **Consider alternate switching strategies**
 - **Clark**
 - **Richard, Guyomar, Audigier, Ching**
- **Estimate effective loss factors**

Switching Strategy 1 (Clark)

- Rate-direction-based, stiffness-motivated
 - Open-circuit when strain magnitude increasing
 - Short-circuit when strain magnitude decreasing



Loss Factor

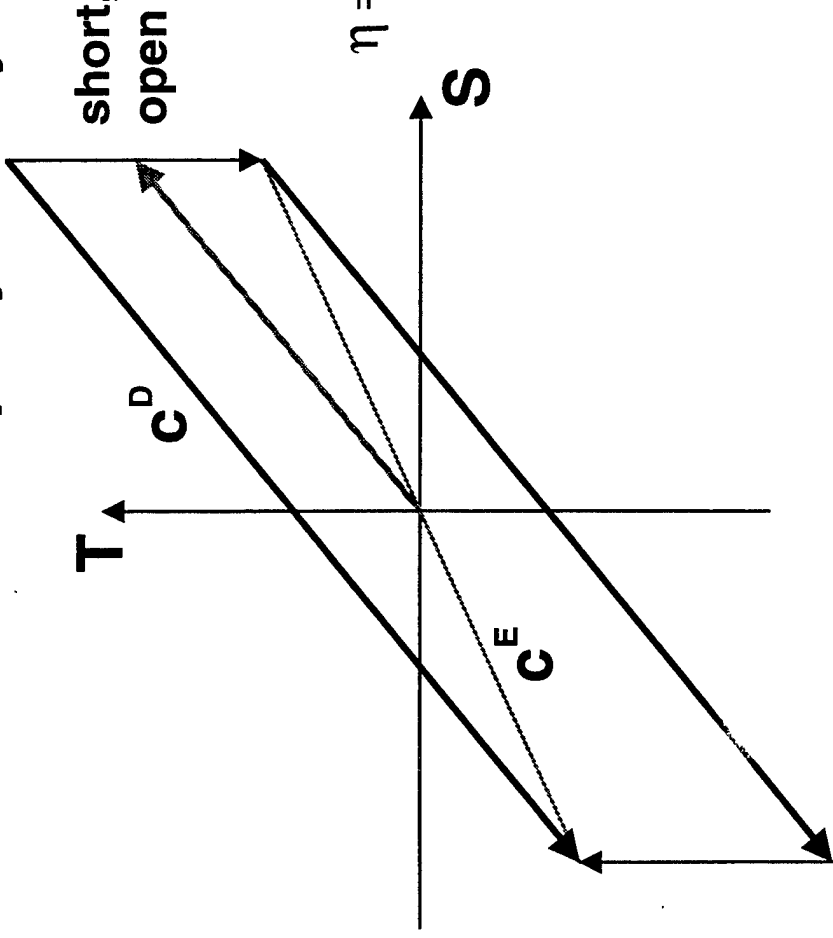
$$\eta = \frac{\Delta U}{2\pi U_D} = \frac{c^D - c^E}{2\pi c^D} k^2 = \frac{k^2}{2\pi}$$

$$k = 0.35 \quad \eta = 0.019$$

$$k = 0.70 \quad \eta = 0.078$$

Switching Strategy 2 (Richard, Guyomar, et al)

- Rate-reversal based
 - Nominally open-circuit
 - Short rapidly, briefly on reversal of strain rate



Loss Factor

$$\eta = \frac{\Delta U}{2\pi U_D} = \frac{2(c^D - c^E)}{2\pi \left(\frac{3}{2}c^D - c^E \right)} = \frac{2k^2}{\pi(2k^2 + 1)}$$

$$k = 0.35$$

$$\eta = 0.063$$

$$k = 0.70$$

$$\eta = 0.158$$

Comparison- Experimental

- Rate-Reversal Based (Richard, Guyomar, Audigier, Ching)

	<u>frequency</u>	<u>loss factor</u>
short-circuit	10.94	0.047
open-circuit	11.05	0.047

$\Delta f \Rightarrow$ coupling coefficient, $k = 0.141$

Switched 11.04 0.058

added damping: $0.058 - 0.047 = 0.011$

prediction based on k_{measured} : 0.012

Conclusions

- **Switched shunting can effectively provide broadband damping**
 - Switch between open and short circuit
 - Damping from shunt resistance and impulsive energy transfer to higher frequency motion
- **Switching strategy**
 - Open, shorting rapidly, briefly on rate reversal
 - Better than rate direction (stiffness) switching
- **Good agreement between theory and test**
- **Active, but very low power needed**

State-Switched Absorber/Damper for Semi-Active Structural Control

Kenneth A. Cunefare, Nader Sadegh, Gregg Larson. The Georgia Institute of Technology. The George W. Woodruff School of Mechanical Engineering. Atlanta, GA 30332-0405

Sergio De Rosa. Dipartimento di Progettazione Aeronautica, University of Naples "Federico II", Via Claudio 21 - 80125 NAPLES, IT, derosa@unina.it

The State-Switched Absorber (SSA) is a novel variation on the concept of a tuned vibration absorber or damper. A system that has the capability to make instantaneous changes in its mass, stiffness, or damping may be termed a state-switchable dynamical system. Such a system will display different dynamical responses dependent upon its current state. For example, state-switchable stiffness may be practically obtained through the control of the termination impedance of piezoelectric stiffness elements. The SSA is such a state-switchable device, and is capable of altering its stiffness state nearly instantaneously. The change in stiffness causes a change in the resonance frequencies of the system, thereby instantaneously 'retuning' the SSA to a new frequency.

The concept behind the SSA is to implement a dynamical system that is capable of instantaneously changing a system property, such as stiffness. A practical, feasible implementation of just such a state-switchable capability is through the use of a piezoelectric material as one element of a series spring in an otherwise normal absorber configuration. The stiffness of a piezoelectric is different when it is open circuited as compared to when it is short circuited. If the circuit impedance (open or shorted, or in-between) is controlled in some fashion, then the stiffness may be switched as fast as the control circuit can respond. If the switch occurs at a point of zero strain in the piezoceramic, then no voltage-induced mechanical transients are introduced in the piezoceramic element of the absorber. If switched at some other strain state, such transients would occur, and could lead to mechanical shock and strong mechanical transients. Theoretically, the stiffness state can be switched transient-free every half-cycle of oscillation of the absorber.

For energy based control of the SSA, the objective of the control law is to reduce the kinetic energy of the base subsystem as much as possible by switching the SSA state at the appropriate time. Consideration of the energy flow into the SSA yields a switching rule (for a 2-state SSA) of

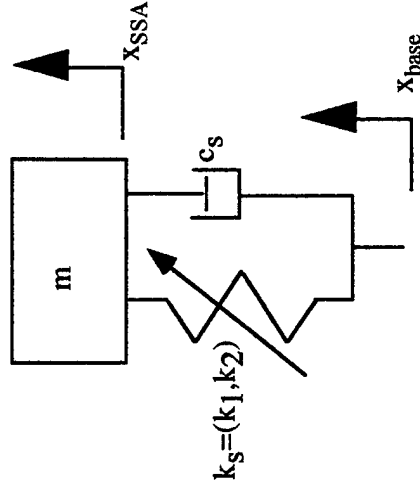
$$k_{SSA}^{next} = \begin{cases} k_{SSA1} & \text{if } v_{base}(v_{SSA} - v_{base}) > 0 \\ k_{SSA2} & \text{if } v_{base}(v_{SSA} - v_{base}) < 0 \\ k_{SSA} & \text{if } v_{base}(v_{SSA} - v_{base}) = 0 \end{cases}$$

where k_{SSA}^{next} is the next value of the SSA stiffness k_{SSA} . This control law is causal and requires no on-line modal analysis. Only estimates of the velocities of the base and SSA masses are needed. An interpretation of this control law is that when the force exerted by the SSA on the base mass opposes the base motion a stiffer spring (hence larger force) removes more energy from the base. On the other hand, a softer spring "pumps" less energy into the base during the periods that it helps the base motion.

At the present stage of SSA development, we have no method that permits us to predict *a priori* whether state-switching is effective as compared to classical passive devices, nor whether one candidate switching rule is better than another. We assess the efficacy of the performance through simulations, as presented in the following section.

Various simulations performed to date indicate potential performance gains in vibration reduction or damping through the use of an SSA as compared to classical passive vibration control devices. Some specific examples of potential SSA applications include the suppression of flight vehicle fuselage vibration levels at gear-box mounts, engine attachment points, automotive chassis structural vibration control, etc. In addition, the state-switching concept is not restricted to use as an absorber or damper. A state-switchable spring could be integrated into an equipment mount or strut. This might provide enhanced isolation of individual systems, or reduced transmission of vibration from one system into another.

State-Switched Device



- State dependent resonances

$$\omega_1 = \sqrt{k_1/m} \quad \omega_2 = \sqrt{k_2/m}$$

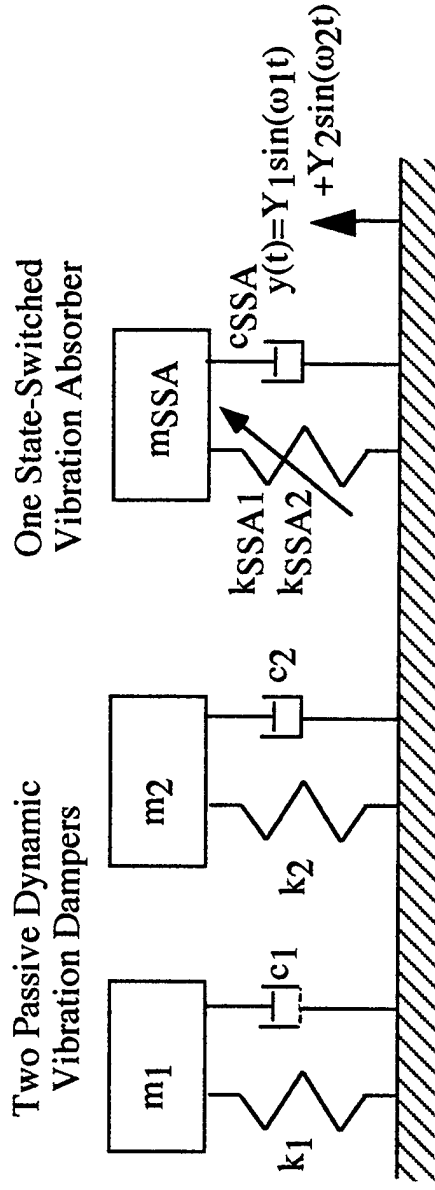
- Transient avoidance: switch at instant to conserve potential in spring: zero relative displacement

- State-Switched Absorber (SSA): device analogous to tuned vibration absorber, but multi-resonance capable

SSA vs. TVD Simulation

- **Objective: maximize work extracted from base**
- **Simulation is straightforward:**
 - Free- and forced vibration response between switches
 - System state at switch time is IC for the system in the next time interval
 - Relative displacement=0 is basic switch criteria
 - Test switch logic at each candidate switch time
- **Modal or time-marching techniques equally applicable**

TVD vs. SSA system



Forcing frequencies: $\omega_1 = 1.0$ r/s, $\omega_2 = 1.2$ r/s

TVD tuning frequencies: $\omega_{TVD1} = 1.0$ r/s, $\omega_{TVD2} = 1.2$ r/s

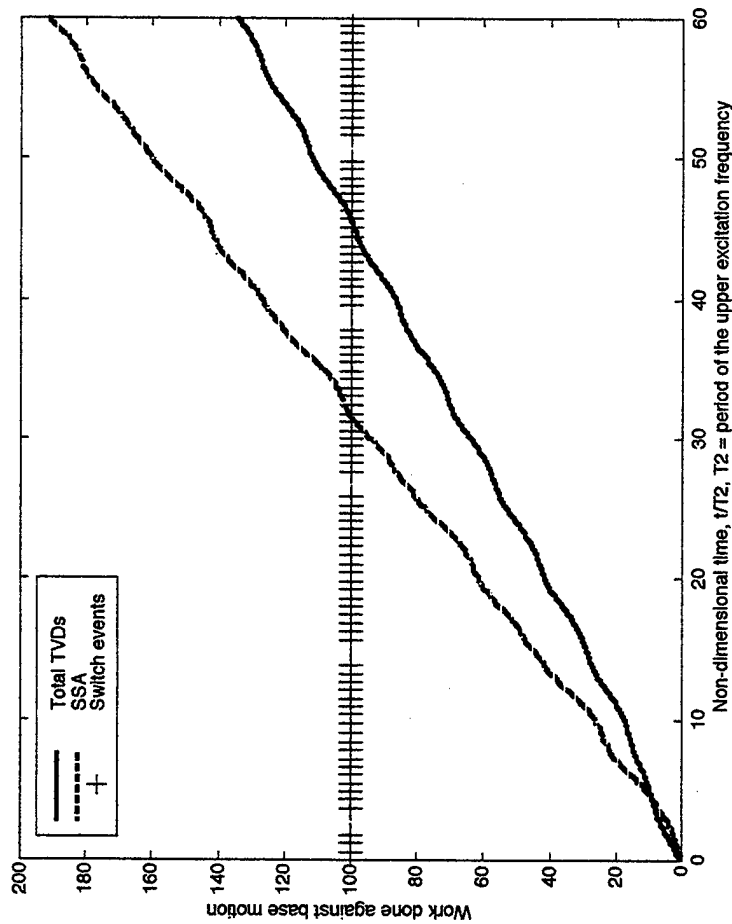
TVD mass: $m_1 = 1.0$ kg, $m_2 = 1.0$ kg

SSA tuning frequencies: $\omega_{SSA1} = 1.0$ r/s, $\omega_{SSA2} = 1.2$ r/s

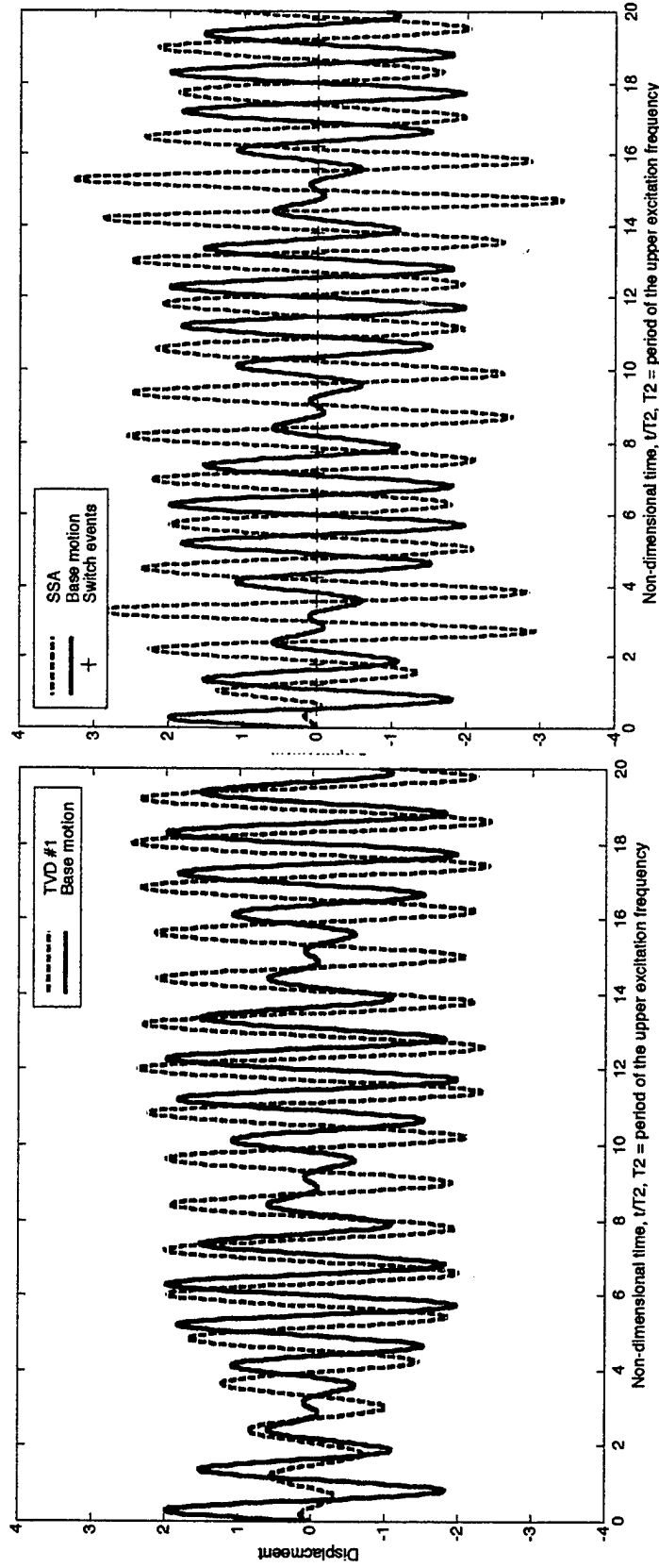
SSA mass: $m_{SSA} = 1.0$ kg

Performance comparison

- The single SSA, with 1/2 the mass of the TVDs, is able to extract more work from the base motion than both TVDs combined



TVD vs. SSA Time History



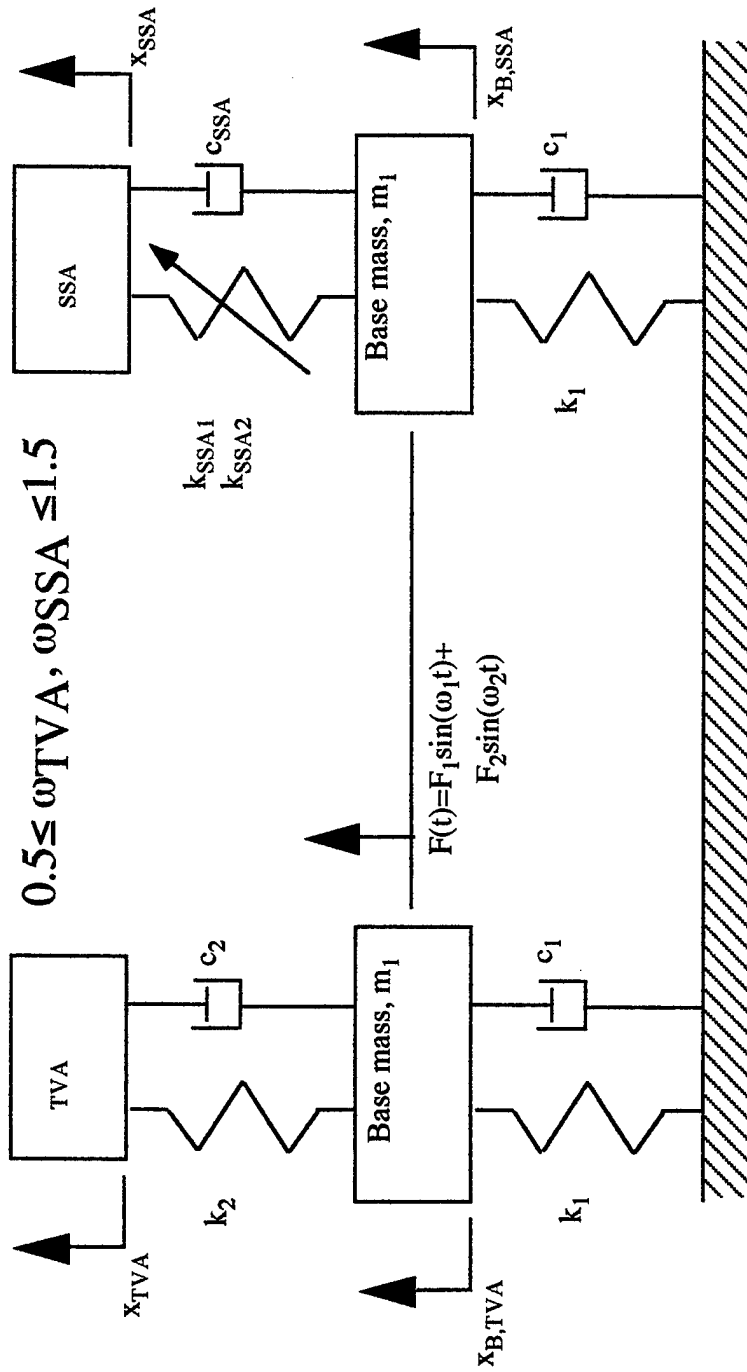
Action of the SSA is to keep the motion of the SSA's mass in opposition to the base motion.

19 July, 1999

*Integrated Acoustics Laboratory
 G. W. Woodruff School of Mechanical Engineering*

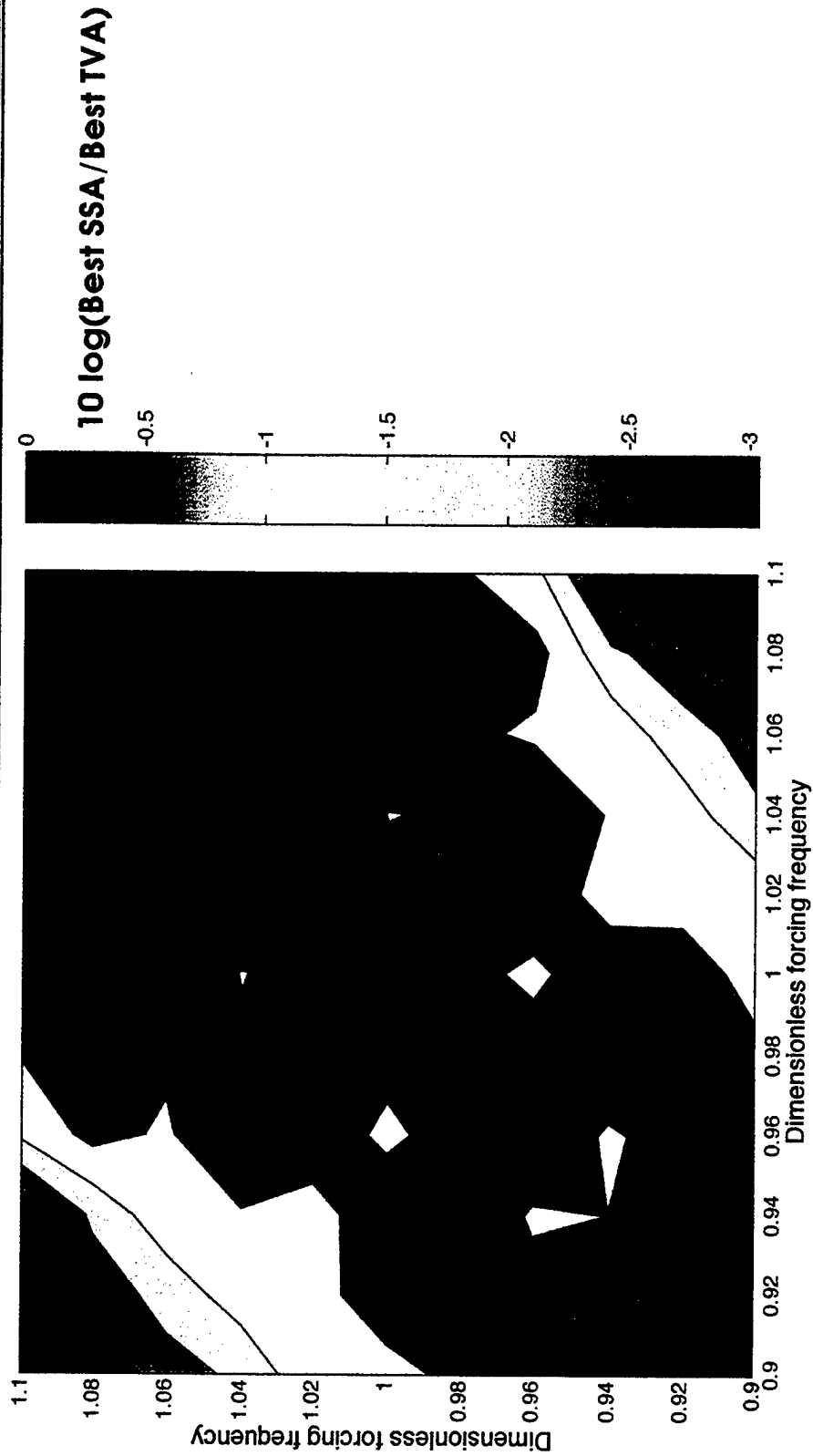
SSA vs. TVA system

Base resonance=1.0 r/s
 Mass ratio=0.1, Damping=5%
 $0.75 \leq \omega_1, \omega_2 \leq 1.25$



$0.5 \leq \omega_{TVA}, \omega_{SSA} \leq 1.5$

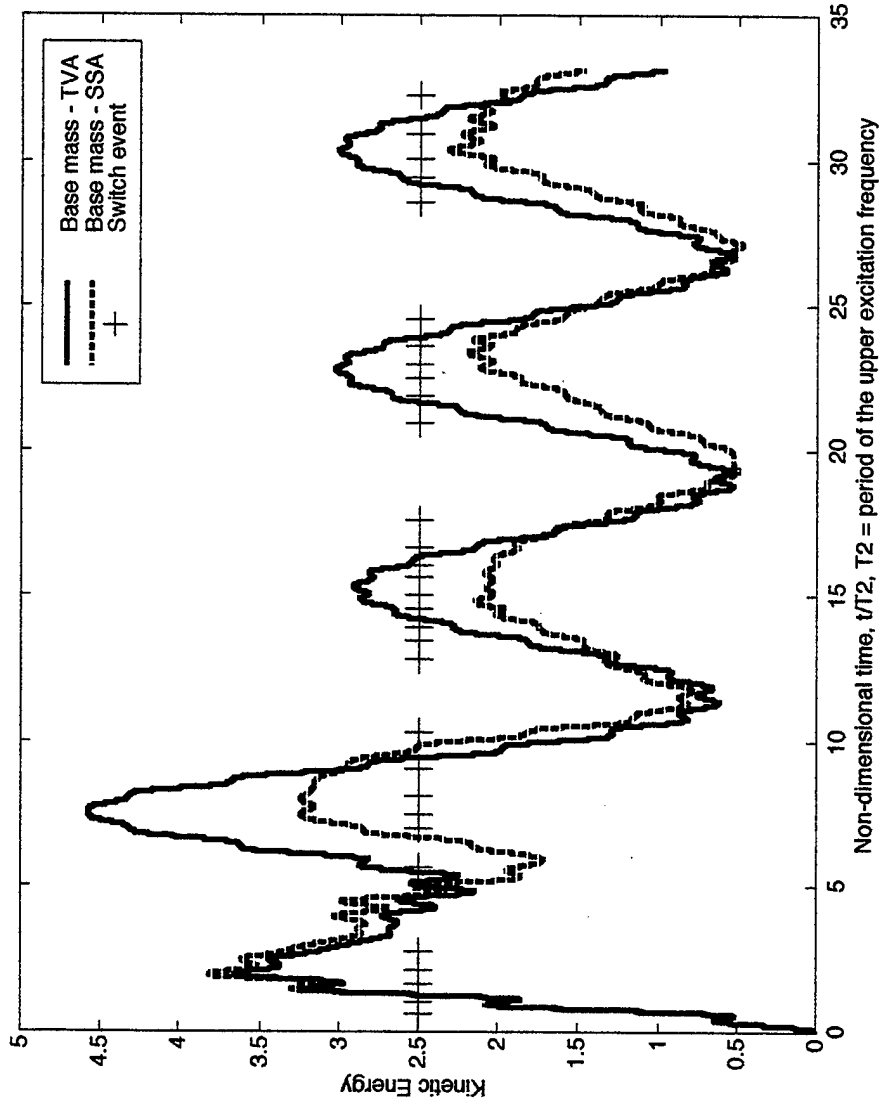
SSA vs. TVA performance



19 July, 1999

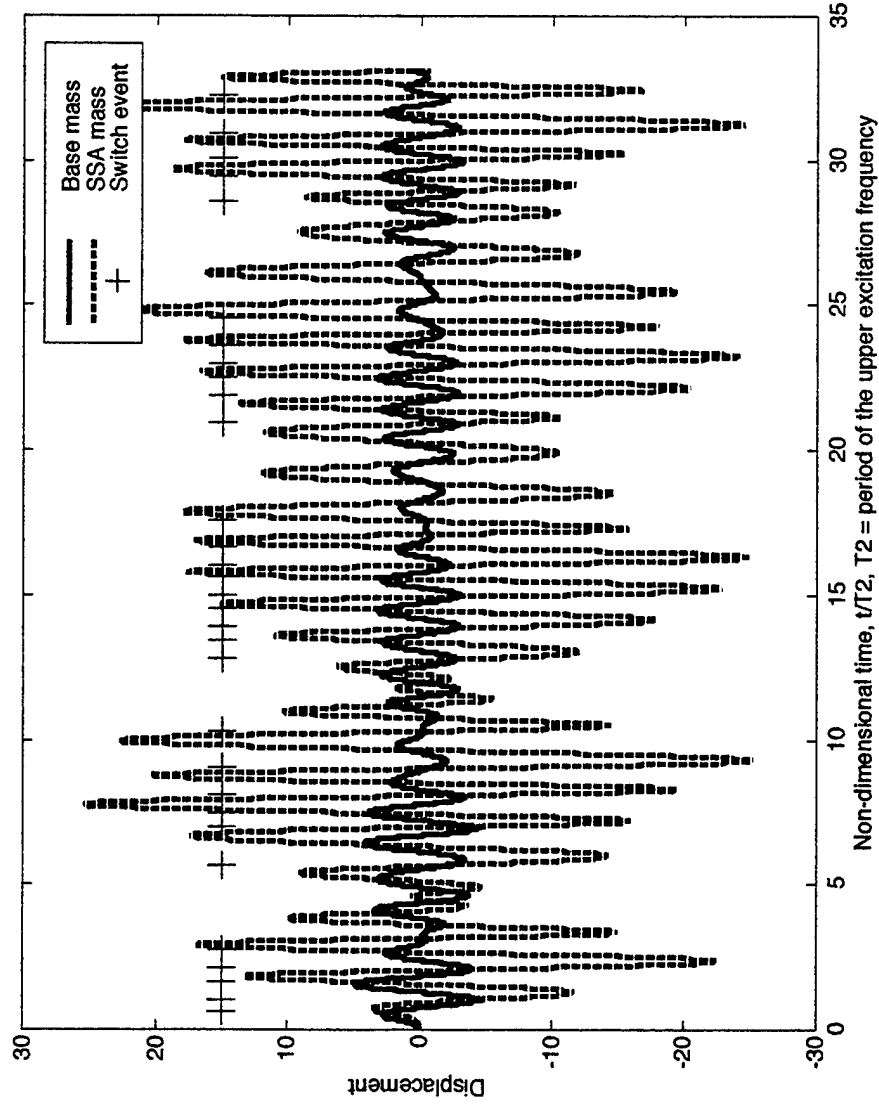
*Integrated Acoustics Laboratory
G. W. Woodruff School of Mechanical Engineering*

Example Energy TVA vs. SSA



- Forcing frequencies:
 $\omega_{f1}/\omega_0 = 0.92$
 $\omega_{f2}/\omega_0 = 1.06$
- Optimal SSA tuning parameters:
 $\omega_{SSA1}/\omega_0 = 0.84$
 $\omega_{SSA2}/\omega_0 = 1.16$

Example Time Response



- Forcing frequencies:
 $\omega_1/\omega_0 = 0.92$
 $\omega_2/\omega_0 = 1.06$
- Optimal SSA tuning parameters:
 $\omega_{SSA1}/\omega_0 = 0.84$
 $\omega_{SSA2}/\omega_0 = 1.16$

EXPERIMENTAL CHARACTERIZATION AND MODELING OF Ni-Ti SHAPE MEMORY ALLOY (SMA) WIRES

Harsha Prahlad¹

Inderjit Chopra²

Monica Vohra³

Alfred Gessow Rotorcraft Center
University of Maryland, College Park, MD 20740

Background and Significance :

Shape Memory Alloys (SMAs) are high stroke 'smart' material actuators that have a number of unique properties such as high stroke, high force, tunable stiffness and damping properties that make it an attractive prospect for 'smart' aerospace structures. However, an extensive characterization of the material is required for accurate prediction of performance. Although the quasi-static characteristics of the material have been modeled, the effects of strain rates, history and loading pattern are a subject of active research.

Research Objectives:

1. To experimentally investigate the stress-strain-temperature behavior of Shape Memory Alloys (SMAs)
2. To model the influences of strain rate and initial state on the state of the material in terms of a simple phenomenological model.

Approach:

1. Determine the factors affecting the quasi-static and dynamic behavior of SMAs
2. Determining the effect of strain rate, loading path, loading pattern and history on the final state of the SMA
3. Comparison of existing models for SMAs with the experimental data and point out areas of significant variation
4. Modeling the variation of the behavior of the SMA incorporating the effect of strain rates

Accomplishments:

1. The quasisteady stress-strain-temperature behavior of the alloy was determined and existing theory validated with experimental results. A tensile test machine and several benchtop machines were used to apply quasisteady loading. The experimental results were compared with four existing theories for quasi-steady behavior – Tanaka, Liang and Rogers, Brinson and Boyd and Lagoudas models. Constants required for the models were obtained from the experiments. It was shown that all the models predicted quasi-steady behavior satisfactorily.
2. Dynamic Testing of SMAs were carried out to determine and quantify properties such as effect of strain rate, Temperature rates, creep, fatigue, impact loading and history on the actuation and damping hysteresis properties of SMAs. Results showed a significant deviation in the behavior of the alloy from the quasi-steady case and showed moderate to poor correlation with the quasi-steady models, underlying the need for further testing and modeling.
3. A parameters based phenomenological model is presented incorporating some of these effects on the behavior of SMAs. The model prescribes a stress-strain-temperature surface for the SMA. The variations of this surface with loading rates is presented, and compared with experimental data.

¹ Graduate Research Assistant

² Professor and Director, to whom correspondence may be addressed, chopra@eng.umd.edu

³ Undergraduate Research Assistant



ALFRED GESSOW ROTORCRAFT CENTER
UNIVERSITY OF MARYLAND



Experimental Characterization and Modeling of Ni-Ti Shape Memory Alloy (SMA) wires

Harsha Prahlad
Grad. Research Asst.

Monica Vohra
Undergrad. Research Asst.

Inderjit Chopra
Professor and Director

Presented at ARO's Workshop
on Smart Structures and Materials, Pennsylvania State University,
August 16-18, 1999



Motivation



- To experimentally investigate the stress-strain-temperature behavior
- To determine the influence of loading pattern, loading rates and loading path on the state of the material
- To examine the factors affecting dynamic characterization of SMA
- To formulate a parameter-based phenomenological model describing SMA behavior



Shape Memory Alloys - Application



Mechanical (Vibration Control, Robotics, Damping Augmentation)

Aerospace (Flap Actuators, Adaptive Composites)

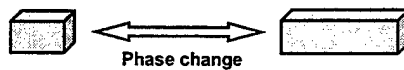
Shape Memory Alloys

Medical (Valve Actuation, Angioplasty)

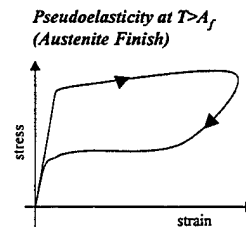
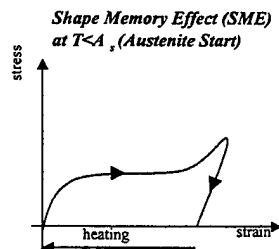
Civil (Structural Control)



Shape Memory Alloys - Mechanism

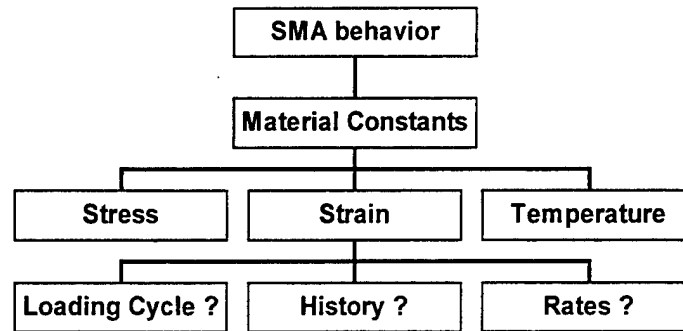


- 'Shape Memory': reversible phase transformation between two crystallographic states
- 2 different mechanisms of recovering large strains :





Factors Affecting SMA Behavior



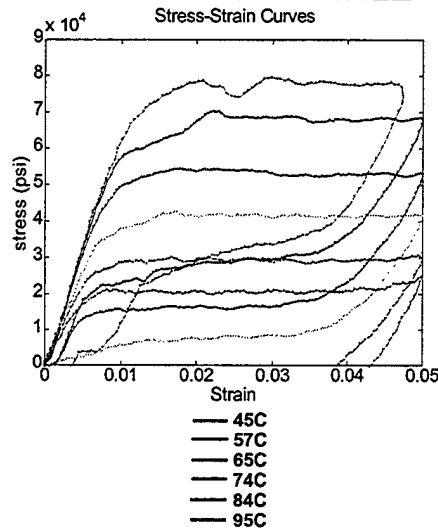
Constitutive Models



- Tanaka Model:** $\sigma - \sigma_o = E(\xi)(\varepsilon - \varepsilon_o) + \Theta(T - T_o) + \Omega(\xi)(\xi - \xi_o)$
 Total Stress Mechanical Stress Thermoelastic Stress Stress Due to Phase Trans.
- Brinson Model :** $\sigma - \sigma_o = E(\xi)\varepsilon - E(\xi)\varepsilon_o + \Theta(T - T_o) + \Omega(\xi)\xi_s - \Omega(\xi_o)\xi_{so}$
- Boyd and Lagoudas Model:** $\sigma - \sigma_o = E(\xi) * (\varepsilon - \varepsilon^i - \alpha \Delta T)$
- Description of martensite volume fraction:**
 - Tanaka: $\xi = \exp(\sigma, T)$ Exponential model
 - Liang and Rogers: $\xi = \cos(\sigma, T)$ Cosine model
 - Brinson: $\xi = \cos(\sigma, T)$ Modified cosine model, separation of martensite variables ($\xi = \xi_s + \xi_T$)
 - Boyd and Lagoudas: $\xi = \xi(\sigma, T)$ Thermodynamic model



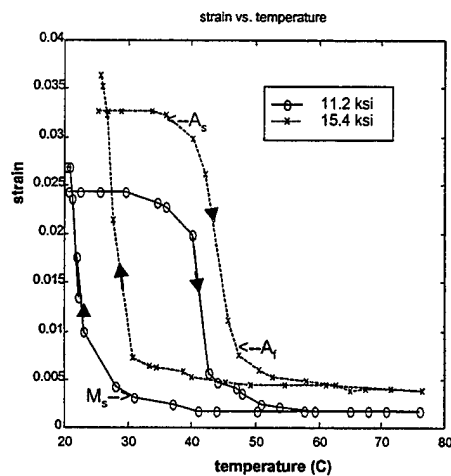
Stress-Strain Characteristics



- ♦ Show Shape Memory and Pseudoelastic effects
- ♦ Critical stress for Martensitic transformation increases with temperature for $T < A_s$
- ♦ Critical transformation stresses for various temperature are obtained from inflection points



Strain-Temperature Behavior

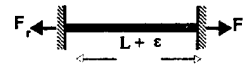
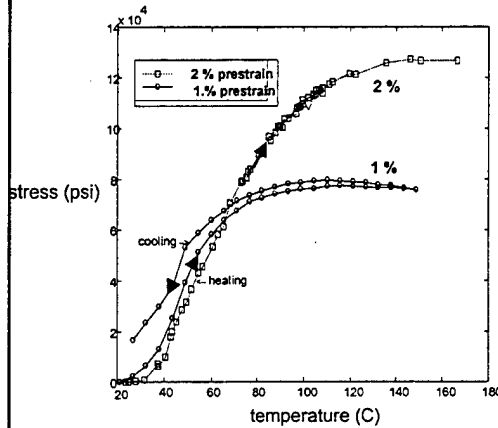


- ♦ Transformation temperatures increase with load
- ♦ Direct indication of the critical transformation temperatures

A_s =Austenite Start, A_f =Austenite Finish
 M_s =Martensite Start, M_f =Martensite Finish



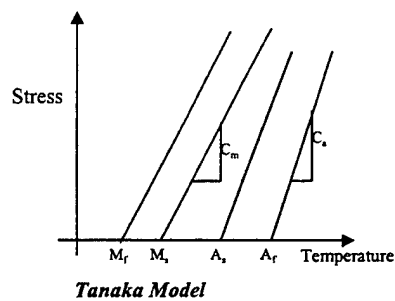
Constrained Recovery



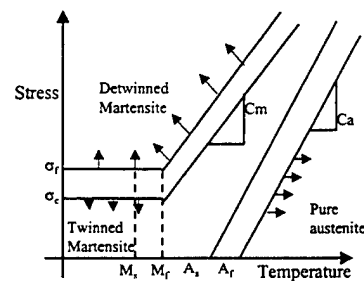
- Very large forces developed by restraining the wire
- Final stress increases with pre-strain
- Some unrecoverable plastic deformation



Critical Stress-Temperature Diagram



Tanaka Model

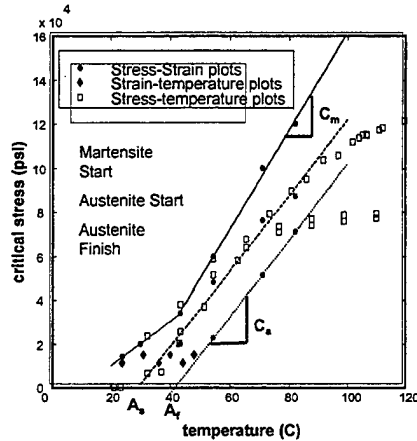


Brinson's model

- ▲ Critical points of stress and temperature for a transformation are obtained from the previous data
- ▲ Material Constants for use in the models determined from this plot



Experimental Critical Points



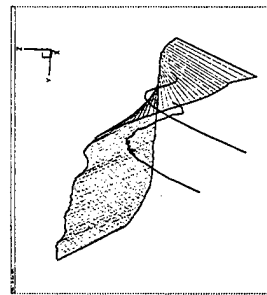
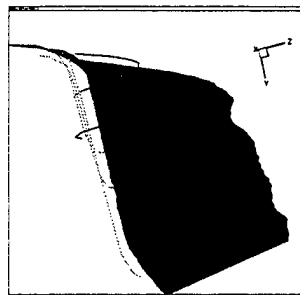
- Critical points obtained from all the tests show good agreement

- Points from recovery stress-temperature plot lie mostly on the A_s and M_s critical curves

$M_s=21\text{ C}$ $A_s=29.4\text{ C}$ $A_f=42\text{ C}$
 $C_m=2080\text{ psi/C}$ ($1.43 \times 10^7\text{ N/m}^2\text{C}$)
 $C_a=1666.6\text{ psi/C}$ (1.14×10^7)



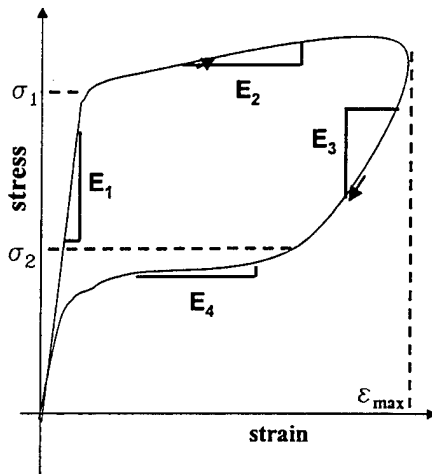
Consolidation of Data



- Surface obtained from stress-strain plots at different temperatures
- Curves from strain-temperature and stress-temperature experiments follow the same general trends, but do not coincide with this surface
- State depends on path, especially during transformation - Variation of the order of 10-15%



Model Parameters



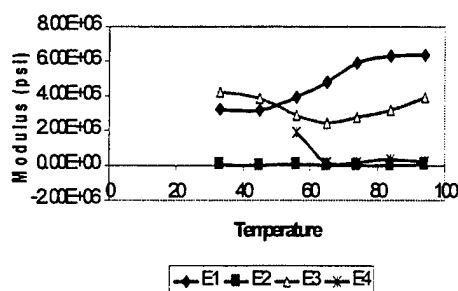
- Parameters :
 E_1, E_2, E_3, E_4 (linear fits)
 σ_1, σ_2
- Function of
temperature T
strain ϵ
strain rate ϵ'
initial martensitic volume
fraction ξ_0



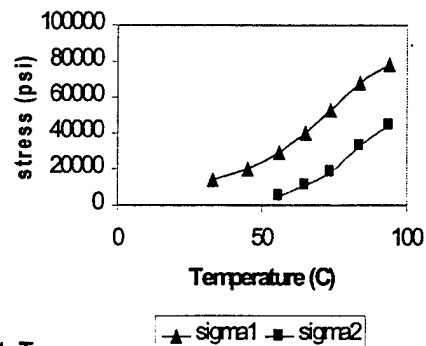
Parameter Variation



Variation of Moduli



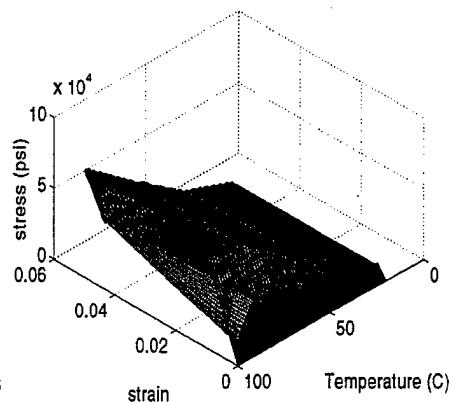
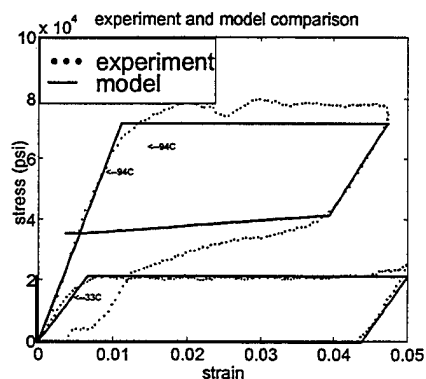
Critical Stresses



Straight Line fits for $E_1, E_4, \sigma_1, \sigma_2$ wrt. T
Quadratic fit for E_3
 $E_2 \sim 0$



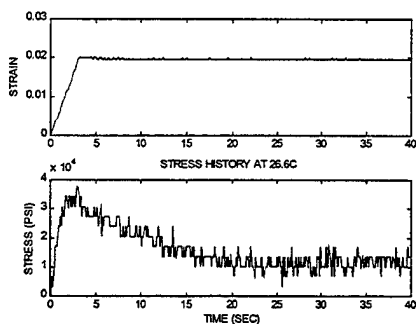
Quasi-static Behavior



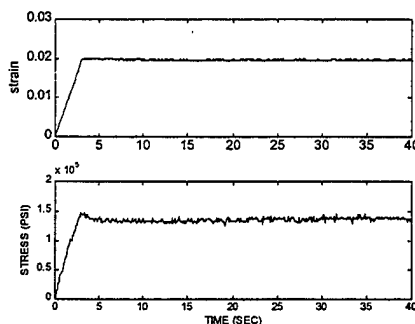
Material state is a point on the surface generated by the model



Effect of Loading Rates Stress-Strain



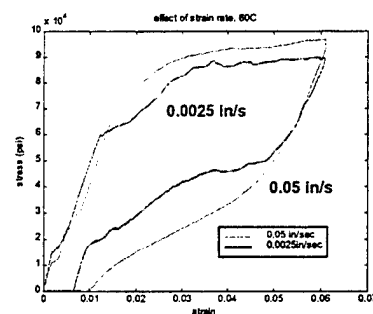
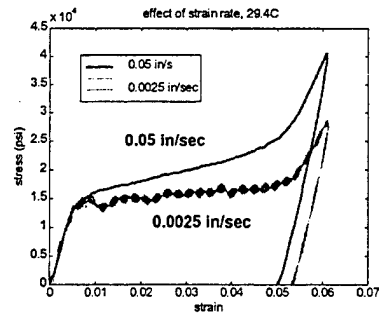
'Stress-Relaxation' at low temperature (26.6C)



No evidence at high temperature (71.1C) : Stress is constant



Effect of Strain Rate



- *Transformation stresses increase with strain rate drastically (upto 30% change in stresses)
- *Likely to be decisive in determining dynamic properties



Conclusions



- ① Critical points of start and end of transformations relatively unique and well defined for quasi-static loading
- ② Dynamic characteristic of the wire likely to vary significantly from the static characteristics
- ③ A parameter-based phenomenological model incorporating some of these effects involving first order fits is proposed
- ④ The model determines key parameters controlling the state of the material, and identifies extent of variation of these parameters with different variables.

Mechanical Characterization of Shape Memory Alloy Composites for Designing Smart Structures

Hugh A. Bruck and Charles L. Moore
Department of Mechanical Engineering
A. James Clark School of Engineering
University of Maryland
College Park, MD 20742

Project Summary

Shape Memory Alloys (SMAs) are being embedded in smart structures for sensing and actuation. The resulting structure is a composite material that can possess a heterogeneous architecture, requiring a system-based approach to optimize its design. In order to develop this approach, it is necessary to determine appropriate constitutive models that can be utilized in Finite Element Analyses for designing heterogeneous smart structures. In this investigation, SMA wire-reinforced fiberglass and epoxy composites are fabricated to determine the relationship between the mechanical response of the composite and the composition of SMA wire reinforcement. A modified linear Rule-of-Mixtures (ROM) formulation is proposed for predicting the mechanical behavior of SMA composites. This simple, uniaxial constitutive model provides a reasonable prediction of SMA composite mechanical behavior, even when the displacement range far exceeded the limit for monolithic SMA wire, and is computationally efficient enough to use with Finite Element Analyses.



Mechanical Characterization of SMA Composites for Designing Smart Structures

Hugh A. Bruck
Charles L. Moore

Department of Mechanical Engineering
University of Maryland
College Park, MD

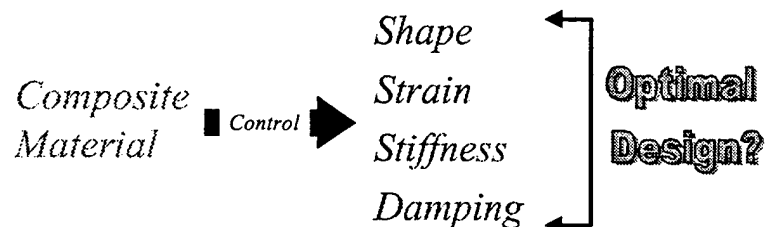
ARO Workshop on Smart Structures

08/17/99



Motivation

- Integration of Shape Memory Alloy (SMA) into structures for sensing and actuation



ARO Workshop on Smart Structures

08/17/99



Design Objectives

- ① *Optimize SMA properties*
- ② *Process composites*
- ③ *Optimize composite microstructure*
- ④ *Optimize architecture of smart structure*
- ⑤ *Fabricate smart structure*
- ⑥ *Verify system performance*

ARO Workshop on Smart Structures

08/17/99



Design Needs

- Fabricate SMA composites and smart structures
- Physical characterization and modeling of SMAs and SMA composites
- System characterization and modeling of smart structures



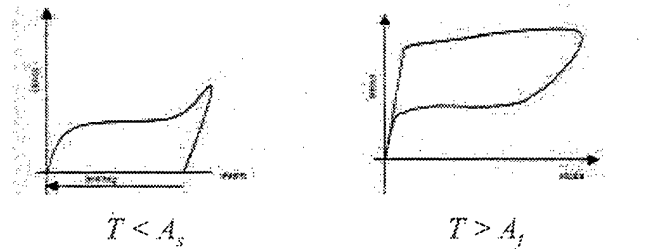
*Systems Design
Approach!!!*

ARO Workshop on Smart Structures

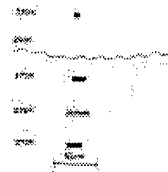
08/17/99



Shape Memory Effect



Two-way
Shape Memory
Effect



ARO Workshop on Smart Structures

08/17/99



SMA Constitutive Models

- Tanaka - Helmholtz free energy
- Liang and Rogers - cosine description of phases
- Brinson - non-constant coefficients, sum of temperature and stress-induced phases
- Boyd and Lagoudis - Gibbs free energy

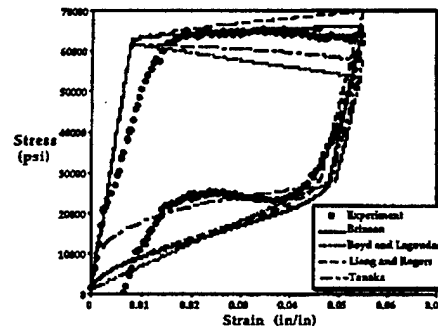
$$(\sigma - \sigma_o) = E(\xi)(\epsilon - \epsilon_o) + \theta(T - T_o) + \Omega(\xi)(\xi - \xi_o)$$

ARO Workshop on Smart Structures

08/17/99



Experimental Comparison with Models

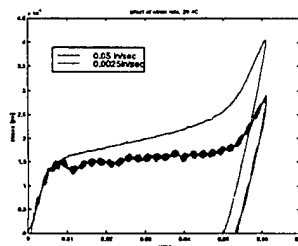


ARO Workshop on Smart Structures

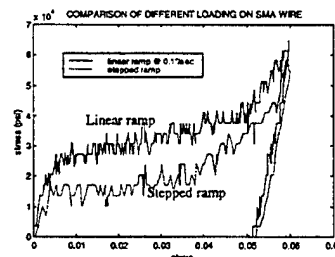
08/17/99



Strain Rate and Loading Path Dependence



Strain rate



Loading path

ARO Workshop on Smart Structures

08/17/99

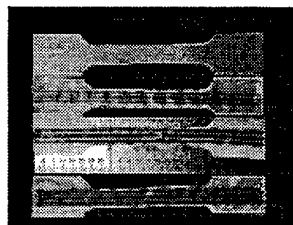


SMA Wire Reinforced GFRPs



• Improve:

- * *strength*
- * *fracture toughness*
- * *buckling resistance*
- * *shape control*

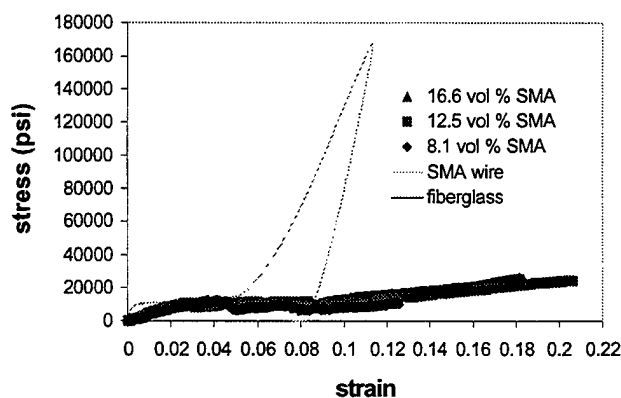


ARO Workshop on Smart Structures

08/17/99



Mechanical Behavior of SMA Wire Reinforced GFRPs

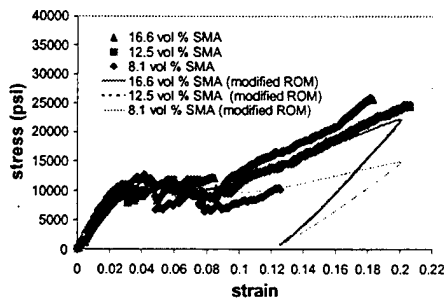


ARO Workshop on Smart Structures

08/17/99



Constitutive Model for SMA Wire Reinforced GFRPs



$$\sigma_{\text{composite}} = V_{\text{matrix}} \sigma_{\text{matrix}}(\epsilon_{\text{composite}}) + V_{\text{fiber}} \sigma_{\text{fiber}}(\epsilon_{\text{composite}})$$

$$\sigma_{\text{matrix}} = E_{\text{matrix}} \epsilon_{\text{composite}} \exp(-\epsilon_{\text{composite}}/a)$$

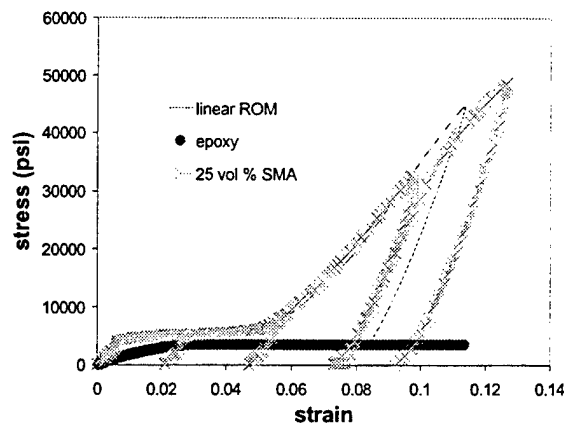
$$\epsilon_{\text{composite}} = \epsilon \exp(b\epsilon_{\text{fiber}})$$

ARO Workshop on Smart Structures

08/17/99



SMA Wire Reinforced Epoxy

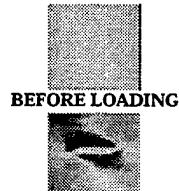


ARO Workshop on Smart Structures

08/17/99



Digital Image Correlation



BEFORE LOADING

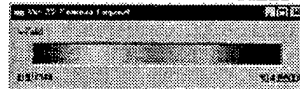


AFTER LOADING

Image of double cracked tensile specimens before and after loading

DIC analysis as performed on the above images

U-DISPLACEMENT FIELD V-DISPLACEMENT FIELD



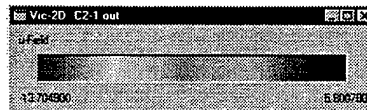
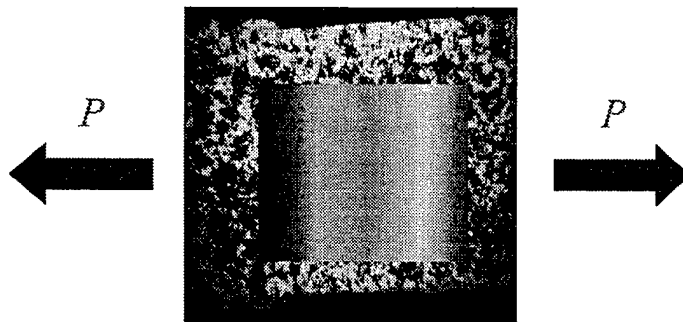
Contour legend as generated for these images

ARO Workshop on Smart Structures

08/17/99



DIC of SMA Composites



ARO Workshop on Smart Structures

08/17/99



Summary

- Brinson model most accurate for SMAs
- Mechanical behavior of monolithic SMAs is strain rate and loading path dependent
- Composites fabricated by embedding SMA wires in fiberglass
- Mechanical behavior of SMA composites can be modeled using simple ROM formulations

ARO Workshop on Smart Structures

08/17/99



Use of SMA Pseudoelastic Hysteresis for Augmentation of Passive Structural Damping

Dr. Farhan Gandhi

Assistant Professor, Aerospace Engineering

**David Wolons, Brendon Malovrh,
and Gautier Chapuis**
Graduate Research Assistants

Rotorcraft Center of Excellence
Pennsylvania State University

Presented at the fourth ARO Workshop on Smart Structures,
Pennsylvania State University, August 16-18, 1999

Background



Shape Memory Alloys are a class of metal alloys that undergo reversible phase transformations through the application of stress or temperature.

- The majority of work has been focused on using the Shape Memory Effect, or Constrained Recovery Effect, to produce high-force (low bandwidth) actuators

Above A_f pseudoelastic stress/strain hysteresis seen in SMAs can be exploited for passive damping of structural vibrations

- Energy dissipation per unit volume (per cycle) is very large
- Can be electrically heated to avoid low temp. performance loss
- This application has received relatively little attention

Background

PENNSTATE



Before SMAs may be widely used as dampers, several important issues must be addressed:

1) In-Depth Material Characterization

(David Wolons, 1/97-12/97)

- Effects of temperature, static strain offset, and strain amplitude at various frequencies

2) Model Development for Incorporation into Dynamic and Aeroelastic Analyses (Brendon Malovrh, 8/98-present)

- Mechanism-based models similar to those used for elastomeric materials and magnetorheological fluids

3) Incorporation of SMAs into Structures for Damping Augmentation (Gautier Chapuis, 8/98-present)

- Finite element analysis, bench-top validation, and optimum design studies

Material Characterization (Background)

PENNSTATE



Previous experimental studies primarily examined SMA behavior at a quasi-static condition, or very low excitation frequency.

- Lin, Tobushi, Tanaka, et al (1996)
- Kawaguchi, Ohashi, Tobushi (1991)
- Ortin (1991)
- others...

**Unsuitable
for Vibration
Damping
Applications**

At Penn State, SMA pseudoelastic hysteretic behavior was experimentally characterized up to an excitation frequency of 10 Hz. Over this frequency range a comprehensive data set was obtained to characterize material behavior at different static strain offsets, strain amplitudes, and temperatures.

Material Characterization (Complex Modulus)

PENNSTATE



The Complex Modulus method was used for characterization of SMA damping behavior

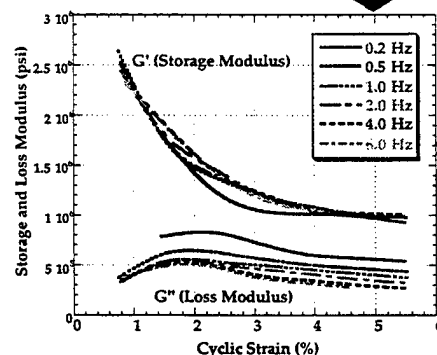
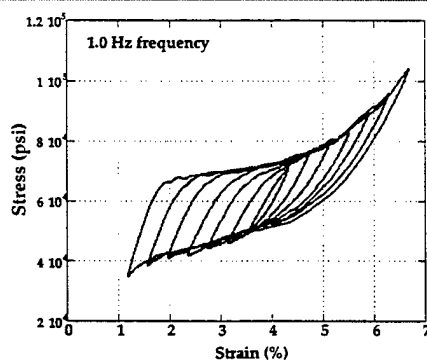
$$\sigma = [G'(\omega) + jG''(\omega)]\epsilon$$

- Storage modulus, G' , representative of stiffness
- Loss modulus, G'' , representative of damping

The use of the complex moduli provides a quick understanding of the variation in stiffness and damping properties with frequency, static offset, strain amplitude and temperature.

Material Characterization (Strain Amplitude Dependence)

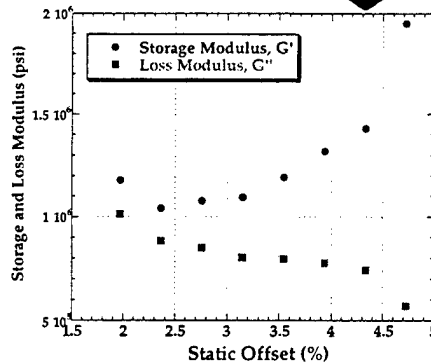
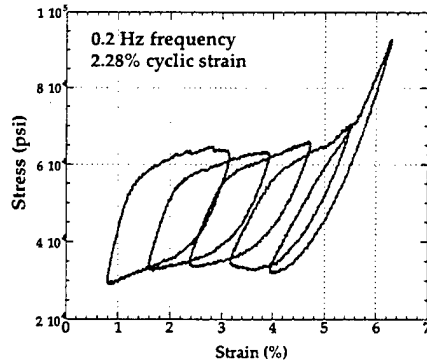
PENNSTATE



- G' decreases sharply (SMA softens) as strain amplitude increases
- Hysteresis cycle slope correspondingly decreases
- G'' attains a maximum value, and then decreases for larger strain amplitudes

Material Characterization (Static Offset Dependence)

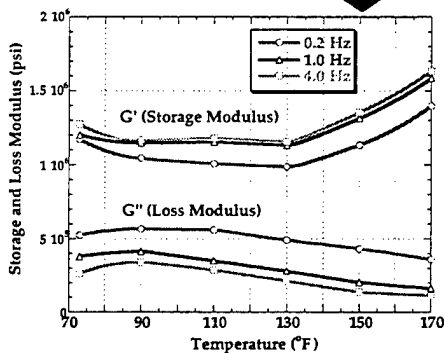
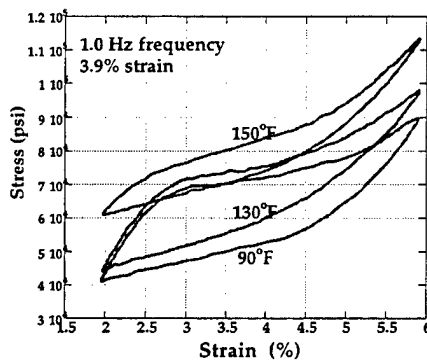
PENNSTATE



- G' first decreases, but then increases with increasing offset
- G' at its lowest when hysteresis cycle entirely within the pseudoelastic range
- G'' generally decreases as static offset increases
- This corresponds to the hysteresis cycle narrowing, and eventually exiting the pseudoelastic range

Material Characterization (Temperature Dependence)

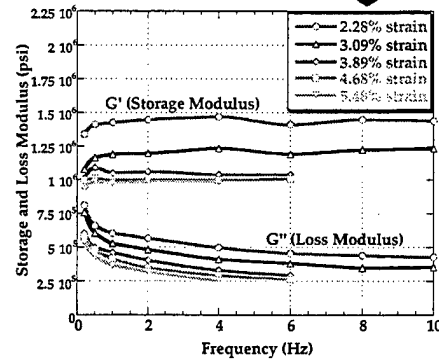
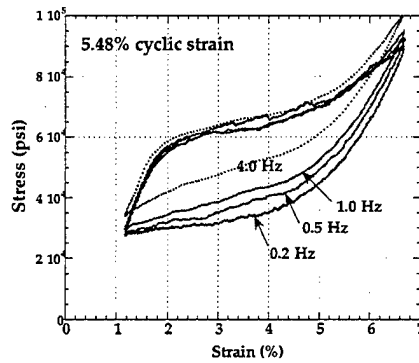
PENNSTATE



- As expected, hysteresis cycle shifts to higher stress levels as temperature increases
- Outside ideal temperature window, G' increases, G'' decreases - thus SMA becomes stiffer and dissipates less energy
- Correspondingly, an increase in peak-to-peak stresses, and a narrowing of the hysteresis cycles is observed

Material Characterization (Frequency Dependence)

PENNSTATE



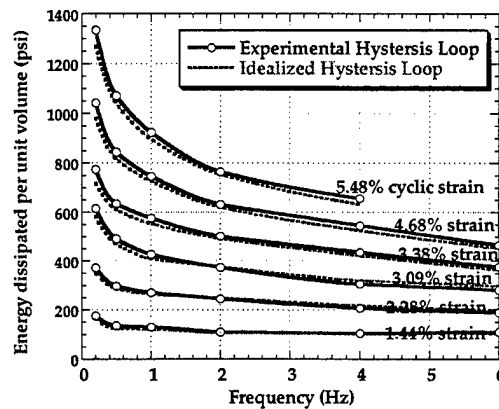
- G'' decreases as frequency increases, G' not very sensitive
- Decrease in G'' results primarily from the reverse transformation commencing at a higher stress level
- G'' drops sharply at low frequencies (0-2 Hz), less change thereafter
- Using quasi-static properties would overpredict damping

Material Characterization (Complex Modulus)

PENNSTATE



- Complex Modulus gives good fundamental understanding of material behavior
- Easily introduced into structural analyses
- Closely matches experimental energy dissipation data

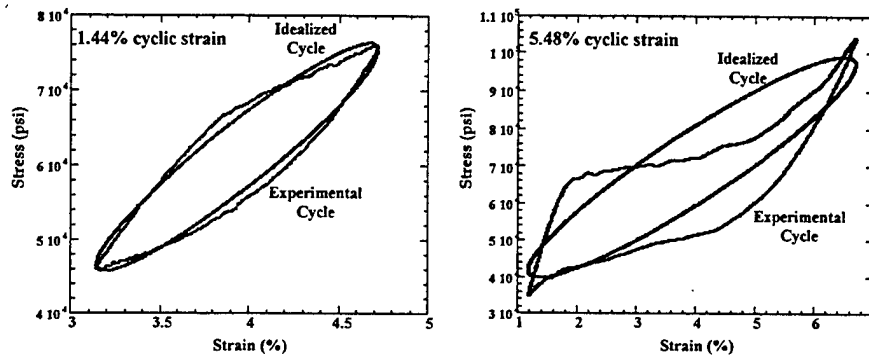


Material Characterization (Complex Modulus, contd.)

PENNSTATE



- However, this approach can only be used for systems subjected to single-frequency periodic excitations
- Further, while the idealized hysteresis cycles (based on complex modulus) accurately predict low strain amplitude hysteresis cycles, discrepancies appear at larger amplitudes

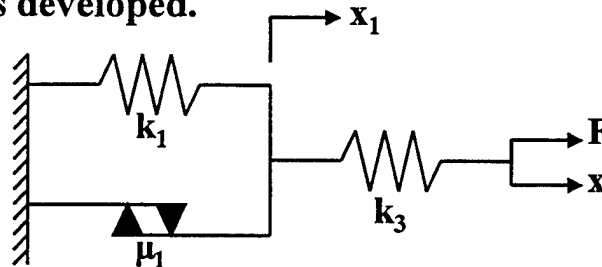


Mechanism-Based Model (Three-Element Model)

PENNSTATE



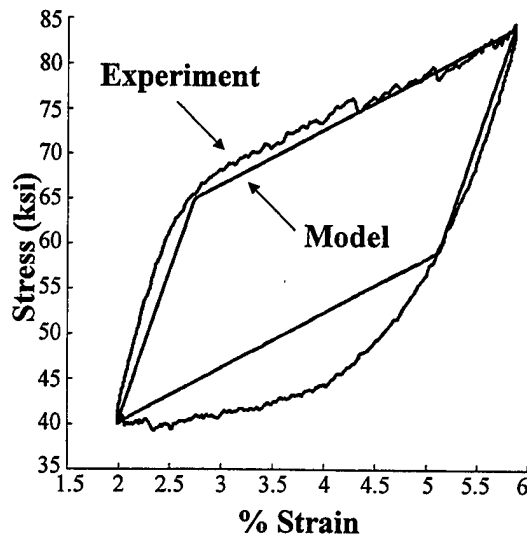
Most existing models have a thermodynamic basis and require complex calculations of phase fractions and transformations, so a Time-Domain Phenomenological Model was developed.



$$F = k_3(x - x_1) \quad x_1 = \frac{k_3 x - \mu_1 \text{sign}(\dot{x}_1)}{k_1 + k_3}$$

Mechanism-Based Model (Three-Element Model)

PENNSTATE

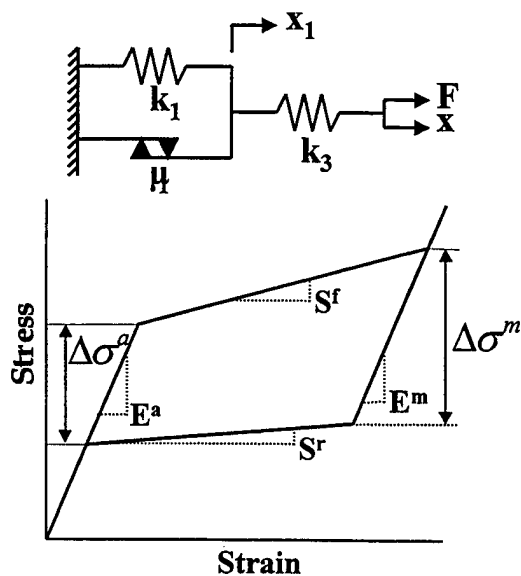


The Three-Element model captures the salient features of the experimental hysteresis curve.

However, the predicted hysteresis cycle necessarily has identical slopes in the austenite/martensite and forward/reverse transformation regions.

Mechanism-Based Model (Parameter Identification)

PENNSTATE



Model parameters may be determined from experimental hysteresis cycles.

$$k_3 = E^{mean}$$

$$k_1 \approx S^{mean}$$

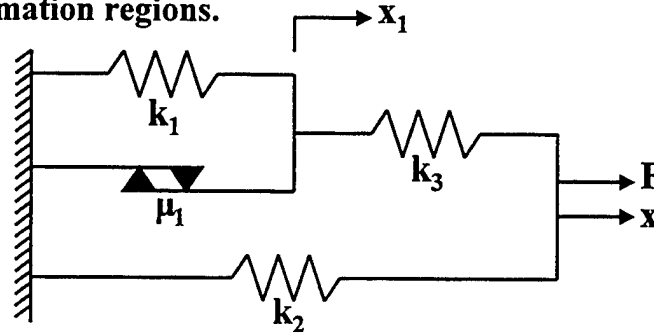
$$\mu_1 = \frac{\Delta\sigma^{mean}}{2}$$

Mechanism-Based Model (Four-Element Piecewise-Linear Model)

PENNSTATE



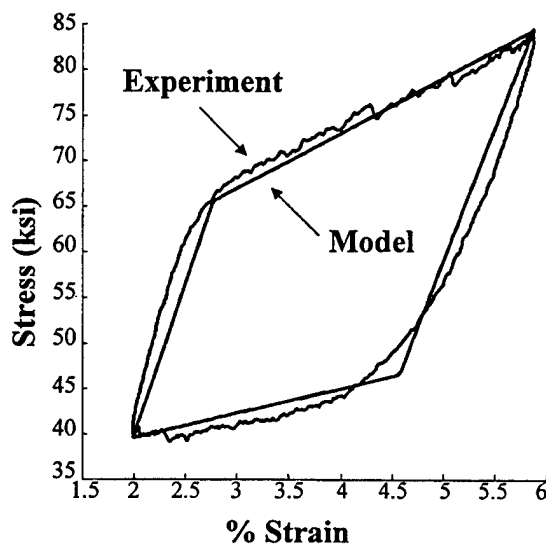
Piecewise-linear behavior in k_1 , k_3 , and μ_1 , along with the addition of a third piecewise-linear spring, k_2 , allows for distinct slopes in austenite/martensite and forward/reverse transformation regions.



$$F = k_3(x - x_1) + k_2x \quad x_1 = \frac{k_3x - \mu_1 \text{sign}(\dot{x}_1)}{k_1 + k_3}$$

Mechanism-Based Model (Piecewise-Linear Model)

PENNSTATE



By allowing distinct moduli in the austenite/martensite phases, and the forward/reverse transformations, experimental hysteresis data is now closely approximated.

Mechanism-Based Model (Parameter Identification)

PENNSTATE



- Four piecewise-linear elements result in eight parameters
- Only five of these parameters are independent
- Comparison of experimental and simulated hysteresis cycles yields the following five equations:

$$\begin{aligned} k_2^f + k_3^f &= E^a & k_2^r + k_3^r &= E^m \\ \frac{k_1^f k_3^f}{k_1^f + k_3^f} + k_2^f &= S^f & \frac{k_1^r k_3^r}{k_1^r + k_3^r} + k_2^r &= S^r & 2\mu_1^f \left(1 + \frac{k_2^f}{k_3^f}\right) &= \Delta\sigma^a \end{aligned}$$

- Two additional constraints ensure continuity:

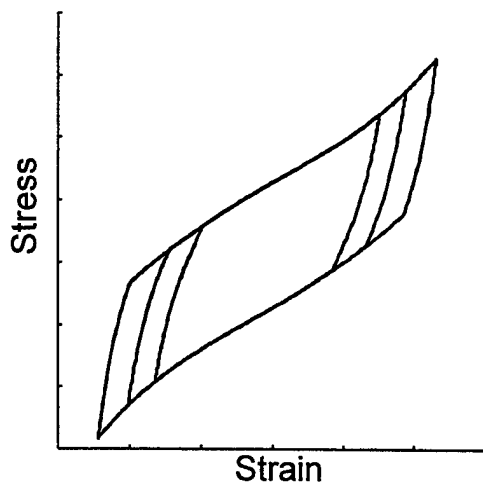
$$k_2^f \bar{x} + k_3^f (\bar{x} - \bar{x}_1) = k_2^r \bar{x} + k_3^r (\bar{x} - \bar{x}_1) \quad \frac{k_3^f \bar{x} - \mu_1^f}{k_1^f + k_3^f} = \frac{k_3^r \bar{x} - \mu_1^r}{k_1^r + k_3^r}$$

- The eighth parameter is arbitrarily assigned a value:

$$k_2^f = 0$$

Mechanism-Based Model (Nonlinear Model)

PENNSTATE



Linear springs in the three-element model are replaced with nonlinear springs, and the system parameters are determined through numerical optimization.

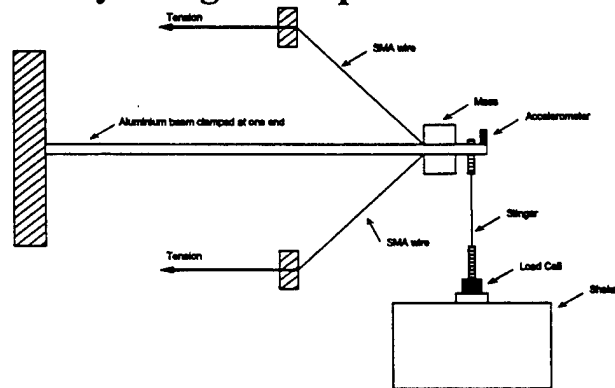
Nonlinear elements produce hysteresis cycles that can approximate the curvature of experimental data.

Influence of SMAs on Structural Damping

PENNSTATE



An experimental setup is being designed to evaluate the influence of SMAs in augmenting structural damping. Finite element models of the system are simultaneously being developed.



Summary

PENNSTATE



- Experimental SMA characterization has focused on influence of excitation frequency (previously ignored, and of importance in vibration damping applications). The effect of temperature, static strain offset, and amplitude have been comprehensively examined over a frequency range of 0-10 Hz.
- Plans being formulated to extend study to higher frequencies
- Using quasi-static hysteresis data overpredicts damping
- Complex modulus characterization provided physical understanding of SMA behavior. Easy to integrate into structural analyses, but unsuitable for transient and non-harmonic excitations.

Summary

PENNSTATE



- **Hierarchy of Time-Domain Mechanism-Based Phenomenological models being developed.** These are physically intuitive and simpler than existing models. Such models suitable for general excitations.
- **Methodology being developed for identification of model parameters from experimental data.**
- **Finite Element analysis of structures with integrated SMAs currently being developed, and experimental setup being designed for validation.** Validated Finite Element analysis to be used in design studies to determine optimal configuration for damping augmentation.
- **Potential for several Army applications - Helicopter lag and landing gear damping, damping in other weapon platforms.**

References

PENNSTATE



Additional details available in the following references

- **Wolons, D., Gandhi, F., and Malovrh, B., "Experimental Investigation of the Pseudoelastic Hysteresis Damping Characteristics of Shape Memory Alloy Wires," *Journal of Intelligent Material Systems and Structures*, Vol. 9, No. 2, Feb. 1998, pp. 116-126.**
- **Gandhi, F., and Wolons, D., "Characterization of the Pseudoelastic Damping Behavior of Shape Memory Alloy Wires using Complex Modulus," *Smart Materials and Structures*, Vol. 8, 1999, pp. 49-56.**
- **Malovrh, B., and Gandhi, F., "Mechanism-Based Phenomenological Models for Pseudoelastic Damping Behavior of Shape Memory Alloys," *Proceedings of the 40th AIAA/ASME/ASCE/AHS/ASC Structures, Structural Dynamics, and Materials Conference*, St. Louis, Missouri, April 1999, pp. 2723-2733, Paper No. AIAA-99-1544.**



Thermo-mechanical Instabilities in Shape Memory Alloys

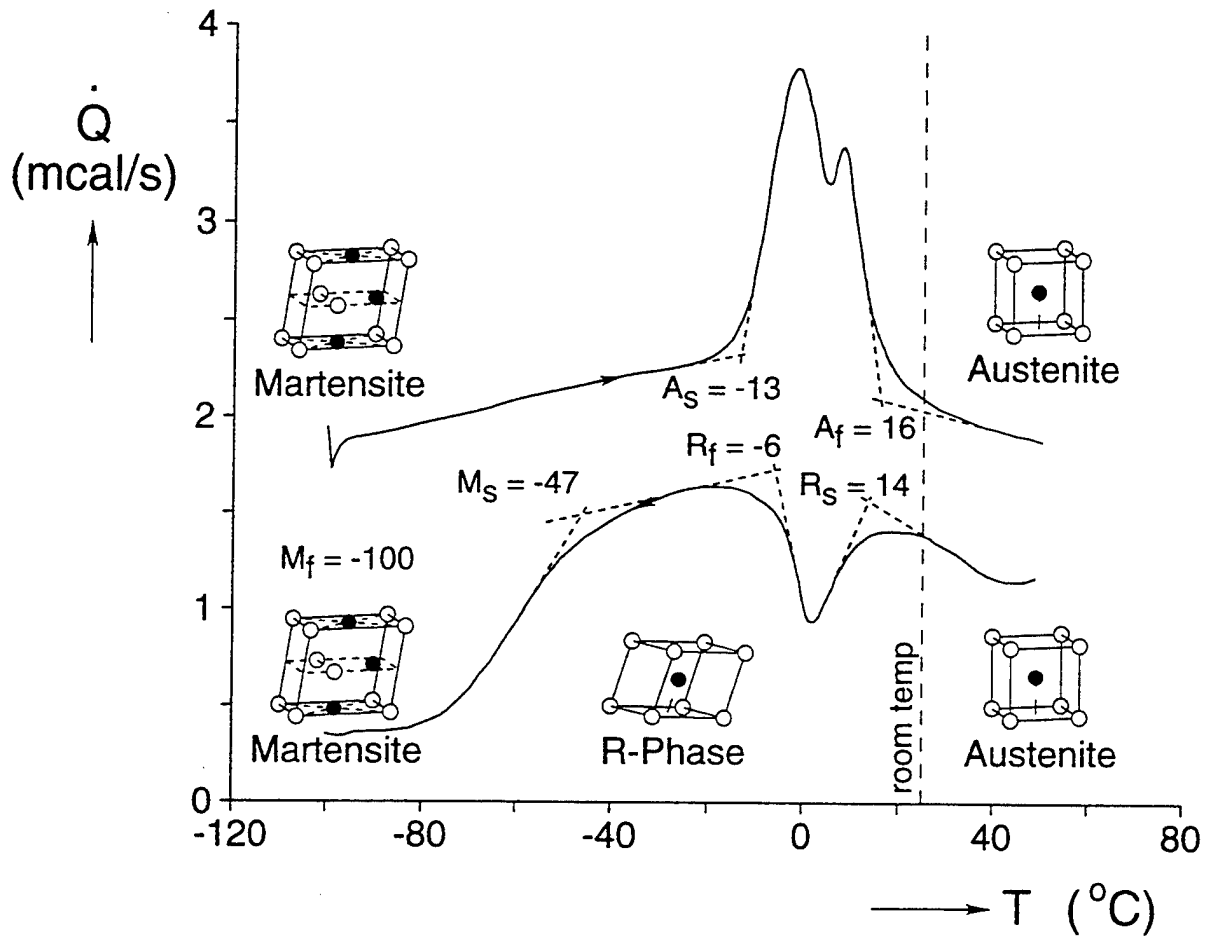
John A. Shaw

Dept. of Aerospace Engineering

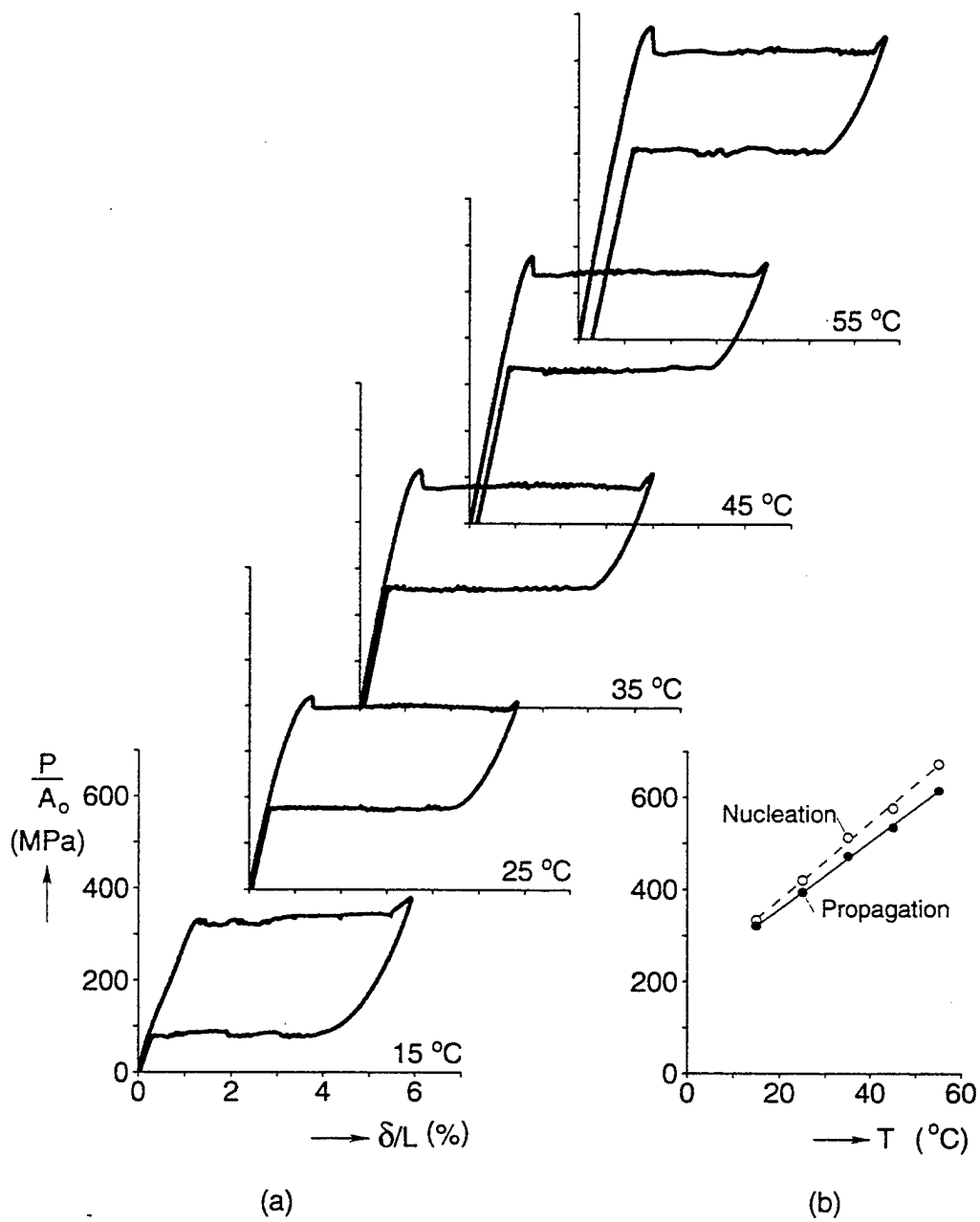
The University of Michigan

Experiments by the author have shown that the stress-induced martensitic transformation in certain polycrystalline NiTi shape memory alloys can lead to strain localization and propagation phenomena when loaded in uniaxial tension. The number of nucleation events and kinetics of transformation fronts was found to be sensitive to the nature of the ambient media and imposed loading rate due to the release/absorption of latent heat and the material's inherent temperature sensitivity of the transformation stress. It is believed that the inhomogeneous deformation and temperature fields have important implications on the material's performance and durability in actuator applications.

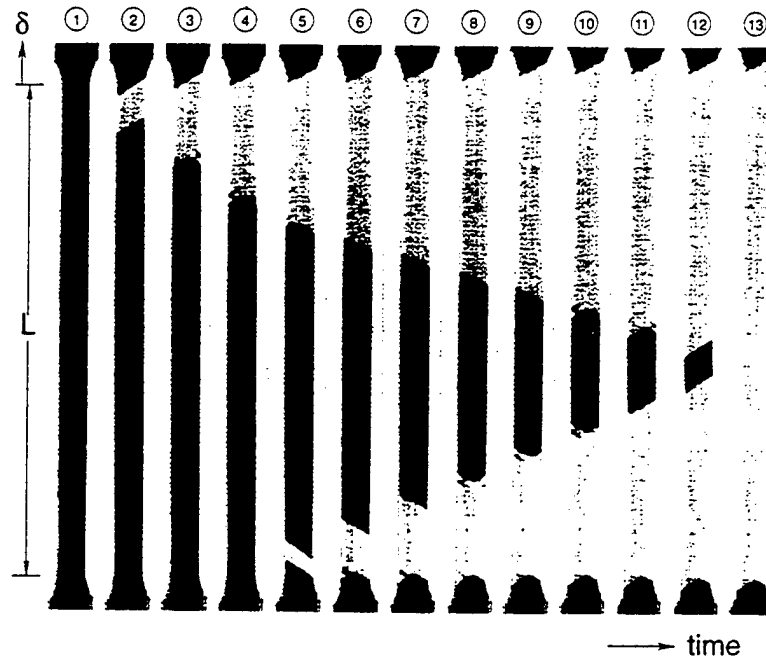
A special plasticity-based constitutive model used within a 3-D finite element framework has previously been shown to capture the isothermal, purely mechanical front features seen in experiments of thin uniaxial NiTi strips. In this talk the approach is extended to include the thermo-mechanical coupling of the material with its environment. The simulations successfully capture the nucleation and evolution of fronts and the corresponding temperature fields seen during the experiments.



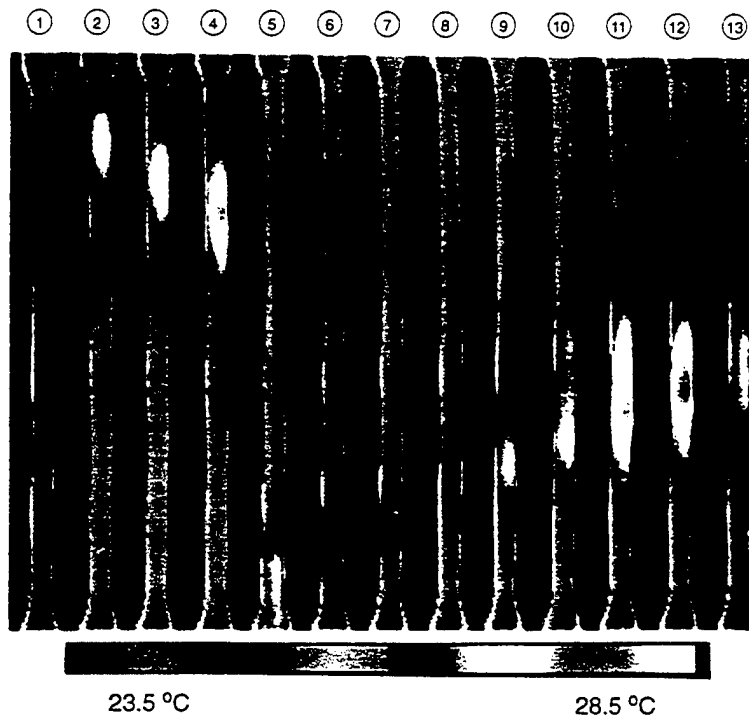
Differential scanning calorimetry of NiTi strip.



(a) Pseudoelastic responses of NiTi strip at $\dot{\delta}_f/L = 10^{-4} s^{-1}$ in water, (b) Fit of nucleation and propagation stresses for $A \rightarrow M$ transformation (loading).

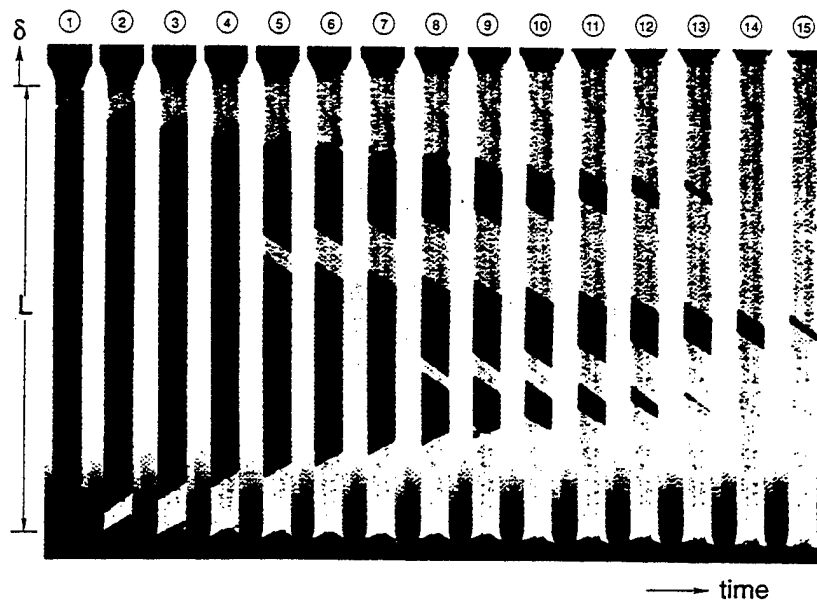


(a)

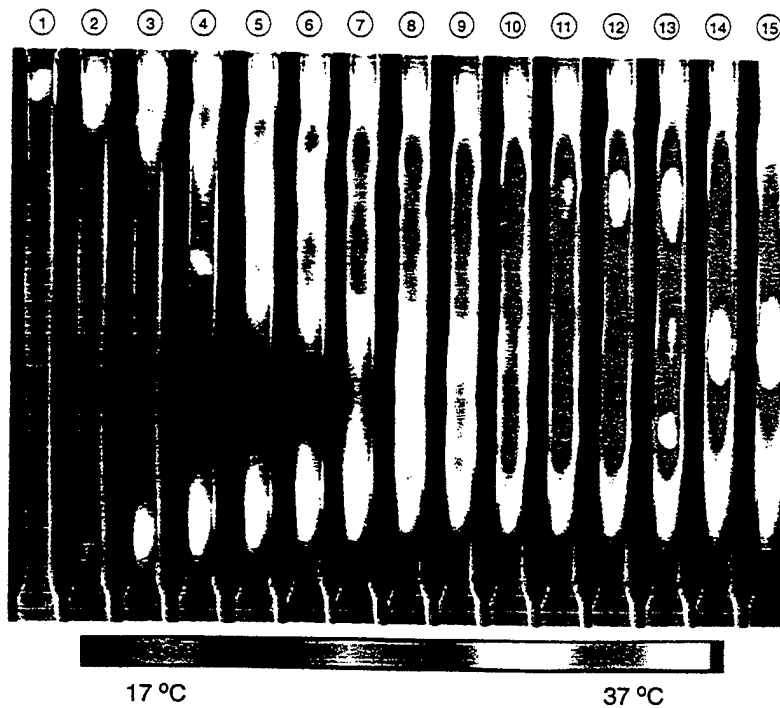


(b)

Experiment 1 – evolution of A→M transformation (loading) at $\dot{\delta}_f/L = 10^{-4} s^{-1}$ in room air; (a) photographs, (b) infrared thermal images. (Experiment taken from *Shaw and Kyriakides* (1997)).

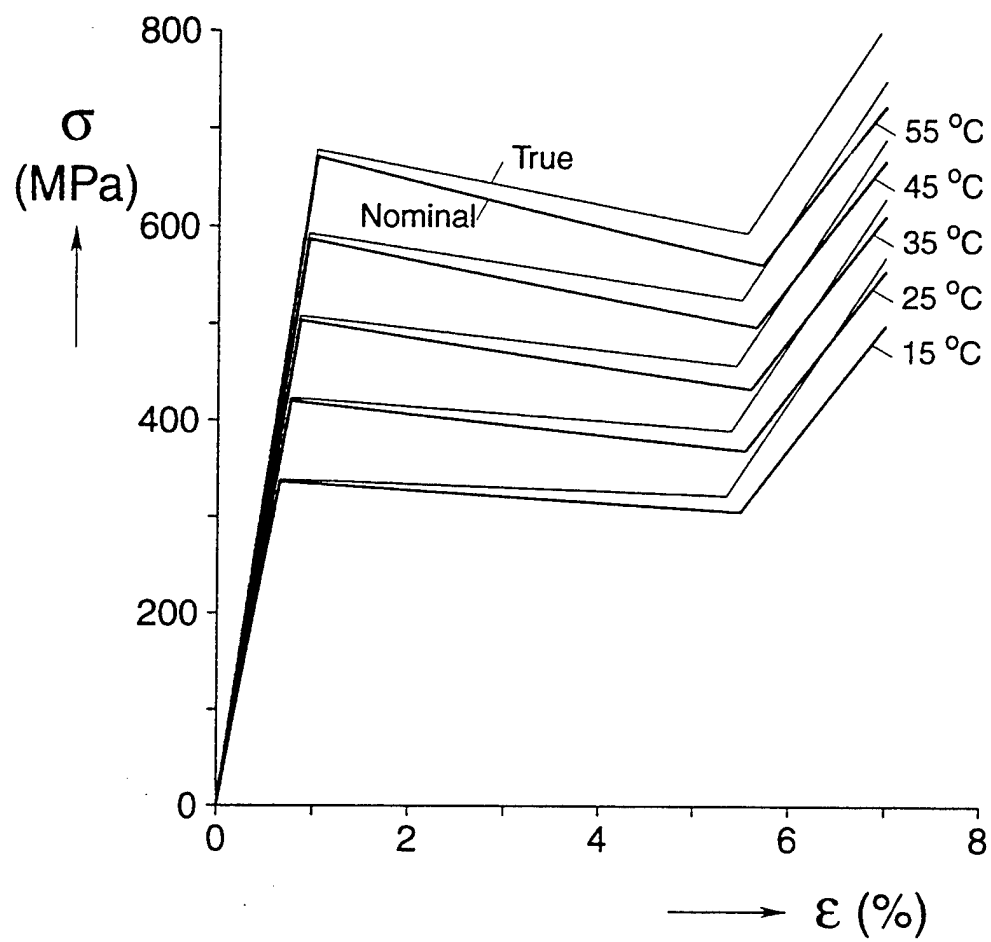


(a)

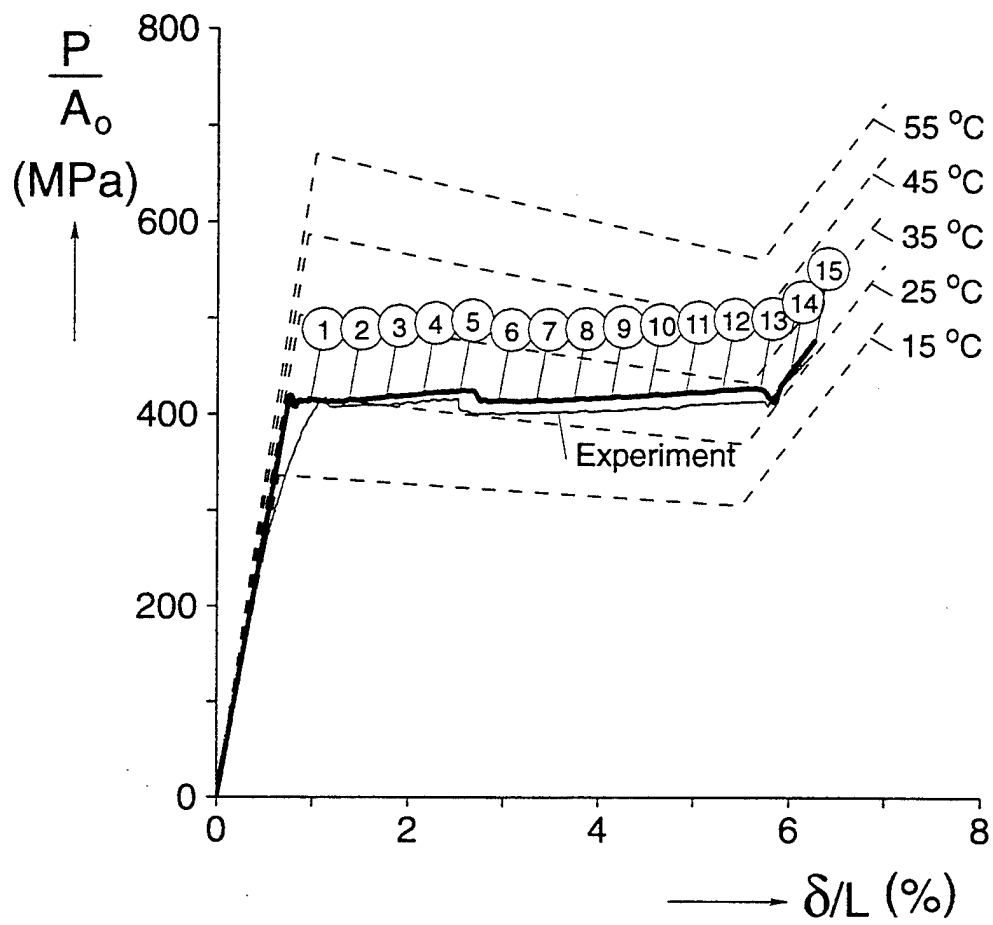


(b)

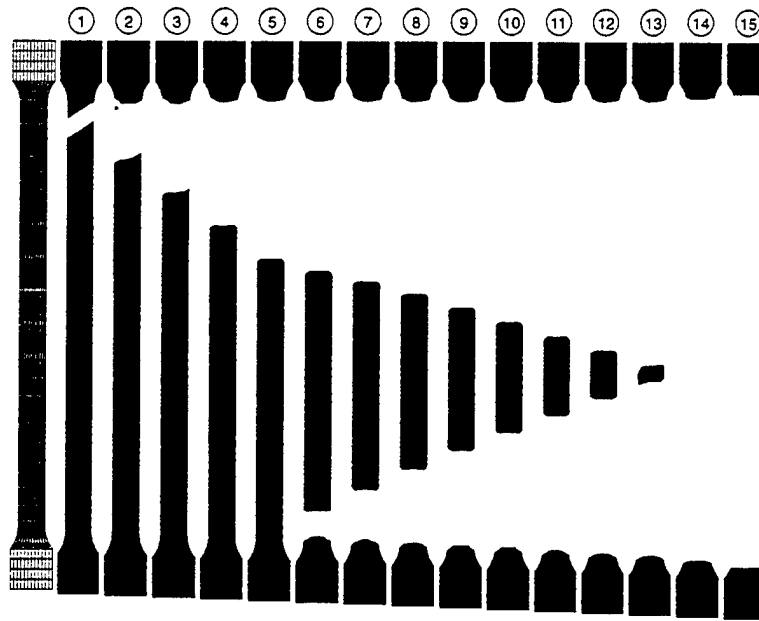
Experiment 2 – evolution of A→M transformation (loading) at $\dot{\delta}_f/L = 10^{-3}s^{-1}$ in room air; (a) photographs, (b) infrared thermal images. (Experiment taken from *Shaw and Kyriakides (1997)*).



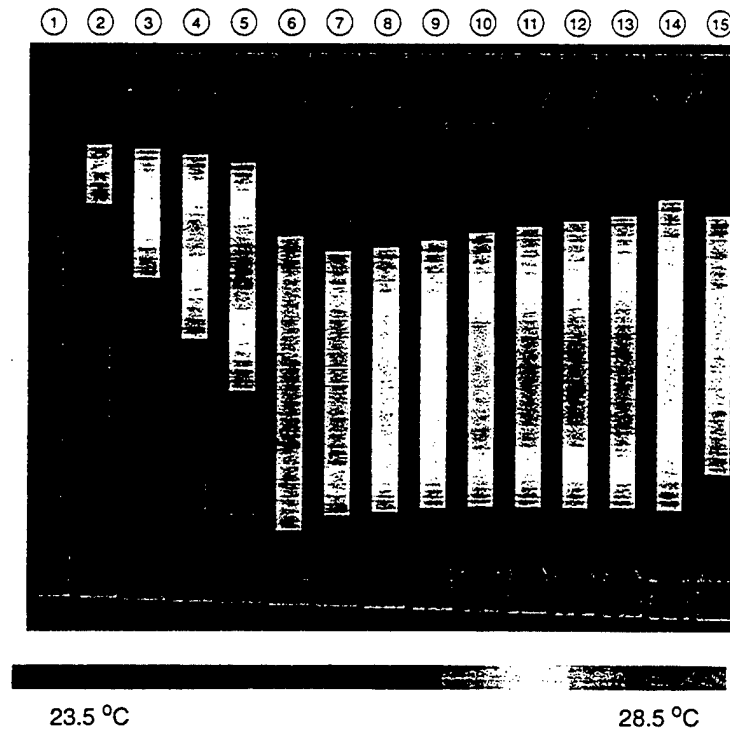
Constitutive model: nominal stress-strain and true stress-log strain.



Simulation 1 - Calculated force-elongation at $\dot{\delta}_f/L = 10^{-4} s^{-1}$ in room air.

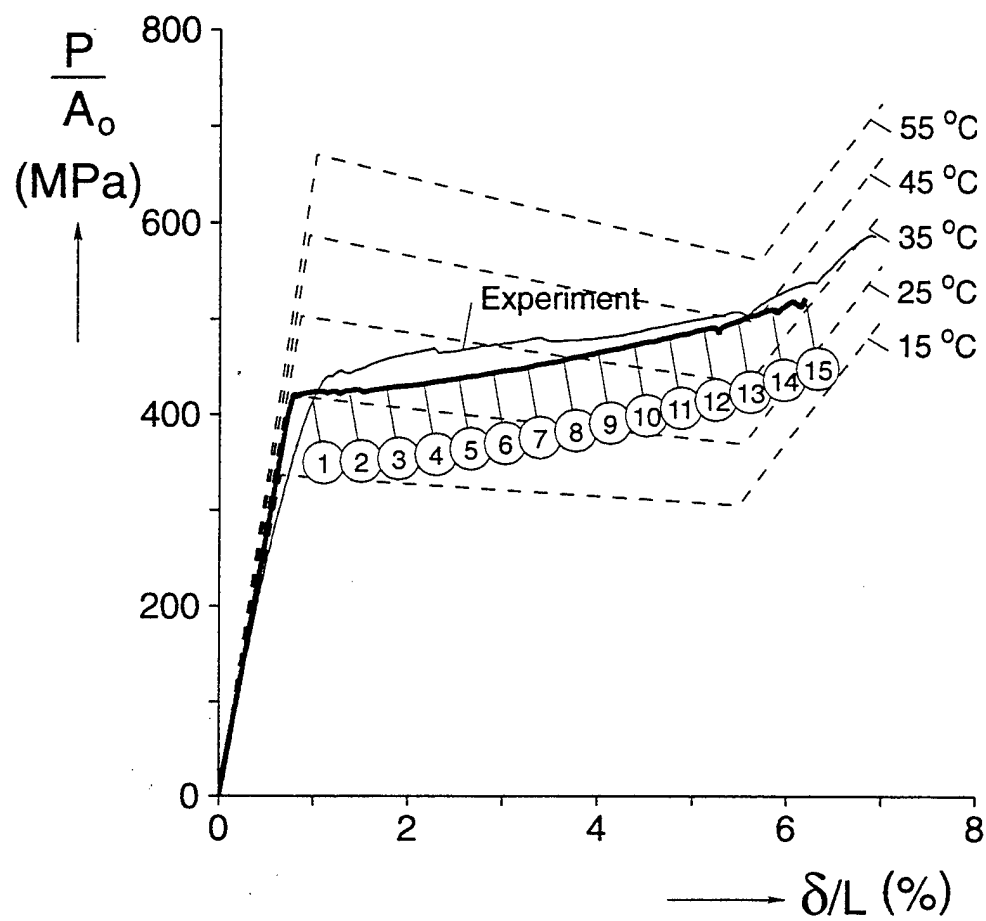


(a)

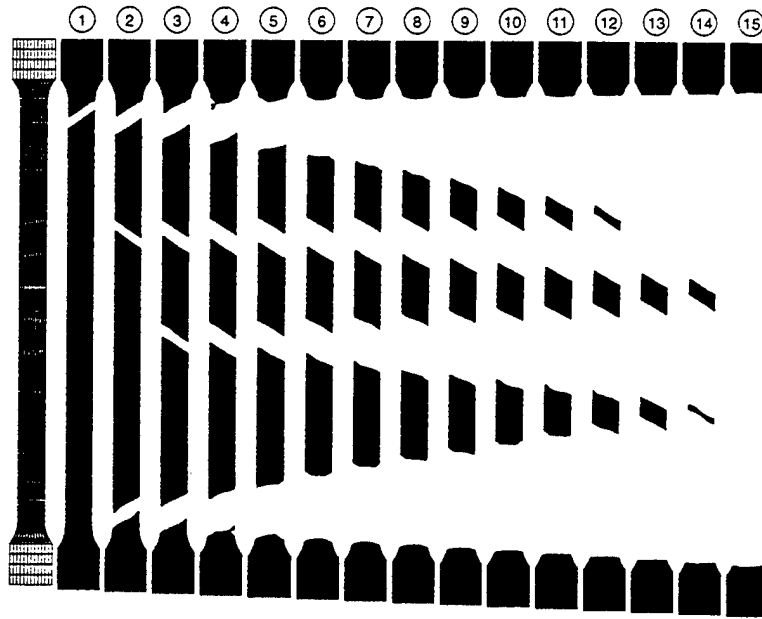


(b)

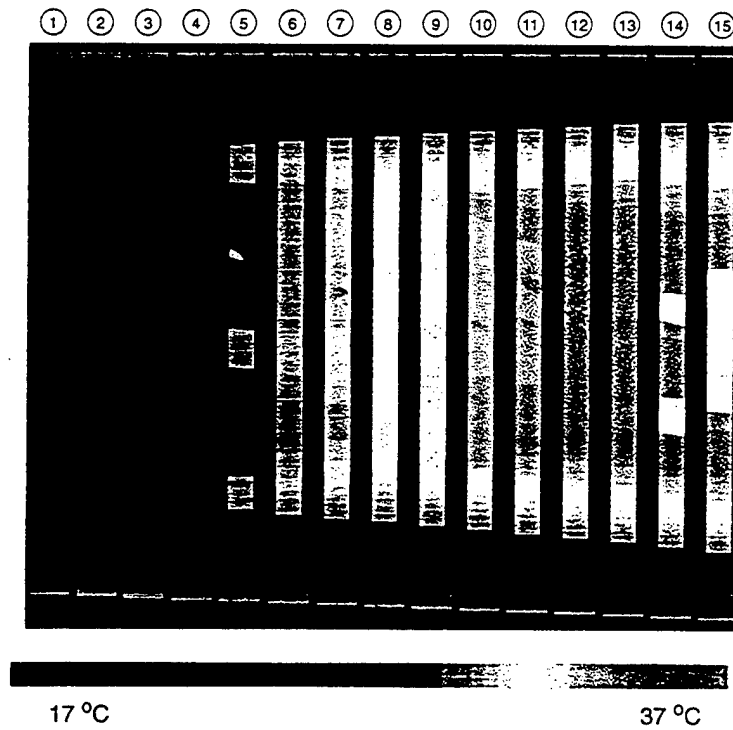
Simulation 1 - evolution of A→M transformation at $\dot{\delta}_f/L = 10^{-4}s^{-1}$ in room air; (a) axial deformation at 3% threshold strain, (b) temperature.



Simulation 2 - Calculated force-elongation at $\dot{\delta}_f/L = 10^{-3}s^{-1}$ in room air.



(a)



(b)

Simulation 2 - evolution of A→M transformation at $\dot{\delta}_f/L = 10^{-3}s^{-1}$ in room air; (a) axial deformation at 3% threshold strain, (b) temperature.

ENVIRONMENTALLY ACTIVATED SMA HYBRID COMPOSITES

Travis L. Turner
Structural Acoustics Branch, M/S 463
NASA Langley Research Center
Hampton, VA 23681-2199
(757) 864-3598, t.l.turner@larc.nasa.gov

Engine and turbulent boundary layer excitations generate substantial fluctuating pressure and thermal loads on portions of high-performance aerospace vehicle structures. Sonic fatigue and noise transmission issues thus emerge as critical considerations in the design of such vehicles. Many smart-structure concepts are not feasible for these applications because of the harsh environment and/or weight associated with the required control electronics. Shape memory alloy (SMA) hybrid composite structures, conventional composite structures with embedded SMA actuators, have significant potential for these applications. These structures adaptively stiffen in response to an elevated thermal environment by design, without the need for control electronics.

A constitutive model capturing the nonlinear thermomechanical behavior of shape memory alloys embedded in a composite matrix is presented. A finite element formulation based upon this constitutive model and the resulting equations governing the response of SMA hybrid composite plate-type structures subjected to thermal and mechanical loads is also shown. The finite element analysis is capable of predicting thermal buckling, geometrically nonlinear thermal post-buckling deflection, and linear vibration responses. A discrete spectral analysis method is incorporated to allow for arbitrary temporal variation of the mechanical load(s).

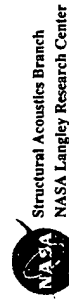
Sample thermal buckling, post-buckling, and base excitation results are presented. Results indicate that two critical buckling temperatures can exist for some structures with SMA compositions exhibiting a phase transformation above ambient temperature. This effect can be avoided by proper alloy selection. The results show that the critical buckling temperature can be shifted by a factor of nearly 400 with a SMA volume fraction of only 12.5%. The fundamental resonance for the structure is increased by a factor of about 10 for the same case. The RMS dynamic response is decreased by a factor of over 20 for the case of random base acceleration excitation spanning the first two symmetric modes of the conventional or inactivated hybrid beams. The inclusion of 12.5% SMA by volume results in a mass increase of 39%. In order to achieve similar performance improvements (unbuckled static equilibrium and corresponding frequency shifts/RMS response reduction) by building up the conventional structure, one would need to increase the mass by a factor of 16.

A SMA hybrid composite fabrication capability is being developed to provide specimens for analysis validation and to improve actuator integration technologies. A Nitinol alloy in a ribbon configuration is being used in this study. A glass-epoxy matrix material is used to allow for simple electrical activation of the SMA actuators. Alloy characterization and beam specimen fabrication is in progress. Beam specimens will be tested in a base excitation configuration. Panel specimen fabrication and testing is planned.

Environmentally Activated SMA Hybrid Composites

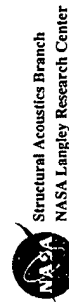
Travis L. Turner
Structural Acoustics Branch
NASA Langley Research Center

Fourth ARO Workshop on Smart Structures
August 16-18, 1999



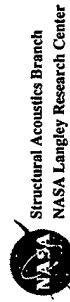
Objective

Develop and validate an analytical tool for predicting the thermomechanical response of composite structures with embedded shape memory alloy actuators and subject to thermal and dynamic mechanical loads.



Outline

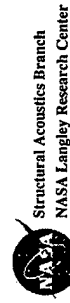
- Approach
- Constitutive Modeling
- Finite Element Formulation
- Solution Capabilities
- Solution Examples
- Fabrication and Testing Status



Approach

- ✓ Develop analytical capability for predicting the thermo-mechanical dynamic response of SMA hybrid composites
- ✓ Validate analysis for conventional structures
- Develop fabrication technology for SMA hybrid composites
- Demonstrate vibration/radiation suppression with SMAs
- Validate/refine analysis and fabrication of SMA composites
- Build practical SMA hybrid composite aircraft structures

- ✓ Completed
- In Progress
- Future Work



SMA 1-D Constitutive Relation

- Recovery Stress Formulation (Rogers 1989, Turner 1994)

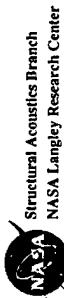
$$\sigma_1 = E\varepsilon_1 + \sigma_r \quad T \geq A_s$$

$$\sigma_1 = E(\varepsilon_1 - \alpha_1 \Delta T) \quad T < A_s$$

- Effective TEC Formulation (Turner 1999)

$$\sigma_1 = E \left[\varepsilon_1 - \int_{\tau_0}^{\tau} \alpha_1(\tau) d\tau \right] \quad T \geq A_s$$

$$\int_{\tau_0}^{\tau} \alpha_1(\tau) d\tau = -\frac{\sigma_r}{E} \quad T < A_s$$



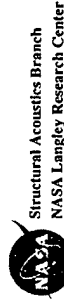
SMA Hybrid Composite Constitutive and Deformation Relations

- General k-th orthotropic layer

$$\begin{Bmatrix} \sigma_x \\ \sigma_y \\ \tau_{xy} \end{Bmatrix}_k = [\bar{Q}]_k \begin{Bmatrix} \varepsilon_x \\ \varepsilon_y \\ \gamma_{xy} \end{Bmatrix}_k - [\bar{Q}]_k \int_{\tau_0}^{\tau} \begin{Bmatrix} \alpha_x(\tau) \\ \alpha_y(\tau) \\ \alpha_{xy}(\tau) \end{Bmatrix}_k d\tau$$

- von Karman strain-displacement relations

$$\begin{Bmatrix} \varepsilon_x \\ \varepsilon_y \\ \gamma_{xy} \end{Bmatrix} = \begin{Bmatrix} u_{,x} \\ v_{,y} \\ u_{,y} + v_{,x} \end{Bmatrix} + \frac{1}{2} \begin{Bmatrix} w_{,x}^2 \\ w_{,y}^2 \\ 2w_{,x}w_{,y} \end{Bmatrix} - z \begin{Bmatrix} w_{,xx} \\ w_{,yy} \\ 2w_{,xy} \end{Bmatrix}$$



Euler-Lagrange Equations

$$\begin{bmatrix} M_b & 0 \\ 0 & M_m \end{bmatrix} \begin{Bmatrix} \ddot{W}_b \\ \ddot{W}_m \end{Bmatrix} + \begin{bmatrix} K_b & K_B \\ K_B & K_m \end{bmatrix} \begin{Bmatrix} W_b \\ W_m \end{Bmatrix} - \begin{bmatrix} K_{\Delta T} & 0 \\ 0 & 0 \end{bmatrix} \begin{Bmatrix} W_b \\ W_m \end{Bmatrix} \\ + \frac{1}{2} \begin{bmatrix} N1_b + (N1_b)_B & N1_{bm} \\ N1_{mb} & 0 \end{bmatrix} + \frac{1}{3} \begin{bmatrix} N2_b & 0 \\ 0 & 0 \end{bmatrix} \begin{Bmatrix} W_b \\ W_m \end{Bmatrix} \\ = \begin{Bmatrix} P_b(t) \\ 0 \end{Bmatrix} + \begin{Bmatrix} F_b(t) \\ 0 \end{Bmatrix} + \begin{Bmatrix} P_{b\Delta T} \\ P_{m\Delta T} \end{Bmatrix} - \begin{bmatrix} M_b & 0 \\ 0 & M_m \end{bmatrix} \begin{Bmatrix} \ddot{U}_g \\ 0 \end{Bmatrix}$$

Separation of Static and Dynamic Systems

- Small motions about potentially large static deflection

$$\{W\} = \{W\}_s + \{W\}_d \quad \text{such that} \quad \{W\}_d \ll \{W\}_s \rightarrow \{W\}_d^2 \approx 0$$

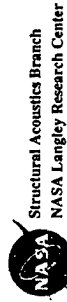
- Static and Dynamic Governing Equations

$$\left([K] - [K_{\Delta T}] + \frac{1}{2} [N1]_s + \frac{1}{3} [N2]_s \right) \{W\}_s = \{P_{\Delta T}\} \quad \text{Static}$$

$$[M] \{\ddot{W}\}_d + ([K] - [K_{\Delta T}] + [N1]_d + [N2]_d) \{W\}_d = \{P(t)\} + \{F(t)\} - [M] \{\ddot{U}_g(t)\} \quad \text{Dynamic}$$

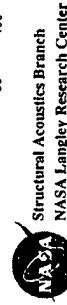
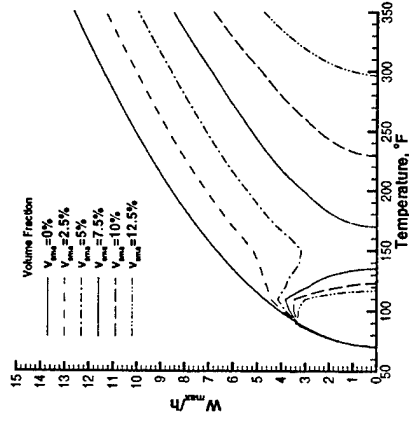
Solution Capabilities

- Thermal buckling (critical buckling temperatures)
- Thermal post-buckling (large thermal deflection)
- Dynamic response to acoustic pressure, concentrated force, and inertial loads
- Acoustic radiation (radiated pressure/intensity, TL)



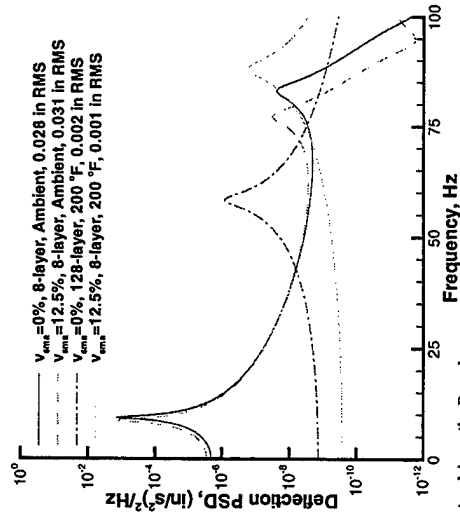
Thermal Post-Buckling Example

Simply-supported 18x1x0.040 inch (45/0_{sm}/-45/90)_{sym} beam, 4% SMA prestrain



Random Inertial Response Example

Same Configuration with Random Base Excitation, 0.1 g RMS



NASA
Structural Acoustics Branch
NASA Langley Research Center

Fabrication Status

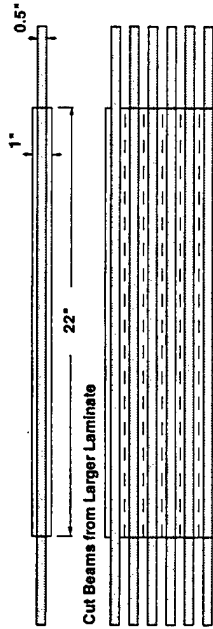
- ✓ Build baseline (no SMA) beam specimens
- ✓ Build SMA hybrid composite beams without prestrain
- Build SMA hybrid composite beams with prestrain
- Build SMA hybrid composite panels w/o and w/ prestrain
- Prestrain and characterize the SMA material
- Experiment with coating technologies

- ✓ Completed
- In Progress
- Future Work

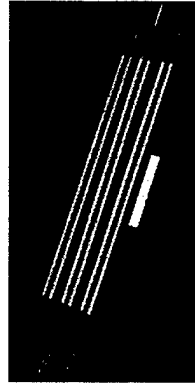
NASA
Structural Acoustics Branch
NASA Langley Research Center

Beam Specimen Fabrication

22"x1"x0.080" Glass-Epoxy/SMA Hybrid Beam (6 Count)
(45/0_{we}/-45/90)_{top} Lamination
SMA in 0° Laminas Only



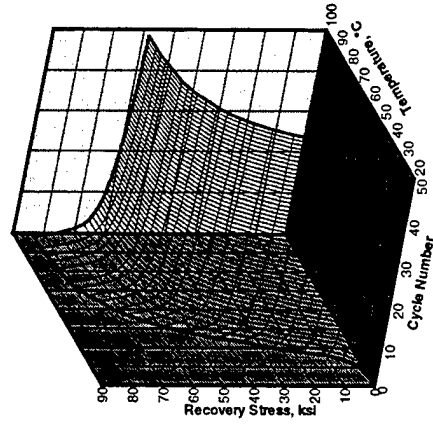
SMA Ribbon:
0.5"x0.005" Cross Section
6" Overhang at Beam Ends



Structural Acoustics Branch
NASA Langley Research Center

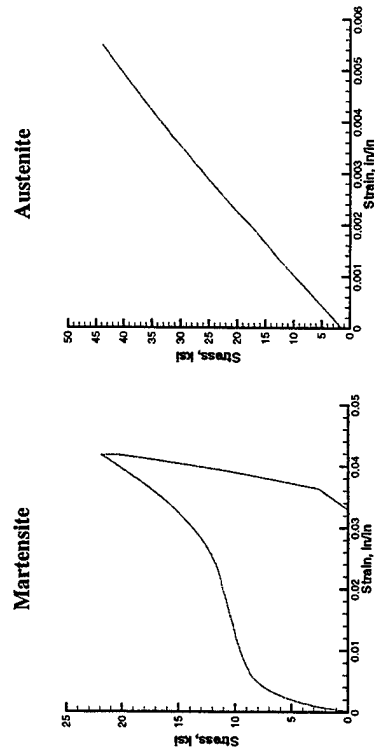
Nitinol Recovery Stress

4% Initial Strain



Structural Acoustics Branch
NASA Langley Research Center

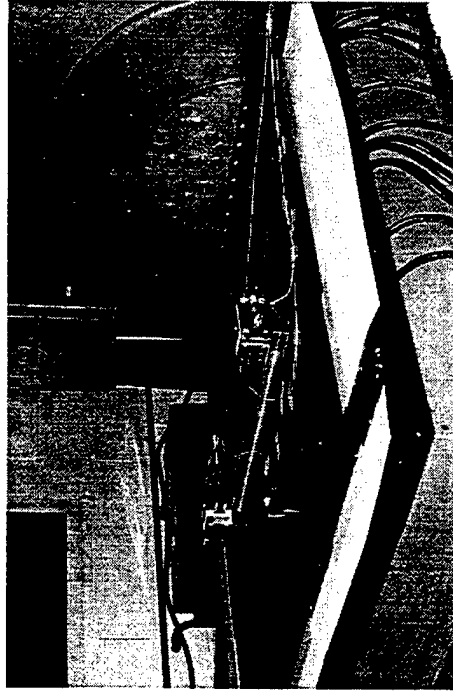
Nitinol Stress-Strain Diagrams




Testing Status/Plans

- Beam specimens
 - Dynamic response suppression (base excitation)
 - Fatigue life enhancement (base excitation)
- Panel specimens
 - Transmission loss testing for vibration/radiation suppression
 - Progressive wave tube testing for sonic fatigue improvement


Base Excitation Test Setup



 Structural Acoustics Branch
NASA Langley Research Center

Summary

- Analysis developed for predicting the dynamic response of SMA hybrids to thermal and mechanical loads
- Predictions indicate significant benefit from embedded SMA
- SMA hybrid composite fabrication processes underway
- Analysis validation testing for beam specimens underway
- Panel specimen vibration/radiation testing planned
- Beam and panel specimen fatigue testing planned

 Structural Acoustics Branch
NASA Langley Research Center

IN-FLIGHT TRACKING OF HELICOPTER ROTOR BLADES USING SHAPE MEMORY ALLOY ACTUATORS

Jeanette J. Epps*

Inderjit Chopra**

Alfred Gessow Rotorcraft Center
Department of Aerospace Engineering
University of Maryland, College Park, Maryland 20742

Helicopters encounter vibratory loads from different sources such as blade dissimilarity and the aerodynamic environment. Reducing and controlling these loads in helicopters continues to be a major topic of research. The present study examines a method to actively reduce the vibratory loads generated due to blade dissimilarity with tab adjustments using shape memory alloy (SMA) actuators.

Blade dissimilarities, in the form of structural, inertial or aerodynamic, can cause a large increase in vibratory forces (primarily at 1/rev frequency) that can introduce more vibrations, lower fatigue life of components and yield less acceptable handling qualities. Currently, to overcome this problem, in-shop tracking of blades is followed periodically resulting in a significant increase in operating cost and helicopter downtime. Tracking is performed manually by adjusting trailing-edge tabs of helicopter blades in an iterative manner. Also to minimize blade dissimilarity, tight manufacturing tolerances are imposed on rotor blades leading to high procurement cost. Although blade tracking and tight tolerances minimizes vibrations, they are time consuming and expensive. In the present study, it is proposed to track helicopter rotor blades while in-flight, as opposed to manually in-shop, using shape memory alloy actuators. The ability to track helicopter blades while in-flight has several advantages: (1) minimization of one per rev vibrations, (2) relaxation in manufacturing tolerance of blades, (3) less downtime, (4) decrease in overall operating and procurement costs, and (5) an increase in fatigue life of structural components and instrumentation. The objective of the current research is to experimentally and analytically examine the feasibility of using shape memory alloy (SMA) wire actuators for tracking of a helicopter rotor.

Actuation of a trailing-edge tab is achieved using the shape memory effect (SME). The shape memory effect involves plastically deforming a SMA wire and then recovering the plastic deformation (also called pre-strain) during transformation via heat activation. The actuator consists of two sets of wires, an upper set and lower set that are thermally and electrically insulated from each other. The SMA wires are clamped at one end to the spar (typically located at the quarter-chord) and, at the other end, are connected to a hinge tube mounted on a shaft. Both wires are assumed to have the same initial length (prior to plastic deformation) and the same initial plastic deformation (pre-strain). To deflect the tab downward, the lower set of wires are heated while the upper wires remains at ambient conditions. When the wires are heated, they contract due to the SME, recovering a portion of its pre-strain and a constraining force develops. Note that this force is dependent upon the load-displacement characteristics of the non-heated wires. The force produces a clockwise moment about the hinge tube's shaft axis, rotating the hinge tube and, consequently, deflecting the tab downward. The top wires are extended plastically the same amount as the contraction of the bottom wires. To bring the tab back to its neutral position, the top wire is heated next. Again upon heat activation, the wire will recover a part of its pre-strain and a recovery force will develop, which will move the tab up. If such a tab system is used for in-flight tracking of a helicopter rotor, it is important to lock the tab at the desired position. This means that heat activation is needed temporarily during an adjustment period and then switched off. A feedback controller is incorporated to achieve the desired tab angle.

In the analysis for the tab actuator, the thermo-mechanical behavior of a SMA wire is predicted using a model adapted from the Brinson constitutive model for SMA. The actuator is modeled as two SMA wires in series. The first wire is clamped at one end and, at the other end, connected to a moveable separator. The second wire is connected to the same moveable separator and clamped at the other end. Assumptions made in model for the wires are that all wires have: 1.) the same length, 2.) the same pre-strain and 3.) the same cross-sectional area. One wire is heated and the other remains at ambient conditions. The constitutive equation for the heated wire determines the recovery force based on the temperature, strain and the martensite volume fraction. The constitutive equation for the non-heated wire is a constant temperature, stress-strain curve equation. Only the strain and the stress-induced martensite volume fraction are changing.

Future work involves testing the actuator dynamics in an open-jet wind tunnel at various angles of attack and freestream velocities and validating the actuator model with test data.

* Graduate Fellow

** Alfred Gessow Professor and Director

Helicopter Blade Tracking



UNIVERSITY OF MARYLAND

Any structural, inertial, or stiffness dissimilarities between rotor blades can cause an aerodynamic imbalance.

This imbalance can cause:

- A tremendous increase in vibratory forces (primarily at 1/rev)
- Lower fatigue life of components
- Yield less acceptable handling qualities



To overcome these problems, it's necessary to carry-out rotor tracking after a certain number of flight hours.

Motivation:

In-flight Tracking Advantages



UNIVERSITY OF MARYLAND

- Minimization of one per rev vibrations
- Reduction in manufacturing tolerances of blades
- Reduction in downtime
- An increase in fatigue life of structural components and instrumentation
- Lower operating costs
- Manual tracking will no longer be necessary

Research Objective and Approach



UNIVERSITY OF MARYLAND

Objective:

Investigate a trailing-edge tab actuated via Shape Memory Alloy (SMA) wire actuators for in-flight tracking.

Approach:

- 1.) Experimentally and theoretically investigate the thermo-mechanical characteristics of NiTi shape memory alloy material.
- 2.) Develop a methodology to actuate a trailing-edge tab using SMA wire actuators for in-flight tracking.

Constrained Recovery Behavior of SMA



UNIVERSITY OF MARYLAND

Heat Activation of Plastically Deformed SMA wire:

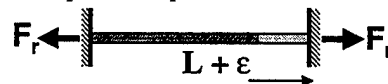
•If the wire is not constrained at other end, then no constraining force develops.

Clamped-free



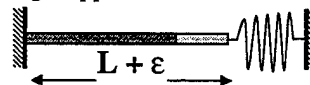
•SMA mechanically constrained both ends and with a pre-strain, ϵ , a tensile force will develop upon heat activation.

Clamped-Clamped



•The recovery force will be modified due to spring flexibility.

Spring-Supported

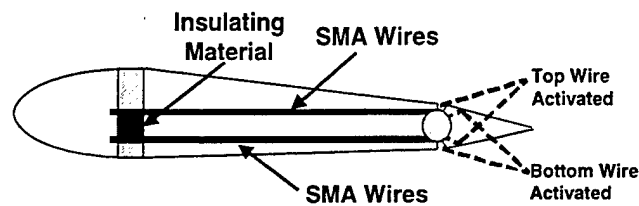


Tab Actuator Configuration



UNIVERSITY OF MARYLAND

- SMA wires fixed to spar at quarter-chord at one end and connected to hinge tube at other end
- Both wires have same initial length and plastic deformation (or pre-strain).



Concept of Trim Tab Actuation

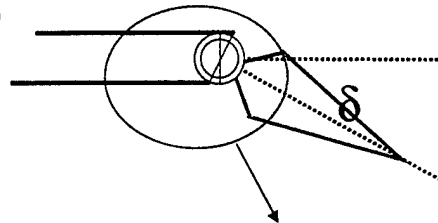


UNIVERSITY OF MARYLAND

To deflect the tab down:

Lower wires heated electrically. Top wires remain at ambient temp.

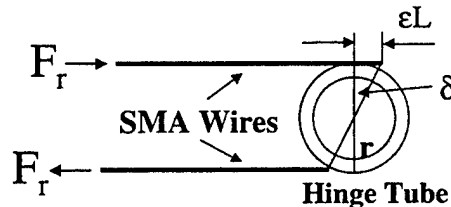
Trim tab deflects down, increasing plastic deformation of top wires.



To deflect the tab up:

Heating top wires causes tab to deflect up and increase plastic deformation of lower wires.

A locking mechanism has to be engaged to maintain desired tab position.



Tab Actuator Embedded in a NACA 0012 Wing Section



UNIVERSITY OF MARYLAND

Tab actuator consists of

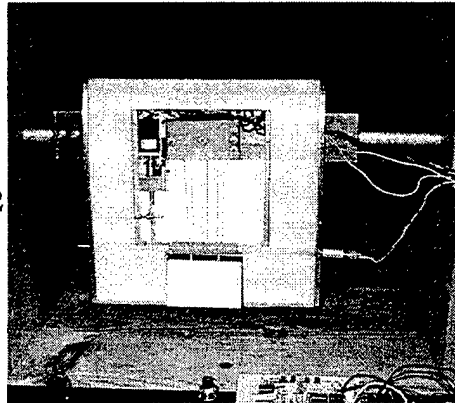
- Three pre-strained 0.015" diameter SMA wires.
- Fiber-glass clamp at the quarter chord spar that electrically insulate the SMA wires.
- Fiber-glass hinge tube, 0.625" diameter and 3.75" long.
- Wires are heated electrically.

Actuator embedded in a NACA 0012 wing section:

- Foam core with fiber-glass skin, fabricated using compression molding technique.
- Span=12", chord= 12", max thickness = 1.44" (12% of chord)

Tab Dimensions:

- Span= 4", chord = 2.4" (20 % of chord)



Gear Locking Mechanism

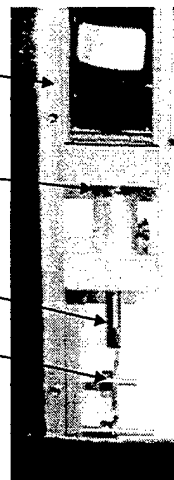


UNIVERSITY OF MARYLAND

The lock consists of:

- Pulling Solenoid (4.375 lbs. @ 0.125") mounted on spar
- Restoring Spring
- Pawl
- Gears

To ensure no rotation of the hinge tube and accuracy of tab angle, another lock is located on the opposite side of the hinge tube.



Actuator Requirements



UNIVERSITY OF MARYLAND

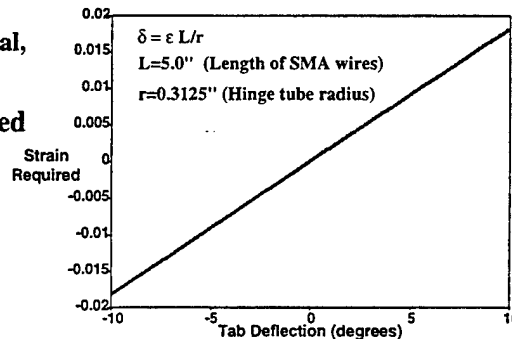
Deflection and Force Requirements for Tab Actuator:

- $\delta = \pm 10^\circ$
- $M_h = 4.6$ in-lbs. (Liang, et al, SPIE '96)

For $r=0.3125''$, the force required of the SMA is:

$$F = \frac{M_h}{r} = 14.72 \text{ lbs.}$$

For $L=5''$, and $r=0.3125''$, the required pre-strain needed for each SMA wire to obtain a tab deflection of $\pm 10^\circ$ is 1.8%.



SMA-SMA Actuator Model



UNIVERSITY OF MARYLAND

The actuator is modeled as two wires in series clamped at one end, and connected to a moveable separator at the other end.



- The wires are electrically and thermally isolated from each other.
- One wire is heated and the other remains at ambient conditions.
- General Assumptions for the Wires:
 - 1.) $L_A = L_B$, same length
 - 2.) $\epsilon_A = \epsilon_B$, same plastic deformation
 - 3.) $\text{Area}_A = \text{Area}_B$, the same cross-sectional area
- Two compatibility requirements:
 - 1.) $F_A = F_B$, magnitude of force in Wire A equals Wire B at the separator.
 - 2.) $x_A = -x_B$, displacement recovered equals displacement elongated.

SMA-SMA Actuator Analysis



UNIVERSITY OF MARYLAND

Assume Wire A remains at ambient conditions, Wire B heated.

Wire A: Stress-strain Equation

$$\sigma^A = E(\xi^A)\varepsilon^A - E(\xi_o^A)\varepsilon_o^A + \Omega(\xi^A)\xi_s^A - \Omega(\xi_o^A)\xi_{so}^A$$

- Constant temperature (T)
- Variables: strain (ε) and martensite volume fraction (ξ).



Wire B: Recovery Stress-temperature Equation

$$\sigma^B = E(\xi^B)\varepsilon^B + \Omega(\xi^B)\xi_s^B - \Omega(\xi_o^B)\xi_{so}^B$$

- Variables: strain (ε), temperature (T), the martensite volume fraction (ξ).

Tab Deflection Controller



UNIVERSITY OF MARYLAND

- A displacement feedback controller

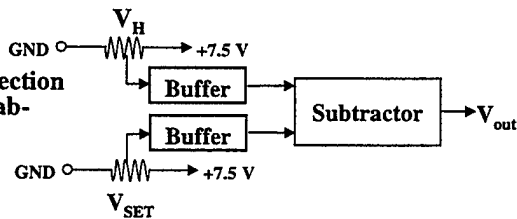
Controller Inputs:

- V_{SET} = the desired tab deflection
- V_H = actual tab position
- Note that the desired tab deflection can be either tab-up or tab-down

Subtractor:

$$V_{OUT} = (V_{SET} - V_H)$$

- V_{OUT} is compared to an error tolerance (e_{tr})



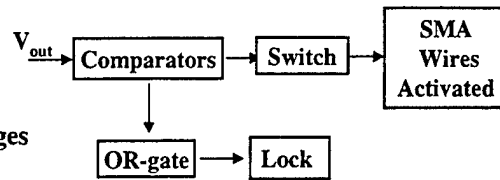
Tab Deflection Controller (cont'd)



UNIVERSITY OF MARYLAND

- If $V_{OUT} > e_{rr}$:
 - Lock disengages to allow free rotation of the tab and the switch closes.
 - The upper pre-strained wires are heat activated. The wires contract causing the tab to deflect up.

- If V_{OUT} is within e_{rr} :
 - The switch opens, de-activating the SMA wires, and the lock engages to prevent any further rotation of the hinge tube.



- As the actual tab position (V_H) approaches the desired tab position (V_{SET}), V_{OUT} approaches e_{rr}
- Note if $V_{OUT} < e_{rr}$
 - The lower pre-strained wires are activated.

Experimental/Theoretical Recovery Strain-Temperature Curve



UNIVERSITY OF MARYLAND

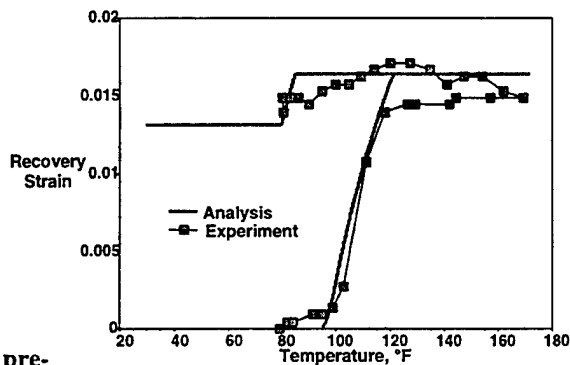


- This plot represents the amount of the plastic deformation that's recovered upon heating.

- Note that upon cooling, the amount of strain recovered decreases slightly then becomes constant.

- Also note that not all of the pre-strain is recovered upon heating.

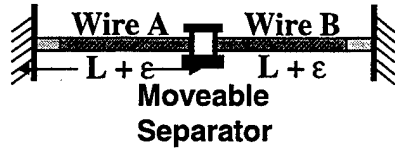
0.015-inch diameter NiTi
2% Initial Pre-strain



Experimental-Theoretical Recovery Stress-Temperature Curve

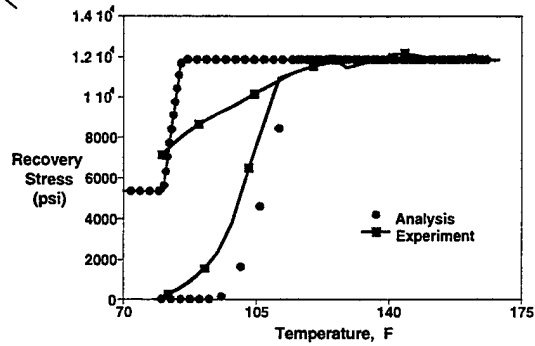


UNIVERSITY OF MARYLAND



- SMA-SMA actuator model (most of the strain is recovered)

- Cooling curve needs improvement



Tab Up/Down Deflection



UNIVERSITY OF MARYLAND

Tab UP



Upper wires heated
Lower wires at room temp

Tab Down



Lower wires heated
Upper wires at room temp

Measured/Predicted Variation of the Tab Angle with Temperature

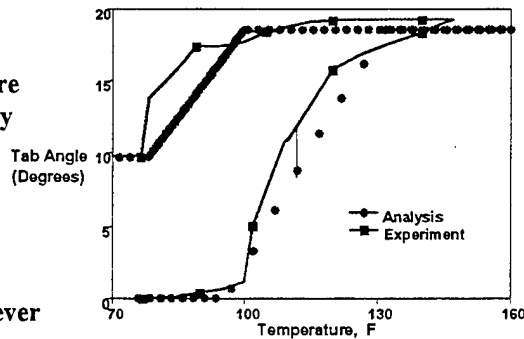


UNIVERSITY OF MARYLAND

3.16% Initial Pre-strain

Tab-up deflection:

- 3 upper SMA wires
- As the upper SMA wires are heated they contract, thereby deflecting the tab up.
- Approx. 18.5° of deflection was obtained.
- Correlation was good, however improvements are needed.



(Data obtained using Laser Sensor.)

Summary and Future Work



UNIVERSITY OF MARYLAND

- Tab actuator built and embedded in a NACA 0012 wing section with a 12" span and 12" chord
- Locking Mechanism constructed
- Tab deflection controller fabricated
- Analysis to predict tab deflection for better control has been developed
- Open-jet wind tunnel tests in progress

Intelligent
Systems
Laboratory

Experiments on the Thermomechanical Fatigue of SMAs

Dimitris C. Lagoudas, David A. Miller and
Lijian Rong

Acknowledgement: Air Force Office of Scientific Research, grant # F49620-98-1-0041
monitored by Major Brian Sanders

TEXAS A&M UNIVERSITY

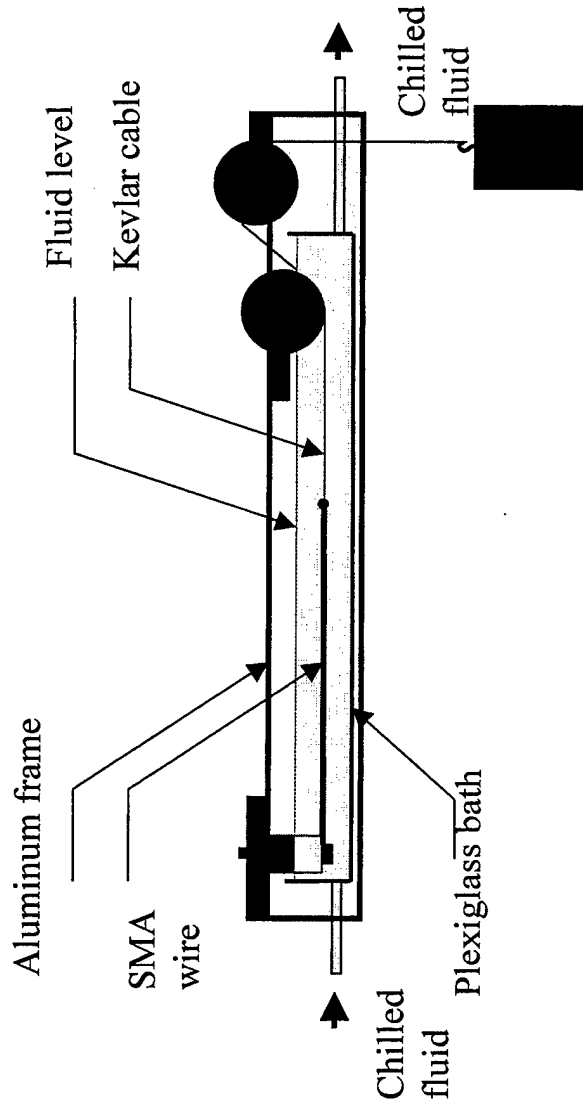
Research Objectives

- Design a test frame for the constitutive measurement of SMAs thermomechanical fatigue life.
- Establish a testing protocol for the evaluation of SMA actuator fatigue life.
- Determine the influence of heat treatment on the thermal fatigue life of NiTiCu SMAs.
- Perform thermal cycles on SMAs with variable mechanical and thermal loading conditions to establish the effect of loading history on thermal fatigue life.

Linear Actuators

□ Fatigue Experiments

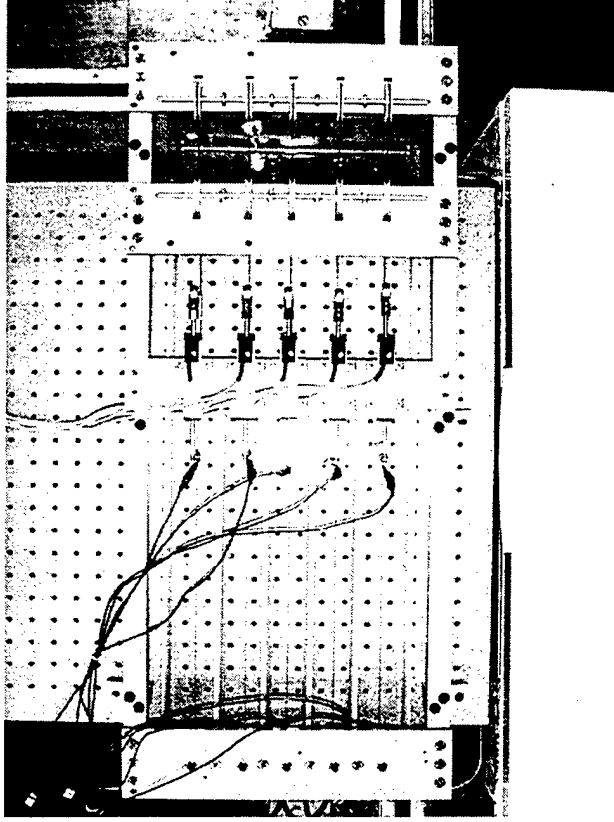
- Custom frame allows for a test rate of up to 1/2 hz., enabling a large number of thermal cycles to be reached quickly.
- Actuation computer controlled to allow for maximum transformation or partial transformation strain during test.



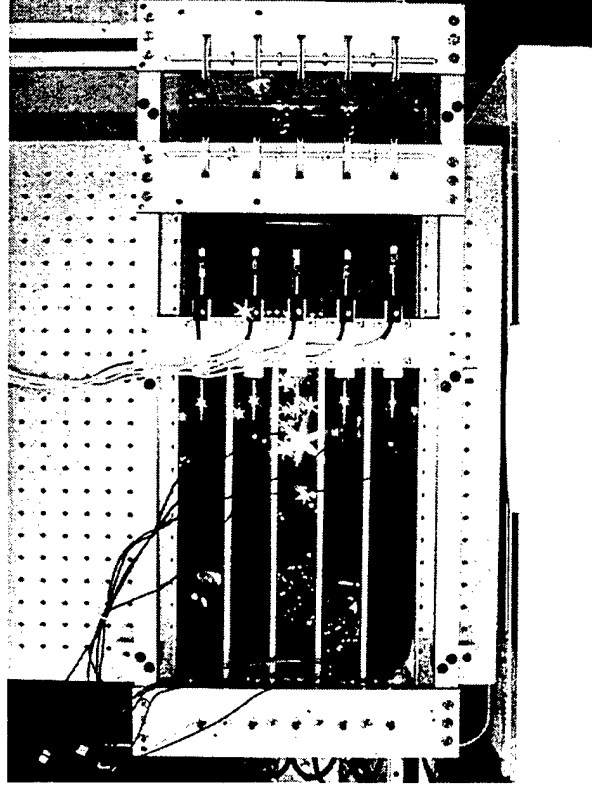
Thermomechanical Thermal Fatigue Test Frame

- Fatigue Experiments
 - Chilled Glycol bath cools wires quickly to achieve high actuation rates

Without glycol

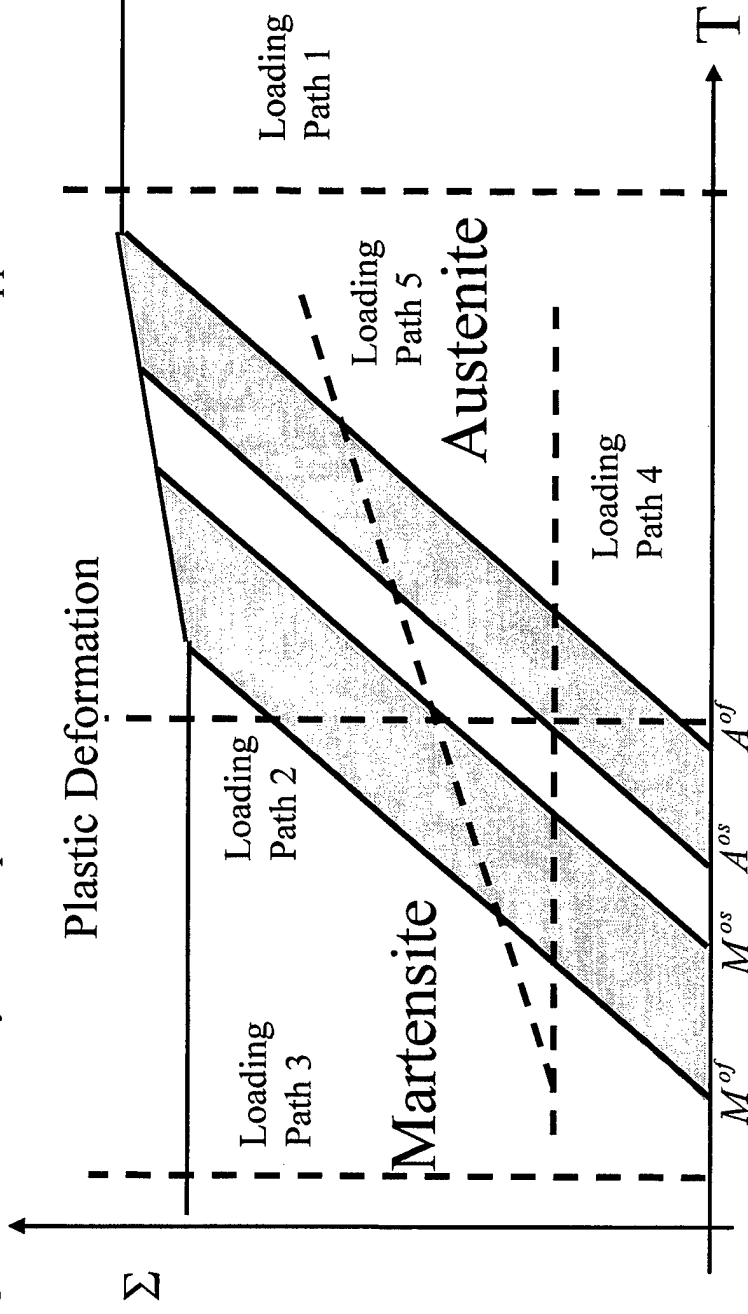


With glycol



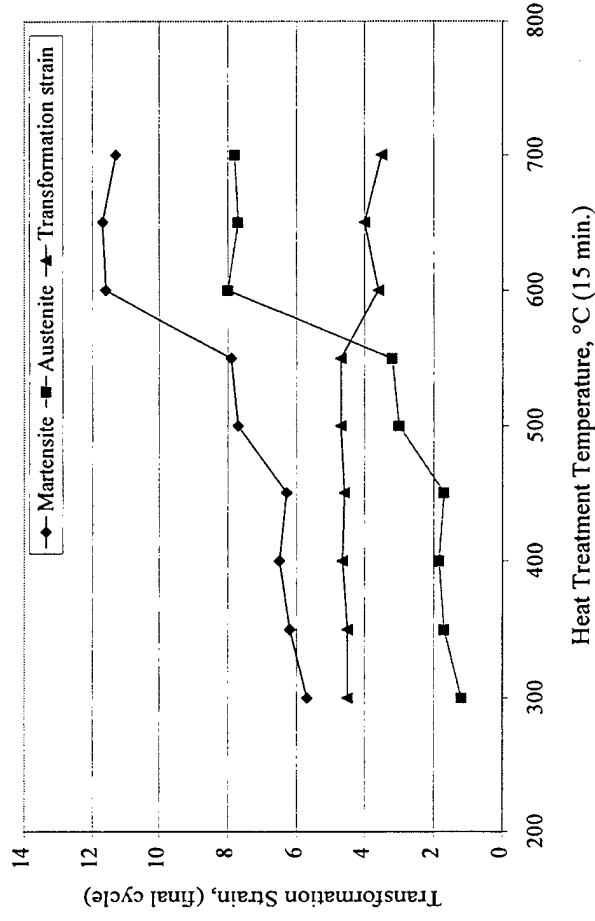
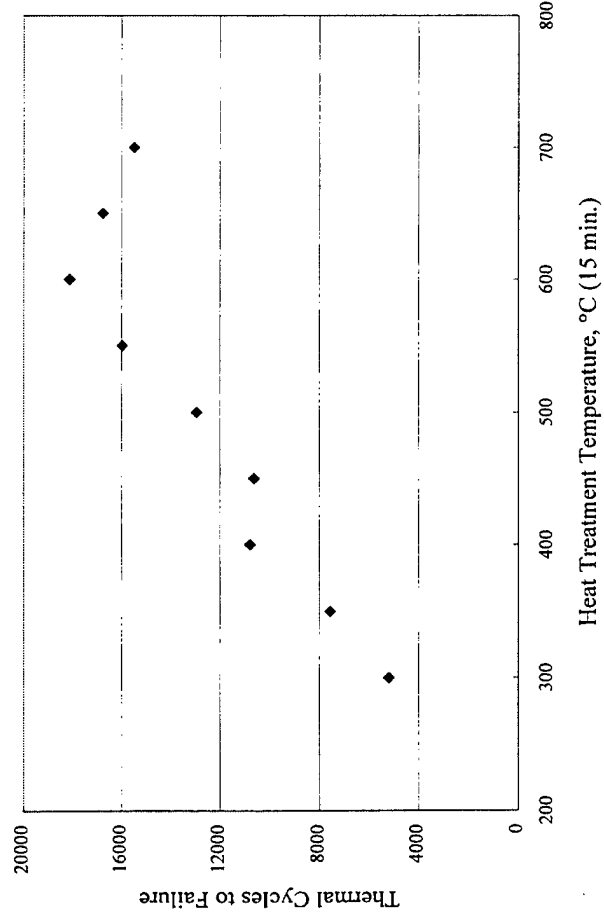
Identification of Fatigue Loading Paths

- ☐ Loading Path 1: Isothermal Austenitic deformation only.
- ☐ Loading Path 2: Isothermal Stress induced Martensitic transformation.
- ☐ Loading Path 3: Isothermal Martensitic detwinning deformation.
- ☐ Loading Path 4: Thermally induced phase transformation under constant applied stress, for complete or partial transformation.
- ☐ Loading Path 5: Thermally induced phase transformation under variable applied stress.



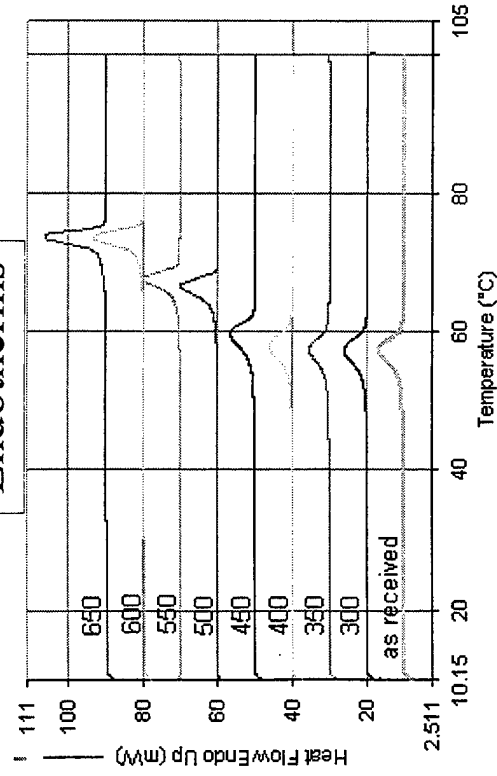
Effect of heat treatment on Thermal fatigue life of NiTiCu

- Thermal cycles to failure at multiple heat treatment temperatures for 15 minutes.
- .0236" dia NiTiCu wire with initial 30% cold work.
- All tests were thermally cycled under a constant stress of 150 MPa.



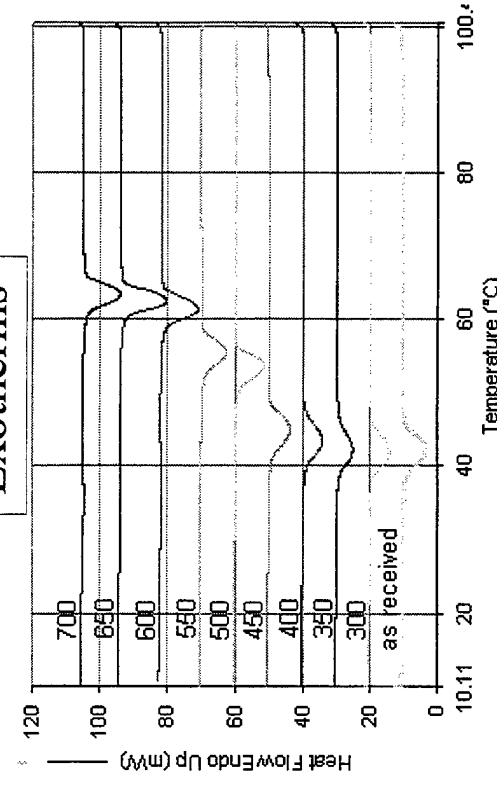
Differential Scanning Calorimeter Results for NiTiCu Specimens

Endotherms

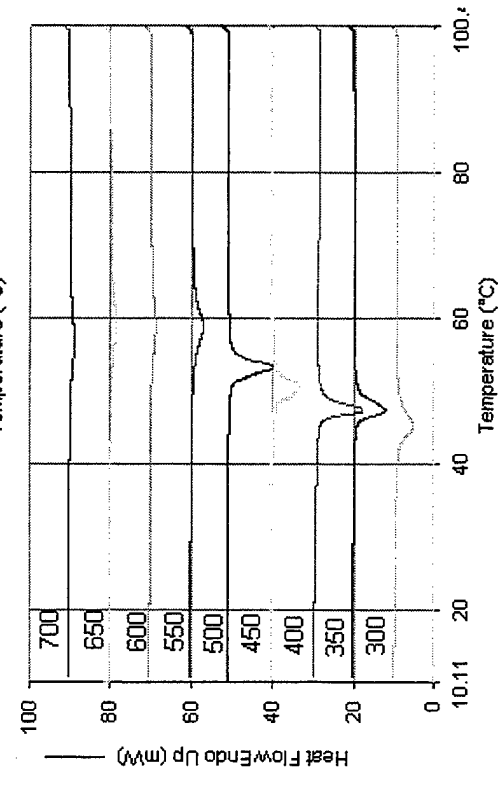
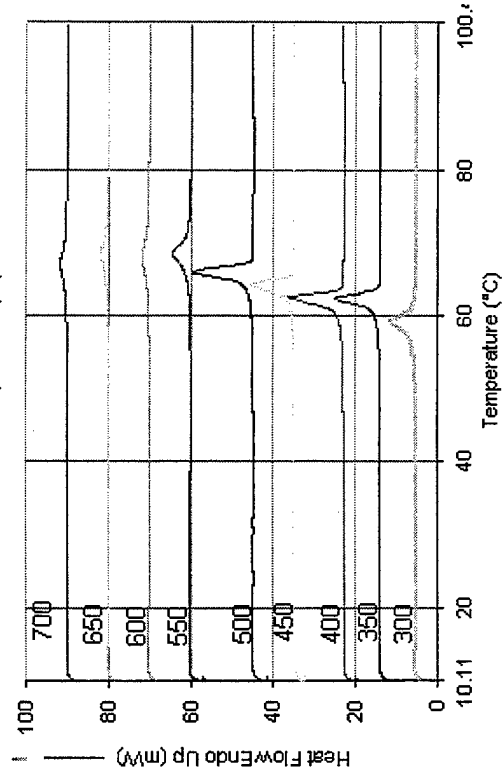


Pre-Test

Exotherms



Post-Test



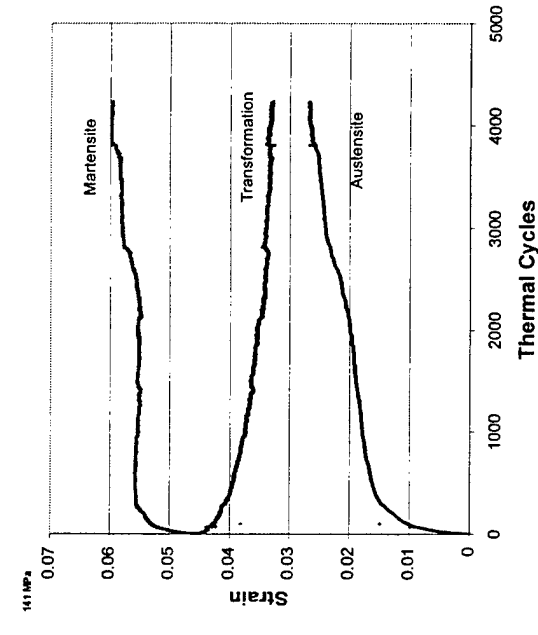
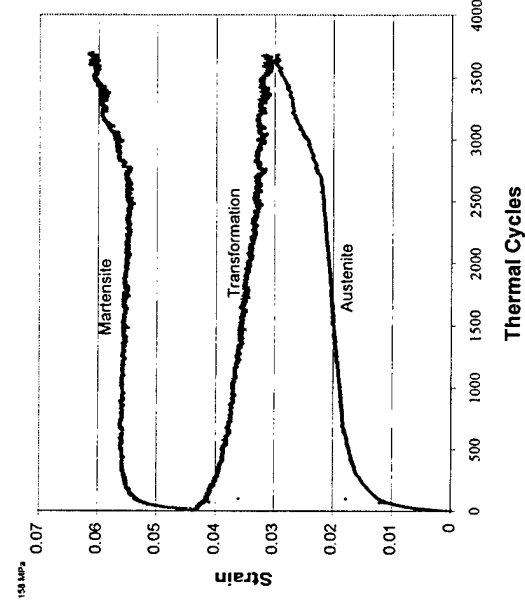
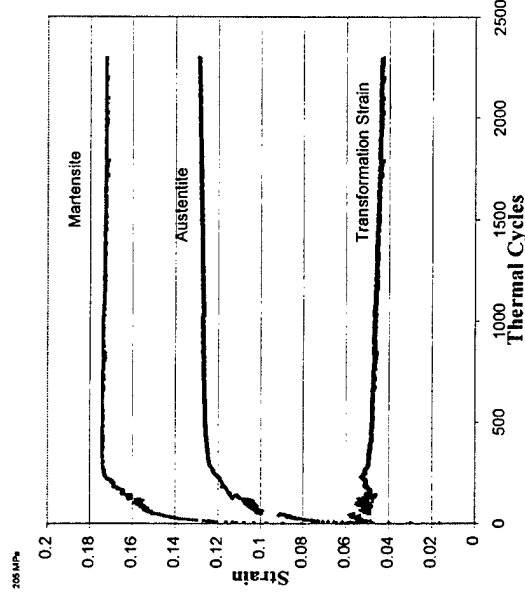
NiTiCu SMA Fatigue Test

heat treated at 600°C for 30 min.

- ☐ Applied Stress, 205 MPa.
- ☐ Cycle frequency, .25 hz
 - 1 second heat
 - 3 second cool
- ☐ Bath Temperature 15°C.

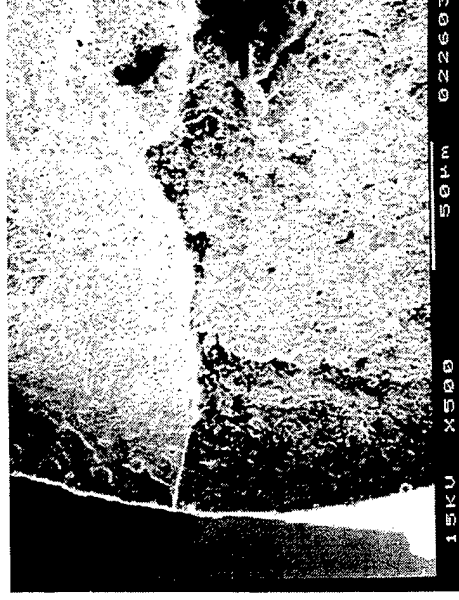
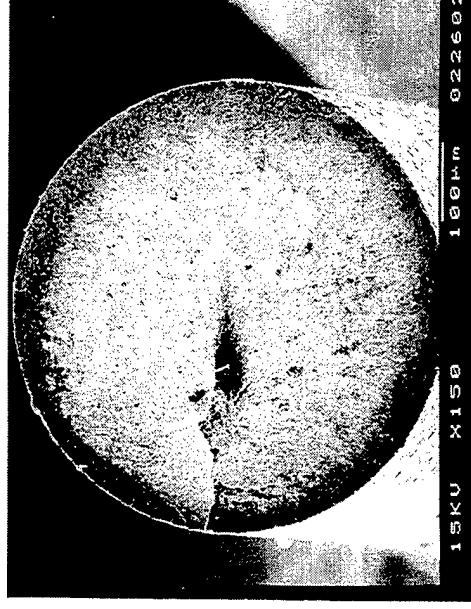
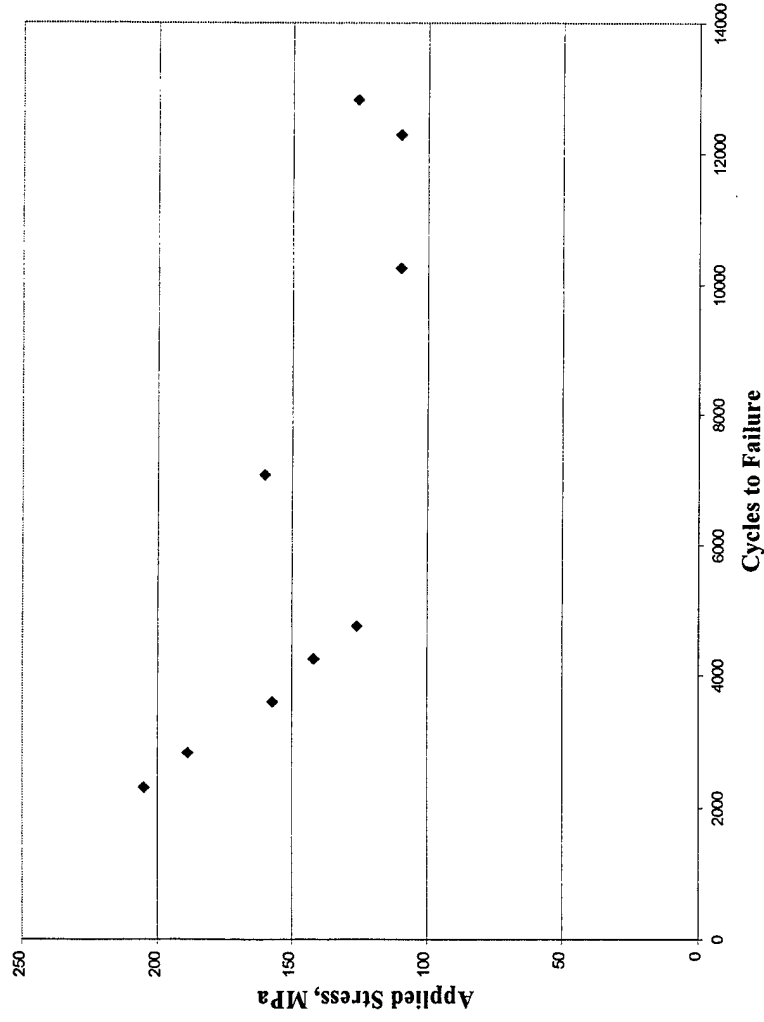
- ☐ Applied Stress, 158 MPa.
- ☐ Cycle frequency, .25 hz
 - 1 second heat
 - 3 second cool
- ☐ Bath Temperature 15°C.

- ☐ Applied Stress, 141 MPa.
- ☐ Cycle frequency, .25 hz
 - 1 second heat
 - 3 second cool
- ☐ Bath Temperature 15°C.



Applied Stress vs. Cycles to Failure and Fracture surfaces for NiTiCu SMA

600°C for 30 min. heat treatment



Future Research Plan

- ☐ Complete constant stress thermal fatigue experiments.
- ☐ Complete experimental study for partial transformation thermal fatigue and variable stress thermal fatigue.
- ☐ Perform further microstructural evaluations to determine and confirm the cause for material failure.
- ☐ Identify the role of the microstructure and processing on thermal fatigue characteristics.

Analytical Solutions for the Cylindrical Bending of Smart Structures: Statics and Vibration

Senthil S. Vel, Postdoctoral Research Associate
senthil@vt.edu

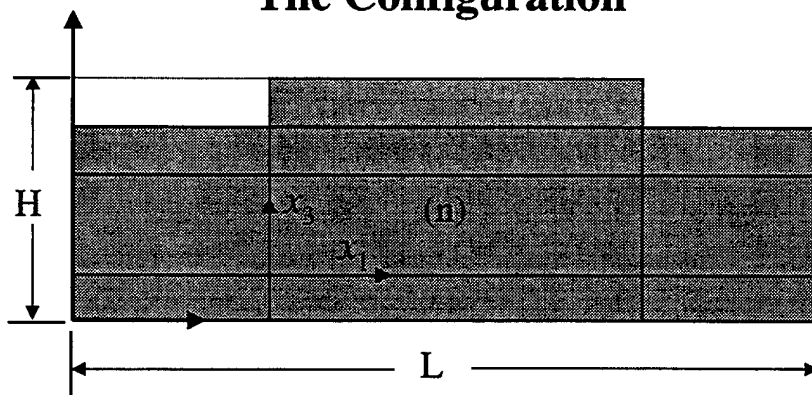
R. C. Batra, Clifton C. Garvin Professor
rbatra@vt.edu

Department of Engineering Science and Mechanics
Virginia Polytechnic Institute and State University
Blacksburg, VA 24061

1

Part I: Static Piezothermoelasticity

The Configuration



Generalized plane piezothermoelastic analysis of laminates:

- coupled quasistatic analysis
- **thick plates**
- **arbitrary boundary conditions**
- distributed or **segmented actuators/sensors**

2

The Governing Equations

Equilibrium equations:

$$\sigma_{ij,j} = 0, \quad D_{i,i} = 0, \quad q_{i,i} = 0.$$

Constitutive equations:

$$\sigma_{ij} = C_{ijkl} u_{k,l} - e_{kij} E_k - \beta_{ij} T,$$

$$D_i = e_{ikl} u_{k,l} + \epsilon_{ik} E_k + r_i T,$$

$$q_i = -\kappa_{ij} T_{,j}.$$

The electric field is related to the electric potential by $E_k = -\phi_{,k}$

Assumption of Generalized Plane Strain:

$$\mathbf{u} = \mathbf{u}(x_1, x_3), \quad \phi = \phi(x_1, x_3), \quad T = T(x_1, x_3).$$

3

A General Solution

Extension of Eshelby-Stroh Formalism:

$$\begin{bmatrix} \mathbf{u} \\ \phi \end{bmatrix} = \mathbf{a} f(z) + \mathbf{c} g(z_\tau), \quad T = g'(z_\tau), \quad (\dagger)$$

where $z = x_1 + p x_3$, $z_\tau = x_1 + \tau x_3$.

Substitution of (†) into the constitutive and equilibrium equations gives $p_\alpha, \mathbf{a}_\alpha, \tau$ and \mathbf{c} ($\alpha = 1, \dots, 4$).

$$\begin{bmatrix} \mathbf{u} \\ \phi \end{bmatrix} = \sum_{\alpha=1}^4 \mathbf{a}_\alpha f_\alpha(z_\alpha) + \mathbf{c} g(z_\tau) + \text{conjugate},$$

$$T = g'(z_\tau) + \text{conjugate}.$$

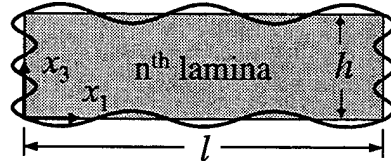
4

A Series Solution

$$f_{\alpha}(z_{\alpha}) = \sum_{m=0}^{\infty} \left\{ v_{m\alpha} \exp(\eta_{m\alpha} z_{\alpha}) + \hat{v}_{m\alpha} \exp(\eta_{m\alpha} (l - z_{\alpha})) \right\} \\ + \sum_{k=0}^{\infty} \left\{ w_{k\alpha} \exp(\lambda_{k\alpha} z_{\alpha}) + \hat{w}_{k\alpha} \exp(\lambda_{k\alpha} (p_{\alpha} h - z_{\alpha})) \right\}$$

where

$$\eta_{m\alpha} = -\frac{m\pi i}{p_{\alpha} h}, \quad \lambda_{k\alpha} = \frac{k\pi i}{l}$$



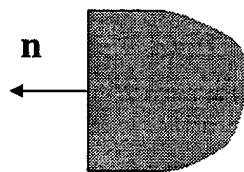
i.e., a single Fourier series on each surface with exponential decay towards the interior.

Series solution for $g(z_r)$ also.

5

Boundary and Interface conditions

If the surface is not in contact with another lamina:



$$\mathbf{J} \begin{bmatrix} u \\ \phi \\ T \end{bmatrix} + \hat{\mathbf{J}} \begin{bmatrix} t_n \\ D_n \\ q_n \end{bmatrix} = \mathbf{r}$$

Example: Mechanical clamped, electrically grounded and thermally insulated surface

$$\mathbf{J} = \text{diag}[1, 1, 1, 1, 0], \quad \hat{\mathbf{J}} = \text{diag}[0, 0, 0, 0, 1], \quad \mathbf{r} = \mathbf{0}$$

6

Boundary and Interface conditions (contd.)

The interfaces are assumed to be perfectly bonded together:

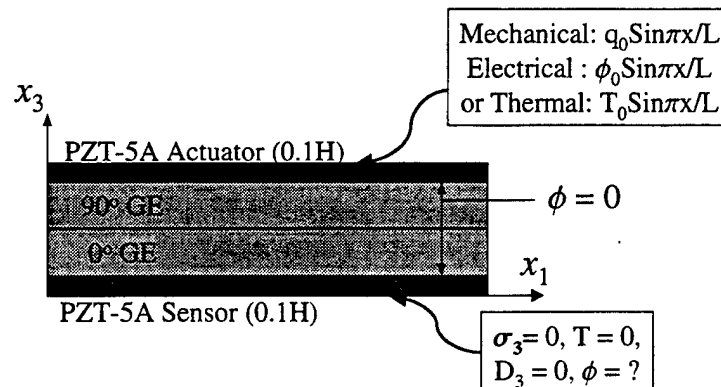
$$[[\mathbf{u}]] = \mathbf{0}, \quad [[\mathbf{t}_n]] = \mathbf{0}, \quad \underbrace{[[\phi]] = 0, \quad [[D_n]] = 0, \quad [[T]] = 0, \quad [[q_n]] = 0}_{\text{replace by } \phi = \Phi \text{ if the interface is electroded}}$$

The boundary conditions and interface continuity conditions are enforced using the classical Fourier series approach

A convergence study was performed from 50 to 400 terms

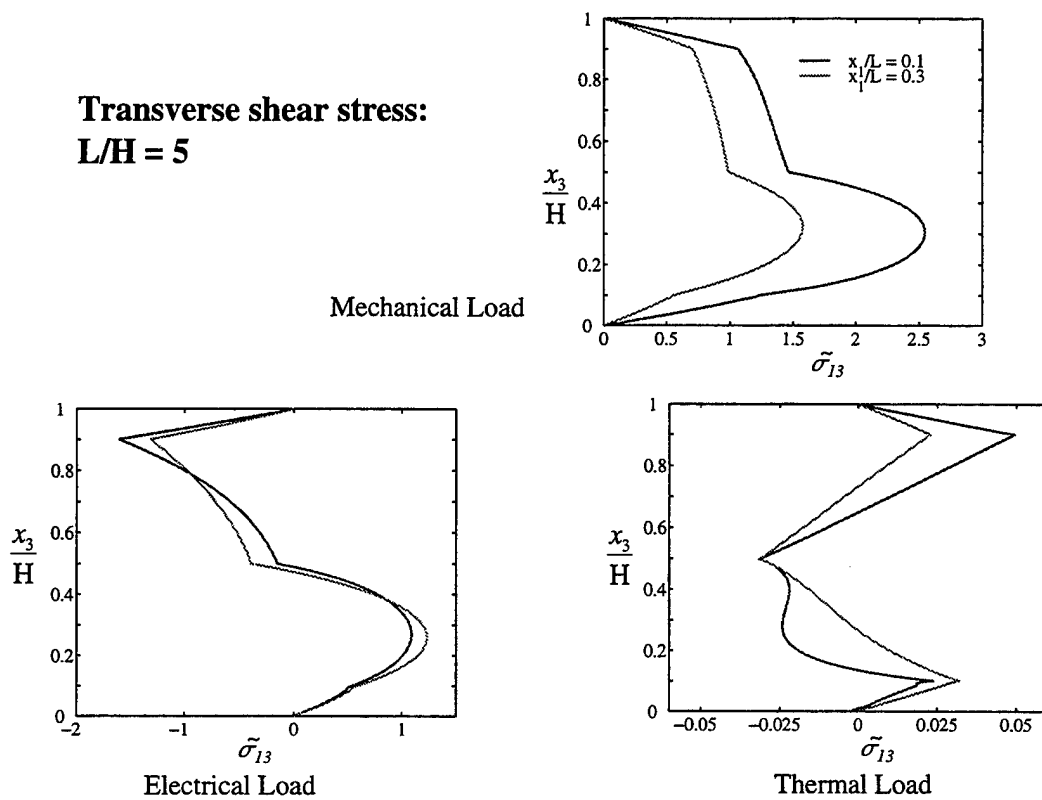
7

Example: Hybrid Laminate with Distributed Actuator and Sensor



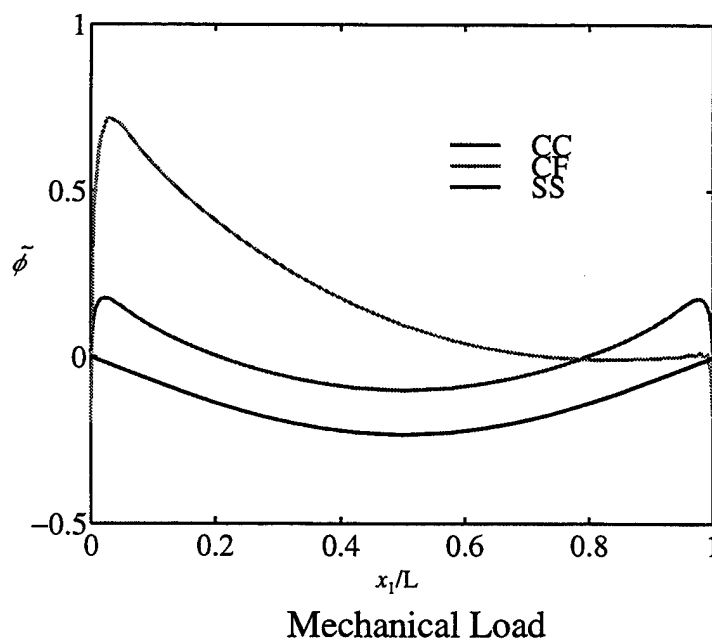
8

**Transverse shear stress:
 $L/H = 5$**



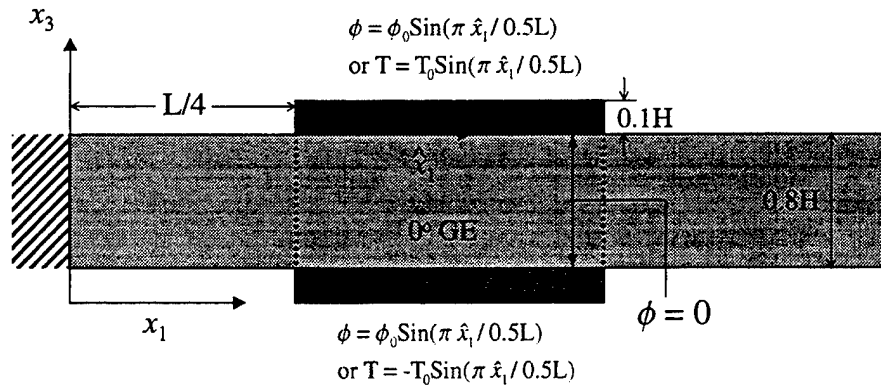
9

Influence of Boundary Conditions on Sensor Voltage



10

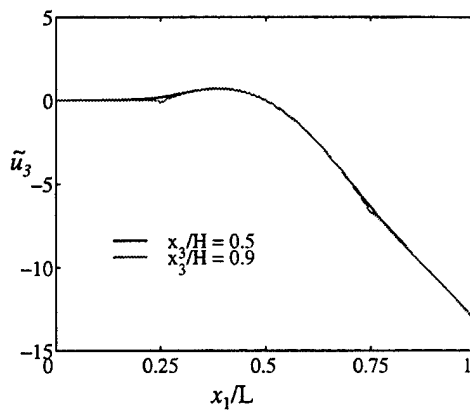
Cantilever plate with actuator patches



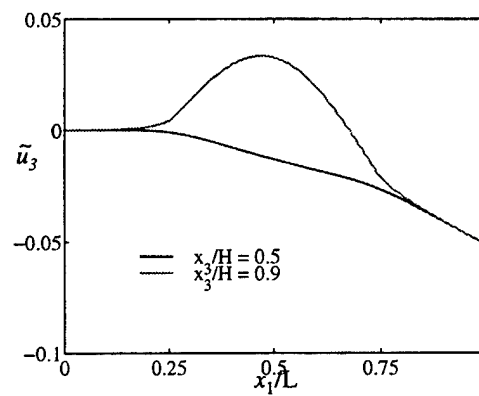
$$L/H = 5$$

11

Transverse deflection



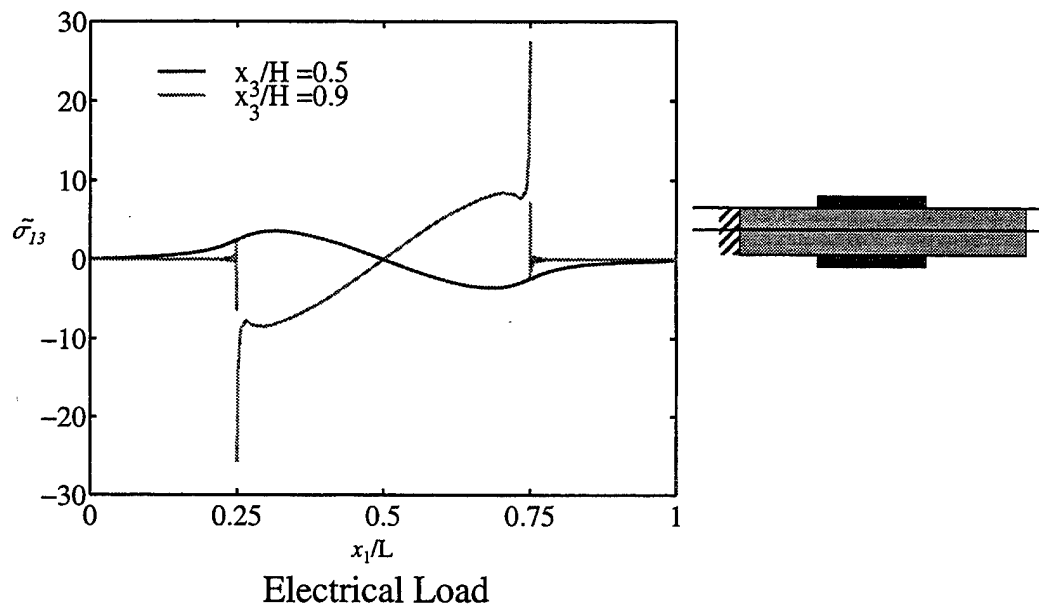
Electrical Load



Thermal Load

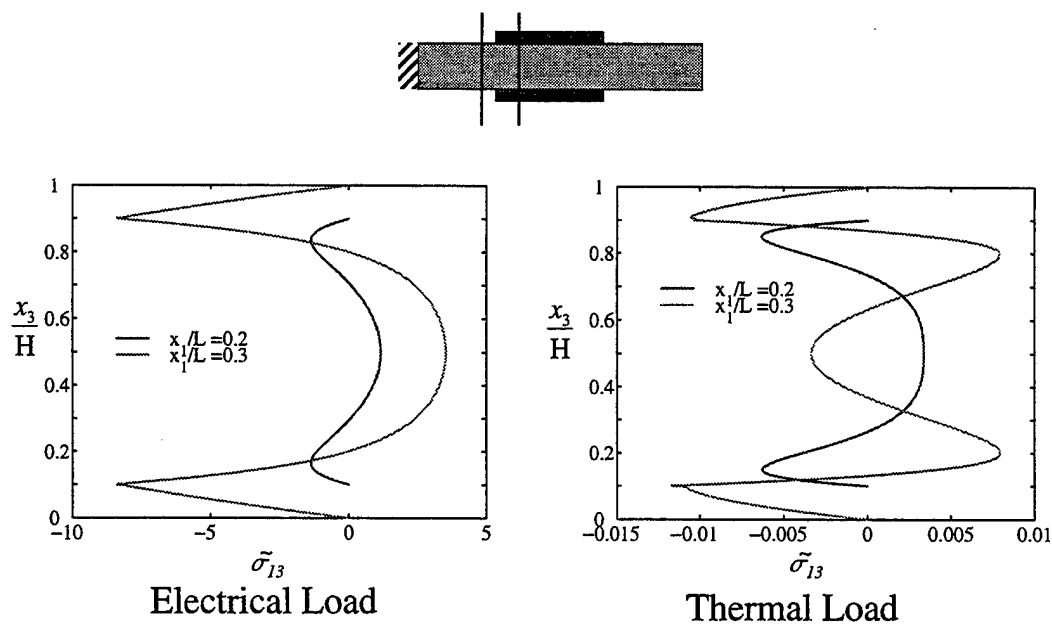
12

Interfacial Shear Stress



13

Transverse Shear Stress



14

Conclusions to Part I

- The Eshelby-Stroh formalism is used to satisfy the governing equations. The analytic functions are chosen as infinite series. The coefficients are determined by satisfying the boundary and interface continuity conditions.
- The method is versatile and capable of analyzing plates with distributed and patched actuators/sensors.
- The interfacial shear stress is unbounded at the edges of a segmented piezoelectric actuator attached to an elastic substrate

Fracture and Fatigue of Piezoceramics Under Electrical and Mechanical Loading

C.T. Sun

School of Aeronautics and Astronautics

Purdue University

W. Lafayette, IN 47907-1282

Tel: 765-494-5130 Fax: 765-494-0307

E-mail: sun@ecn.purdue.edu

Abstract

The use of piezoceramics as actuators in smart structures demands that these materials perform under increasingly high electric and mechanical loads. Durability and reliability of piezoceramic actuators have become an important issue. Therefore, fracture and fatigue behavior of piezoceramics should be understood and predictive models should be developed.

Under intensive electrical and mechanical loads, piezoceramics could undergo polarization switching resulting from microstructural domain wall switching. Such domain wall switching often occurs near the tip of a crack (or flaws) in a piezoelectric material under electrical and mechanical loads because of the singular nature of the stress and electric fields. Domain switching, if occurs, may alter the near tip stress field and, consequently, change the apparent fracture toughness of the material.

In this study, an energy-based criterion for domain switching in piezoelectric materials is proposed. It is assumed that domain switching occurs and is completed instantly if the change of internal energy exceeds a critical value. The criterion is verified using experimental results for PZT and PLZT piezoceramics. A finite element based algorithm in conjunction with the domain switching criterion is developed to analyze the stresses and electric fields in compact tension specimen with a single edge crack. Domain switching zones in the vicinity of the crack tip corresponding to various combined electrical and mechanical loads are obtained. It is found that the size, shape and mode (90° or 180° switching) of domain switching zone near the crack tip depend on the magnitude and direction of the electric field. Moreover, the stress intensity factor and, consequently, the fracture toughness are now affected by the electric field through domain switching. Experimental fracture and fatigue data for PZT4 are presented and compared with the theoretical predictions.

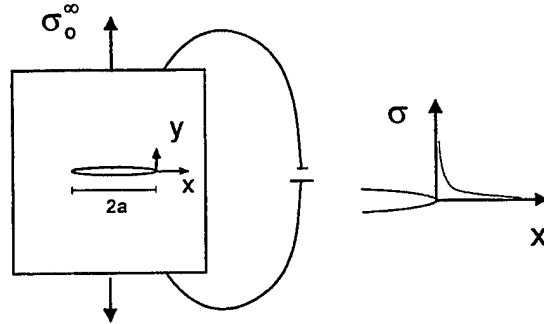
Classical Fracture Criteria

1. Stress Intensity Factors

- Fracture occurs when intensity of stress reaches a critical value

$$\sigma = \frac{K_I}{\sqrt{2\pi x}}$$

$$K_I = \sqrt{\pi a} \sigma_o^\infty$$



- Fully decoupled between mechanical and electrical fields: Stress Intensity Factor is not affected by the electrical field, thus cannot account for electric field effect on fracture

2. Total Energy Release Rate

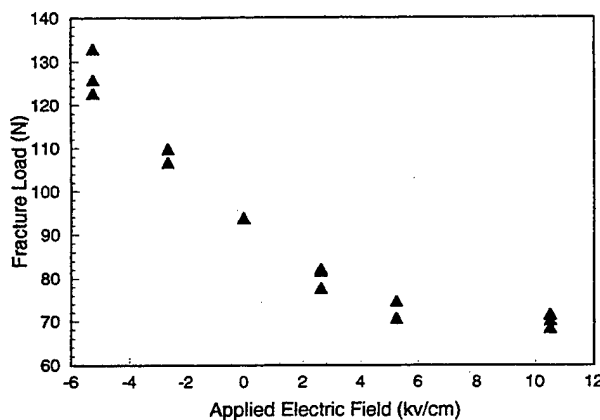
$$G = G_c \Rightarrow \text{Fracture}$$

$$G = \lim_{\Delta a \rightarrow 0} \frac{1}{\Delta a} \int_0^{\Delta a} \{ \sigma(x)u(x - \Delta a) + D(x)\phi(x - \Delta a) \} dx$$

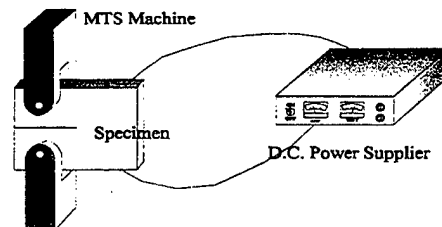
- Predictions are way off when comparing with experimental data

Motivation:

1. Experimental Results



(Park & Sun, 1995, PZT-4)



Observation: Negative electric field increases fracture load while positive electric field decreases fracture load.



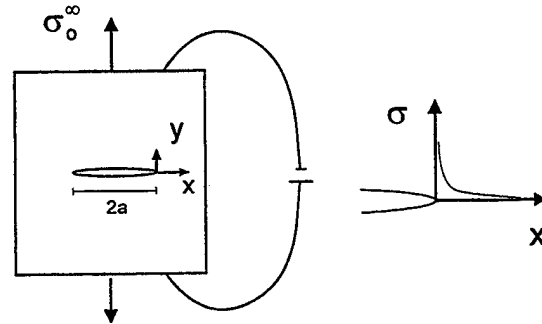
Classical Fracture Criteria

1. Stress Intensity Factors

- Fracture occurs when intensity of stress reaches a critical value

$$\sigma = \frac{K_I}{\sqrt{2\pi x}}$$

$$K_I = \sqrt{\pi a} \sigma_0^\infty$$



- Fully decoupled between mechanical and electrical fields: Stress Intensity Factor is not affected by the electrical field, thus cannot account for electric field effect on fracture

2. Total Energy Release Rate

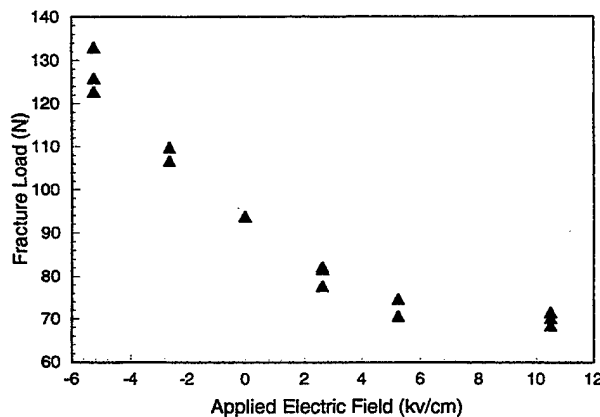
$$G = G_c \Rightarrow \text{Fracture}$$

$$G = \lim_{\Delta a \rightarrow 0} \frac{1}{\Delta a} \int_0^{\Delta a} \{ \sigma(x)u(x - \Delta a) + D(x)\phi(x - \Delta a) \} dx$$

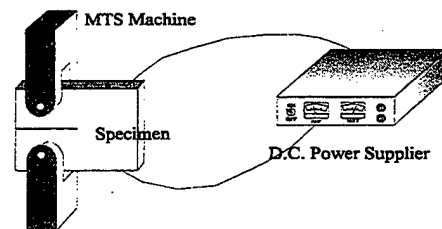
- Predictions are way off when comparing with experimental data

Motivation:

1. Experimental Results



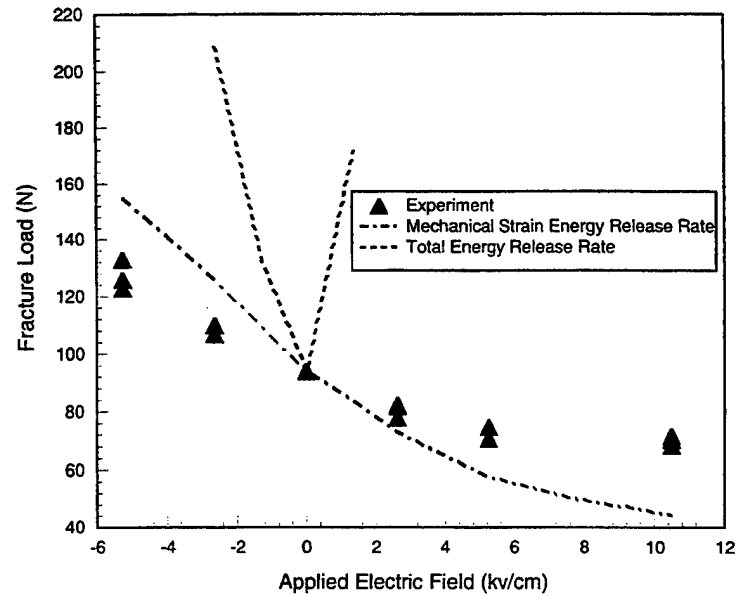
(Park & Sun, 1995, PZT-4)



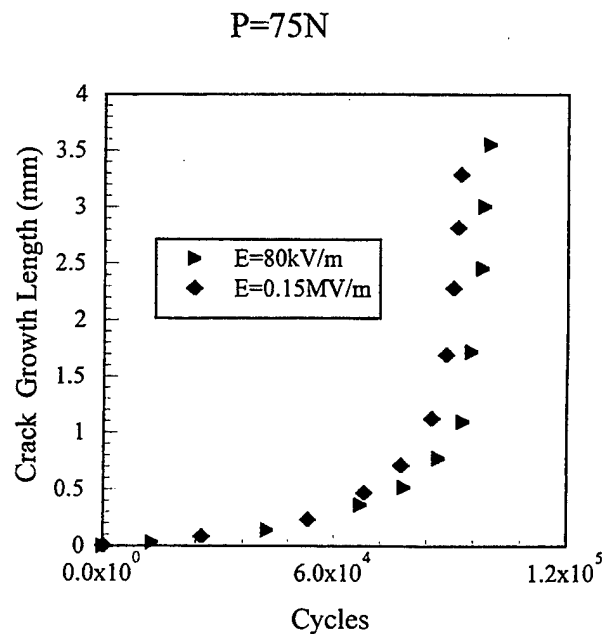
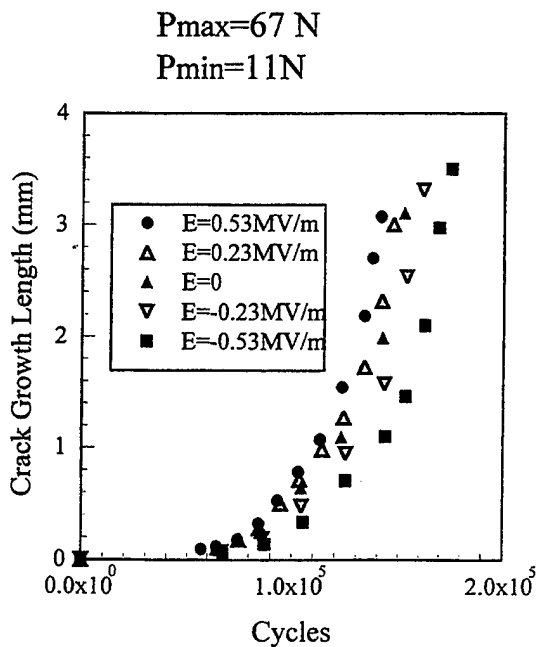
Observation: Negative electric field increases fracture load while positive electric field decreases fracture load.



Fracture Load Prediction by different Criteria

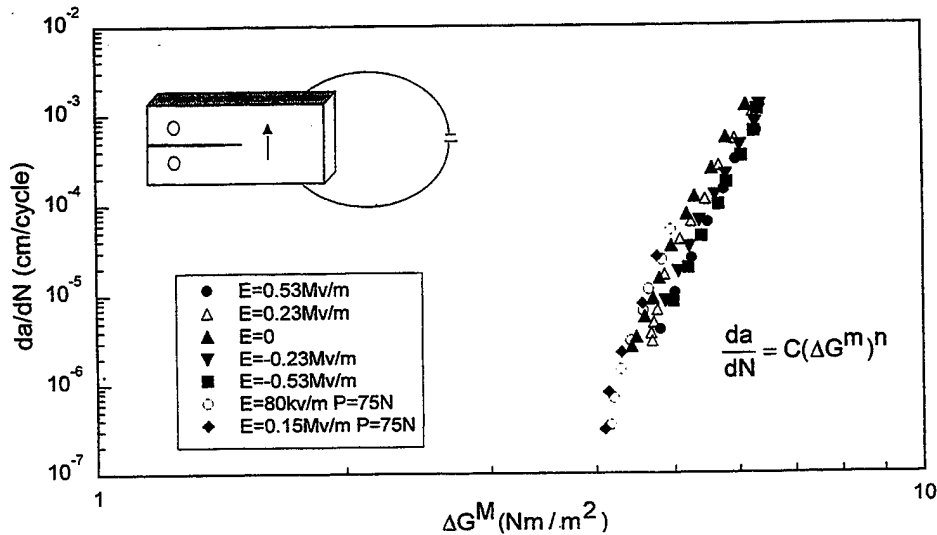


Fatigue Crack Growth Data from CTS Specimen

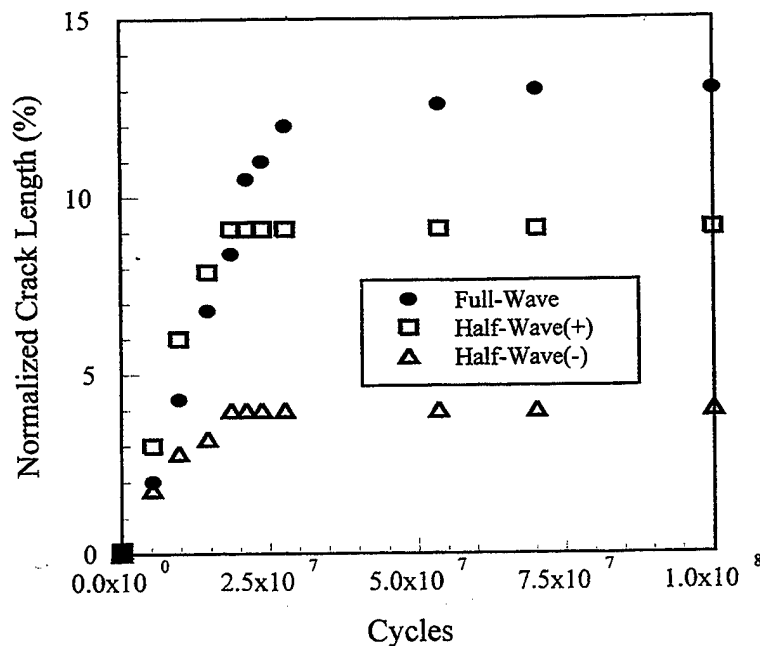


Paris Law Using Mechanical Energy Release Rate

The crack growth curve under different mechanical and electric loads all collapse into a single master curve. The mechanical strain energy release rate rather than the total energy release rate is able to capture the fracture and fatigue behavior of piezoceramics in the presence of electric fields.



Indentation Crack Under Electric Loading



Domain Switching Criterion

Sun and Jiang (1998) proposed that domain switches once the change of internal energy density G reaches a critical value G^c , i.e.,

$$G = \sigma_{ij} dy_{ij} + E_i dD_i \geq G_k^c, \quad k = 90^\circ, 180^\circ$$

where the change of strains and electric displacements include two parts: crystal structure change and piezoelectric effect.

- For 180° switching

$$G_{180^\circ}^c = 2P^s |E_{180}^c|$$

- For 90° switching

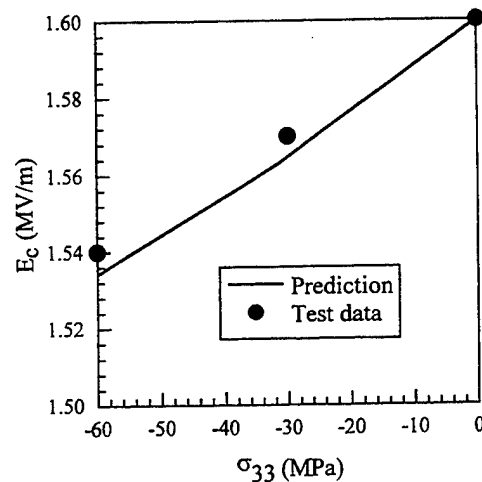
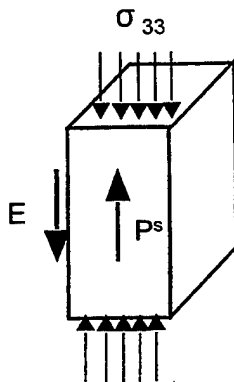
$$G_{90^\circ}^c = P^s |E_{90}^c| = \gamma^s |\sigma_{33}^c|$$

Switching criterion was shown to be accurate for experimental results using PZT and PLZT.

Experimental Verification

- 180° Ferroelectric Switching (PZT-4)

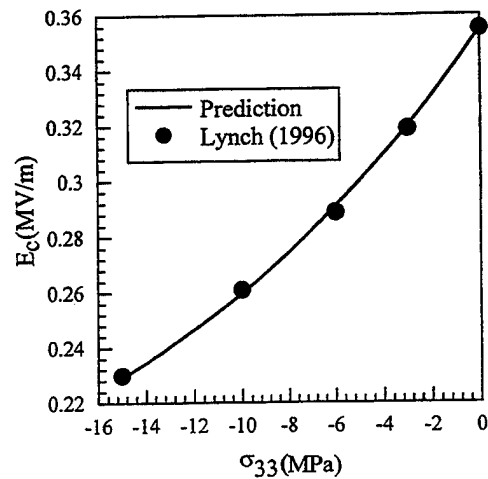
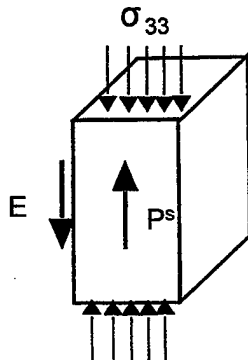
$$E_3^c = - \frac{|E_{180}^c|}{1 - \frac{2d_{23}}{P^s} \sigma_{33}}$$



Experimental Verification (cont.)

• 180° Ferroelectric Switching (PLZT)

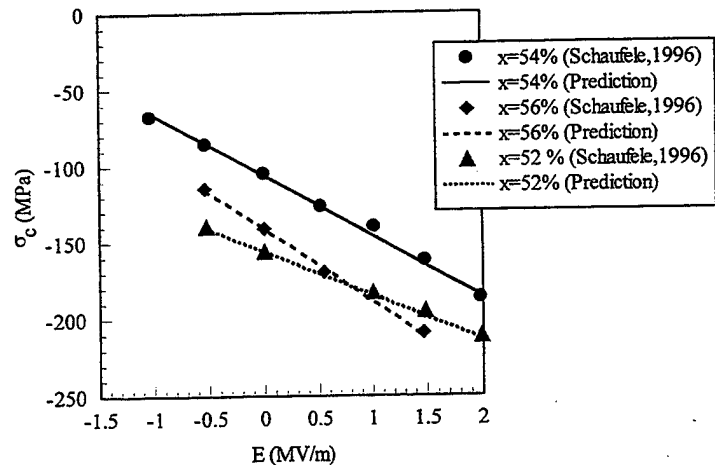
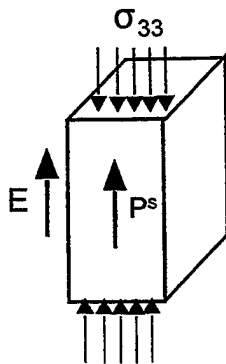
$$E_3^c = -\frac{|E_{180}^c|}{1 - \frac{2d_{23}}{P^s} \sigma_{33}}$$



Experimental Verification (cont.)

• 90° Ferroelastic Switching

$$\sigma_{33} = -|\sigma_{33}^c| - \frac{P^s}{Y^s} E_3$$

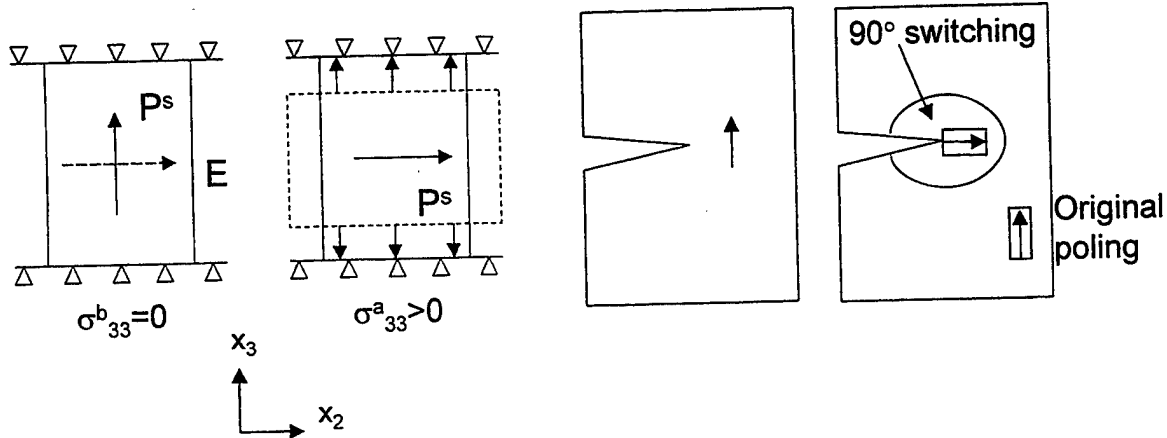


hard PZT- ($\text{Pb}(\text{Zr}_x\text{Ti}_{1-x})_{0.985}\text{Fe}_{0.015}\text{O}_{2.9925}$)



Non-Uniform Stress and Electric Field

- Stresses are different after including the crystal change induced by switching



Modified Domain Switching Criterion

It is proposed to use the average values of the stress and electric field before and after switching

$$G = \frac{\sigma^b_{ij} + \sigma^a_{ij}}{2} dy_{ij} + \frac{E^b_i + E^a_i}{2} dD_i \geq G^c_k, \quad k = 90^\circ, 180^\circ$$

where $\sigma^b(E^b)$ and $\sigma^a(E^a)$ stand for the stresses (electric fields) before and after switching.

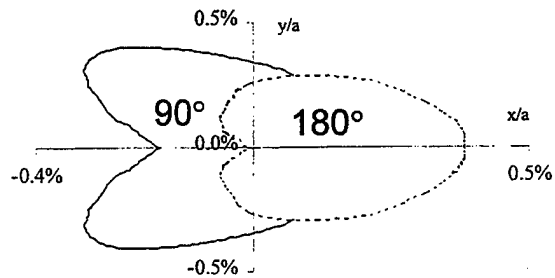
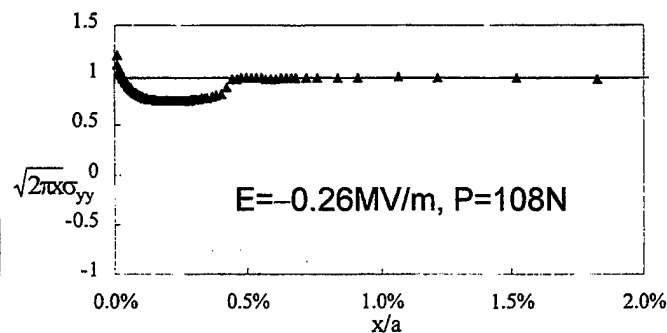
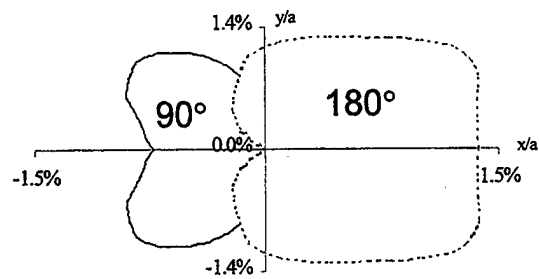
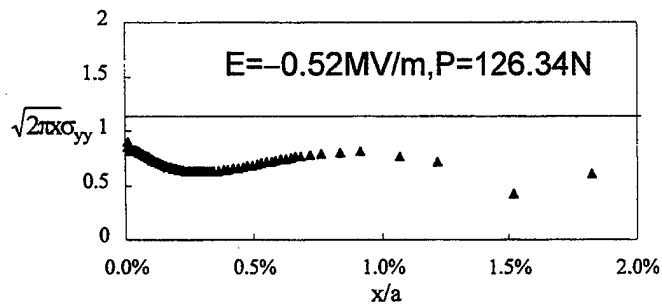
In order to determine which type of switching would take place, compare $G/G^c_{180^\circ}$ and $G/G^c_{90^\circ}$, and.

$$G^c_{180^\circ} = 1.36 \text{ MN/m}^2$$

$$G^c_{90^\circ} = 1.05 \text{ MN/m}^2$$

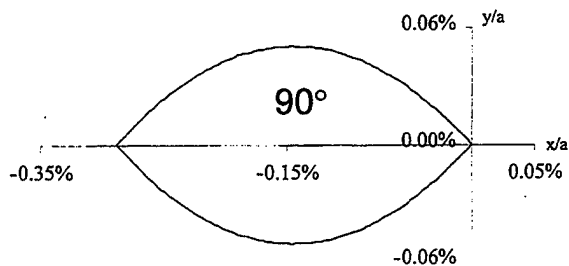
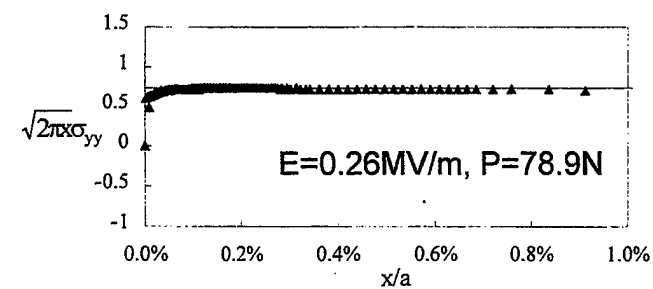
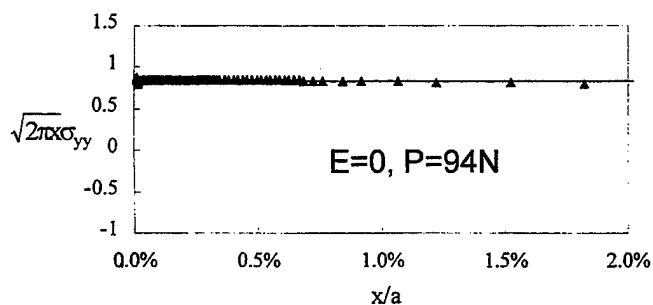


Determination of Effective Stress Intensity Factor

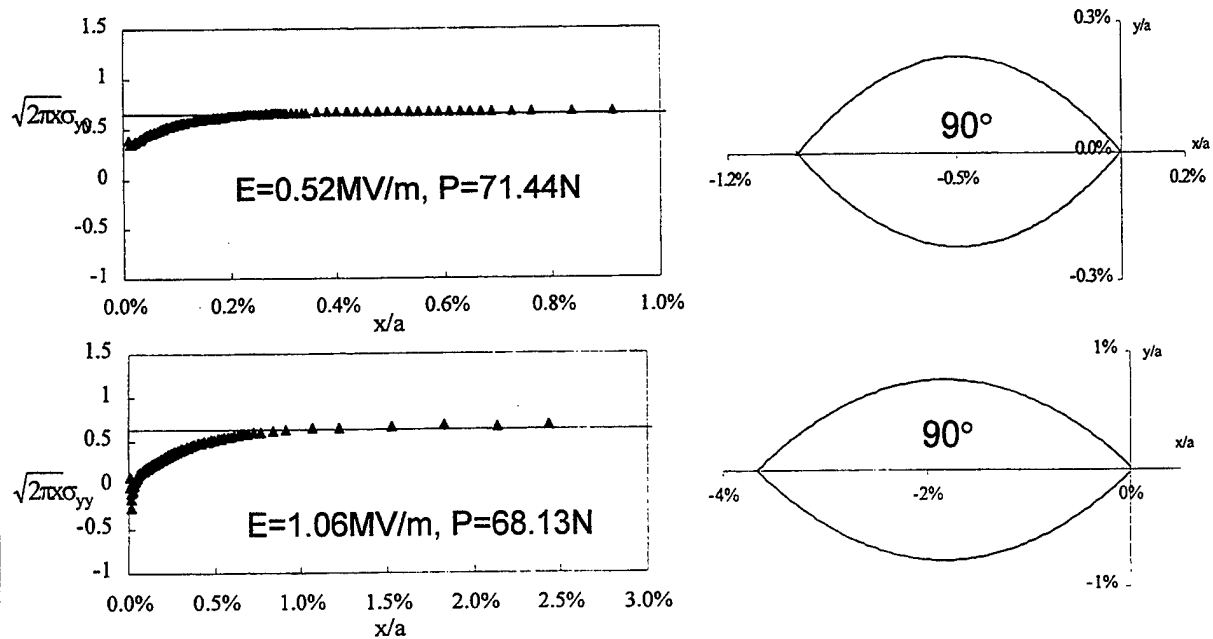


For negative electric field: averaging over the 180° switching zone range

Determination of Effective Stress Intensity Factor (cont.)



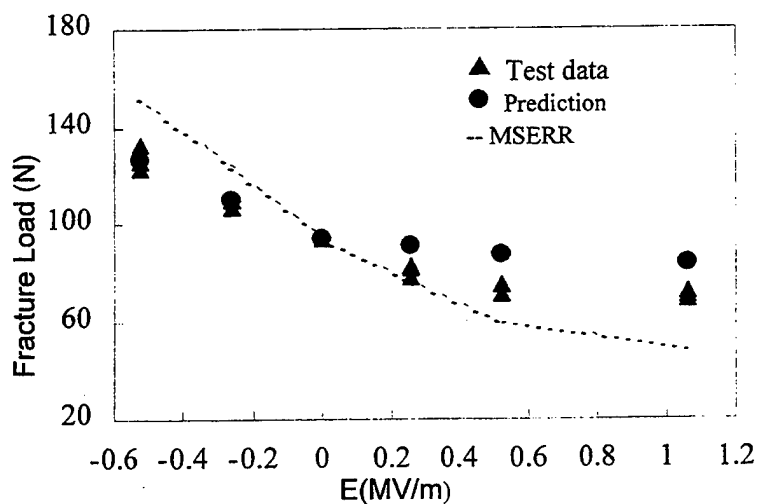
Determination of Effective Stress Intensity Factor (cont.)



For positive electric field: determining at some distance ahead of the tip

Comparison

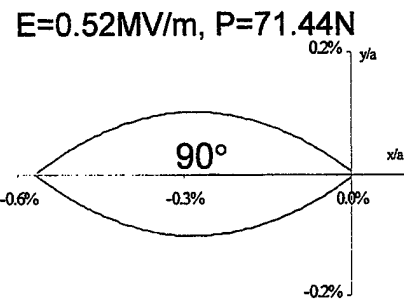
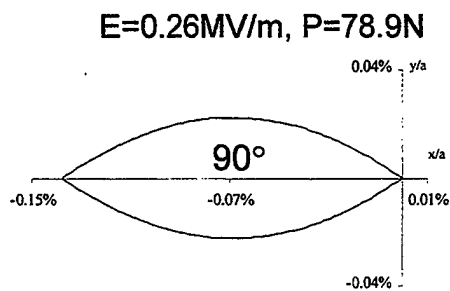
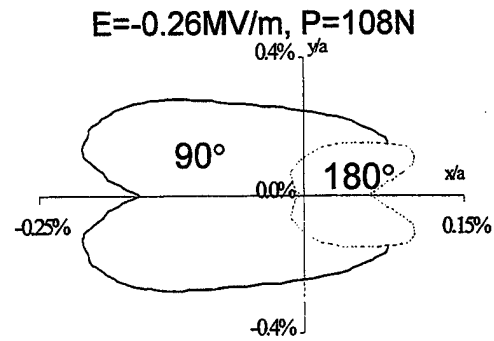
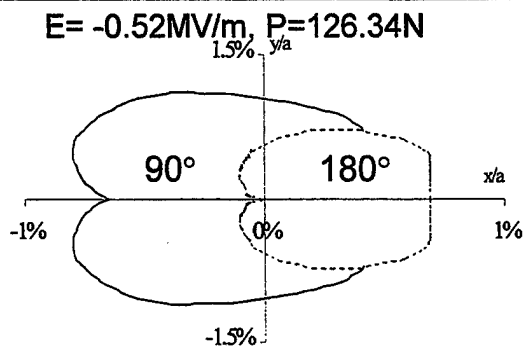
- Choose fracture toughness for $E=0$, $P=94\text{ N}$ as the critical value



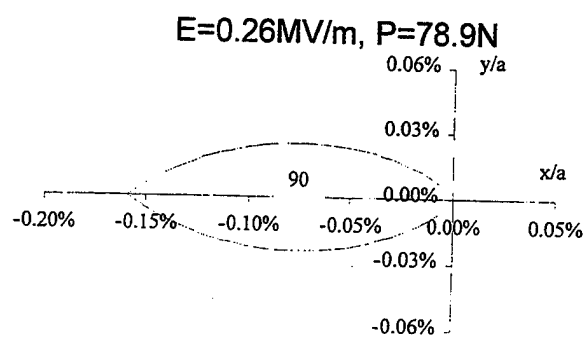
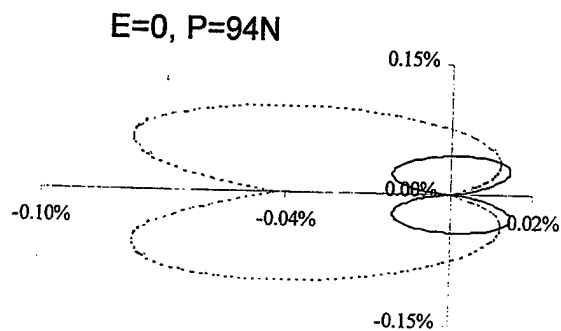
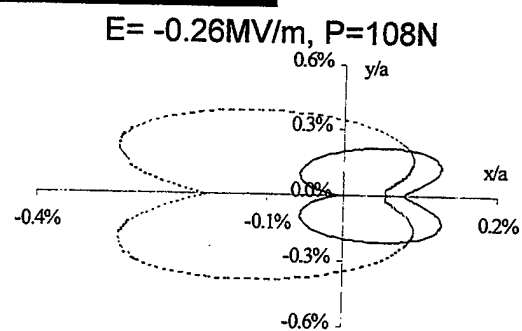
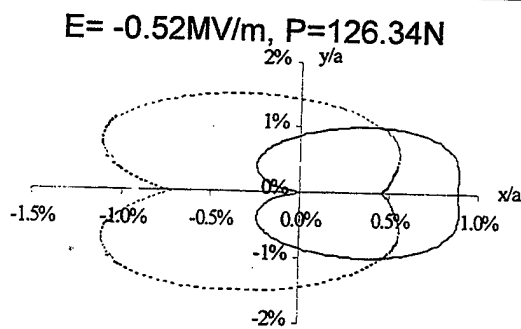
Observation: prediction from FEM is quite good comparing with test result



One Step Solution



Near Tip Solution



Prediction of the As-Manufactured Shapes of Rectangular and Circular Piezoceramic Benders

M.W. Hyer and A.B. Jilani

Department of Engineering Science and Mechanics

219 Norris Hall, Campus Code 0219

Virginia Polytechnic Institute and State University

Blacksburg VA 24061

for first author - tel: 540-231-5372, fax: 540-231-4574, email: hyerm@vt.edu

Benders, which usually consist of a number of layers of metals, plastics, and active materials such as piezoceramics, can be laminated in such a way that as they are cooled from the cure temperature of the adhesives bonding the layers together, they deform significantly out of plane. This occurs because the laminated construction is such that the material properties of the layers, particularly the elastic constants and the coefficients of thermal expansion, are not symmetric with respect to the bender geometric midsurface. As a result, as the device cools to room temperature, differences in thermally-induced strains and stiffnesses of the layers cause out-of-plane deformations. These out-of-plane deformations are an advantage because they amplify the displacements caused by activating the piezoceramic material. An example of this construction is a class of devices commonly referred to as THUNDER. The purpose of this paper is to present an analysis that can be used to predict the out-of-plane deformations associated with the manufacturing processes of these devices. What makes the study of these manufacturing deformations so interesting is that the deformations are large enough that they cause geometrically nonlinear effects during cooling, and the cause of these effects can be traced to the geometry and material properties of the device. A change in the length and width of a rectangular bender, or the diameter of a circular bender, and the cure temperature of the adhesive are but two parameters that control the as-manufactured shape. Furthermore, under certain rather general conditions, more than one as-manufactured shape is possible for a given set of material and geometric properties. Thus the study is felt to be useful for determining the sensitivity of the as-manufactured shape to the various material and geometric parameters of the device so that the design process can be simplified.

The analysis is based on a Rayleigh-Ritz approach to minimizing the total potential energy of the bender as it is cooled from the processing temperature to room temperature. Because the problem is geometrically nonlinear, stability is an issue. Thus the first and second variations of the total potential energy are used. The key to the analysis is the proper choice of the approximate displacement fields required by the Rayleigh-Ritz procedure. The end result of the Rayleigh-Ritz approach is a set of nonlinear algebraic equations that are solved numerically. The equations can have multiple roots, the multiple roots corresponding to the multiple room-temperature configurations. The stability of each of the roots is considered to access whether or not a particular configuration will be observed.

Reference

Hyer, M.W. and A.B. Jilani, 'Predicting the deformation characteristics of rectangular unsymmetrically laminated piezoceramic materials,' *Smart Materials and Structures*, 7 (1998) 784-791

***Prediction of the As-Manufactured Shapes of Rectangular
and Circular Piezoceramic Benders***

Michael W. Hyer and Adel B. Jilani

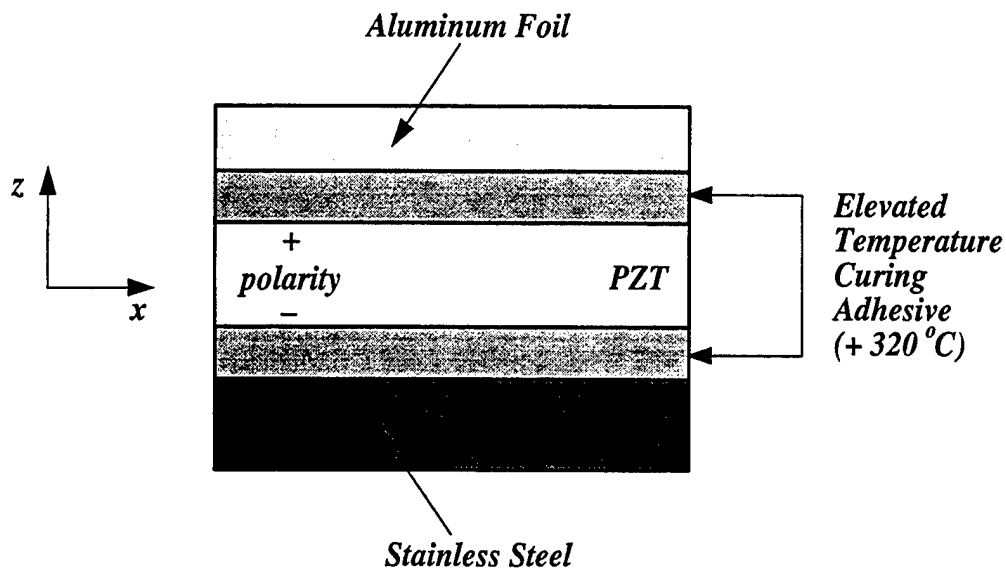
*Department of Engineering Science and Mechanics
Virginia Polytechnic Institute and State University*

*Fourth ARO Smart Structures Workshop
Penn State, University Park Campus, Pennsylvania
August 16–18, 1999*

*Acknowledgement
NASA Langley Research Center Grant NCC-1-304*

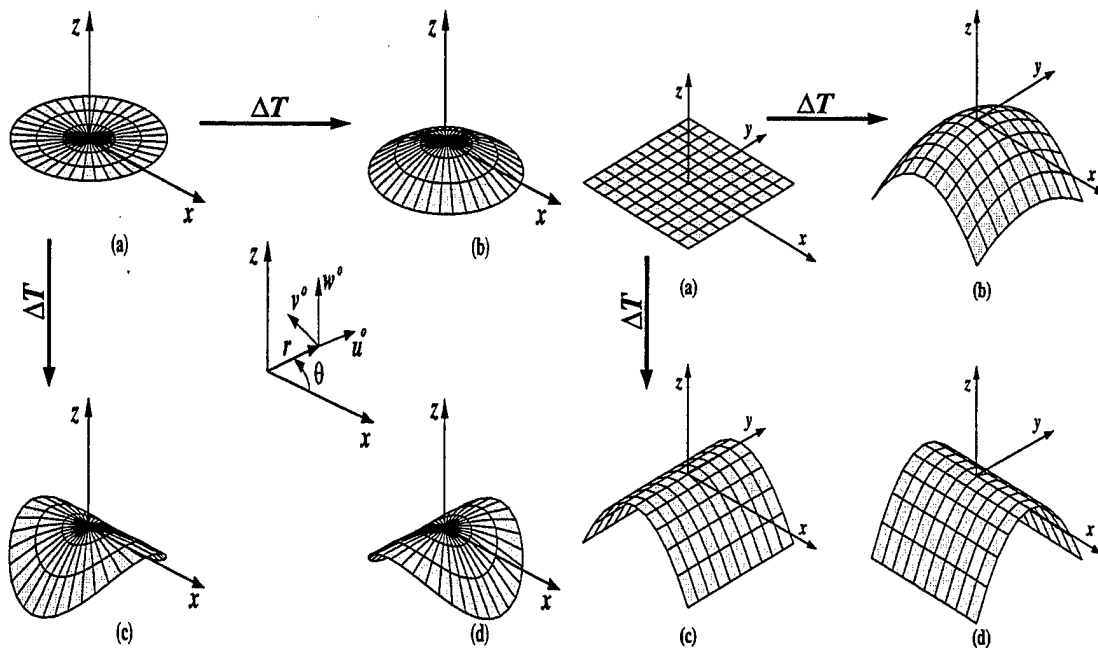
VaTech

The Cross-Section of THUNDER Bender



VaTech

Circular and Rectangular THUNDER Room–Temperature Shapes



VaTech

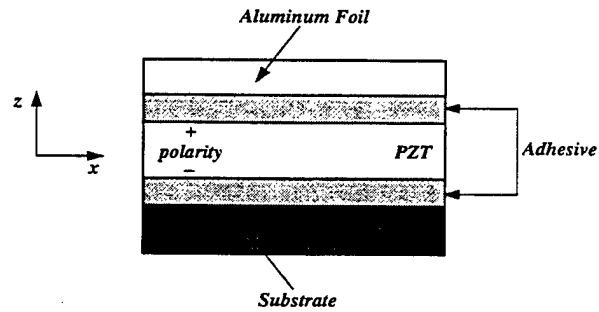
Modeling Approach for THUNDER Room–Temperature Shapes

Overview

- Use Rayleigh–Ritz approach with Total Potential Energy
- Consider geometrically nonlinear effects
- Assume material is linear elastic
- Assume Kirchhoff plate theory
- Use first variation of Total Potential Energy to find equilibrium configuration
- Use second variation of Total Potential Energy to study stability

VaTech

Numerical Results

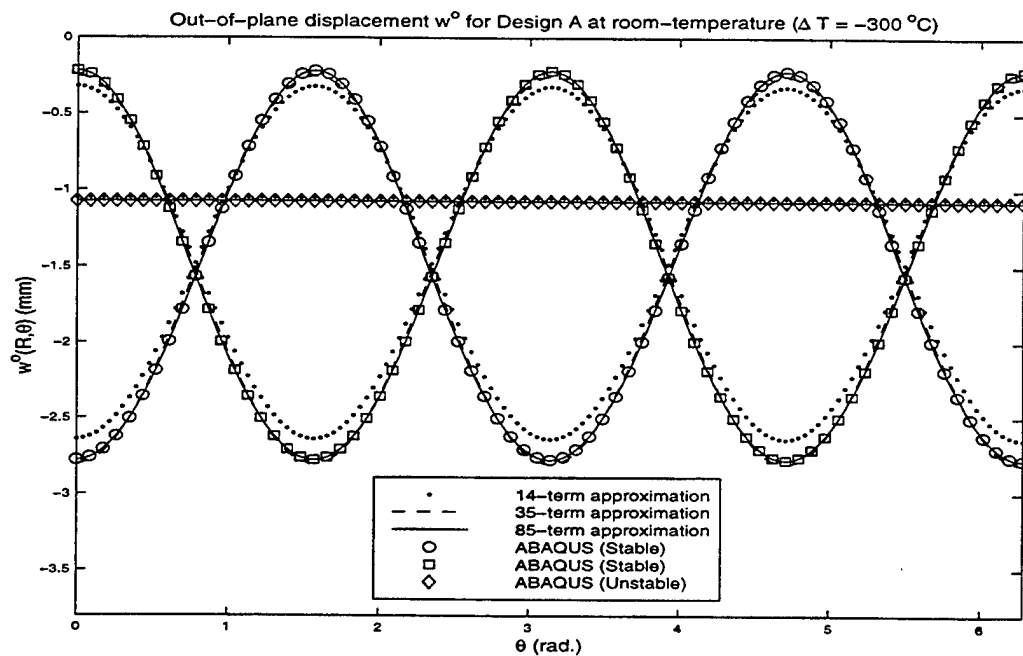


Design	R (mm)	PZT Thickness (mils)	Substrate	
			Thickness (mils)	Material
a	25.40	10	6	Stainless Steel
A	38.1	10	6	Stainless Steel
b	15.88	10	6	Stainless Steel

Material Properties				
	Stainless Steel	Aluminum Foil	PZT5A	Adhesive
E (GPa)	207.0	70.0	69.0	3.45
ν	0.30	0.30	0.31	0.40
α ($10^{-6}/^{\circ}\text{C}$)	10.8	23.4	2.0	45.0

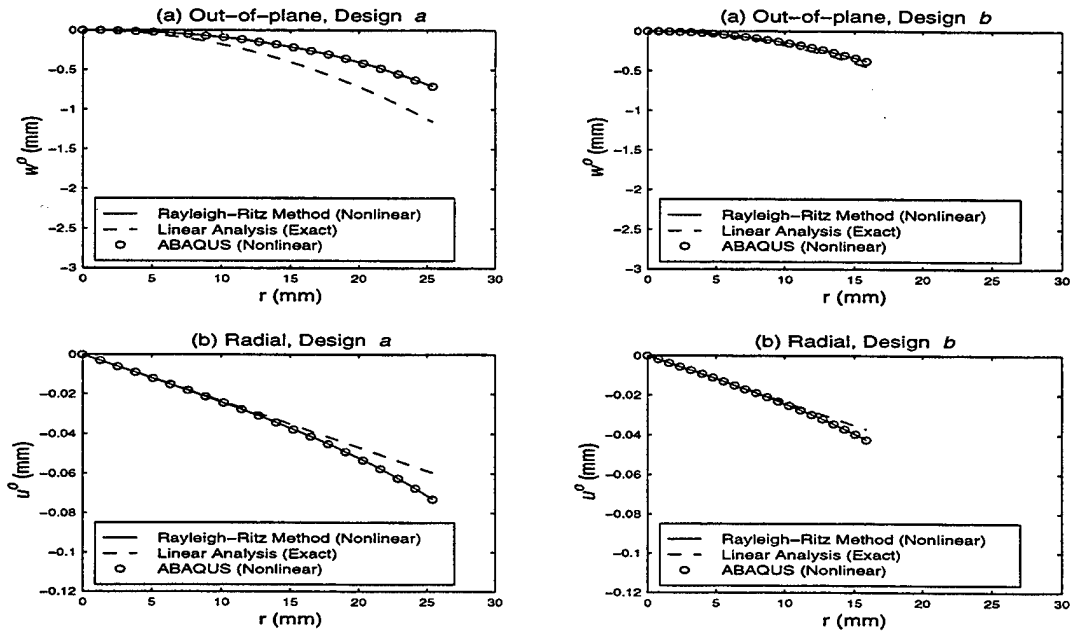
VaTech

Convergence of the Rayleigh-Ritz Method



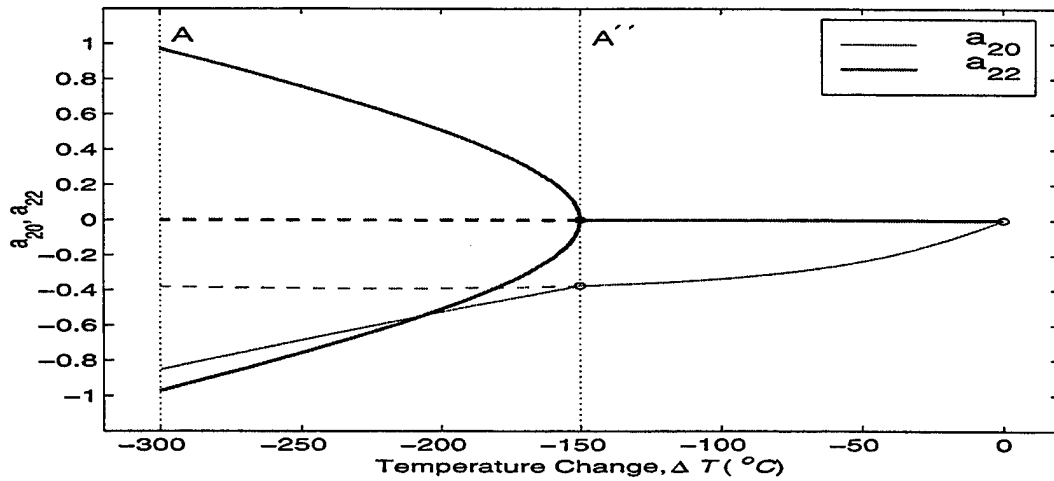
VaTech

Displacements of Designs a and b



VaTech

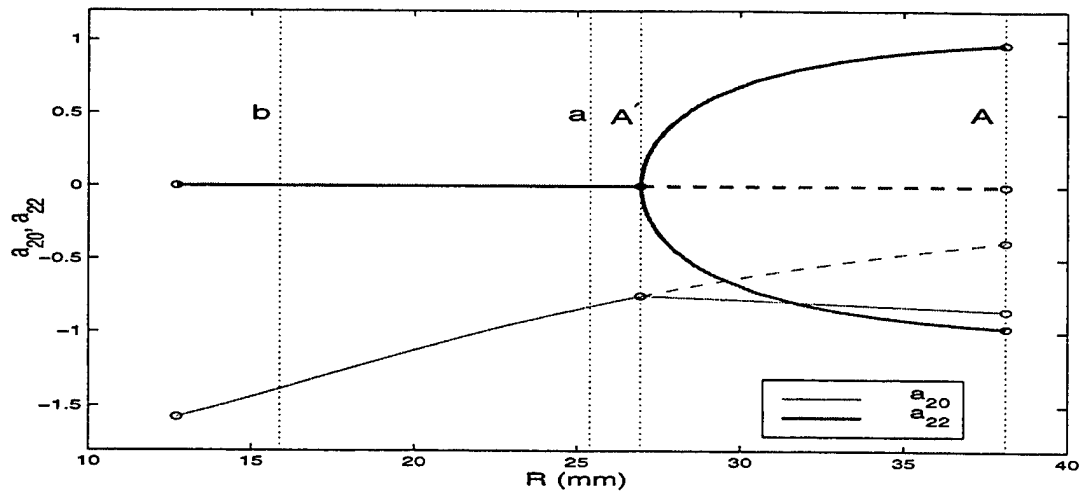
Curvatures of Design A vs. Temperature



$$\begin{aligned}\kappa_r^0 &= -2a_{20} - 6a_{30}r - 12a_{40}r^2 - 20a_{50}r^3 - 30a_{60}r^4 \\ &\quad - (2a_{22} + 6a_{32}r + 12a_{42}r^2 + 20a_{52}r^3 + 30a_{62}r^4) \cos(2\theta) \\ \kappa_\theta^0 &= -2a_{20} - 3a_{30}r - 4a_{40}r^2 - 5a_{50}r^3 - 6a_{60}r^4 \\ &\quad + (2a_{22} + a_{32}r - a_{52}r^3 - 2a_{62}r^4) \cos(2\theta) \\ \kappa_{r\theta}^0 &= 4(a_{22} + 2a_{32}r + 3a_{42}r^2 + 4a_{52}r^3 + 5a_{62}r^4) \sin(2\theta)\end{aligned}$$

VaTech

Curvatures vs. Radius at $\Delta T = -300^\circ \text{C}$



$$\begin{aligned}\kappa_r^o &= -2a_{20} - 6a_{30}r - 12a_{40}r^2 - 20a_{50}r^3 - 30a_{60}r^4 \\ &\quad - (2a_{22} + 6a_{32}r + 12a_{42}r^2 + 20a_{52}r^3 + 30a_{62}r^4) \cos(2\theta) \\ \kappa_\theta^o &= -2a_{20} - 3a_{30}r - 4a_{40}r^2 - 5a_{50}r^3 - 6a_{60}r^4 \\ &\quad + (2a_{22} + a_{32}r - a_{52}r^3 - 2a_{62}r^4) \cos(2\theta) \\ \kappa_{r\theta}^o &= 4(a_{22} + 2a_{32}r + 3a_{42}r^2 + 4a_{52}r^3 + 5a_{62}r^4) \sin(2\theta)\end{aligned}$$

VaTech

Conclusions

- Analysis developed agrees very well with ABAQUS
- Analysis directly gives multiple roots (if necessary)
- Analysis addresses stability directly
- Geometric nonlinearities are important
 - Flattening
 - Multiple shapes
- Shape(s) of circular THUNDER are a strong function of radius
- Cure temperature can influence shape(s)

VaTech



Measurement of the Constitutive and Fracture Behavior of PZT

**Christopher S. Lynch
The Georgia Institute of Technology**

The G.W. Woodruff School of
Mechanical Engineering



Overview

- **Characterization of Ferroelectric Ceramics**
 - Need for Characterization
 - **Improve device reliability**
 - **Develop design tools for devices**
 - Measured Fracture Toughness
 - Measured Constitutive Behavior of Ferroelectrics
 - Modeling Constitutive Behavior
 - **Micromechanics Models**
 - **Phenomenological Models**
 - Finite Element Analysis
 - **Crack Tip Field Concentrations**
 - **Multilayer Design**

The G.W. Woodruff School of
Mechanical Engineering

Stress and electric field concentrations in PLZT



Electric Field



Stress

The G.W.Woodruff School of
Mechanical Engineering

R-curve Testing

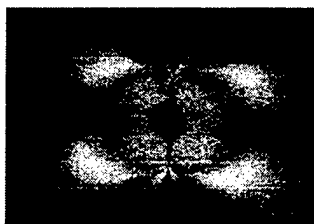


Side view showing
shape of the
indentation



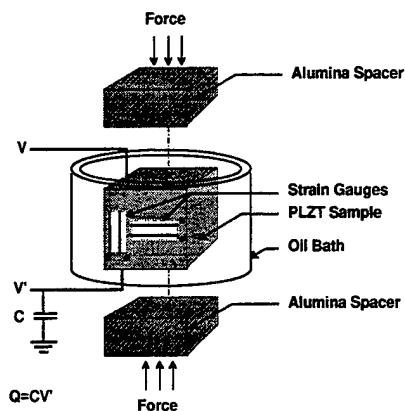
Micrograph
showing
fracture surface

Top view showing
residual stress induced
by birefringence



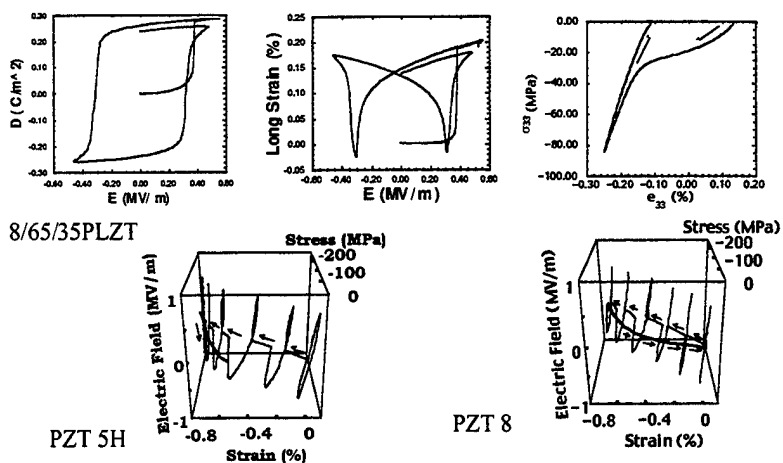
The G.W.Woodruff School of
Mechanical Engineering

Uniaxial Experimental Arrangement



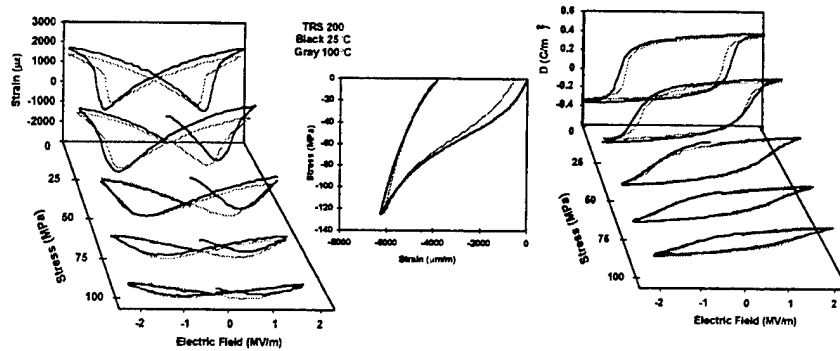
The G.W. Woodruff School of Mechanical Engineering

Hysteresis Behavior of Three Compositions



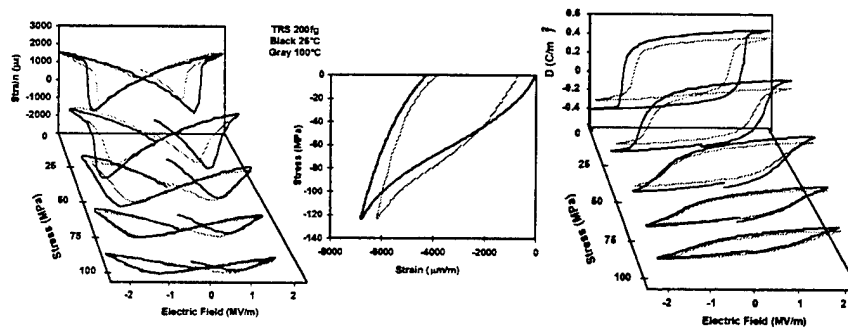
The G.W. Woodruff School of Mechanical Engineering

TRS 200 Stress and Temperature Dependence



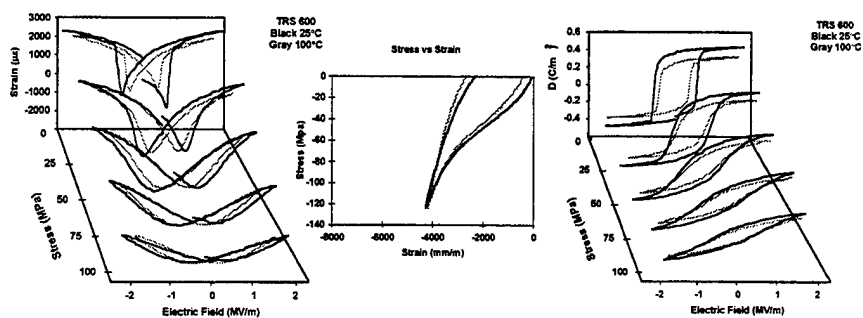
The G.W. Woodruff School of
Mechanical Engineering

TRS 200fg Stress and Temperature Dependence



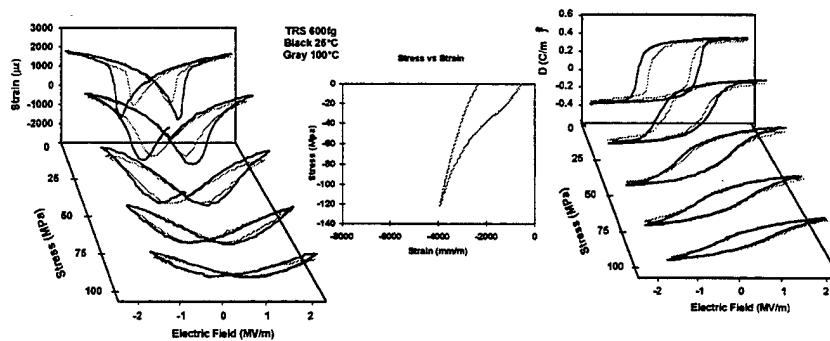
The G.W. Woodruff School of
Mechanical Engineering

TRS 600 Stress and Temperature Dependence



The G.W. Woodruff School of Mechanical Engineering

TRS 600fg Stress and Temperature Dependence



The G.W. Woodruff School of Mechanical Engineering

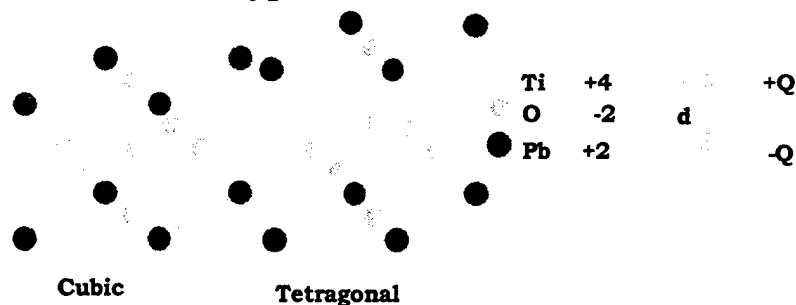
Micromechanics Modeling of the Constitutive Behavior of Ferroelectric Ceramics

- Step like switching at the unit cell scale
 - Work / energy criterion
 - 90° vs 180° switching
- Modified switching law at the multiple cell scale
 - Hard PZT, Phase Changers, Electrostrictors
- Switching law at the single crystal scale
 - Multiple variants, Evolution of volume fraction of variants
- Micromechanics at the polycrystal scale
 - Grain orientation
 - Intergranular interaction (inhomogeneity problem)
 - Volume averaging

The G.W. Woodruff School of Mechanical Engineering

Curie Point Phase Transition

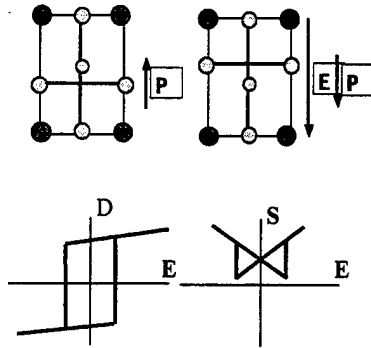
Perovskite Type Structure



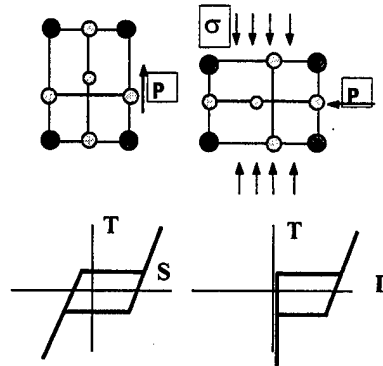
The G.W. Woodruff School of Mechanical Engineering

Ferroelectric and Ferroelastic Switching

Ferroelectric

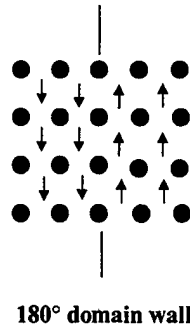
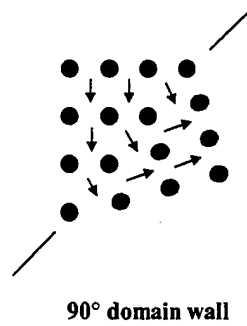


Ferroelastic



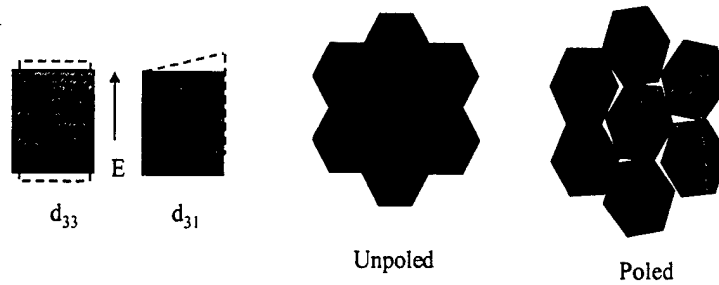
The G.W. Woodruff School of Mechanical Engineering

Behavior at the Single Crystal Scale



The G.W. Woodruff School of Mechanical Engineering

Behavior at the Ceramic Scale



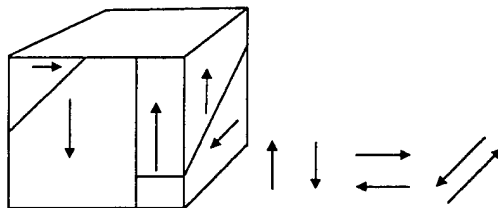
Anisotropic Actuation

Intergranular Stress

Intergranular E-Field

The G.W. Woodruff School of
Mechanical Engineering

Polarization Reorientation



$f_1, f_2, f_3, f_4, f_5, f_6$

$$\sum f_i = 1$$

Each crystal can be
polydomain. 90°
domain walls
accommodate strain

Six tetragonal variants
corresponding to the
possible polarization
directions

Evolution of the
volume fraction of
each variant is tracked

The G.W. Woodruff School of
Mechanical Engineering



Structural Modeling and Design for Reliability

- **Reliability**
 - Field concentrations
 - Crack problems
 - Electrode edge problems
 - Stack actuator design
- **Finite element analysis**
 - Linear piezoelectric analysis
 - ABAQUS
 - Non-linear analysis
 - Micromechanics handles non-linearity and switching
 - Phenomenological model handles non-linearity and evolution

The G.W. Woodruff School of
Mechanical Engineering



Summary

- **Micromechanics Modeling**
 - Energy wells for different material behavior
 - Evolution of variants
 - Inclusion analysis
- **Phenomenological Modeling**
 - Calibrate for proportional loading
 - Extend to non-proportional loading
- **Finite element analysis**
 - Continue development of custom code
 - Develop code with library of material behavior
 - Produce code as design tool for ferroelectric actuators
 - Alternate approach
 - Develop user designed material subroutines for ABAQUS

The G.W. Woodruff School of
Mechanical Engineering

Thin Film NiTi Shape Memory Actuators

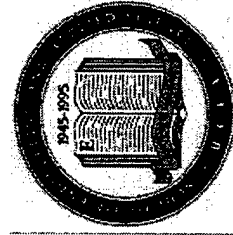
By:

Ken Ho, John Gill, Jenna Favelukis, Peter Jardine, and Greg P.

Carman

Mechanical and Aerospace Engineering Department
University of California, Los Angeles

<http://aml.seas.ucla.edu>



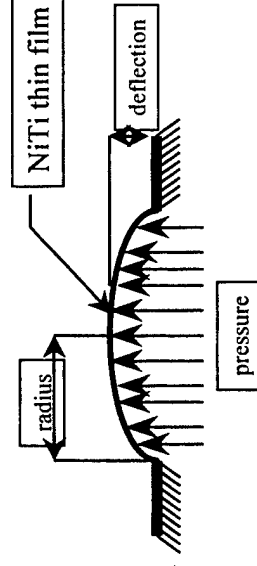
Sponsored by AFOSR F49620-98-1-0058 Brian Sanders
and partially by ARO DAAD19-99-1-0138 Bushnell/Anderson

Active Materials Lab



Objectives

- Requirements for application of MEMS bubble actuators are:
 - a frequency response of at least 100Hz upon cooling
 - the ability to withstand mechanical loads of at least 5psi (35kPa)
 - the ability to give a deflection on the order of 1mm, keeping maximum strain less than 4% (fatigue limit)

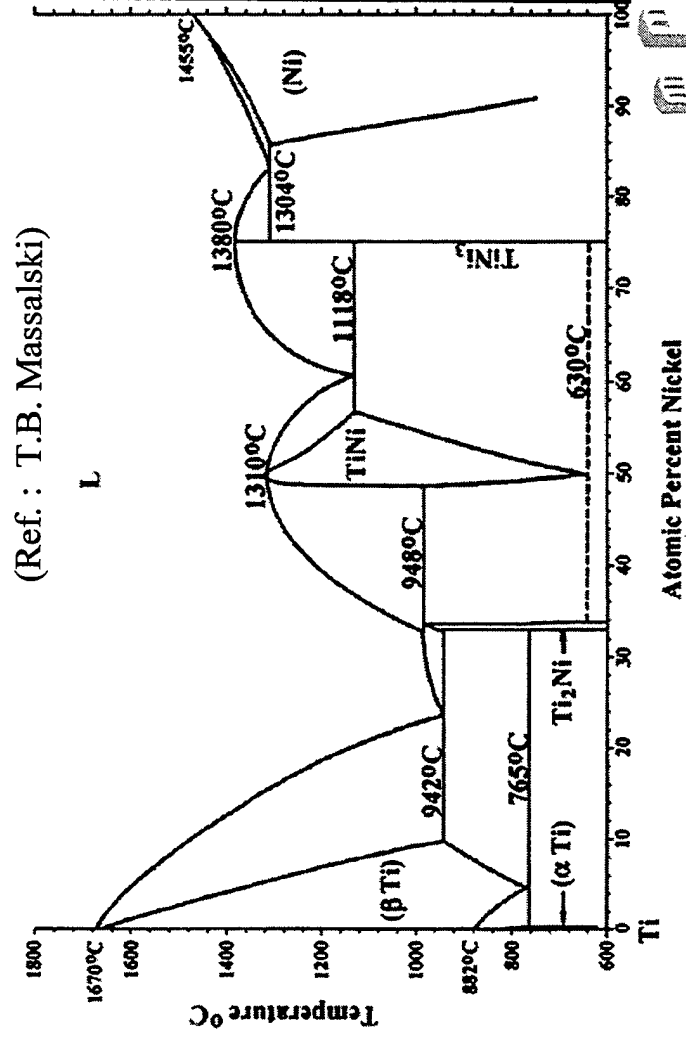
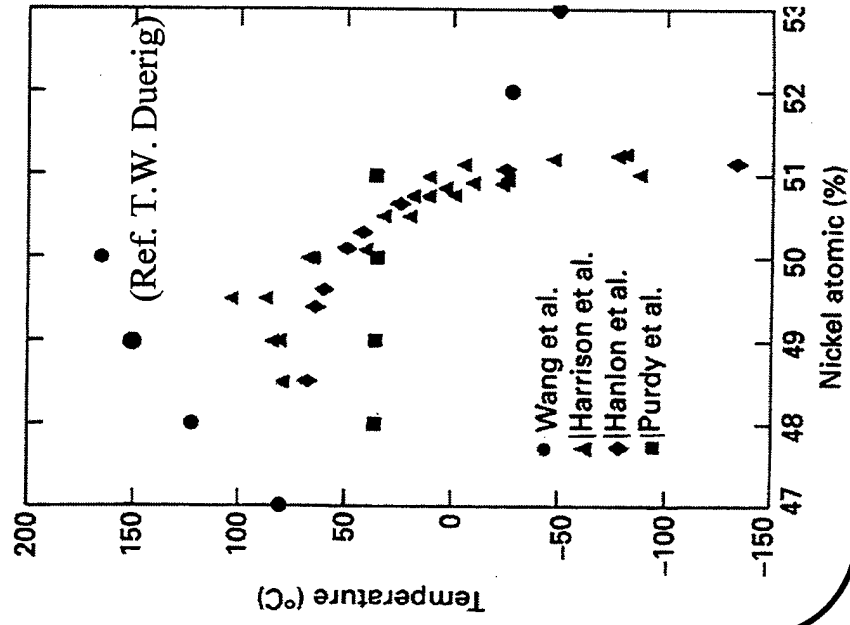


Schematics of the bubble

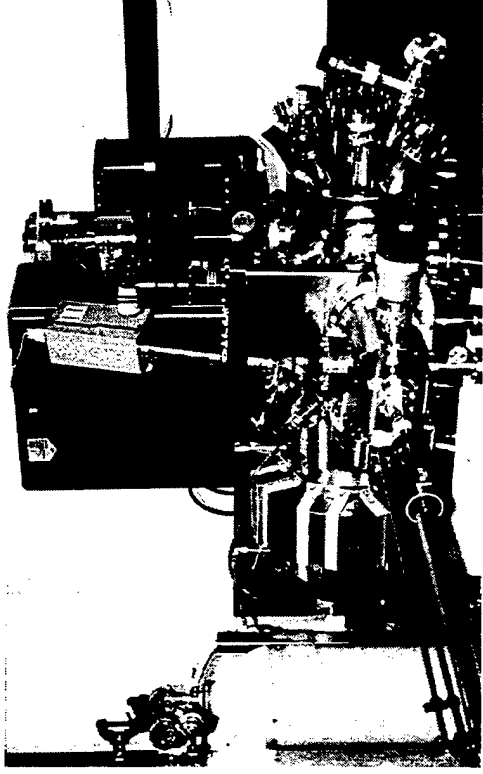
↕
millimeter size

Problem Description - Compositional Sensitivity

- T_f Highly sensitive to composition
- Narrow phase region \Rightarrow easily forms precipitates



Sputtering Process



Control Temperature of Target

- cold target (room temperature)
- hot target (above 500 C)
- transition target temperature

Discussion

• Why??

- Substrate Heating
- Target surface profile or cleanliness
- Magnetic effects
 - > Curie temperature of Ni = 358°C
- Decreased bond energy
 - > increase sputtering yield
- Sputtering angle

$$S \propto \frac{K}{U} \left(\frac{M_t}{M_i} \right)$$

• Benefits

- Control of film transformation temperature (stoichiometry)
- Gradation of film properties possible
 - > Two way effect 2-D structure

substrate

target

S- sputtering yield

K- kinetic energy of incident ion

U- binding energy

M- mass of target and incident atoms

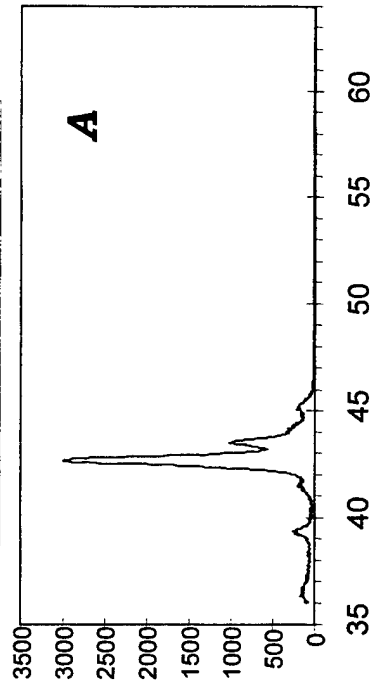
*Gradation film properties
(i.e. superelastic/SMA)*

Active Materials Lab

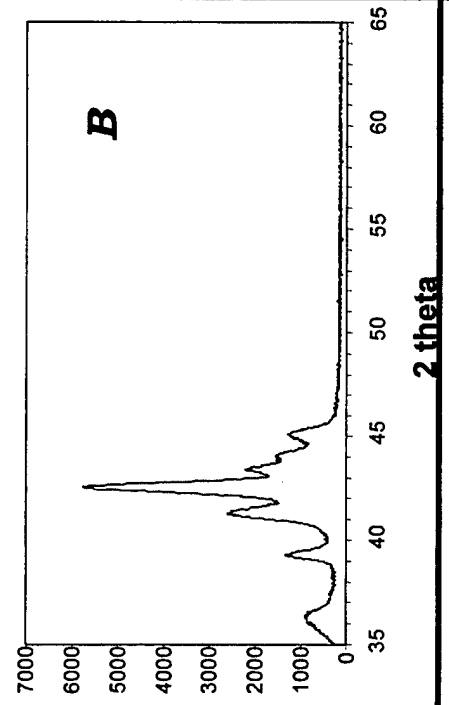


X-Ray Diffraction Results (Martensite/Austenite)

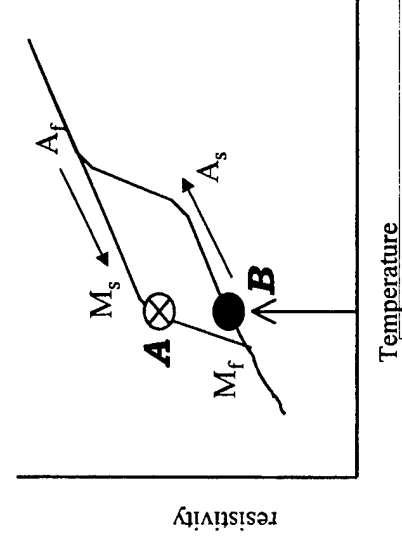
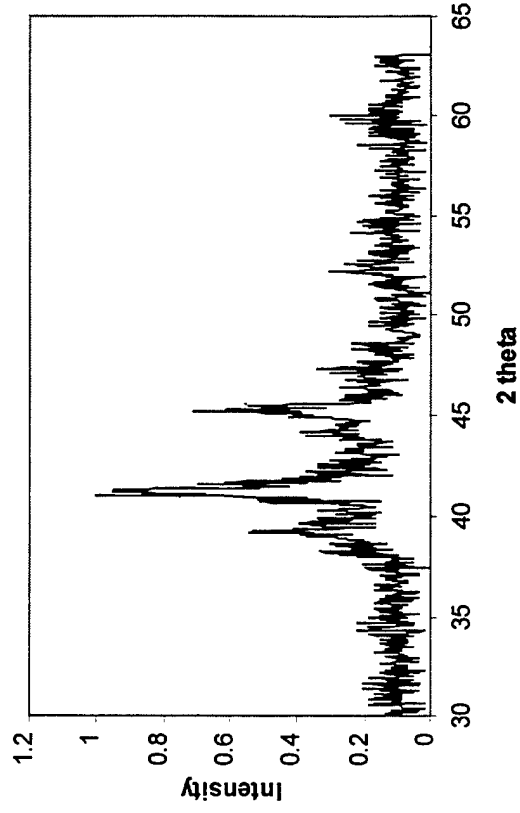
XRD (hot/cold target)



after cooling to -100 °C (hot/cold target)

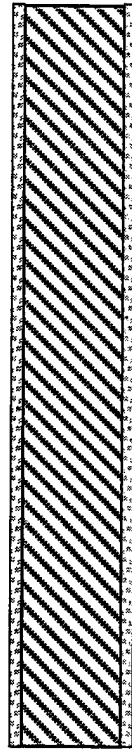


XRD NiTi Target



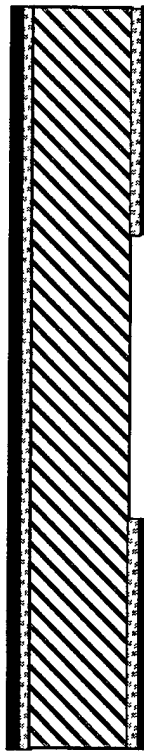
Active Materials Lab

Actuator Fabrication



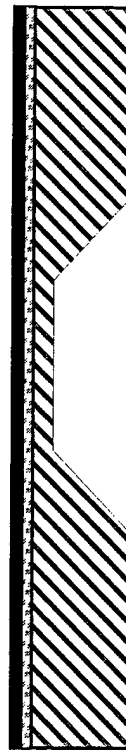
(a)

Wet oxidation



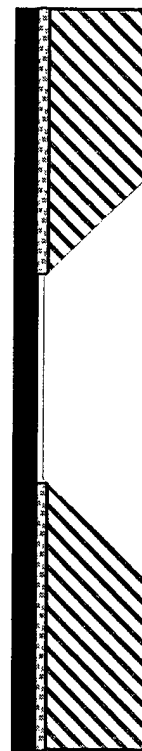
(b)

LPCVD nitride deposition
Pattern the nitride and oxide



(c)

KOH etching of Si



(d)

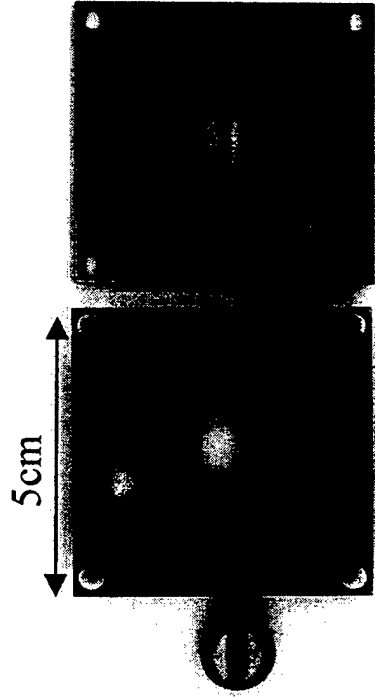
NiTi deposition and patterning
DRIE of Si membrane

 - Silicon dioxide
 - Silicon
 - Nitride
 - NiTi film

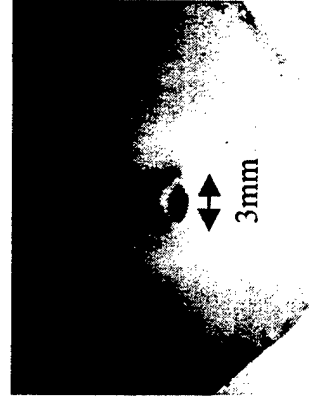
Active Materials Lab



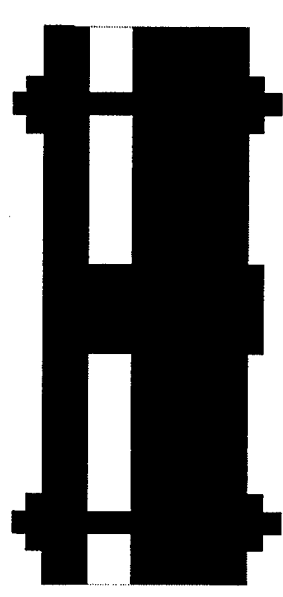
Hot Shaping



(a) Jig for hot shaping



vertical disp: 500µm

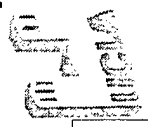


- - NiTi
- - Jig
- - Clamp
- - Silicon
- - Deflector

(b) Schematic diagram of cross section view of NiTi film hot shaping

Hot shaping condition

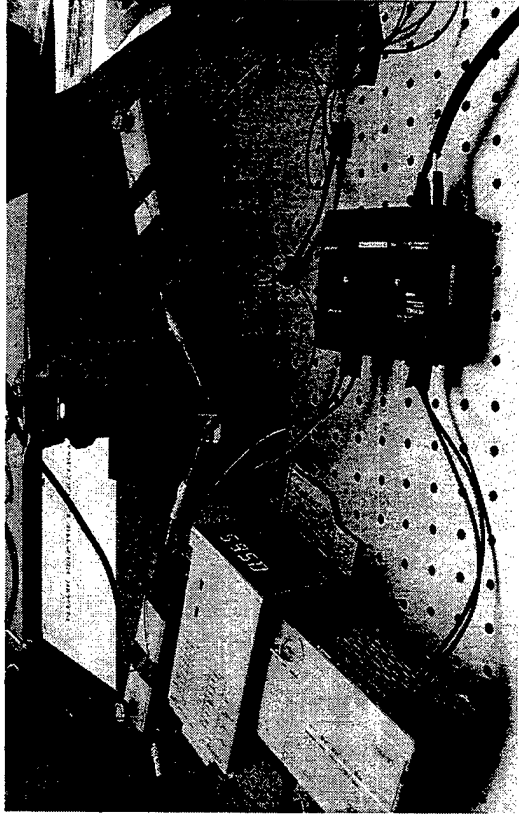
- in vacuum to prevent oxidation
- 500 °C for 20 mins



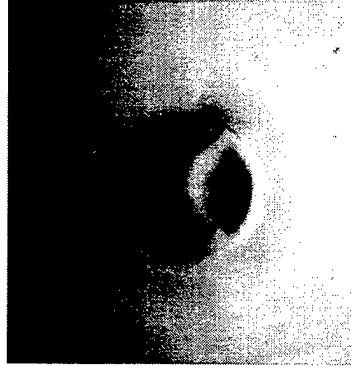
Active Materials Lab

Characterization of Thin Film Actuator

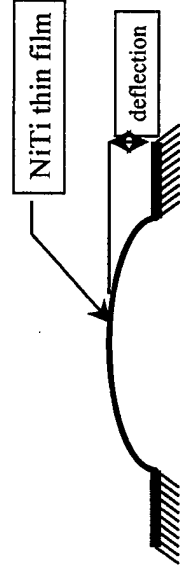
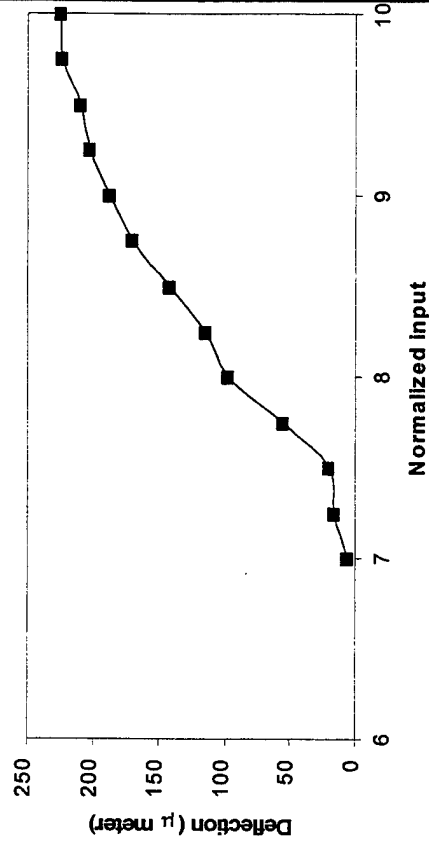
Displacement/Frequency Measurement



Microbubble
actuator



Displacements up to 500 μm achieved



Active Materials Lab

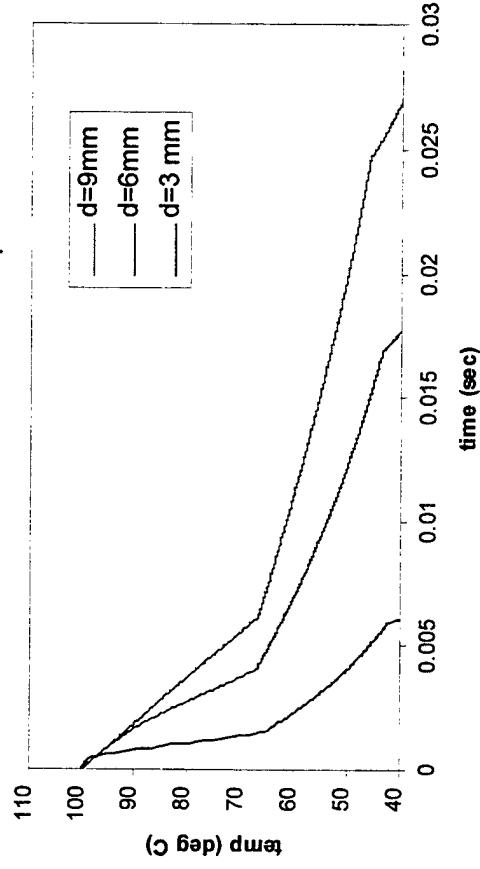


Frequency Response of NiTi Bubble

- Cooling profile of NiTi bubble actuator for various diameters with fixed thickness of $3\mu\text{m}$
- Incorporate forced air flow
- 100Hz frequency response possible

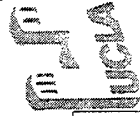
Cooling Profile

bubble: thickness of $3\mu\text{m}$



Conclusions

- Target temperature influences quality of film
- Controlling target temperature allows
 - tailoring of film structure
 - 2 way effect
- Microbubble actuator w/ 2way effect fabricated and tested
- Displacements of 0.5mm achieved
- Frequency response over 100 Hz possible



**Nonlinear Static and Transient Response
of Smart Beams and Shells
with Piezoelectric Layers**

J. Chróścielewski
Politechnika Gdańska

R. Schmidt
Aachen University of Technology

Contents

- Geometrically Nonlinear Theory of Beams and Shells
with Piezoelectric Layers
- Numerical Method
- Numerical Simulation
 - Statics:
 - Stress Analysis
 - Shape Control
 - Shift of Bifurcation and Limit Points
 - Symmetric/Unsymmetric Buckling
 - Dynamics:
 - Shift of Eigenfrequencies
 - Vibration Control
 - Dynamic Instability

Geometrically Nonlinear Theory of Arches

Based on the Bernoulli-Hypothesis

Green-Lagrange strain tensor :

$$\varepsilon_{11} = \gamma + \theta^3 \kappa$$

with the membrane and bending strains

$$\gamma = \theta + \frac{1}{2} \theta^2 + \frac{1}{2} \varphi^2, \quad \kappa = -(1 + \theta) \varphi_{,1} + \varphi \theta_{,1}$$

and the notation

$$\theta = u_{,1} - b_{11} w, \quad \varphi = w_{,1} + b_{11} u$$

Constitutive equations :

$$S_{11} = C_{1111} \varepsilon_{11} - e_{311} E_3, \quad D_3 = e_{311} \varepsilon_{11} + \xi_{33} E_3$$

Stress resultants :

$$N = \int_A S_{11}(\theta^3) dA = \sum_i \int_A (C_{1111}^{(i)} \varepsilon_{11}(\theta^3) - e_{311}^{(i)} E_3^{(i)}) dA,$$

$$M = \int_A S_{11}(\theta^3) \theta^3 dA = \sum_i \int_A (C_{1111}^{(i)} \varepsilon_{11}(\theta^3) - e_{311}^{(i)} E_3^{(i)}) \theta^3 dA$$

Principle of virtual displacements :

$$\int_L (N \cdot \delta \gamma + M \cdot \delta \kappa) ds - \int_S \mathbf{f} \cdot \delta \mathbf{u} dS - \int_V \rho \mathbf{b} \cdot \delta \mathbf{u} dV + \int_V \rho \mathbf{u} \cdot \delta \mathbf{u} dV = 0$$

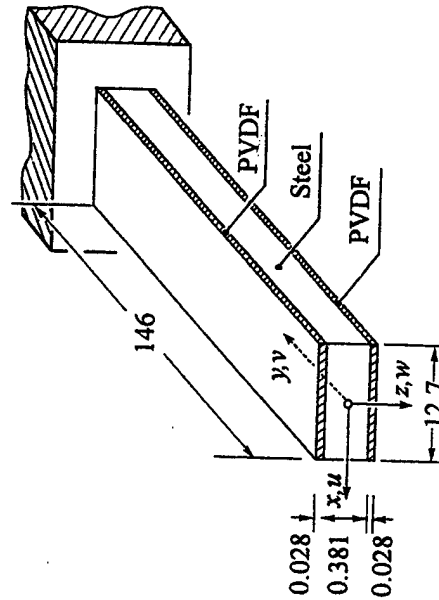
Finite Element Method :

Incremental form of the equations of motion :

$$[\mathbb{K}_t] \Delta \mathbf{q} = \mathbb{R}_{t+\Delta t} - \mathbb{F}_t$$

Incremental form of the equations of motion :

$$\mathbb{M} \Delta \ddot{\mathbf{q}} + \mathbb{C} \Delta \dot{\mathbf{q}} + [\mathbb{K}_t] \Delta \mathbf{q} = \mathbb{R}_{t+\Delta t} - (\mathbb{M} \ddot{\mathbf{q}}_t + \mathbb{C} \dot{\mathbf{q}}_t + \mathbb{F}_t)$$



Steel:

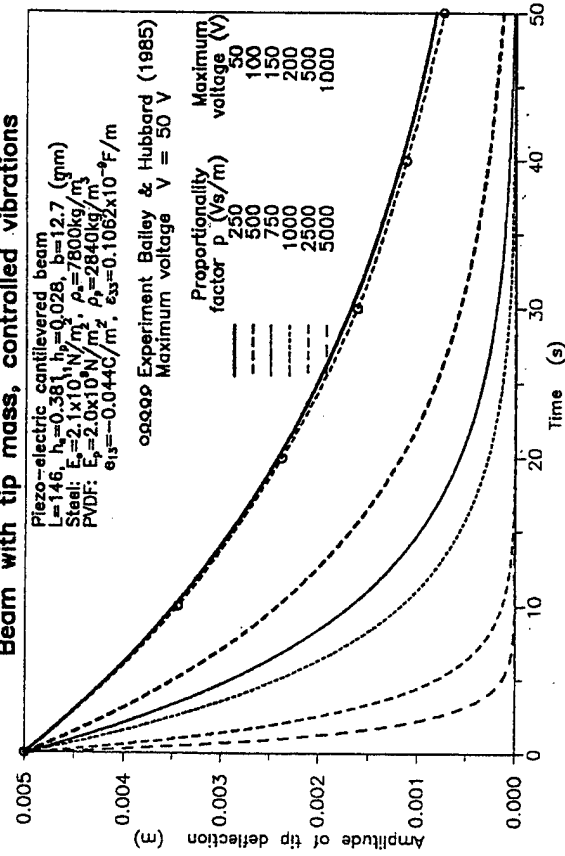
$E = 2.1 \times 10^{11} \text{ N/m}^2$, $\nu = 0.3$,
 $\rho = 7800 \text{ kg/m}^3$

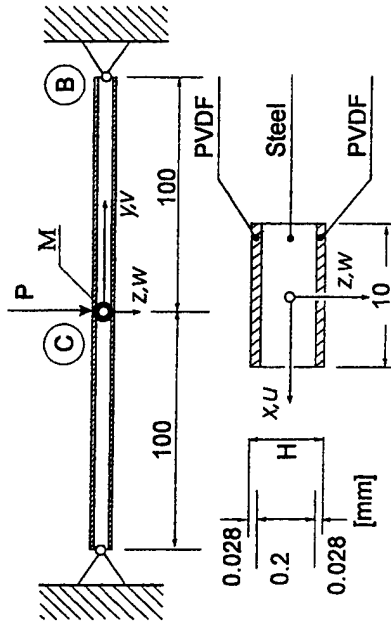
PVDF:

$E = 2.0 \times 10^{10} \text{ N/m}^2$, $\nu = 0.3$,
 $\rho = 2840 \text{ kg/m}^3$,
 $e_{13} = -0.044 \text{ C/m}^2$,
 $\epsilon_{33} = 0.1062 \times 10^{-9} \text{ F/m}$

Tip mass: $M = 6.73 \times 10^{-3} \text{ kg}$

Beam with tip mass, controlled vibrations

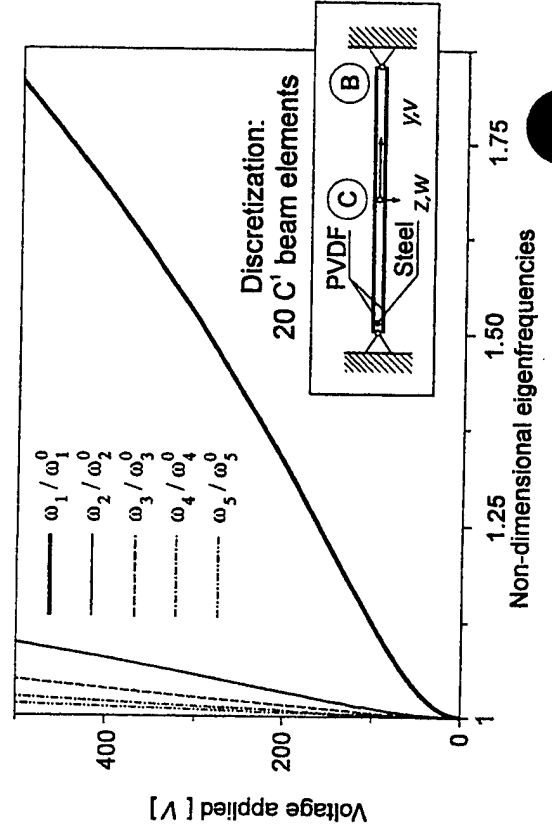
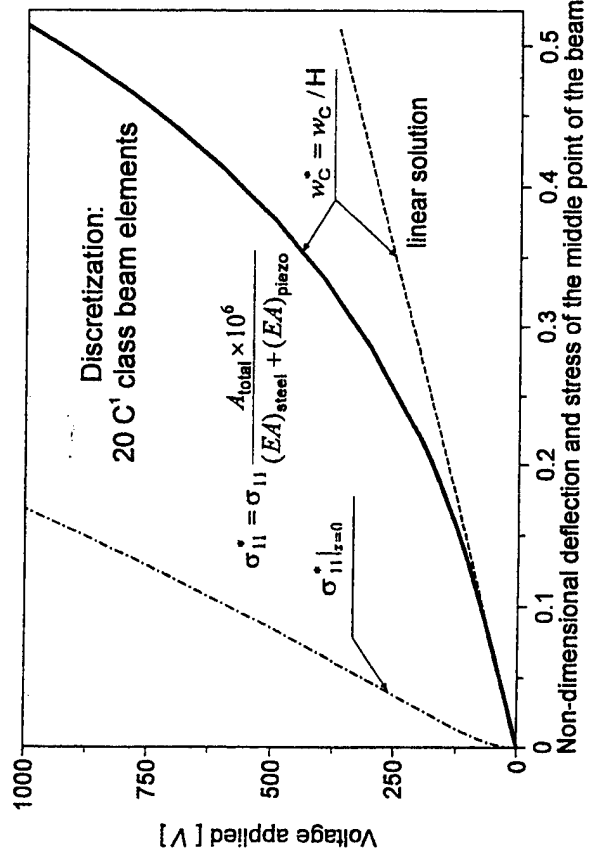
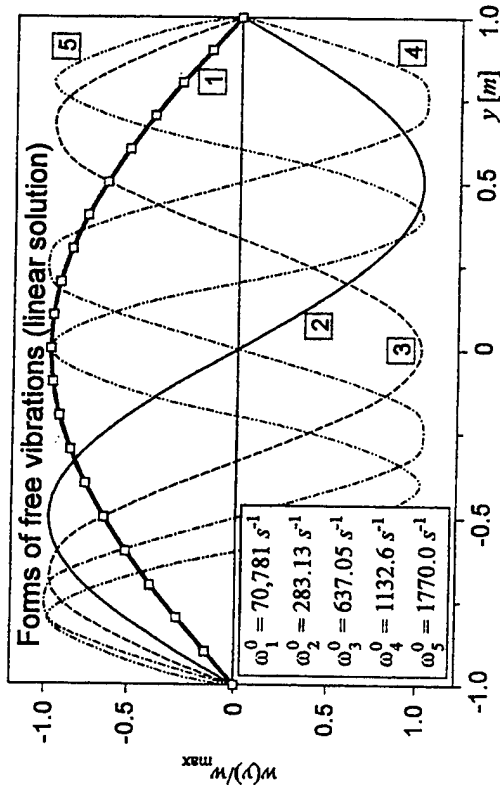




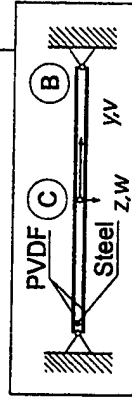
Steel:
 $E = 2.1 \times 10^{11} \text{ N/m}^2$,
 $\nu = 0.3$,
 $\rho = 7800 \text{ kg/m}^3$

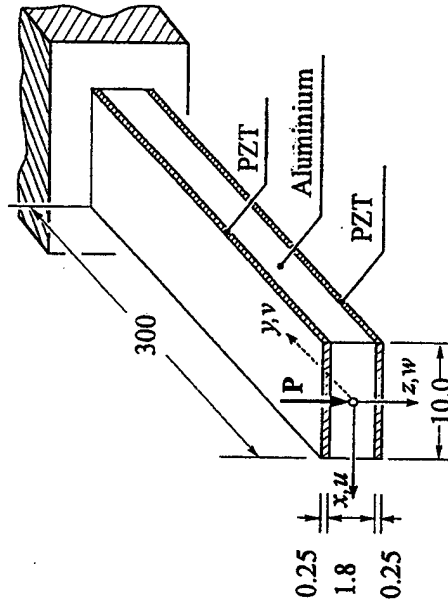
PVDF:
 $E = 2.0 \times 10^9 \text{ N/m}^2$,
 $\nu = 0.3$,
 $\rho = 2840 \text{ kg/m}^3$,
 $\epsilon_{13} = -0.044 \text{ C/m}^2$,
 $\epsilon_{33} = 0.1062 \times 10^{-9} \text{ F/m}$

Mass:
 $M = 6.73 \times 10^{-3} \text{ kg}$



Discretization:
 20 C1 beam elements

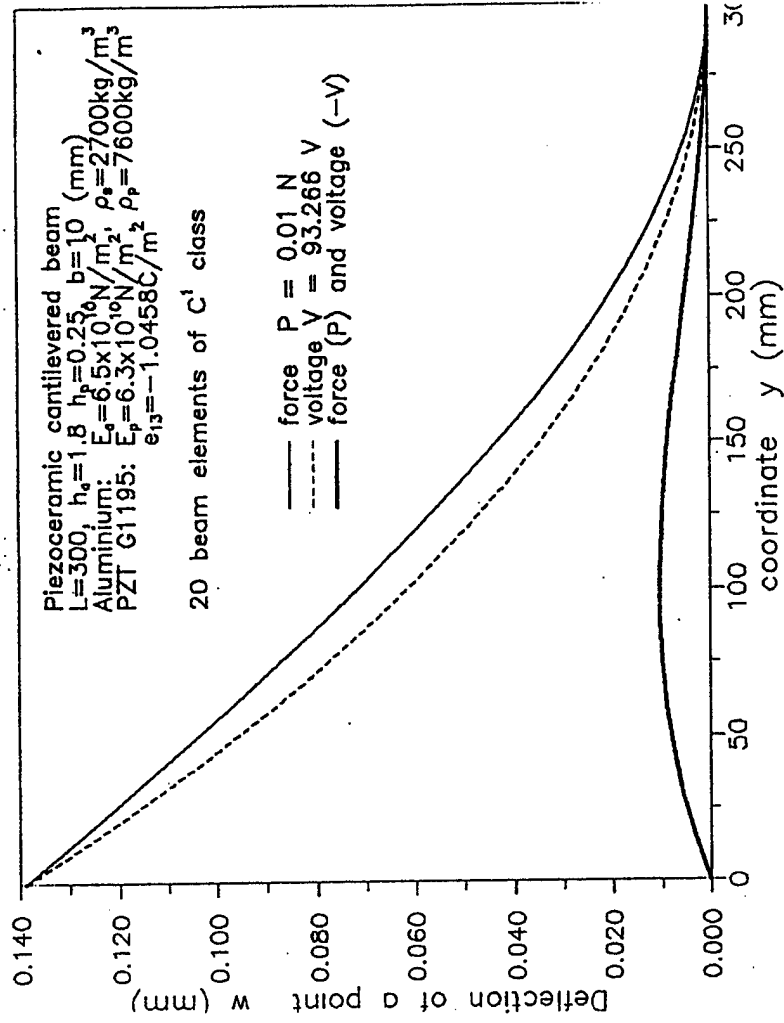




Aluminium:
 $E = 6.5 \times 10^{10} \text{ N/m}^2$, $\nu = 0.3$,
 $\rho = 2700 \text{ kg/m}^3$

PZT G1195:
 $E = 6.3 \times 10^{10} \text{ N/m}^2$, $\nu = 0.3$,
 $\rho = 7600 \text{ kg/m}^3$,
 $e_{13} = -1.0458 \text{ C/m}^2$

$P = 0.01 \text{ N}$



PIEZOELECTRICALLY CONTROLLED CIRCULAR ARCH

FEM: 100 elements, 2 nodes, C' class

integration: Newmark method $\Delta t=2 \times 10^{-5} \text{ s}$

PVDF (10 independent sections)

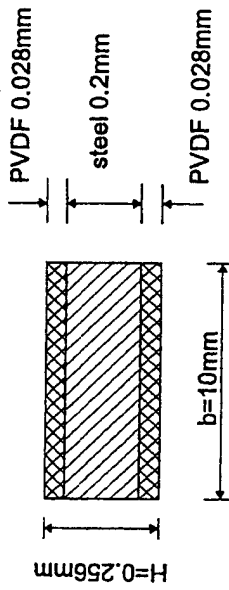
q hydrostatic pressure

H=7.90mm

B=120mm

30°

$$R = \frac{60}{\sin 15^\circ} = 231.822 \text{ mm}$$



Steel:

$$E_s = 2.1 \times 10^{11} \text{ N/m}^2$$

$$\rho_s = 7800 \text{ kg/m}^3$$

PVDF:

$$E_p = 2.0 \times 10^9 \text{ N/m}^2$$

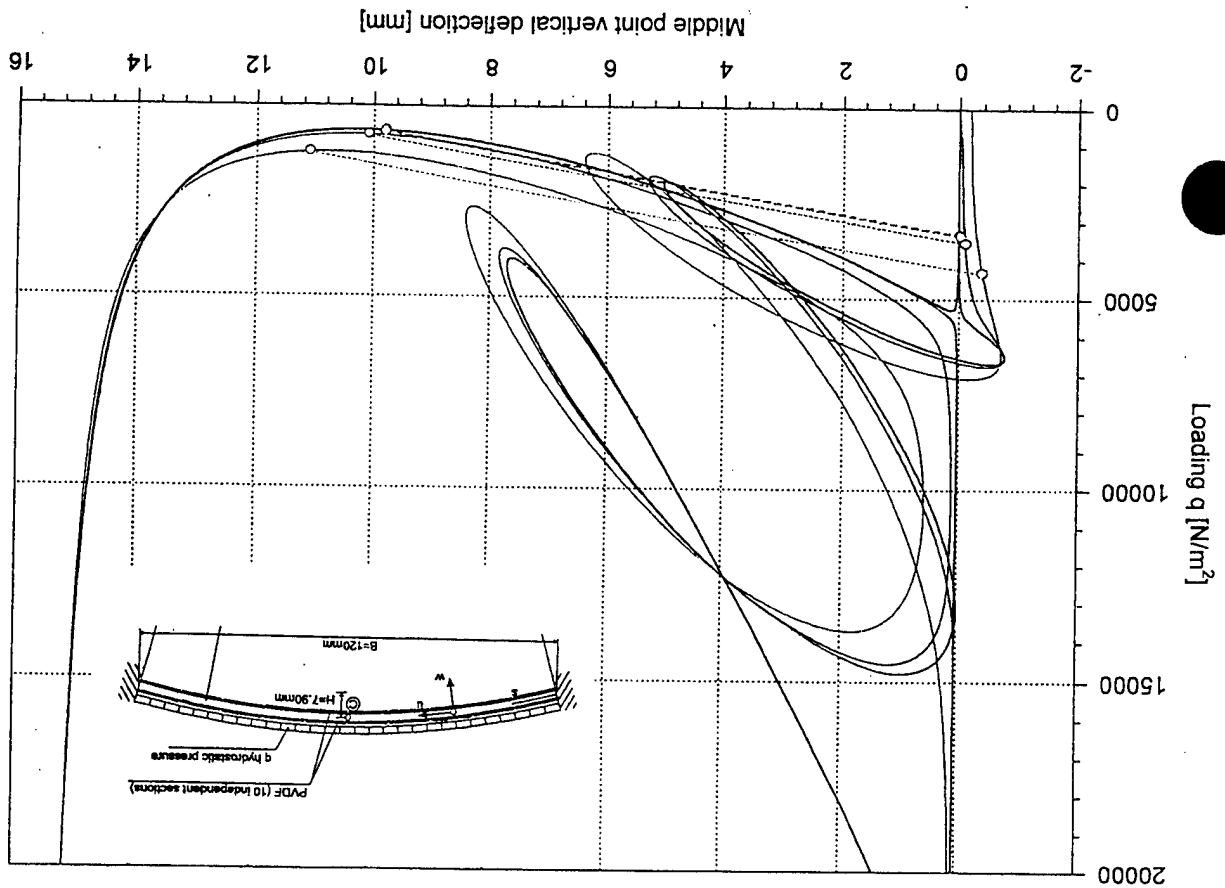
$$\rho_p = 2840 \text{ kg/m}^3$$

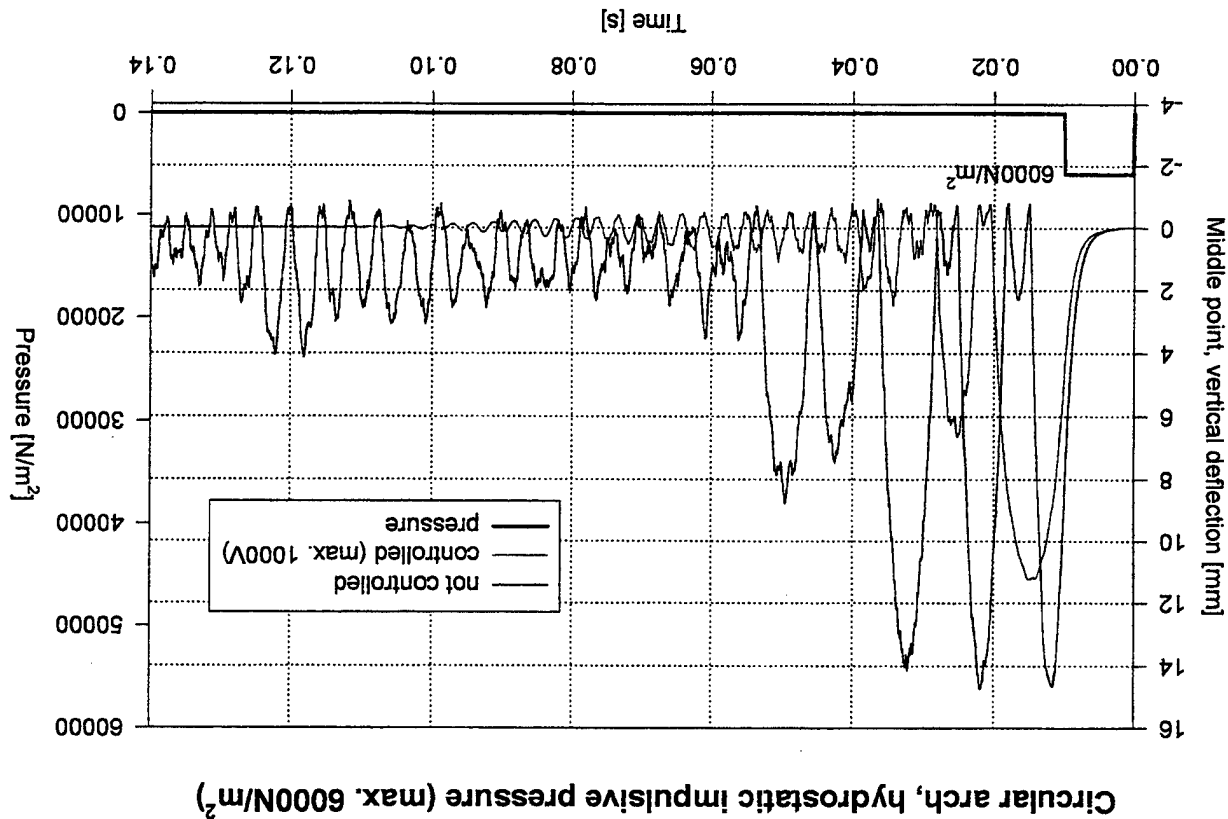
$$e_{13} = 0.044 \text{ C/m}^2$$

$$p = 10000 \text{ V/s/m}$$

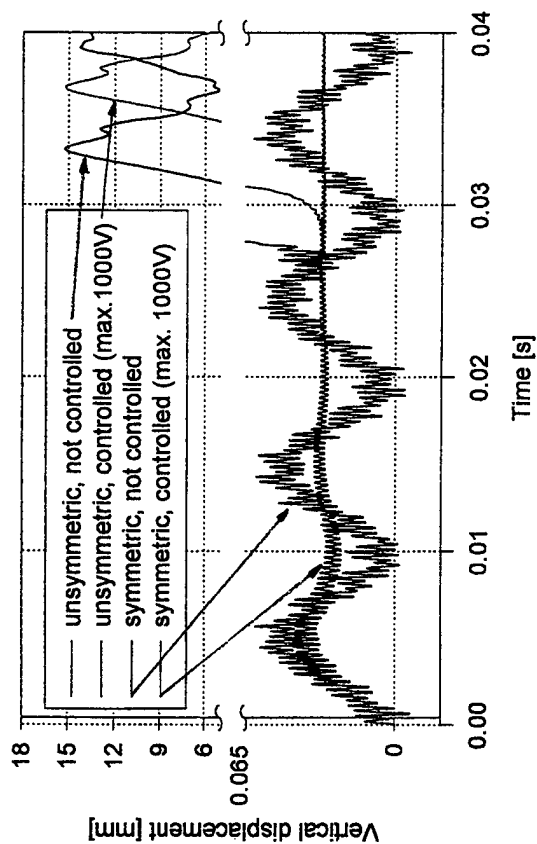
$$\text{max. voltage} = 1000 \text{ V}$$

$$V = p \cdot \dot{w}_{\text{average}}$$

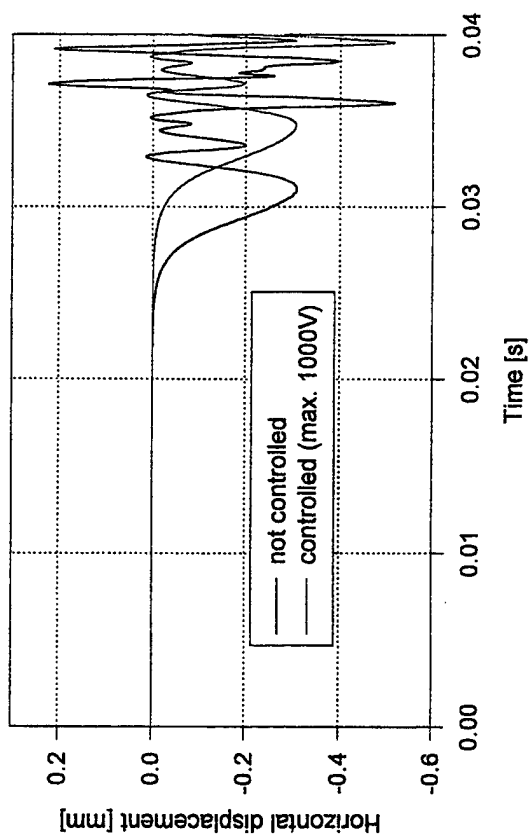


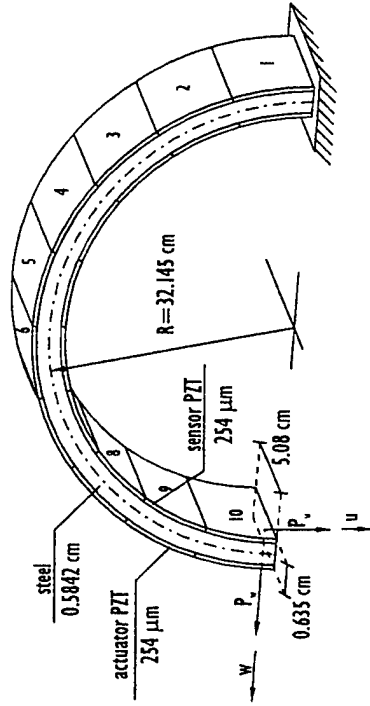
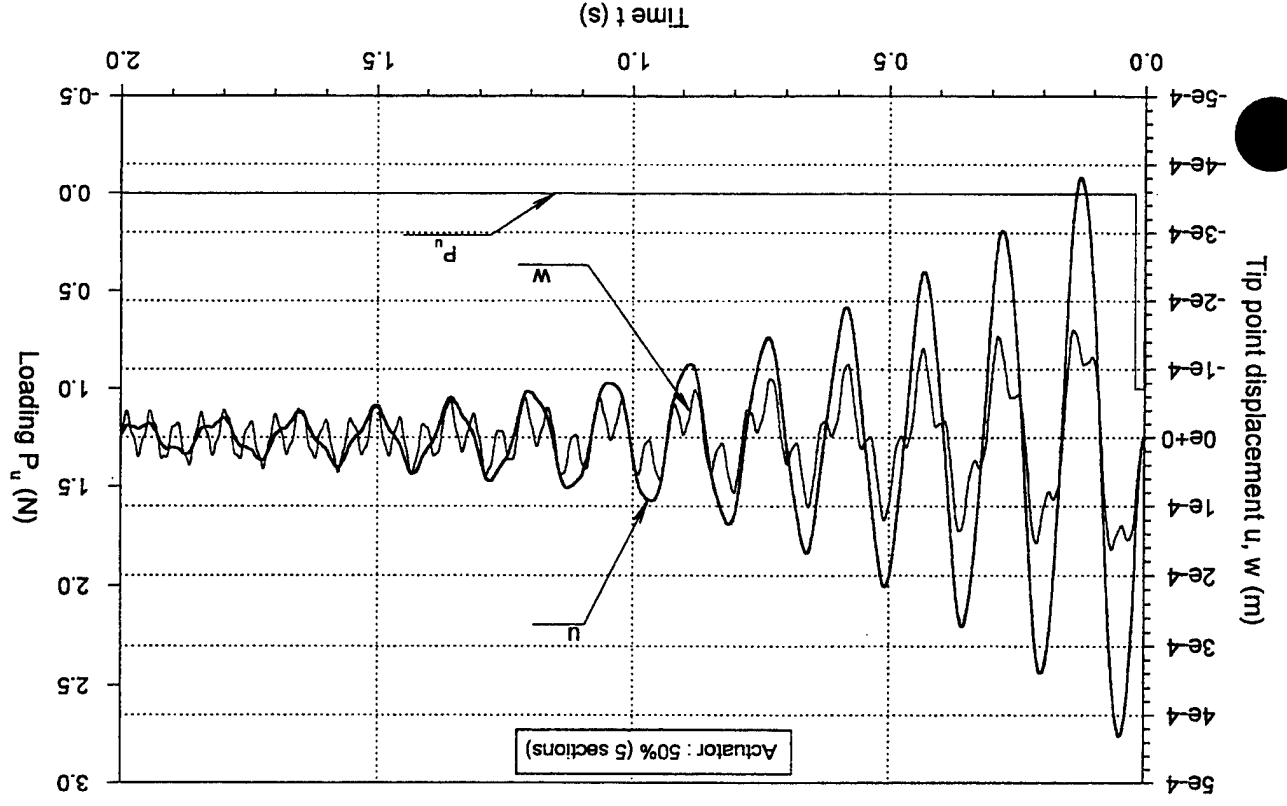


Middle point displacements (step load $q=5000\text{N/m}^2$)

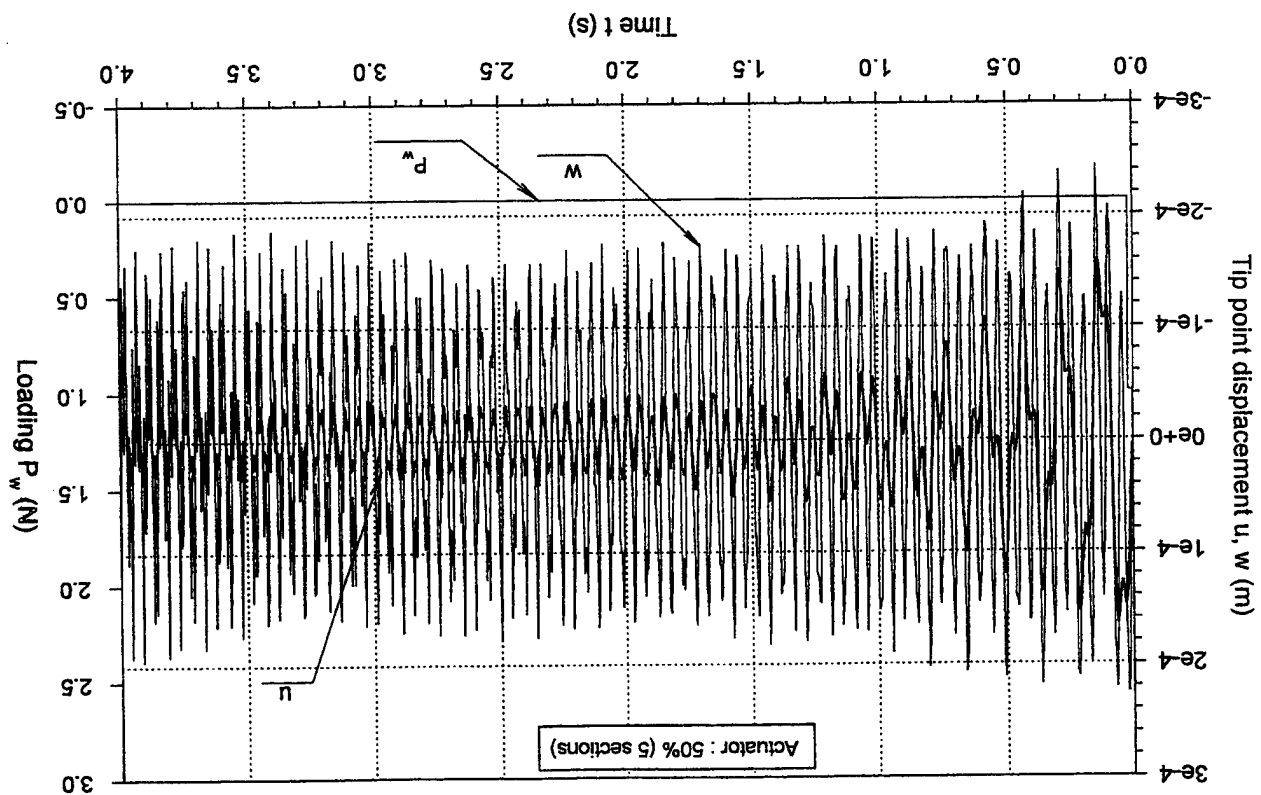
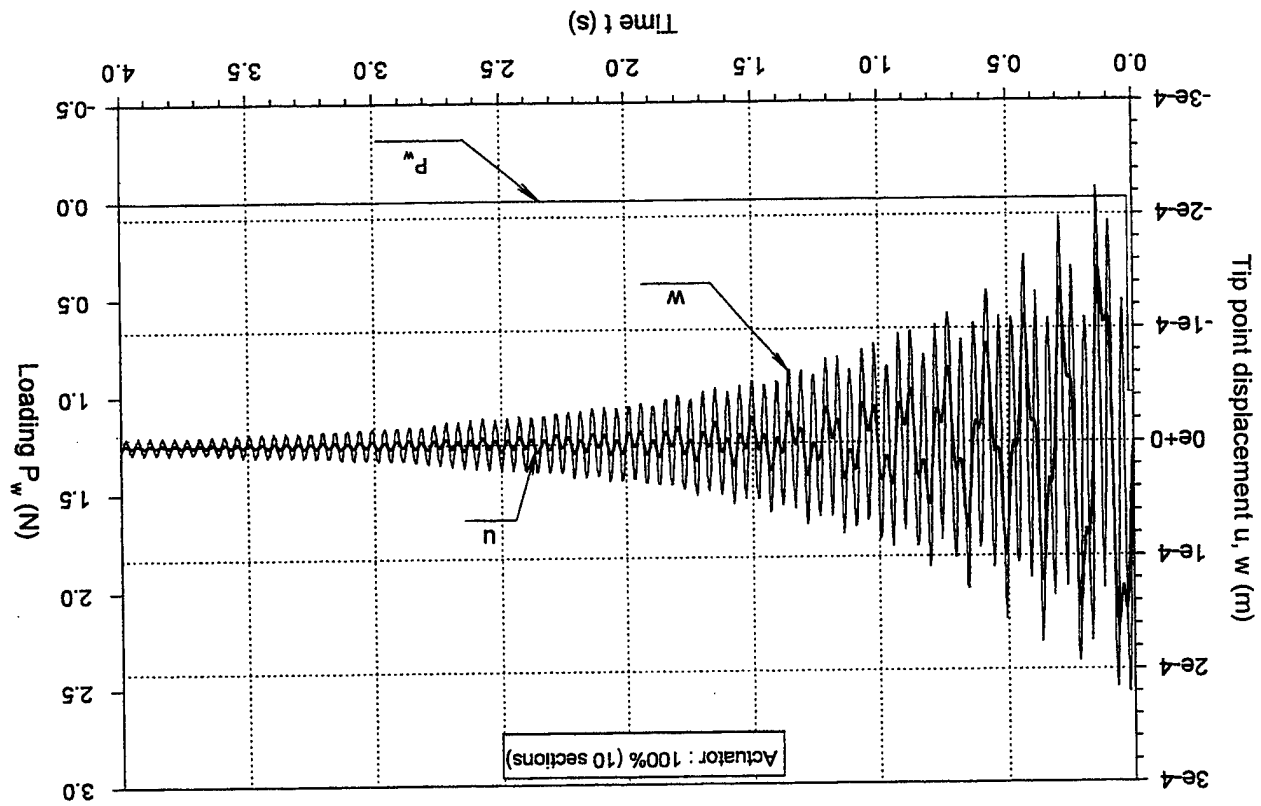


Horizontal displacements - unsymmetric cases





Properties	PZT	Steel
Density, ρ , kg m^{-3}	7.600×10^3	7.750×10^3
Young's modulus, Y , Pa	6.300×10^{10}	2.100×10^{11}
Poisson's ratio, μ	0.300	0.300
Piezoelectric constant, d_{31} , m V^{-1}	1.790×10^{-10}	
Electric permittivity, ϵ_{33} , F m^{-1}	1.650×10^{-8}	
Capacitance, C , F m^{-2}	3.080×10^{-4}	



**IMPEDANCE MATCHING CONTROL
OF
ACTIVE CONSTRAINED LAYER DAMPING**

S. Poh and A. Baz

**Mechanical Engineering Department
University of Maryland
College Park, MD 20742**

**Tel: 301-405-5216
e-mail: baz@eng.umd.edu**

**Fourth ARO Workshop on Smart Structures
Penn State, August 16-18, 1999**

University of Maryland



IMPEDANCE MATCHING CONTROL OF ACTIVE CONSTRAINED LAYER DAMPING

S. Poh and A. Baz
Mechanical Engineering Department
University of Maryland
College Park, MD 20742

ABSTRACT

An Impedance Matching Controller (IMC) is developed to control the operation of Active Constrained Layer Damping (ACLD) treatments for vibrating beams. The IMC aims at maximizing the power dissipation from the vibrating beams over a wide frequency band. The controller is realized using the dereverberated impedance of the structure in order to ensure its robustness.

The performance of the controller is evaluated theoretically and experimentally for a beam which is fully-treated with an ACLD treatment. The beam is subjected to swept sinusoidal excitation and operating at different ambient temperature. The performance characteristics of the IMC are determined and compared with those of beams controlled by a Direct Velocity Feedback Controller (DVFC). Such a comparison clearly demonstrates the effectiveness of the IMC in attenuating the structural vibration with control efforts which are much lower than those required by the DVFC. The obtained results emphasize also the robustness of the IMC in the presence of varying operating temperatures. [Work is funded by ARO].

OUTLINE OF PRESENTATION

1. Introduction
2. Impedance Controller
3. Implementation Issues
4. Control of Beams with ACLD treatment
5. Summary

University of Maryland



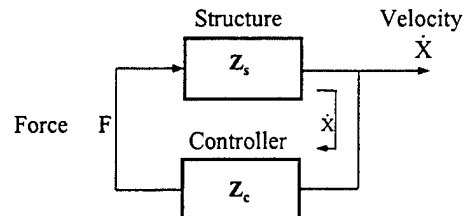
IMPEDANCE CONTROL (IMC) BACKGROUND

1. Procopio & Hubbard 1984.
2. von Flotow & Schafer 1986.
3. Guicking, Melcher and Wimmel 1989.
4. MacMartin & Hall 1991.
5. Betros, Alvarez-Salazar & Bronowicki 1993.
6. Berkman, Owen & Preuss 1997.
7. Hiram 1997.

University of Maryland



IMPEDANCE CONTROL (IMC)



Impedance of structure $Z_s = R_s + j\chi_s$ and Impedance of Controller $Z_c = R_c + j\chi_c$

The total impedance $Z_t = Z_s + Z_c = (R_s + R_c) + j(\chi_s + \chi_c)$

Power dissipated P in controller is: $P = R_c \dot{X}^2$

University of Maryland



IMPEDANCE CONTROL (IMC)

Velocity is: $\dot{x} = F/Z_t = \frac{F}{[(R_s + R_c)^2 + (\chi_s + \chi_c)^2]^{1/2}}$

Power is: $P = R_c \frac{F^2}{[(R_s + R_c)^2 + (\chi_s + \chi_c)^2]}$

For a given R_c , the dissipated power is maximum when: $\frac{\partial P}{\partial \chi_c} = 0, \Rightarrow \chi_c = -\chi_s$

Hence, $P_{\max} = \frac{R_c F^2}{(R_s + R_c)^2}$

This power can further be maximized again such that:

$\frac{\partial P}{\partial R_c} = 0, \Rightarrow R_c = R_s \Rightarrow Z_c = R_s - j\chi_s = Z_s^*$

i.e. The controller impedance matches the complex conjugate of structural impedance.

University of Maryland



IMPEDANCE CONTROL (IMC)

IMPLEMENTATION PROBLEMS

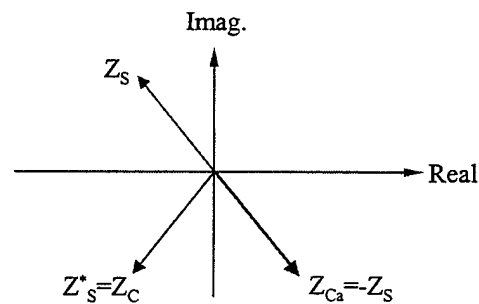
1. Controller is **NON-CAUSAL** (improper transfer function)
2. Controller cancels completely the poles and zeros of the structure
3. For low-damping structures, the controller does not dissipate energy

University of Maryland



IMPEDANCE CONTROL (IMC)

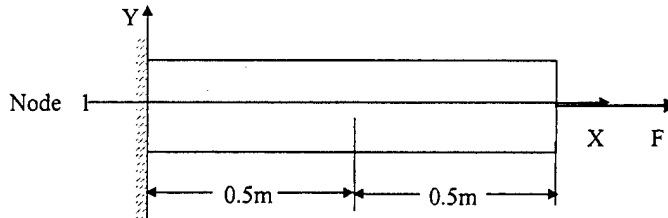
REALIZATION OF IMC using DEREVERBERATED FIELD METHOD



University of Maryland



MOTIVATION: IMPEDANCE CONTROL (IMC)



Transfer Function $G(s) = [C [sI_{2n \times 2n} - A]^{-1} B + D]$

where $A = \begin{bmatrix} 0_{n \times n} & I_{n \times n} \\ -[M]^{-1}[K] & 0_{n \times n} \end{bmatrix}$, $B = \begin{bmatrix} 0_{n \times m} \\ [M]^{-1}B_0 \end{bmatrix}$, $C = \{0 \ 1 \ 0 \ 0\}$ and $D=0$.

$$[M] = \frac{mL}{12} \begin{bmatrix} 4 & 1 \\ 1 & 2 \end{bmatrix} \text{ and } [K] = \frac{2EA}{L} \begin{bmatrix} 2 & -1 \\ -1 & 1 \end{bmatrix}.$$

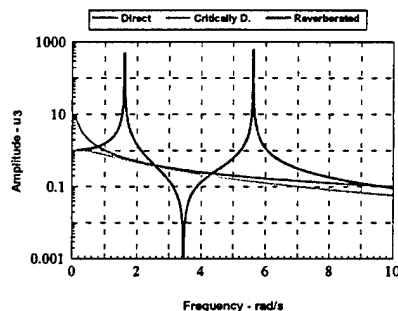
University of Maryland



IMPEDANCE CONTROL (IMC)

Transfer Function $G = \frac{6.857(s - 3.464i)(s + 3.464i)}{(s - 5.629i)(s + 5.629i)(s - 1.6114i)(s + 1.6114i)}$

➡ Two zeros at $\pm 3.464i$ and poles at $\pm 5.629i$ and $\pm 1.6114i$.



Dereverberated Transfer Function

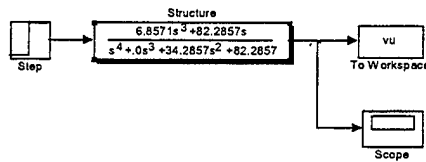
$$G_c = \frac{6.857(s + 3.464)^2}{(s + 5.629)^2(s + 1.6114)^2}$$

University of Maryland



IMPEDANCE CONTROL (IMC)

Uncontrolled



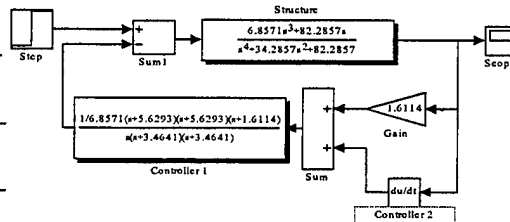
Controlled

$$K_c = Z_d = \frac{(s+5.629)^2(s+1.6114)^2}{6.857s(s+3.464)^2}$$

$$= K_{c1} K_{c2}$$

$$K_{c1} = \frac{(s+5.629)^2(s+1.6114)}{6.857s(s+3.464)^2}$$

$$K_{c2} = (s+1.6114).$$

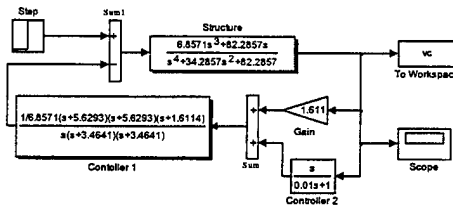


University of Maryland

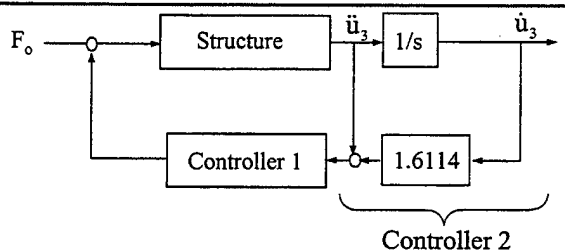


IMPEDANCE CONTROL (IMC)

Configuration 1



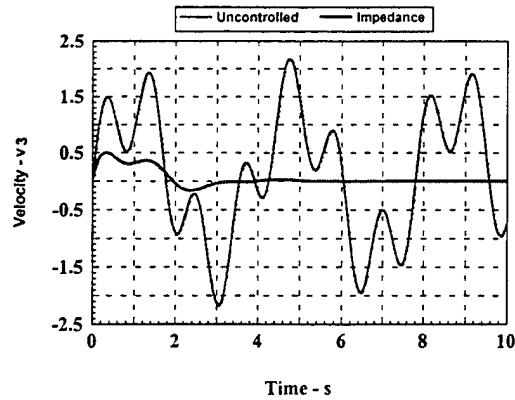
Configuration 2



University of Maryland



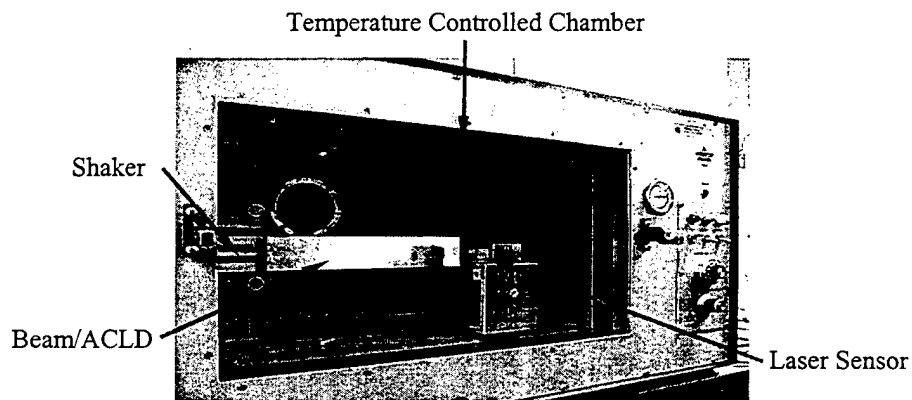
IMPEDANCE CONTROL (IMC)



University of Maryland



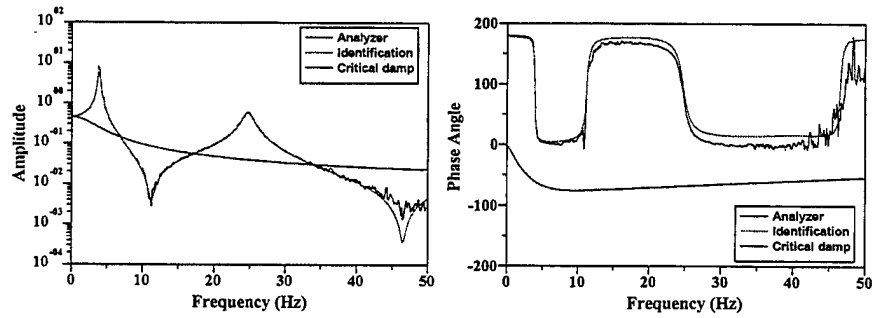
EXPERIMENTAL SET-UP



University of Maryland



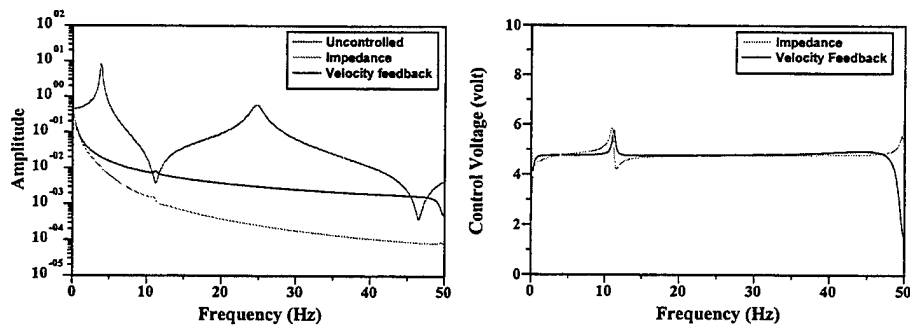
IDENTIFICATION AT 65 Deg. F.



University of Maryland



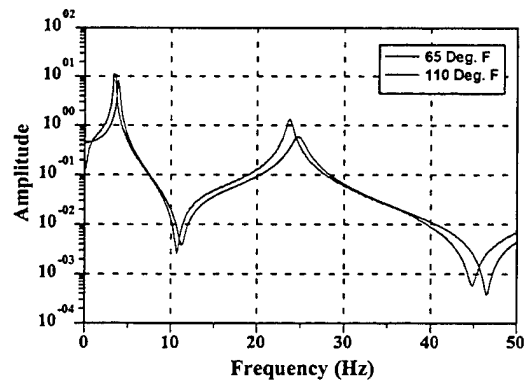
IMC & DVFC at 65 Deg. F



University of Maryland



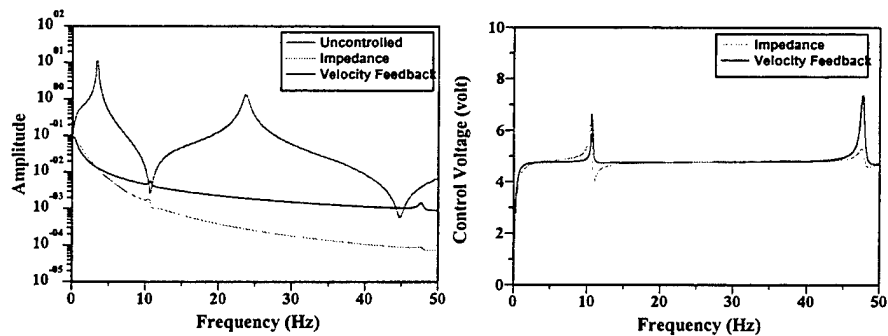
TRANSFER FUNCTIONS at 65 and 110 Deg. F.



University of Maryland



IMC & DVFC at 110 Deg. F



University of Maryland



SUMMARY

1. Impedance Matching Controller (IMC) maximizes power dissipation from vibrating structures.
 2. Suitable for controlling complex structures with closely-spaced modes.
 3. The IMC is a Direct Velocity Feedback Controller (DVFC) with a frequency-dependent gain.
 4. The IMC is more effective than DVFC in controlling structural vibration & requires less control efforts.
 5. The IMC is robust to variations in structural parameters.
-

University of Maryland





FOURTH ARO WORKSHOP ON SMART STRUCTURES
Penn State, University Park Campus, Pennsylvania
August 16-18, 1999

Using Piezoelectric Materials for Vibration Damping in Mechanical Systems

Valder Steffen, Jr(*) Daniel J. Inman

Center for Intelligent Material Systems and Structures
Virginia Polytechnic Institute and State University
Blacksburg, Virginia 24061-0261

(*) on leave from the Federal University of Uberlandia
Mechanical Engineering Department
Uberlandia, Minas Gerais, Brazil



PRESENTATION SCHEME

1- INTRODUCTION

2- VIBRATION SUPPRESSION THROUGH COLLOCATED DAMPING CONTROL

- 2.1- Basic Equations for the Piezoelectric Actuated Beam
- 2.2- Mathematical Model for the Piezo-actuated Beam
- 2.3- Passive Damped Beam
- 2.4- Optimization Strategy
- 2.5- Application 1

3- VIBRATION SUPPRESSION WITH RESONANT SHUNTS

- 3.1- The Single-Mode Damper
- 3.2- Vibration Suppression over a Frequency Band
- 3.3- Optimization Strategy
- 3.4- Applications

4- CONCLUSIONS / FUTURE WORK

5- ACKNOWLEDGEMENTS





1- INTRODUCTION

- Vibration Reduction: common design situation in a variety of engineering applications
- Two basic approaches for vibration reduction:
 - 1- active vibration control
 - 2- passive techniques
- Self-sensing actuator: single piezoelectric element (Dosh, Inman and Garcia, 1992)

Actuator + sensor

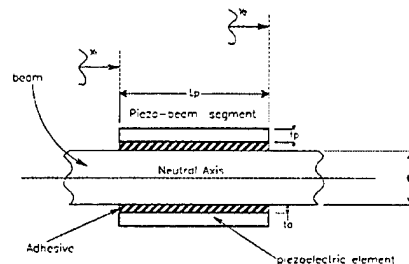


Collocated control



2- VIBRATION SUPPRESSION THROUGH COLLOCATED DAMPING CONTROL

2.1- Basic equations for the piezoelectric actuated beam (Crawley, de Luis, Anderson)



v1: voltage top piezo
v2: voltage bottom piezo
d31: piezo constant
Ep: elastic modulus piezo

$$v1 = -v2 = v$$

The moment generated by the voltage applied to the piezoceramics is given by

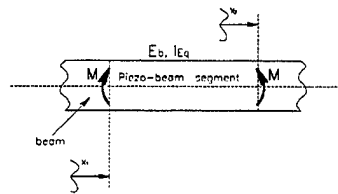
$$M^* = b_p E_p d_{31} (t_b / 2 + t_a + t_p / 2) (v_1 - v_2) = K^* (v_1 - v_2) / 2$$

$$M^* = K^* v$$





The effect of the piezoelectric on the beam is represented by two equal and opposite concentrated moments: $M=Kv$



The output of the sensor piezoelectric elements can be written as a linear combination of the modal amplitudes:

$$V_s(t) = \sum_{i=1}^{\infty} C_i \eta_i(t)$$

For design purposes the system representation is truncated to n modes:

$$V_s(t) = \sum_{i=1}^n C_i \eta_i(t)$$

$$z(t) = [\eta_1 \ \eta_2 \ \dots \ \eta_n \ \dot{\eta}_1 \ \dot{\eta}_2 \ \dots \ \dot{\eta}_n]^T \quad \bar{A} = \begin{bmatrix} O_n & I_n \\ -\Omega^2 & O_n \end{bmatrix} \quad \bar{B} = \begin{bmatrix} O_{n \times 1} \\ \hat{B} \end{bmatrix} = \begin{bmatrix} O_{n \times 1} \\ B_1 \\ \vdots \\ B_n \end{bmatrix}$$

$$\dot{z}(t) = \bar{A} z(t) + \bar{B} v(t)$$

$$\bar{C} = [\hat{C} \ O_{1 \times n}] = [C_1 \ C_2 \ \dots \ C_n \ O_{1 \times n}]$$

$$V_s(t) = \bar{C} z(t)$$

$$\Omega_1 = \text{diag}[\omega_1 \ \dots \ \omega_n]$$



The transverse response of a beam subject to initial conditions is

$$y(x,t) = \sum_{i=1}^{\infty} \Phi_i (\eta_{i0} \cos \omega_i t + \dot{\eta}_{i0} / \omega_i \sin \omega_i t)$$

Where $\Phi_i(x)$ depends on the boundary conditions

Obs- if damping is included a similar equation is obtained.

2.3- Passive Damped Beam

Collocated control is introduced \Rightarrow damping is maximized uniformly in the modes

Control law: $v(t) = k_d \hat{C} \dot{\eta}$

\Rightarrow Vector equation of motion $\ddot{\eta} + k_d \hat{B} \hat{C} \dot{\eta} + \Omega^2 \eta = 0$

state-space representation:

$$\dot{z}(t) = A z(t) \quad A = \begin{bmatrix} O_n & I_n \\ -\Omega^2 - k_d \hat{B} \hat{C} \end{bmatrix}$$





2.5 Application 1

Simply supported beam

the i-th eigen-function is $\Phi_i(x) = \sqrt{2/L_b} \sin(i\pi x / L_b)$

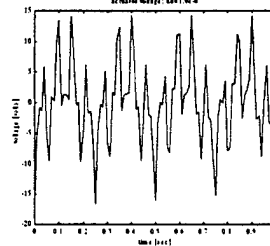
$$\text{and } \omega_i = \frac{i^2 \pi^2}{L_b^2} \sqrt{E_b I_b / (\rho_b A_b)}$$

Initial velocity is given by impact to a short portion δ of the beam at a distance d from the left hand support

$$y(x,t) = \frac{2v\delta}{L_b} \sum_{i=1}^{\infty} \frac{1}{\omega_i} \sin \frac{i\pi x}{L_b} \sin \frac{i\pi d}{L_b} \sin(\omega_i t)$$

For $n = 3$; $kd = 1.0e-6$:

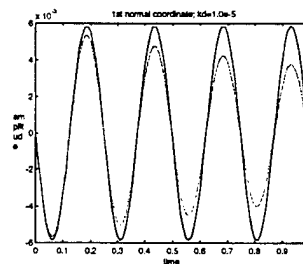
Obs- when damping is introduced to more modes, kd has to be increased.



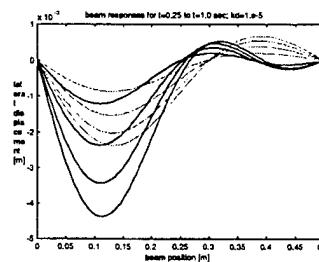
Virginia
e



The first normal coordinate - optimal design configuration



Beam response for different time instants



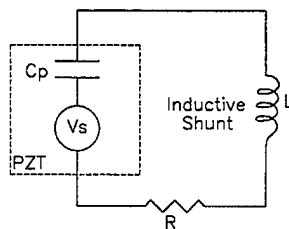
Virginia
e



3- VIBRATION SUPPRESSION WITH RESONANT SHUNTS

piezoelectric element attached to a structure: is strained as the structure deforms and a portion of the vibration energy is converted into electrical energy

piezoelectric element: behaves electrically as a **capacitor**



can be combined with a shunt network for vibration control

Shunt: **resistor + inductor**

piezoelectric element + shunt = **RLC** resonant network

optimal case: RLC frequency is tuned to structural resonance



3.1- The single-mode-damper(Hagood and von Flotow,1991)

$$v(s) = F(s) / \{Ms + K / s + Z^{RSP}(s)\}$$

$$Z_i^{SU} = Ls + R \quad \text{"i": impedance applied across the ith direction of the piezo = direction that the piezo is poled (usually sheets across the thickness)}$$

the electrical impedance of the RLC network is:

$$Z_i^{EL}(s) = \frac{Ls + R}{LC_{pi}^T s^2 + RC_{pi}^T s + 1} \quad \text{"T": capacitance value is measured at constant stress}$$

non-dimensional impedances:

$$\bar{Z}_i^{EL}(s) = \frac{Z_i^{EL}}{1 / (C_{pi}^T s)} = \frac{LC_{pi}^T s^2 + RC_{pi}^T s}{LC_{pi}^T s^2 + RC_{pi}^T s + 1} \quad \bar{Z}_{ij}^{ME}(s) = \frac{1 - k_{ij}^2}{1 - k_{ij}^2 \bar{Z}_i^{EL}}$$

kij: electromechanical coupling coefficient





3.2- Vibration Suppression over a Frequency Band

Multi-mode damper: introducing additional electronic components to the system to increase the number of electronic resonances



Use a different shunt for each suppressed mode: the shunt parameters (L,R) are obtained through an optimization scheme (similar to DVA's).

The undamped n d.o.f. system is written in normal coordinates as:

$$\ddot{q}_i(t) + \omega_i^2 q_i(t) = \{\Theta_i\}^T \{f(t)\}, \quad i = 1, 2, \dots, n$$

The excitation force is applied at the coordinate k:

$$\{f(t)\} = f_k(t) \{e_k\}$$

$\{e_k\}$ is the kth column of the identity matrix

For the harmonic case: $f_k(t) = F_k e^{j\omega t}$; $q_i(t) = Q_i(t) e^{j\omega t}$



$$H_{mk}(\omega) = \frac{X_m}{F_k} = \left[\sum_{i=1}^n \frac{\Theta_{ki}}{(\omega^2 - \omega_i^2)} \Theta_{mi} \right]$$

It can be concluded that the FRF of the n d.o.f. system is a *linear combination* of the FRFs obtained for each one of the modal coordinates, in which the coefficients of the linear combination are the components of the eigenvectors corresponding to the coordinates where the response is measured. This result can be easily extended for damped systems provided that the equations of motion are uncoupled and the equations of motion are written in the modal space .

The transfer function for the single-mode damper is written in the Laplace domain. It corresponds to the FRF when transformed to the frequency domain. The shunt parameters for each suppressed mode have to be determined from the appropriate linear combination of FRFs over the interest frequency band.





3.3- Optimization Strategy

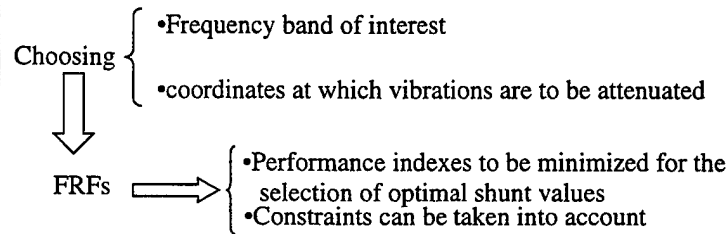


Illustration: - harmonic force F_k is applied at coordinate k
 - the response at the coordinate m is to be minimized
 - frequency band $\omega_L \leq \omega \leq \omega_U$: p frequency lines
 - a single shunt is attached to the structure

Performance indexes: $J(L, R) = \max\{abs[H_{mk}(\omega_m)]\}$
 (examples)

$$J(L, R) = \sum_{i=1}^p \bar{H}_{mk}(\omega_i) w_i H_{mk}(\omega_i)$$

w_i , $i=1$ to p : weighting factors to be ascribed to each frequency line within the band



Optimization Method

For certain cases: classical optimization \Rightarrow poor convergence

Genetic algorithms: random search techniques
 "survival of the fittest" theories

Genetic Algorithms overview

Goldberg (1989): G.A. for optimization problems
 objective function do not posses properties such as
Continuity, Differentiability, Satisfaction Lipschitz cond.

Basic Genetic Algorithm (Michalewicz, 1996):

•Evaluation

fitness of each population member: adaptation grade of the individual
 individual: set of design variables

•Selection

-choosing members of the current generation to produce the prodigy of the next generation
 -designs presenting better fitness functions are more likely to be chosen as parents





Crossover

design information is transferred to the prodigy from the parents

→ new individuals are formed from existing ones
new parts of the solution space is explored

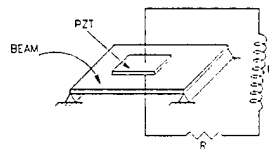
Mutation

low probability random operation used to perturb the design represented by the prodigy

One individual is mutated → A single new solution that is copied to the next generation: diversity

3.4 Application 2

Simply supported beam represented by its finite element model

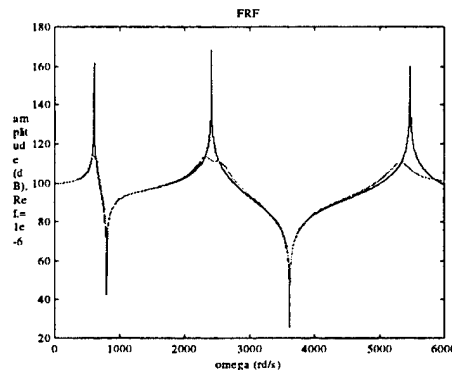


3 shunted PZTs are installed on the structure at position corresponding to the maximum strain energy for each mode, respectively
 $C_p = 150 \text{ nF}$; $K=0.12$



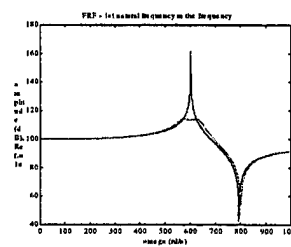
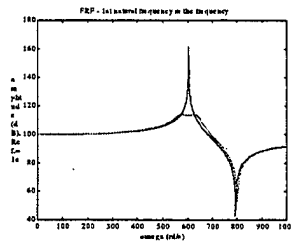
Optimal shunt values obtained using G.A.

	Inductance [Henry]	Resistance [Ohm]
Shunt 1	18.2	1680.5
Shunt 2	1.1	399.4
Shunt 3	0.2	173.4





FRFs limited to frequency bands including the first and the second modes



In this application: modes uncoupled and well spaced in frequency

Application 3

Natural frequencies: 610, 640, 850 rd/s

Modal damping factors: 3%, 1%, 1%

Two shunts: reduce the vibration of first two modes

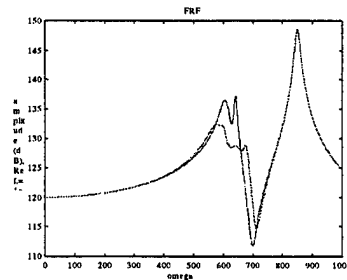


Shunt parameters	Single-mode damper		Present technique	
L_1, L_2 (henry)	17.8	16.0	17.4	16.5
R_1, R_2 (ohm)	1794.3	1601.8	1343.5	570.7

Shunt parameters not well tuned: lose efficiency



System FRF with and without the optimal shunts:



For general applications



- a certain number of modes may be coupled
- frequencies are close together

The technique presented should be used to determine the optimal shunt parameters.





4- CONCLUSIONS

- ✦ General methodology for the optimal design of piezoelectric elements for vibration damping in mechanical systems.
- ✦ Several natural frequencies in the frequency band.
- ✦ Two different approaches: - active vibration control
- passive shunt
- ✦ Active vibration
 - very effective for optimal position and geometry configuration
 - when the number of modes to be damped increase
 - Actuator gain value becomes unaffordable
 - in the optimal solution, a significant part of the structure surface is covered by the piezo-element
 - optimization technique: SUMT
- ✦ Passive electric shunt
 - system FRF is a linear combination of the FRFs obtained for each one of the modal coordinates
 - the technique presented is valid for the general case (coupling)
 - optimization technique: genetic algorithms



FUTURE WORK

- ✦ Applications involving large flexible structures with a significant \ number of modes in the frequency band of interest
 - investigate the use of different techniques for vibration reduction, concurrently: DVA, active control, shunts
 - avoid inherent limitations of available techniques (actuator voltage limits, free space for shunt installation, feasible parameter values, DVA constraints)
 - use hybrid optimization techniques when convergence difficulties appear: classical methods, G.A., simulated annealing



6- ACKNOWLEDGEMENTS

CAPES Foundation (Brazil)
Fulbright Commission (USA)
Air Force Office of Scientific Research (grant No. F49620-99-0822)



HIGH AUTHORITY AND NONLINEARITY ISSUES IN ACTIVE-PASSIVE HYBRID PIEZOELECTRIC NETWORKS FOR STRUCTURAL DAMPING

J. Tang

K. W. Wang

Structural Dynamics and Controls Lab

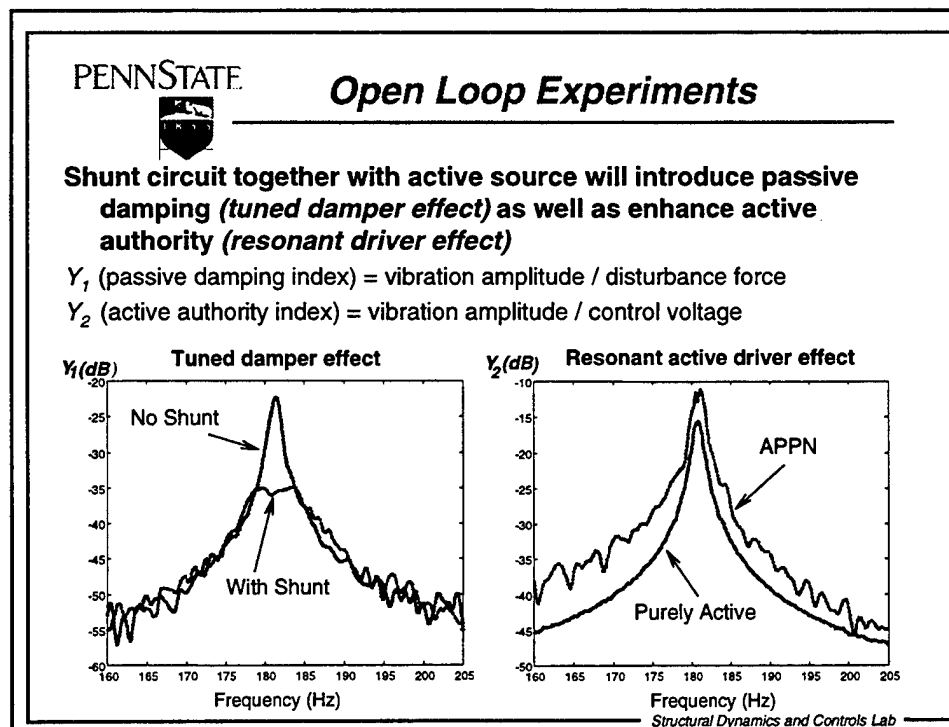
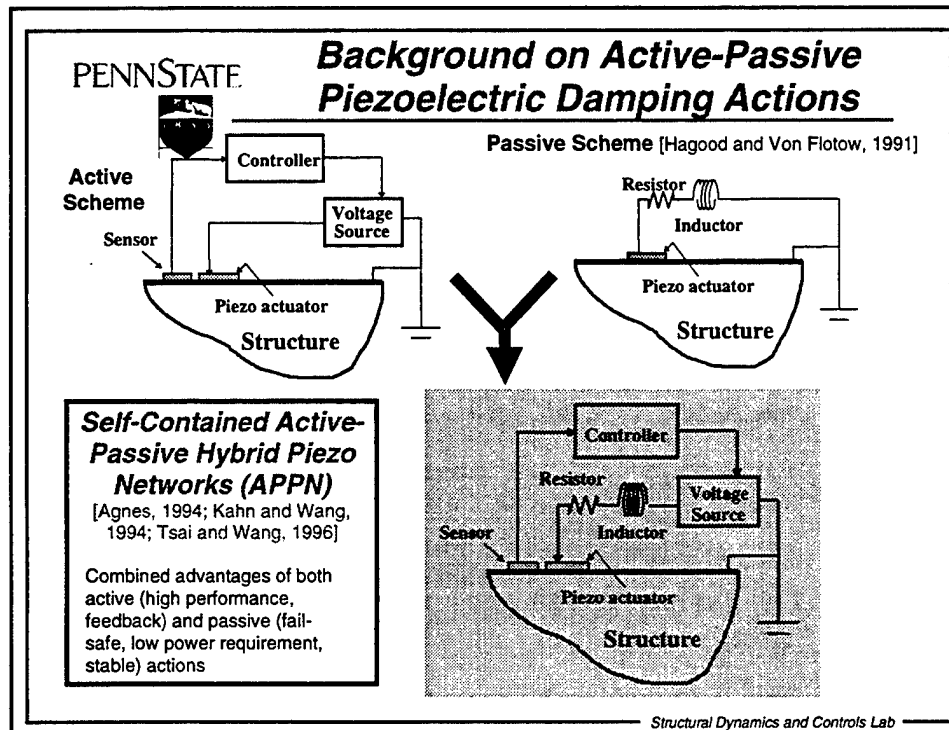
The Pennsylvania State University

University Park, PA

Because of their active and passive damping features, piezoelectric materials have been explored for their active-passive *hybrid* vibration control abilities, which could have the advantages of both the passive (stable, fail-safe, low power requirement) and active (high performance, feedback or feedforward actions) systems. An active-passive hybrid piezoelectric network (APPN) concept has been proposed [Kahn and Wang, 1994; Agnes, 1994; Tsai and Wang, 1996] for this purpose. This actuator configuration integrates the piezoelectric material with an active voltage source and a passive R (resistance) L (inductance) shunting circuit. The function of an effective APPN system is two-fold. On one hand, structural vibration energy is transferred to electrical energy and dissipated in the tuned shunt circuit passively. This will often result in high charge and current in the circuit and high voltage across the piezoelectric actuator. On the other hand, the control voltage will drive the piezoelectric actuator through the circuit to suppress vibration, where the circuit will increase the active authority by amplifying the voltage input to the piezoelectric actuator. Therefore, the more effective the APPN, the more likely that high electrical field will occur across the piezoelectric material, especially under high load conditions. Due to this fact, the linear assumption often made in most piezoelectric actuator based control systems (the linear constitutive relation between the stress, strain, electrical field and electrical displacement of the piezoelectric material) might not be valid in some APPN applications. This is because that the material hysteresis and the high order nonlinear relationship between the mechanical response and electrical field could become very significant when high field occurs on the piezoelectric actuators. Therefore, in order to fully utilize the high authority characteristics of the APPN actuator, the nonlinear effects need to be considered in the controller design.

The goal of this research is to develop a control law for the APPN configuration with piezoelectric nonlinearities being taken into account, such that the actuator authority and system performance can be maximized. A robust control algorithm based on the sliding mode theory is proposed for this purpose. The advantage of employing the sliding mode technique is that the controller can be designed to be robust with respect to system uncertainties, provided that the uncertainty *bounds* can be estimated. In this case, the piezoelectric nonlinearities (which are in general difficult to model) can be treated as uncertainties (partially or completely) and need not be accurately modeled. Clearly, in addition to the piezoelectric hysteresis and the higher order nonlinearity, the system could be synthesized to be robust against other possible uncertainties as well. These other uncertainties include the drift and the external stress dependency of the induced strain in the piezoelectric materials⁹, the system parameter modeling errors, and the unknown external disturbances.

In this paper, the nonlinear behavior of the piezoelectric material is first investigated experimentally. The nonlinearity and uncertainty bounds are extracted from the test results. Based on the experimental data, the sliding mode controller is formulated. Two schemes are discussed. One is to use the linear system as the baseline and treat all nonlinearities as unknowns. The second scheme is to utilize the high order nonlinearity in the model and controller, while treating the others as uncertainties. Analysis results are given to demonstrate the validity of the proposed approach.



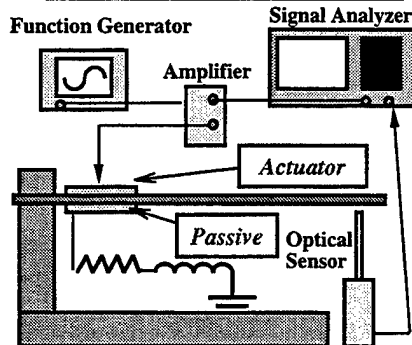


Experimental Observation on Integrated and Separated Systems

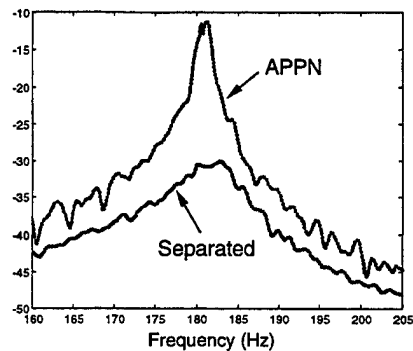
A comparison between integrated and separated system

- Both have the same passive damping ability
- The active authority of integrated system is much higher than separated configuration

Separated Configuration



Active Authority Index



Structural Dynamics and Controls Lab



Active-Passive Hybrid Piezo Networks (APPN)

Previous Work

- A simultaneous controller/circuit optimization process [Tsai and Wang, 1996]
 - A well-designed APPN can outperform a purely active system in terms of both damping performance and power requirement
- An adaptable circuit [Morgan and Wang, 1997]
 - A "Semi-Active" APPN with power flow management could further enhance the efficiency of the device

Summary of Previous Observations

- APPN could combine the advantages of both purely active and passive approaches and outperform them

Structural Dynamics and Controls Lab



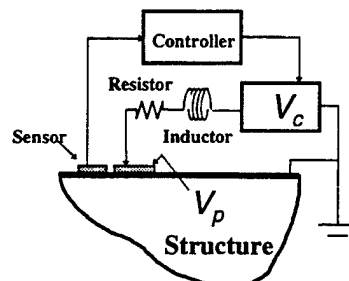
Active-Passive Hybrid Piezo Networks (APPN)

Summary of Previous Observations (cont.)

- Shunt circuit could enhance **both** passive damping and active authority in APPN
 - Integrated self-contained design is better than the separated
 - Shunt circuit amplifies voltage input to the piezoelectric actuator around tuned frequency ($V_p \gg V_c$) -- An increase of more than 500% has been observed in experiments

Issue

High electrical field is likely to occur



Structural Dynamics and Controls Lab



Piezoelectric Material Property

**Under high electrical fields --
nonlinearity becomes significant**

[Devonshire, 1954; Crawley and Lazarus, 1990;
Sirohi and Chopra, 1998; etc.]

- **Material hysteresis**
- **The mechanical response and electrical field exhibits high order relation**

Structural Dynamics and Controls Lab



Problem Statement and Objective

Despite the nonlinear behavior, linear relationship has been assumed in most applications [IEEE, 1987]

$$\tau = E_p \varepsilon - h_{31} D$$

$$E = -h_{31} \varepsilon + \beta_{33} D$$

– valid for low field cases

To take full advantage of the APPN concept, the piezoelectric nonlinearities need to be taken into account in system control design

Objective - To utilize and/or compensate for the piezoelectric nonlinearity in APPN, such that high authority damping can be achieved



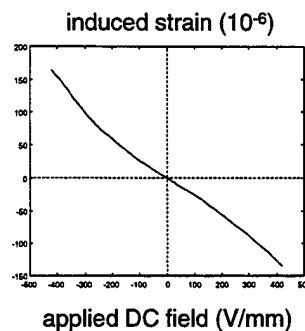
Experimental Observations on Piezoelectric Material Property

Experiment setup

- PZT-5A piezoelectric patch
- Use surface bonded strain gage to measure the induced strain

Static free strain

- Quasi-static induced strain curve
 - Slope of the curve increases as the field level increases
 - Third order (or higher) relation between the induced strain and applied field

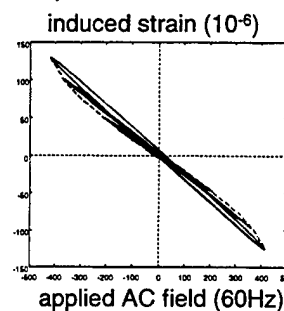
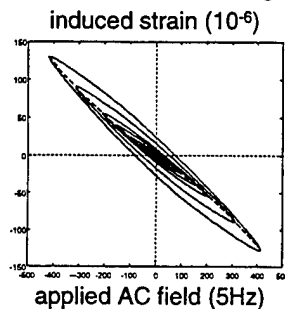




Experimental Observations on Piezoelectric Material Property

Dynamic strain response (induced strain vs AC voltage input)

- Significant hysteresis at high field level
- Slope of "peak" induced strain curve increases as applied field increases -- high order relationship



- These phenomena have been reported [Crawley and Lazarus, 1990; Sirohi and Chopra, 1998].

Structural Dynamics and Controls Lab



Technical Challenge and Proposed Idea

- **Piezoelectric nonlinearity phenomena** - difficult to have precise model

- **Idea**

Treat the piezoelectric nonlinearities (partially or completely) as bounded uncertainty and develop nonlinear robust controller to compensate for the uncertainty -- only need to estimate the "bounds", and do not need the precise model of nonlinearity

Structural Dynamics and Controls Lab



Proposed Tasks

- **Determine baseline and propose constitutive equations with bounded uncertainty**
 - Linear baseline - treat all nonlinearities as unknowns
 - Nonlinear baseline - treat some nonlinearities (e.g., the high order terms) as known elements and utilize their characteristics, treat others as unknowns
- **Extract nonlinear uncertainty bounds from experimental investigations**
- **Design a controller based on the Sliding Mode control theory**
 - Nonlinear controller - can include the modeled piezoelectric nonlinearities in the nonlinear baseline
 - Robust controller - can compensate for the unmodeled nonlinearities as uncertainties

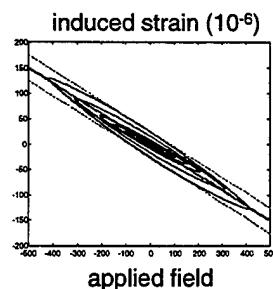
Structural Dynamics and Controls Lab



Proposed Constitutive Equations with Linear Baseline

Constitutive equations with bounded uncertainty

- use linear constitutive relation as basic model (green solid line)
- actual induced strain = linear deterministic value + uncertainty
- uncertainty bound (red dashed lines) is extracted from experimental observations -- can cover the piezoelectric nonlinearities



Proposed constitutive equations:

$$\tau = E_p \varepsilon - h_{31} D$$

$$E = -h_{31} (\varepsilon - \varepsilon_0) + \beta_{33} D$$

where

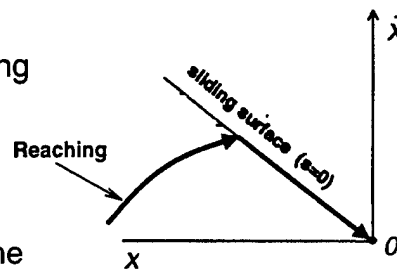
$$|\varepsilon_0| < \varepsilon^*$$

Structural Dynamics and Controls Lab



Basic Principle

- Design sliding surface $s(x)=0$ in state space, on which the system is asymptotically stable with sufficient damping -- *to ensure final vibration suppression*
- Design a controller which forces the states to reach the sliding surface in finite time -- *to ensure minimal transient behavior*



Structural Dynamics and Controls Lab



• Sliding surface

- define a sliding surface $s = \lambda_1 x_1 + \lambda_2 x_2 + \lambda_3 x_3 - x_4 = 0$
- dynamics on the sliding surface

$$\begin{Bmatrix} \dot{x}_1 \\ \dot{x}_2 \\ \dot{x}_3 \end{Bmatrix} = \begin{bmatrix} 0 & 1 & 0 \\ 0 & 0 & 1 \\ 0 & 0 & 0 \end{bmatrix} \begin{Bmatrix} x_1 \\ x_2 \\ x_3 \end{Bmatrix} + \begin{Bmatrix} 0 \\ 0 \\ 1 \end{Bmatrix} [\lambda_1, \lambda_2, \lambda_3] \begin{Bmatrix} x_1 \\ x_2 \\ x_3 \end{Bmatrix}$$

• Determination of sliding mode by optimal control theory

- define a cost function

$$J = \int (\hat{x}^T W_s \hat{x} + r_s v^2) dt \quad \hat{x} = [x_1, x_2, x_3]^T \quad \begin{array}{l} x_1: \text{displacement} \\ x_2: \text{velocity} \\ x_3: \text{related to charge} \end{array}$$

$$v = [\lambda_1, \lambda_2, \lambda_3] \hat{x}$$

- **do not penalize x_3**

Structural Dynamics and Controls Lab



Sliding Mode Control

- Control input is determined by reaching condition

$$\dot{s} = -\alpha \operatorname{sgn}(s) \rightarrow u = \hat{u} - \frac{\alpha}{\bar{\omega}_m^4 \delta^2 c^2} \operatorname{sgn}(s)$$

$$\hat{u} = \frac{1}{\bar{\omega}_m^4 \delta^2 c^2} [-\lambda_1 x_2 - \lambda_2 x_3 - \lambda_3 x_4 - \bar{\omega}_m (2\zeta + r\delta^2) x_4 - \bar{\omega}_m^2 (1 + 2\zeta r\delta^2 + \delta^2) x_3 - \bar{\omega}_m^3 \delta^2 (r + 2\zeta) x_2 - \bar{\omega}_m^4 \delta^2 (1 - c^2) x_1]$$

- Include uncertainty bounds

$$\alpha = \alpha^* + \gamma$$

α^* positive number, relate to uncertainty bounds, to compensate for uncertainties

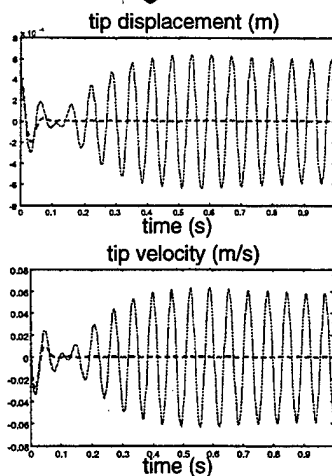
γ arbitrary positive number, to adjust transient behavior

- Control can be made smooth by replacing $\operatorname{sgn}(s)$ by a saturation function

Structural Dynamics and Controls Lab



Analysis Results -- Compare with Optimal Passive System



- Vibration suppression of beam with initial displacement and subject to sinusoidal external excitation

- R and L are optimal values for passive shunt
- voltage across the PZT is in the nonlinear range but below the depoling limit

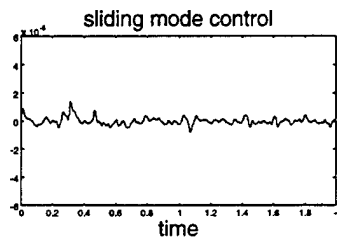
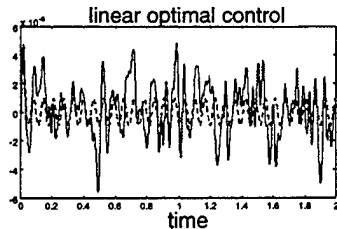
- Significantly outperforms optimal passive system

green solid line: optimal passive system
red dashed line: sliding mode control

Structural Dynamics and Controls Lab



Analysis Results -- Compare with Linear Controller



- Linear optimal control (LQR) -- not considering nonlinearity in control design
 - green dashed line: without simulating nonlinearity (ideal situation)
 - blue solid line: with nonlinearity being simulated (real situation)
 - performance degraded by piezoelectric nonlinearity
- Sliding mode control (with the same RMS control power input)
 - capable of compensating for piezoelectric nonlinearity

Structural Dynamics and Controls Lab



Concluding Remarks

Methodology is developed to utilize the high authority nonlinear piezoelectric actions in APPN damping treatments

- Piezoelectric nonlinearities at high electrical fields are investigated experimentally and constitutive relations with bounded uncertainty are proposed based on experimental observations
- A robust sliding mode controller is designed, which is capable of compensating for piezoelectric nonlinearity, system modeling error, and external disturbance

Structural Dynamics and Controls Lab

Active Magnetostrictive Free Layer Damping

B. Bhattacharya and G.R. Tomlinson

Department of Mechanical Engineering, University of Sheffield, Sheffield, S1 3JD, UK.

1 Introduction:

Magnetostrictive composites are found to have useful applications as sensors and actuators. These composites are composed of two phases - magnetostrictive particles of Terfenol-D (T-D) like material and a compliant inactive polymer or metal powder as the matrix. Sandlund *et al*¹ developed magnetostrictive particulate composites in rod form by embedding T-D particles in epoxy resin. Anjappa *et al*² characterised the static macroscopic behaviour of such actuators. It is observed that the volume fraction, modulus of elasticity of the matrix, prestress and orientation of magnetostrictive particles play a significant role in the actuator performance. These observations are also substantiated by the theoretical modelling of Herbst *et al*³ and Nan⁴. Lim *et al*⁵ investigated the performance of magnetostrictive particles embedded in a phenol type polymer binder. Similar studies were carried out by Chen *et al*⁶ with Fe+Glass, Al+Glass, CeFe₂+Glass and E Glass powder as the binder matrix. It was observed that the elastic modulus of the matrix in such two-phased composites has to be carefully chosen to achieve high magnetostriction.

In the present study, numerical simulations of magnetostrictive composites are considered. A comparison between magnetostrictive free composite layers and hard ceramic coatings applied to a steel blade is carried out. The effects of volume fraction, thickness of magnetostrictive layer and elastic modulus of the matrix on the dynamic characteristics are presented.

2 Active vs. Passive Coatings:

In order to compare the performance of hard ceramic coatings with active magnetostrictive layers, a cantilever steel blade model (as shown in Fig 1A and B) is considered. The blade is considered to have coatings of the same thickness of magnetostrictive composites/hard ceramic coating on both the sides for comparison. Two types of coating thickness are considered, 0.006" (0.1524mm) and 0.02" (0.508mm). For the active coating, a magnetic field in the range of 0.5×10^6 to 1×10^6 A/m is applied. It is assumed that the particles in the composite are aligned along the longitudinal axis of the beam by applying suitable magnetic field during the fabrication. The frequency and Q-factor for the two models corresponding to the first and second bending modes are obtained using a Rayleigh-Ritz model^{7,8}. The temperature effects are not considered in this work. The results are shown in Tables 1 and 2 respectively. It is observed that both for passive and active coating a considerable amount of damping is achieved. The Q-factor obtained with T-D+Fe-Glass powder is of the same order as the hard coating. More damping is achieved with T-D+E-Glass powder. For the first two bending modes, the

Fourth ARO Workshop on Smart Structures, August 16-18, 1999

magnetostrictive coating with phenol binder is found to be the most effective amongst all the coatings. However, the resonant frequencies reduce significantly with the polymer coating. It is also of interest to note that the damping achieved by the hard coating is more uniform than the active coatings.

3 Dynamic Characterisation of Active Magnetostrictive Composite Coating:

In order to study the dynamic characteristics of the magnetostrictive coatings three different parameters are studied. These are the thickness ratio of the magnetostrictive layer to the host, the volume fill fraction and the elastic modulus of the matrix.

In the first study, the thickness of the magnetostrictive layer is varied from 0.1 to 1mm for a beam of size 75x50x3 mm. The base material was chosen to be titanium. The composite is considered to be T-D+Fe-Glass powder [10/90 vol%]. The damping characteristics for the first three bending modes are shown in Fig 2. It is observed that for all the three modes, the Q-factor decreases (i.e. damping improves) with respect to the increase in thickness ratio. However, beyond the thickness ratio of 0.2, the effect gets saturated signifying very small amount of gain in damping with respect to the change in the composite layer thickness.

It is known from the HCP theory³ that the effective magnetostriction λ (the ratio of the magnetostriction of the composite to that of the magnetostrictive component) varies with the fill fraction f and the Poisson's ratio of the magnetostrictive material as follows:

$$\lambda = \frac{f}{1-1.25\nu} (1.1538 - 1.2628\nu - 0.2122f^{2/3})$$

Following this theory the effective magnetostriction of three composites having Fe-Glass Powder, E-Glass Powder and Phenol as the binder respectively are evaluated with respect to the change in the fill fraction. The base beam is chosen to be Titanium (of size same as in Fig 1A), and the patch of magnetostrictive coating is considered to be from 0 to 25% of the length of the beam from the fixed end. The data are plotted in Fig 3. It is found that for all the cases the effective magnetostriction increases with f and the maximum value is obtained when f is around 1 (that is the composite is almost full of magnetostrictive particle). The effect of volume fraction on the resonant frequency of the beam is plotted in Fig 4. It is found that for higher %volume of the Fe-Glass powder, the frequency of the beam has increased significantly from the sixth mode onwards.

However, in terms of damping, the situation is somewhat different. In Fig 4, the variation of Q-factor for the first five modes of the cantilever beam (size 75x50x3 mm) are plotted for four different compositions of the composite [Matrix/T-D by vol. 10/90, 20/80, 30/70 and 40/60 respectively]. It is found that for the first two modes maximum damping is achieved for $f = (20/80)$ whereas for the next three modes maximum damping is achieved for $f = (30/70)$.

Chen et al⁶ have shown that the elastic modulus of the matrix plays an important role in the magnetostrictive strain in the composite. It is suggested that to obtain high magnetostriction, the elastic moduli of the magnetostrictive phase and the matrix should be as close as possible. However, in dynamic applications, the choice of the elastic

Fourth ARO Workshop on Smart Structures, August 16-18, 1999

modulus of the composite layer must be done suitably with respect to the elastic modulus of the base beam. In Fig 5, the variation of Q-factor in the first four bending modes with respect to the change in effective composite elastic modulus is plotted for the same titanium beam as above. With the exception of the second mode of vibration, the modal damping increases as the effective elastic modulus of the composite increases. This signifies that the elastic modulus of the matrix and the volume fill fraction indirectly play a significant role in the damping of vibration.

4 Conclusions

- (a) Active magnetostrictive composite layers, applied as surface coatings, offer significant damping in the flexural modes of vibrating structures. Compared with hard passive coatings of equivalent modulus, the modal damping is not very different.
- (b) By optimising the modulus of the matrix, the thickness ratios of the magnetostrictive coatings and the magnetic field significant improvement in the damping can be achieved. However, no consideration is given to the manufacturability of the magnetostrictive composite coating of thickness in the range of 0.02" to 0.006" which may become significant during the actual fabrication of such coatings.
- (c) While from effective magnetostriction point of view, the higher volume fill fraction produces more magnetostriction, however, from damping point of view an optimal fill fraction could be found out which could be considerably lower than the highest permissible value of f depending on the frequency range of interest.

REFERENCES

1. Sandlund L, Fahlander M, Cedell T, Restorff J and Clark A E, "Magnetostriction, elastic moduli and coupling factors of composite Terfenol-D", *Journal of Applied Physics*, 75 (10), 5656-5658, 1994.
2. Anjanappa M, Wu Yuefei, "Magnetostrictive particulate actuators: configuration, modeling and characterization", *Smart Materials and Structures*, Vol.6, 1997, pp.393-402
3. Herbst J F, Capehart T W, Pinkerton F E, "Estimating the effective magnetostriction of a composite: A simple model", *Applied Physics Letter*, Vol.70, N0.22, 1997, pp.3041-3043
4. Nan C W, "Effective magnetostriction of magnetostrictive composites", *Applied Physics Letter*, Vol.72, N0.22, 1998, pp.3041-3043
5. Lim S H, Kim S R, Kang S Y, Park J E, Nam J T and Son D, "Magnetostrictive properties of polymer-bonded Terfenol-D composites", *Journal of Magnetism and Magnetic Materials*, Vol.191, 1999, pp.113-121

Fourth ARO Workshop on Smart Structures, August16-18, 1999

6. Chen Y, Snyder JE, Schwichtenberg C R, Dennis K W, Falzgraf D K, "Effect of the elastic modulus of the matrix on magnetostrictive strain in composites", *Applied Physics Letters*, Vol.74, No.8, 1999, pp. 1159-1161.
7. Rongong J A, Wright J R, Wynne R J and Tomlinson G R, "Modelling of a hybrid constrained layer/piezoceramic approach to active damping", *ASME Journal of Vibration and Acoustics*, 119, 120-130, January 1997.
8. Bhattacharya B, Rongong J A and Tomlinson G R," Vibration Suppression Performance of Piezoceramic and Magnetostrictive Materials in Constrained Layer Damping", Paper 3672-27, SPIE 6th Annual International Symposium on Smart Structures and Materials, Newport Beach, CA, USA, 1-5 March , '99.

COMPARISON OF ACTIVE VS PASSIVE COATINGS

Beam Type	Increase in weight of the host Beam (%)	1B Mode		2B Mode	
		Frequency	Q-factor	Frequency	Q-factor
Steel Blade without any coatings	Nil	477	700	2942	2000
With Metco 212 Hard Coat (WBC)	1.42	481	206	2963	205
With MS layer (40/60 T-D + Fe-Glass Powder Vol. %)	4.82	460	123	2860	213
With MS layer (40/60 T-D + E-Glass Powder Vol. %)	4.48	440	60	2780	94
With MS layer (4/96 T-D + Phenol Wt. %)	5.80	425	15	2758	35

Table 1: Comparison of Q-factors and Frequencies for a Steel Blade with Active and Passive Coatings: Coating thickness = 0.1524 mm(0.006")

COMPARISON OF ACTIVE VS PASSIVE COATINGS

Beam Type	Increase in weight of the host Beam (%)	1B Mode		2B Mode	
		Frequency	Q-factor	Frequency	Q-factor
Steel Blade without any coating	Nil	477	700	2942	2000
With Metco 212 Hard Coat (WBC)	4.73	495	74	3049	73
With MS layer (40/60 T-D + Fe-Glass Powder Vol.%)	16.06	467	43	2880	59
With MS layer (40/60 T-D + E-Glass Powder Vol.%)	14.94	450	18	2800	22
With MS layer (4/96 T-D + Phenol Wt.%)	19.36	430	4	2750	6

Table 2: Comparison of Q-factors and Frequencies for a Steel Blade with Active and Passive Coatings: Coating thickness = 0.508 mm(0.02")

SUMMARY OF ACTIVE VS PASSIVE COATINGS

- ♦ It is observed that both for passive and active coatings a considerable amount of modal damping is achieved with Q factor in the range 5-200.
- ♦ Damping achieved with the hard coating is more uniform (in a modal context) than the active coatings.
- ♦ The highest damping is achieved with T-D+E-Glass powder, volume fraction $\approx 40/60$.
- ♦ For the first two bending modes, the magnetostrictive composite with phenol binder was found to be the most effective coating with Q values in the range 15-35.
- ♦ With the polymer coatings there is a significant reduction in the resonant frequencies due to the added mass effect.

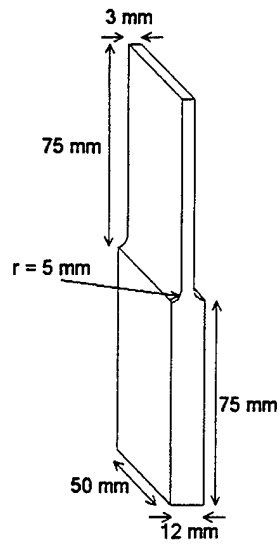


Fig 1A: Geometry of the Blade

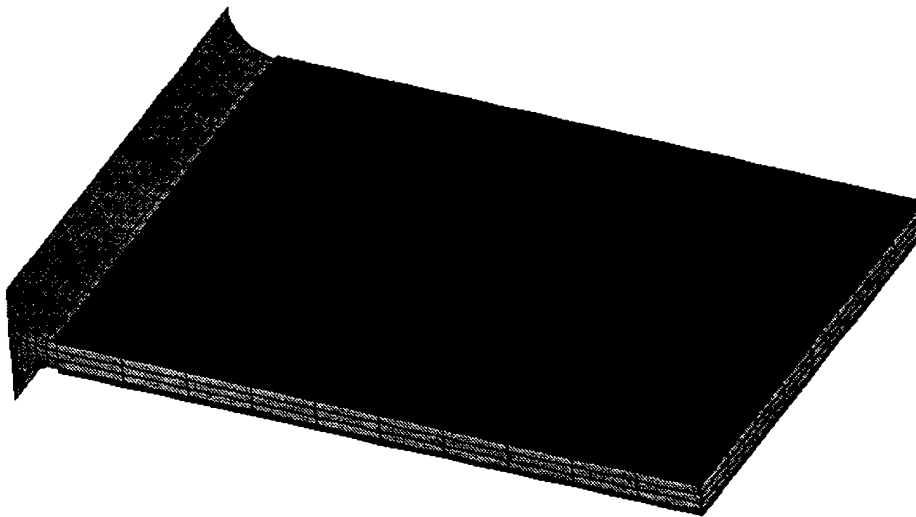


Fig 1B: FEM Model of the Blade with Coating

Dynamic Characterisation of Active Magnetostrictive Composite Coat

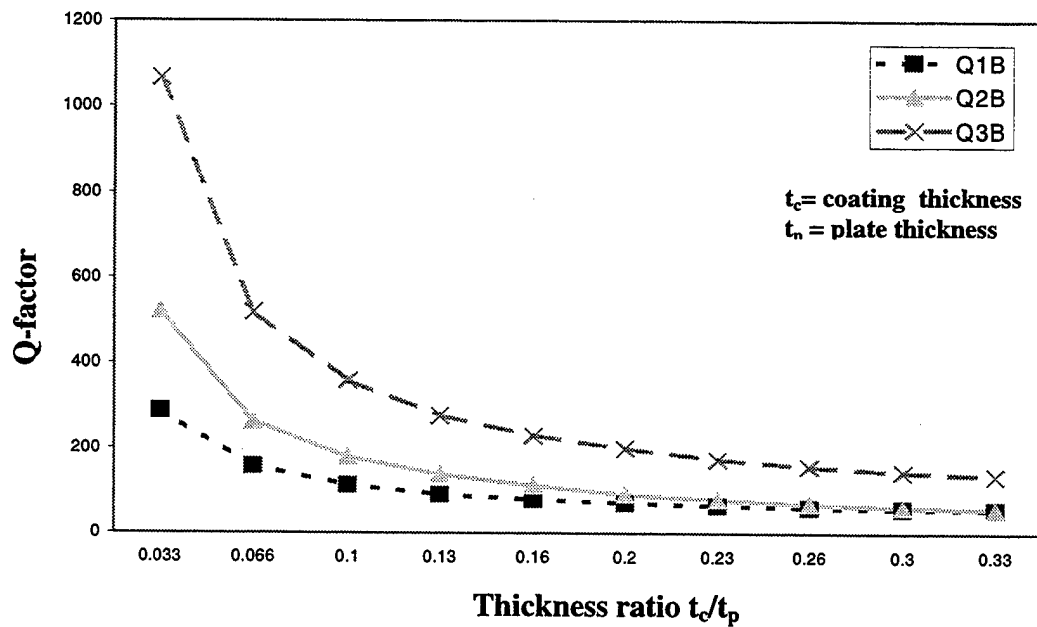


Fig 2: The effect of thickness of active coat over the Q-factor

- ◆ For all the three modes, the Q-factor decreases with respect to the increase in thickness ratio.
- ◆ Beyond the thickness ratio of 0.2, the effect gets saturated signifying a very small amount of gain in damping with respect to the change in the composite layer thickness.

Dynamic Characterisation of Active Magnetostrictive Composite Coat

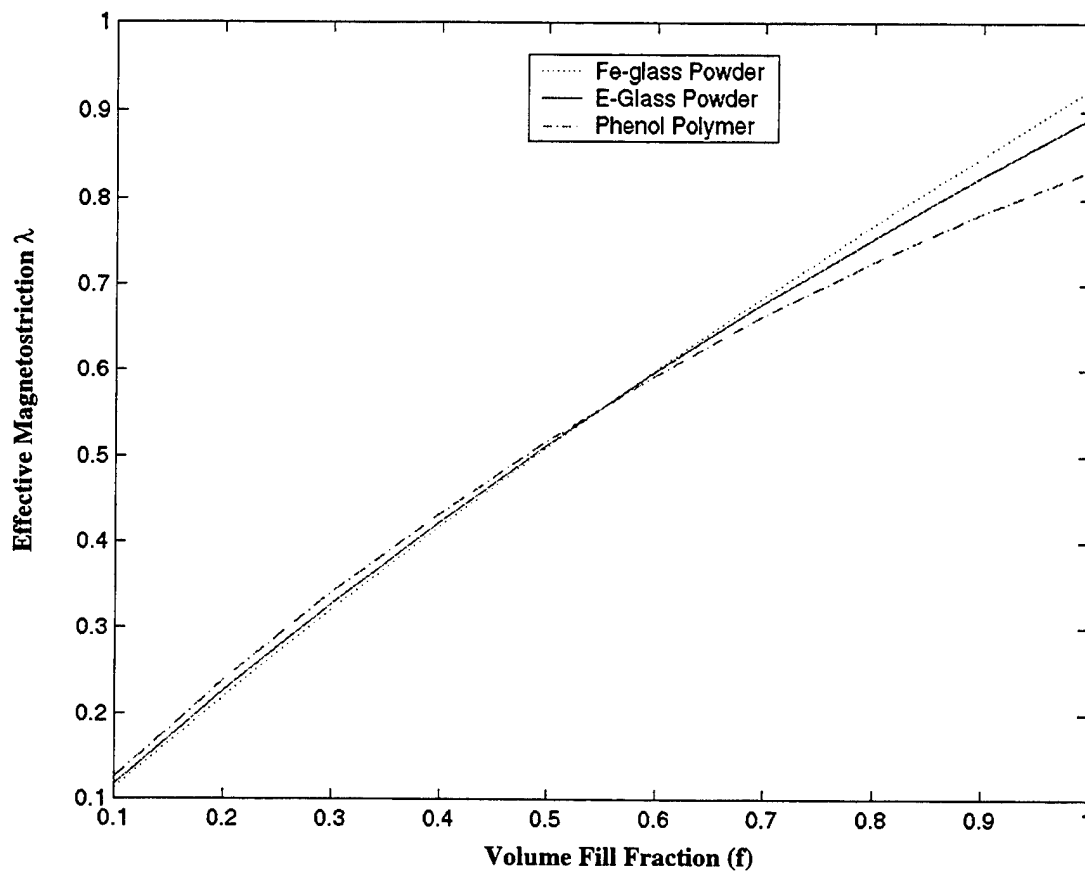


Fig 3: The effect of volume fill fraction over the effective magnetostriction

- ◆ For all the cases the effective magnetostriction increases with f and the maximum value is obtained when f is around 1 (that is the composite is almost full of magnetostrictive particle).

Dynamic Characterisation of Active Magnetostrictive Composite Coat

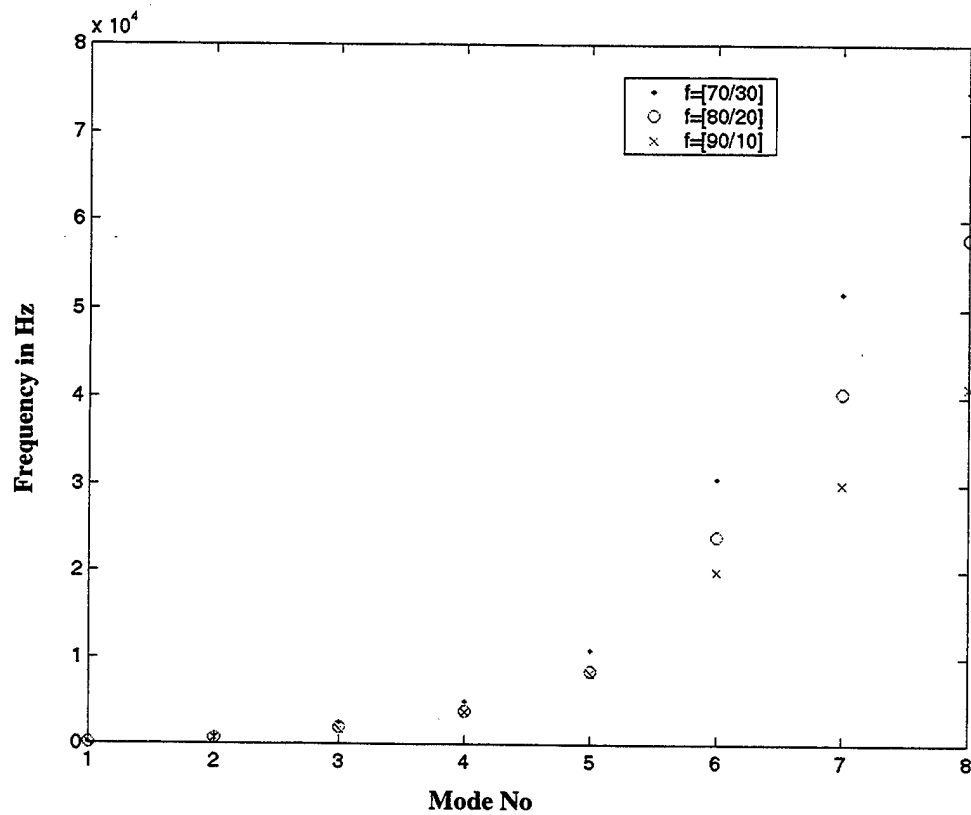


Fig 4: The effect of volume fill fraction on the resonant frequencies of the beam

For higher % volume of the Fe-Glass powder, the frequency of the beam has increased significantly from the sixth mode onwards.

Dynamic Characterisation of Active Magnetostrictive Composite Coat

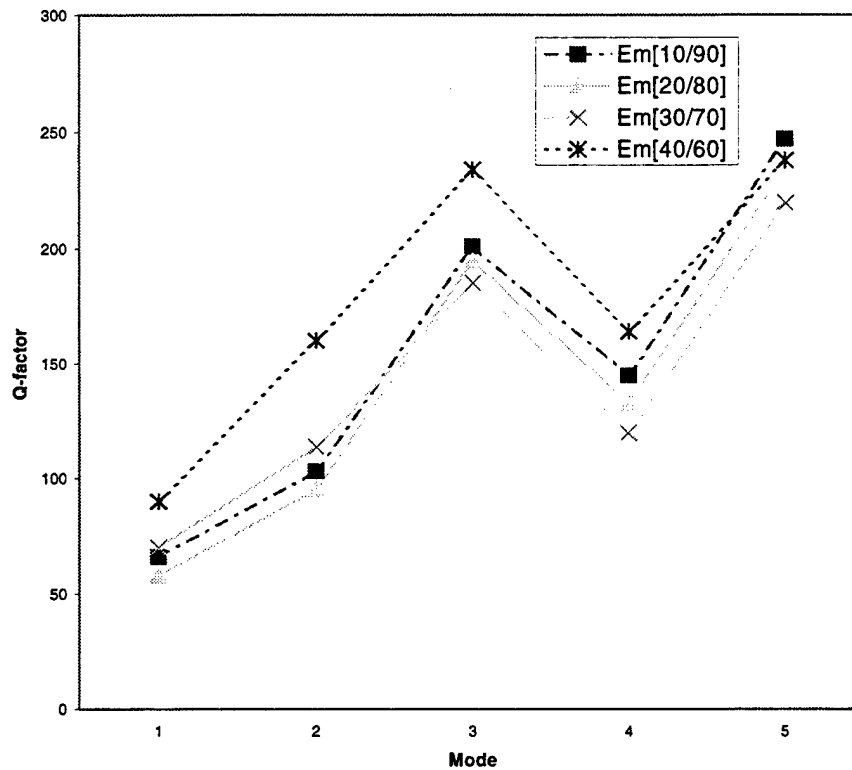


Fig 5: The effect of volume fill fraction on Q-factor

- ◆ For first two modes of vibration maximum damping is achieved for the volume fraction $f = (20/80)$ whereas for the next three modes maximum damping is achieved for the volume fraction $f = (30/70)$.

Dynamic Characterisation of Active Magnetostrictive Composite Coat

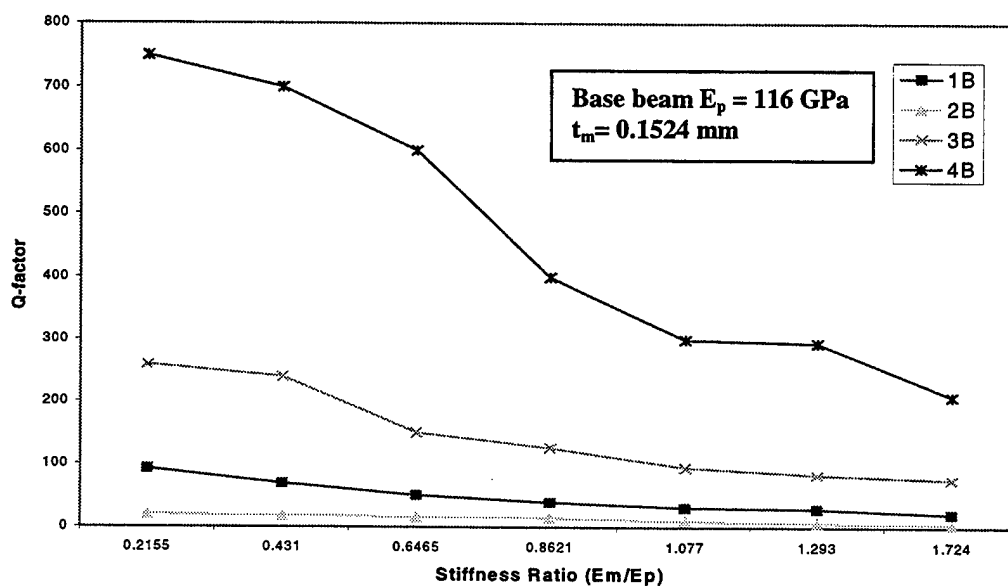


Fig 6: The effect of the Elastic Modulus of the matrix on Q-factor

- ◆ Except for the second mode of vibration, high damping is achieved corresponding to the effective elastic modulus of the magnetostrictive composite which are substantially higher than the Young's modulus of the base beam.

Modeling Issues for Cyclic and Step-Strain Relaxation Deformations of Elastomers

Arthur R. Johnson
Army Research Laboratory
Analytical and Computational Methods Branch
NASA Langley Research Center
Hampton, VA

**Fourth ARO Workshop on Smart Structures
August 16-18, 1999
Penn State, University Park Campus
Pennsylvania**

Outline

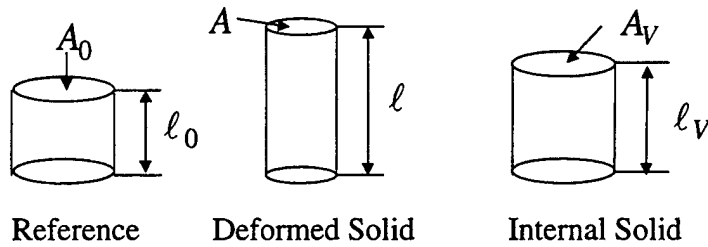
- 1.) Viscohyperelastic solids in tension.
- 2.) Test data for compression of pill coupons.
- 3.) Energy functions and viscous constants
for internal solids.
- 4.) Viscohyperelastic numerical simulations.
- 5.) Numerical simulations for modified
models.
- 6.) Summary.

ViscoHyperelastic Solid in Tension

$\ell_0, A_0 =$ Reference length, area for hyperelastic solid.

$\ell, A =$ Deformed length, area of physical solid.

$\ell_V, A_V =$ Reference length, area of internal time dependent solid (viscohyperelastic.)



Force on Physical Solid

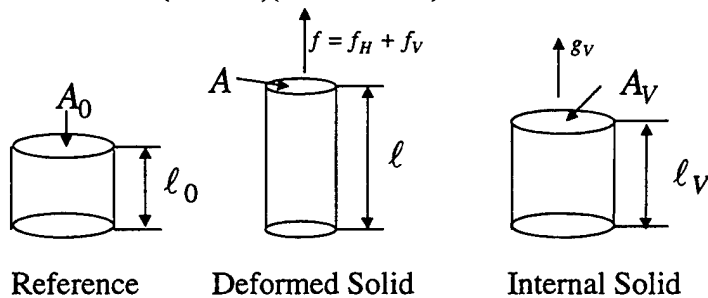
$$f = f_H + f_V$$

$$f_H = 2A \left(\lambda^2 - \frac{1}{\lambda} \right) \left(\frac{\partial W_H}{\partial I_{1H}} + \frac{1}{\lambda} \frac{\partial W_H}{\partial I_{2H}} \right)$$

$$f_V = 2A_V \left(\lambda_V^2 - \frac{1}{\lambda_V} \right) \left(\frac{\partial W_V}{\partial I_{1V}} + \frac{1}{\lambda_V} \frac{\partial W_V}{\partial I_{2V}} \right)$$

$$\lambda = \frac{\ell}{\ell_0}$$

$$\lambda_V = \frac{\ell}{\ell_V}$$



Physical Solid's Internal Energy

$$W = W_H + W_V \quad \text{Total internal energy.}$$

$$W_H = \sum_{\ell+m \geq 1}^3 \sum_{\ell+m \geq 1}^3 C_{\ell m}^H (I_{1H} - 3)^\ell (I_{2H} - 3)^m \quad \text{Hyperelastic part.}$$

$$W_V = \sum_{\ell+m \geq 1}^3 \sum_{\ell+m \geq 1}^3 C_{\ell m}^V (I_{1V} - 3)^\ell (I_{2V} - 3)^m \quad \text{Viscous part.}$$

$$I_1 = \lambda^2 + \frac{2}{\lambda} \quad I_2 = 2\lambda + \frac{1}{\lambda^2} \quad \text{For tension.}$$

$$\text{Recall} \quad \lambda = \frac{\ell}{\ell_0} \quad \lambda_V = \frac{\ell}{\ell_V}$$

Internal Solid's Evolution Equation

ℓ_V is relaxing to ℓ

$$\Lambda = \frac{1}{\lambda_V} = \frac{\ell_V}{\ell} \quad \text{Reference is now } \ell$$

$$\hat{W}_V = W_V(\Lambda) \quad \text{Energy function for evolution stress.}$$

$$g_V = 2 \left(\Lambda^2 - \frac{1}{\Lambda} \right) \left(\frac{\partial \hat{W}_V}{\partial \hat{I}_{1V}} + \frac{1}{\Lambda} \frac{\partial \hat{W}_V}{\partial \hat{I}_{2V}} \right) \quad \text{Stress relaxing length } \ell_V \text{ to length } \ell$$

$$-\eta \frac{\partial g_V}{\partial t} \Big|_{\ell} = g_V \quad \text{Stress is assumed proportional to its decay rate.}$$

$$\frac{d\ell_V}{dt} = \frac{-g_V \ell}{\eta \frac{\partial g_V}{\partial \Lambda}}$$

Evolution equation for ℓ_V

Comments:

- Can superimpose a number of internal solids.
- Data can be included for tension, shear, biaxial, 3D.
- Results for large deformation relaxation are generally good.

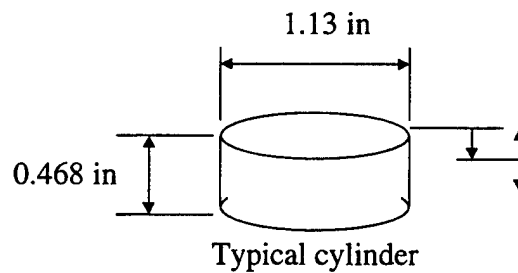
Problem:

- When the above nonlinear relaxation model is used for dynamics, the results are not valid for ranges of strain rates.

Proposal:

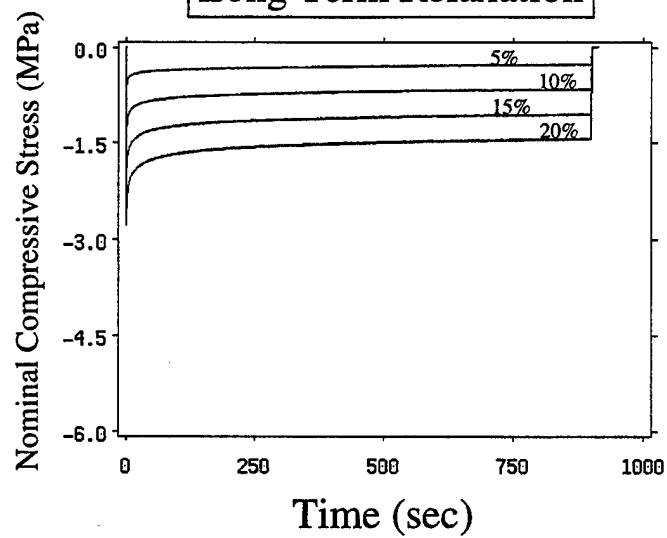
- Modify the above model by making $\eta = \eta$ (strain rate) and possibly $W_V = W_V$ (strain rate.)

Pill Shaped Coupons

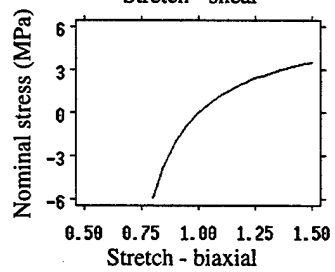
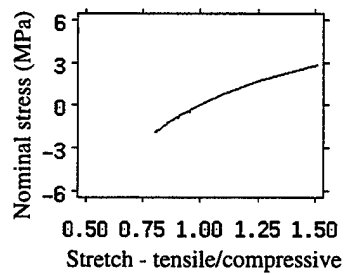
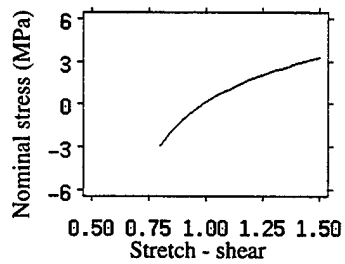


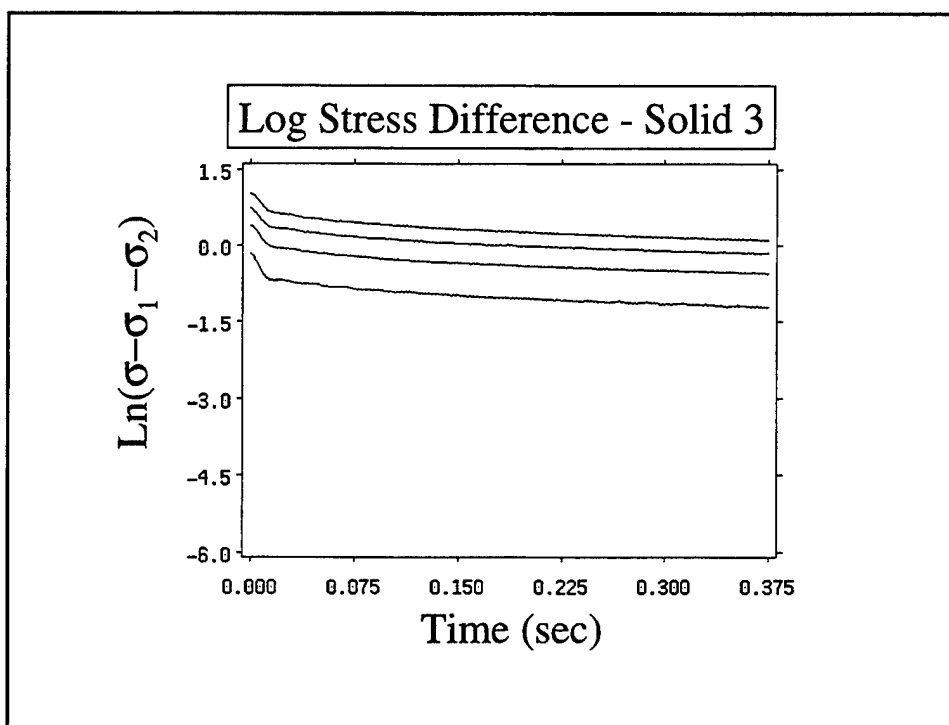
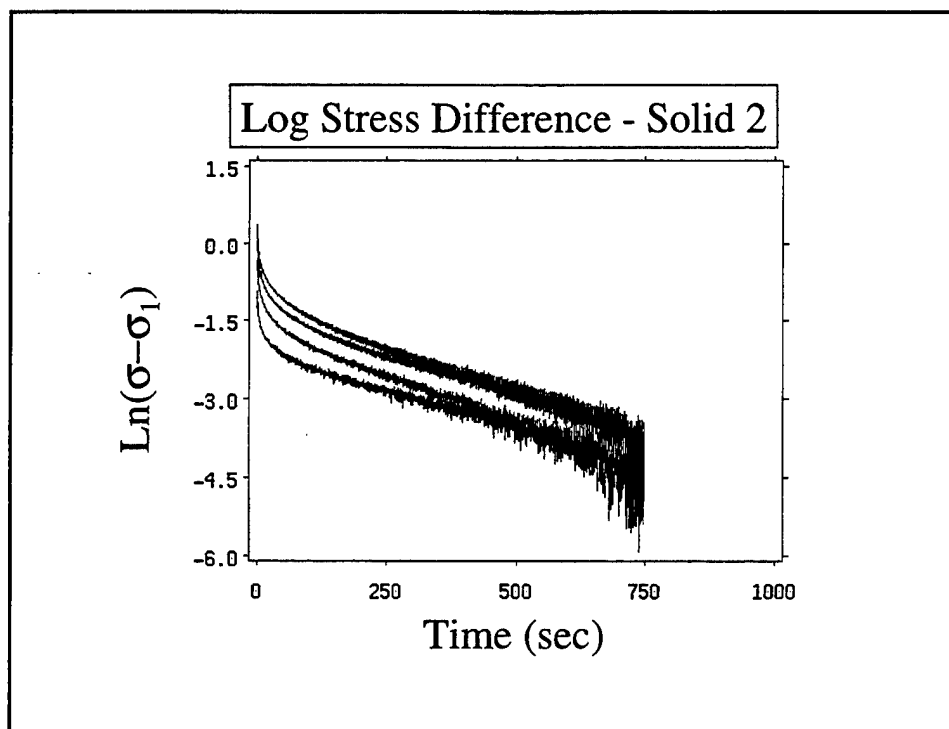
Conditioned 5 - 30 % at 0.5 Hz for 20 cycles.
Rest 15 min.

Long Term Relaxation



Tensile, pure shear, and biaxial stresses for solid 1





Energy Density Functions and Viscosity Constants

$$W_{Total} = W_1(X_1, x(t)) + \sum_{s=2}^5 W_s(X_s(t), x(t))$$

$$W_1 = 0.95928(I_1 - 3)$$

$$W_2 = 0.2177(I_{1,2} - 3)$$

$$W_3 = 1.0247(I_{1,3} - 3)$$

$$W_4 = 0.441(I_{1,4} - 3)$$

$$W_5 = 2.661(I_{1,5} - 3) + 17.23(I_{2,5} - 3)$$

$$\eta_1 = \infty \quad \leftarrow \text{Elastic Solid}$$

$$\eta_2 = 329.$$

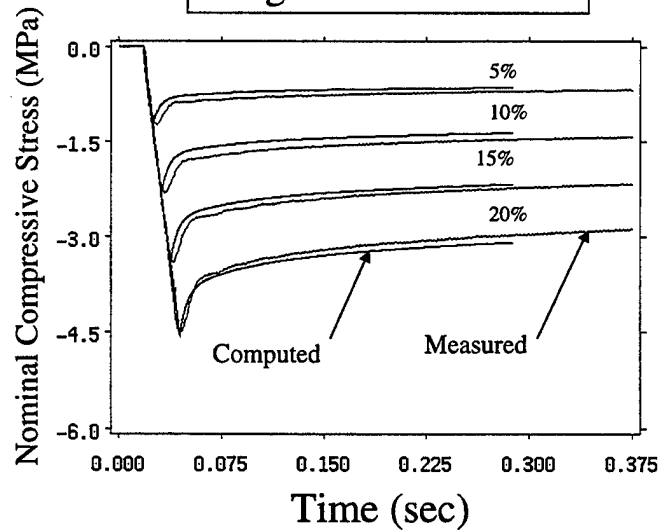
$$\eta_3 = 1.58$$

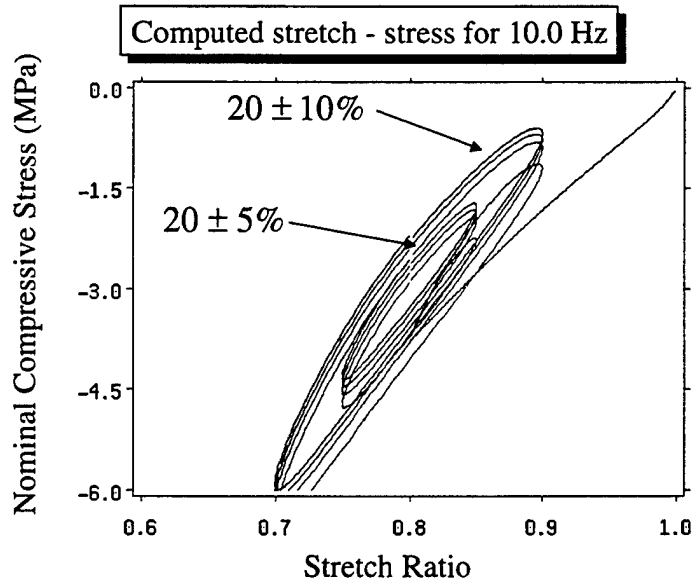
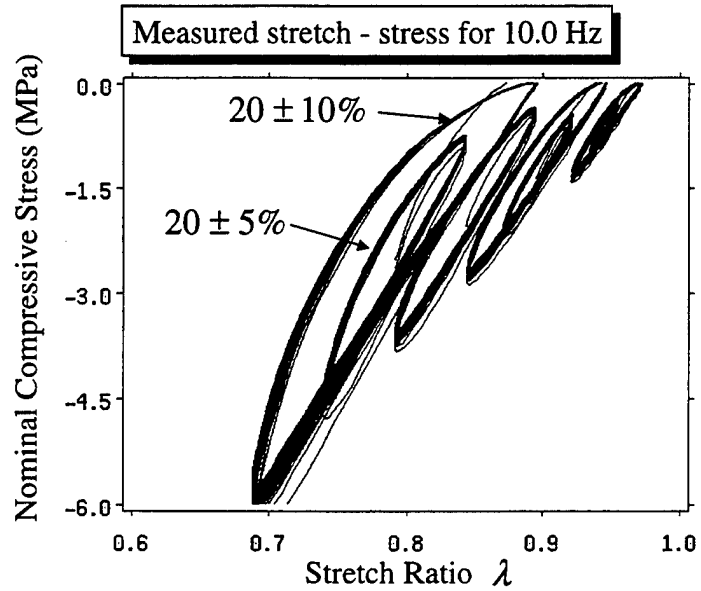
$$\eta_4 = 0.0562$$

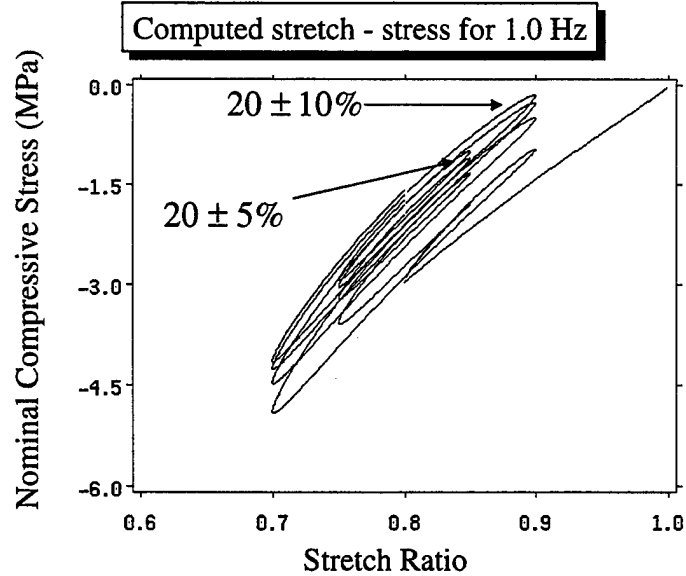
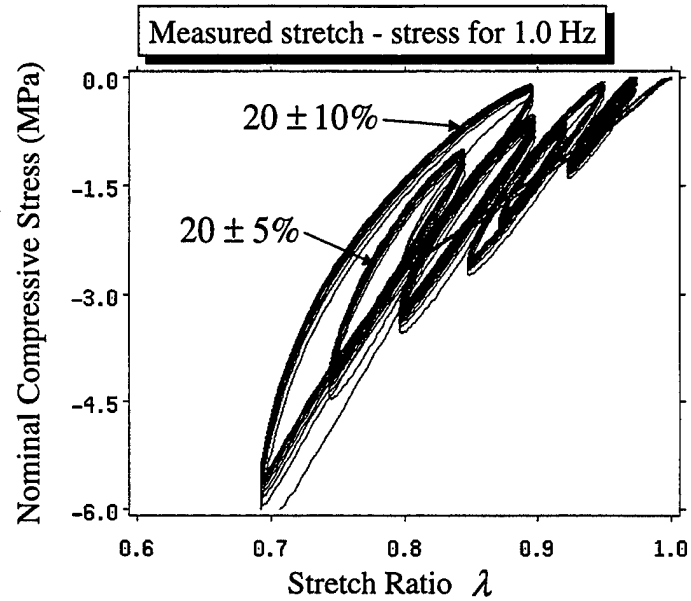
$$\eta_5 = 0.005$$

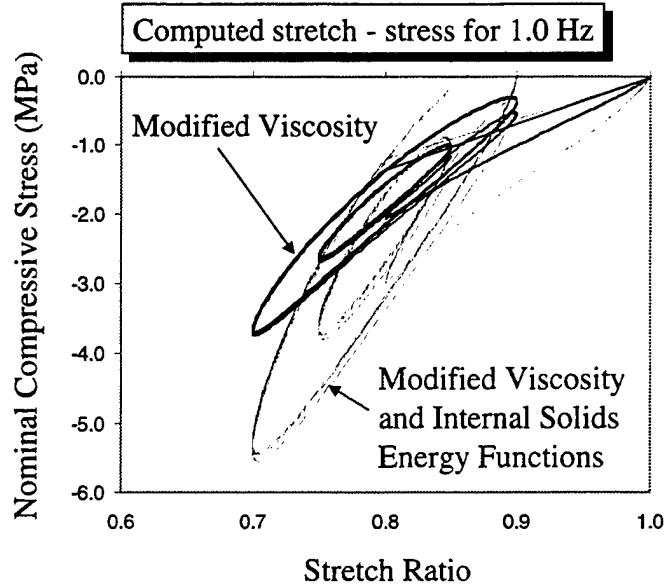
Internal Solids

Long Term Relaxation









Summary

- 1.) Test data for relaxation and dynamic compression of pill coupons were modeled using viscohyperelasticity.
- 2.) Numerical simulations indicated that **both** rate dependent viscosities **and** rate dependent energy functions (moduli in a Maxwell model) are needed for one model to be capable of simulating both relaxation and dynamics.

An Overview of Magnetostrictive Device Design and Performance

Alison Flatau, Marcelo Dapino
Iowa State University

F. Tad Calkins
The Boeing Company

David L. Hall	Rick Kellogg	Nick LaPointe
F. Tad Calkins	LeAnn Faidley	Brian Lund
Marcelo Dapino	Ralph Smith (NCSU)	

supported by the NSF Civil & Mechanical Systems Division, NASA Marshall, and NASA Langley

Fourth ARO Workshop on Smart Structures
8/18/99

Outline

- **Background on magnetostriction**
 - stress
 - applied magnetic field
 - (temperature)
- **Transducer design basics**
 - magnetic circuit, prestress, power supply
 - (composite devices)
- **General Performance Trends**
 - stress, bias fields, drive level, frequency blocked force rating
- **Applications**
 - sensors
 - actuators

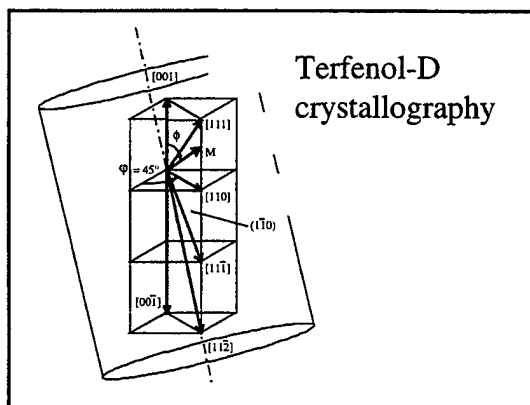
Magnetostriction

Nominal saturation strains of various ferromagnetic materials

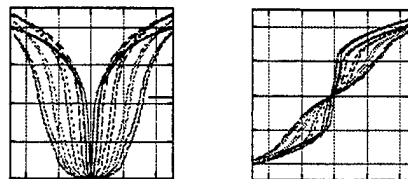
Material	Strain (ppm)
Iron	20
Nickel	-40
Alfenol 13	40
NiCo	186
Terfenol-D	2000

Terfenol-D Tb_xDy_{1-x}Fe_y

- Terfenol-D is a giant magnetostrictive material
 - *Ter*: terbium, *fe*: iron, *nol*: Naval Ordnance Laboratory, *D*: dysprosium
 - $0.27 < x < 0.3$, $1.90 < y < 2.0$
- 1960's Arthur Clark, NOL (NSWC)
 - quasi-static room temperature strains up to 2000 ppm
- 1980's Dale McMasters, Ames Laboratory
 - bulk manufacturing process

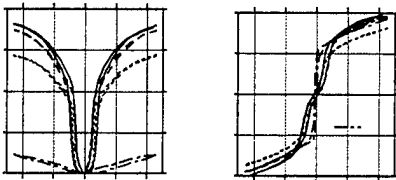


Magnetization/mechanical
prestress



Etrema Products Inc.

Temperature



Clark 1992

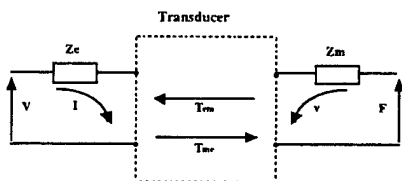
Magnetostrictive Transduction

$$\epsilon = \sigma / E_y + dH + \alpha \Delta T$$

$$B = d^* \sigma + \mu^* H = P \Delta T$$

Action	Effect
$\Delta H \rightarrow F, \epsilon$	Joule
$\Delta \sigma \rightarrow \Delta B, \Delta \mu$	Villari
$\Delta H \rightarrow T, \theta$	Wiedemann
$\Delta \tau \rightarrow \Delta B, \Delta \mu$	Matteucci

Electroacoustics model of transduction

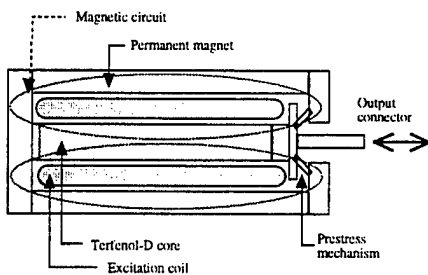


$$V = Z_e I + T_{em} v \quad F = T_{me} I + Z_m v$$

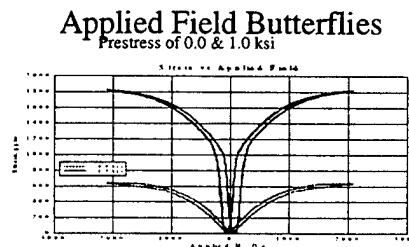
Transducer Design Features

- Magnetic Circuit
 - need for flux in material; eddy currents
- Prestress to maximize strain
 - nonlinear spring effects
- Accommodate brittle material
 - need to remain under compressive load at resonance!
- Coil design
 - inductance vs. high field per amp
- Power supply
 - voltage vs. current control; back emf

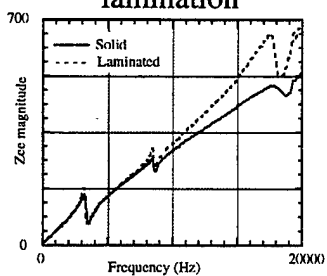
Terfenol-D Transducer



Effect of Prestress on Strain vs. Applied Field Butterflies



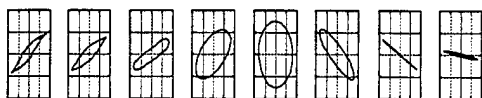
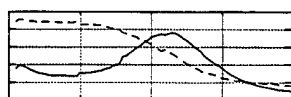
Effect of Terfenol-D core lamination



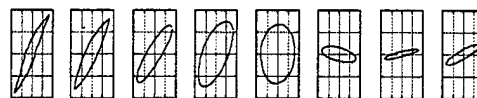
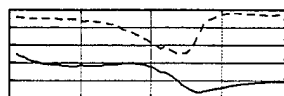
Effect of magnetic bias



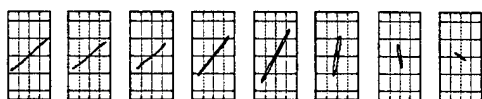
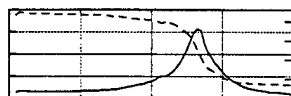
Frequency response function $\lambda-H$



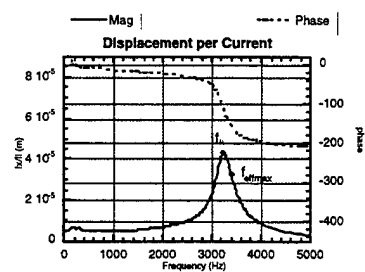
M-H



$\lambda-M$

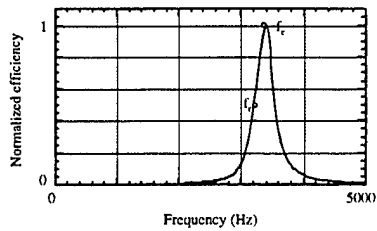


Mechanical resonance



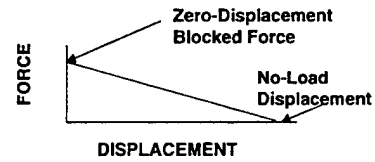
Electromechanical resonance

mechanical output/electrical input power



Blocked Force

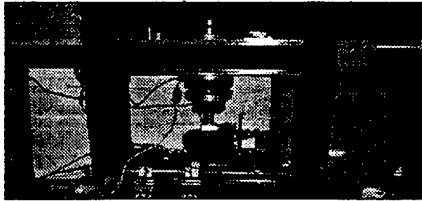
- DC Load Line



$$F_B \equiv AE\epsilon$$

- E in T-D is a function of stress,
- temp, & applied magnetic field.

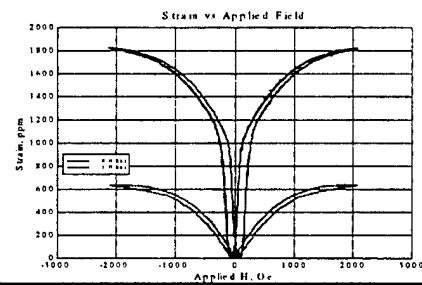
Computer Controlled Phoenix MTS System



- Techron 7780 Amplifier
- NI DAQ Board/LabView
- Continuous Data Acquisition- 50 Hz
- Displacement Rate - 15 mils/min

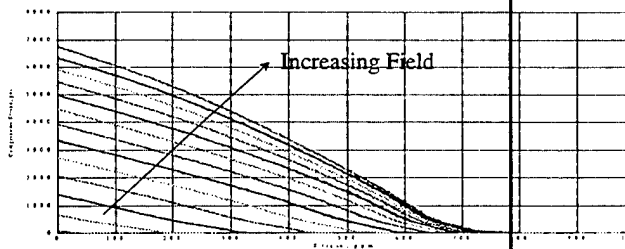
Strain-Field Butterflies

Prestress of 0.0 & 1.0 ksi

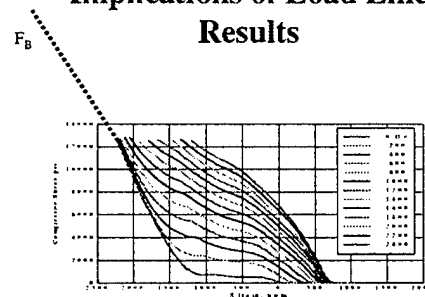


Load Lines 0.0 ksi Preload

Applied field H increasing 0-2400 Oe by 200

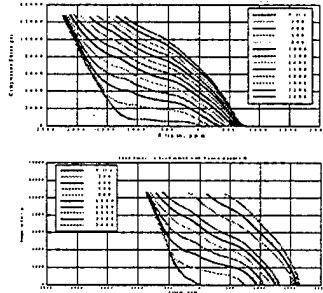


Implications of Load Line Results



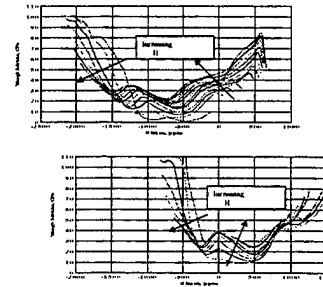
Load Lines 0.0 & 1.0 ksi Preloads

Applied field H increasing 0-2400 Oe by 200



Elastic Modulus 0.0 & 1.0 ksi Preload

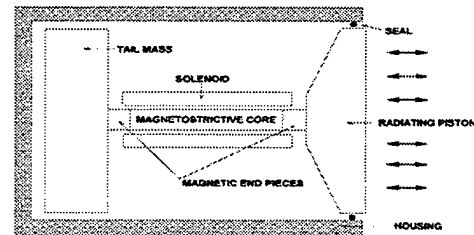
Applied field H increasing 0-2400 Oe by 200



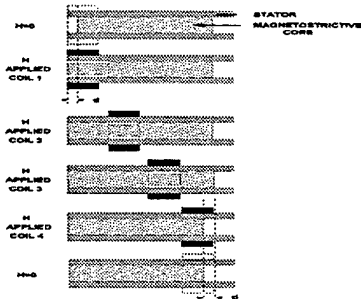
Actuation

- Linear motion (Joule effect)
 - sonar, vibration control, ultrasonics (cleaners and high power motors), tuned vibration absorbers, positioners, inch worm motors, ...
- Rotary motion (Wiedemann effect)
 - positioners, torque drivers, tuned vibration absorbers,

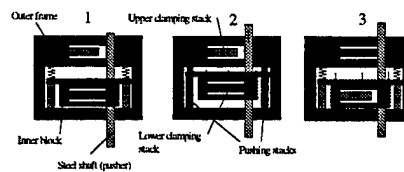
Tonpilz Transducers



Kiesewetter Inchworm Motor

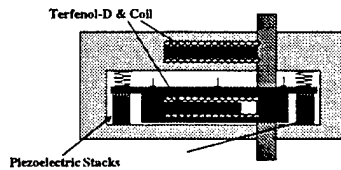


Inch-worm Linear Motor Design



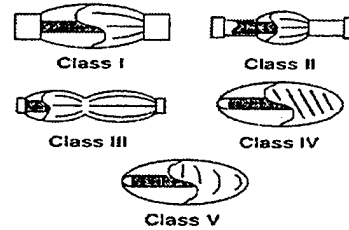
- Step 1: Moving clamp activates
 Step 2: Pushers move inner block forward
 Step 3: Stationary clamp activates and pushers return inner block to original position.

Hybrid motor

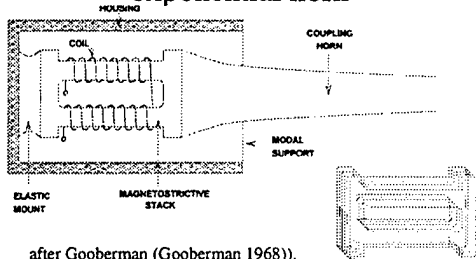


- Possibility: resonant RLC circuit
 - very little input energy needed.
 - C => piezoelectric
 - L => magnetostrictive

Brigham & Royster's Flextensional classifications



Ultrasonic motor with exponential horn

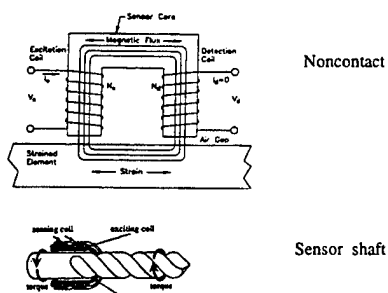


after Gooberman (Gooberman 1968)).

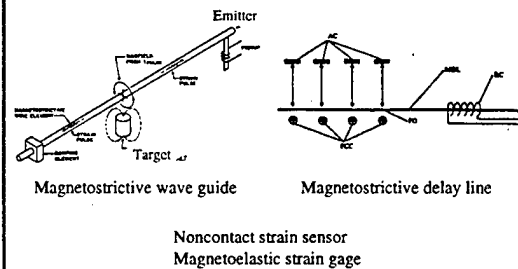
Sensors

- Active and Passive
 - health monitoring
 - displacement/rotation
 - force/torque
 - magnetization
 - crack/corrosion detection
 - ...

Torque sensor

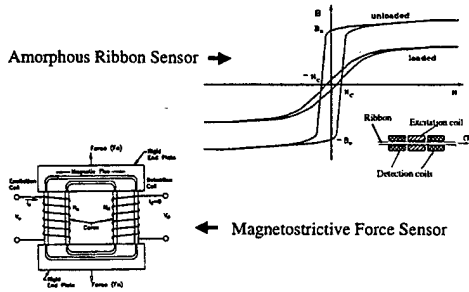


Motion and position sensors



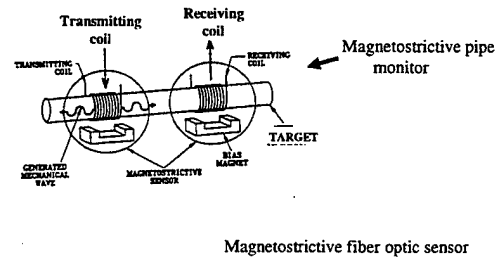
Force and stress sensors

Amorphous Ribbon Sensor →



← Magnetostrictive Force Sensor

Material characterization sensor



Magnetic field sensor

Terfenol-D magnetometer
Magnetostrictive fiber optic sensor

Magnetic field sensor

Hearing aids
magnetoelastic delay line digitizer
magnetoacoustic keyboard
thermometer
magnetic tagging for composite monitoring

Future directions for advances in magnetostrictive applications?

- Composites
- low cost materials
- low hysteresis materials
- magneto-shape memory alloys

Actuator Power Reduction Using a Tuned L-C Oscillator Circuit

Jayant Sirohi* and Inderjit Chopra†

Alfred Gessow Rotorcraft Center,
Department of Aerospace Engineering,
University of Maryland, College Park, MD 20742

ABSTRACT

Piezoelectric actuators are widely used in smart structural systems to actively control noise and vibration and improve performance. Due to the highly capacitive nature of these actuators, the power factor of the driving circuit is close to zero. The efficiency can be improved by making the power factor as close to unity as possible, which can be achieved by adding an inductance in the circuit, either in series or in parallel with the capacitance. In the case of the parallel configuration, at the resonant frequency, the impedance of the circuit goes to infinity and the net current drawn from the power supply is zero. The parallel L-C oscillator concept is therefore investigated further in an attempt to minimize the absolute value of current drawn from the supply.

Power reduction techniques by means of power factor correction¹ have been explored in the past. This work presents a detailed analysis of the power factor correction technique by means of a tuned L-C oscillator circuit. Non-ideal circuit performance is addressed, along with theoretical limits to possible power savings, and practical difficulties in achieving them. In addition, a novel use of an active pseudo-inductor to simulate the inductance in the oscillator circuit is investigated.

The values of capacitance in the range of interest vary from $\approx 0.1\mu F$, which is a typical value for piezoceramic sheet actuators, to $\approx 7\mu F$, which represents a typical stack actuator. The range of operating frequencies of interest is 1-100 Hz, which corresponds to the application of the stack in a smart trailing edge flap system.² The required value of the inductance to achieve resonance increases rapidly in the operating region of interest, and are difficult to implement in practice.

This problem can be circumvented by using an pseudo-inductor constructed with an operational amplifier. Energy is no longer stored in a magnetic field, but as a charge on a capacitor in the pseudo-inductor circuit.³⁻⁵ Two circuits were investigated for this purpose. The desired characteristics of such a pseudo-inductor circuit include low complexity, ease of tuning and ability to operate in an AC coupled mode, since stack actuators are normally operated under unipolar excitation. The circuit with the best characteristics will be chosen and incorporated along with a commercially available linear power supply to achieve a compact, low power actuator drive circuit. This drive circuit will be tested on smart rotor actuators currently under development, in benchtop tests and on a hoverstand, with a view to reducing the current passed through the slipring to the rotating system.

REFERENCES

1. Niezrecki, C. and Cudney, H.H., "Power Factor Correction Methods Applied to Piezoelectric Actuators", AIAA-93-1688-CP, Proceedings of the 34th AIAA/ASME/ASCE/AHS/ASC Structures, Structural Dynamics and Materials Conference, pp. 3261-3268, April 1993.
2. Lee, T., and Chopra, I., "Design and static testing of a trailing edge flap actuator with piezostacks for a rotor blade", Proceedings of the SPIE Smart Structures and Materials, Vol. 3329, pp.321-332, March 1998.
3. Berndt, D.F., and Dutta Roy, S.C., "Inductor Simulation using a Single Unity Gain Amplifier", IEEE Journal of Solid State Circuits, Vol. SC-4, , pp.161-162, June 1969.
4. Dutta Roy, S.C., and Nagarajan, V., "On Inductor Simulation using a Unity Gain Amplifier", IEEE Journal of Solid State Circuits, Vol. SC-5, No. 3, pp.95-98, June 1970.
5. Prescott, A.J., "Loss compensated active gyrator using differential-input operational amplifiers", Electronic Letters, vol. 2, pp. 283-284, July 1966.

* Graduate Research Assistant

† Alfred Gessow Professor and Director



ACTUATOR POWER REDUCTION USING A TUNED L-C OSCILLATOR CIRCUIT

Jayant Sirohi
Graduate Research Assistant

Inderjit Chopra
Professor and Director

Alfred Gessow Rotorcraft Center,
Department of Aerospace Engineering,
University of Maryland at College Park

4th ARO Workshop on Smart Structures, 16 - 18 August 1999



Outline



- ➡ Introduction
 - Piezoelectric actuation
 - Constitutive relations
- ➡ Power Consumption
 - Theoretical relations
 - Impedance method
 - Prediction of current drawn
- ➡ Power reduction
 - Concept of LCR oscillator circuits
 - Pseudo-inductance
 - Circuit construction
- ➡ Results
- ➡ Conclusions

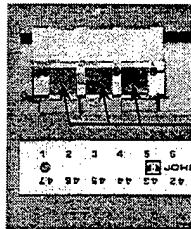


Introduction

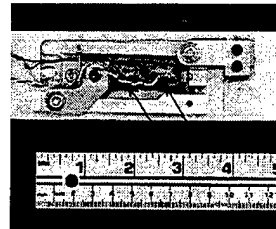


PZT(lead zirconate titanate) actuators are widely used in the development of smart rotors and other systems

T.E. FLAP ACTUATION



Multi-layered
piezoceramic
bender actuators



Piezoceramic
stack
actuators

It is necessary to accurately characterize and predict the response of piezoceramic actuators in order to develop efficient systems



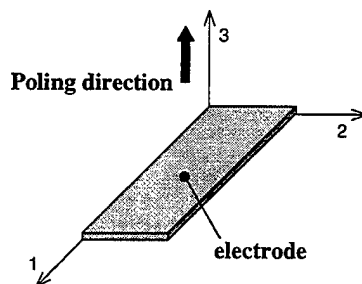
Constitutive relations



Under small signal conditions,

$$D_i = e_{ij}^T E_j + d_{im}^d \sigma_m \quad \text{Sensor}$$

$$\epsilon_k = d_{jk}^c E_j + s_{km}^E \sigma_m \quad \text{Actuator}$$



PZT-5H 2"x1"x0.01"

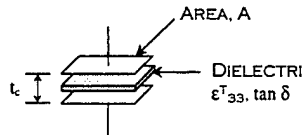
D: electric displacement (Coulombs/m²)
e: dielectric permittivity (Farads/m)
 σ : stress (N/m²)
 ϵ : strain
d: piezoelectric coefficients (m/V)
E: electric field (V/m)
s: elastic compliance (m²/N)



Power Consumption



For an ideal parallel plate capacitor, the capacitance C is given by:



$$\text{Impedance } Z = \frac{1}{j\omega C} = \frac{t_c}{j\omega \epsilon A}$$

A free PZT sheet is treated as a lossy capacitor (complex permittivity)

$$Z_{\text{freePZT}} = \frac{t_c}{j\omega \epsilon_{33}^T (1 - j \tan \delta) A}$$

ϵ_{33}^T : dielectric permittivity
 $\tan \delta$: dissipation factor



Power Prediction



Power consumption by a pair of actuators surface bonded onto a beam is predicted using the Impedance method (Rogers et. al., 1993)

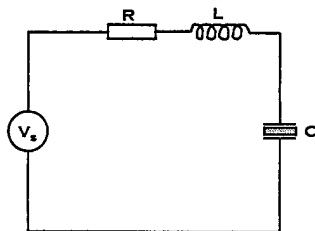
Current consumed is given by:

$$I = j\omega E w_c l_c \left(\frac{d_{31}^2 \bar{Y}_{11}^E Z_A \tan(kl_c)}{(Z_A + Z) kl_c} + \bar{\epsilon}_{33}^T - d_{31}^2 \bar{Y}_{11}^E \right)$$

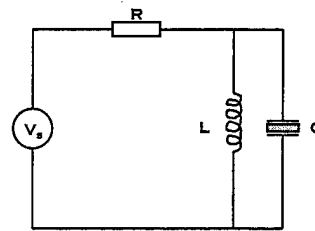
the empirical variation of ϵ_{33}^T and $\tan \delta$ is also incorporated.



Ideal LCR Circuits



SERIES



PARALLEL

AT RESONANT FREQUENCY

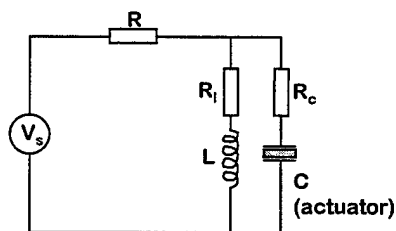
$$\omega_{oIDEAL} = \frac{1}{\sqrt{LC}}$$

Reactance $\rightarrow 0$
Current Drawn $\rightarrow V_s/R$

Reactance $\rightarrow \infty$
Current Drawn $\rightarrow 0$



Parallel LCR Circuit



Non-ideal components:

$$\bullet Z_C = \frac{\tan \delta}{\omega C} + \frac{1}{j\omega C}$$

$$\bullet Z_L = R_L + j\omega L$$

$$Z_{TOT} = R + Z_P$$

Resonant Frequency is the frequency at which the total reactance becomes zero

$$\omega_o = \omega_o \text{ Ideal only if } R_C = R_L$$



Parallel LCR circuit



$$Z_{P(REAL)} \approx \frac{L}{2R_L C} + \frac{R_L}{2}$$

For a large value of Z_p ,

- Need a large L/C ratio
- Small R_i

Consider the case of a stack actuator:

$$C_{act} = 7 \mu F$$

For a resonant frequency of 15 Hz,

$$L_{req} = 16 H$$

Such a large value of inductance is difficult to realize in practice, especially with a sufficiently small value of R_i



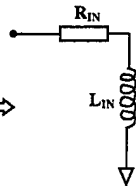
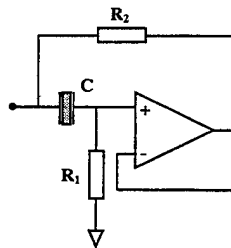
Pseudo-inductance



- Constructed using an active element, namely an op-amp
- High values of inductance can be easily achieved
- R_i values are comparatively small
- Energy is stored in a capacitor rather than in a magnetic field
- Pseudo-inductances have been investigated before for
 - » Integrated Circuit applications
 - » Semi-passive damping

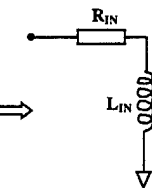
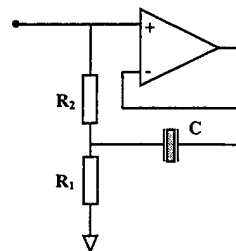


Pseudo-inductance



Circuit A

$$L_{IN} = C R_1 R_2$$



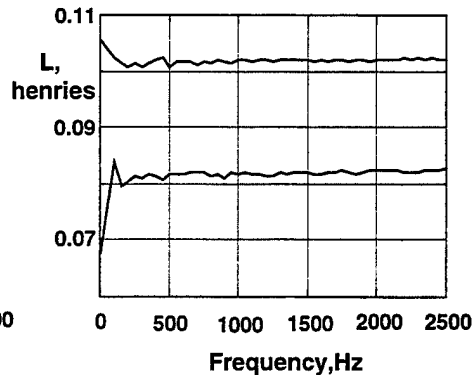
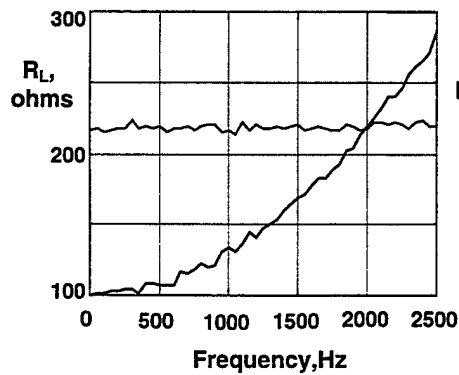
Circuit B



Pseudo-inductance



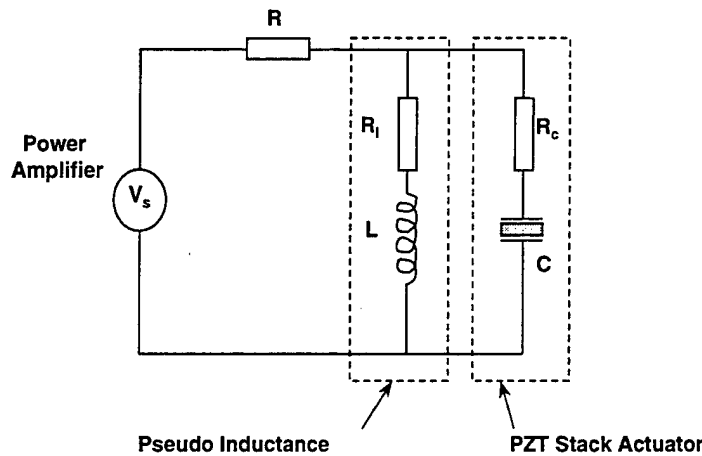
Comparison of pseudo-inductance and choke coil



— Choke coil
- - - Pseudo-inductance



Experimental Setup



Prototype Circuit A



Circuit built with a high power PA-88 op amp $V_{EX}=50V$

Freq. Hz	I_{ACT} (mA)	I_{ACT} (mA)	I_{IND} (mA)	Actuator Power, Watts ($V_{pk} * I_{pk}$)		% actuator power reduction	% total power reduction
	(w/o ind.)	(with ind.)		(w/o ind.)	(with ind.)		
5	5.88	0.28	0.70	0.21	0.01	95.24	71.85
7	8.26	4.68	0.24	0.3	0.17	43.33	37.63
10	11.90	9.24	0.07	0.43	0.33	23.26	21.20
15	17.80	16.12	0.02	0.64	0.58	9.38	9.22
25	28.97	27.98	0.01	1.04	1.01	2.88	2.42

- Reduction in net power consumption by 70%
- Directly translates into a power supply weight saving
- Total power consumption can be improved at different frequencies by tuning the pseudo-inductance circuit

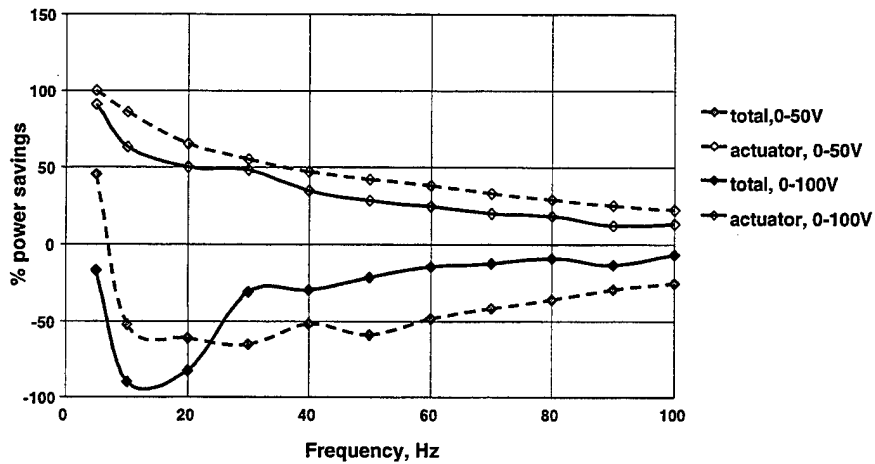


Effect of actuation voltage

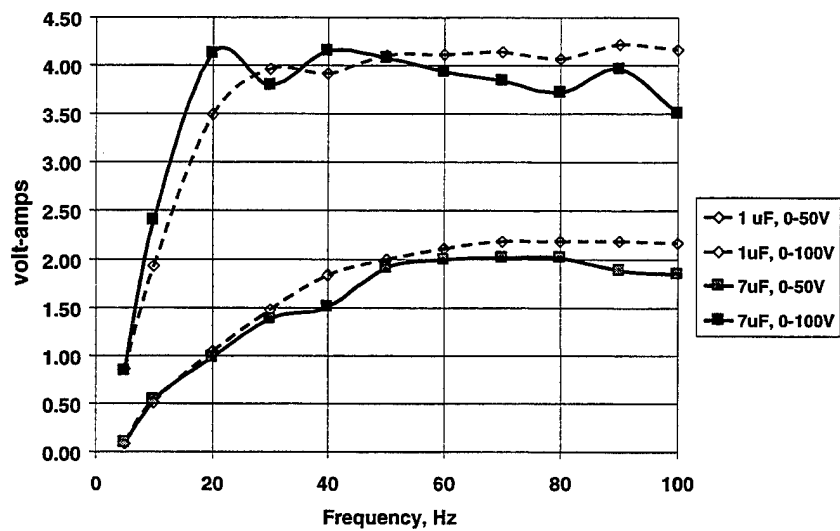


C=7uF

Circuit A, continuously tuned



Pseudo inductor power





Conclusions



- Power consumption can be predicted using the impedance method, taking into account the variation of properties with field. Accuracy goes down at higher frequencies and field strengths.
- Power consumption from the supply can be decreased using power factor correction methods.
- Pseudo-inductances with desirable properties can be synthesised for use in such resonant circuits.
- Higher power pseudo-inductances need to be built in order to drive the actuators at sufficient excitation levels.

Controlling Power Flow Through Electronically Integrated Smart Devices

Douglas K. Lindner, Sriram Chandrasarkaren, and Jeffrey Scruggs

Bradley Department of Electrical and Computer Engineering

Virginia Tech

Blacksburg, VA 24061

(540) 231-4580

lindner@vt.edu

Fourth ARO Workshop on Smart Structures

Penn State, University Park Campus, PA

August 16 -18, 1999

In this talk we consider smart materials as actuators driven by switching amplifiers. The amplifier is an electronic device which connects the electrical power bus to the actuator (piezoelectric, say). Therefore, we adopt the view that the amplifier is really an energy switch the conditions the raw electrical power, and delivers it to the actuator in response to a command signal. The switching amplifier also supports reverse power flow. By configuring the control loops around the device in the appropriate way, the power flow through the smart device can be controlled [1]. In the proper configuration, the smart device can draw power from the disturbance source and direct it to the electrical energy storage device. This type of operation could be advantageous in situations where electrical energy is in limited supply because the amount of electrical energy needed to drive the actuator is minimized.

In this talk we will discuss the effect of the control loops on the power flow through the smart device. These results are similar to recent result on controlling the power flow through proof-mass actuators [2]. The effects of the internal amplifier control loops are studied along with the outer structural control loops. The nonlinearities of the actuation material are taken into account.

1. Zvonar, G. A. and D. K. Lindner, "Power Flow Analysis of Electrostrictive Actuators Driven by Switchmode Amplifiers," *Journal on Intelligent Material Systems and Structures*, special issue on the 3rd Annual ARO Workshop on Smart Structures, Vol. 9, No 3, March, 1998, pp. 210 - 222.

2. Lindner, D. K. and S. Chandrasekaran, "Control of Regenerative Power From Piezoelectric Actuators," accepted for the Adaptive Structures Forum at the AIAA/ASME/ASCE/AHS/ASC 40th Structures, Structural Dynamics, and Materials Conference, St. Louis, CA, April 12 - 15, 1999.



Renewable Fuel Cell Power Sources for Active Structures

Donald J. Leo

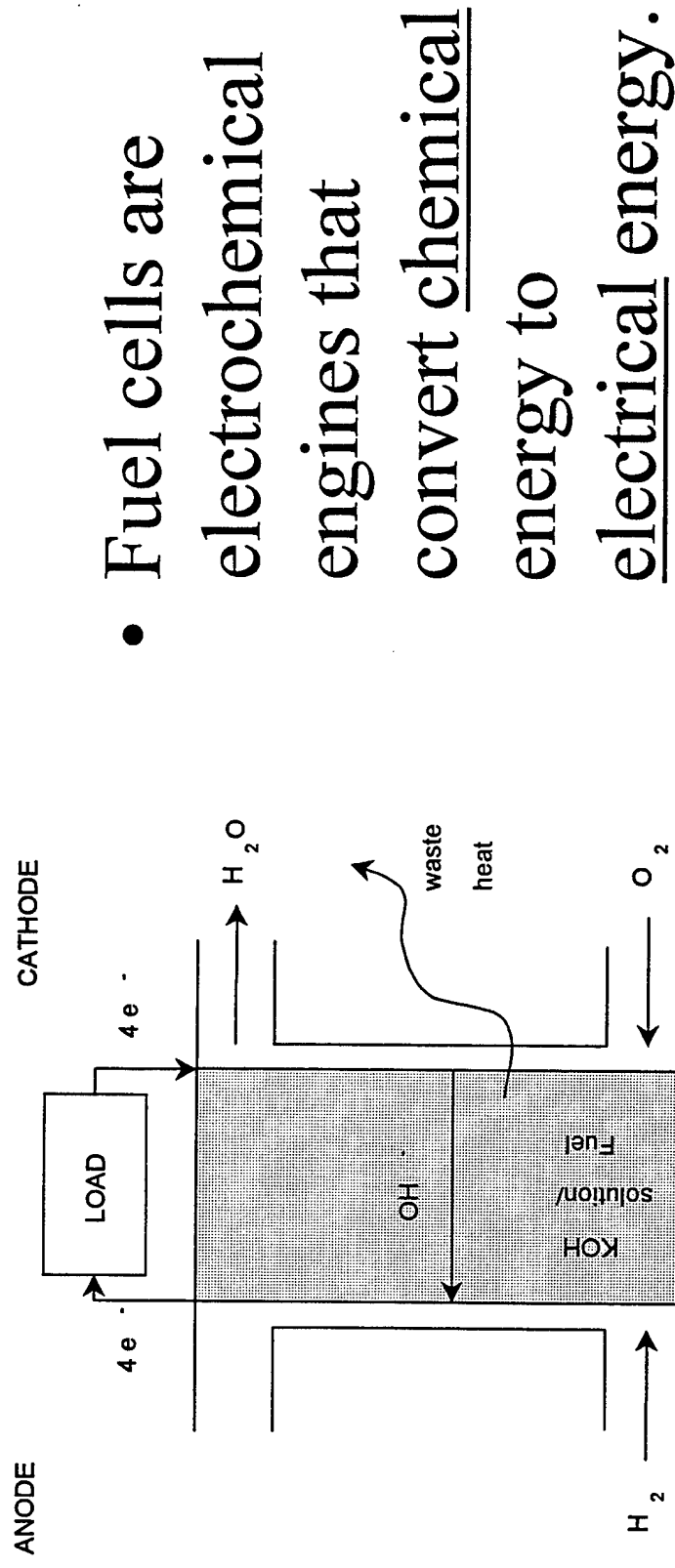
CIMSS - Mechanical Engineering Department
Virginia Tech
Blacksburg, VA

Fourth ARO Workshop on Smart Structures
The Pennsylvania State University
State College, PA
August 15-18, 1999

Objective

- Investigate the use of fuel cells as power sources for active structures
 - Motivation
 - System Issues
 - Efficient Actuation

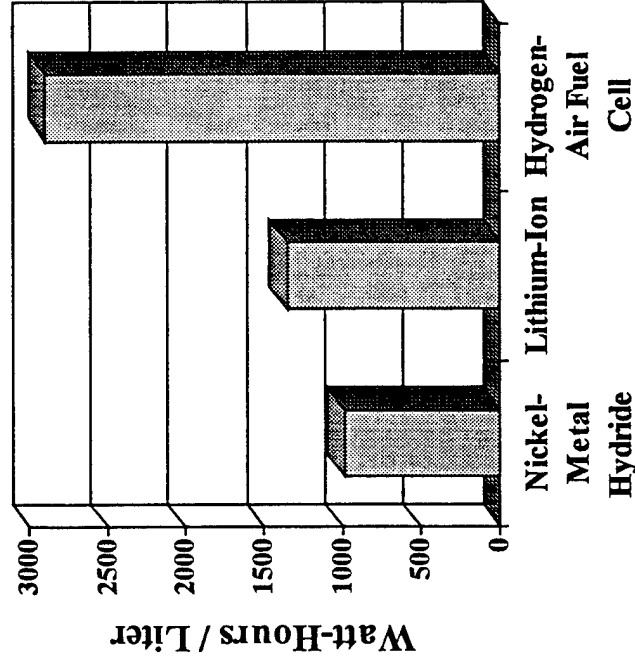
Fuel Cells



- Fuel cells are electrochemical engines that convert chemical energy to electrical energy.

Fuel Cells versus Batteries

Maximum energy density for two common secondary cells and a hydrogen-air fuel cell

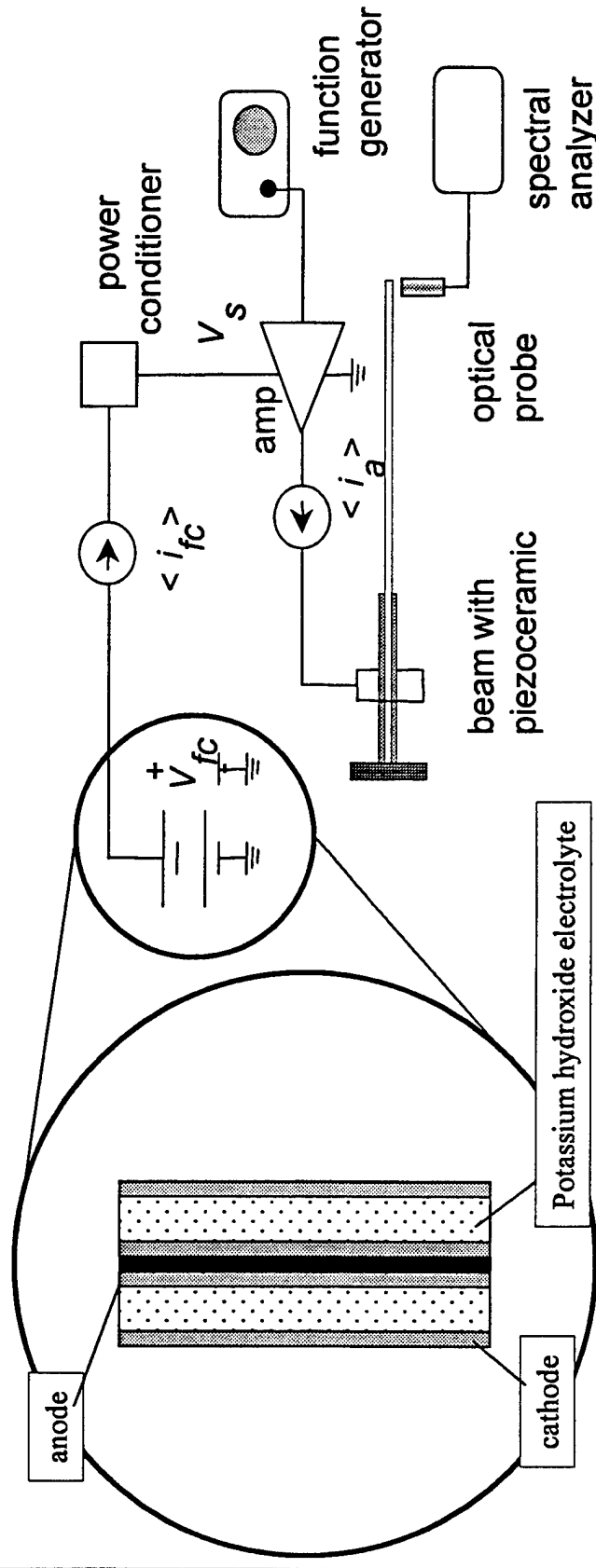


- Advantages
 - Higher *maximum achievable* energy density
 - Instantly ‘recharged’ with the addition of fuel
- Disadvantages
 - Lower *achievable* energy density due to lower *packaging efficiency*.
 - Will work on any fuel as long as it is hydrogen.

Why Fuel Cells?

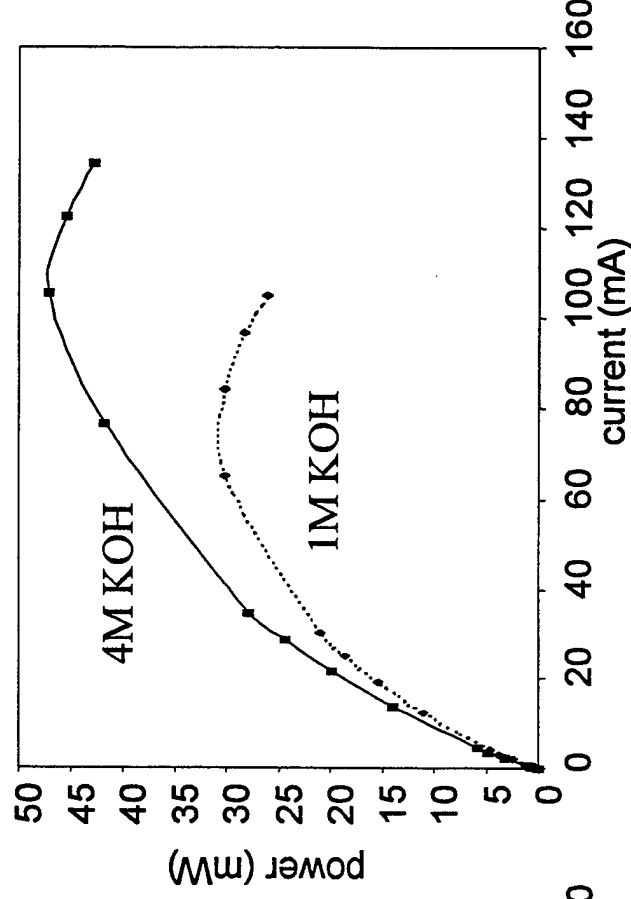
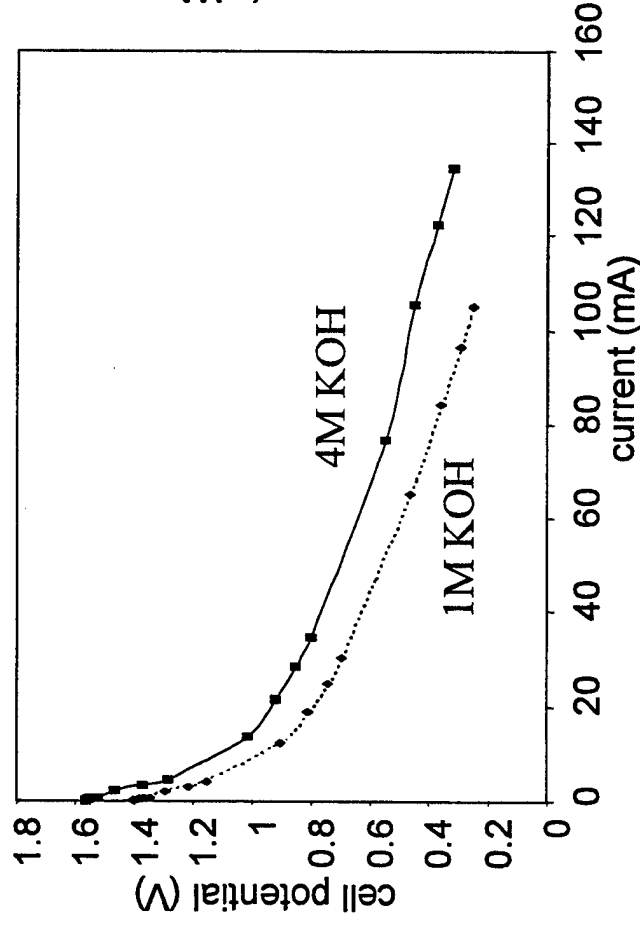
- Miniature fuel cells are being developed by several sources (100 mW - 10 W)
 - Cellular phone and pager applications
- Fuel cells represent a renewable source of power that does not require recharging
 - Autonomous systems
- It might be possible to achieve a high level of structural / power integration

Preliminary Experiments



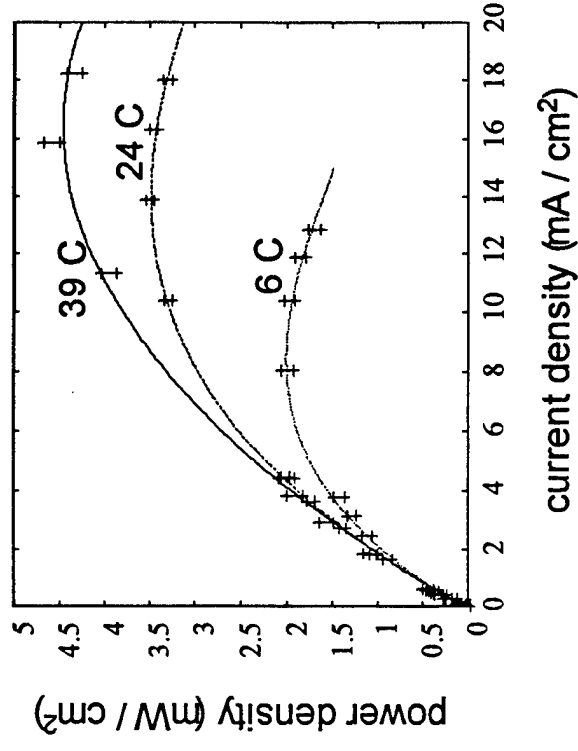
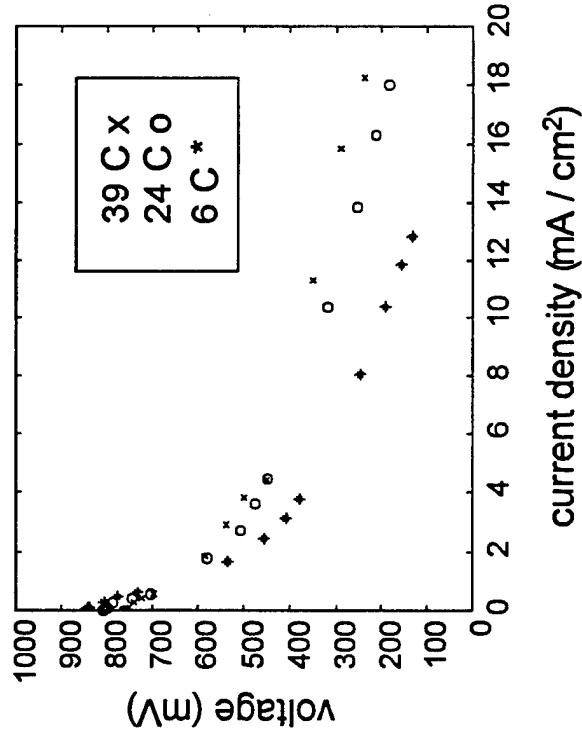
- The objective of the initial experiment was to power a piezoceramic bimorph with an alkaline fuel cell and investigate the parameters affecting fuel cell performance.

Polarization Curves and Power Output



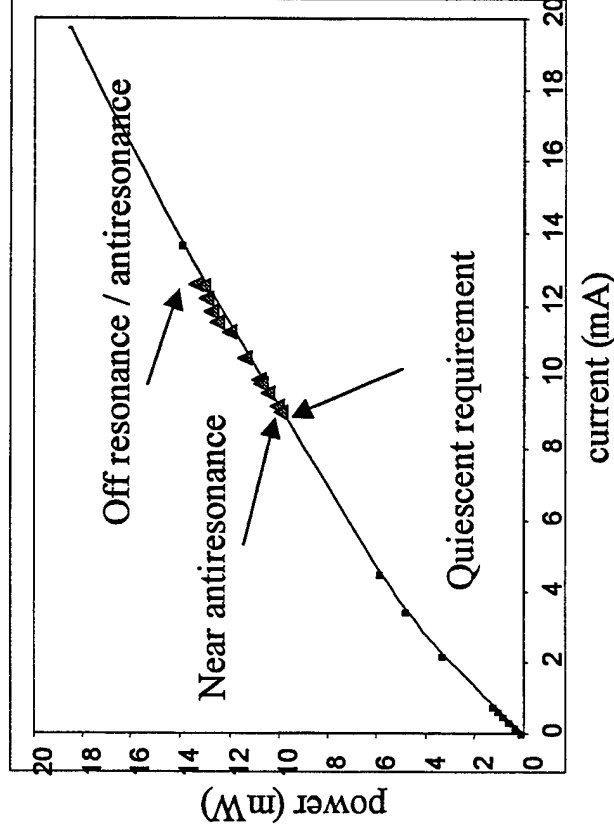
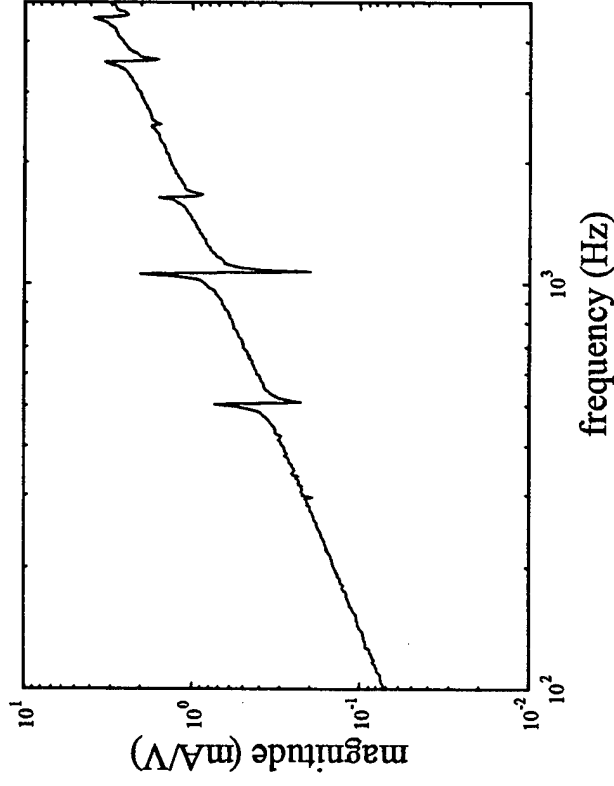
- Increasing the molarity of the electrolyte increases the power output and increases the maximum current output of the cell.

Temperature Effects



- Increasing temperature increases the power output of the cell.

Efficient Actuation



- Electromechanical coupling can be exploited to reduce the energy requirements of the cell (4 times reduction in power).
- Current fuel cell and power conditioner is not matched properly to the actuator.

Summary

- Fuel cells are DC power sources that can be renewed with the addition of fuel.
- Systems issues include
 - air flow control
 - temperature control
 - compact design for minimum weight and volume
- Future experiments will focus on matching the fuel cell power output to the active structure.

Micro-Scale Electrohydrodynamic Pumped High Performance Actuation

Reza Kashani¹ Kevin Hallinan

Mechanical & Aerospace Dept.

The University of Dayton

The success of most active noise/vibration control solutions depends on the performance of the actuator driving those systems. This is especially true when the noise control solution is intended for a real-life structure/machine (not a laboratory scale device). The most elegant active noise/vibration control strategy, which works wonderfully in simulation, might not perform satisfactorily in practice because the actuators are saturated and/or do not have enough agility (bandwidth).

Performance, in terms of high force, displacement, and bandwidth, has always been the primary objective of actuator builders and users alike. Numerous research activities have been conducted in recent years to exploit smart materials as the actuator drive mechanism. However, all existing smart material actuators lack at least one of the above-mentioned attributes. For example, piezoelectric and magnetostrictive actuators have high bandwidth and adequate force but not high displacement. The current state of the art for block force and free displacement is on the order of 100s of Newtons and 10s of micrometers. The actuator package required to provide such features, not to mention more effective features, is rather large and heavy. Moreover, *such actuators are restricted for use in low-temperature applications only.*

A new type of actuation device has been conceptualized that meets the needs of both large displacement, force and bandwidth within a package more compact than currently available magnetostrictive and stack-type piezo actuators of similar rating. This concept relies on micro-scale electrohydrodynamic (EHD) pumping of a dielectric liquid with a small concentration of free charges. Configured as an actuator, the EHD pump(s) would be used to move fluid between two reservoirs—each having a compliant membrane that interfaces to the world to provide the means to achieve vibration cancellation or microactuation.

Ordinarily limited to generating flow in macro-scale applications, the EHD pump is shown to exhibit an attractive scaling benefit as its size is reduced. Heuristically, the scaling benefit is derived from the fact that in an EHD pump a time averaged electrohydrodynamic force is induced when travelling electric fields are imposed within the fluid. These forces are maximum near the fluid-structure interface. In steady-state, the energy added to the fluid by these electro-hydrodynamic forces can be dissipated viscously or can be used to increase the potential energy (pressure) of the fluid—where the latter acts over the volume of fluid in the pump. *As the pump volume to surface area decreases, the energy going toward increasing pressure in the pump has an increasingly larger effect.* Since

¹ The corresponding author. Address: Mechanical and Aerospace Dept.; The University of Dayton; 300 College Park; Dayton, OH 45469-0210. Email: rkashani@engr.udayton.edu

volume/surface area is inversely proportional to the characteristic width or diameter of the pump, the pressure head generated scales similarly. Analytical and numerical studies have shown the EHD-pumped actuator to be capable of delivering equal force and bandwidth to magnetostrictive and stack-type piezo actuators, but with considerably greater displacement and roughly $1/10^{\text{th}}$ of the size. This type of actuator offers the possibility for deployment in active vibration control or microactuation applications. Moreover, compared to smart material transducers, it is tolerant of significantly greater temperatures.

Electrohydrodynamic Pumping Background

EHD pumping is made possible by the generation of electrohydrodynamic forces within a dielectric fluid with a small concentration of free charges due to the application of electrostatic fields. There has been significant progress in the development of both thermally induced and ion drag EHD pumps. But outside of the work by a handful of research groups, the work has focused on macroscopically large sizes. They showed that generating head was possible for a micro-sized EHD pump but were far from pushing the envelope of possibility for generating head with their micro EHD pump system. None have considered taking advantage of this head generation for the purpose of actuation.

EHD Pumped Actuator

An electrohydrodynamically pumped actuator concept has been established to provide similar force and bandwidth to the smart material²-driven actuators, but which can be designed to provide significantly larger displacement in a smaller package. This actuator relies upon the use of an electrohydrodynamically driven pump array to provide force in a controlled manner.

Figure 1 shows a possible configuration of the new actuator concept. In this design, two liquid reservoirs, which are separated by a compliant membrane, are connected by an array of electrohydrodynamically driven micro-pumps. In operation, when the actuator experiences a disturbance force, an electric field is advanced against the direction of the flow caused by the disturbance to provide a reactive force. As the direction of the applied load changes, the direction of the advancing electric field within the pump is likewise reversed.

Central to the operation of the actuator is the array of mesoscale electrohydrodynamic (EHD) pumps. These pumps can be configured in a combination of series (to provide high pressure leading to high force) and parallel

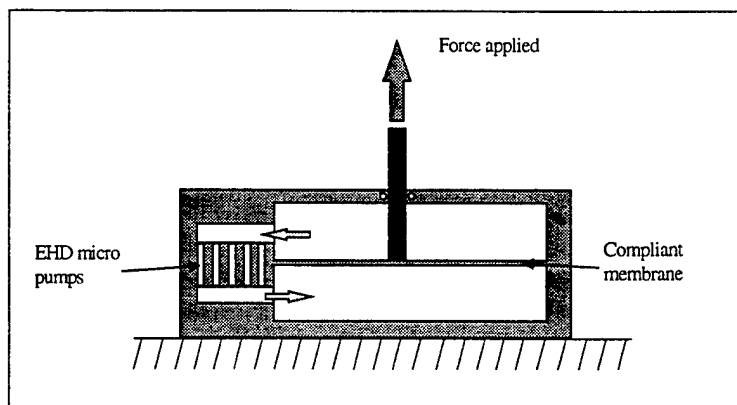


Figure 1 Schematic of a design for the new actuator concept

² Piezoelectric and magnetostrictive material

(to provide high flow leading to high displacement) arrangements to achieve the desired force response and displacement capabilities. Depending on the application, a combination of series and parallel stacks can be used to achieve the desired actuation specifications.

Benefits of the New Actuator Concept

There are three primary benefits of the new actuator concept:

1. Increased displacement potential

In contrast to smart material-driven devices, the displacement that can be tolerated by the EHD actuator is limited only by the size of the reservoir shown in Figure 1.

Therefore, displacements of greater than several millimeters are feasible, limited only by the compliance of the membranes containing the liquid in the two reservoirs.

2. Significant force generation

This benefit is a consequence of the scaling and practical benefits associated with the miniaturization of EHD pumping. As in the MEMS (Micro Electro-Mechanical Systems) area, a number of applications have led to tremendous scaling benefits at micro sizes, particularly when the physics is influenced by the ratio of the surface area to volume. Decreasing size increases this ratio.

3. High bandwidth

The nearly instantaneous nature of the electrohydrodynamic forces acting on the fluid, containing free charges, and the small mass of the fluid in a single channel make this actuation mechanism highly agile. A parametric study of a thermal induction EHD pumped actuator has been conducted to determine the effects of: 1) electric field intensity, 2) aspect ratio, 3) pressure drop and 4) radius, on the performance (in terms of responsiveness) of EHD pumping. In this study, a disturbance force acts on the actuator made of a single EHD pump. This in turn imposes a disturbance pressure on the fluid causing it to flow. After the flow becomes fully developed, the electric shear stress is applied on the surface of the channel of the pump to arrest the flow. The time it takes to stop the bulk flow near the entrance region is determined. This time is called "time to zero flow" and is an indication of the agility of actuator. The shorter the time to fully arrested the flow, the faster (higher bandwidth) the actuator.

Response times of about 10 microseconds were observed.

Accomplished Work

Computational simulations of the micro-scale EHD actuator concept have been conducted. The model effectively solves the Navier-Stokes equations, modified to include time-averaged electrohydrodynamic

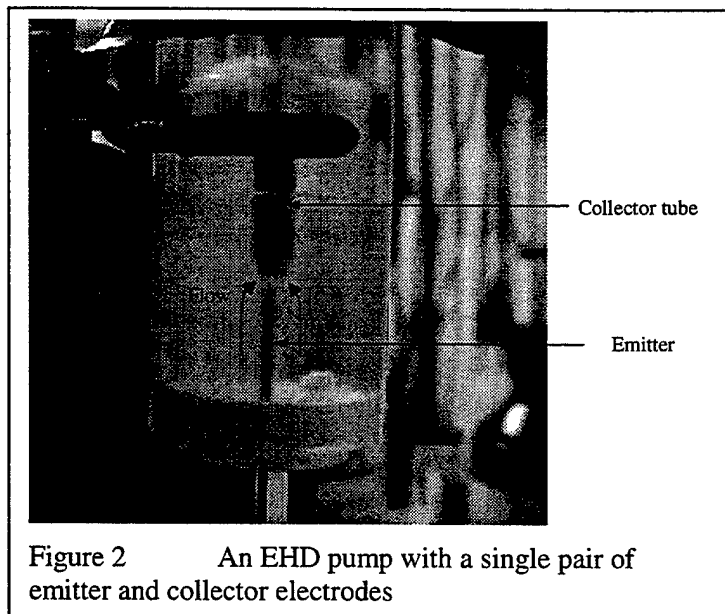


Figure 2 An EHD pump with a single pair of emitter and collector electrodes

stresses induced in the fluid as a result of the electric field imposed.

From the simulations, the following basic trends consistent with the scaling arguments were observed:

- The pressure rise produced increases by the square of the electric field constrained to the maximum electric field corresponding to the breakthrough voltage of the liquid.
- The pressure rise produced increases linearly with increasing channel or pore length.
- The pressure rise produced increases nearly linearly with increasing the amount of charged particles.
- The pressure rise produced per unit length increases with the inverse of the diameter.

Additional efforts have focused on the development of an experimental prototype of an EHD pump that could be configured as an actuator. Decane has been chosen as the working fluid. A multitude of electrode configurations has been considered. The final configuration was designed to deliver an electric force that was distributed over the full extent of the fluid moving through a 1.5-mm diameter channel. It was based on the Stuetzer's spherical emitter electrode-spherical collector electrode design, having a sharp tip emitter electrode and a collector that encompassed the whole of the channel. In this arrangement, shown in Figure 2, a needle like emitter electrode was positioned 1.5 mm from the entrance to the 1.5-mm diameter metal tube, which also served as the collector electrode. The benefit of this design is that the sharp needle tip produces a locally high electric field near the tip of the emitter electrode. The ionization of the molecules occurs here resulting in the generation of free charges. In between the emitter and the tube, the field is sufficiently high to generate an ion drag force on all of the fluid entering the tube.

The single-channel milli-EHD pump of Figure 2 with the single pair axisymmetric electrodes produces a pressure head of 21 cm of decane when an electric field of 1.2×10^7 V/m is imposed. The 21 cm of decane of head produced, is equivalent to 1573 N/m^2 or 0.015 atm. The theoretical head that can be generated for the ion drag pumping is proportional to the square of the electric field. For the given electric field of 1.2×10^7 V/m, the measured head is almost identical to the theoretical value. Further, if the electric field were to be increased by an order of magnitude³, the head generated by the single electrode pair would be 1.5 atm. This magnitude of electric field was not considered solely due to the limitations in the hardware and instrumentation used.

Note that the theoretical head is linearly proportional to the number of electrode pairs used in the pump. Using the electrode pair spacing of 0.1 mm and the slot length of 10 mm will allow the deposition of 100 electrode pairs. Considering that the pressure build up varies linearly with the number of electrode pairs, the 1.5 atm pressure achievable with a single electrode pair will be amplified to 150 atm when 100 electrode pairs are used. Note that the amplification is not achieved through the use of leveraging mechanism (which is how it is done in piezoelectric or magnetstrictive type actuators) and is not at the expense of other attributes (such as flow) of the pump. The slot width/diameter of 50 microns allows the stacking of up to 100 slots in parallel in a 1mm by 1mm cross-section, resulting in 15 N force. Extending the cross-sectional area to 10 mm by 10 mm (which is

³ The voltage requirement for generating $1e8$ V/m electric field with an electrode spacing of a few micrometers is in par with the voltage requirement of driving a stack-type piezoelectric actuator.

still a small cross section compared to the currently available actuators), increases the force 100 times to 1500 N. In other words, **a 10 mm cube type actuator will be capable of developing 1500 N force, *theoretically*.**

Research is needed to further analyze the new concept and establish a parametric understanding of the actuator with respect to geometry, fluid, and temperature constraints. Research is also proposed to experimentally verify the viability of the promising concept. A multitude of prototypes will be designed, fabricated, and tested to provide experimental benchmarking of the model predictions. At the same time, this experimental benchmarking will provide practical experience in both fabricating the concept and incorporating it into various applications of interest to DOD.

We envision having developed tools for the design, fabrication, and deployment of the EHD pumped actuator. We envision having working prototypes providing force, bandwidth, and size capabilities superior to comparable magnetostrictive and piezo type devices. We envision having demonstrated the feasibility for incorporating such actuators in noise control applications of interest to DOD by active control of the vibration of the structure emanating the noise or active isolation of that structure from the source of vibration such as power plant, propulsor, gear box, motor, and pump. High performance feature of the proposed actuation mechanism make it viable for controlling the vibration of large and sometimes very stiff structures.

Broader Impact of EHD-Actuation

The advancement in EHD pumping that will be achieved through this project will also be used in variety of other applications. For example abating machinery noise via active isolation of the machinery such as gearboxes and pumps from being transmitted to radiating structures using active hydraulic mounts. In this application, EHD pumping action will be used as a pump to actively displace liquid in the inertia track of these isolators.

Another application of the EHD pump concept is microfluidic pumping for use in control of turbulent shear flows. Currently, most research on the development of microfluidic pumping is based on miniaturizing mechanical pumps. This brings with it all the undesirable attributes associated with mechanical devices, e.g. friction, backlash in gearing, etc. EHD pumping contains no moving part and is an attractive alternative to the current practice.

Decentralizing the power generation system in a flight vehicle is another potential application for EHD actuator. Currently, centralized generation and supply of hydraulic power to hydraulic actuators distributed in an aircraft is very common. Decentralizing the power generation, will reduce flight vehicle control system complexity, size, and weight and will improve the overall control system and reliability. Such scheme requires a compact, high performance actuation (high force and displacement along with the reasonable agility, simultaneously⁴), which are beyond the capabilities of currently available smart material transducers.

⁴ The commonly used approach of *levering* that amplifies the force at the expense of displacement and vice versa, is not the viable solution to this actuation problem.

Current Actuation Mechanisms

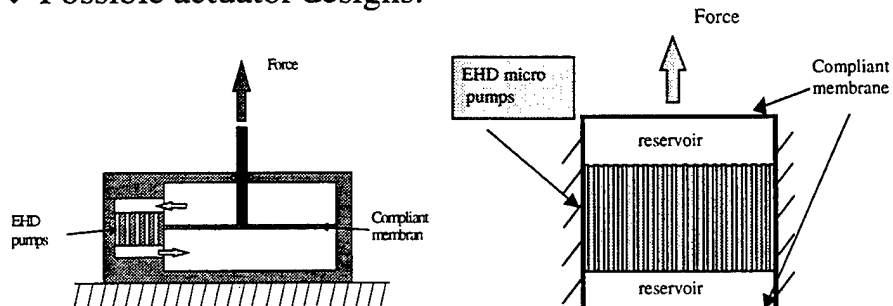
- ◆ Piezoelectric ceramics
 - Patches
 - Rods/stacks
 - Fibers
- ◆ Magnetostrictive alloys
- ◆ Shape memory alloys

Issues:

- Temperature
- Displacement/force limitations

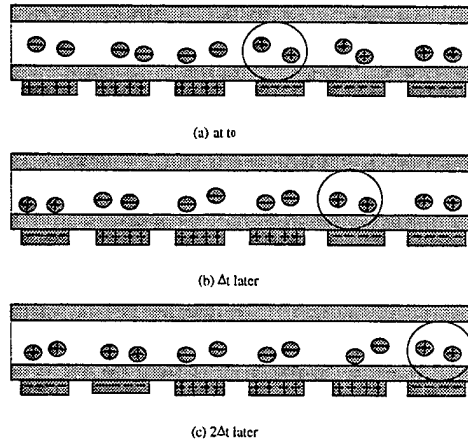
Electrohydrodynamic Pumping

- ◆ EHD pumping, in micro-scale
 - the driving mechanism of the actuator
- ◆ Possible actuator designs:



EHD Pump Operation

- ◆ Ions can be generated by
 - Thermal induction
 - Ion injection
 - Field ionization
 - » High electric field ionizes the molecules of a unipolar fluid



Alternative Stack Arrangements

High force

Stacked channels in series

$$\Delta P = \Delta P_{\text{channel}} \times (\# \text{ of channels})$$



Stacked channels in parallel

$$\text{Flow rate} = \text{Flow rate} \times (\# \text{ of channels})$$



High stroke

Stacked channels in a combination of series and parallel to increase flow and ΔP :



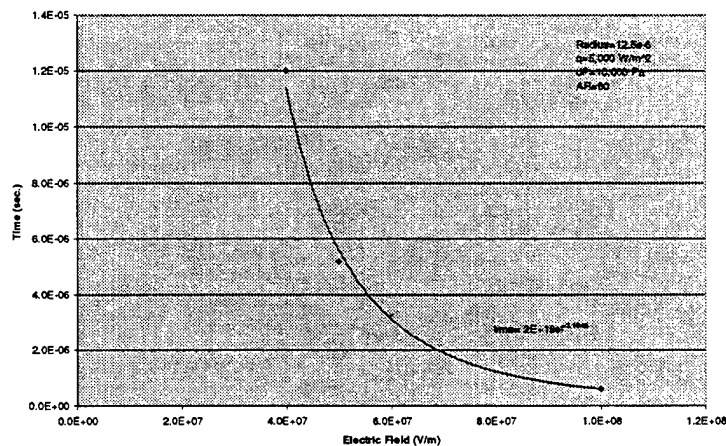
Optimal compromise

Parametric Study

Parametric study of each control variable

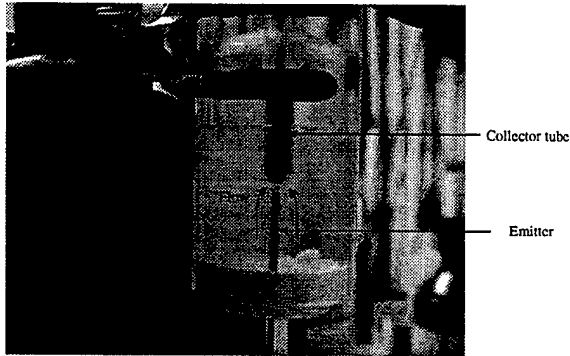
- Responsiveness and performance are nearly proportional to
 - » Electric field intensity²; (ϵE^2)
 - » Aspect ratio
 - » Amount of charged particles
 - » 1/Radius

Time to Zero Flow

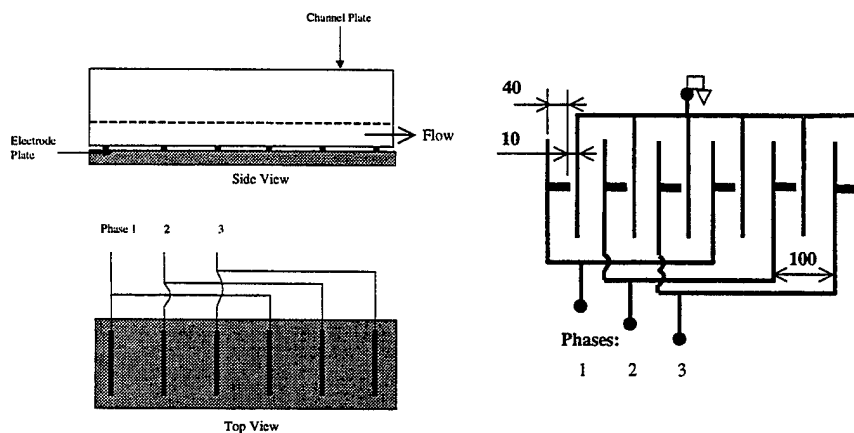


Experimental Results

- ◆ An emitter electrode was positioned 1.5 mm from the entrance to the 1.5-mm diameter metal tube (served as the collector electrode)
- ◆ For $E=1.2 \times 10^7$ V/m, pressure of 0.015 atm was built up
- ◆ For $E=1.2 \times 10^8$ V/m, the pressure build up will be 1.5 atm



Configuration and Electrode Arrangement



Extrapolation of the Results

- ◆ The slot width/diameter of 50 microns
 - 10 mm length and 100 μm electrode pair spacing results in 100 electrode pairs
 - » 1mm by 1mm cross-section can accommodate 100 slots in parallel
 - ◆ 15 N force
 - » Extending the cross-sectional area to 10 mm by 10 mm
 - ◆ 1500 N force
 - A 10 mm cube actuator will be capable of developing 1500 N force, theoretically
- ◆ Our current manufacturing capabilities
 - Chemical etching of silicon
 - Ultrasonic milling of dielectric ceramics such as glass
 - » Electrode spacing: 0.1 mm - 1 mm
 - » Slot width/diameter: 20 microns - 200 microns
 - » Slot lengths: 1 cm - 10 cm

Summary

- ◆ Fast tool servoing
 - » Operation with uncertain parameters
 - » Effective disturbance rejection
 - » Enables production of parts using fewer operations
 - » Requires high performance actuation
- ◆ EHD-pumped actuator
 - » A High-performance, high-bandwidth, compact actuator is conceptualized
 - ◆ The actuator relies on the use of EHD pumping in micro-scale
 - ◆ Capable of achieving 1000s of Newtons of force and millimeters of stroke

The Department of Defense
Multidisciplinary Research Program of
the University Research Initiative

ACOUSTIC TRANSDUCTION
- MATERIALS AND DEVICES

- Overview 1998-

Principal Investigator: Kenji Uchino
Materials Research Laboratory
The Pennsylvania State University

GRANT NO.: N00014-96-1-1173

PERIOD: July 31, 96 through December 31, 99

GRANT AMOUNT: \$ 3 Million

GRANTEE: The Pennsylvania State University
Materials Research Laboratory (MRL)
Applied Research Laboratory (ARL)
Center for Acoustic and Vibration (CAV)

PROGRAM OFFICER: Jan F. Lindberg, ONR

PROJECT OBJECTIVES

LONG TERM GOALS

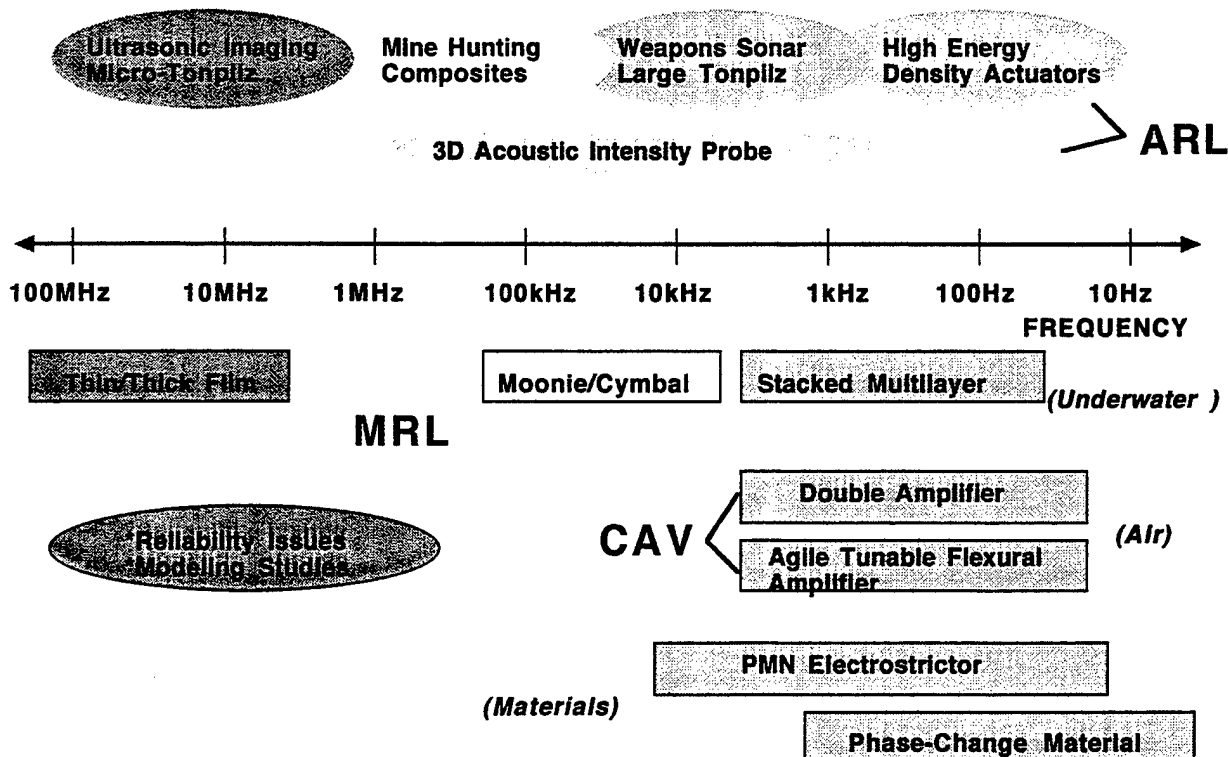
To develop improved and reliable air and underwater acoustic transducers, encompassing a wide frequency spectrum from 10 Hz to 100 MHz with systematic and conjunct studies on materials, devices, modeling and electronics.

OBJECTIVES

The technical objectives are to develop:

- (1) high performance piezoelectric materials (high strain, agile, low loss piezoelectrics and related ecological materials) with advanced reliability, aiming at the applications to
- (2) Cymbal and Tonpilz transducer arrays for 3 - 50 kHz sonars,
- (3) thin/thick film transducers for 10 - 100 MHz medical acoustic devices and
- (4) underwater intensity sensors for low-frequency surveillance,
- (5) flexural amplification mechanisms of the solid state strain for air acoustic transduction, as well as
- (6) modeling/computer simulations of domain motions and structural vibrations and
- (7) supporting electronics.

DEVICES



MATERIALS / COMPONENTS

Materials Research Laboratory (MRL)

Piezoelectric Materials and Actuator Components

- | | |
|---|---|
| (1) New MPB and tungsten bronze materials | <u>A. S. Bhall</u>
<u>R. Guo</u>
<u>L. E. Cross</u>
Baomin Xu
E. F. Alberta |
| (2) Improved lead magnesium niobate-lead titanate electrostrictors for multilayer Tonpilz transducers | <u>T. R. Shrout</u>
W. Hackenberger |
| (3) Flexensional cymbal transducers for sonar applications | <u>R. F. Newnham</u>
J. F. Tressler
J. Zhang |
| (4) Thin film lead zirconate titanate (PZT)-based ceramics for micro tonpilz applications | <u>S. Trolier-McKinstry</u>
Wei Ren |
| (5) Compact ultrasonic motors | <u>K. Uchino</u>
B. Koc |

Reliability of Ceramic Actuators

- | | |
|---|---|
| (6) High power/voltage piezoelectrics | <u>K. Uchino</u>
Y. H. Chen |
| (7) High stress dependence/polarization mechanism in relaxor ferroelectrics | <u>Q. M. Zhang</u>
J. Zhao
Yi Bai |
| (8) Destruction mechanisms and AE measurements | <u>K. Uchino</u>
H. Aburatani |

Modeling and computer simulation studies

- | | |
|-------------------------------------|--------------------------------------|
| (9) Ferroelectric domain structures | <u>C. A. Randall</u> |
| (10) Structural vibrations | <u>W. Cao</u>
J. Erhart
S. Zhu |

Applied Research Laboratory

- | | |
|---|---|
| (1) Cymbal arrayed projectors | <u>W. J. Hughes</u>
R. W. Dashem
G. A. Granville |
| (2) PMN Tonpilz tunable transducers | <u>W. J. Hughes</u>
P. G. Bednarchik
R. W. Dashem
G. A. Granville |
| (3) Thin film micro-Tonpilz transducers | <u>W. J. Hughes</u>
<u>R. J. Davis</u>
<u>R. L. Tutwiler</u>
D. Van Tol
Li-Peng Wang
K. Majahan
S. Madhvan
R. Dave |

Center for Acoustics and Vibrations

- | | |
|--|--|
| (1) Integrated mechanical amplifiers | <u>G. H. Koopmann</u>
<u>A. D. Belegundu</u> |
| (2) Inchworm Actuators | <u>G. H. Koopmann</u>
<u>A. D. Belegundu</u>
M. Lysena
M. Yang
J. Frank |
| (3) Actively-tuned vibration absorber / Agile tunable flexural transducers | <u>G. A. Lesieutre</u>
C. A. Hebert
J. Bernard
C. L. Davis |
| (4) Underwater acoustic intensity probes | <u>G. C. Lauchle</u>
J. A. McConnell
J. Wang
D. E. Capone
K. J. Bastyr
K. Kim |

SIGNIFICANT RESULTS

- (1) The phase diagrams and piezoelectric properties of several relaxor-based systems have been systematically explored for use in piezoelectric/electrostrictive transducers: PIN-PMN, PSN-PT, PIN-PT, PIT-PT.
- (2) It was shown from the Neutron data that the intrinsic volumetric electrostrictive coefficient Q_h for PMN-PT is on the same level as those of normal ferroelectrics due to the large contribution of the nanopolar regions to the macroscopic polarization response of the material.
- (3) The measured and calculated results of the cymbal transducer array showed it to be a viable medium to higher power transducer for shallow water projector applications from 5 kHz to about 50 kHz.
- (4) A prototype two-geophone underwater acoustic intensity sensor has been successfully developed.
- (5) Using a combination of rapid thermal annealing and a post-crystallization heat-treatment step, films with remanent polarizations above $40 \mu\text{C}/\text{cm}^2$ and dielectric constants of >1200 at room temperature have been prepared on platinized Si substrates. We have found that an HF etch followed by a quick HCl cleanup etch at 40°C results in a clean surface with good resolution of the desired PZT structures.

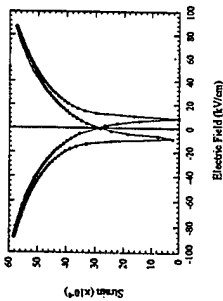
SIGNIFICANT RESULTS

(continued)

- (6) For a flexural fixed-fixed bimorph loaded axially to one-half of its critical buckling load, the resonance frequencies associated with both the voltage and current responses shifted by more than 25%. In addition, the device coupling coefficient increased by 30% at the same load.
- (7) Using an optimized design strategy for flexensional devices, an inchworm driven by three PZT stacks has been fabricated.
- (8) A semi-actively tuned piezoceramic vibration absorber was developed using a tunable capacitive shunt circuit. Within the tunable frequency band, increases in performance beyond those of a purely passive system were as great as 20 dB and averaged more than 10 dB.
- (9) A compact ultrasonic rotary motor ("windmill") as tiny as 3 mm in diameter has also been developed: the maximum revolution 600 rpm and the maximum torque 1 mN·m.
- (10) Phenomenological calculation for PZT suggests that near the morphotropic phase boundary on the rhombohedral side, the $d_{33(001)}/d_{33(111)}$ rapidly increases, while $d_{33(111)}/d_{33(001)}$ increases only moderately, leading to large enhancement of $d_{33(001)}/d_{33(111)}$ more than 4. The k_{33} more than 90 % can be expected.

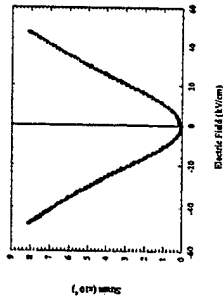
PSN:PT

High k_{33} , low Q_m
 $d_{33} \sim 600$ pC/N



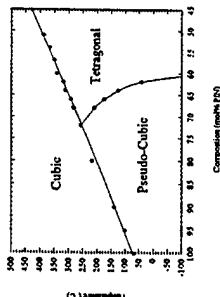
PMN:PIN

Low hysteresis: χ_{ij} vs E



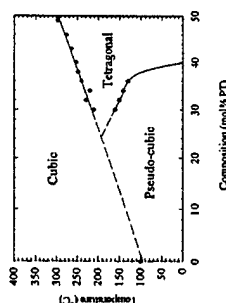
PIN:PT

Moderate d_{33}



PIT:PT

First report on the synthesis of
phase-pure PIT:PT ceramics.



PSN:PZN:PT

Comp (% PSNT)	d_{33} (pC/N)	$-d_{31}$ (pC/N)	k_p (%)	k_{31} (%)	K_{13} (%)	σ
75.0	375	162	66.5	38.7	72	0.29
50.0	435	186	63.3	38.8	46	0.25
25.0	300	131	51.0	30.0	73	0.33

RELIABILITY

Since the ceramic actuators are occasionally used under high voltage/power and high stress, systematic data accumulation on these characteristics is important to realize reliable transducer materials.

High Power Piezoelectric Measurement (K. Uchino)

- * Measuring system - resonance technique at a constant current (i.e. constant vibration level) condition.
- * PMN-PT ceramics near the morphotropic phase boundary have been examined with Mn or Fe doping to test the acceptor doping effect. When the temperature rise is around 200C, the vibration velocity of 0.3 m/s can be obtained for a sample with 0.5 wt.% Mn doping.

High Stress Measurement (Q. Zhang)

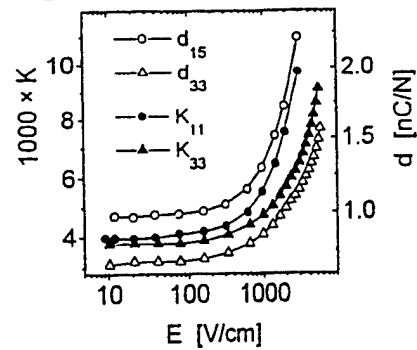
- * The effect of mechanical pre-stress on the electromechanical properties of 0.9PMN-0.1PT ceramic over a broad temperature and DC bias field range has been measured.
- * Using neutron diffraction and dilatometry, both the intrinsic electrostrictive coefficients (lattice coefficients) and the contribution from the nano-polar regions were determined.
The intrinsic volumetric electrostrictive coefficient Q_h for PMN-PT is on the same level as those of normal ferroelectrics. The measured Q_h from the macroscopic strain response, which is much smaller than that of the lattice Q_h , is a direct consequence of the large contribution of the nanopolar regions to the macroscopic polarization response of the material.

--- How do the materials behave under a high driving field, what are the general rules describing the non-linear behaviors?

The non-linear response of PZT piezoceramics with electric field:

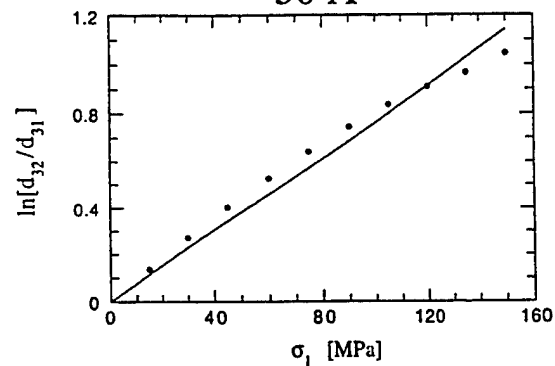
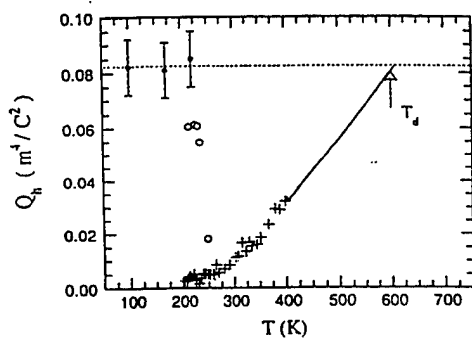
$$d = d_{lin}(1 + (d_{nli}E)^a)$$

where the exponent a and prefactor d_{nli} of the nonlinear term exhibit a universal behavior



The comparison electrostrictive coefficients measured by neutron diffraction and macro-strain:

The size of the micropolar regions determined by the dependence of d_{32}/d_{31} on T_1
 $\sim 50 \text{ \AA}$



PENNSTATE



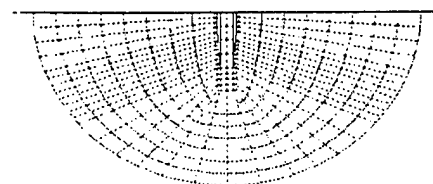
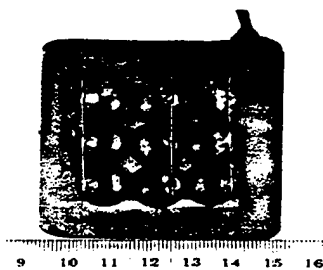
MURI: Acoustic Transduction

Cymbal Transducers

Cymbal Transducers

Objective

- Improve the pressure tolerance of cymbal transducer
- Model underwater performance and optimize cymbal structure (materials and dimension)
- Develop cymbal array to achieve high source level and desired beam pattern
- Study failure mechanism to improve its reliability



In Water

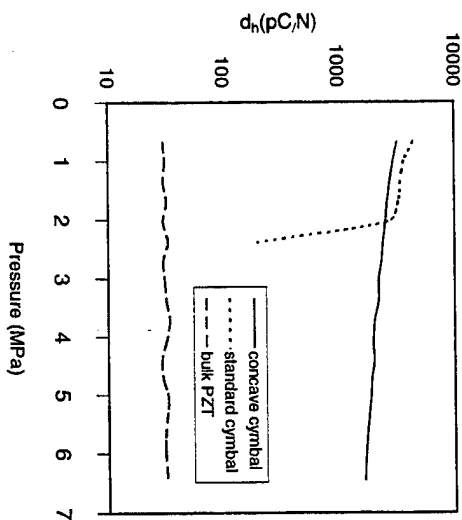
CURRENT WORK

Modeling

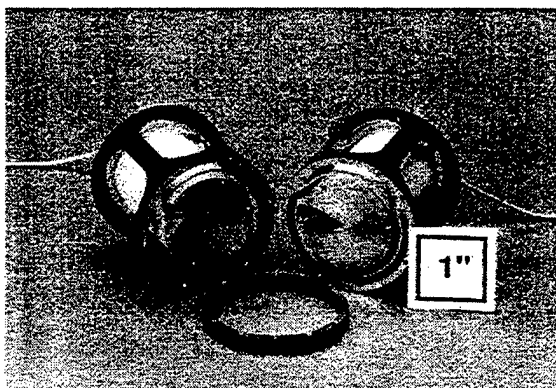
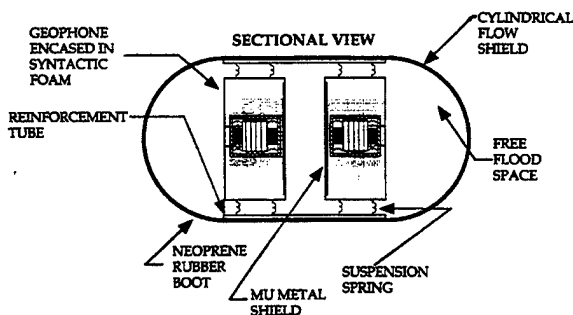
- ATILA FEA code used to predict underwater performance
- TVR, FFVS and beam pattern calculated
- Very good agreement between model results and measurements

Concave Cymbal

- PZT ring used instead of disk
- Weight is lower
- Pressure capability extended from 2MPa(200m) Standard cymbal to 6Mpa(600m) Concave cymbal



UNDERWATER ACOUSTIC INTENSITY SENSORS



- u-u sensors invented (patent pend.), prototyped, and calibrated
- Standing wave field calibration successful
- geophone phase mismatch an issue as with p-p probe
- flow noise measurable for low source strength, but not a serious issue
- Current research transitioning to platform S&T applications (NVMS)



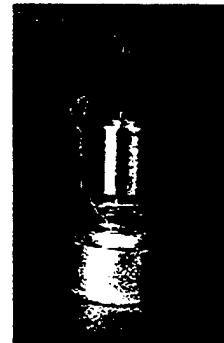
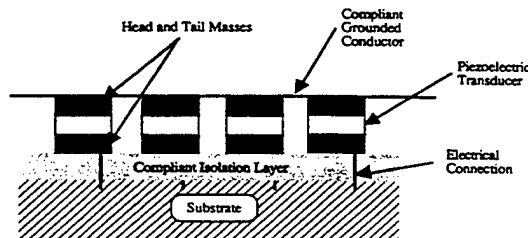
Micro-Tonpilz Transducer

OBJECTIVE

- Use a thick film PZT tonpilz design to fabricate arrays at frequencies of 30 to 80 MHz
- Build low megaHertz tonpilz transducers to verify the concept and compete with present designs for medical applications

CONCEPTS

- Utilize thick film PZT (about 8 microns) technology with sonar tonpilz transducer design to produce silicon mounted very high frequency transducers



TONPILZ: German for "sound mushroom"

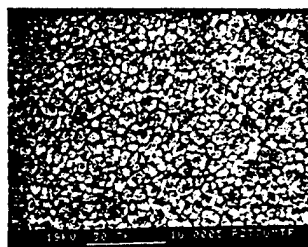
- A longitudinal mass-spring-mass vibrator



Micro-Tonpilz Transducer

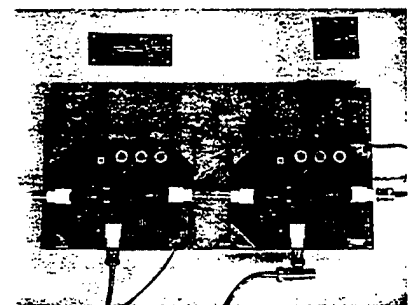
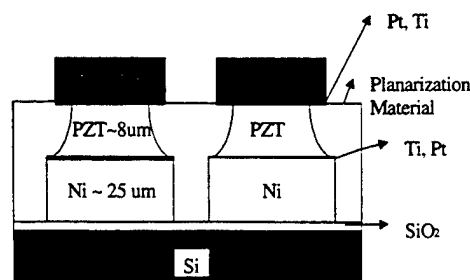


2 MHz Tonpilz Transducer



Thin film PZT

- Grain Size ~ 0.1 - 0.3 μm
- Good remnant polarization



Electronics
Preamp & Time-Gain
Compensation circuits

*Micro Fabrication
Option 1: Straight-up Structure*



Advanced Material (PMN) Tonpiliz

OBJECTIVE

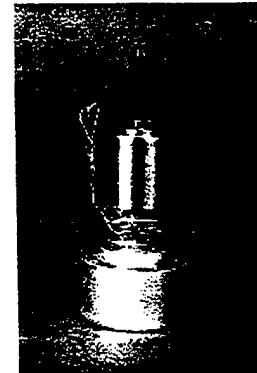
- Develop a common cross-discipline understanding of design parameters so that more optimum materials can be developed for increased transducer performance
- Evaluate PMN and other advanced materials at high frequencies (above 10 kHz) for high source level transmit and high sensitivity receive modes of operation

MOTIVATION

- PMN (a high energy density, electrostrictive material) has high interest for Navy transducer application.
- Establish a baseline tonpiliz element for evaluating piezoceramic and ferroelectric transducer materials.

INNOVATIONS/GOALS

- Investigate PMN characteristics as a receiver and projector.
- Evaluate promising advanced materials in Navy transducer designs.
- Design a direct drive transducer without a voltage step-up transformer.



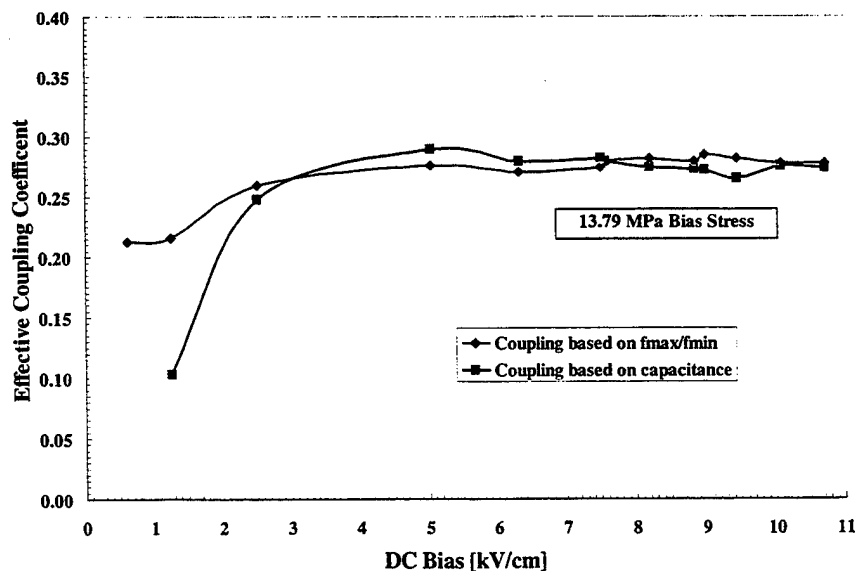
Pmn98-PGB.PPT



Measurement of BPT Transducer Coupling Coefficient PMN-PT-La 90/10/1 22°C

• Coupling coefficient

$$k = \sqrt{1 - \frac{\text{Frequency of Maximum Admittance}}{\text{Frequency of Maximum Impedance}}} = \sqrt{\frac{\text{Mechanical Stiffness}}{\text{Total Capacitance}}}$$



Pmn98-PGB.PPT



Optimal Design of Piezoceramic Actuators

PI's: Professor Gary H. Koopmann, CAV Director
Professor Ashok D. Belegundu, Mech Engr

Affiliated Faculty: Dr. Weicheng Chen, CAV

Graduate Students:

Mark Lesyna, MS ME 1998

Jeremy Frank, Ph.D. Candidate 1998

Center for Acoustics and Vibration



FREQUENCY-AGILE PIEZOCERAMIC TRANSDUCERS OBTAINED THROUGH APPLICATION OF IN-PLANE LOADS

Chad A. Hébert

M.S. Candidate

George A. Lesleuire
Advisor

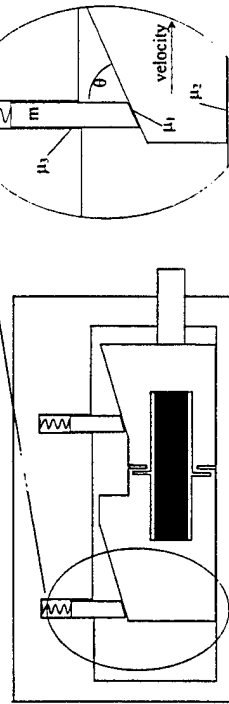
July 14, 1998

Dept. of Aerospace Engineering

Center for Acoustics and Vibration



Small, self-locking, self-contained piezoceramic wedge-worm type actuators are being designed for embedding in flow control foils. Studies to optimize a self-locking mechanism are conducted to create wedge surfaces that alternately produce high clamping and high actuation forces.



Actuator Top View

Optimization Parameters

Center for Acoustics and Vibration



Conclusions

• Frequency-agile piezoceramic transducers were obtained through application of compressive in-plane loads

• Change the effective bandwidth

- > TPB - frequency change of 36%
- > TAPD - frequency change of 13%

• Increase device coupling coefficient

- > TPB - increase in k_{sys} of 38%
- > TAPD - increase in k_{sys} of 15%

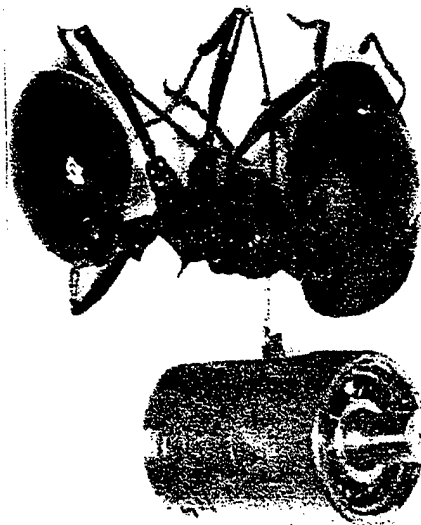
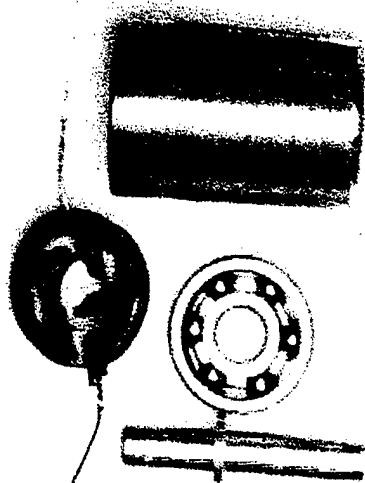


Dept. of Aerospace Engineering

Center for Acoustics and Vibration

"Windmill" Compact Ultrasonic Motor
(K. Uchino)

3 mm ϕ (800 rpm, 1 mN·m)



PENNSTATE



Modeling and Fundamental studies

(W. Cao, C. Randall)



Perfected the finite element modeling methods and used it to design array transducers. The finite element code has been integrated with acoustic beam computation and the modeling results were verified by experiments.



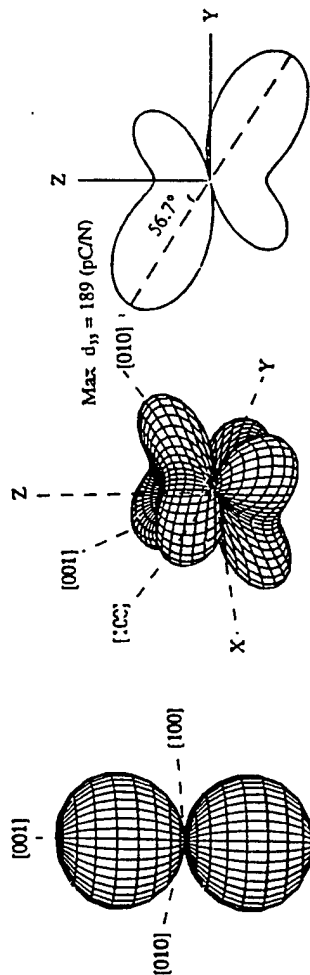
A simulation model was developed to study the formation of ferroelectric domains. The new computation model is used to study the size effects and surface effects in the formation of stable domains. New fast computation algorithm was used which can substantially reduce the computation task, making real dimension simulation practical.



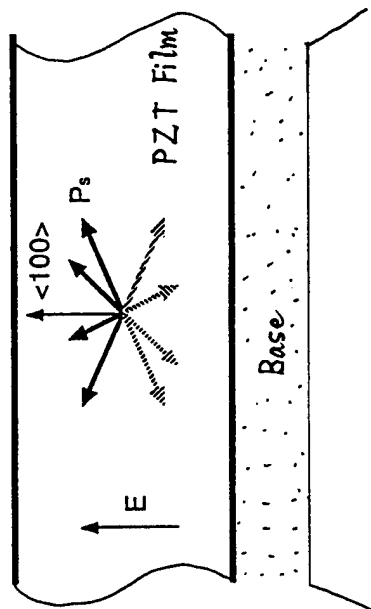
Nucleation mechanism on domain switching was investigated experimentally. It is found that the number of nucleation sites grows with the increase of electric field. The pre-existing nuclei also facilitate the growth of the stable domains.

Crystal Orientation Dependence of Piezoelectric d33 in Pb(Zr,Ti)O3 (K. Uchino)

PZT 40/60 (Tet) PZT 60/40 (Rhomb)



Rhombohedral compositions with the $\langle 100 \rangle$ orientation may provide the max d and k!



SUMMARY STATISTICS OF FY98

PUBLICATION/PATENTS/PRESENTATIONS/HONORS/PARTICIPANTS
(Number Only)

	ONR	nonONR
a. Number of Papers Submitted to Refereed Journal but not yet Published:	0	0
b. Number of Papers Published in Refereed Journals:	93	0
General Summary/Review	12	
Materials Studies	43	
Composite Transducers	17	
Device Structures	13	
Modeling/Theory	8	
c. Number of Books or Chapters Submitted but not yet Published:	3	0
d. Number of Books or Chapters Published:	2	0
e. Number of Printed Technical Reports & Non-Refereed Papers:	15	0
f. Number of Patents Filed:	6	0
g. Number of Patents Granted:	2	0
h. Number of Invited Presentations at Workshops or Prof. Society Meetings:	38	0
i. Number of Contributed Presentations at Workshops or Prof. Society Meetings:	77	0
j. Honors/Awards/Prizes for Contract/Grant Employees: (selected list attached)	13	0
k. Number of Graduate Students and Post-Docs Supported at least 25% This Year on Contract Grant:	21	0
	Grad Students:	TOTAL
		Female
		Minority
	Post Doc:	TOTAL
		Female
		Minority
l. Number of Female or Minority PIs or CO-PIs		
	New Female	0
	Continuing Female	1
	New Minority	0
	Continuing Minority	0

An Analytical and Experimental Analysis for a One-Dimensional Passive Stand-off Layer Damping Treatment

Jessica M. Yellin, I.Y. Shen, Per G. Reinhall, and Peter Y. H. Huang

University of Washington
Mechanical Engineering Department, Box 352600
Seattle, Washington 98195-2600

Project Summary

Passive stand-off layer (PSOL) damping treatments are presently being implemented in many commercial and defense designs. In a PSOL damping treatment, a stand-off or spacer layer is added to a conventional passive constrained layer (PCL) damping treatment. To investigate how the bending and shearing rigidities of the stand-off layer (SOL) affect the damping performance, an analytical model has been developed for a PSOL damping treatment applied to an Euler-Bernoulli beam.

The equations of motion were derived and solved in order to simulate the frequency responses of several beams treated with PSOL. A series of experiments was conducted in order to test this analytical model. These experiments measured the frequency responses of a variety of beams treated with PSOL damping treatments. The experimentally measured results were normalized and calibrated and then compared with the theoretical predictions using the new analytical model. This comparison showed that the analytical model was able to predict very accurately the frequency responses of the beams treated with PSOL.

Author e-mail addresses:

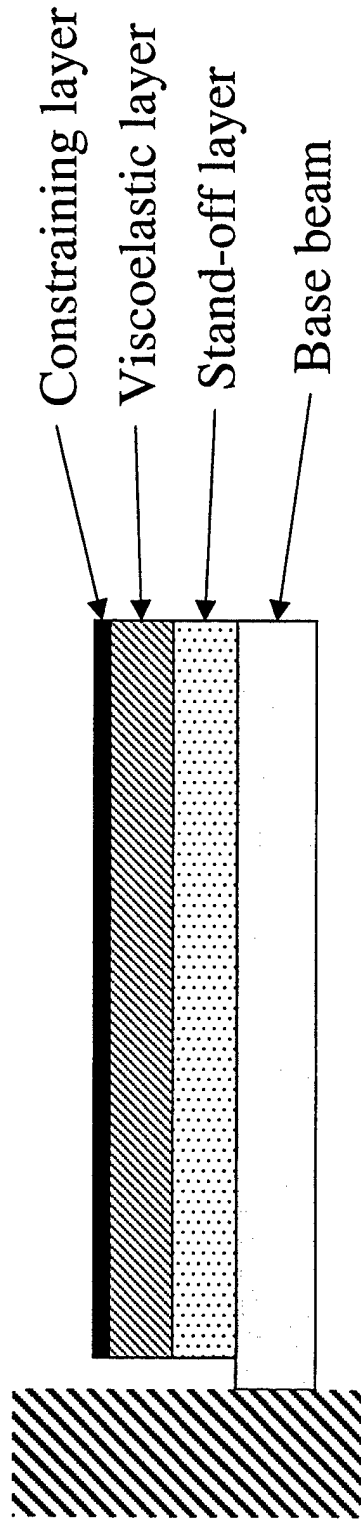
Jessica M. Yellin:	jmyellin@u.washington.edu
Professor I.Y. (Steve) Shen:	ishen@u.washington.edu
Professor Per G. Reinhall:	reinhall@u.washington.edu
Peter Y.H. Huang:	yahuang@u.washington.edu

Passive Stand-off Layer Damping: Analytical Model for Continuous SOL

Objectives:

- To develop an analytical model that accurately predicts the frequency response function of a beam treated with passive stand-off layer (PSOL) damping.
- To verify this analytical model experimentally.

Cantilever beam treated with PSOL



PSOL applications

Space and Defense:

- Reduce vibration:
 - satellite panels
 - launch vehicle fuselages
- Reduce acoustical noise:
 - wing skins and fuselages (F-15)
 - rotorcraft cabins
 - squeal in vehicle brake pads

Commercial:

- Reduce acoustical noise:
 - airplane passenger cabins
 - car and truck cabins
- Damp vibration:
 - disk drives
 - computer circuit boards
 - consumer electronics

Why use a stand-off layer?

- Enhances damping by increasing shear angle in viscoelastic (VEM) layer.
 - Increases distance of VEM layer to neutral axis of the structure
- Viscoelastic stand-off layer can provide additional damping to structure.

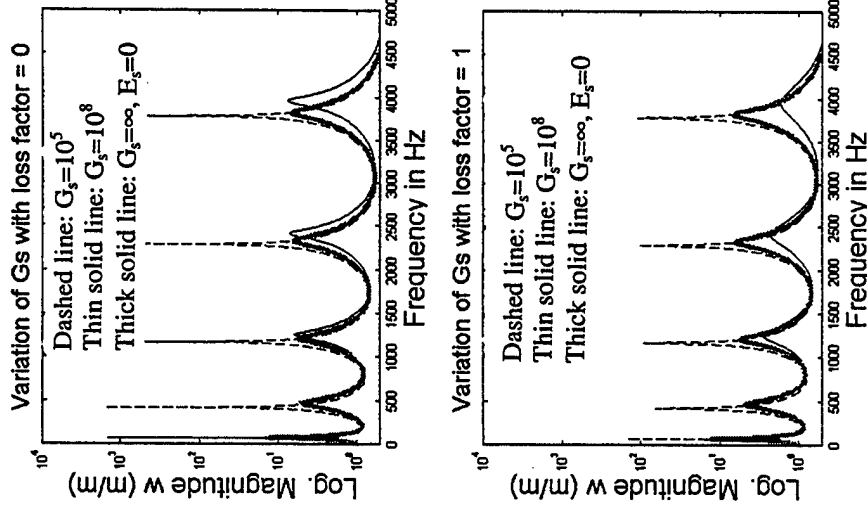
PSOL Analytical Model

Previous models:

- Assumed ideal case of SOL with $G_s = \text{infinity}$, $E_s = 0$

PSOL analytical model:

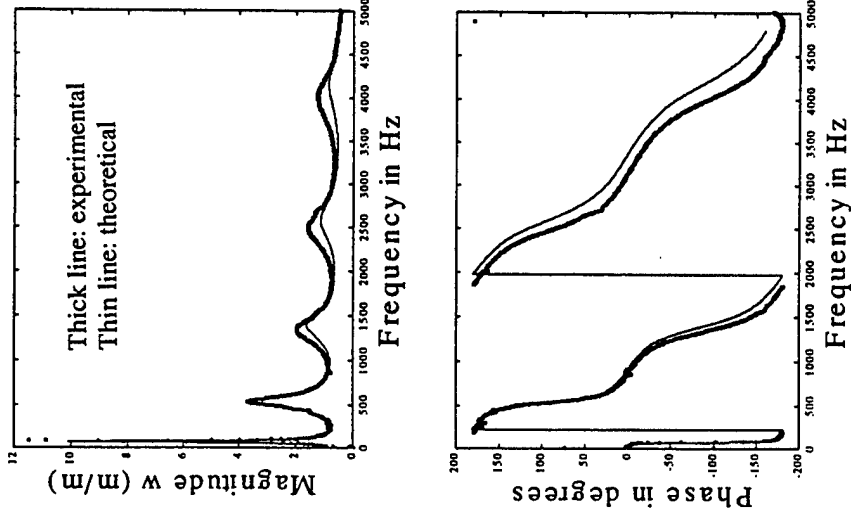
- Allows SOL to have finite G_s , non-zero E_s .
- Allows SOL to have internal damping properties.
- Frequency response differs significantly from ideal case if physically realistic values for E_s , G_s , and loss factor are used.



Comparison of Theoretical Predictions with Experimental Results

Experimental results verify
theoretical model:

- predicted frequency of
modes within 5% of
experimental results
- predicted amplitude and
phase of modes accurately



Spectral Element Method for Sandwich Beam with Passively Constrained Viscoelastic Damping Layers

Gang Wang
Graduate Research Assistant

Norman M. Wereley
Associate Professor

Alfred Gessow Rotorcraft Center
Department of Aerospace Engineering
University of Maryland, College Park, MD, 20742

SUMMARY

We present a spectral finite element model (SFEM) for the analysis of cantilevered sandwich beam with passively constrained layer damping (PCLD) excited via a pair of piezoelectric actuators. The sandwich beam consists of aluminum face layers sandwiching a viscoelastic core. The viscoelastic core has a complex modulus that varies with frequency. The actuators are mounted on top and bottom of the beam, and are excited with equal, but out-of-phase, voltages to excite bending motion of the sandwich beam. The SFEM is formulated in the frequency domain using dynamic shape functions based on the exact displacement solutions from wave propagation methods, where we implicitly account for the frequency dependent complex modulus of the viscoelastic core. A small number of spectral elements are required to calculate the frequency response functions of the sandwich beam. The SFEM results are compared to frequency response functions calculated using conventional finite element (CFEM) and Galerkin assumed modes methods (AM), where Golla-Hughes-McTavish method is used to account for frequency dependent complex modulus of viscoelastic core. SFEM shows improved accuracy and the potential for improved computational efficiency, because many more elements or assumed modes must be incorporated into CFEM or AM analyses for comparable accuracy. The analysis is validated using frequency response functions measured for cantilevered sandwich beams with passive constrained layer damping treatments having 50% and 75% coverage of the beam length.

ACKNOWLEDGEMENT

Research supported by U.S Army Research Office under the FY96 MURI in Active Control of Rotorcraft Vibration and Acoustics. (Dr. Gary Anderson and Dr. Tom Doligalski, technical monitors). Lab equipment support was provided under the FY96 Defense University research Instrumentation Program (DURIP) contract No. DAAH-0496-10301 (Dr. Gary Anderson, technical monitor).



Motivation



- Reduce the interior cabin noise in aircraft, rotorcraft and other vehicles
- Helicopter interior cabin noise caused by rotor/transmission noise (100dB): air and structure borne
- Goal: *"Jet-Smooth Quiet Ride"*
 - Increase passenger and pilot comfort
 - Reduce structural fatigue levels
 - Reduce communication interference



Acoustic Control Hybrid Damping



Propose a hybrid scheme for controlling interior acoustics...

- Sandwich structure with viscoelastic core to enhance structural damping: high frequencies (> 300 Hz)
- Surface-mounted piezo-actuators for active control via feedforward/feedback techniques: lower frequencies (< 300 Hz)

Models of sandwich beam/plate that are suitable for use in feedback or feedforward control system



Modeling of Viscoelastic Materials



- Goal: To account for the frequency dependent complex shear modulus of viscoelastic core
- Golla-Hughes-McTavish (GHM) Method
 - Golla & Hughes(1985); McTavish & Huges (1992)
 - spring-mass-dashpot systems in series (mini-oscillators)
- Anelastic Displacement Field
 - Lesieutre & Mingori (1990)

Adding internal dissipation coordinates to account for the frequency dependent property of viscoelastic core



Progressive Wave Method



- 3-layer sandwich beam (Mead & Marcus, 1969)

$$\frac{\partial^6 w}{\partial x^6} - g(Y + 1) \frac{\partial^4 w}{\partial x^4} + \frac{m}{D_t} \frac{\partial^4 w}{\partial x^2 \partial t^2} = \frac{mg}{D_t} \frac{\partial^2 w}{\partial t^2}$$

- Douglas (1979): consider the sandwich beam with fully and partially PCLD treatment.
- Assuming: $w(x, t) = W(x, \omega) e^{j\omega t}$

$$W = a_1 e^{-k_1 x} + a_2 e^{k_1 x} + a_3 e^{-k_2 x} + a_4 e^{k_2 x} + a_5 e^{-k_3 x} + a_6 e^{k_3 x}$$

- Boundary and compatibility conditions are used to calculate those wave coordinates



Progressive Wave Method: Pros and Cons



- Advantages
 - Direct calculation of the frequency response from the governing equation without resorting to internal dissipation coordinates
 - Introduce a new element only when the impedance changes
- Disadvantages
 - Each time the boundary condition or a new impedance change is introduced - must REDO the model
 - Not as convenient as finite element method
- Need methods that captures convenience of FEM, but retains advantages of progressive wave methods to calculate the frequency response



Spectral Finite Element Model (SFEM)



- SFEM is formulated in frequency domain
- Develop SFEM analysis for 1-dimensional sandwich beams with passive constrained layer damping (PCLD)
 - Doyle (1997) "Wave propagation in structures"
 - Developed SFEM for isotropic structures like beams and rods
 - Extend Doyle's methods to beams with PCLD
- Other efforts in SFEM...
 - Longitudinal extension of rods with active constrained layer damping (ACL D) examined using SFEM (Baz, 1998)
 - Here, we are examining bending of a beam with PCLD



Objectives



- Develop spectral finite element (SFEM) analysis in frequency domain
 - Combine advantages of progressive wave and conventional finite element methods
 - Calculation of frequency response in the frequency domain
 - No internal dissipation coordinates needed to account for viscoelastic core
 - Reduce computational burden relative to internal dissipation coordinate methods (CFEM and AM method)



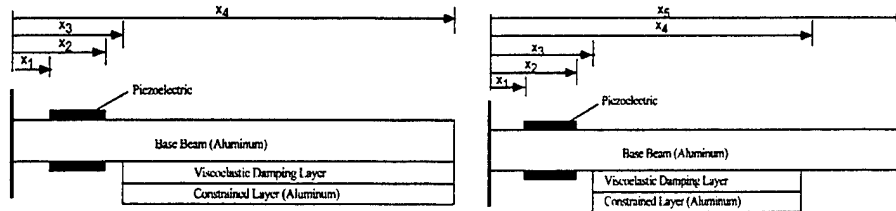
Cont.



- Compare SFEM to conventional finite element method (CFEM) and assumed modes (AM) results
- Experimentally validate analysis for cantilevered sandwich beam with isotropic faces and viscoelastic cores
 - modal frequencies
 - frequency response functions



SFEM Analysis for Sandwich Beam



- Isotropic beam and rod spectral dynamic stiffness matrix (Doyle, 1997)
- Spectral dynamic stiffness matrix for beam with PCLD



Governing Equations for Sandwich Beam



- Consider the inertia of face plates and Euler-Bernoulli assumption for face plates (layer 1&3)

$$m \ddot{w} + Dw_{xxxx} = \frac{Gbd}{h_2} (u_1' - u_3' + dw_{xx})$$

$$-m_1 \ddot{u}_1 + E_1 A_1 u_1'' = \frac{Gbd}{h_2} (u_1 - u_3 + dw_x)$$

$$-m_3 \ddot{u}_3 + E_3 A_3 u_3'' = -\frac{Gbd}{h_2} (u_1 - u_3 + dw_x)$$



Continued



- We assume

$$w = We^{j\omega t}; u_1 = U_1 e^{j\omega t}; u_3 = U_3 e^{j\omega t}$$

- where

$$W = a_1 e^{-k_1 x} + a_2 e^{k_1 x} + a_3 e^{-k_2 x} + a_4 e^{k_2 x} + a_5 e^{-k_3 x} + a_6 e^{k_3 x} + a_7 e^{-k_4 x} + a_8 e^{k_4 x}$$

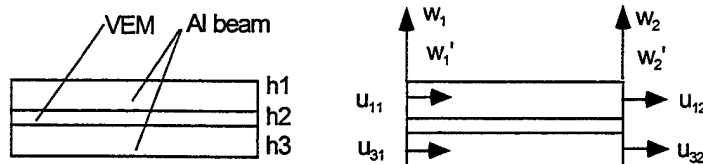
$$U_1 = b_1 e^{-k_1 x} + b_2 e^{k_1 x} + b_3 e^{-k_2 x} + b_4 e^{k_2 x} + b_5 e^{-k_3 x} + b_6 e^{k_3 x} + b_7 e^{-k_4 x} + b_8 e^{k_4 x}$$

$$U_3 = c_1 e^{-k_1 x} + c_2 e^{k_1 x} + c_3 e^{-k_2 x} + c_4 e^{k_2 x} + c_5 e^{-k_3 x} + c_6 e^{k_3 x} + c_7 e^{-k_4 x} + c_8 e^{k_4 x}$$

- Here b_i and c_i can be expressed by a_i



Spectral Finite Element for Sandwich Beam



- The nodal displacement chosen as follows, only six degrees of freedom needed

$$q^T = \left[U_{11} \quad U_{31} \quad W_1 \quad \frac{dW_1}{dx} \quad U_{12} \quad U_{32} \quad W_2 \quad \frac{dW_2}{dx} \right]$$



Spectral FEM



- So after mathematical manipulation

$$W = \{z\} N_w \{q\}$$

$$U_1 = \{z\} N_{u1} \{q\}$$

$$U_3 = \{z\} N_{u3} \{q\}$$

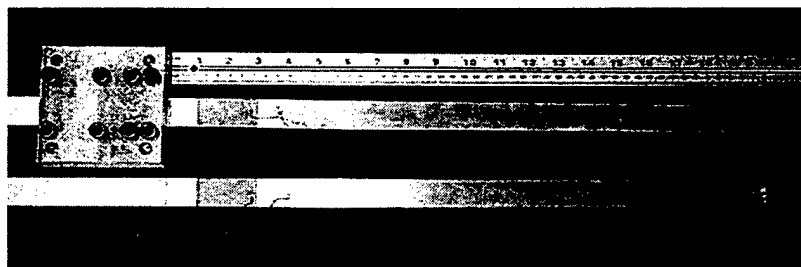
- where

$$z = \begin{bmatrix} e^{-k_1 x} & e^{k_1 x} & e^{-k_2 x} & e^{k_2 x} & e^{-k_3 x} & e^{k_3 x} & e^{-k_4 x} & e^{k_4 x} \end{bmatrix}$$

- Recall the energy expressions to calculate the dynamic stiffness element.
- Assembly procedure same as CFEM
- Calculate the frequency response at each given frequency



Experimental Set Up



Aluminum Base beam: 20"x1"x1/16"

Constrained layer: (15" or 10") x1"x1/64"

3M Scotchdamp ISD 112 VEM (5 mil)

PZT-5H actuator pair: Size: 2"x1"x5 mil ; 1" from end

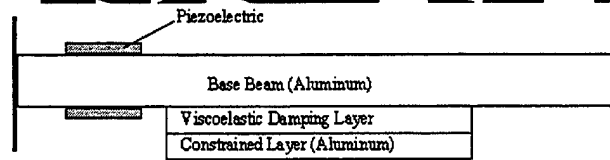
2 test specimens: 75 % & 50% PCLD treatment



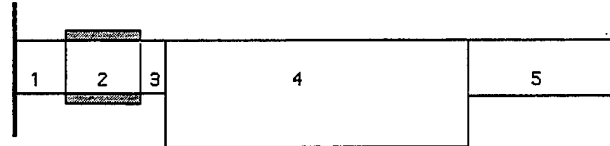
Element Meshes



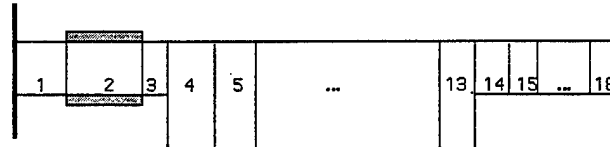
50% PCLD



SFEM

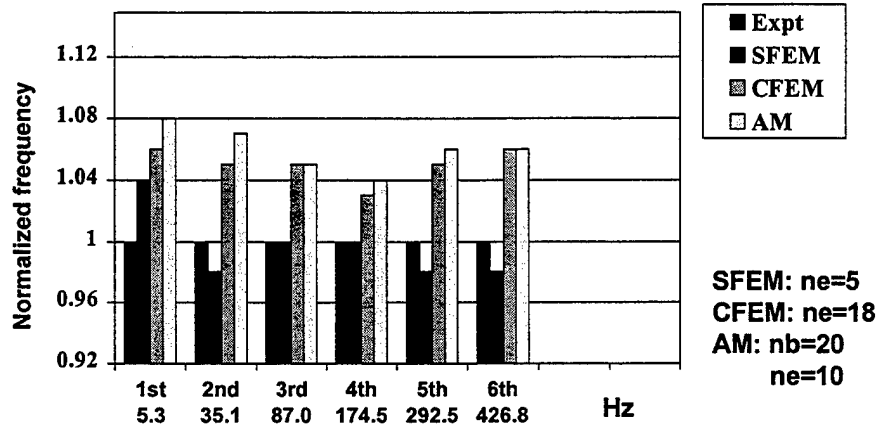


CFEM



Results...

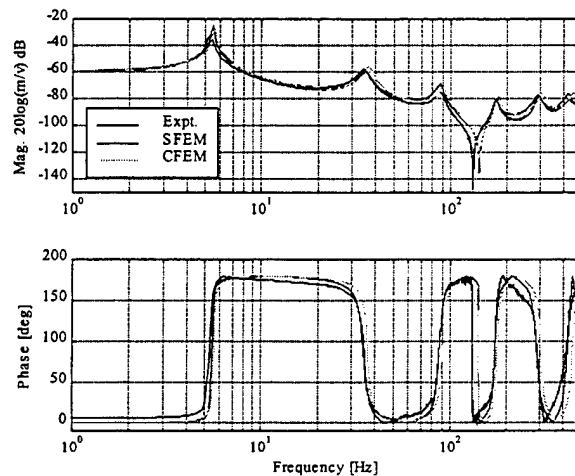
Comparison of modal Frequencies (50% PCLD Treatment)





Results...

Frequency Response Functions (50% PCLD Treatment)



Conclusions



- Spectral finite element model
 - Shape functions duplicated from exact progressive wave solutions
 - Minimum number of elements coincides with the number of different impedance in the structures having uniform sections.
 - Accurately account for the mass/inertia contributions compared to the consistent mass matrix in CFEM
 - Implicitly account for the frequency dependent properties of viscoelastic core
 - High computational efficiency, leads to parallel algorithm in the calculation of frequency response functions

Thickness Deformation of Constrained Layer Damping: An Experimental Evaluation

Peter Y. H. Huang, Per G. Reinhall, I. Y. Shen, and Jessica M. Yellin

Mechanical Engineering Department, University of Washington

Seattle, Washington 98195-2600, USA

SUMMARY

Constrained layer damping treatments have been assumed to dissipate energy mainly through shear deformation of the viscoelastic layer. Almost without exception, the mathematical models of structures that incorporated these treatments are based on the theory developed by Mead and Markus (1969) approximately 30 years ago. One important assumption used in their theory is that the thickness deformation of the viscoelastic layer can be neglected. The purpose of this study is to evaluate the accuracy of this assumption by experimentally investigating the vibration characteristics of constrained layer damped beams. The experimental results were compared to two mathematical models. One was based on the theory of Mead and Markus. The other was based on a model developed by Miles and Reinhall (1986) to account for the thickness deformation of the viscoelastic layer. Experimental results show that the thickness deformation phenomenon is significant in the high frequency range, and that the consideration of the thickness deformation of the viscoelastic layer improves the accuracy of the analytical model.

Introduction

Mathematical Models for Constrained Layer Damped Beam

- The Mead-Markus Model

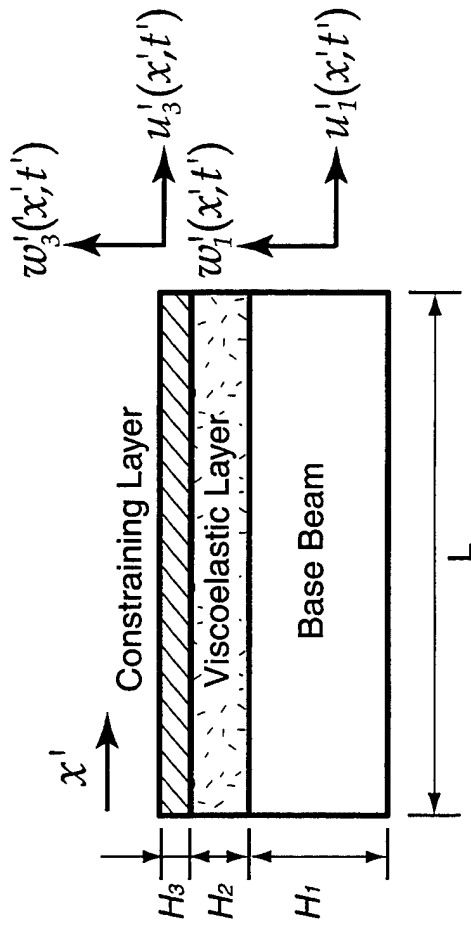
$$w_1' = w_3' \text{ and } u_1' = \frac{E_3 A_3}{E_1 A_1} u_3'$$

- The Modified Mead-Markus Model

$$w_1' = w_3' \text{ and } u_1' \neq u_3'$$

- The TD Model

$$w_1' \neq w_3' \text{ and } u_1' \neq u_3'$$



Experiment Setup and Procedure

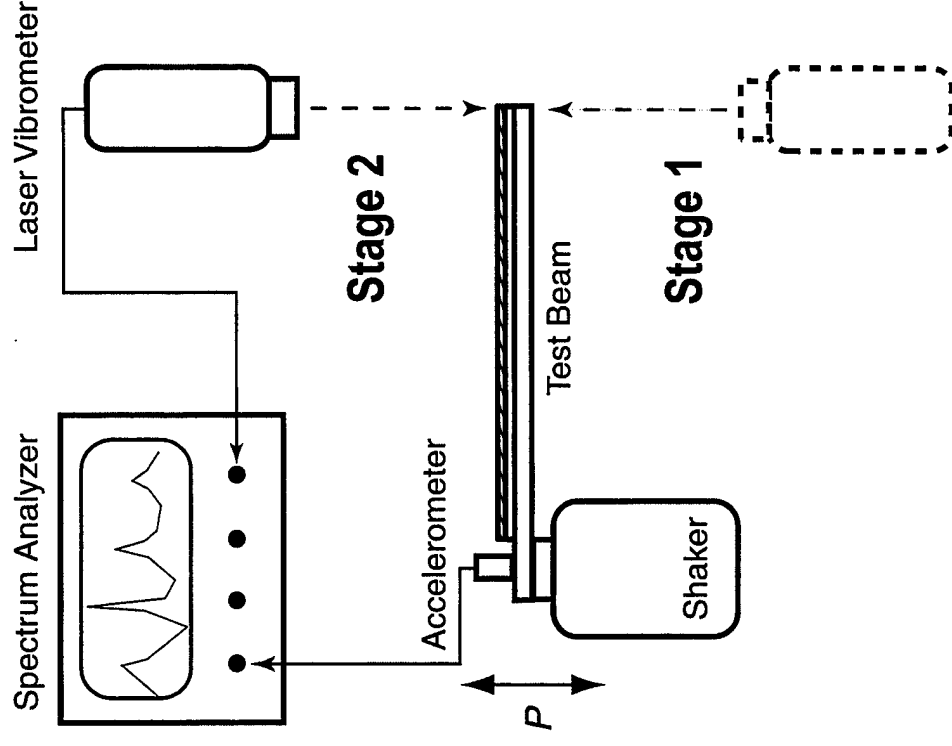
• Procedure

Stage 1-

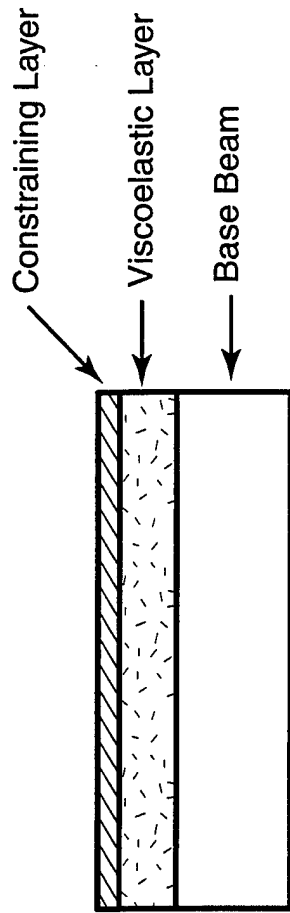
Measure the frequency response of the base beam

Stage 2-

Measure the frequency response of the constraining layer



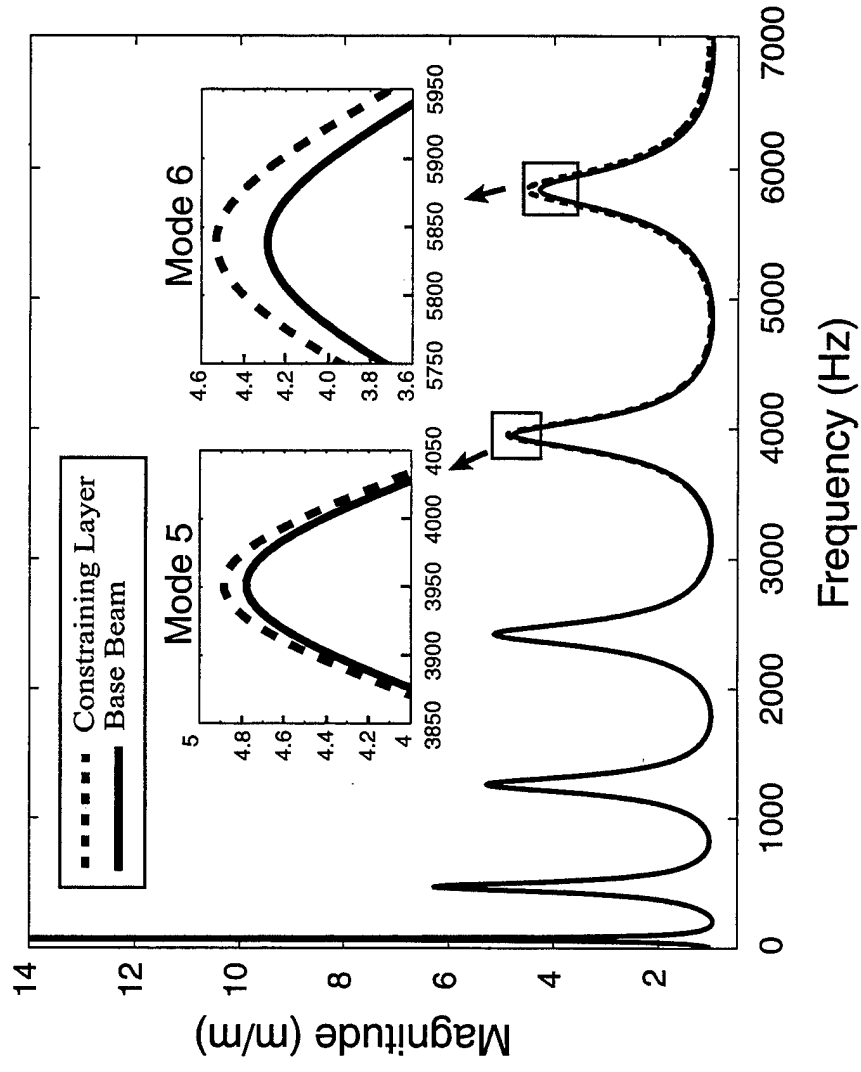
• Configurations of Specimens



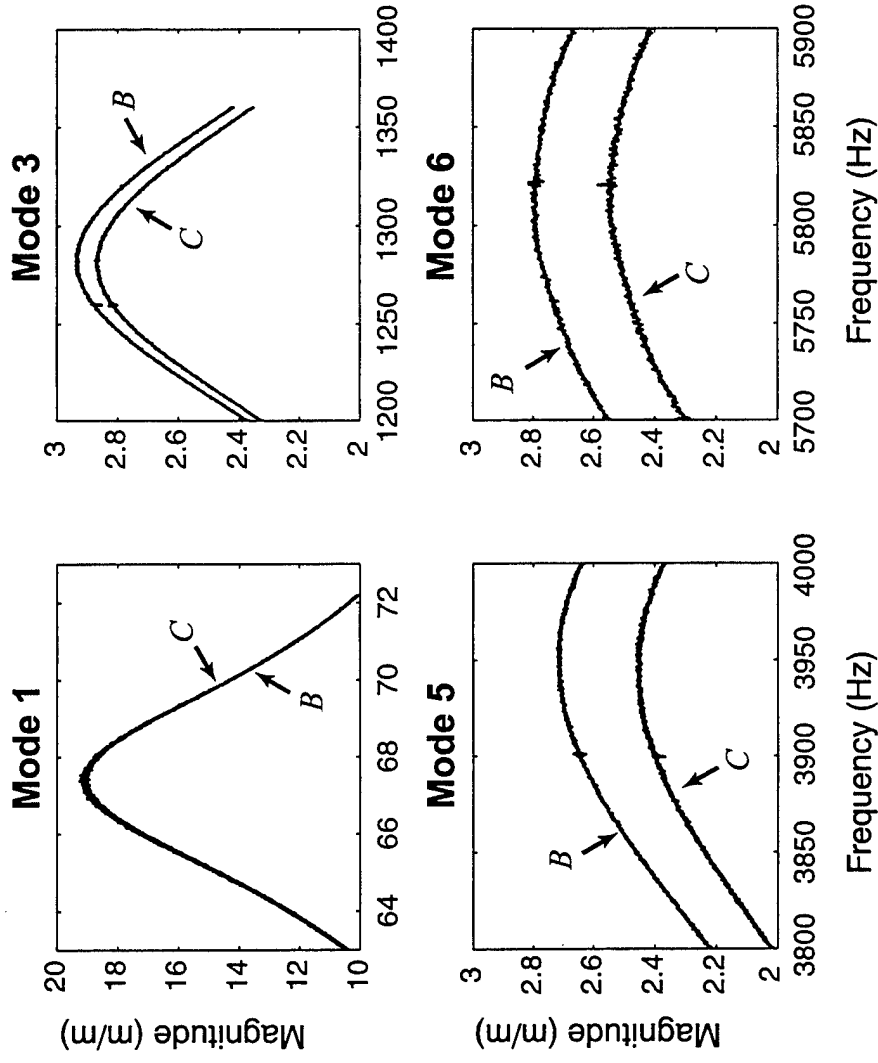
Specimen 1	Base Beam	Viscoelastic Layer	Constraining Layer
Length (mm)	150	150	150
Width (mm)	12	12	12
Thickness (mm)	2.2	0.75	0.80
Material	Al 2024	ISD 112	Al 2024
Modulus (MPa)	E: 69000	G: 0.1 ~ 0.6	E: 69000
Loss Factor (%)	0.29 ~ 0.04	30 ~ 90	0.29 ~ 0.04
Mass density (Kg/m ³)	2700	1060	2700

Results

• Theoretical Prediction (the TD Model)



• Experimental Results

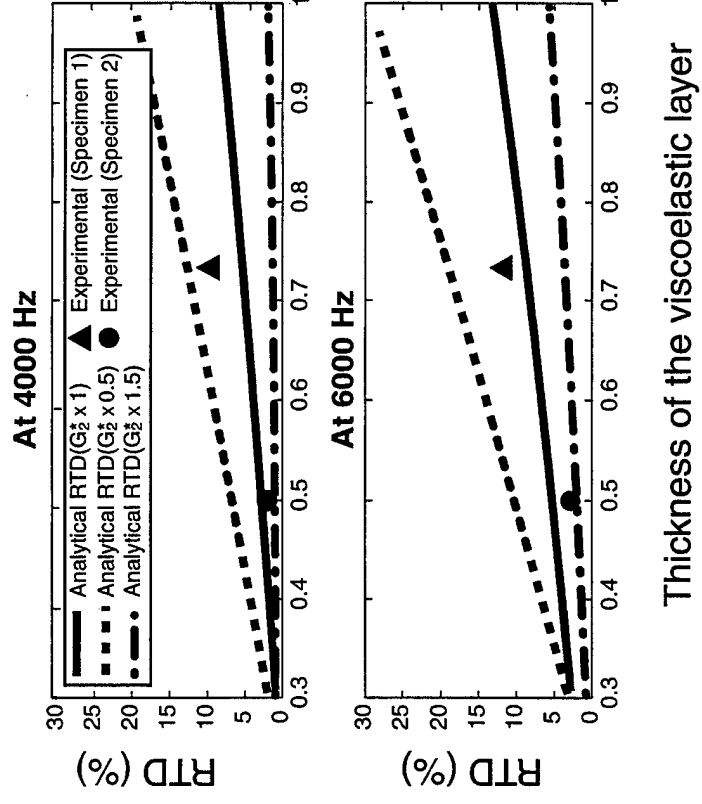
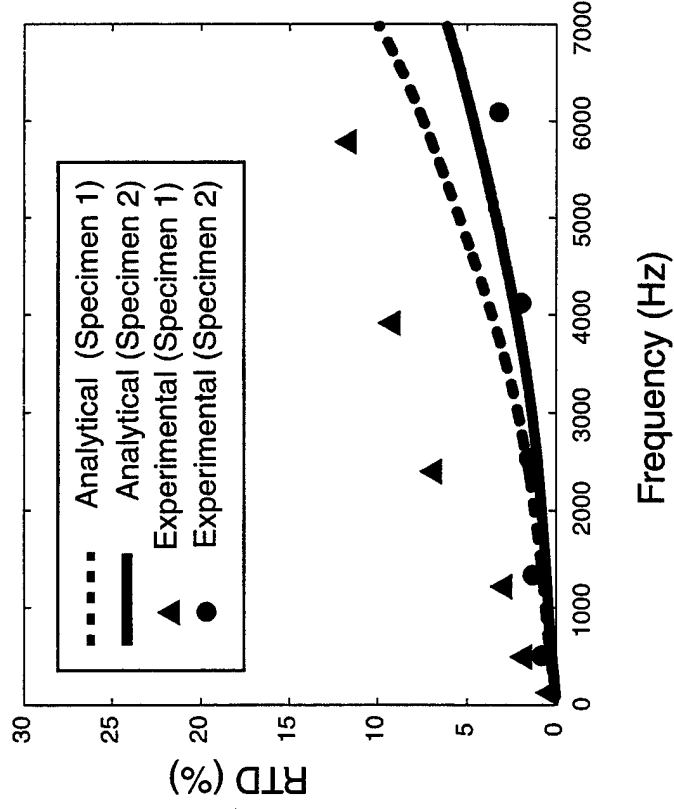


B = frequency response of the base beam

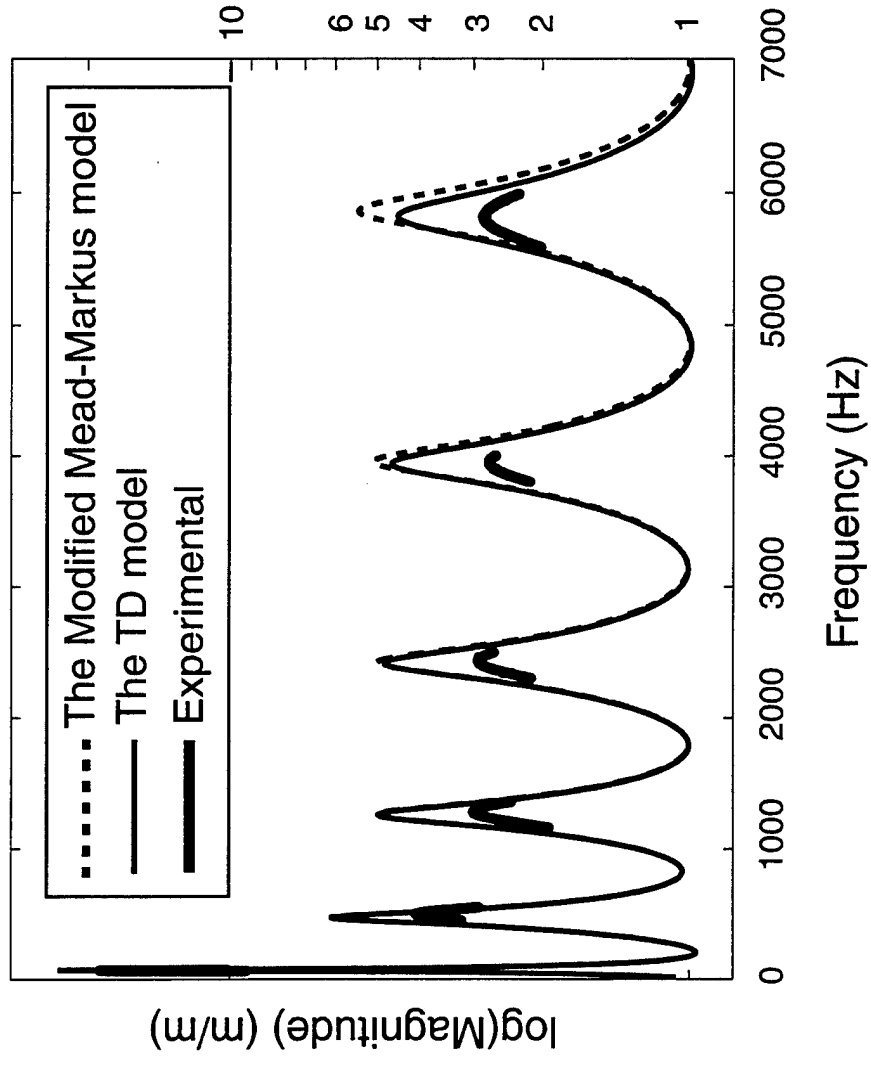
C = frequency response of the constraining layer

Discussion

- $RTD \left(= \left| \frac{w'_1 - w'_3}{w'_1} \right| \right)$



•Frequency Response of the Base Beam



Active Control of Turbulent Boundary Layer Induced Sound Radiation from Aircraft Style Panels

by

Gary P. Gibbs
Structural Acoustics Branch
NASA Langley Research Center
Hampton, VA 23681

Kenneth W. Eure
Naval Surface Warfare Center
PHD Dam Neck Detachment
1922 Regulus Avenue
Virginia Beach, VA 23461-2097

John W. Lloyd
Department of Mechanical Engineering
Virginia Tech
Blacksburg, VA 24061

ABSTRACT:

Reduction of interior noise in commercial and military aircraft has been a strong focus for many years. Active methods have been proposed for noise control for the low frequency range because of their potential weight and size savings over conventional passive systems. Considerable work in tonal noise control has been conducted over the last two decades, and commercial systems are available on several types of commercial and general aviation aircraft. Boundary layer noise transmission is one of the dominant noise source in sub-sonic and supersonic aircraft. Recently active control technology has been expanded to handle TBL type noise sources that are, for all practical purposes, spatially and temporally incoherent.

In this paper, the results of active control of TBL induced sound radiation will be presented. The active control approach was experimentally investigated at the Arnold Engineering Development Center (AEDC) in the von Karman tunnel A. In this test, a panel was constructed similar to the sidewall of an aircraft; however, the panel was flat to allow a simple incorporation into the wind tunnel wall. The panel included three frames and three stringers similar in cross section to the Boeing 717 aircraft, and provided a net arrangement of 6 aircraft bays. The static in plane stress normally associated with aircraft cabin pressurization was provided via a tensioning fixture. Tensioning was applied to simulate the aircraft in flight at 40,000 feet. The panel was mounted in place of the model injection doors in the tunnel floor. Thus the smooth "exterior" side was subjected to TBL flow inside the tunnel, and the other (interior) side radiated sound into the model preparation room. Accelerometers were mounted on the interior side of the panel, and microphones were positioned in the model preparation room to monitor sound radiation.

The control method employed an Active Structural Acoustic Control (ASAC) strategy in a feedback control topology. The system utilizes structurally mounted piezoceramic (PZT-5A) control actuators, accelerometers with sound radiation filters, and a Generalized Predictive Control (GPC) technique to minimize the total sound power radiating from the structure. In this method sound radiation is estimated using surface mounted accelerometers and a sound radiation estimation technique termed "radiation modal expansion" to estimate the orthogonal sound radiation components in real time. These radiation components are fed through GPC derived compensators to drive the PZT control actuators (feedback topology).

Experiments were conducted at both Mach 0.8 and Mach 2.5 flow conditions, and active control was performed on a single bay, and two bays. The results demonstrate reductions in total radiated sound power on the order of 10 - 15 dB at resonances, and 5 - 10 dB integrated over the band width of 150 - 800 Hz. Although the goals was to reduce sound radiation the vibration levels were also reduced. For example, the results demonstrate reductions of the center mounted accelerometer of 10 - 20 dB at panel resonances, and 5 - 11 dB integrated over a bandwidth of 150 - 800 Hz.

Active Control of Turbulent Boundary Layer Induced Noise Transmission

Gary P. Gibbs, NASA LaRC

Ken Eure, NRC

John Lloyd, Virginia Tech



Structural Acoustics Branch
NASA Langley Research Center

Overview

- **Overview**
- **von Karman tunnel A {AEDC} test**
 - **Test configuration**
 - **Control system configuration**
 - ♦ **Radiation Modal Expansion (RME)**
 - ♦ **Generalized Predictive Control (GPC)**
 - **Test conditions**
 - ♦ **Mach 0.8**
 - ♦ **Mach 2.5**
- **Conclusions**
- **Future work**



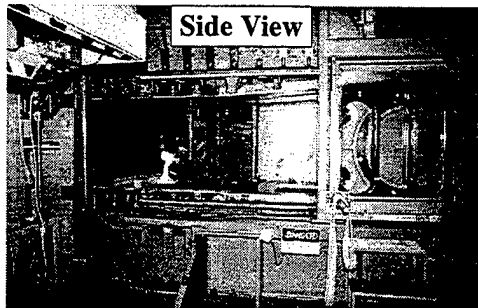
Structural Acoustics Branch
NASA Langley Research Center

von Karman Gas Dynamics Facility Tunnel A

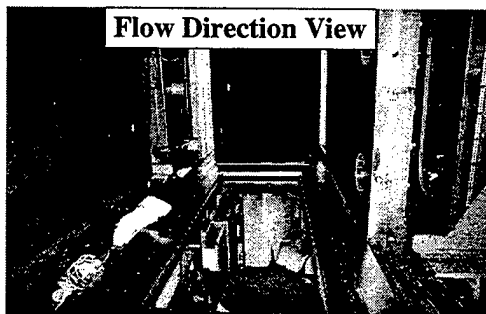
Arnold Engineering Development Center (AEDC)

Features

- 40" x 40" test section
- Flow speeds from 0.7M to 5.5 M
- Relatively low background noise
- Continuous operation



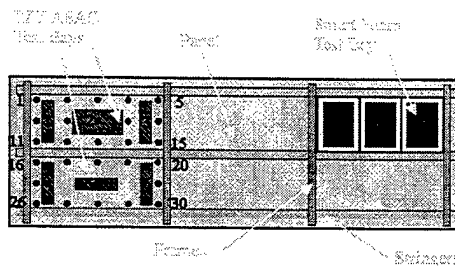
Flow Direction View



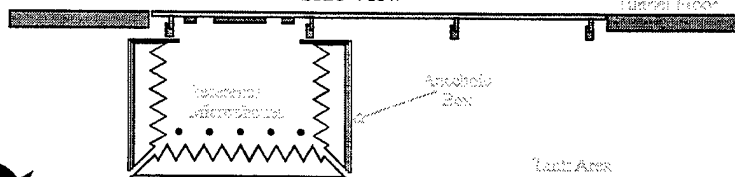
Structural Acoustics Branch
NASA Langley Research Center

AEDC Test Panel Schematic

Bottom View

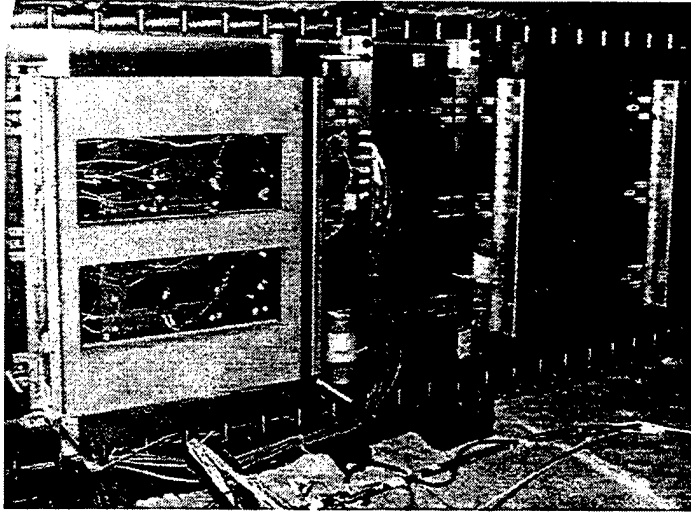


Side View



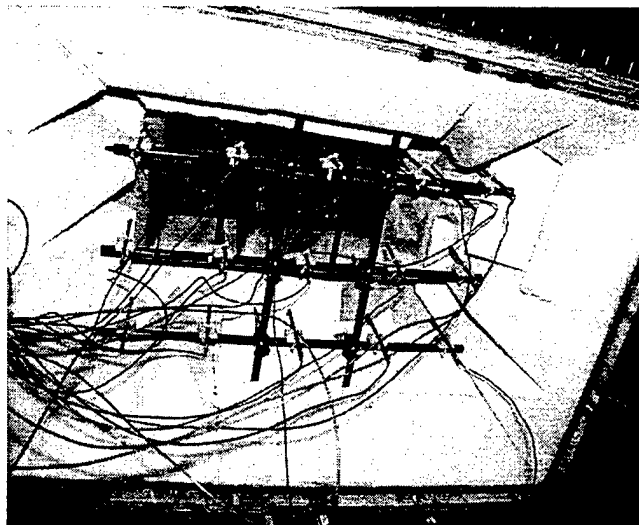
Structural Acoustics Branch
NASA Langley Research Center

NASA panel viewed from tank



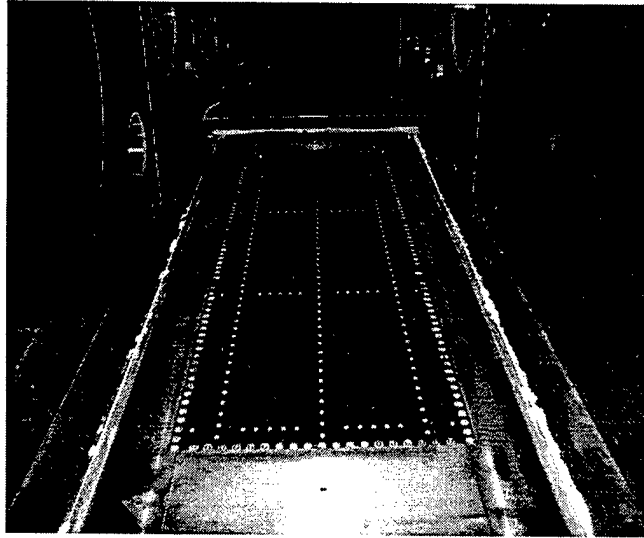
Structural Acoustics Branch
NASA Langley Research Center

Microphone configuration



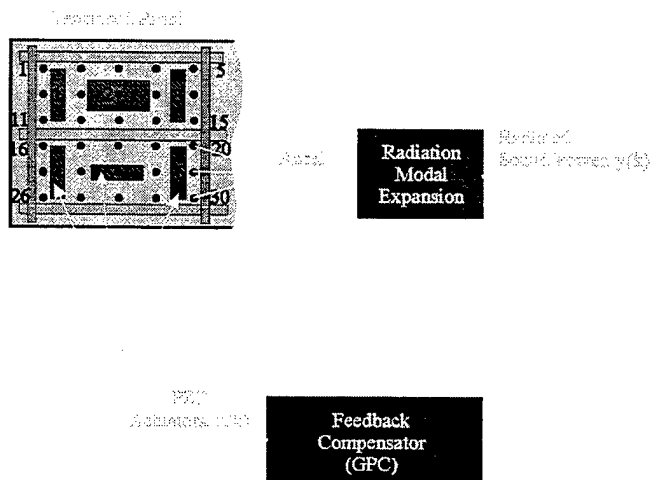
Structural Acoustics Branch
NASA Langley Research Center

NASA panel viewed from tunnel



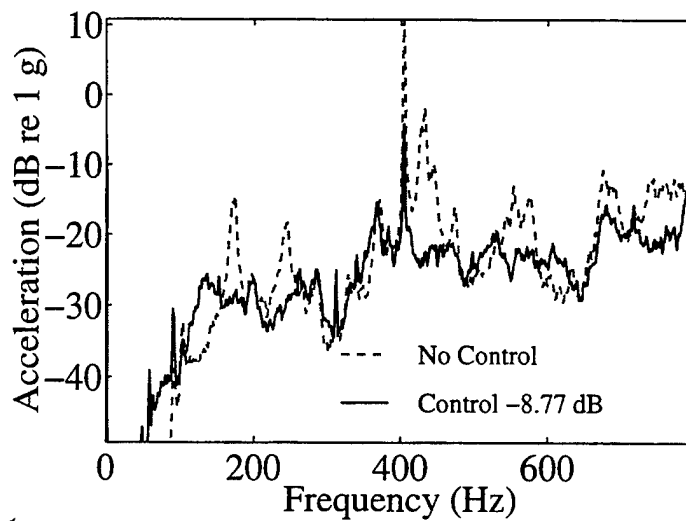
Structural Acoustics Branch
NASA Langley Research Center

ASAC controller schematic Generalized Predictive Control and Radiation filters



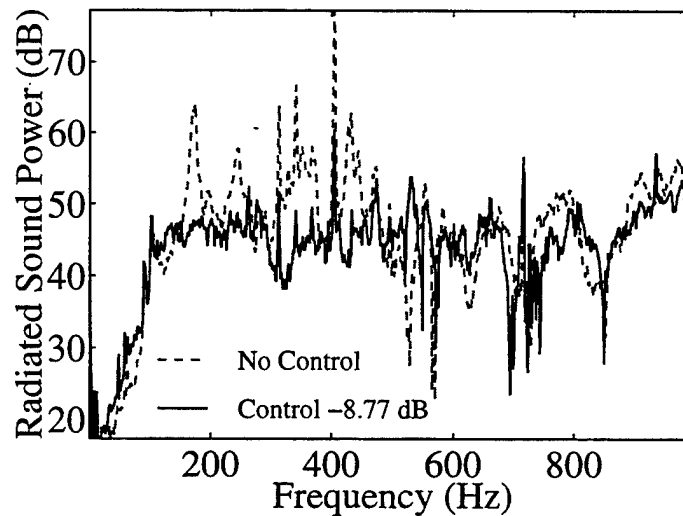
Structural Acoustics Branch
NASA Langley Research Center

Autospectrum of center mounted Accel (#8) Bay 1, Mach 0.8



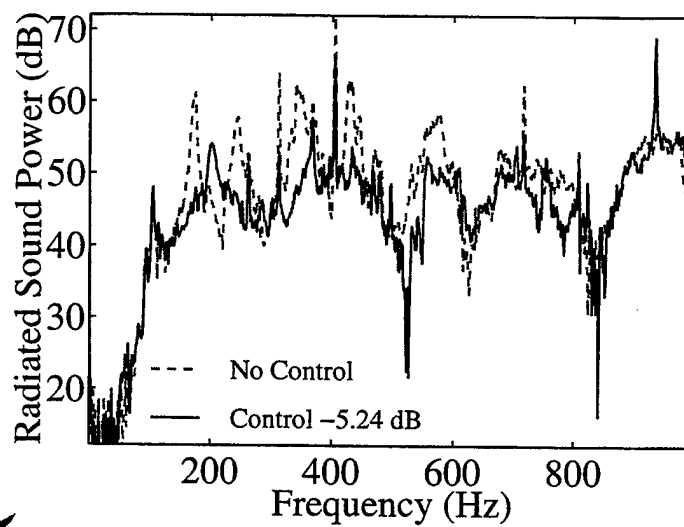
Structural Acoustics Branch
NASA Langley Research Center

Radiated sound power estimated using radiation filters Bay 1, Mach 0.8



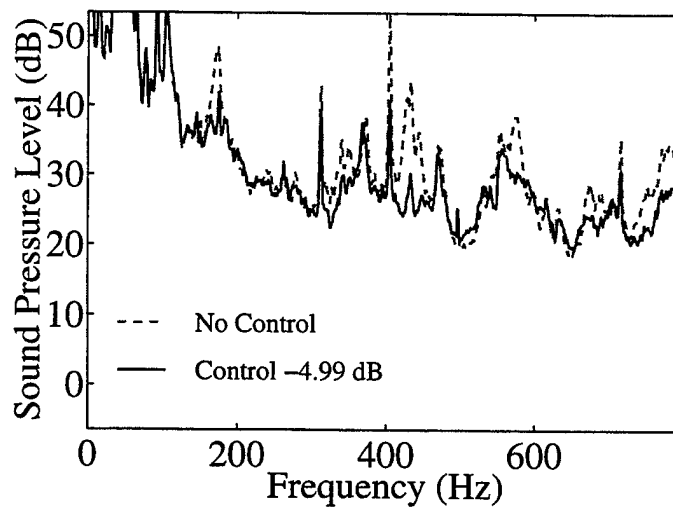
Structural Acoustics Branch
NASA Langley Research Center

Radiated sound power estimated using radiation filters
Bay 2, Mach 0.8



Structural Acoustics Branch
NASA Langley Research Center

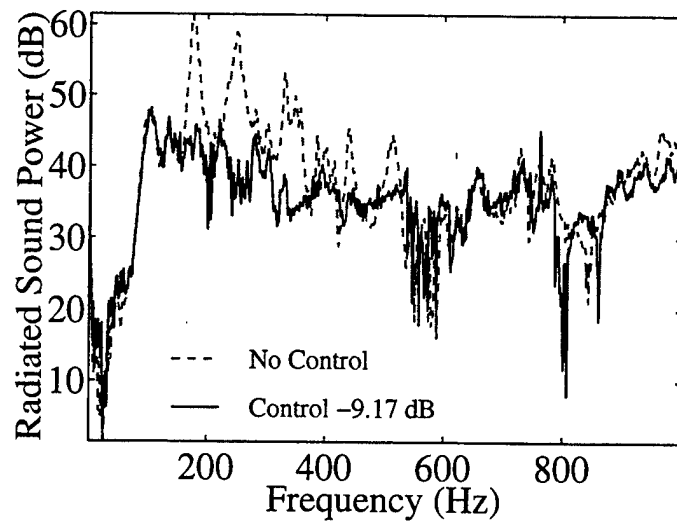
Radiated sound power summed over 15 microphones
Mach 0.8



Structural Acoustics Branch
NASA Langley Research Center

Radiated sound power estimated using radiation filters

Bay 1, Mach 2.5



Structural Acoustics Branch
NASA Langley Research Center

Conclusions

- ASAC of aircraft style panels
 - 10 - 15 dB reduction of peak responses
 - 5 - 10 dB reduction (150 - 800 Hz)
- ASAC of two bays simultaneously with independent I.D.
- Active/passive control of aircraft style panels
 - 2 - 8 dB active reduction (400 - 800 Hz)
 - 10 - 12 dB overall reduction (150 - 2000 Hz)



Structural Acoustics Branch
NASA Langley Research Center

PENNSTATE



*Enhanced Low Frequency Transmission Loss
of Light Weight Trim Panels Using PZT
Inertial Actuators*

Wenchao Huang

Aircraft Structure Research Institute, Xi'an, P.R.C.

G. Koopmann, W. Chen, S. Sharp

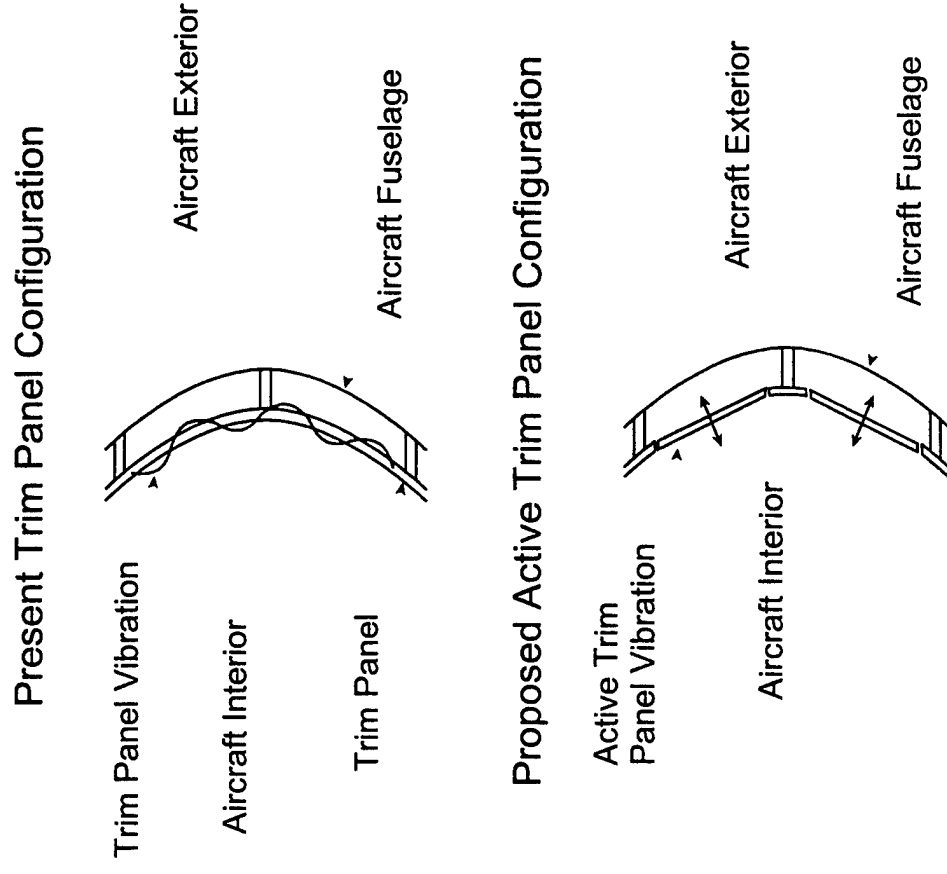
The Pennsylvania State University



Enhanced Low Frequency Transmission Loss

Overall Approach

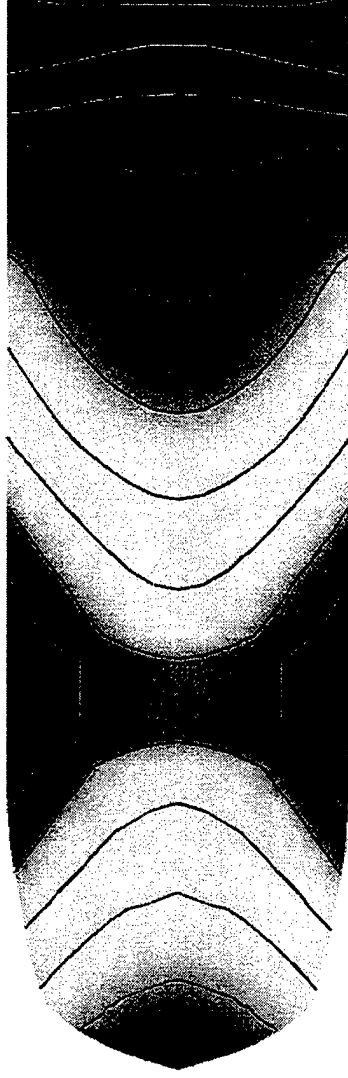
- Segment larger trim panels into an array of smaller trim panels
- Design trim panel to be very stiff allowing only rigid body motion over frequency range of control
- Attach sensors and actuators to control the motion of individual trim panels
- Minimize the motion of each individual trim panel to achieve global sound level reductions



Enhanced Low Frequency Transmission Loss

Targeted Interior Noise Characteristics

Sound Pressure Level (dBA) Inside a Prop Engine Boeing Aircraft



Green Aircraft



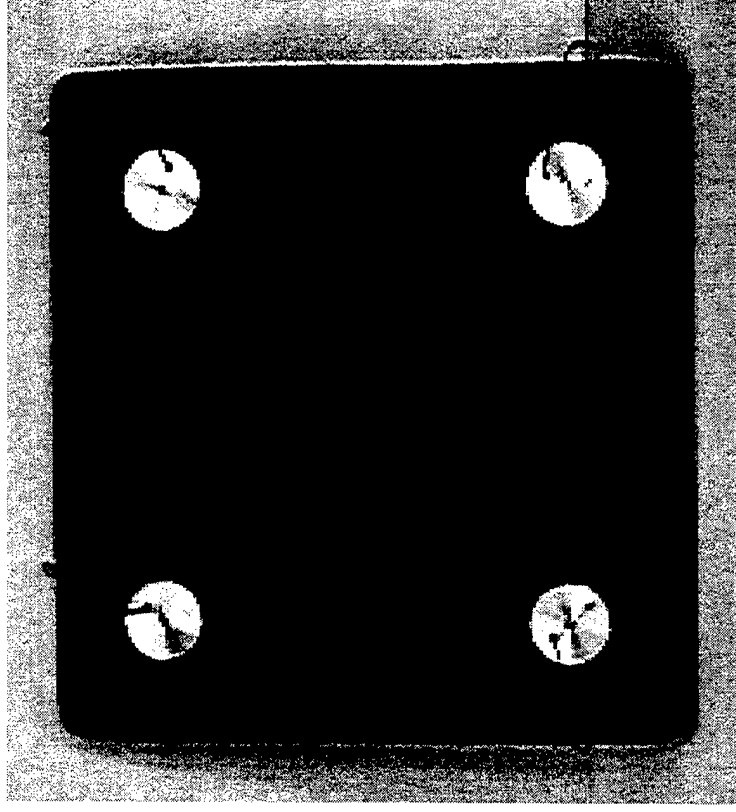
- Figure shows regions of high energy transmission into aircraft cabin at blade tone frequency



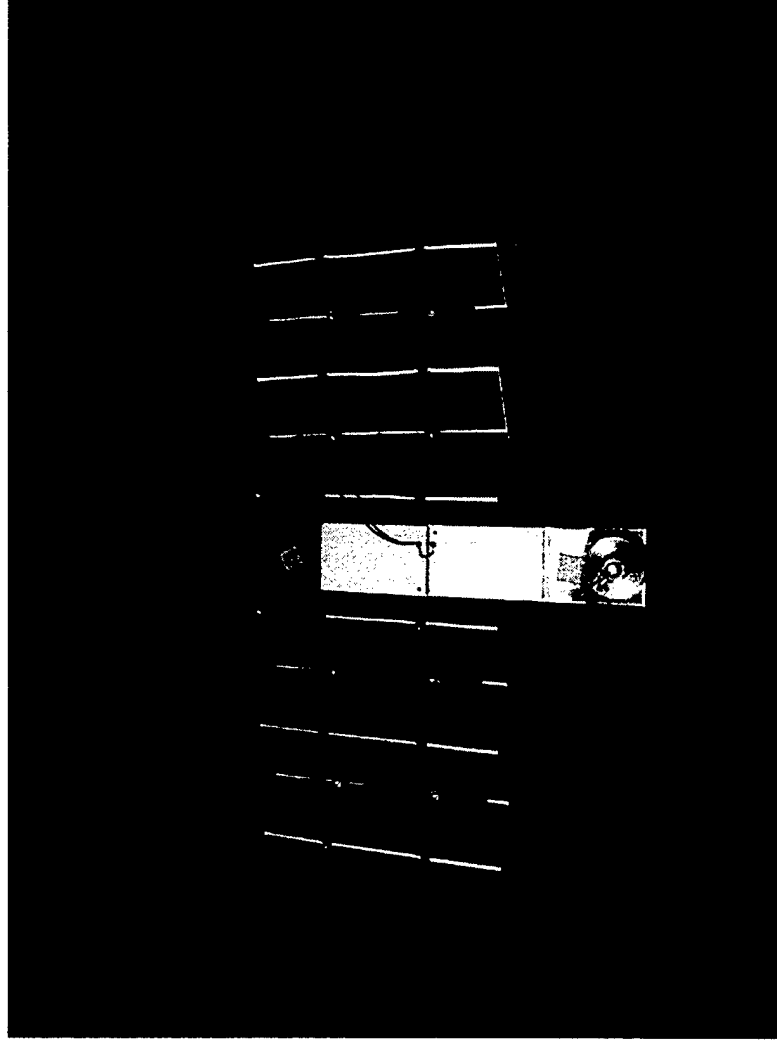
Overview of Presentation

- Overall Approach
- Past Research
- Current Trim Panel and Actuator Design
- Control System
- Experimental Results
- Conclusion and Future Work

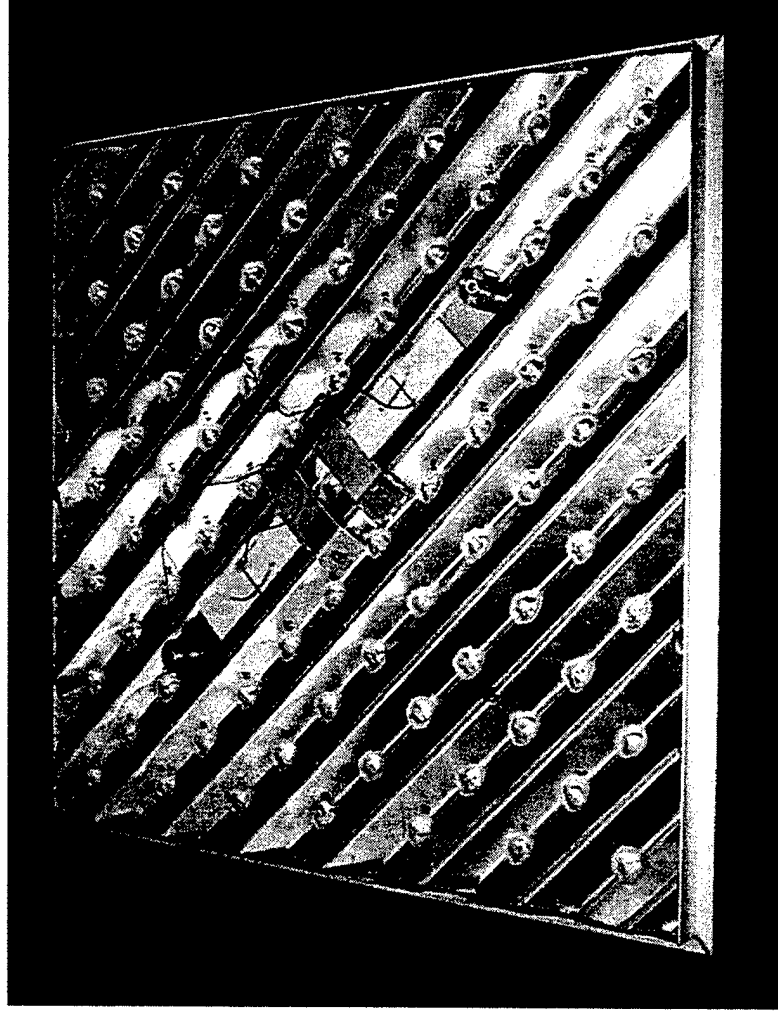
- Honeycomb composite panel
 - 18 x 18 x 1 inches
 - Aluminum core
 - Carbon fiber face sheets
 - 1.55 lb/ft²
- Inertial shakers and accelerometers embedded at 4 corners
- Laboratory experiments produced an increase of 6 - 10 dB in transmission loss in the 80 Hz and 125 Hz 1/3 octave bands

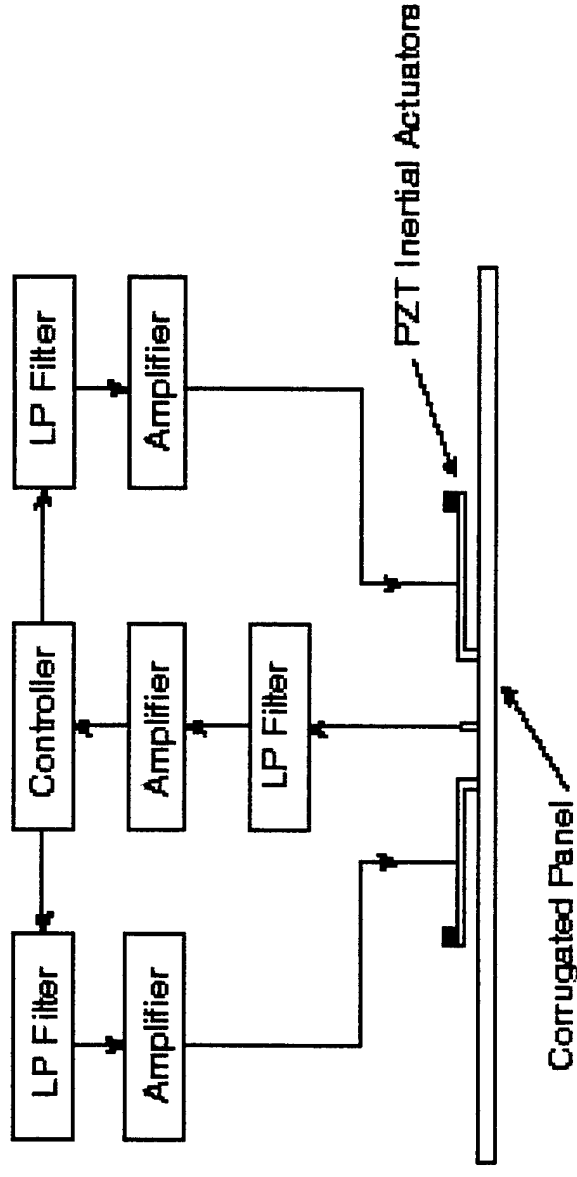


- Piezoceramic driven beam with an attached mass
- Weighs 45 grams
- 0.1 N force
- First resonance at 25 Hz



- Two corrugated aluminum panels attached orthogonally
- First bending mode occurs above 250 Hz
- 1.0 lb/ft²
- A second pair of actuators are mounted symmetrically on opposite side



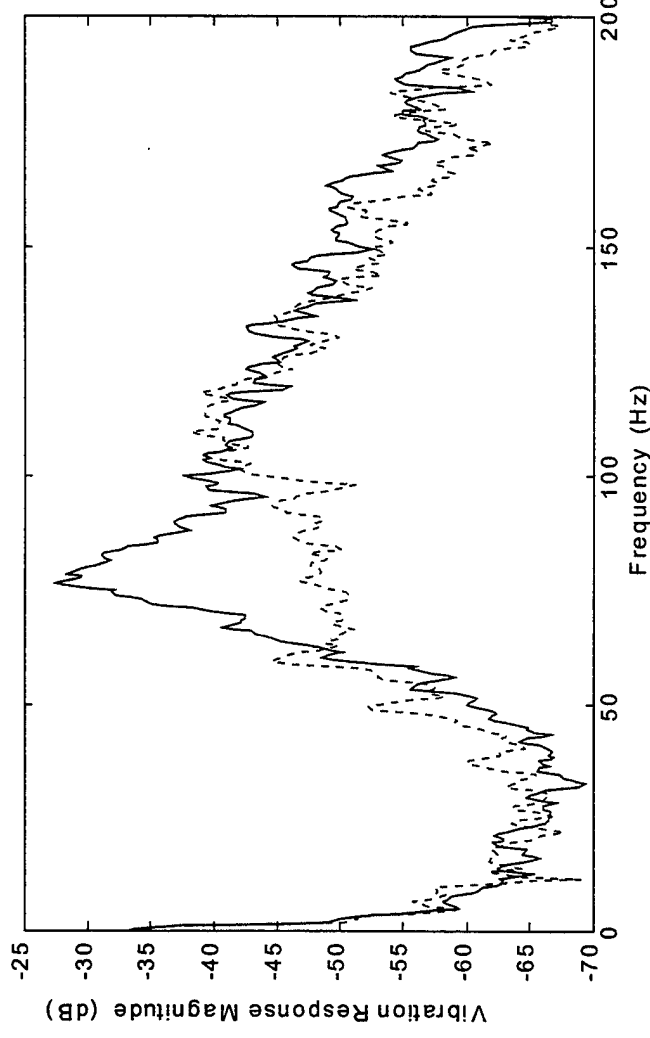


- Control system is SISO feedback control whose error signal is the acceleration at the panel's center
- Analog control circuit consists of serially connecting three Tow-Thomas biquad filters



Enhanced Low Frequency Transmission Loss

Experimental Results - Vibration Reduction

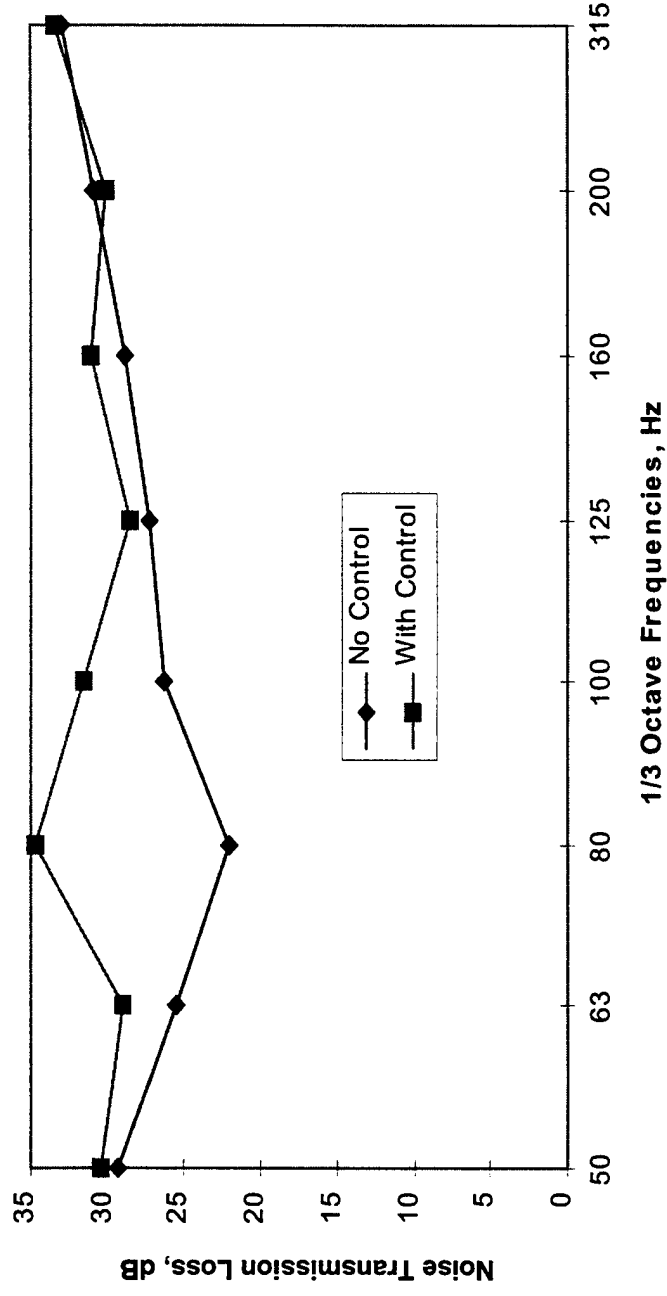


- Greater than 15 dB vibration reduction in acceleration at resonance; solid line - no control; dash line - with control



Enhanced Low Frequency Transmission Loss

Experimental Results - Noise Transmission Loss



- Increase of up to 15 dB in transmission loss due to active control

*Conclusions***Conclusions:**

- Developed trim panel which is lightweight and ultrastiff
- Designed PZT driven inertial actuators and simple feedback control circuit
- Demonstrated both the reduction in vibration sound transmission loss reductions

Future Work:

- Demonstrate the method with multiple trim panels mounted on an aircraft fuselage to confirm that locally controlled trim panels produce global reductions in overall sound power within the cabin



ACTIVE CONTROL OF WAVE TRANSMISSION THROUGH STRUTS

I. Pelinescu, B. Balachandran, and D. Ortel
Department of Mechanical Engineering
University of Maryland
College Park, MD 20742-3035

Project Summary

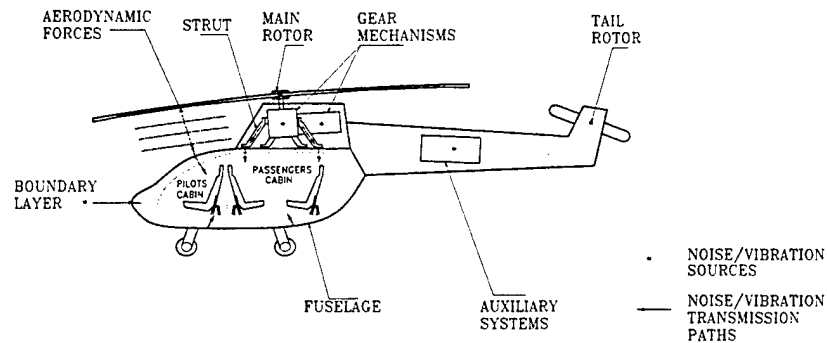
The work presented in this paper is a part of an extended research effort, which is being pursued with the aim of reducing interior noise and vibration levels in a helicopter cabin in a frequency range extending up to 6 kHz. Noise in a helicopter cabin can arise due to air borne and structure borne mechanisms. The overall objective of this work is to address the problem of reducing structure borne noise transmitted into a helicopter cabin by reducing the vibrations transmitted from the gearbox mechanisms through the gearbox support struts to the fuselage. Specific objectives include the following: a) development of mechanics based models for mechanisms of noise/vibration transmission through finite length strut-like structures including integration of actuation schemes and b) investigation and validation of schemes to control noise/vibration transmission through strut-like structures over different frequency bandwidths. For attenuating longitudinal and flexural vibrations at the fuselage attachment end, piezoelectric stack and magnetostrictive actuators are placed at the end of the strut along axial and transverse directions, respectively. A linear model of the actuator accounting for mechanical and electrical or magnetic boundary constraints respectively is developed and integrated with the mechanics model of the cylindrical strut. The resulting ensemble is analyzed in the frequency domain, and the control force input generated by the actuator and related control parameters are determined. The longitudinal and flexural displacements at the end of the strut attached to the fuselage are calculated in numerical simulations of the open-loop system. The potential to attenuate both longitudinal and flexural vibrations transmitted to a host structure through a support strut was thus examined. Furthermore displacement feedback control of flexural wave transmission through a cylindrical strut by using multiple piezoelectric stack actuators has been investigated numerically with the help of a mechanics based model.

In this work, piezoelectric stack and magnetostrictive actuators were considered to reduce longitudinal and flexural vibrations transmitted to a host structure through a finite length strut. The electro-mechanics and magneto-mechanics of the actuators were integrated with the strut mechanics. A mechanics model of the strut-actuator assembly, which can be used in the studies of active control of wave transmission, was developed and presented. The results of the simulations point to the potential for actively controlling longitudinal and flexural wave transmission by using multiple piezoelectric actuators. The current work points out to the importance of considering near field effects when controlling flexural waves transmitted through a finite strut and appropriately locating the actuators. High frequency tones inside a helicopter cabin are primarily due to structure borne noise transmission through the gearbox struts. The outcome of this work demonstrates the viability of using active materials for controlling noise/vibration transmission through gearbox struts into rotorcraft cabins.

Acknowledgments

The support received from the U.S. Army Research Office under contract number DAAH 049610334 is gratefully acknowledged. Drs. Tom Doligalski and Gary Anderson are the technical monitors for this contract.

Motivation



- Control of interior noise levels in rotorcraft:
 - Sources
 - Transmission paths
 - Receiving space
- Active control of structure borne noise and vibration:
 - Path treatment
- Vibration transmitted through gearbox struts into rotorcraft cabin in frequency range 10 Hz - 6000 Hz

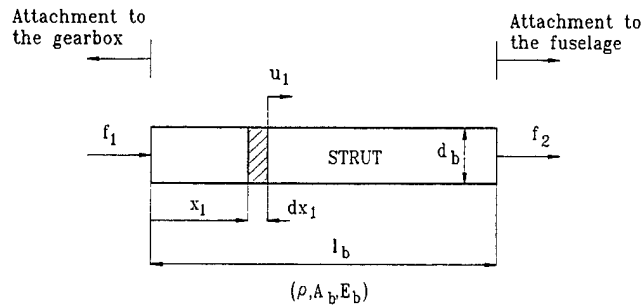


Previous Work

1. Papers and reports related to the following projects:
 - (a) Reduction of Helicopter Interior NOise (RHINO); Joint European Project, 1993/1995
 - (b) Agusta A-109 Cabin Noise Quieting Program, 1976/1978
 - (c) EH101 Vibration Control Program, Westland Helicopter Ltd., 1988/1990
2. Papers by I. Pelinescu and B. Balachandran, proceedings of SPIE, March 1998 and March 1999
3. Paper by D. Ortel and B. Balachandran, proceedings of SPIE, March 1999
4. US Patents - Helicopters vibrations control
5. NASA Technical Reports



Cylindrical Strut - Longitudinal Wave Transmission



- Equation of motion:

$$\frac{\partial^2 u_1}{\partial x_1^2} - \frac{1}{c^2} \frac{\partial^2 u_1}{\partial t^2} = 0$$

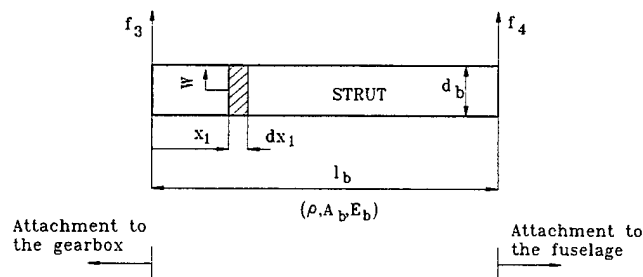
- Wave type solution:

$$u_1 = U_1(x_1, \omega)e^{j\omega t} = (C_1 e^{-jk_l x_1} + C_2 e^{jk_l x_1})e^{j\omega t}$$

- Boundary conditions: forces



Cylindrical Strut - Flexural Wave Transmission



- Equation of motion:

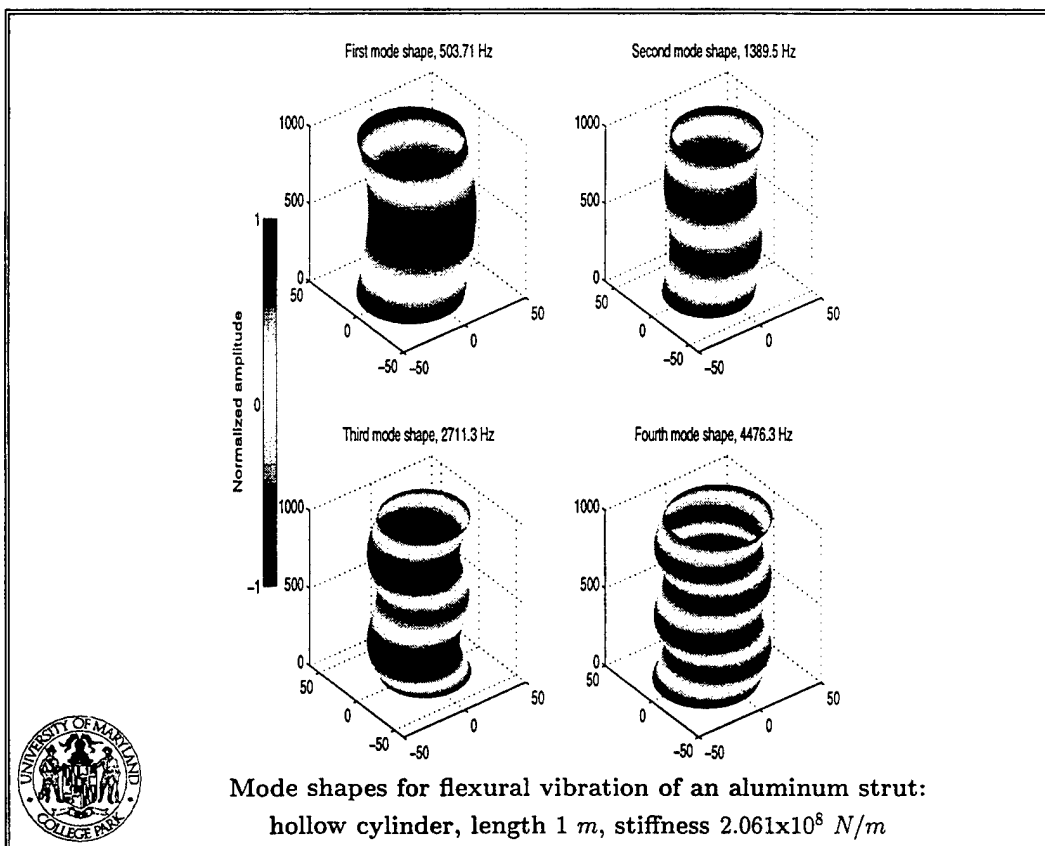
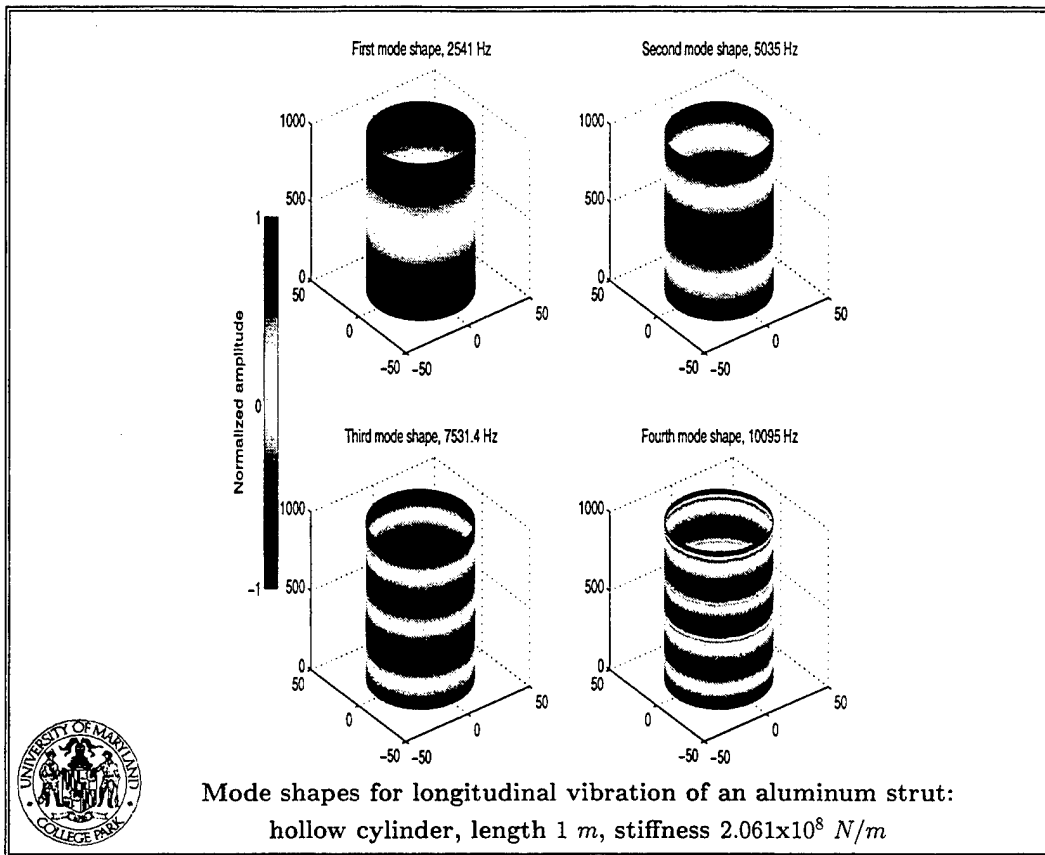
$$\frac{\partial^4 w}{\partial x_1^4} + \frac{\rho A_b}{E_b I_b} \frac{\partial^2 w}{\partial t^2} = 0$$

- Wave type solution:

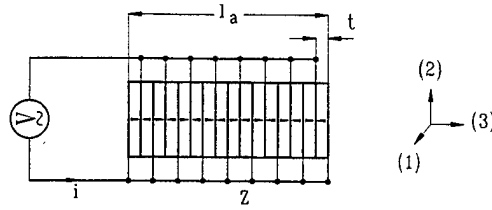
$$w = W(x_1, \omega)e^{j\omega t} = (C_1 e^{k_f x_1} + C_2 e^{-k_f x_1} + C_3 e^{jk_f x_1} + C_4 e^{-jk_f x_1})e^{j\omega t}$$

- Boundary conditions: forces & moments





Actuation Mechanism - Piezoelectric Actuator Model



- Constitutive equations:

$$S_3 = s_{33}^D T_3 + g_{33} D_3$$

$$E_3 = -g_{33} T_3 + \beta_{33}^T D_3$$

- Electric potential on the surface of the electrodes:

$$\varphi|_{x_2=0; x_2=l_a} = \pm V e^{j(\omega t + \theta)}$$

- Electric boundary conditions:

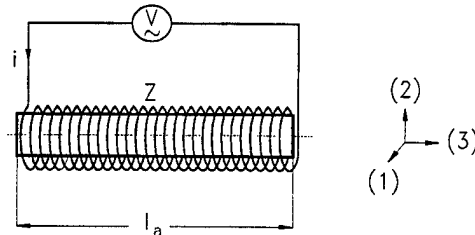
$$D_3 = \frac{2V}{j\omega A_a Z} e^{j(\omega t + \theta)}, \quad Z = \frac{1}{j\omega C}$$

- Equation of motion:

$$\frac{\partial^2 u_2}{\partial x_2^2} - \frac{1}{(v_3^D)^2} \frac{\partial^2 u_2}{\partial t^2} = 0$$



Actuation Mechanism - Magnetostrictive Actuator Model



- Constitutive equations:

$$S_3 = s_{33}^H T_3 + d_{33}^m H_3$$

$$B_3 = d_{33}^m T_3 + \mu_{33}^T H_3$$

- Driving current applied:

$$i = \frac{2V}{Z} e^{j(\omega t + \theta)}$$

- Magnetic boundary conditions:

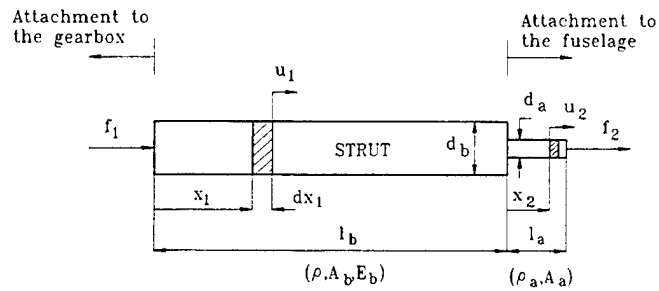
$$H_3 = \frac{N 2V}{l_a Z} e^{j(\omega t + \theta)}, \quad Z = j\omega L$$

- Equation of motion:

$$\frac{\partial^2 u_2}{\partial x_2^2} - \frac{1}{(v_3^H)^2} \frac{\partial^2 u_2}{\partial t^2} = 0$$



Active Strut - Mechanics Model Longitudinal Wave Transmission



- Equation of motion in strut:

$$\frac{\partial^2 u_1}{\partial x_1^2} - \frac{1}{c^2} \frac{\partial^2 u_1}{\partial t^2} = 0$$

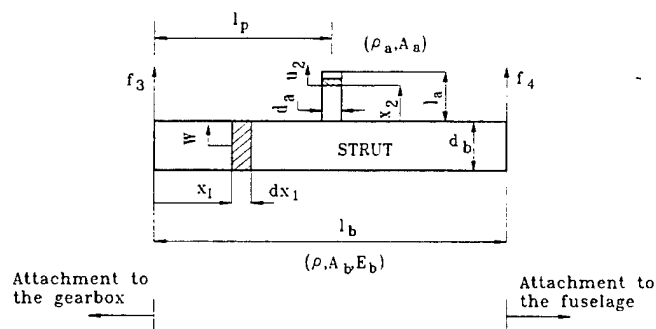
- Equation of motion in actuator:

$$\frac{\partial^2 u_2}{\partial x_2^2} - \frac{1}{(v_3^*)^2} \frac{\partial^2 u_2}{\partial t^2} = 0$$



superscript * corresponds to piezoelectric or magnetostrictive actuator

Active Strut - Mechanics Model Flexural Wave Transmission



- Equation of motion in strut:

$$\frac{\partial^4 w}{\partial x_1^4} + \frac{\rho A_b}{E_b I_b} \frac{\partial^2 w}{\partial t^2} = 0$$

- Equation of motion in actuator:

$$\frac{\partial^2 u_2}{\partial x_2^2} - \frac{1}{(v_3^*)^2} \frac{\partial^2 u_2}{\partial t^2} = 0$$



superscript * corresponds to piezoelectric or magnetostrictive actuator

Frequency Domain Analysis

- Wave type solutions:

$$u_1 = U_1(x_1, \omega)e^{j\omega t} = (C_1e^{-jk_l x_1} + C_2e^{jk_l x_1})e^{j\omega t}$$

$$u_2 = U_2(x_2, \omega)e^{j\omega t} = (Ae^{-jk_{l2} x_2} + Be^{jk_{l2} x_2})e^{j\omega t}$$

$$w = W(x_1, \omega)e^{j\omega t} = (C_3e^{k_f x_1} + C_4e^{-k_f x_1} + C_5e^{jk_f x_1} + C_6e^{-jk_f x_1})e^{j\omega t}$$

- Boundary conditions: forces & moments

- Displacements at the ends of the strut:

$$\rightarrow \begin{Bmatrix} U_1(0, \omega) \\ U_1(l_b, \omega) \end{Bmatrix} = \begin{bmatrix} \alpha_{11} & \alpha_{12} \\ \alpha_{21} & \alpha_{22} \end{bmatrix} \begin{Bmatrix} F_1 \\ F_2 \end{Bmatrix} + \begin{Bmatrix} \beta_1 \\ \beta_2 \end{Bmatrix} F_c^*$$

$$\rightarrow \begin{Bmatrix} W(0, \omega) \\ W(l_b, \omega) \end{Bmatrix} = \begin{bmatrix} \gamma_{11} & \gamma_{12} \\ \gamma_{21} & \gamma_{22} \end{bmatrix} \begin{Bmatrix} F_3 \\ F_4 \end{Bmatrix} + \begin{Bmatrix} \delta_1 \\ \delta_2 \end{Bmatrix} F_c^*$$

- Control input force amplitude:



Piezoelectric actuator:

$$F_c^* = \frac{g_{33}}{s_{33}^D} \frac{2V}{\omega Z} e^{j\theta}$$

Magnetostrictive actuator:

$$F_c^* = \frac{d_{33}^m A_a N}{s_{33}^H l_a} \frac{2V}{Z} e^{j\theta}$$

Numerical Simulations

- Aluminum hollow cylindrical strut with longitudinal stiffness: $2.061 \times 10^8 \text{ N/m}$ and length 1 m

- Rod shaped multiple layer piezoelectric actuator:

- Material PZT 5H, Morgan Matroc Inc.

- Length $l_a = 38.1 \text{ mm}$

- Diameter $d_a = 6.35 \text{ mm}$

- Layer thickness $t = 50 \text{ }\mu\text{m}$

- Rod shaped magnetostrictive actuator:

- Material Terfenol-D, ETREMA Inc.

- Length $l_a = 75 \text{ mm}$

- Diameter $d_a = 12.7 \text{ mm}$

- Bias stress $T = 32 \text{ MPa}$

- Bias magnetic field strength $H = 79.6 \text{ kA/m}$

- Number of turns of the driving coil $N = 1600$

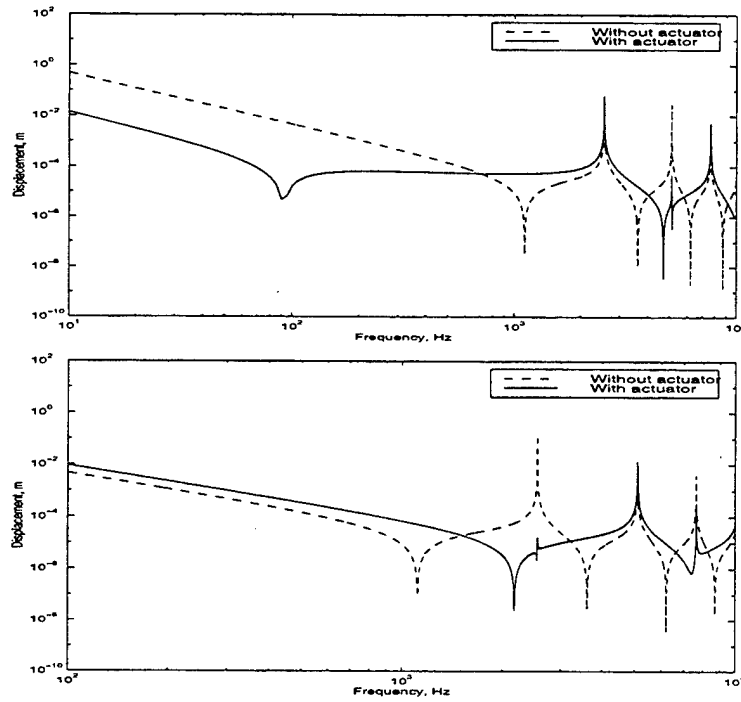
- Amplitudes of external forces:

- Longitudinal forces: $F_1 = 15 \text{ kN}$ and $F_2 = 500 \text{ N}$

- Transverse forces: $F_3 = 500 \text{ N}$ and $F_4 = 50 \text{ N}$

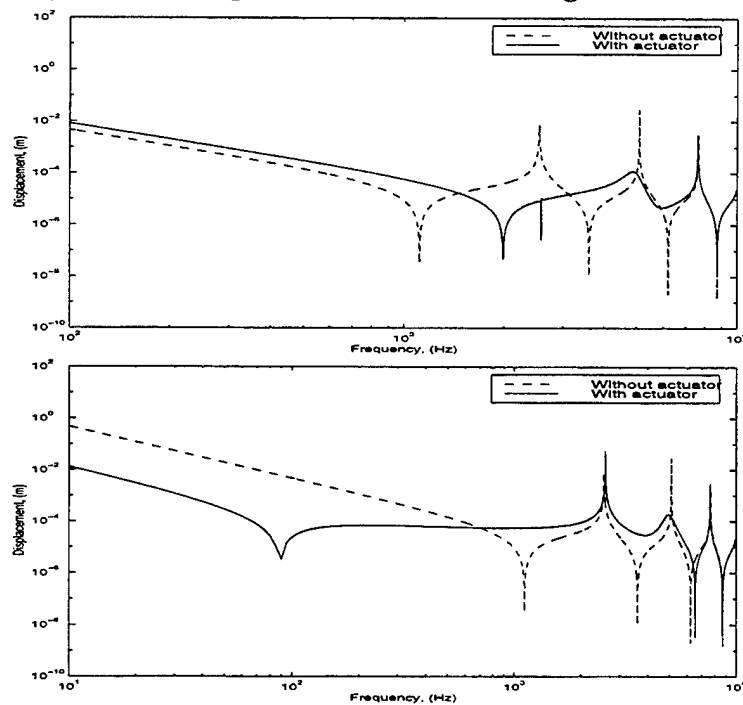


Longitudinal Displacement U_1 at Fuselage Attachment



Open-loop control using piezoelectric actuator: a) electric current $i = 7.66 \text{ A}$ and phase $\theta = 0^\circ$, b) electric current $i = 8.43 \text{ A}$ and phase $\theta = -90^\circ$. Voltage $V = 80 \text{ V}$

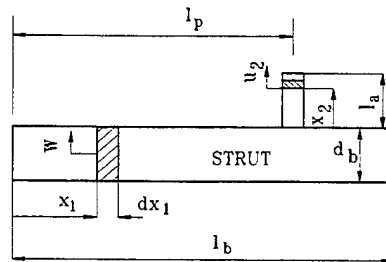
Longitudinal Displacement U_1 at Fuselage Attachment



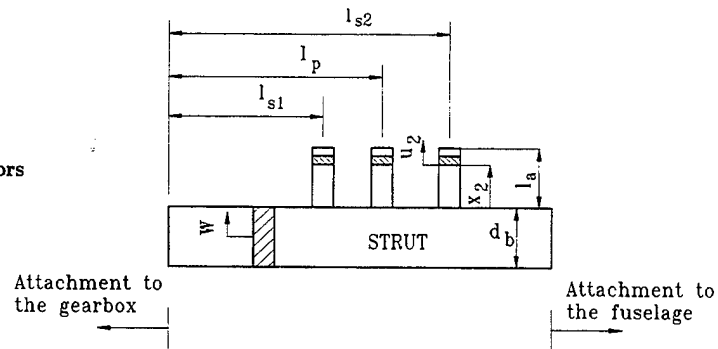
Open-loop control using magnetostrictive actuator: a) electric current $i = 8.05 \text{ A}$ and phase $\theta = 0^\circ$, b) electric current $i = 9.0 \text{ A}$ and phase $\theta = 180^\circ$

Flexural Wave Control - Actuator Arrangements

One actuator arrangement



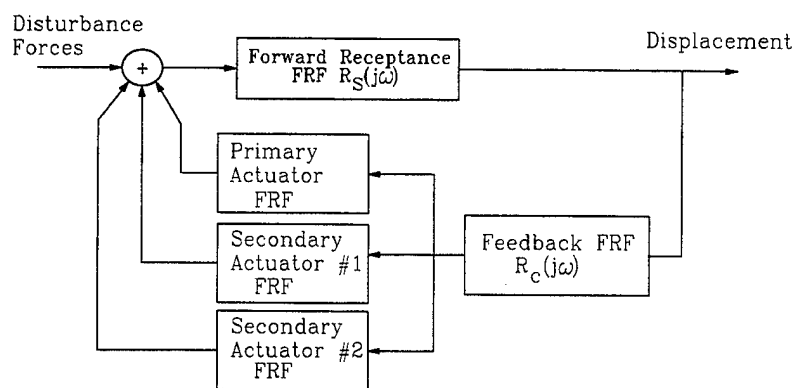
Three actuators arrangement



$$u_2 = U_2(x_2, \omega) e^{j\omega t} = (Ae^{-jk_{l2}x_2} + Be^{jk_{l2}x_2}) e^{j\omega t}$$

$$w = W(x_1, \omega) e^{j\omega t} = (C_3 e^{k_f x_1} + C_4 e^{-k_f x_1} + C_5 e^{jk_f x_1} + C_6 e^{-jk_f x_1}) e^{j\omega t}$$

Displacement Feedback Controller

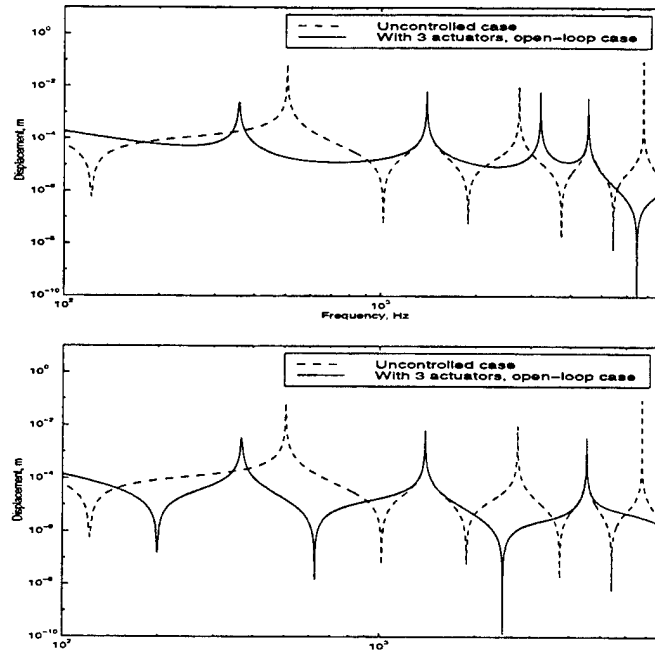


Model based controller

- One and three piezoelectric actuators
- Controller designed for each tone over a frequency bandwidth
- Performance function used to minimize mechanical power supplied to the strut

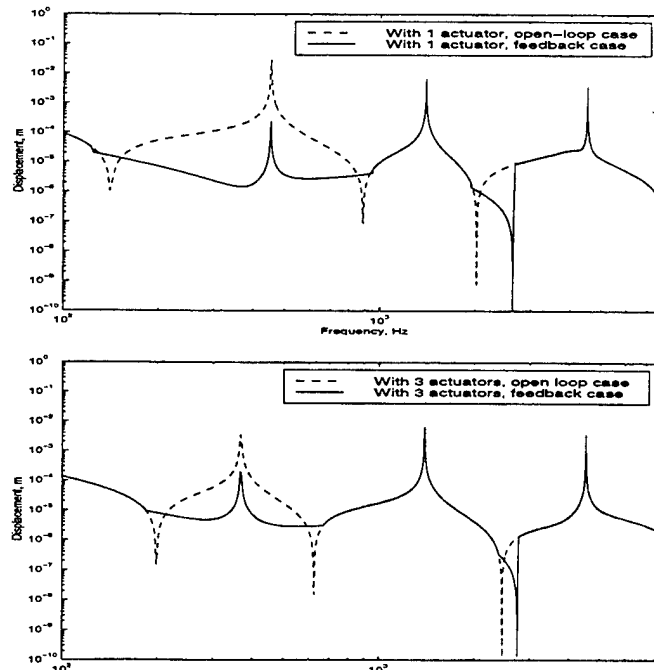


Lateral Displacement W at Fuselage Attachment



Open-loop control using three piezoelectric actuators located at: a) 0.75 m, 0.52 m, 1.0 m and b) 0.61 m, 0.54 m, 0.68 m. Input current $i = 0.08$ A to primary actuator and $i = 0.2$ A to each secondary actuator

Lateral Displacement W at Fuselage Attachment



Feedback control using piezoelectric actuators: a) one actuator and b) three actuators

Modal Vibration Control for PVDF Coated Plates

Lothar Gaul and Uwe Stöbener

Institute A of Mechanics, University of Stuttgart
Pfaffenwaldring 9, D-70550 Stuttgart, Germany
phone +49-(0)711-685-6278, fax +49-(0)711-685-6282
e-mail l.gaul@mecha.uni-stuttgart.de

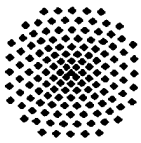
Since complex technical systems, such as aircrafts, space structures and automobiles, have to combine high performance with low weight, passive vibration absorbers often reach their limits. This is why active control of structural dynamics has gained more importance. In this presentation a modal based control concept for a PVDF coated rectangular aluminum plate is proposed. Different from other concepts the PVDF elements are used as sensors and actuators. The purpose is twofold, the reduction of the vibration level coupled with the reduction of transmitted sound intensity if an acoustic excitation source is considered. The main advantage of PVDF elements compared to piezo ceramics, e.g. PZT, is their flexibility. This advantage becomes significant for mechanical structures with non plane surfaces because PVDF elements can even be bonded to curved surfaces. The drawback of using PVDF elements as actuators is their small piezoelectric activity which is approximately ten times smaller than that of PZT. This drawback can be compensated by a segmentation of the PVDF actuators in matrix design. Combined with an actuator management system the segmentation leads to variable quasi modal actuator areas. These areas cover a large part of the surface of the structure and can be adapted to the excited mode shape.

The presentation starts with the plate model. Since PVDF has less weight and is softer than aluminum and the PVDF elements are ten times thinner than the plate there is no significant change of the mass and the stiffness of the structure due to the additional PVDF segments. Therefore the classical plate theory is used to calculate the eigenfrequencies and the mode shapes. These modal data are used to calculate the placement of the sensors and to design the modal controller.

The real time measurement of the modal displacements is carried out with an array of point sensors and a modal filter. The effectiveness of the measurement depends on the placement of the point sensors. The placement has to fulfil the observability of the vibration and the non singularity of the modal filter matrix. To ensure this conditions a costfunction is defined which contains an observability index and the condition number of the modal filter matrix. Six different sensor array configurations are selected and the best configuration is experimentally tested by evaluating the amplitude frequency response. It is shown that the experimental results validate the analytical solution nicely.

The modal filtered feedback controller consists of four parts. The first part is called mode analyzer. The mode analyzer is identical with the pseudo inverse of the modal filter matrix. The inputs of the mode analyzer are the sensor signals of six PVDF point sensors and the outputs are modal displacements for six selected modes. The modal displacements are the inputs for the second part of the controller which is called the gain matrix. The gain matrix has two components. The first component is a constant factor and the second component is a linear function of the modal amplitudes. The outputs of the gain matrix are read in the mode synthesizer which is the third part of the controller. The mode synthesizer is programmed with the modal actuator matrix and has the task to transform the controller output from the modal coordinates into physical coordinates. The last part of the controller is the so called actuator management system (AMS). The AMS analyses the excited modes and adapts the actuator areas by switching the mode synthesizer.

In order to check the performance of this concept experimentally a plate with nine actuators and six sensors is manufactured and the controller is digitally implemented on a controller board. The test results show a reduction of the vibration amplitudes up to 70 % and a reduction of the transmitted sound pressure up to 50 %.



Universität Stuttgart

INSTITUT FÜR
MECHANIK

Prof. Dr.-Ing. habil. Lothar Gaul

Dipl.-Ing. Uwe Stöbener

Pfaffenwaldring 9, 70550 Stuttgart,
Germany

Allmandring 5 B, 70550 Stuttgart,
Germany

phone +49-(0)711-685-6278

phone +49-(0)711-685-8166

fax +49-(0)711-685-6282

fax +49-(0)711-685-8169

l.gaul@mecha.uni-stuttgart.de

u.stoebener@mecha.uni-stuttgart.de

<http://www.mecha.uni-stuttgart.de>

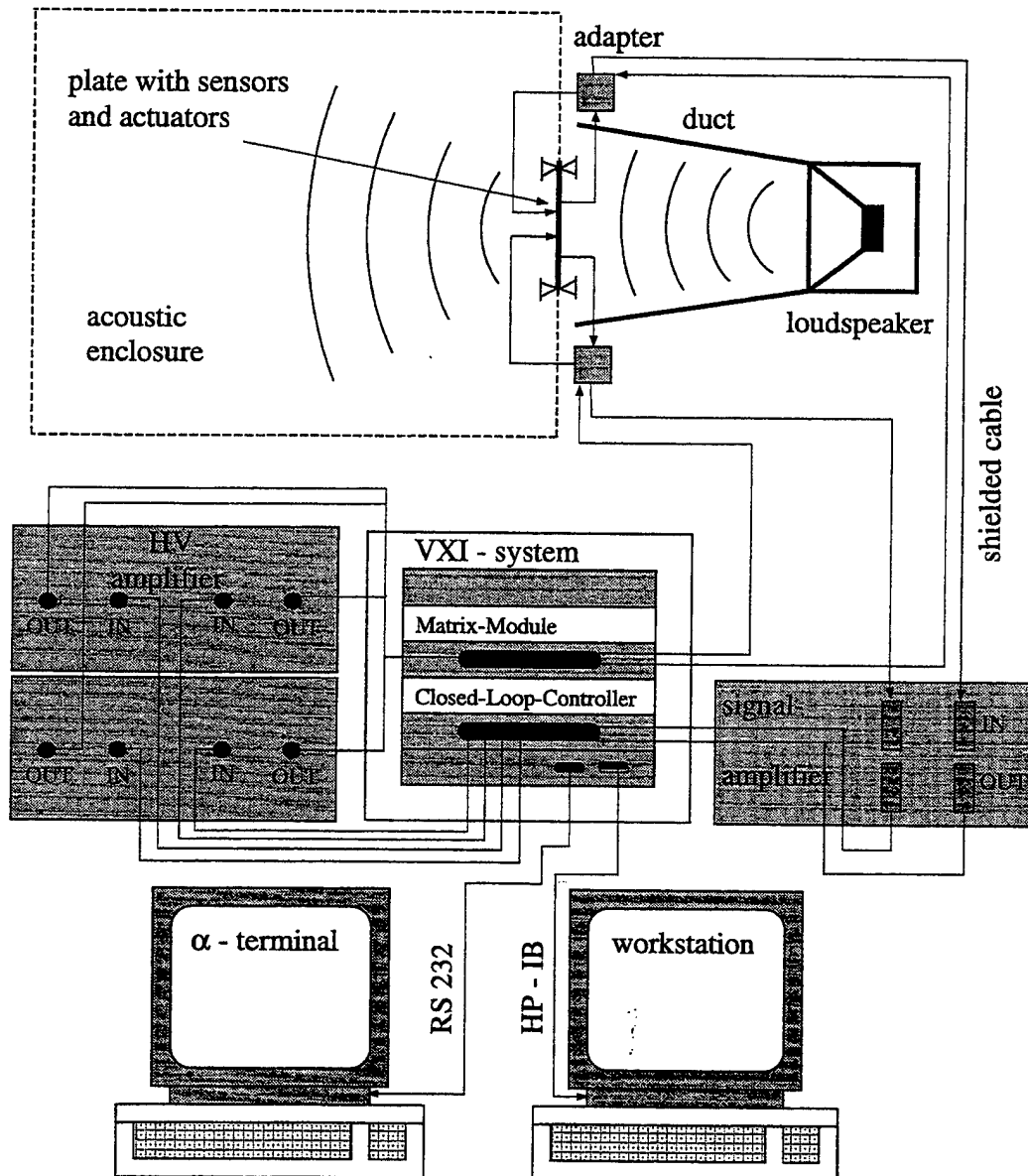
<http://www.mecha.uni-stuttgart.de>

Modal Vibration Control for PVDF Coated Plates

- Plate Model and Mode Shapes
- Placement of Sensors and Actuators
- Modal Controller Concept
- Experimental Tests
- Conclusion and Outlook

Plate Control Setup

Excitation by sound field and sound transmission through plate



Optimal Placement of PVDF-Sensors

singular value decomposition

$$\tilde{\Psi} = \mathcal{U} \mathcal{W} \mathcal{V}^T$$

$$\mathcal{W} = \begin{pmatrix} s_1 & & & \\ & s_2 & & \\ & & \dots & \\ & & & s_N \end{pmatrix}$$

$$\text{condition number } \sigma = \frac{s_{max}}{s_{min}}$$

sensitivity

$$\tilde{\Psi} = \begin{pmatrix} \frac{\tilde{\psi}_{11}}{max(\tilde{\psi}_{i1})} & \frac{\tilde{\psi}_{12}}{max(\tilde{\psi}_{i2})} & \dots & \frac{\tilde{\psi}_{1N}}{max(\tilde{\psi}_{iN})} \\ \frac{\tilde{\psi}_{21}}{max(\tilde{\psi}_{i1})} & \frac{\tilde{\psi}_{22}}{max(\tilde{\psi}_{i2})} & \dots & \frac{\tilde{\psi}_{2N}}{max(\tilde{\psi}_{iN})} \\ \dots & \dots & \dots & \dots \\ \frac{\tilde{\psi}_{N1}}{max(\tilde{\psi}_{i1})} & \frac{\tilde{\psi}_{N2}}{max(\tilde{\psi}_{i2})} & \dots & \frac{\tilde{\psi}_{NN}}{max(\tilde{\psi}_{iN})} \end{pmatrix}$$

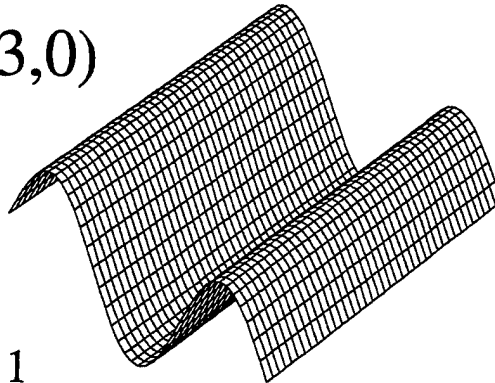
$$\alpha_k = \sum_{i=1}^N \frac{|\tilde{\psi}_{ik}|}{N}, \quad k: \text{ number of the column}$$

$$\text{sensitivity index } \beta = \prod_{k=1}^N \alpha_k$$

$$\text{costfunction } f_{cost} = \frac{\beta}{\sigma}$$

Optimal Placement of PVDF-Sensors

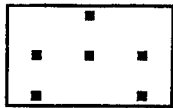
mode (3,0)



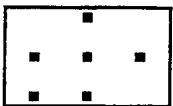
configuration 1



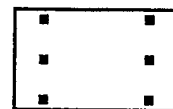
configuration 2



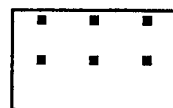
configuration 3



configuration 4



configuration 5



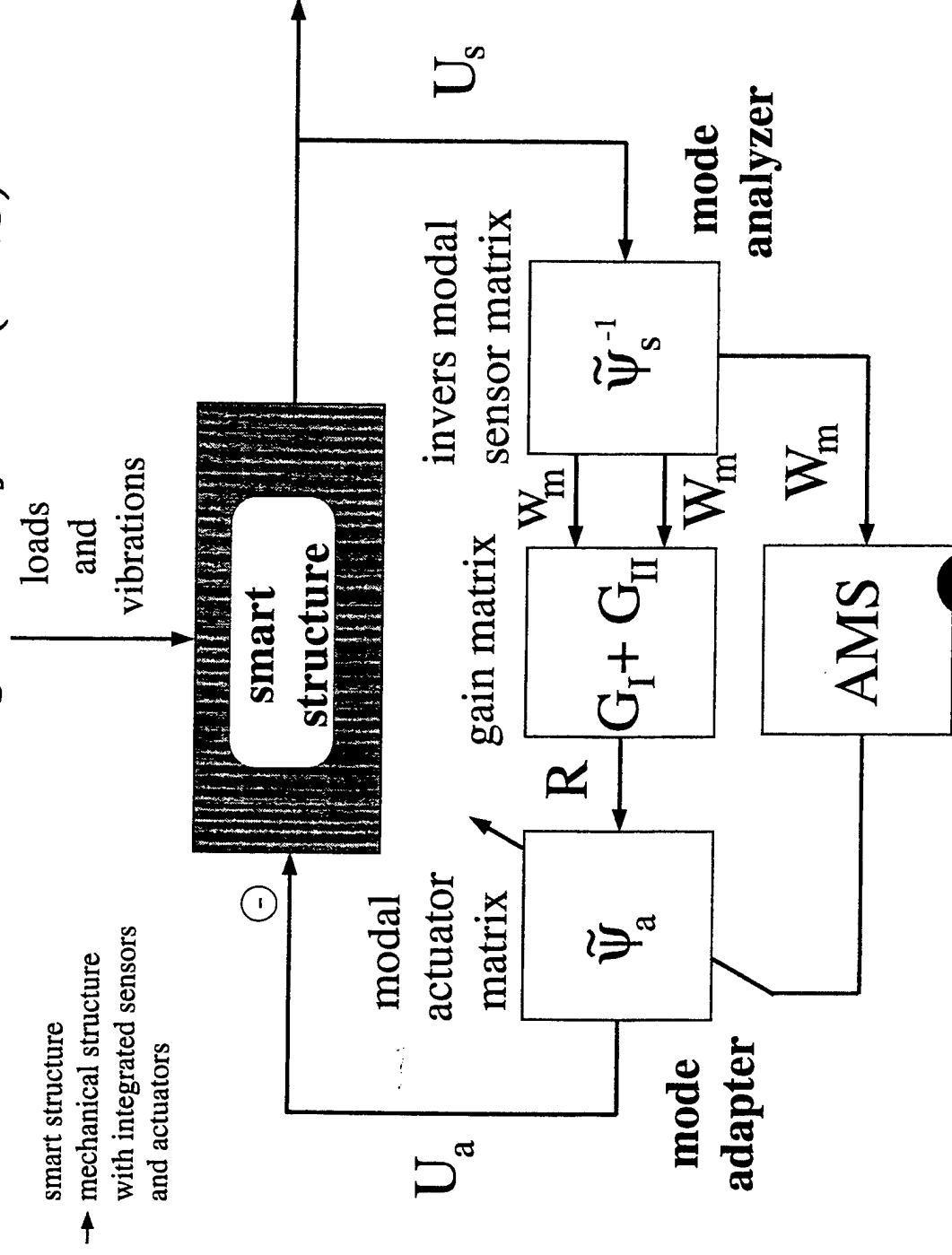
configuration 6



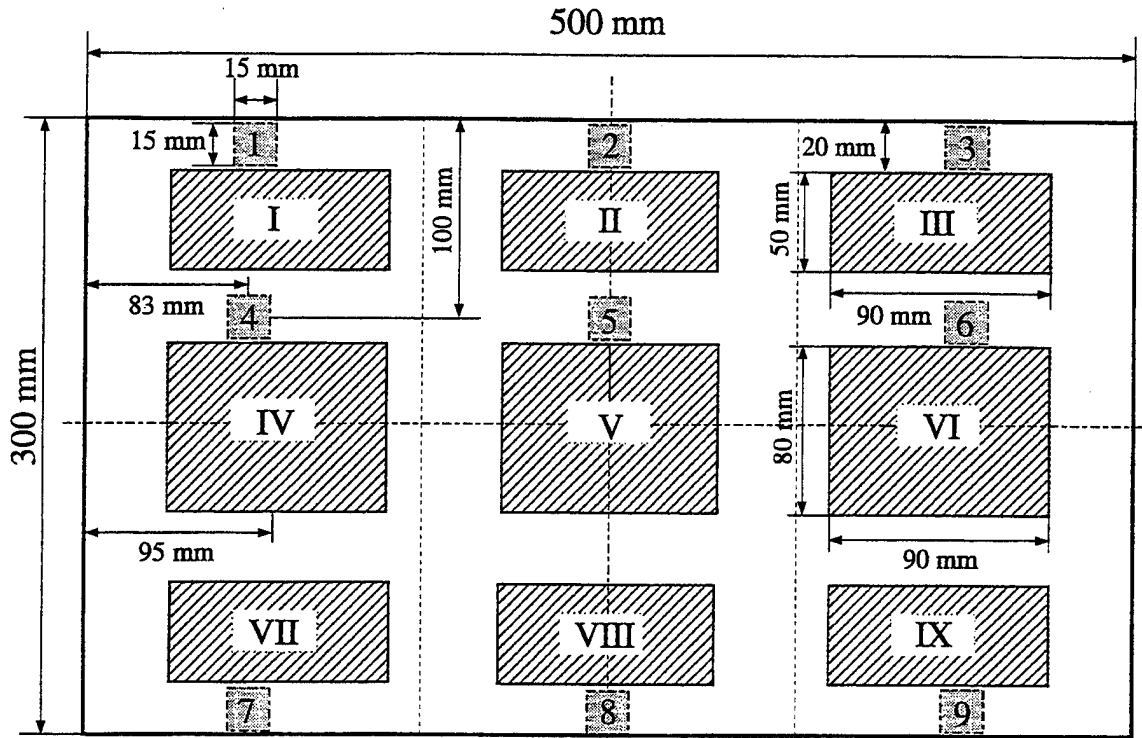
configuration	1	2	3
sensitivity index β	0,00512	0,00397	0,002629
condition number σ	4,34	4,02	5,00
costfunction f_{cost}	0,00127	0,00099	0,00052
configuration	4	5	6
sensitivity index β	0,00507	0,00397	0,00428
condition number σ	∞	∞	∞
costfunction f_{cost}	0,00000	0,00000	0,00000

Control of Structures

Modal Filtered Feedback (MFF) and
Actuator Management System (AMS)



Test plate with sensors and actuators



sensors in use : 1, 4, 5, 6, 7, 9

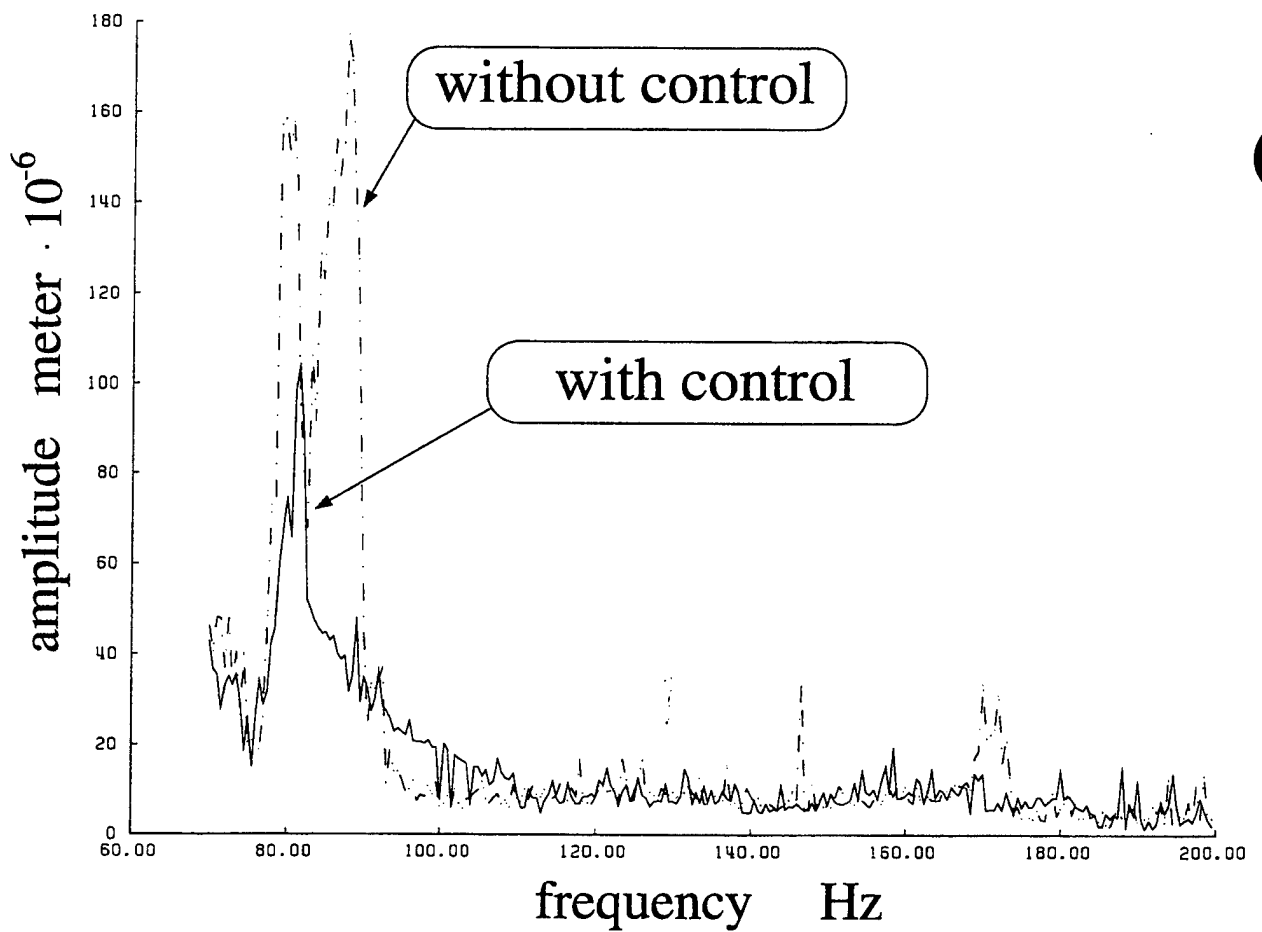
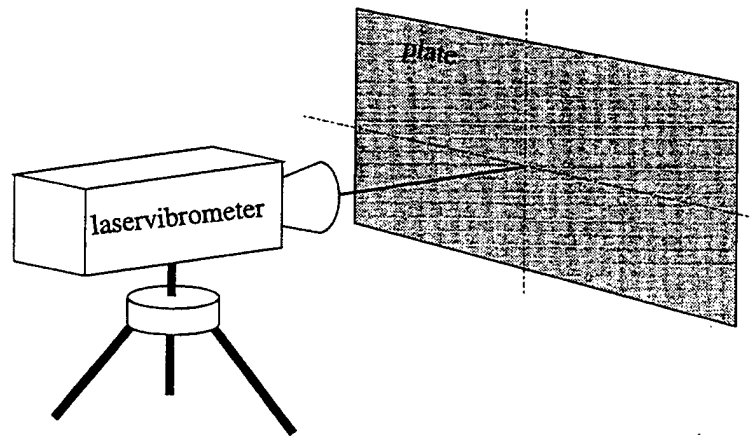
for modes (1,2), (3,0), (3,1), (2,2), (4,0) and (3,2)

$$\tilde{\Psi}_s = \begin{pmatrix} +112.37 & +2261.72 & +2218.67 & +0812.73 & +3489.99 & +2129.71 \\ -490.03 & +2261.72 & +0000.00 & -1457.57 & +3489.99 & -2888.43 \\ -983.66 & -2261.76 & +0000.00 & -0000.16 & -0000.74 & +2888.49 \\ -490.11 & +2261.72 & +0000.00 & +1457.73 & -3489.25 & -2888.43 \\ +112.37 & +2261.72 & -2218.67 & +0812.73 & +3489.99 & +2129.71 \\ +112.39 & +2261.72 & -2218.67 & -0812.81 & -3489.25 & +2129.71 \end{pmatrix}$$

actuators

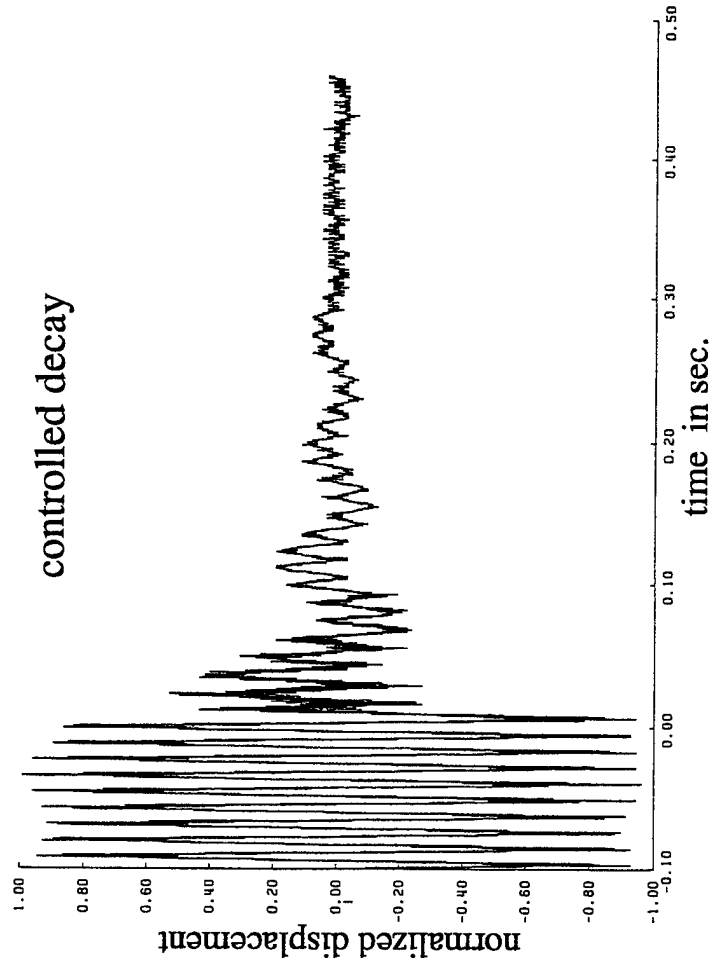
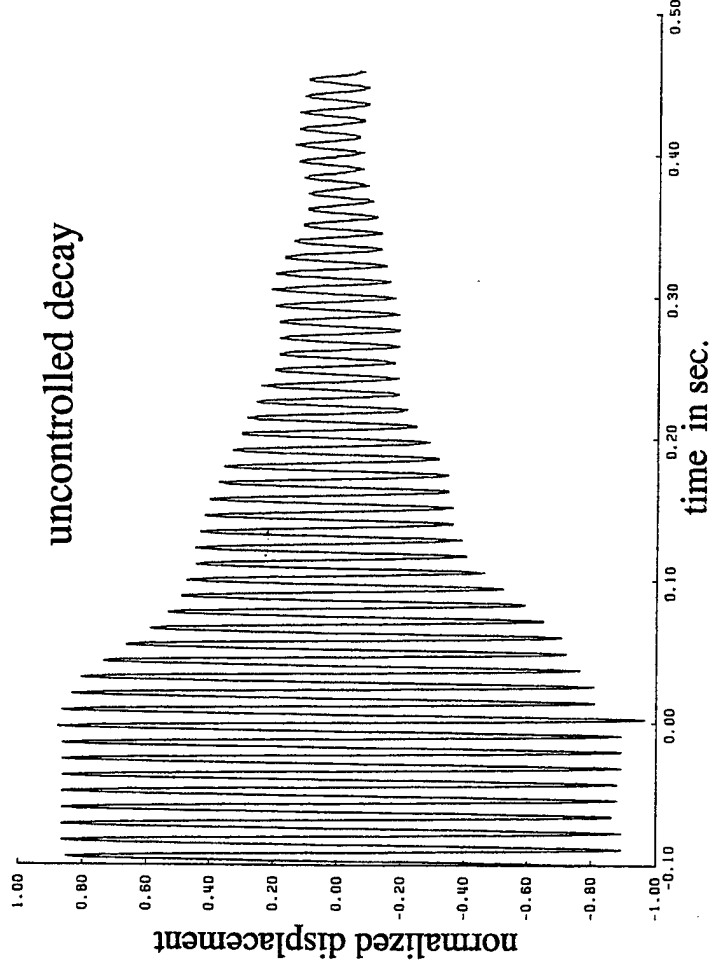
$$\tilde{\Psi}_a = \begin{pmatrix} +0.000001174 & +0.000053149 & +0.000018265 \\ +0.000002089 & -0.000054460 & -0.000018715 \\ +0.000001174 & +0.000053145 & +0.000018264 \\ -0.000002313 & +0.000053149 & -0.000039074 \\ -0.000004116 & -0.000054460 & +0.000040038 \\ -0.000002314 & +0.000053145 & -0.000039072 \\ +0.000001174 & +0.000053149 & +0.000018265 \\ +0.000002089 & -0.000054460 & -0.000018715 \\ +0.000001174 & +0.000053145 & +0.000018264 \end{pmatrix}$$

Experimental FRF results

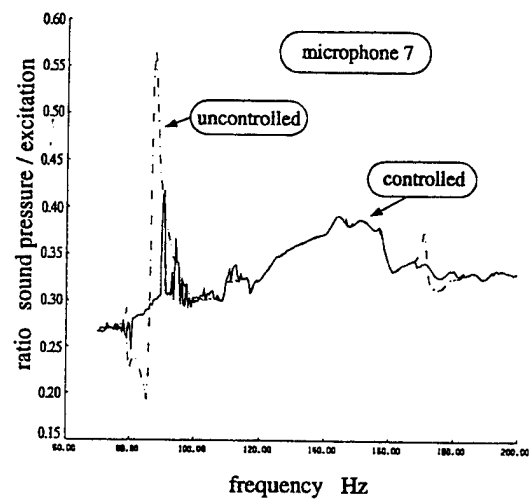
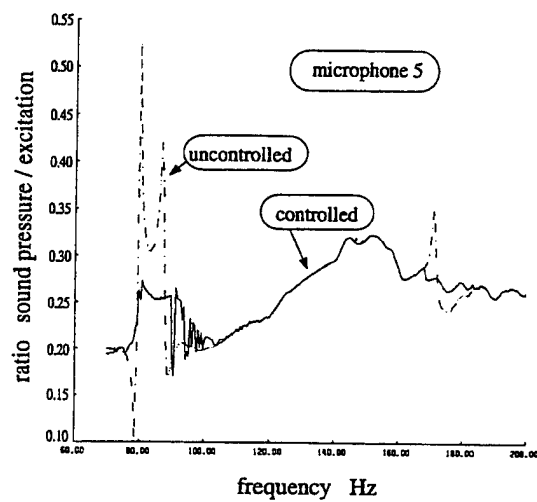
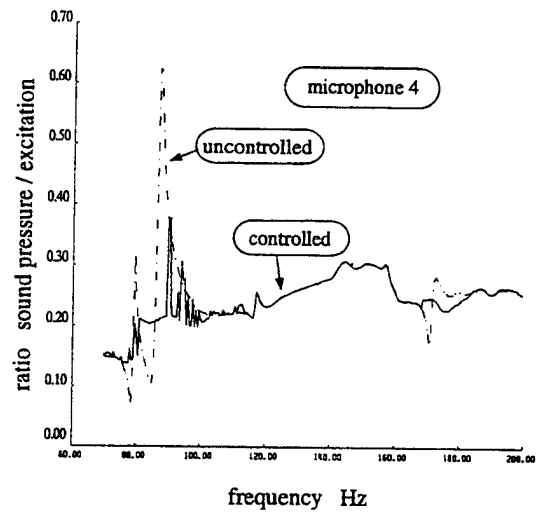
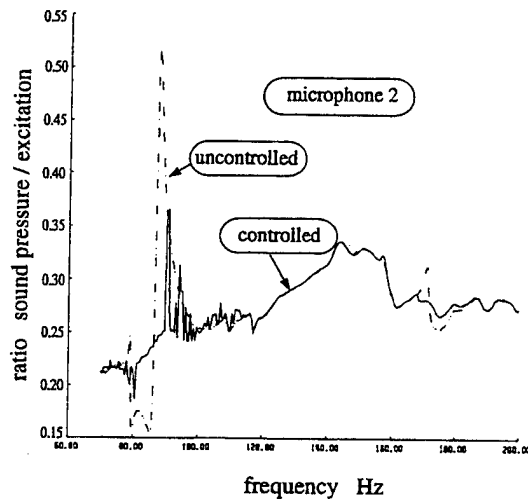
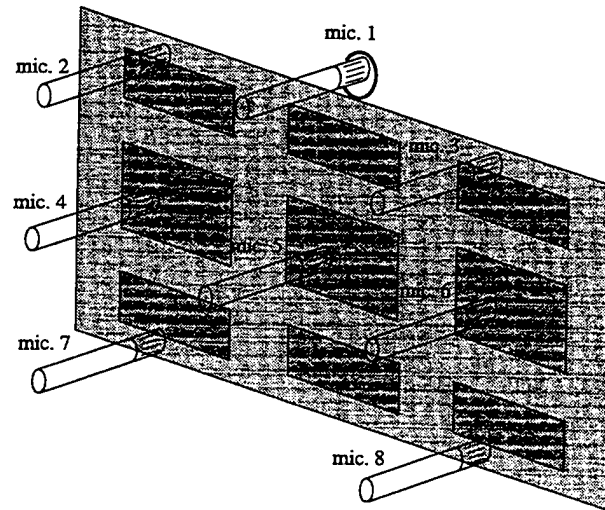


Decay of Plate Vibration

Experimental results



Experimental FRF results



VIBRATION SUPPRESSION USING A LASER VIBROMETER AND PIEZOCERAMIC PATCHES

E.A. WHEATER, A. GHOSHAL, C.R. ASHOK KUMAR, M. J. SUNDARESAN,

M. J. SCHULZ, and M. HUMAN

Department of Mechanical Engineering
North Carolina A&T State University

Greensboro, NC 27411, U.S.A.

Phone: 336-334-7620 ext 313, Fax: 336-334-7417, Email: schulz@ncat.edu

P. F. PAI

Department of Mechanical and Aerospace Engineering
University of Missouri-Columbia

Columbia, MO 65211, U.S.A.

Ph: 573-884-1474, Fax: 573-884-5090, email: paip@missouri.edu

INTRODUCTION:

- **Active Vibration Suppression:** Improves reliability and safety of structures by reducing fatigue cracking and damage.
- **New Smart Structures Concept:**
 - **Scanning Laser Doppler Vibrometer (SLDV)** measures the velocity of the structure in the direction of the scanning laser for feedback.
 - **Piezoceramic lead zirconate titanate (PZT)** patches measure strains used for control signals or apply actuation forces to counteract structural vibration.
 - **Hybrid Approach:** Laser velocity sensing and PZT strain sensing used simultaneously.
 - **Advantages:** The structural velocity is maximum and the strain is zero when the structural vibration mode passes through equilibrium, and the structural strain is maximum and the velocity is zero when the vibration mode is at its peak amplitude.

CONTROL SIMULATION:

Figure 1 shows a cantilever beam 0.838 meters long, 4.45 centimeters wide, and 3.175 millimeters thick with PZT patches near the root. This was used for Finite Element Analysis. The disturbance force $f(t)$ is a 50Hz sine input acting perpendicular to the beam. The time step for the simulation is $dt=2e-6$ seconds. The highest frequency of the FEM model is 587Hz.

SIMULATION USING GAIN SWITCHING CONTROL

- The gain switching was simulated at different switching speeds.
- The scanning laser using gain switching control gave only a small performance improvement compared to using the fixed laser. This is because only the current measurement coordinate is used in the control, and information on past measurements is not used.

SIMULATION USING LQR CONTROL WITH TIME DELAY

- When the update of the state vector is sampled at 500Hz the simulation becomes unstable. The RMS displacement of the three translational dof's for this case is 0.71 mm.
- This simulation is rerun with a sampling time of 10,000Hz for the full state vector. In this case (Figure 2) the vibration response is suppressed very quickly, and the RMS displacement of the three translational dof's is 0.32 mm. When the update of the state vector is sampled faster than 587Hz the control is stable and the performance is better than gain switching control.

- Table 1 shows that the natural frequencies have only a very small change due to the control. The LQR control provides a large increase in the damping ratios for all modes. The fixed laser control adds moderate damping to only the first mode.
- This suggests that a new control technique that incorporates time delay into distributed sensing and using the LQR method may give the best performance for the scanning laser.

Table 1: Beam FEM natural frequencies and damping ratios

Vibration mode no.	Natural Frequencies (Hz)			Damping Ratios		
	No control	Fixed laser sensor	LQR with fast scan	No control	Fixed laser sensor	LQR with fast scan
1	3.9131	3.9130	3.9229	.0286	.0415	.1521
2	24.601	24.601	24.595	.0053	.0012	.0511
3	69.513	69.513	69.537	.0038	.0024	.0197
4	156.54	156.54	156.78	.0056	.0097	.0485
5	294.61	294.61	293.73	.0096	.0058	.0545
6	587.34	587.34	586.69	.0186	.0203	.0304

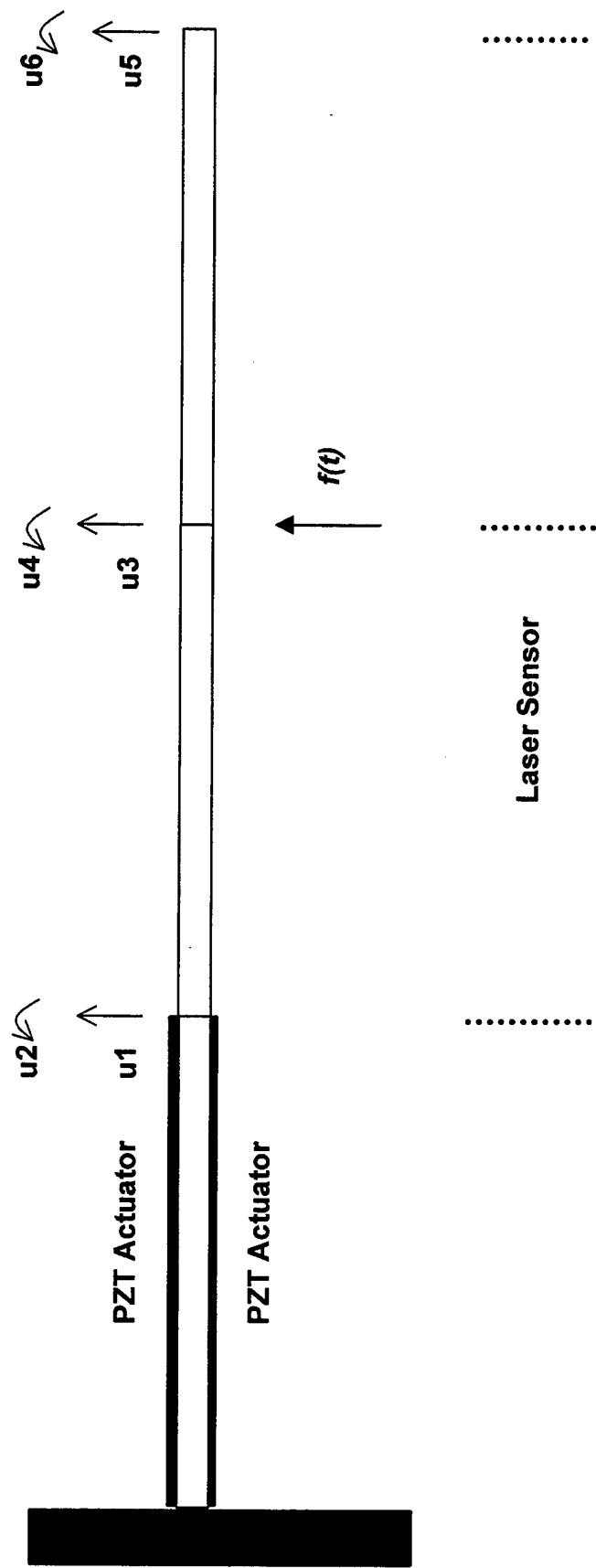


Figure 1: Finite element model of a cantilever beam for the control simulation.

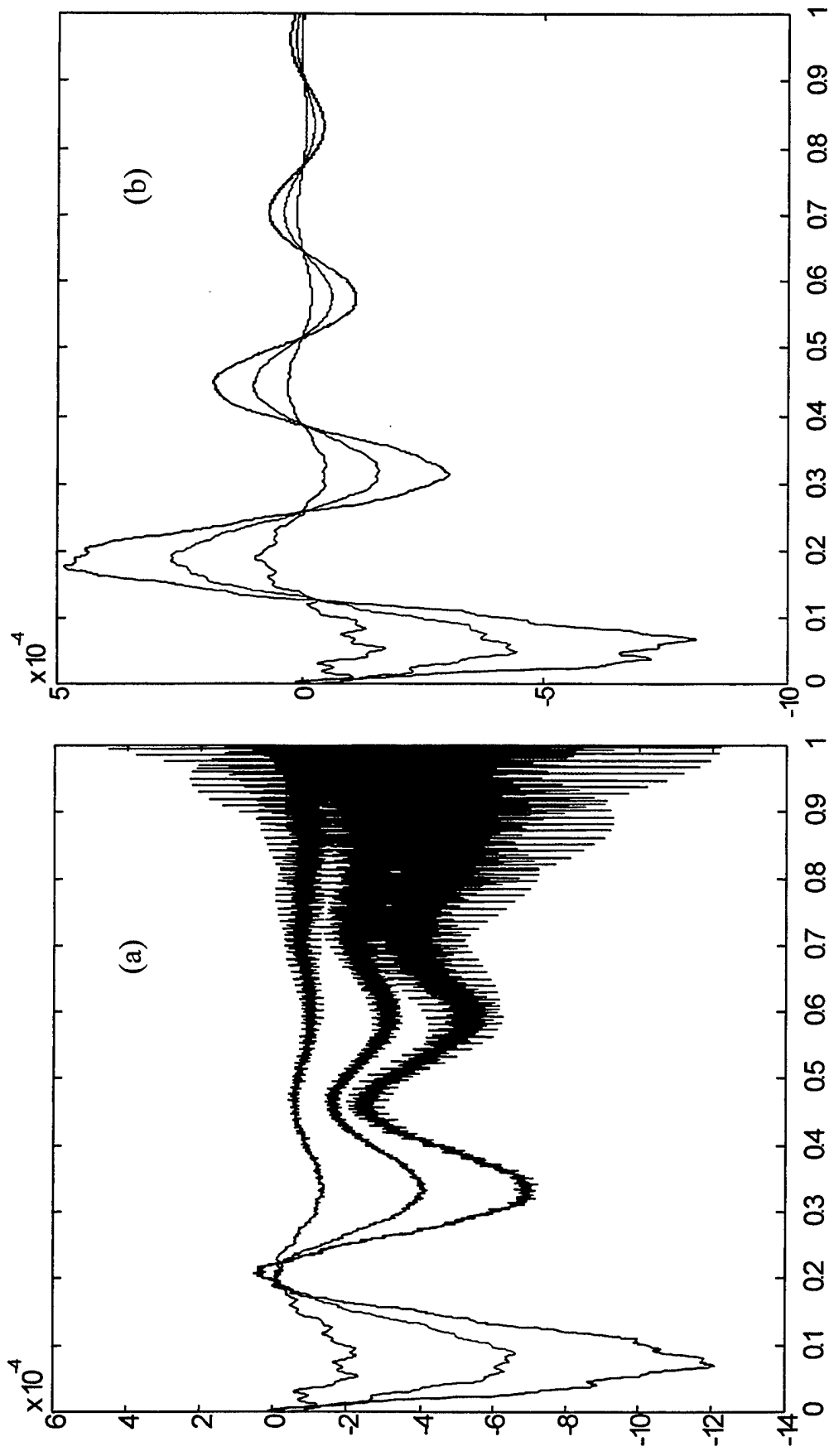


Figure 2: Simulation of the cantilever beam translational displacements versus time using laser scanning with LQR velocity feedback control for the cases of (a) the scanning update time is $ts=2e-3$ seconds, and (b) scanning update time is $ts=1e-4$ seconds.

EXPERIMENTATION USING A SCANNING LASER SENSOR:

Test Apparatus:

- Alpha DEC high-speed processor
- A Polytec PI fixed laser vibrometer
- A mirror scanner developed at NCA&TSU (Figure 7(b)).
- One piezoceramic sensor patch to drive the scanning mirror and for the actuation control signal. Two piezoceramic patches are used for actuation of the cantilever beam structure. The dimensions of the PZT patches are 5.08 cm X 3.81 cm X 0.254 mm.
- A SIMULINK control diagram (Figure 6) with filters and gains was downloaded to the controller for real-time hardware in the loop simulation.

Why PZT?

- A Polyvinylidene Fluoride (PVDF) film of size 5.08 cm X 5.08 cm X 0.05 mm, bonded directly to the aluminum beam, was initially used as the sensor.
 - Advantage of PVDF: A large sensor can be used to spatially filter the response.
 - Disadvantage: In this experiment the voltage output of the PVDF film was small and contained some 60Hz noise. The voltage output from the PZT was about 100 times greater than the PVDF.

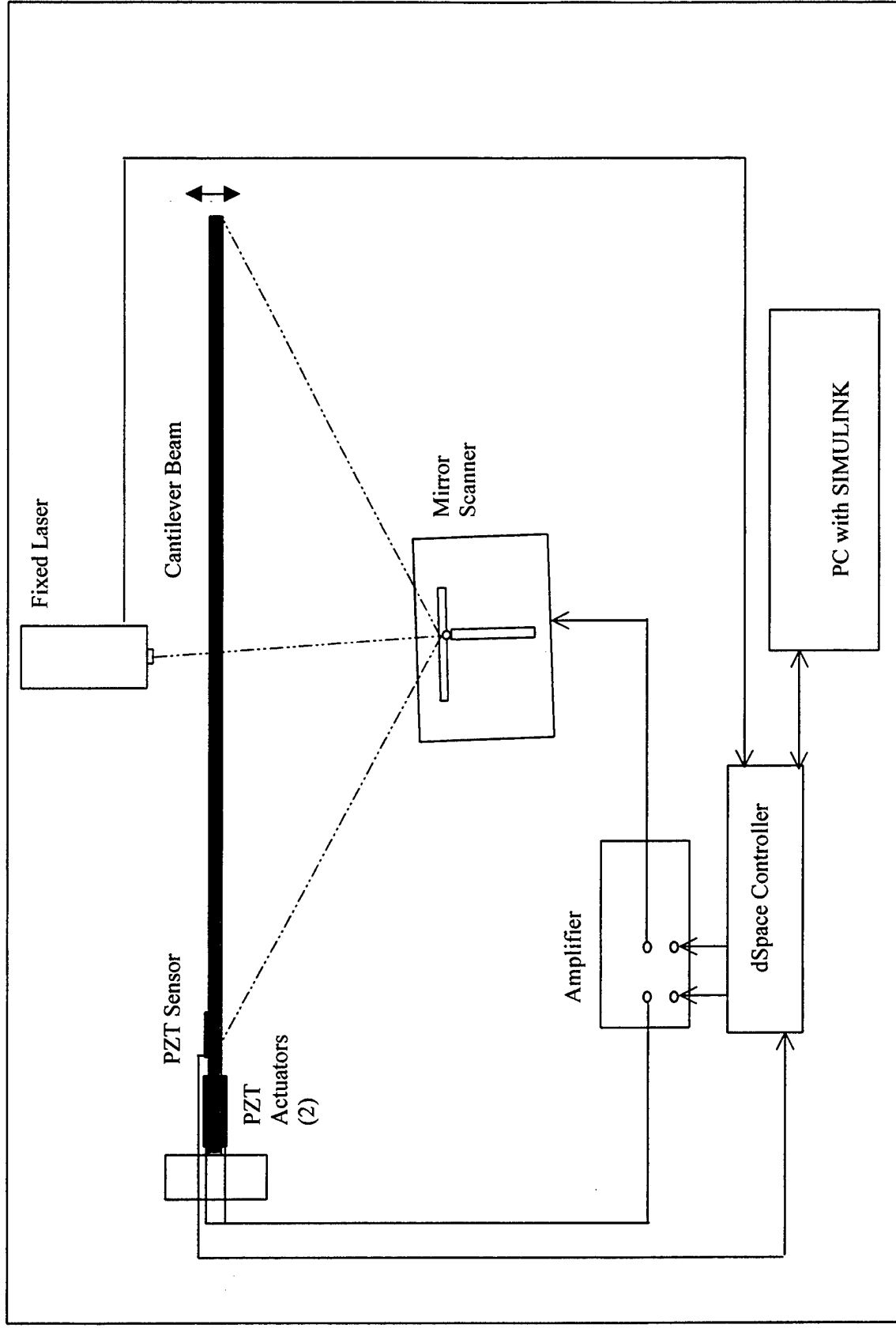


Figure 6: Schematic of the vibration suppression control system using a scanning laser and PZT patches.

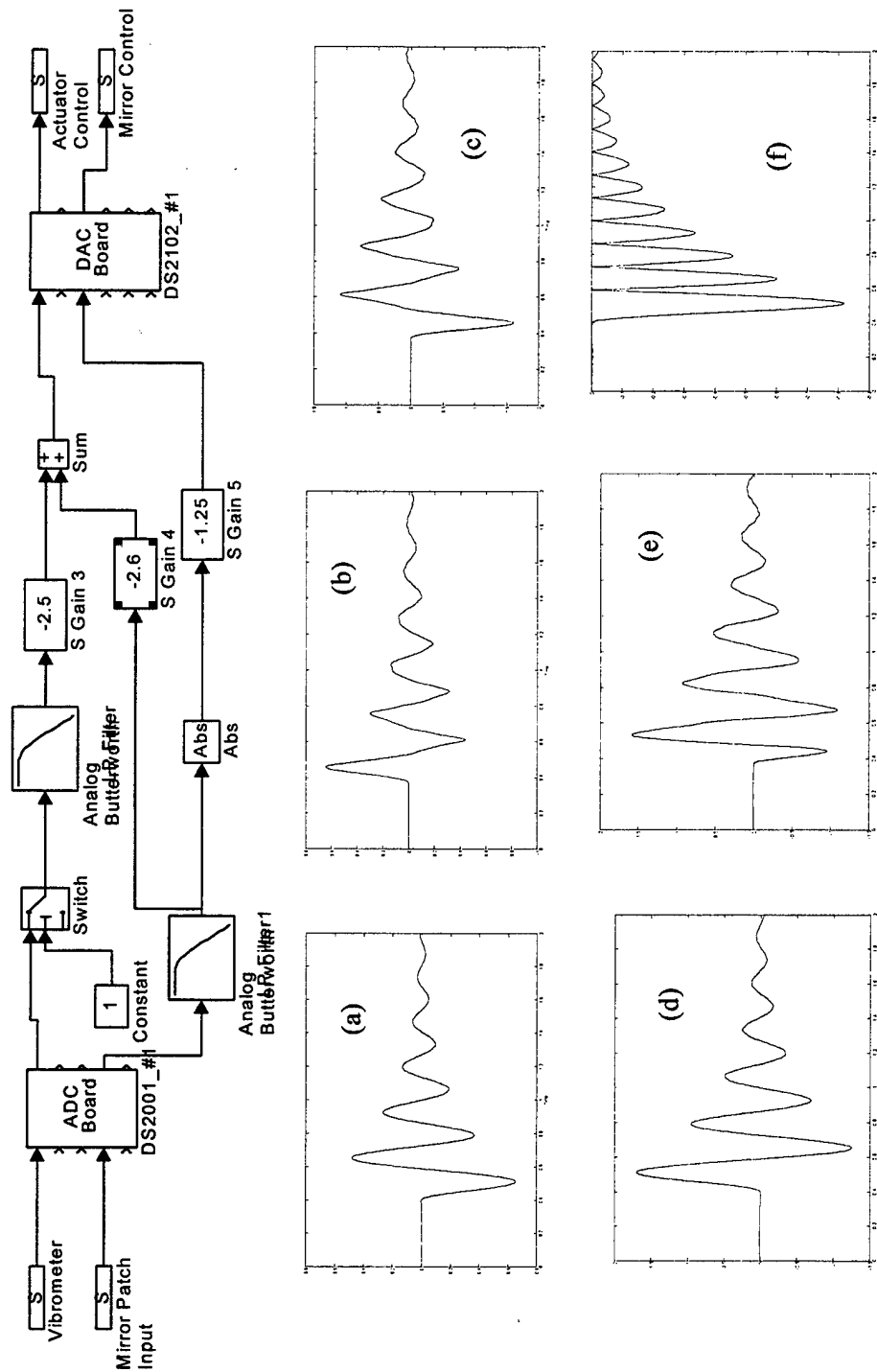


Figure 12: SIMULINK diagram and system variables using hybrid control: (a) the PZT sensor signal after filtering, (b) the vibrometer signal after filtering, (c) the laser feedback control signal sgain3, (d) the PZT feedback control signal sgain4, (e) the control signal from the DAC to the actuators, and (f) the control signal from the DAC to the mirror. The laser control gain is -2.5 , the sensor PZT patch gain for the actuator control is -2.6 , and the mirror control gain is -1.25 .

CONCLUSIONS:

- The laser sensing control technique was demonstrated to effectively suppress vibration of a cantilever beam structure.
- A hybrid control system was shown to have advantages of improved performance and stability.
- The experiment in which damage (a 50% height crack) was put in the beam showed that the performance of the hybrid control was not significantly affected.
- The damage was indicated by drop out of the laser signal during the free vibration of the beam.
- The technique presented can potentially be extended to large complex structures where the advantages of laser sensing are the capability to provide centralized control, simplified sensing and communication, and the ability to improve control performance by measuring the response at many points on the structure by scanning the laser.

ACKNOWLEDGEMENT:

This work was sponsored by the Army Research Office under the research grant DAAH04-96-1-0048 (technical monitor, Dr. Gary Anderson), by the Army Research Office under the equipment grant DAAG55-97-1-0299 (technical monitor, Dr. Thomas L. Doligalski), and by the NASA Center of Aerospace Research at NCA&TSU under the grant NCC-1-255. This support is gratefully acknowledged.

**BUFFET ALLEVIATION:
AN ADAPTIVE STRUCTURES APPROACH**

S. Hanagud, M. Bayon de Noyer and H. Luo,
Georgia Institute of Technology, School of Aerospace Engineering
Atlanta, Georgia 30332-0150

D. Henderson,
Air Force Research Laboratory, WPAFB, Ohio 45433

K.S. Nagaraja,
Rohini International, 3354 Southfield Drive,
Beavercreek, Ohio 45434

Outline

- Tail Buffet : Causes and Effects
- Actuator : Choice and Design
- Controller : Choice and Design
- Experimental Validation:
 - Full Scale Vertical Tail Sub-Assembly
 - 1/16th Scale Model Wind Tunnel Tests



Tail Buffet

- Terms appeared for the first time in early 1930's when British Aeronautical Research Committee concluded that the cause of the accident of a commercial airplane was severe "buffeting" of the tail.
- For High Performance Twin-Tail Aircraft (F-15, F/A-18), tail buffet was first noticed through its destructive effects of induced fatigue cracks in the early seventies.

Tail Buffet

High Angle of Attack
Maneuver



Unsteady Pressure:

- Separated Flow
- Vortices



Excitation of some
Vibration Modes
of the Vertical Tails



- Fatigue of Tail
Structural Assembly
- Limitation of
Flight Envelope



Tail Buffet

Different Aircraft Different Problems

- **F-15 Cracks in Upper Part of the Vertical Tails**
 - Unsteady flow contains a narrow band of frequencies
 - Band contains first torsion mode of the vertical tails
 - Pods mounted on the upper tip of the tails
 - » Cracks at the connection between vertical tail and pod
- **F/A-18 Cracks in Lower Part of the Vertical Tails**
 - Broadband excitations resulting from bursting of the Leading-Edge Extension (LEX) vortices
 - First bending mode absorbs most of the energy
 - » Cracks at the root of the vertical tail

Tail Buffet Alleviation Systems

- **Aerodynamic Approaches:**
 - Addition of fences on wings or fuselage:
 - LEX Fences on the F/A-18
 - Wing Fences (Klein and Komerath, 1997)
 - Air Blowing:
 - Tangential Leading Edge Blowing (Mabey and Pine, 1991, Bean and Wood, 1993 and 1996)
 - Forebody Tangential Slot Blowing (Gee, Rizk, and Schiff, 1994)
- **Passive Structural Approaches:**
 - Reinforcement of vertical tail structural assembly
 - Exoskin (Ferman et al. 1993)

Tail Buffet Alleviation Systems

- **Adaptive (Smart) Structure Approaches**

- Ashley et al. (1994) simulated the use of a rudder for the F/A-18 and a tip vane for the F-15 with direct feedback controllers
- Lazarus et al. (1995, 1996) developed and simulated a Buffet Load Alleviation system with PZT wafers and LQG controllers
- Hauch et al. (1996) experimentally studied an Active Vertical Tail (5%-scale aeroelastically scaled structure based on a generic aircraft) with PZT wafers and PID controllers
- Nitzsche et al. (1997) compared simulations using rudder or PZT wafers and LQG controllers
- Moses (1997) experimentally compared the use of rudder and PZT wafer with frequency domain compensation controller

Choice of Actuator

Piezoelectric Actuator

versus

Aerodynamic Control Surface

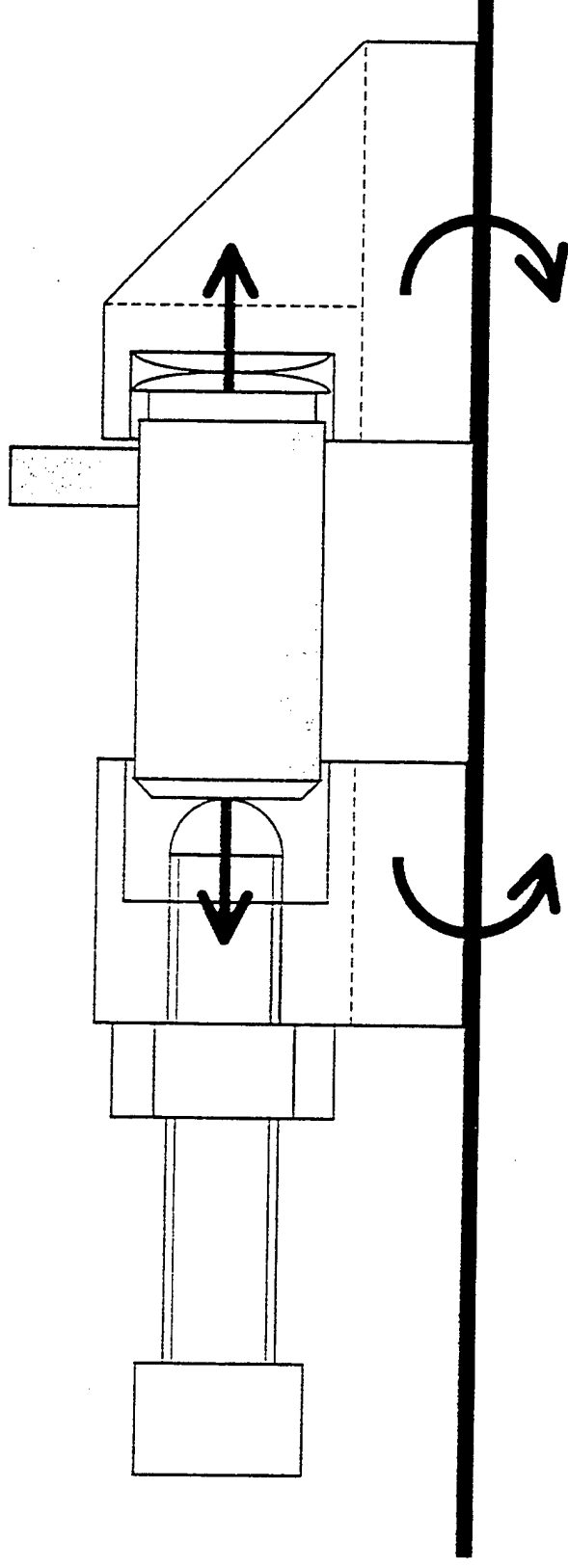
- Buffet alleviation system operates independently of the flight controls
 - No restriction of the maneuverability of the aircraft
- Ability to place the actuators
 - Optimal number of Actuators
 - Optimal placement of Actuators

Choice of Actuator

Piezoceramic Stack versus PZT Wafer

- Uses of direct d_{33} instead of the transverse d_{31} piezoelectric charge constant
- Force and elongation are added along the stack
- Successfully used in vibration control as:
 - Force Actuators
 - for trusses (Preumont et al., 1992)
 - for plates by being placed between the plate and a stiffener (Young and Hansen, 1996)
 - Bending Moment Inducing Actuators
 - for stiff beams and plates by being mounted in cutouts (Redmond and Barney, 1997).

Offset Piezoceramic Stack Actuator



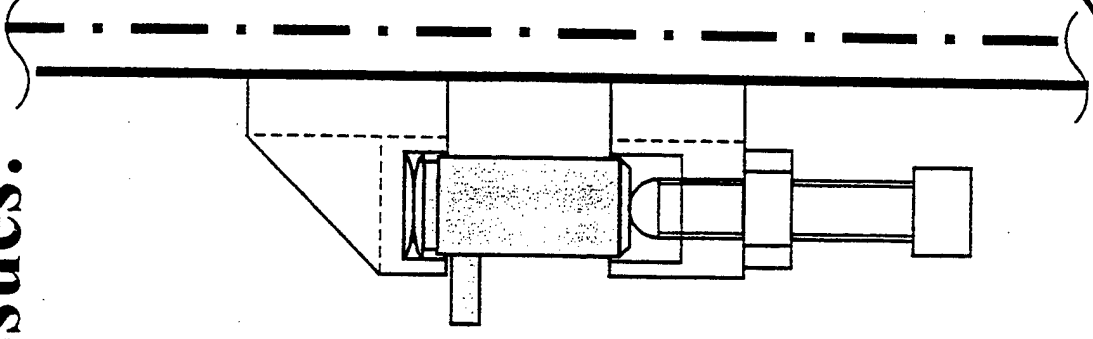
Transform the longitudinal forces into control moments by:

- Placing the stack parallel to the controlled structure at an offset distance from its neutral axis

Offset Piezoceramic Stack Actuator

Reliability and Maintainability Issues:

- **Principal piezoceramic stack failure mode happens under local tension**
- **Piezoceramic stack compressed between two blocks bonded to the host structure**
 - ⇒ No linkage between stack and controlled system
 - ⇒ Tensile loads are not transmitted to the stack
- **Rounded point contact between stack and mounts**
 - ⇒ Bending loads are not transmitted to the stack
- **Bolt to facilitate the removal of the stack**
 - ⇒ Insures stack is removable while mount is bonded on controlled structure



Offset Piezoceramic Stack Actuator

Sizing Considerations:

- Maximum control authority
 - Actuator resultant forces maximum
- Minimum power requirement
 - Smallest needed control authority of the actuator
- Different types of piezoceramic stacks possible:
 - Low-voltage (100V) piezotranslators can generate blocked force in the range of 180N to 3kN
 - High-voltage (1000V) piezotranslators can generate blocked force in the range of 1.5kN to 30kN
- Optimization of actuator assembly depends on:
 - Selected piezoceramic stack
 - Controlled system

Choice of Controller

Acceleration Feedback Control

- Goh and Caughey (1985) introduce Second Order Compensator with Positive Position Feedback (PPF) Controller
- Juang and Phan (1992) introduce an approach to unconditionally stable second order compensators, based on acceleration feedback
- Sim and Lee (1993) derive the unconditional stability for multi-mode acceleration feedback control with multiple collocated sensor-actuator pairs
- Goh and Yan (1996) propose a pole placement method to obtain the parameters of the acceleration feedback compensators for multi-mode control with collocated sensor-actuator pairs. (Critically Damped Compensators)

Single DOF Representation of AFC

- The equation describing the active damping of a single degree of freedom system using Classical Acceleration Feedback Control consists of:
 - a Structural Modal Equation with Feedback Force due to the Actuator and Disturbance Force,
 - a Compensator Modal Equation with Acceleration Sensing Component,

$$\begin{cases} \ddot{\xi} + 2\zeta_s\omega_s\dot{\xi} + \omega_s^2\xi = -a_1\gamma\omega_c^2\eta + f \\ \ddot{\eta} + 2\zeta_c\omega_c\dot{\eta} + \omega_c^2\eta = a_2\ddot{\xi} \end{cases}$$

ξ is the modal coordinate of the structure,
 ζ_s is the structural damping ratio,
 ω_s is the structural natural frequency,
 a_1, a_2 are the sensitivities of the actuator and sensor respectively.

η is the modal coordinate of the compensator,
 ζ_c is the compensator damping ratio,
 ω_c is the compensator natural frequency,
 γ is the scalar gain applied to the feedback signal.

Cross-Over AFC Design

- The only practical design condition from the previous restriction is:

$$\omega_c = \omega_s$$

since all the other conditions yield to large shifting of the closed loop natural frequency.

- The other cross-over condition is given by:

$$\gamma = \frac{(\zeta_s - \zeta_c)^2}{a_1 a_2}$$

- And the closed-loop natural frequency and damping ratio are given by:

$$\omega_f = \omega_s \quad \text{and} \quad \zeta_f = \frac{1}{2}(\zeta_s + \zeta_c)$$

Cross-Over AFC Design

- 5 design parameters: ω_f , ζ_f , ω_c , ζ_c and γ ,
- Only 1 free design parameter, since there are 4 cross-over conditions. The choice of the free design parameter, between ζ_f , ζ_c and γ , is left to the designer.
- Single DOF Design Procedures
 - Fix final closed loop value of damping ratio ζ_f then solve for compensator parameters ω_c , ζ_c and γ
 - Fix compensator damping ratio ζ_c then solve for other compensator parameters ω_c and γ
 - Fix compensator scalar gain γ then solve for other compensator parameters ω_c and ζ_c .

AFC SDOF H_2 Optimal Design

Minimize H_2 norm of closed-loop system transfer function between modal response and external disturbance force

$$\|G\|_2 = \left(\frac{1}{2\pi} \int_{-\infty}^{+\infty} \|G(j\omega)\|_F^2 d\omega \right)^{1/2} = \left(\int_0^{+\infty} \|H(t)\|_F^2 dt \right)^{1/2} = \|H\|_2$$

Equivalent to

Minimize the RMS of impulse modal response of closed loop system due to unit impulse load

Minimize the covariance of closed loop modal response due to unit white noise disturbance

$$\|y\|_2 = \left(\int_0^{+\infty} y^T(t)y(t)dt \right)^{1/2} \quad \|y\|_2 = \left(\lim_{t \rightarrow \infty} \mathbf{E} \left\{ \frac{1}{t} \int_0^t y^T(\tau)y(\tau)d\tau \right\} \right)^{1/2}$$

AFC SDOF H_2 Optimal Design

- State space model of closed loop system based on modal states of controlled system and controller states:

$$\begin{cases} \dot{\mathbf{x}}(t) = \tilde{\mathbf{A}}\mathbf{x}(t) + \tilde{\mathbf{B}}\mathbf{w}(t) \\ \mathbf{y}(t) = \tilde{\mathbf{C}}\mathbf{x}(t) \end{cases}$$
- Define a functional J , which depend on the controller parameters

$$J(\omega_c, \zeta_c, \gamma) = \|\mathbf{G}\|_2^2 = \text{tr}(\mathbf{P}\tilde{\mathbf{B}}\tilde{\mathbf{B}}^T)$$

where \mathbf{P} is the observability Gramian and satisfies the Lyapunov equation:

$$\tilde{\mathbf{P}}\tilde{\mathbf{A}} + \tilde{\mathbf{A}}^T\tilde{\mathbf{P}} + \tilde{\mathbf{C}}^T\tilde{\mathbf{C}} = 0$$

- Set derivatives of J with respect to ω_c , ζ_c and γ to zero :
 - There is no optimal gain γ ,
 - For a given scalar gain γ , we have:

$$\omega_{c,\text{opt}} = \omega_s$$

$$\zeta_{c,\text{opt}} = \frac{1}{2} \sqrt{a_1 a_2 \gamma}$$

AFC SDOF H_2 Optimal Design

- Robust Stability since $a_1 a_2 \gamma = 4 \zeta_{c,opt}^2 > 0$
- Robust Performance
- Define Departure From Optimality

$$D_{opt} = \frac{\|G_{cl,controller \text{ based on identified parameters}}\|_2 - \|G_{cl,controller \text{ based on true parameters}}\|_2}{\|G_{cl,controller \text{ based on true parameters}}\|_2}$$

- Assume small uncertainties in ω_s , ζ_s and $a_1 a_2$ of the form $q_{s,true} = q_{s,identified} (1 + \varepsilon_q)$
- Taylor Expansion of D_{opt} gives (with $\alpha = \zeta_s / \zeta_c$) :

$$D_{opt} \approx \frac{1}{4} \left[\left(1 - \frac{3}{2} \alpha (1 + \varepsilon_\zeta) \right) \varepsilon_a + \left(1 - \frac{5}{2} \alpha + \frac{\alpha^2}{\zeta_s^2} \left(1 - \frac{7}{2} \alpha \right) \right) \varepsilon_\omega^2 + \frac{1}{4} \left(\frac{3}{2} \alpha - 1 \right) \varepsilon_a^2 \right] + O(\varepsilon^3)$$

Choose γ such that $49 \zeta_s^2 < a_1 a_2 \gamma < 4$

Multi-Mode AFC

- The general equations for a n-DOF System Multi-Mode Acceleration Feedback Control are as follow:

$$\begin{cases} [M]\{\ddot{x}\} + [C]\{\dot{x}\} + [K]\{x\} = -[\Gamma_{act}][G][\Omega_c]\{\eta\} + \{f\} \\ \{\ddot{\eta}\} + [\Lambda_c]\{\dot{\eta}\} + [\Omega_c]\{\eta\} = [S][\Gamma_{acc}]\{\ddot{x}\} \end{cases}$$

with:

$\{x\}$ Structural Geometric Coordinates,
 $[M]$ Mass Matrix,
 $[C]$ Damping Matrix,
 $[K]$ Stiffness Matrix,
 $\{f\}$ Disturbance Force Vector,
 $[\Gamma_{act}]$ Location and Sensitivity Matrix of the Actuator,
 $[\Gamma_{acc}]$ Location and Sensitivity Matrix of the Accelerometer,

$\{\eta\}$ Compensator Modal Coordinates,
 $[\Lambda_c]$ Diagonal Damping Values Matrix of the Compensator,
 $[\Omega_c]$ Diagonal Natural Frequencies Matrix of the Compensator,
 $[G]$ Feedback Scalar Gain Matrix,
 $[S]$ Sensor Influence Matrix.

Multi-Mode AFC for Single Actuator

- Design Methodology
 - Obtaining a mathematical model for the transfer function of the plant (sensor signal divided by control signal) in the form of a partial fraction expansion,
 - Design of p independent AFC compensators using cross-over design, each being as selective as possible,
 - Check of the stability of the closed-loop system using root locus procedure.

Non Collocated Multi-Mode AFC

- The general equations for multi-mode acceleration feedback control are as follow:

$$\begin{Bmatrix} [M]\{\ddot{x}\} + [C]\{\dot{x}\} + [K]\{x\} \\ \{\ddot{n}\} + [\Lambda_c]\{\dot{n}\} + [\Omega_c]\{n\} \end{Bmatrix} = -[\Gamma_{act}][G][\Omega_c]\{n\} + \{f\}$$

with:

$\{x\}$ n Structural Geometric Coordinates,	$\{n\}$ p Compensator Modal Coordinates,
$[M]$ n \times n Mass Matrix,	$[\Lambda_c]$ p \times p Diagonal Damping Values
$[C]$ n \times n Damping Matrix,	Matrix of the Compensator,
$[K]$ n \times n Stiffness Matrix,	$[\Omega_c]$ p \times p Diagonal Natural Frequencies
$\{f\}$ n \times 1 Disturbance Force Vector,	Matrix of the Compensator,
$[\Gamma_{act}]$ n \times m Location and Sensitivity	$[G]$ m \times p Feedback Gain Matrix,
Matrix of the Actuator,	$[S]$ p \times m Parallel Influence Matrix.
$[\Gamma_{acc}]$ m \times n Location and Sensitivity	
Matrix of the Accelerometer,	

Wind Tunnel Experimental Setup

Georgia Tech Research Institute

Model Test Facility (MTF)

Low Speed Wind Tunnel

Test Section: 30"H x 43"W x 90"L

Equipment

1/16th Scaled Model

Two PCB 303 A02 Accelerometer

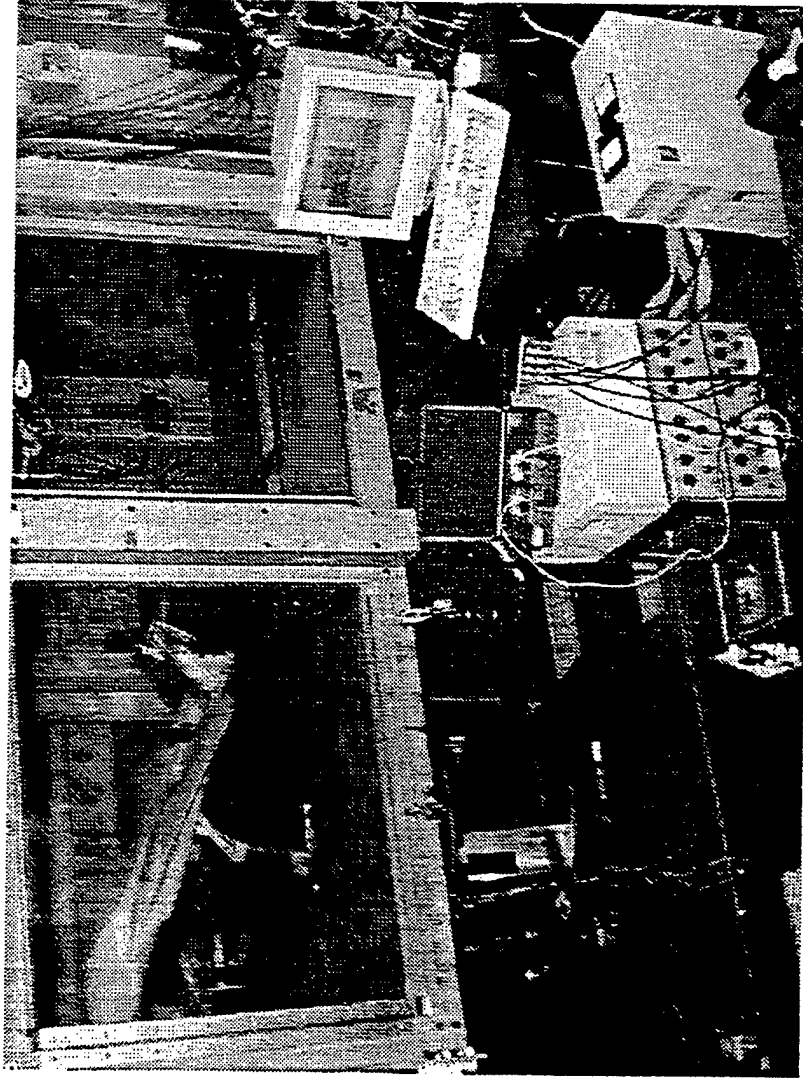
Four Offset Piezoceramic Stack

Actuators with:

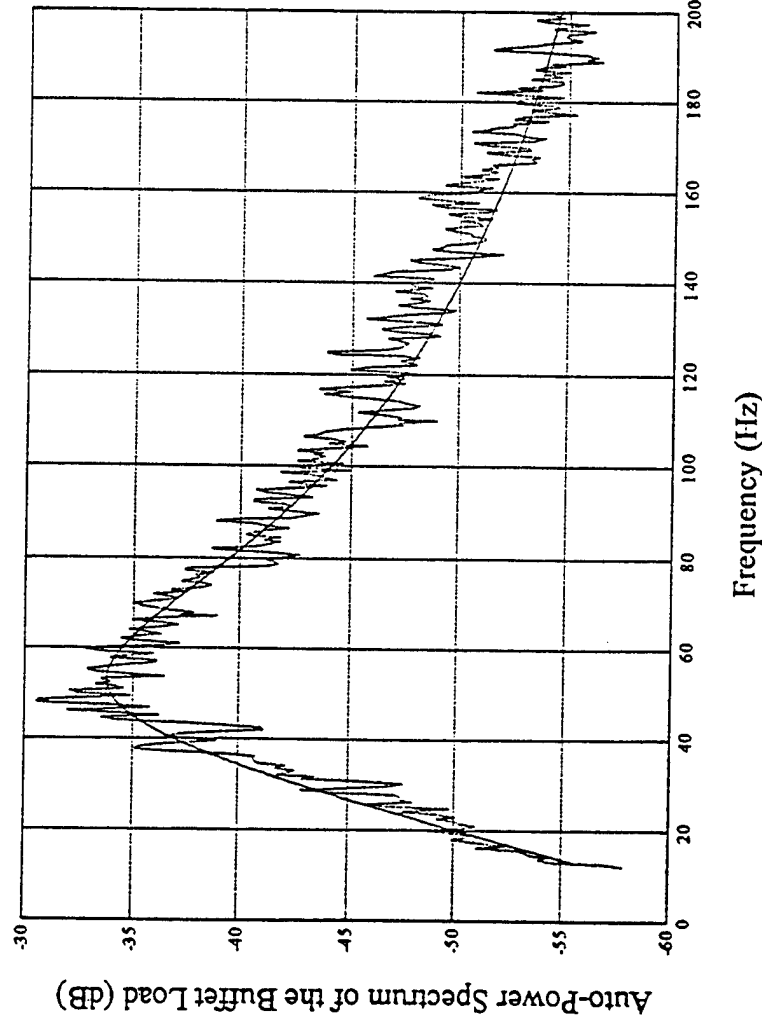
- PI P-830.10 (1kN) Stacks

dSpace Alpha Combo (600MHz DSP)

Amplifiers, Filters, Noise Generator, Computer



Aeroelastically Scaled Empennage



Auto-Power Spectrum of the Buffet Load
on the Outboard Trailing Edge Tip

Scaling based on reduced
frequency:

$$r = \frac{f \cdot b}{U}$$

Characteristic length ratio:

$$b_{\text{model}} = b_{\text{full-scale}} / 16$$

Free stream velocity

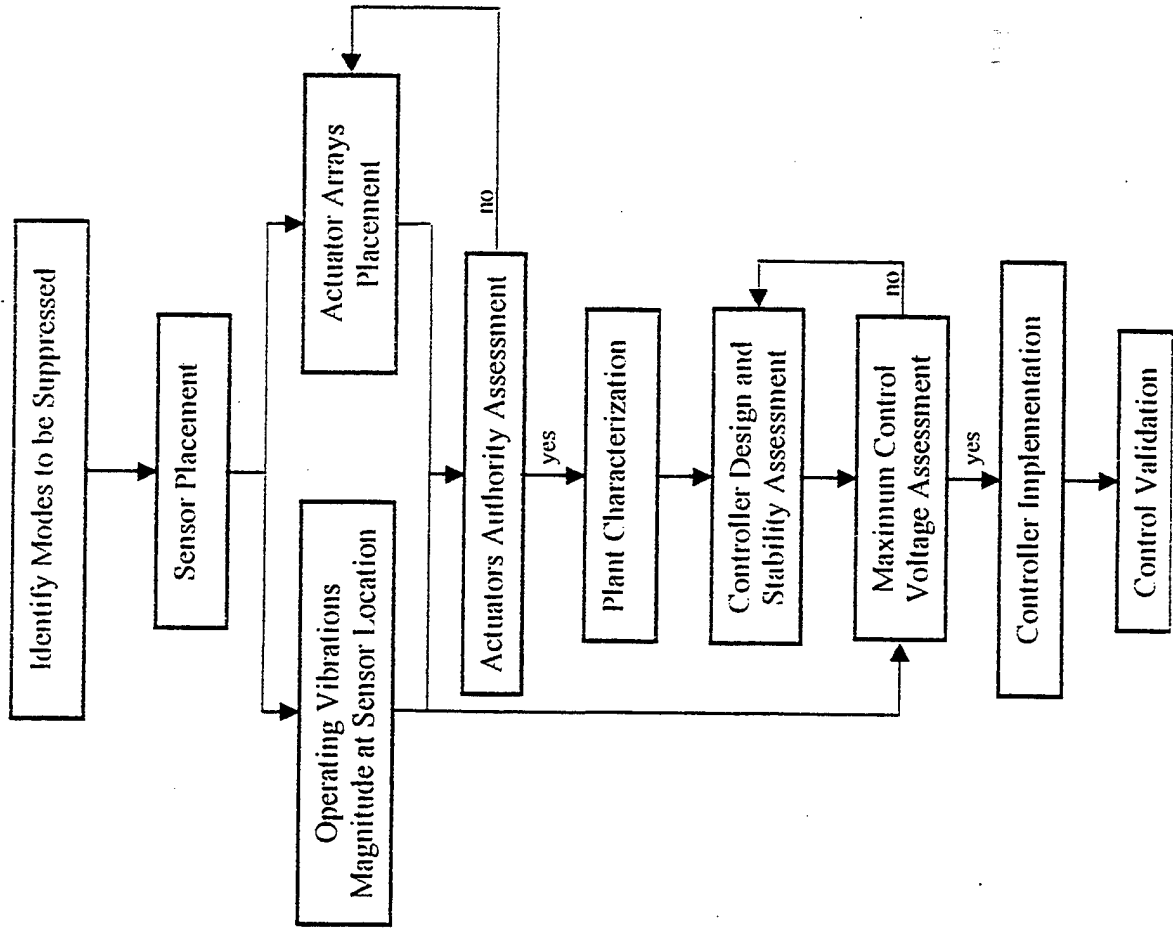
$$U_{\text{model}} = 26.9 \text{ m/s} \quad @300\text{ft}$$

$$U_{\text{full-scale}} = 0.6 \text{ Mach} \quad @20,000\text{ft}$$

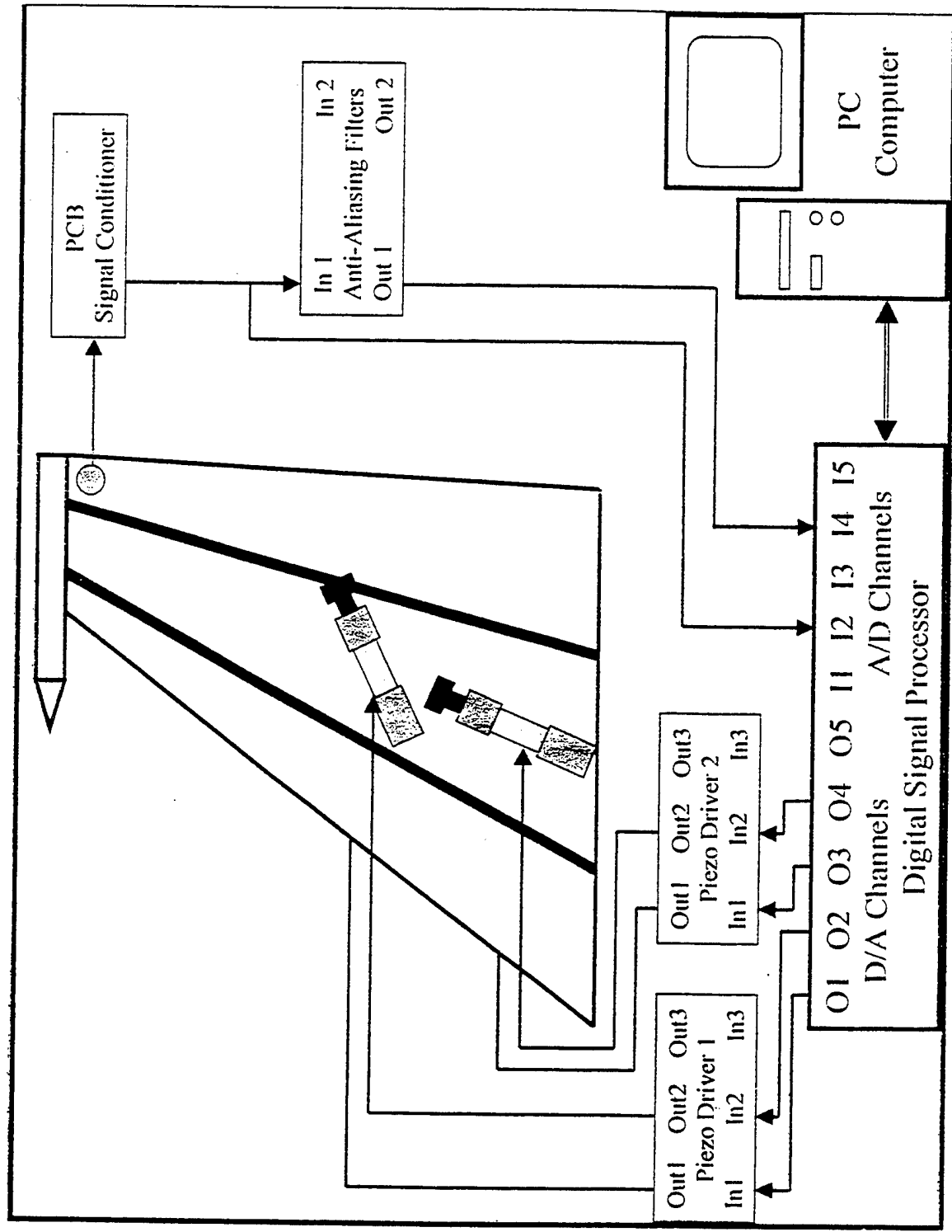
Gives frequency ratio:

$$f_{\text{model}} = 2.25 f_{\text{full-scale}}$$

Control System Design Procedure

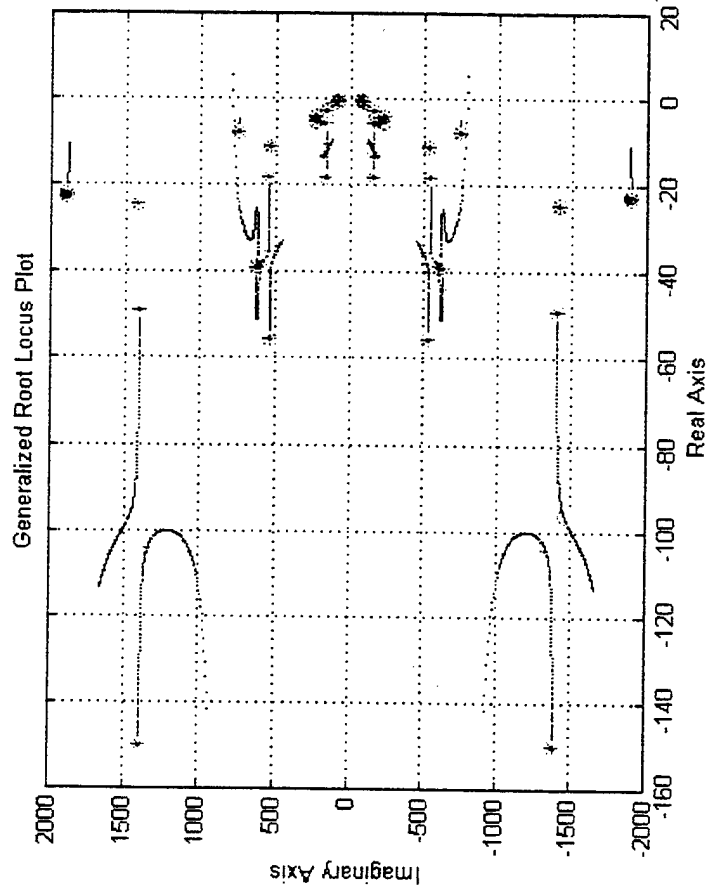
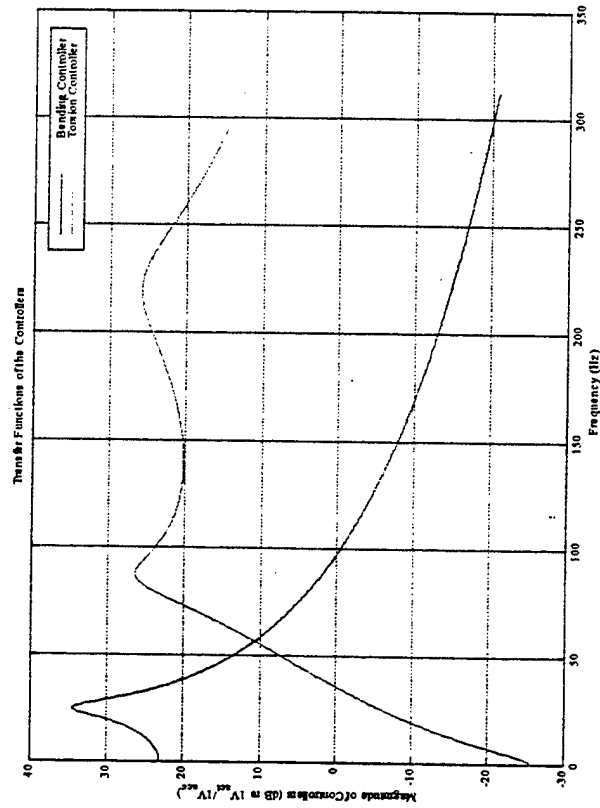


Wind Tunnel Experimental Wiring



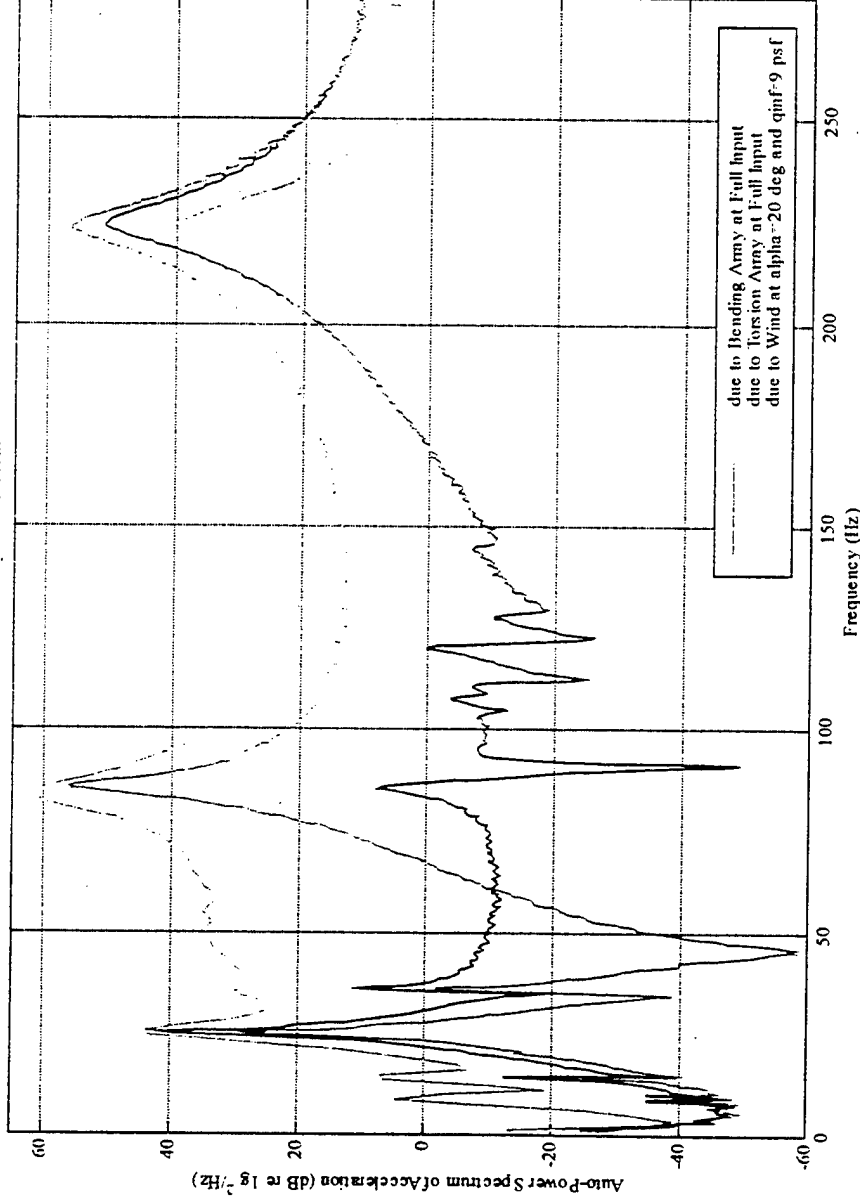
Wind Tunnel Controllers

	Frequency (rad/s)	Damping Ratio (%)	Scalar Gain
First Bending	157.22	13.464	-14.153
First Torsion	538.05	11.998	-4.8485
Second Torsion	1403.3	12.384	4.7967



Wind Tunnel Tests Actuator Authority

Actuator Authority Assessment



First bending mode : bending array has enough authority to suppress vibrations

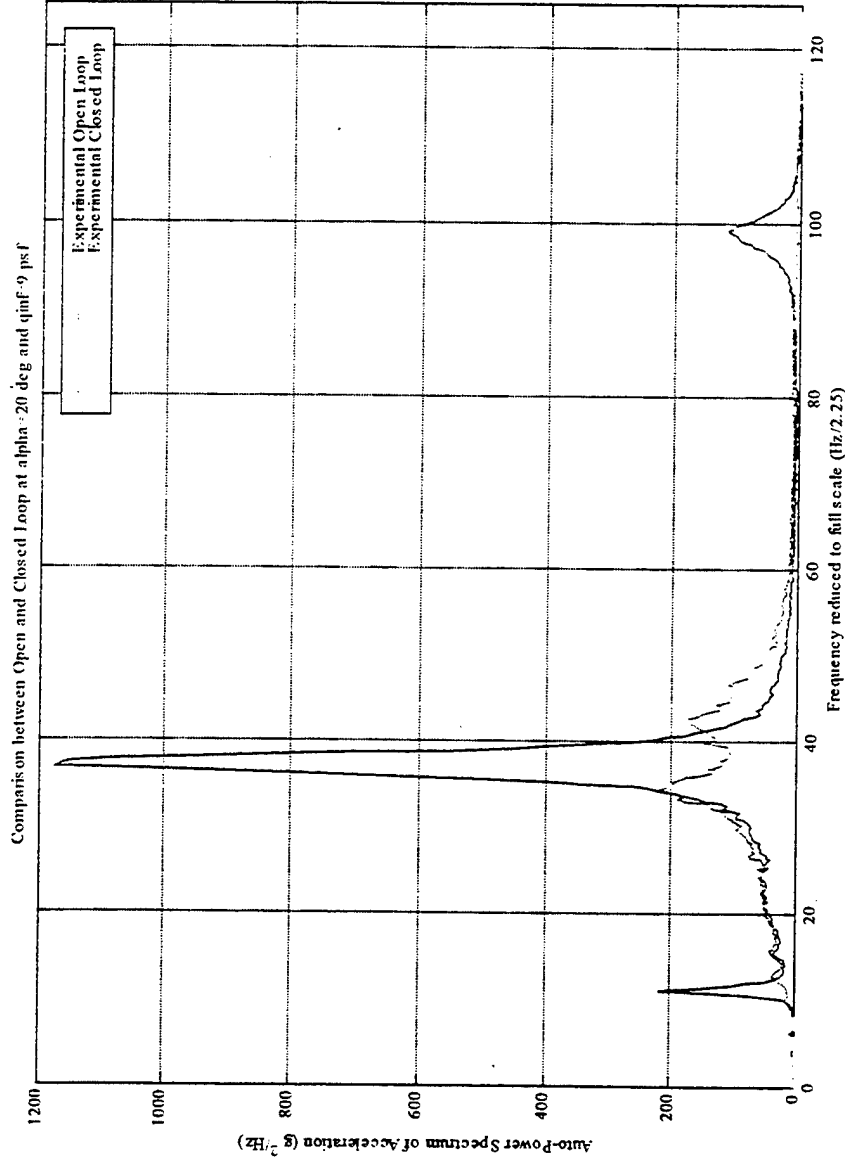
First torsion mode: torsion array produces slightly smaller response than wind, however difference is not large enough to require extra actuator

Second torsion mode: both of actuator arrays produce larger response than wind.

Controller Implementation

- **Objective:** Implement the designed controller digitally on a Digital Signal Processor (DSP)
- **Method**
 - Controller is built using block programming capability of Simulink
 - Controller is converted to DSP machine language through the Real Time Workshop of Mathworks and Real Time Interface of dSPACE
 - Time integration are performed using a fifth order Runge-Kutta algorithm
 - To avoid aliasing the controller rate is set at a frequency much higher than twice maximum controlled frequency

Wind Tunnel Tests Results



- Angle of Attack 20° and Free Stream Dynamic Pressure 9psf
- Auto-Power Spectrum of each of the controlled frequency reduced by a factor of at least 6 (more than 15dB reduction)
- RMS acceleration response of the Trailing Edge Tip of the tail was reduced by more than 17%

HEALTH MONITORING OF HELICOPTER ROTOR SYSTEMS

by

Mark J. Schulz, Anindya Ghoshal, Mannur Sundaresan

Structural Dynamics and Control Laboratory

Department of Mechanical Engineering

North Carolina A&T State University

Greensboro, NC 27411

Tel: (336) 334-7620 x 313, email: schulz@ncat.edu

P. F. Pai

Department of Mechanical and Aerospace Engineering

University of Missouri-Columbia

Columbia, MO 65211, U.S.A.

Ph: 573-884-1474, Fax: 573-884-5090, email: paip@missouri.edu

Professor Ed Smith

Technical Monitor

PSU Rotorcraft Center of Excellence

ARO Workshop on Smart Structures

August 16-18, 1999

HEALTH MONITORING OF HELICOPTER ROTOR SYSTEMS

FACULTY:

**MARK SCHULZ, ANINDYA
GHOSHAL, MANNUR
SUNDARESAN** (North
Carolina A&T SU)

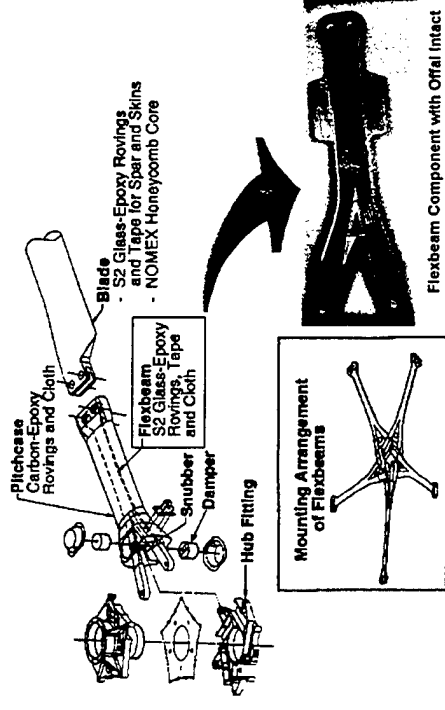
P. FRANK PAI (U.
Missouri - Columbia)

SPONSORS:

NRTC (Technical Monitor
Professor Ed Smith)
Boeing Mesa (Test article
from P. Shanthakumar)

PROBLEM STATEMENT & RELEVANCE

- The rotor system has no redundant load path and rotor components require a high level of maintenance
- Health Monitoring of the rotor system can increase safety and reduce operational costs



Helicopter rotor system (Picture Courtesy of Boeing)

PROJECT OBJECTIVES

- Develop a technique for detecting damage to the flexbeam part of a bearingless rotor
- Extend the technology to other rotor components

TECHNICAL BARRIERS:

- Aerodynamic loads and geometry of the flexbeam are changing in the airborne (rotating blades) condition; signal coupling between rotating & fixed frames difficult
- PZT sensors/actuator are used to actively interrogate the flexbeam using vibrations
- FEM Modeling of simple beams is used to develop damage detection algorithms
- Passive AE technique to be investigated

APPROACH:

RESULTS:

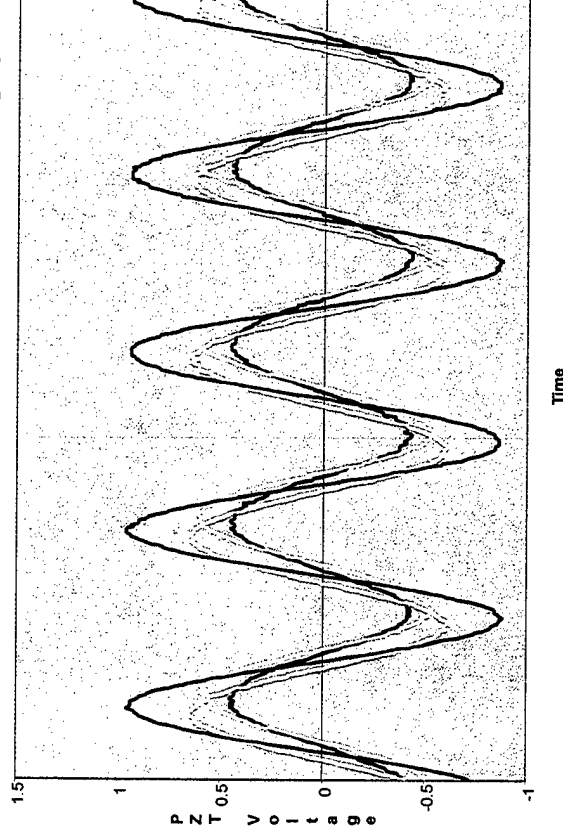
- Damage detection using longitudinal vibration promising because amplitude change of symmetric PZT's indicates damage with minimal pre-damage data

FLEXBEAM HEALTH MONITORING



Mass-Actuator

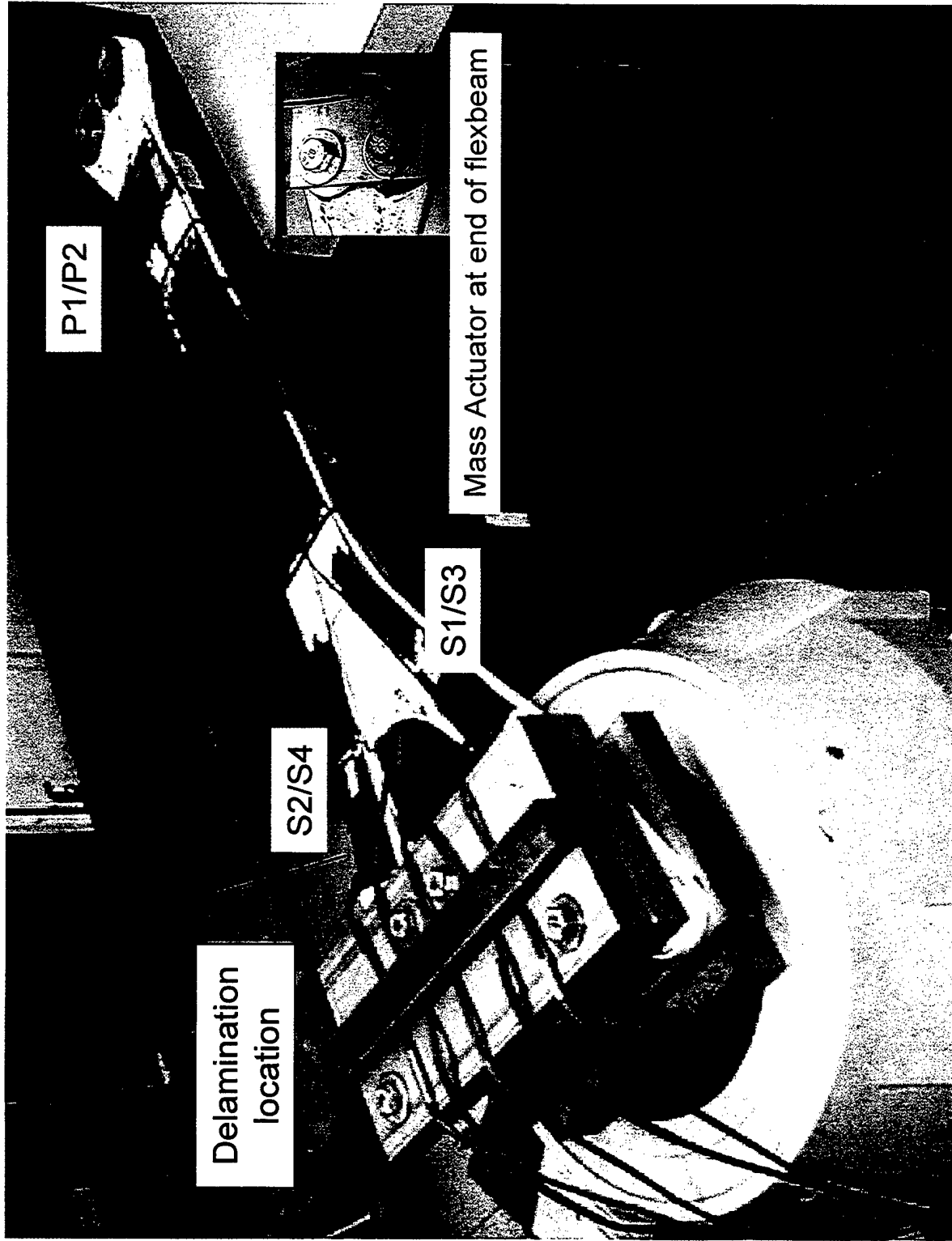
Vibration response of PZT patches at 900Hz (red curve is nearest damage)



Bot left(black), top left(white), bot right(yellow), top right(red), damage is at right leg

Helicopter crash due to rotor blade failure





Helicopter flexbeam with PZT patches/piezo-inertial actuator

Experimental Results (100 volts excitation):

Table 1. PZT Voltage vs. Frequency

Case number	Frequency (Hz)	C1	C3	C2	C4	P1	P2
1	100	0.12	0.18	0.14	0.18	0.14	0.18
2	200	0.12	0.18	0.14	0.18	0.14	0.18
3	500	0.2	0.22	0.18	0.22	0.18	0.22
4	600	0.24	0.22	0.22	0.34	0.22	0.34
5	800	0.16	0.18	0.14	0.22	0.14	0.22
6	840	0.2	0.22	0.18	0.22	0.18	0.22
7	860	0.28	0.3	0.18	0.3	0.18	0.3
8	880	0.32	0.34	0.3	0.42	0.38	0.46
9	900	0.42	0.56	0.64	0.94	0.66	0.74
10	920	0.2	0.3	0.3	0.46	0.3	0.34
11	940	0.16	0.22	0.22	0.34	0.22	0.22
12	960	0.16	0.22	0.18	0.3	0.18	0.22

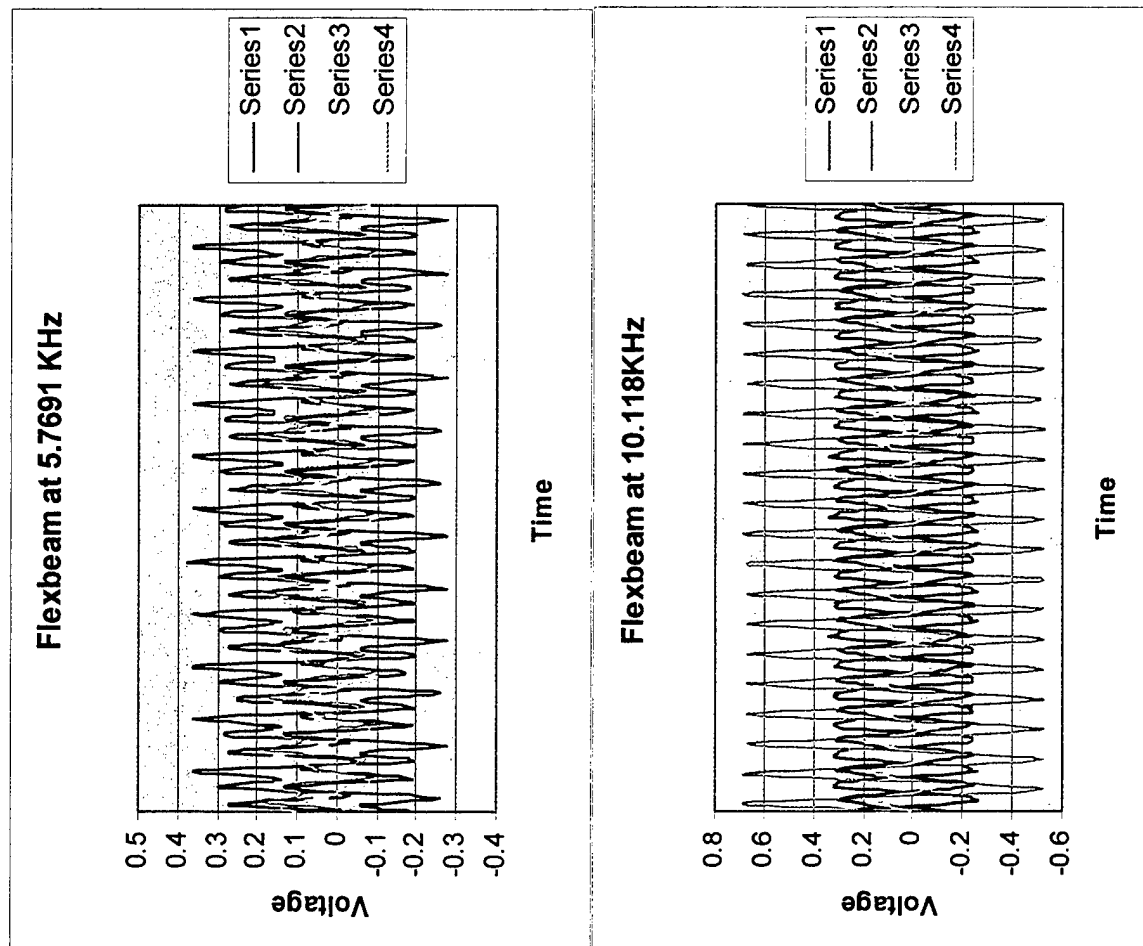
(C1-bottom patch left leg, C3-top patch left leg, C2-bottom patch right leg, C4-top patch right leg, P1-top patch end, P2-bottom patch end)

Results of Flexbeam Testing Using PZT Patch Excitation:

- High frequency response (10.1 KHz) different between legs, possibly indicates delamination on one leg
- Nonlinear response at (5.8 KHz) not understood

Results of Flexbeam Testing Using PZT Inertial Actuator:

- Resonant comparison method used to compare symmetric sensor outputs at resonances of damage
- Difference in vibration response between top and bottom collocated patches is greatest at leg with delamination
- Away from resonance damage not obvious
- A higher frequency actuator is needed



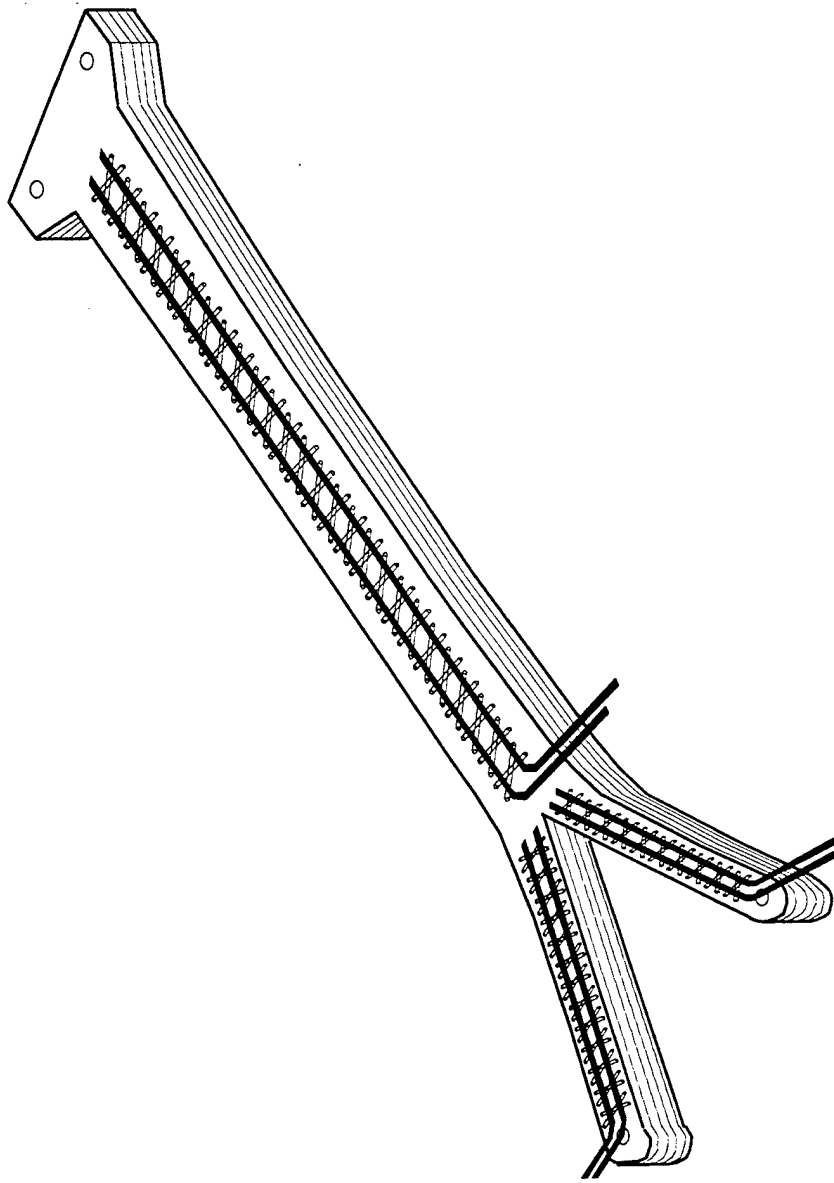
Flexbeam PZT patch response for PZT patch excitation (Series 1= sensor S1, series 2=sensor S2, series 3=sensor S3, Series 4=sensor S4 near delamination)

Conclusions

- **Damage detection using longitudinal vibration promising because amplitude change of symmetric PZT's indicates damage with minimal pre-damage data**
- **Testing during loading is needed**
- **Testing for different damages is needed**
- **An actuator that has a higher frequency may be more sensitive for damage detection using longitudinal vibration**

New Approach

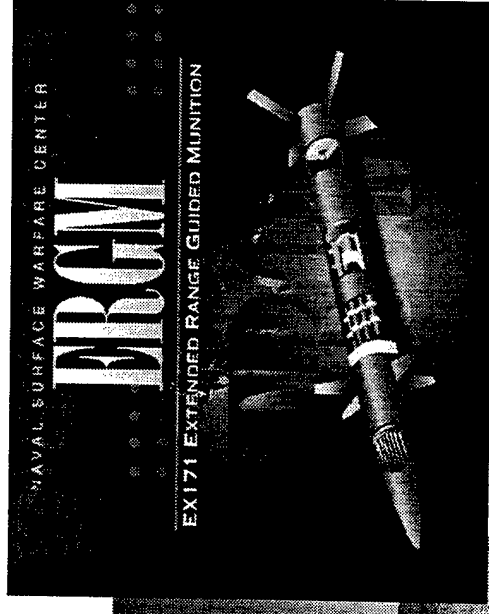
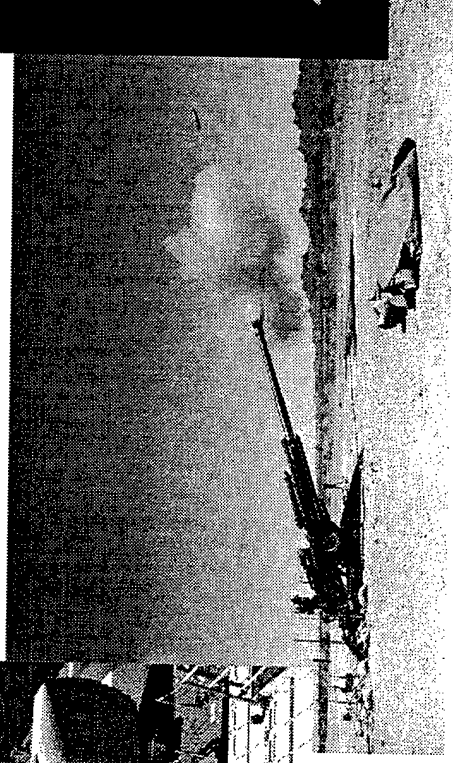
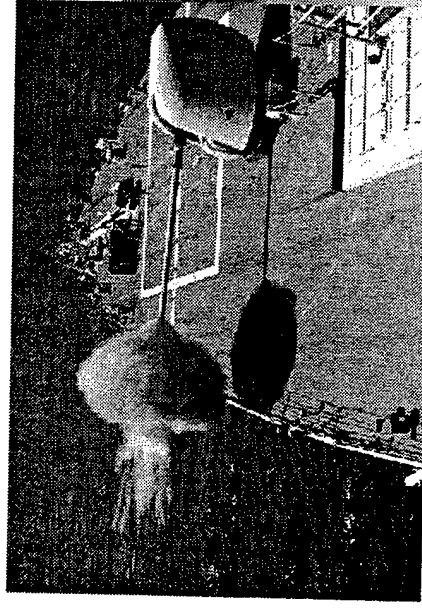
- **A distributed sensor is being developed**



Distributed sensor concept for rotorcraft flexbeam

Application of Magneto-Rheological Dampers for Controlling Gun Recoil

Mehdi Ahmadian
James C. Poynor
Advanced Vehicle Dynamics Laboratory
Department of Mechanical Engineering
Virginia Tech
Blacksburg, VA 24061-0238
(540) 231-4920
ahmadian@vt.edu



Background

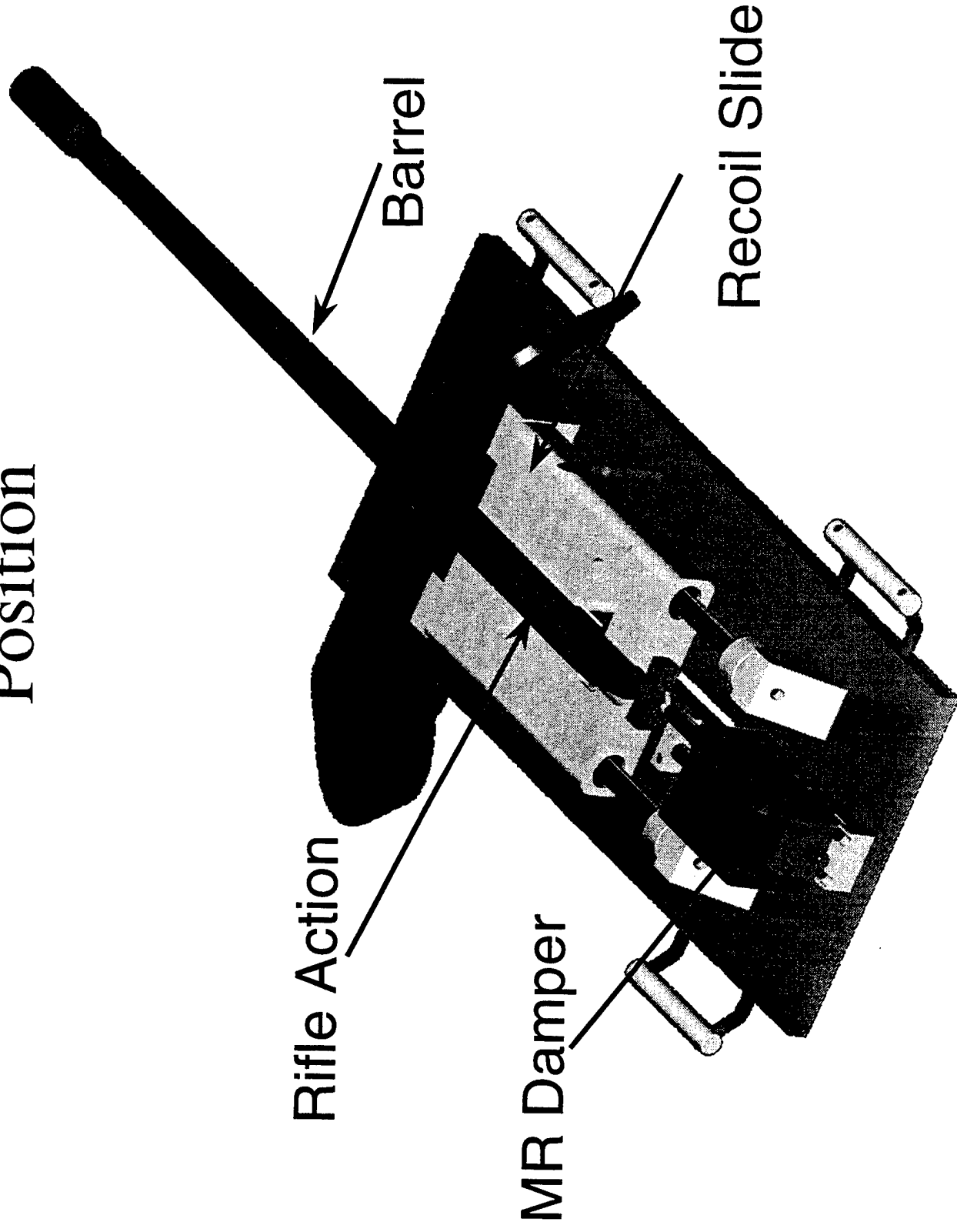
- *The project was started in August 1998, as a result of contacts between Naval Surface Warfare Center (NSWC) and Virginia Tech*
- *It was intended to demonstrate the benefits of MR technology for better controlling gun recoil*
 - ◆ *alternative for existing recoil mechanisms?*
 - ◆ *future weapons?*

Objective: Do the capabilities of MR technology help the versatility and adaptability of future or existing weapons

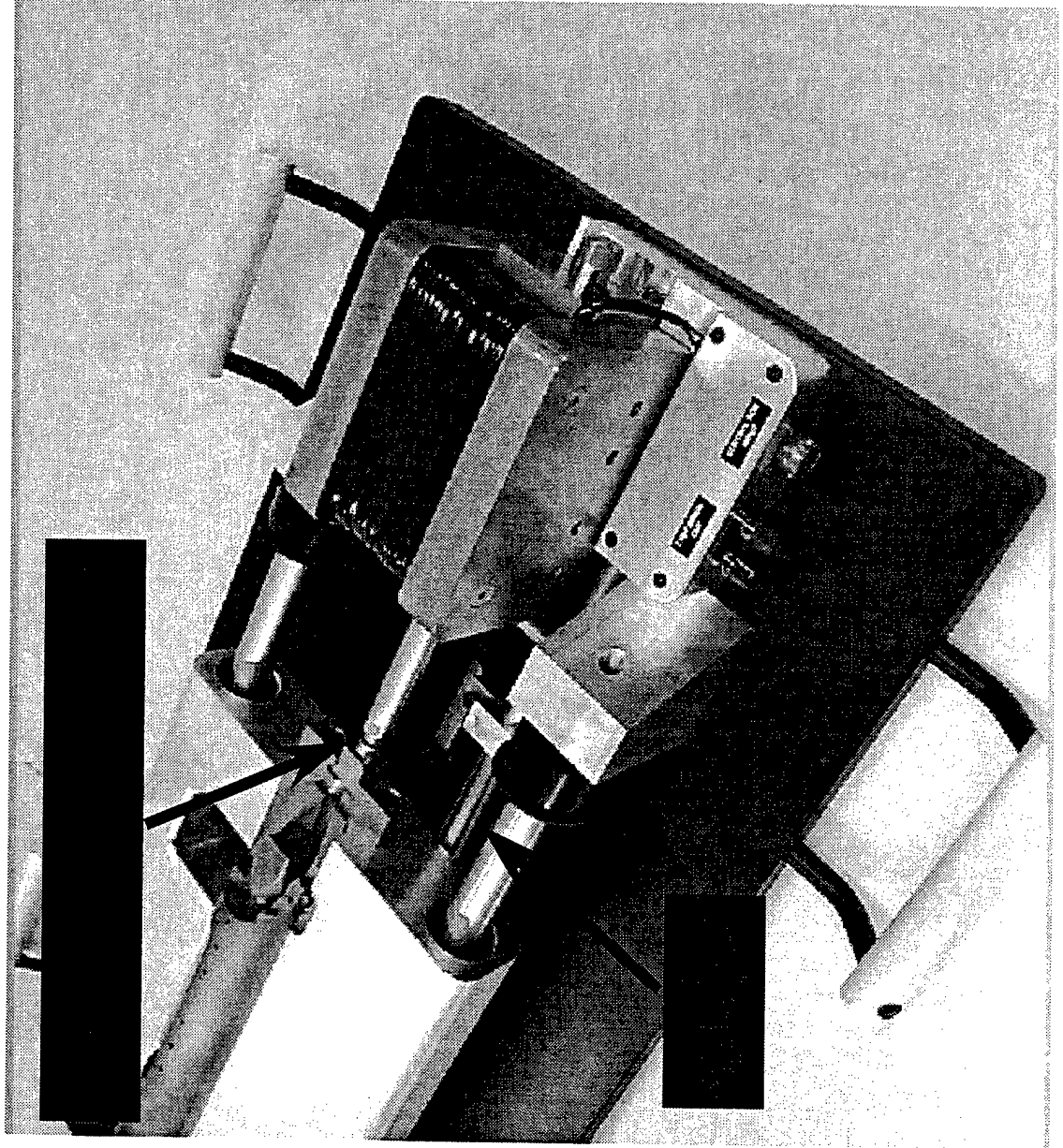
Approach

- Reviewed information on MK45 (provided by NSWCC)
- Evaluated recoil force and velocity requirements for MK45
- Brain stormed on various demonstrator designs
- Chose a 50 caliber BMG
 - ◆ live ammunition
 - ◆ reasonable recoil energy (force/velocity)
 - ◆ readily available
 - ◆ impressive!

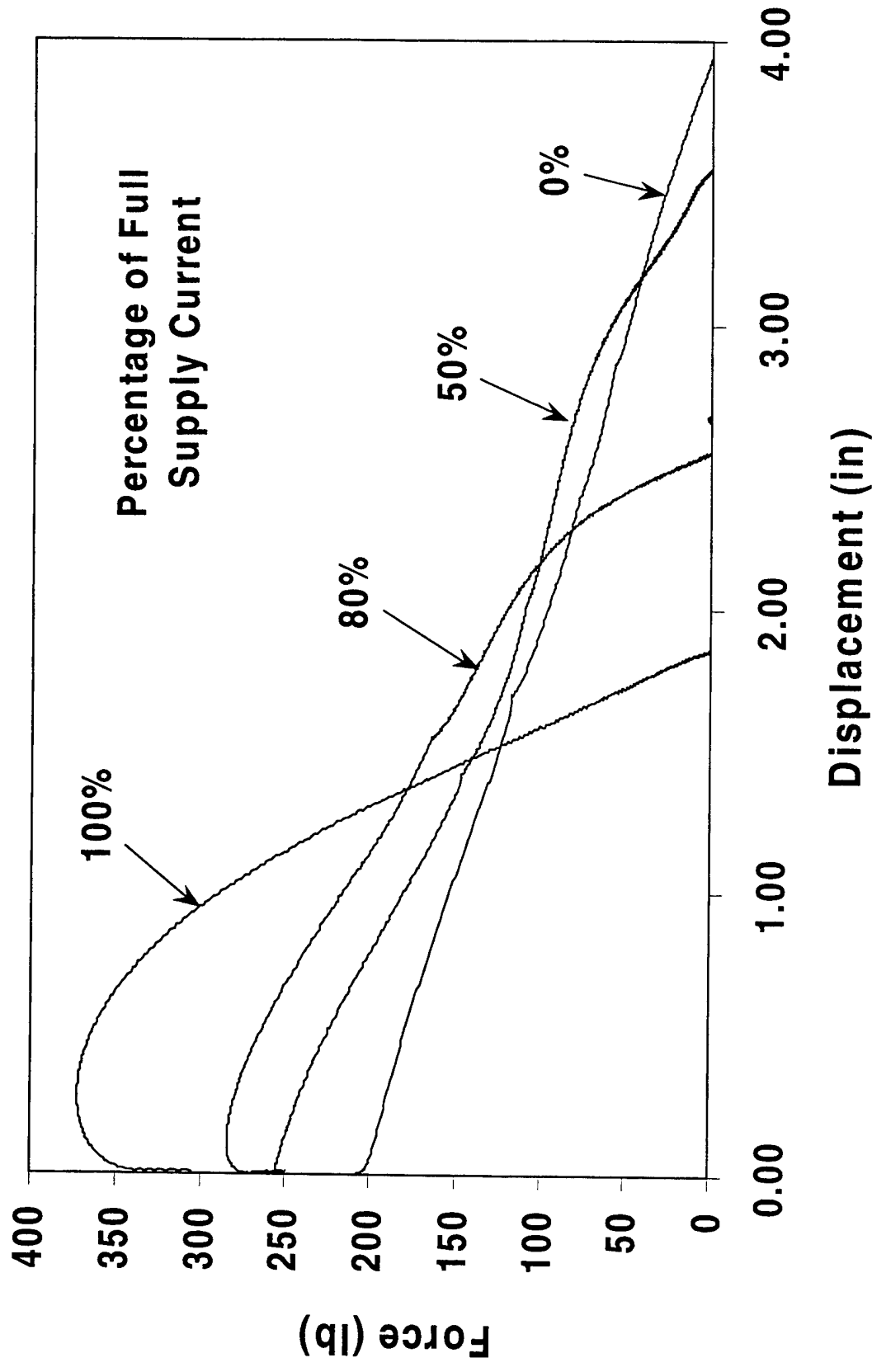
Recoil Demonstrator in Battery Position



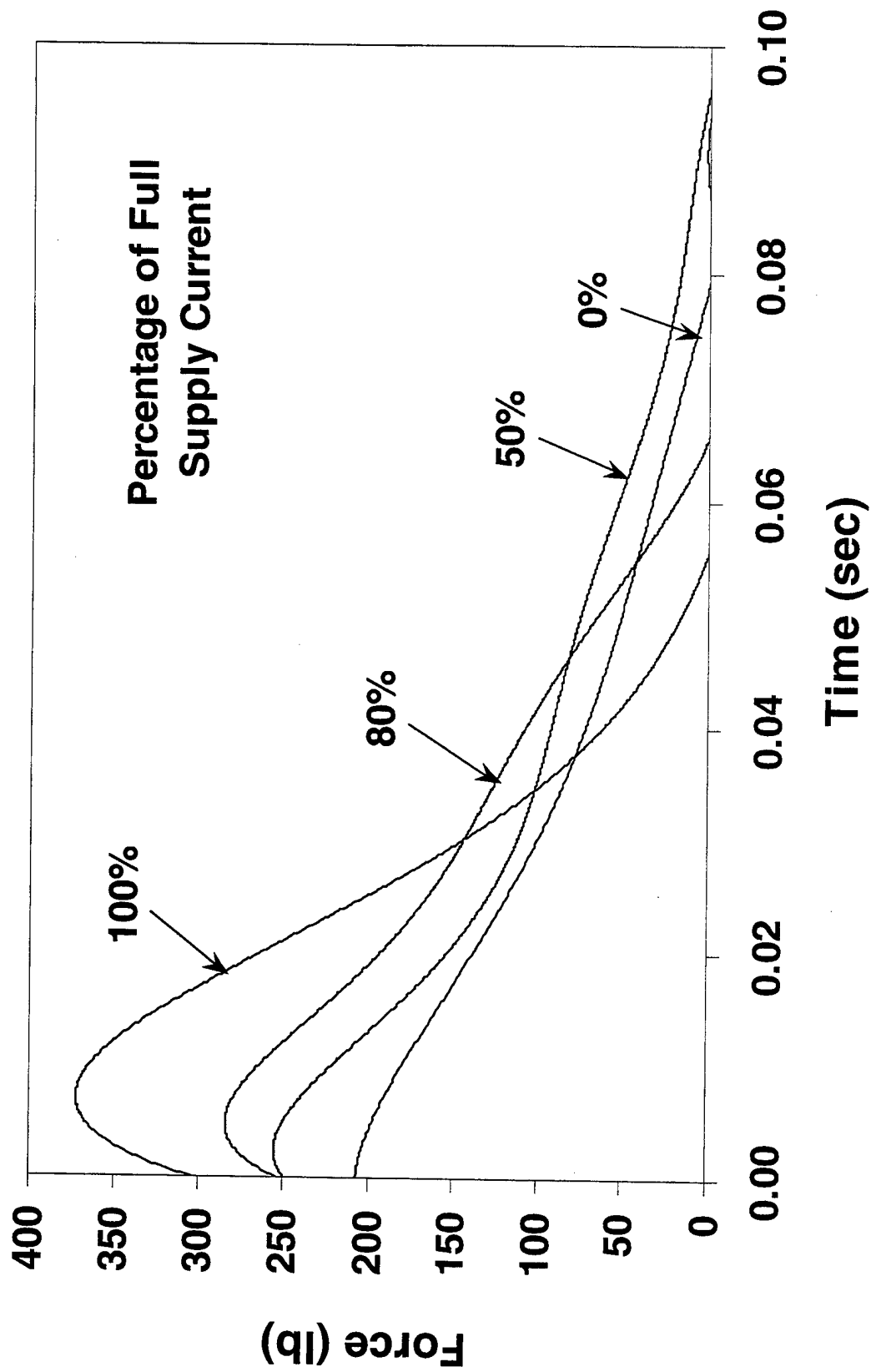
Instrumentation



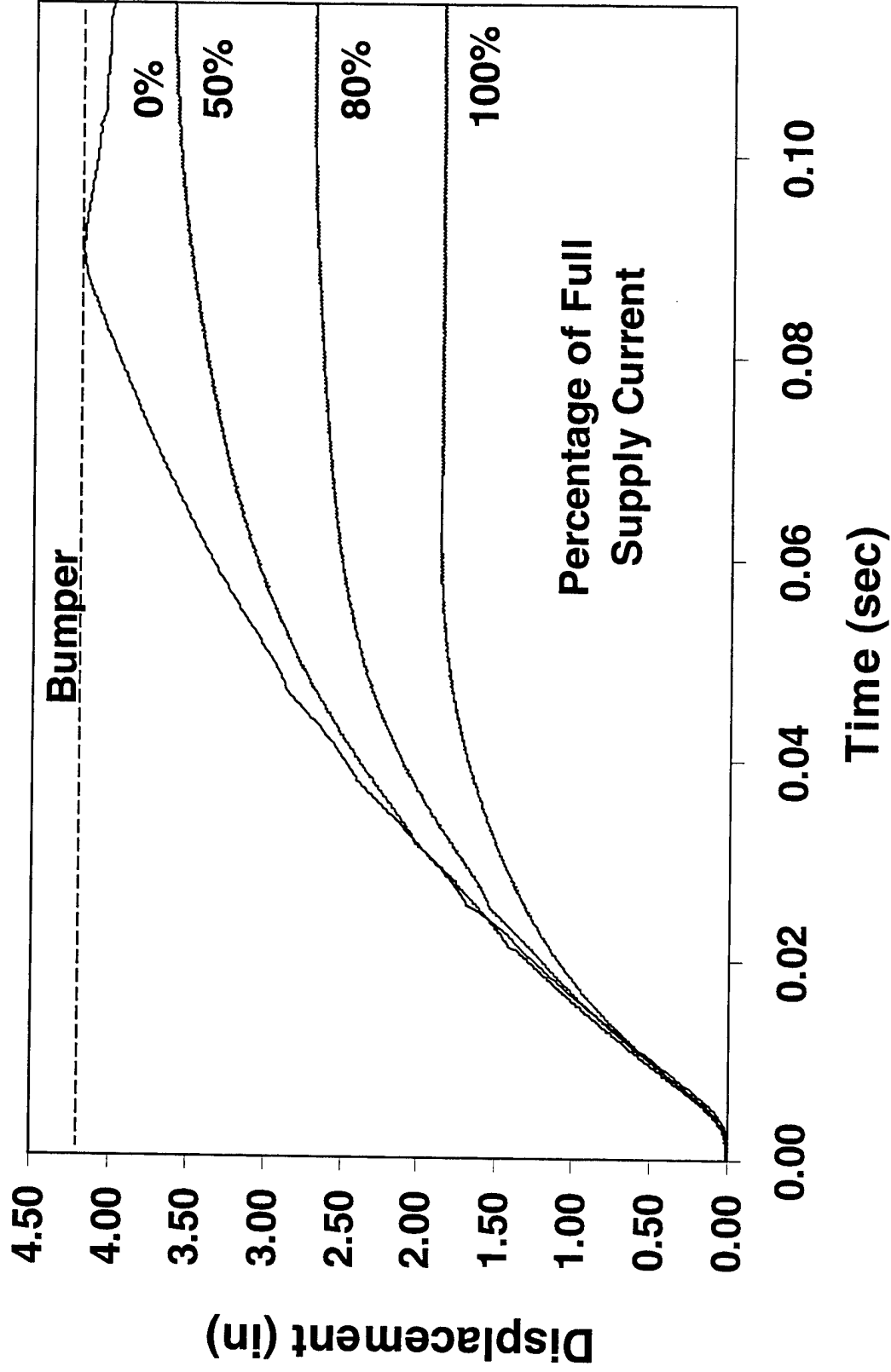
Recoil Force-Displacement Spectrum



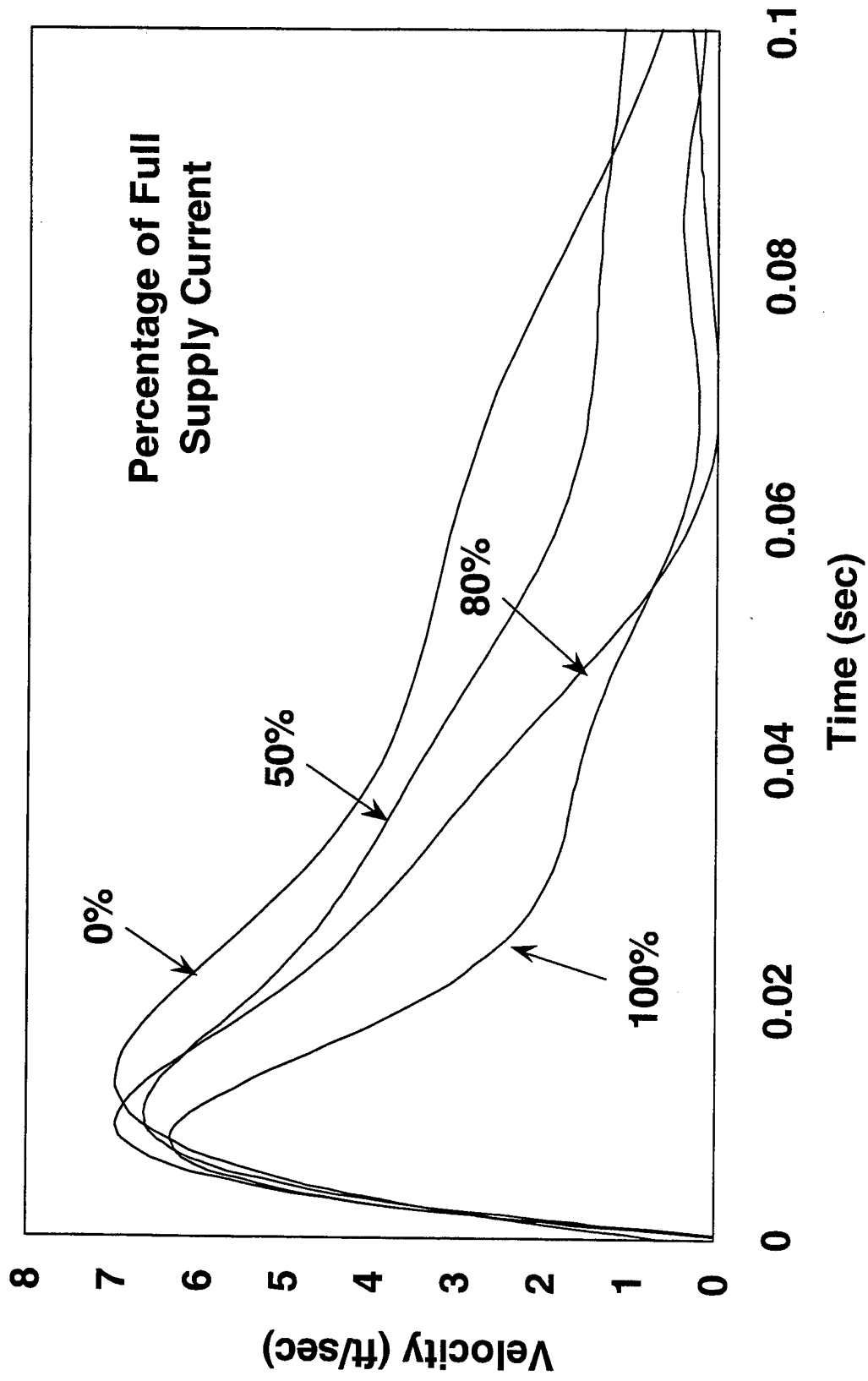
Recoil Force Profile



Recoil Displacement Profile



Recoil Slide Velocity



Summary

- *Evaluated the feasibility of MR technology for weapons applications*
- *Designed and built a live ammunition demonstrator*
- *Designed and built a magneto-rheological damper*
- *Showed that MR dampers are effective in controlling gun recoil; i.e., we can use the damper to control the recoil force and stroke*

PIEZOELECTRIC MINIATURE MOTOR USING A RADIAL-TORSIONAL STATOR VIBRATOR

Burhanettin Koc, Philippe Bouchilloux¹ and Kenji Uchino

International Center for Actuators and Transducers, Materials Research Laboratory,
The Pennsylvania State University, University Park, PA 16802, USA

¹Active Materials and Smart Structures Laboratory
Department of Mechanical Engineering, Aeronautical Engineering and Mechanics
Rensselaer Polytechnic Institute, Troy, NY 12180-3590, USA

Abstract:

This study presents design and operating principle of a 3.0mm diameter piezoelectric ultrasonic motor. The stator in this motor has a bi-layer structure, where a uniformly-electroded piezoelectric element is bonded to a metal ring. The metal ring has four inwardly oriented arms placed 90° apart on its inner circumference. The tips of the arms are truncated and a rotor with a conical end touches to the tips of the arms. The length and cross-sectional area of each arm were selected such that the resonance frequency of the second bending mode of the arms is close to that of the radial mode of the stator. The rotor is placed at the center of the stator and rotates when an electric field is applied at a frequency between the radial and bending resonance modes. The truncated cone shape at the end of the rotor guarantees a permanent contact with the tips of the arms.

The behavior of the free stator was analyzed using the ATILA finite element software. Torque vs. speed relationship was measured from the transient speed change with a motor load. A starting torque of 17 μNm was obtained at 20 Vrms when the motor was driven at 558 kHz. The main features of this motor are low cost and easy assembly owing to a simple structure and less number of components.

PIEZOELECTRIC MINIATURE MOTOR USING A RADIAL-TORSIONAL STATOR VIBRATOR

Burhanettin Koc, Philippe Bouchilloux¹ and Kenji Uchino

International Center for Actuators and Transducers, Materials Research Laboratory,
The Pennsylvania State University, University Park, PA 16802, USA

¹Active Materials and Smart Structures Laboratory
Department of Mechanical Engineering, Aeronautical Engineering and Mechanics
Rensselaer Polytechnic Institute, Troy, NY 12180-3590, USA

Background History

- Contrary to common belief, piezoelectric ultrasonic motors have a long tradition.
- In 1942, Williams and Brown proposed the first investigation of piezoelectric ultrasonic motor.
- Although the working mechanisms of ultrasonic motors had been known for more than 50 years, only a few different types of ultrasonic motors have been developed until 1980s.

Kleesattel et al, 1959

Tehon, 1962

Arkhangeldky, 1963

Lavrenko, 1964

H.V Barth, in 1973

Wischnewski, 1975

Lavrinenko et al., 1980

- Intense research on piezoelectric ultrasonic motor starts after Sashida's travelling wave ultrasonic motor design in 1982.

Motivation

- Emerging technology demand smaller, more accurate and more powerful motion systems for micromechatronic device applications
- Conventional motional systems, utilize electromagnetic motors, can provide partial solutions to the needs of today's marketplace.
- Since miniaturization of conventional electromagnetic motors is difficult, these motors are not suitable for micromechatronic device applications
- The piezoelectric ultrasonic motors have a great potential for micromechatronic device applications because of the following features
 - high resolution of displacement control
 - frictional locking at the power-off stage
 - high thrust to weight ratio
 - absence of a parasitic magnetic fields

Current miniaturized piezoelectric ultrasonic motors, which use travelling wave, have a size limitation

- to produce a traveling wave on a piezoelectric element two AC power sources with 90 degree phase difference are needed
- sectors on the piezoelectric active element are poled in alternately opposite directions which causes a high stress concentration between two electroded sectors resulting in sample damage

Objective

- to design, fabricate, and characterize a miniature piezoelectric ultrasonic motor that can be used in micromechatronic devices.

Applications

- Medical industry (catheter)
- Microrobotics (desktop manufacturing)
- Mobile communication devices (silent alarm)
- Automotive (adaptive lighting)

Approaches

- Keeping the structure and poling configuration of the active piezoelectric element simple so as to be manufactured in small size;
- Reducing the number of components used in the motor as few as possible to decrease the production cost.

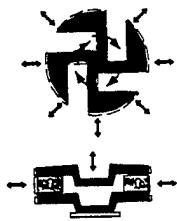
Material : commercial bulk PZT ring (high Q_m , Low dielectric loss)

Design: Metal-Ceramic Composite structure

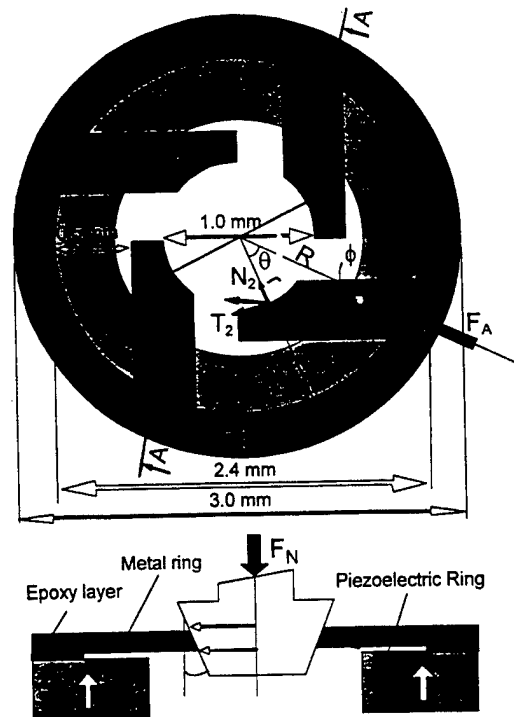
FEM: understand the free stator behavior and optimize the structure

Top and cross-sectional view of the miniaturized stator

Initial Design*

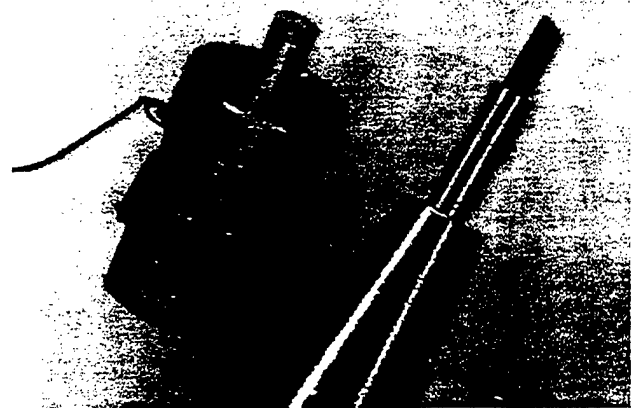
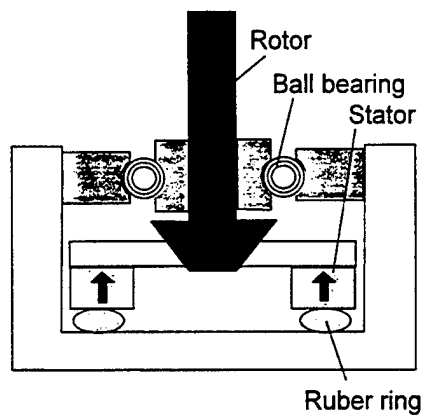


- remove bottom metal coupler
- remove center part of the top metal coupler
- adjust the bending frequency of the inward oriented arms to the radial resonance frequency
- understand stator behavior using ATILA
- characterize the motor



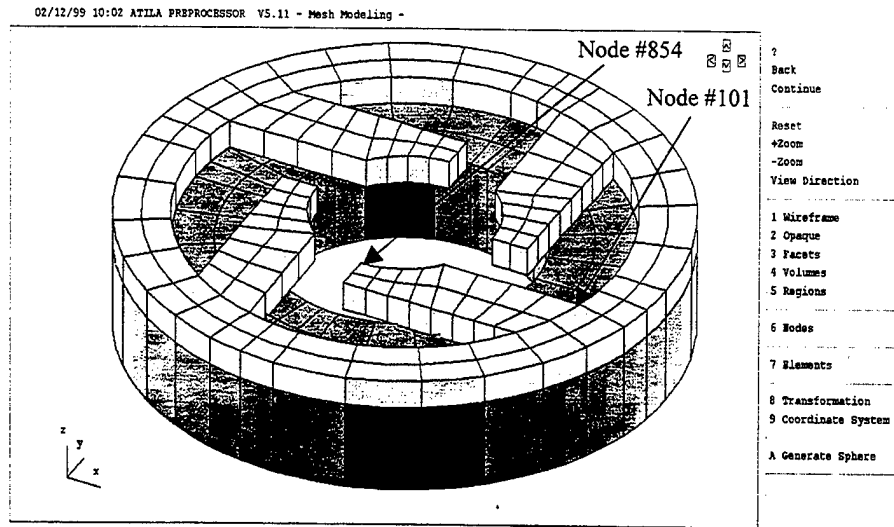
* Koc et. al. Jpn. J. Appl. Phys. Vol. 37, pp.5659-5662
Part 1, No. 10 October 1998

The 3 mm Motor



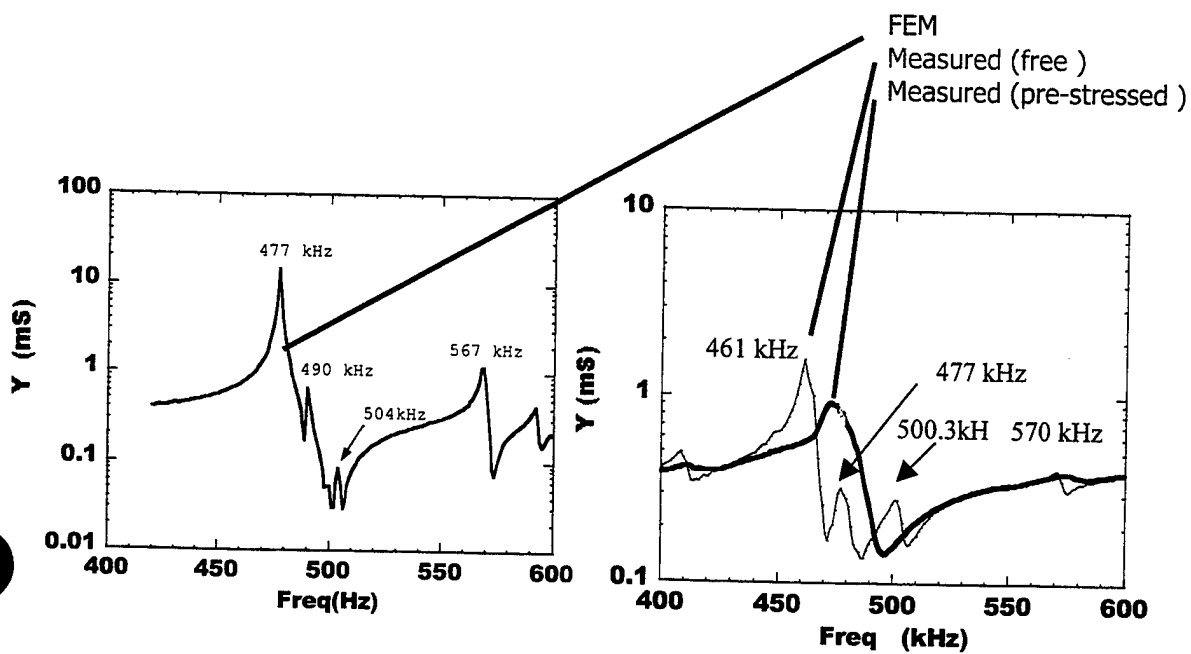
Encapsulated motor next to a 0.5 mm metallic pencil
(Steel housing was coated with an epoxy insulator)

ATILA Finite Element Modeling

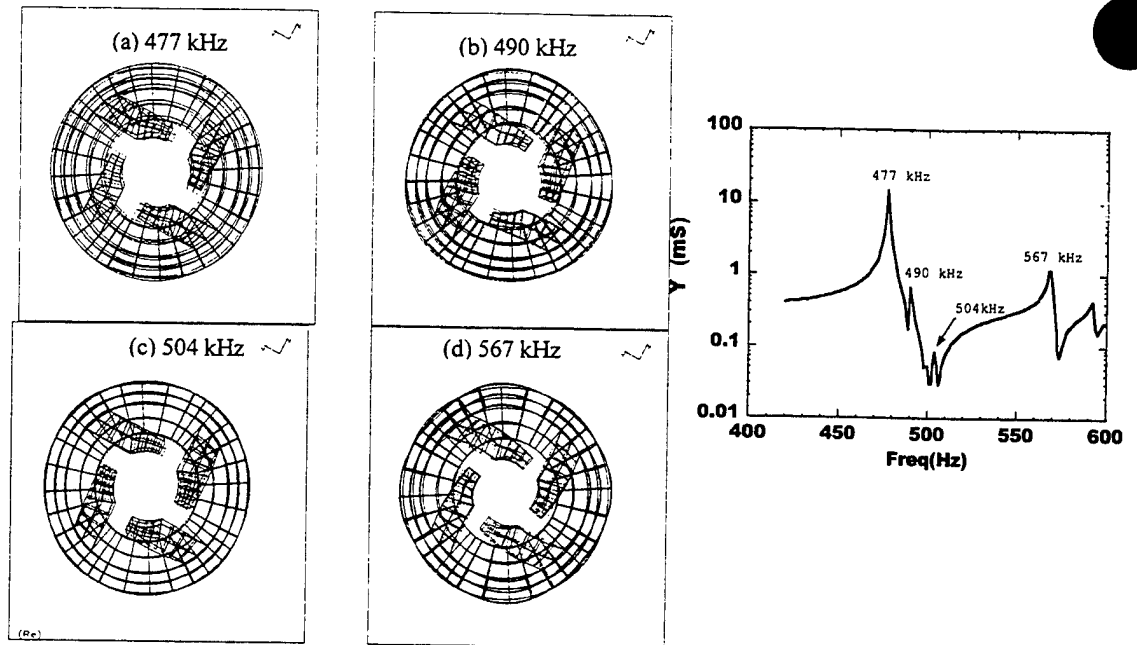


ATILA 3D mesh of the stator vibrator
(256 brick elements were used in the model with 2036 nodes)

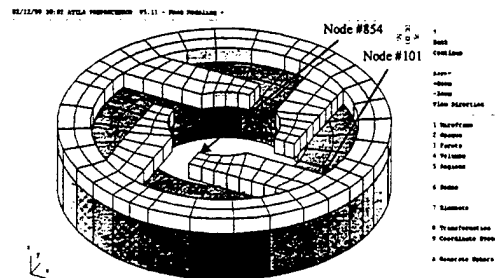
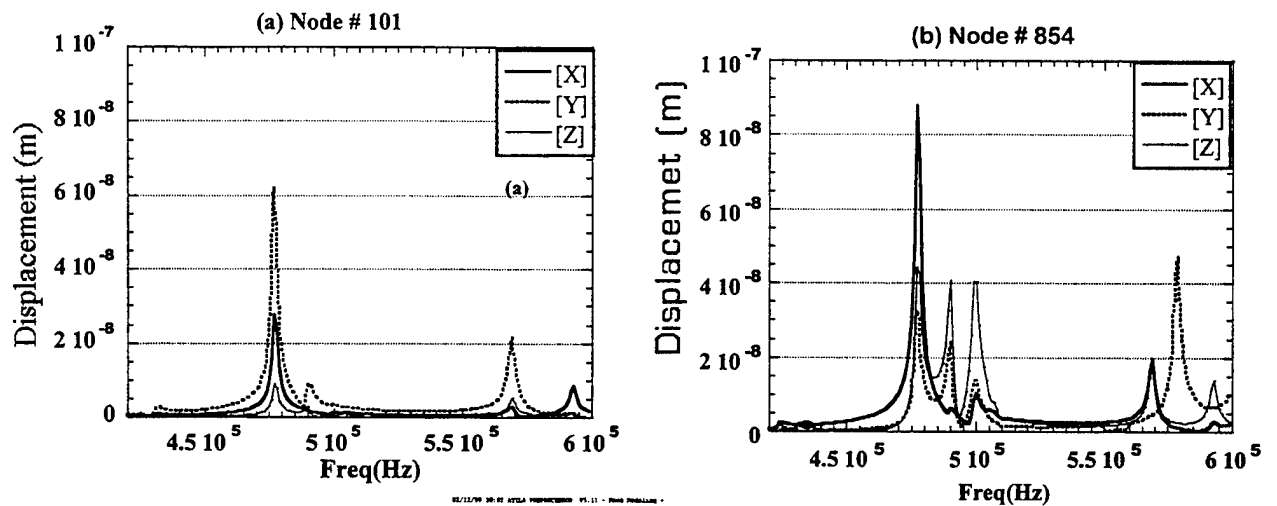
Admittance Spectrum



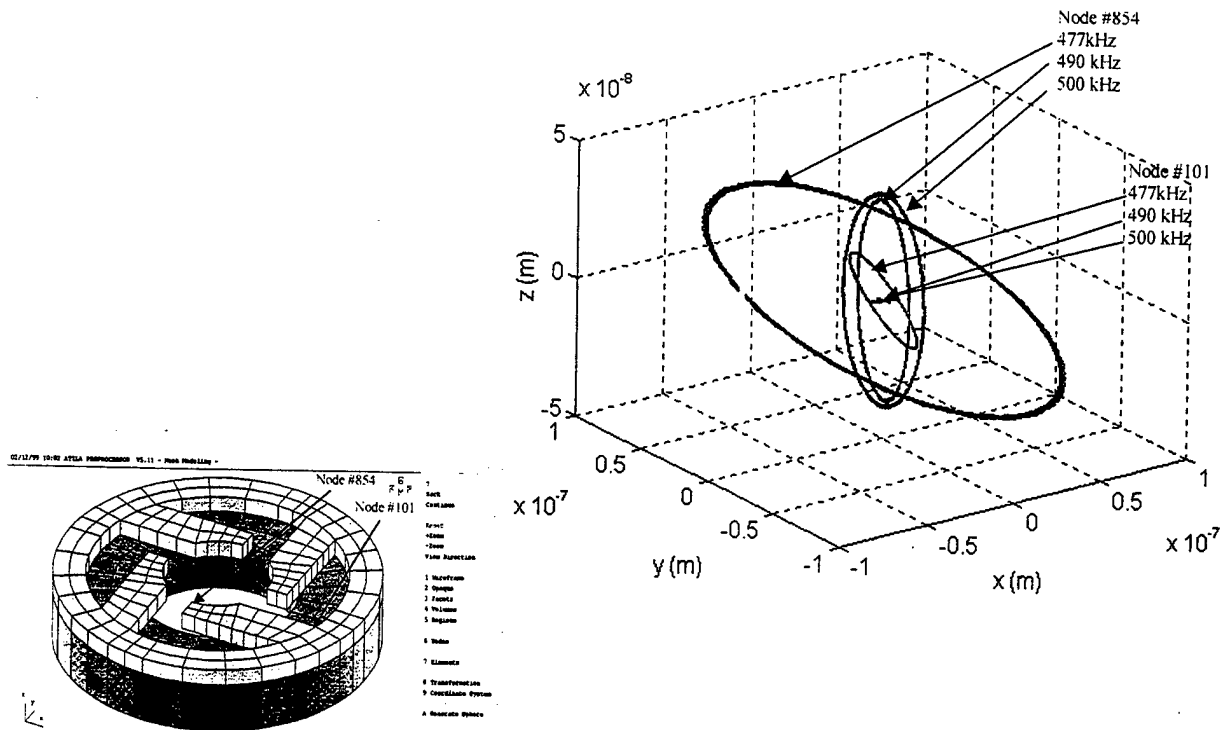
Simulated Mode Shapes of the Free Stator



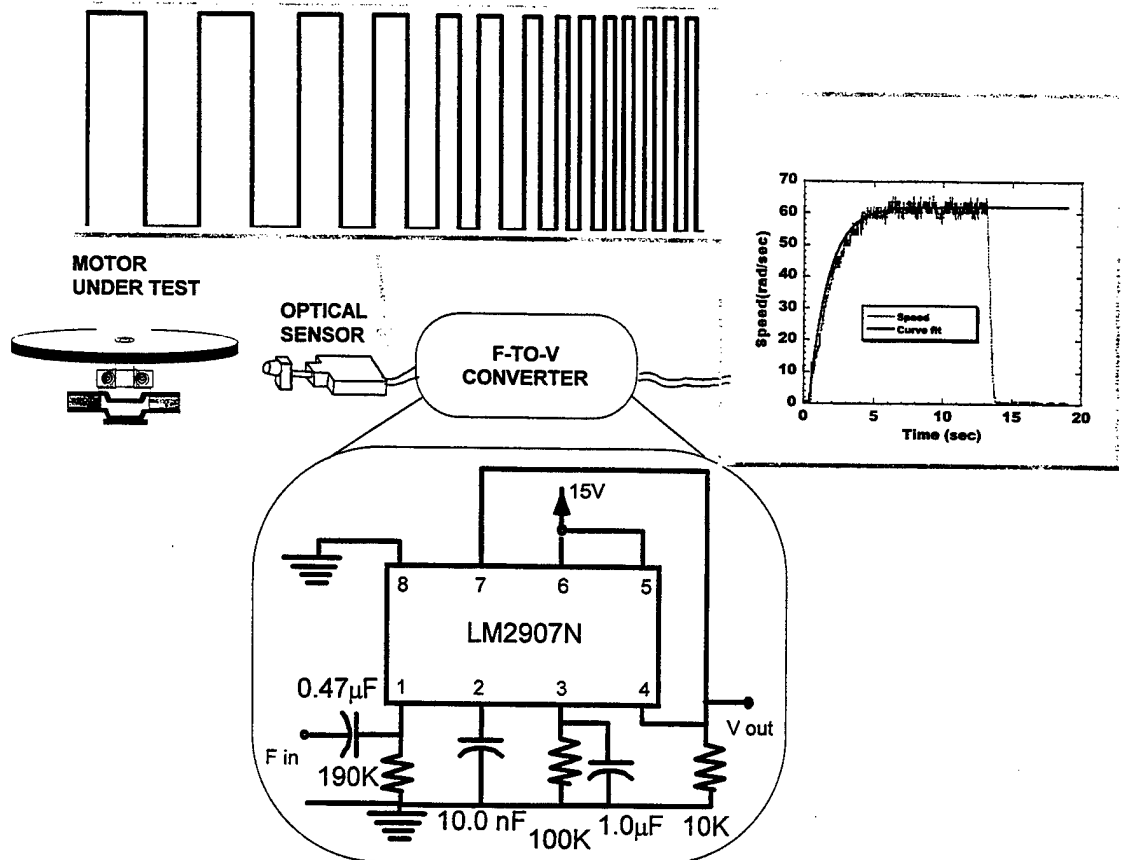
Magnitude of calculated displacement



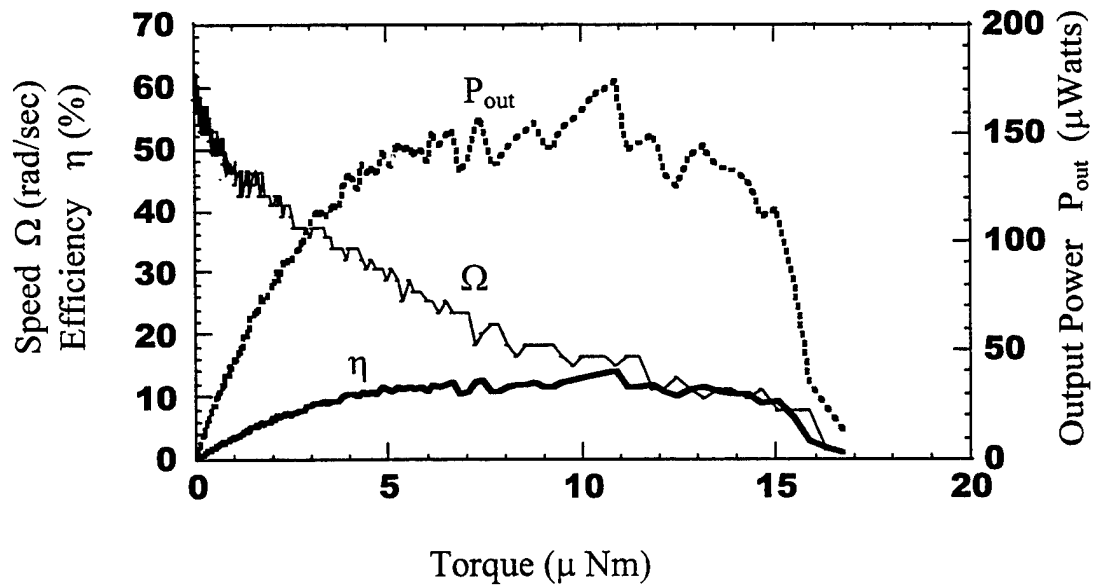
Amplification of Elliptical Trajectories



Angular Position and Transient Speed Detection



Load characteristics of the motor



Load characteristics of the motor was estimated from transient speed measurement

Conclusions

- We proposed a new Multi-Mode-Single-Vibrator Type Piezoelectric Ultrasonic Motor design using metal-ceramic composite radial-torsional stator vibrator. The diameter of the motor is 3mm.
- The structure of the motor is simple and highly scalable.
- The rotation in this motor take place by exciting the stator with a combination of two modes: the fundamental radial mode of the stator and the second bending mode of the arms.
- The stator was analyzed using the ATILA finite element code, and its dynamic behavior was predicted.
- The major applications of this motor can be micromechatronic devices for the medical and microrobotic areas.



On Constrained Layer Damping Treatments - Influence of Nonlinear Viscoelastic Material Characterization

Farhan Gandhi

Asst. Professor of Aerospace Engineering
Pennsylvania State University

Presented at the Fourth ARO Workshop on Smart Structures
University Park, Pennsylvania, August 16-18, 1999



Motivation

When Constrained Layer Damping Treatments are applied to big heavy structures (buildings, bridges, submarines.....)

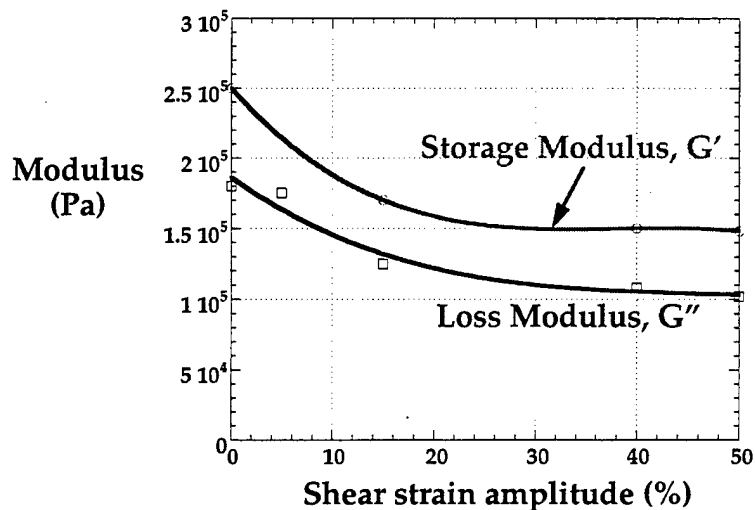
damping materials used will likely be

ELASTOMERS such as **SILICONE RUBBER***

(*Used by Lord Corporation in design of its dampers)

Shear Modulus of silicone rubbers is strongly dependent on strain amplitude

Nonlinear Variation of G' and G'' for Elastomeric Materials



Motivation (contd.)

PENNSTATE



Constrained layer treatments (PCL and ACL) seek to maximize shear in the damping layer (VEM)

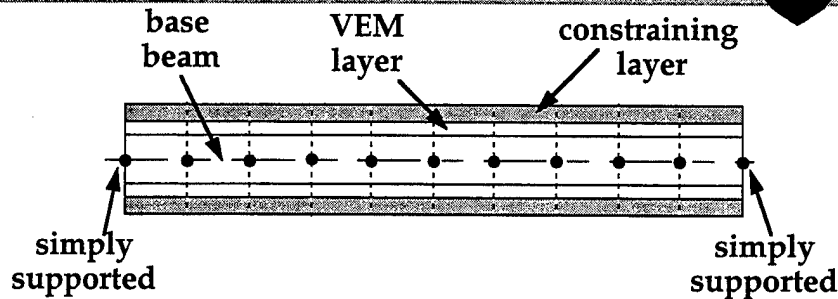
However, previous studies have not considered nonlinear material characterization of the VEM

The shear modulus (G' and G'') is strain dependent even at small values of strain amplitude

What is the influence of the VEM nonlinear behavior on the performance of the constrained layer damping treatment?

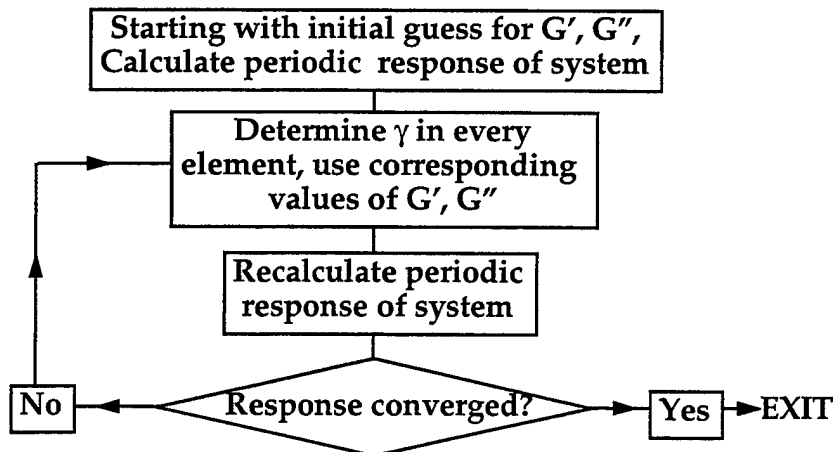
Model Description

PENNSTATE



- Beam simply supported at both ends
- Treatment symmetric - on upper and lower surfaces
- Analysis using Finite Element Method
- 3 DOF at each node - w , w' , and γ (VEM shear angle)
- (Amplitude dependent) Complex modulus for VEM
- Excited by sinusoidal force $P = P_0 e^{j\Omega t}$ at mid-point

Solution Procedure



- Repeat for different Ω s to get frequency response function
- Half-power bandwidth method used to calculate damping
- Repeat for different excitation amplitude

Properties of Beam with Constrained Layer Treatment

PENNSTATE



Material Properties

Young's Modulus of Beam	$7.1 \times 10^{10} \text{ N/m}^2$
Young's Modulus of PZT	$6.49 \times 10^{10} \text{ N/m}^2$
Mass density of Beam	2700 Kg/m^3
Mass density of PZT	7600 Kg/m^3
Mass density of VEM	1250 Kg/m^3

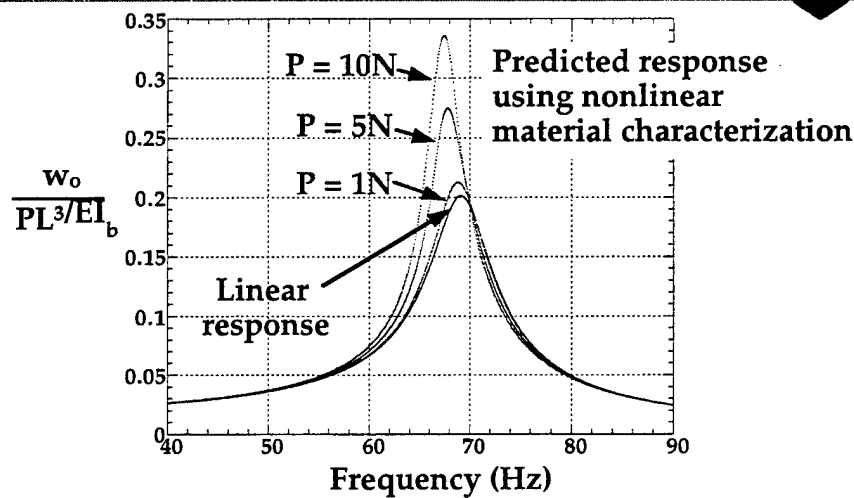
Geometric Properties

	Beam I	Beam II
Thickness of Beam	$4.0 \times 10^{-3} \text{ m}$	$4.0 \times 10^{-3} \text{ m}$
Thickness of VEM	$1.0 \times 10^{-3} \text{ m}$	$0.5 \times 10^{-3} \text{ m}$
Thickness of PZT	$1.0 \times 10^{-3} \text{ m}$	$1.0 \times 10^{-3} \text{ m}$
Width of Beam	$20.0 \times 10^{-3} \text{ m}$	$20.0 \times 10^{-3} \text{ m}$
Length of Beam	$300.0 \times 10^{-3} \text{ m}$	$500.0 \times 10^{-3} \text{ m}$

VEM Shear Modulus $\frac{\text{Shear Modulus of Beam II}}{\text{Shear Modulus of Beam I}} = 20$

Frequency Response Function (Beam I)

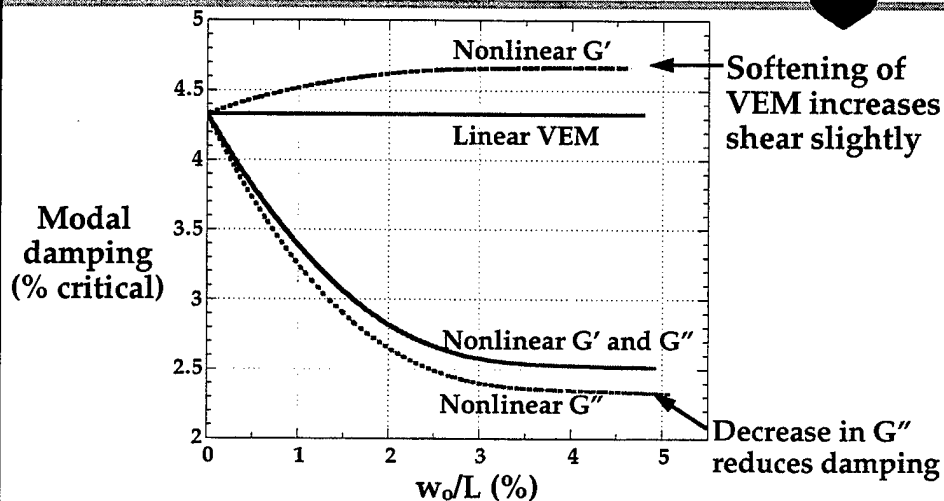
PENNSTATE



For larger excitations - resonant amplitude increases
- damping decreases

Influence of Nonlinear Characterization of VEM on Modal Damping (Beam I)

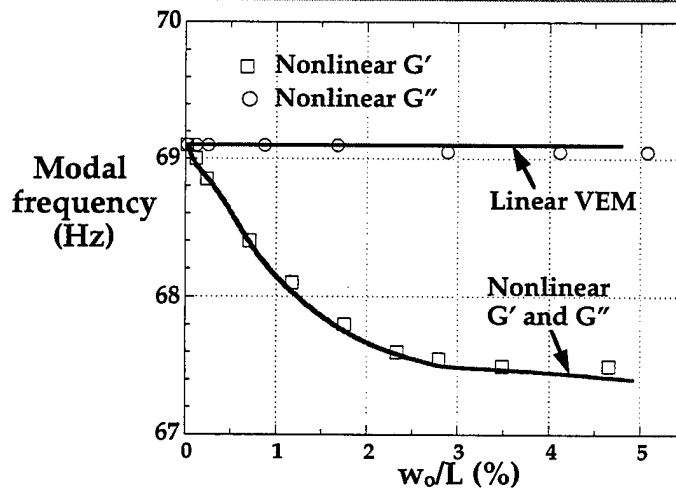
PENNSTATE



Decrease in G'' dominates - damping reduced by up to 42%

Influence of Nonlinear Characterization of VEM on Modal Frequency (Beam I)

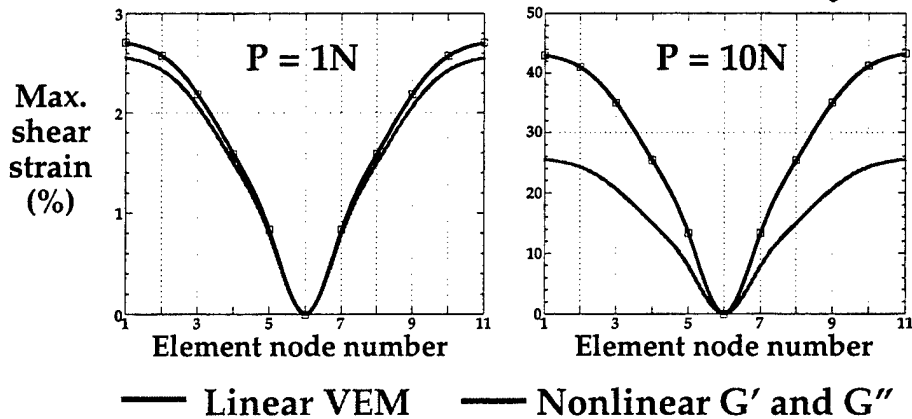
PENNSTATE



Negligible change in frequency (due to change in G')

Shear Strain Variation at Resonance Condition (Beam I)

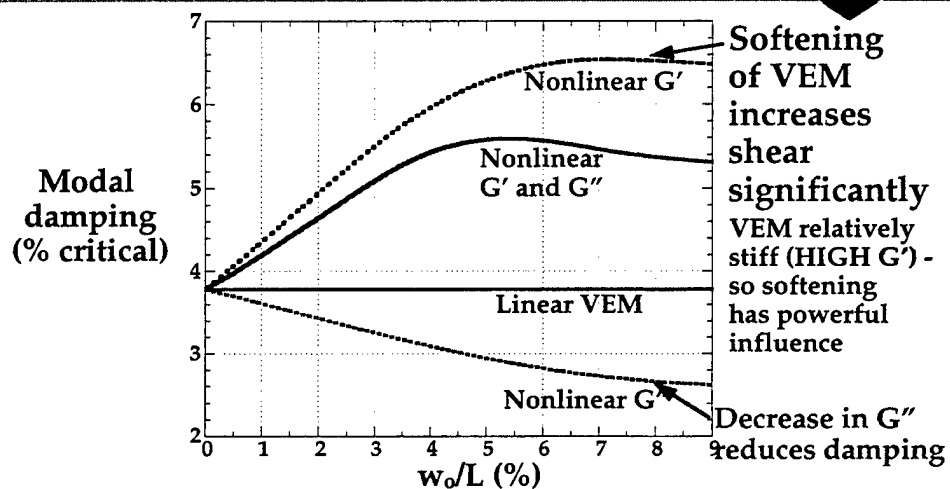
PENNSTATE



When nonlinear VEM characterization considered shear strain increases due to decrease in damping

Influence of Nonlinear Characterization of VEM on Modal Damping (Beam II)

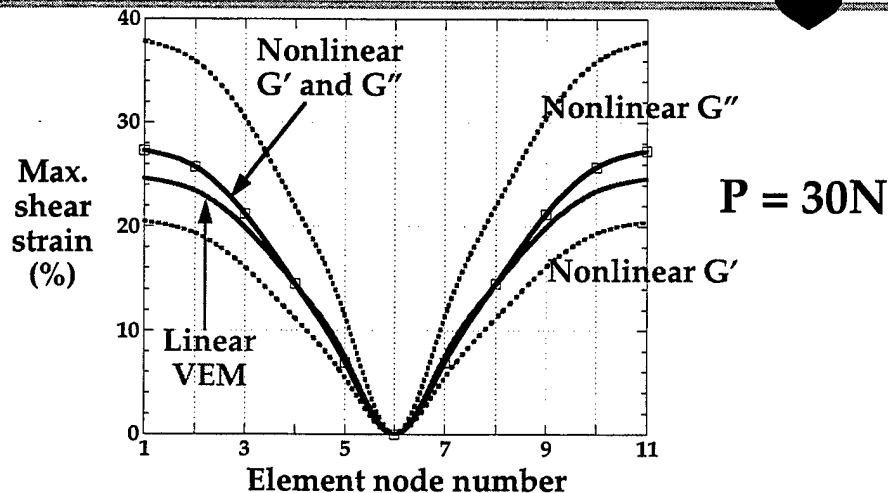
PENNSTATE



Decrease in G' dominates - damping increased by up to 47%

Shear Strain Variation at Resonance Condition (Beam II)

PENNSTATE



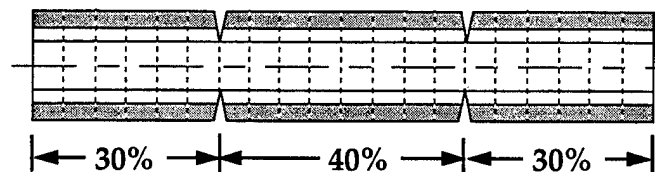
Decrease in G' - increases damping by "unlocking" shear layer
 Decrease in G'' - decreases damping, thus producing more shear

Segmented Constrained Layer Damping Treatment

PENNSTATE



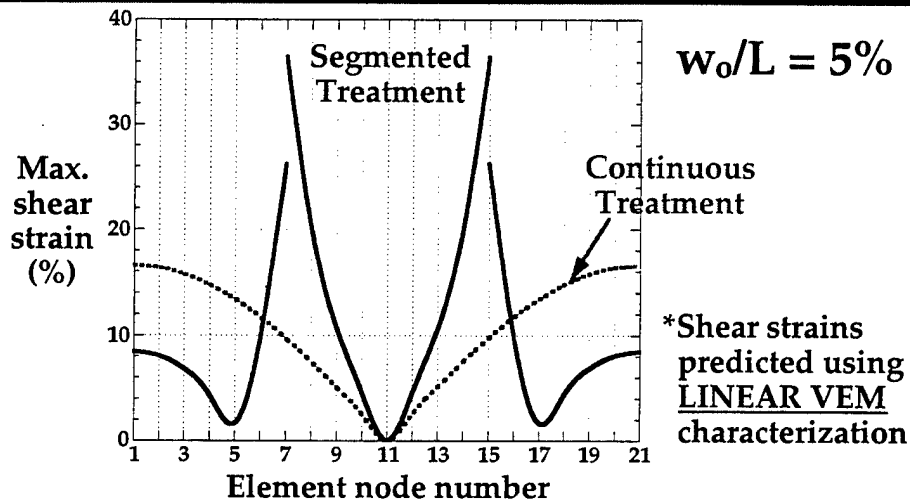
Treatment on Beam II segmented as shown...



... to produce higher damping (due to an overall increase in shear)

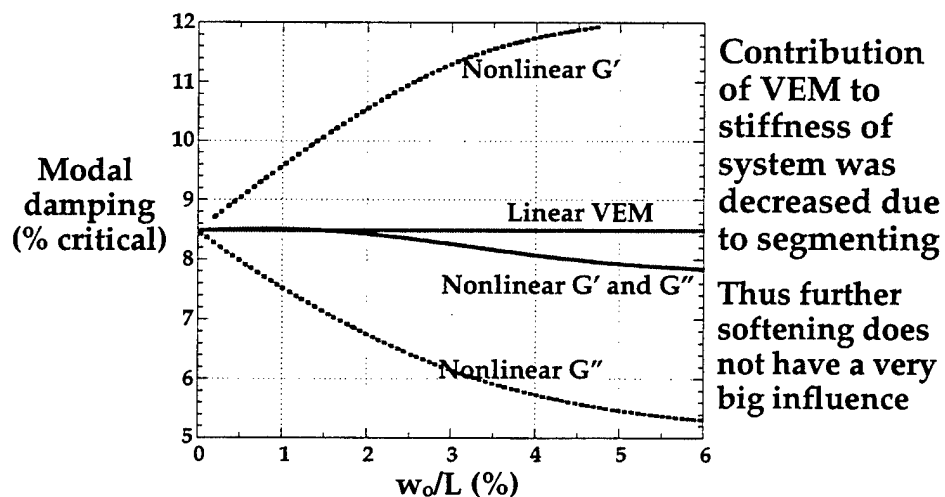
Note that segmentation also reduces the frequency (from 44.8 Hz - 32.2 Hz) - associated with reduced stiffness of "stiff" damping layer

Shear Strain Variation at Resonance in Continuous and Segmented Treatments



Regions of higher shear strain in segmented treatment will provide increased damping

Influence of Nonlinear Characterization of VEM on Modal Damping of Beam II with Segmented Treatment



Decrease in G'' dominates - damping reduced slightly

Influence of Nonlinear VEM Behavior on Modal Damping of Beam II with Continuous & Segmented Treatments

For Continuous Treatment -

Damping increased from 3.8% to about 5.6% critical

For Segmented Treatment -

Damping decreased from 8.5% to about 7.8% critical

Using Linear characterization

Segmentation provided additional 4.7% damping

If Nonlinear behavior considered

Segmentation provided a more modest 2.2% damping

If parameters are changed it is conceivable that while linear model may predict that segmentation would be beneficial, nonlinear model may show it actually produces less damping

Concluding Thoughts

PENNSTATE



- **When treatment is applied to large, heavy structures (bridges, buildings, helicopters, submarines, tanks...) it is likely that SILICONE RUBBER/ELASTOMERS will be used - they display nonlinear behavior**
- **Nonlinear material characterization very important**
- **When nonlinear behavior is considered, the available damping may be-**
 - significantly lower (if material is relatively soft),**
 - or significantly higher (if material is relatively stiff)**
- **Segmentation may prove to be not quite as advantageous**
 - MANY CONCLUSIONS WILL CHANGE -**

HERSCHEL-BULKLEY ANALYSIS OF CONTROLLABLE FLUID DAMPERS IN FLOW MODE

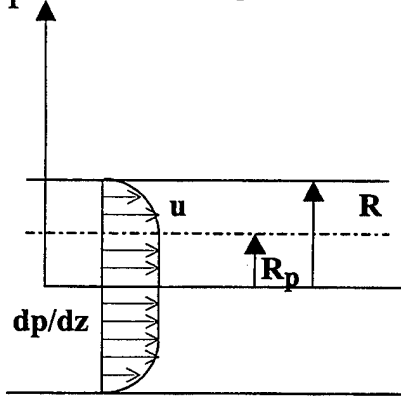
Xiaojie Wang¹ and Faramarz Gordaninejad²

Department of Mechanical Engineering, University of Nevada, Reno, NV 89557

Phone: 775-784-6990, Fax: 775-784-1701, E-mail: faramarz@unr.edu

Bingham plastic constitutive model has been widely used to predict the post-yield behavior of electro- and magneto-rheological fluids (ER and MR fluids). However, if these fluids experience shear thinning or shear thickening, Bingham plastic model may not be an accurate predictor of behavior, since the post-yield plastic viscosity is assumed to be constant. In our recent study, it was theoretically and experimentally demonstrated that the Herschel-Bulkley fluid model can be successfully employed when evaluating non-Newtonian post-yield behavior of ER and MR fluids. In this paper, Herschel-Bulkley model is adapted to include a detailed analysis of ER and MR fluid dynamics through pipes and parallel plates. In addition, non-dimensionalized equations are derived. Moreover, simplified explicit expressions for the exact formulation are developed. It is shown that the proposed simplified model to the Herschel-Bulkley steady flow equations for pipes and parallel plates can be used as an accurate design tool while providing a convenient and generalized mathematical form for modeling ER and MR fluid materials.

Flow Through a Circular Pipe with a Constant Cross section:



The Herschel-Bulkley constitutive equation is adopted in Eq. (1) to describe the flow of ER and MR fluids through a circular pipe with a constant cross sectional area. where τ_{rz} is shear stress; $\frac{du}{dr}$ is shear strain rate, and k and n are fluid index parameters. τ_y is the yield stress and is a function of the external field.

Figure 1. Flow profile of a non-Newtonian fluid in pipe geometry.

$$\begin{cases} \tau_{rz} = \tau_y + k \left| \frac{du}{dr} \right|^n & |\tau_{rz}| \geq \tau_y \\ \frac{du}{dr} = 0 & |\tau_{rz}| \leq \tau_y \end{cases} \quad (1)$$

Using a cylindrical coordinate system, the flow rate can be developed as follows:

$$Q = \frac{\left(\frac{p'R}{2} - \tau_y \right)^{\frac{n+1}{n}} \pi R^3}{\left(\frac{pR}{2} \right)^3 k^{\frac{1}{n}}} \left[\frac{\left(\frac{p'R}{2} - \tau_y \right)^2}{\frac{3n+1}{n}} + \frac{2\tau_y \left(\frac{p'R}{2} - \tau_y \right)}{\frac{2n+1}{n}} + \frac{\tau_y^2}{\frac{n+1}{n}} \right] \quad (2)$$

¹ Graduate Research Assistant

² Professor

where $p' = -dp/dz$. The following dimensionless parameters are introduced:

$$X = \frac{4\tau_y}{p'D} = \frac{R_p}{R}; (D=2R) \text{ and, } Y = \left(\frac{3n+1}{n} \frac{8Q}{\pi D^3} \right)^n \frac{4k}{p'D} \quad (3)$$

Where X represents the dimensionless plug thickness or dimensionless shear stress. When $X=1$, the plug radius equates to the pipe radius and the yield stress of the fluid is equal to its shear stress at the wall which implies that there is no flow in the pipe. Y is the dimensionless volumetric flow rate. Therefore, a linear approximation to Eq. (2), for all n , when $X < 0.5$, can be presented as:

$$Y = 1 - \left[(na+1) - \frac{3}{8}(na - bn + \frac{n(n-1)}{2}a^2) \right] X \quad (4)$$

When $X > 0.5$, the plug radius reaches half of the pipe radius, the yield stress will play an important role in determining pressure loss. A simplified expression for Eq. (2) is obtained as follows:

$$Y = A'X(1-X)^\alpha \quad (5)$$

Where A' and α are functions of n . These values are presented in Table 1. The dimensioned version of the pressure loss can be derived as follows:

$$\frac{dp}{dz} = \frac{4\tau_y}{D \left[1 - A' \left(\frac{3n+1}{n} \frac{8Q}{\pi D^3} \right)^{\frac{n}{\alpha}} \left(\frac{k}{\tau_y} \right)^{\frac{1}{\alpha}} \right]}; \left(\frac{R_p}{R} > 0.5 \right), A_0 = (A')^{-\frac{1}{\alpha}} \quad (6)$$

Table 1. Values of A' , α and A_0 for Different n .

n	α	A'	$A_0 = (A')^{-\frac{1}{\alpha}}$
1	2.260	3.289	0.590
0.8	2.105	3.031	0.591
0.4	1.784	2.700	0.573

Similar expressions were also developed for parallel plates flow mode case. The proposed exact, Eq. (2), and the simplified, Eqs. (4) and (5), for the Herschel-Bulkley pipe flow relationships are presented in Figure 2.

ACKNOWLEDGEMENTS

This study is funded by the Army Research Office Grant Number DAAG55-97-1-0077. The authors are thankful for the encouragement by Dr. Gary Anderson, the Program Director.

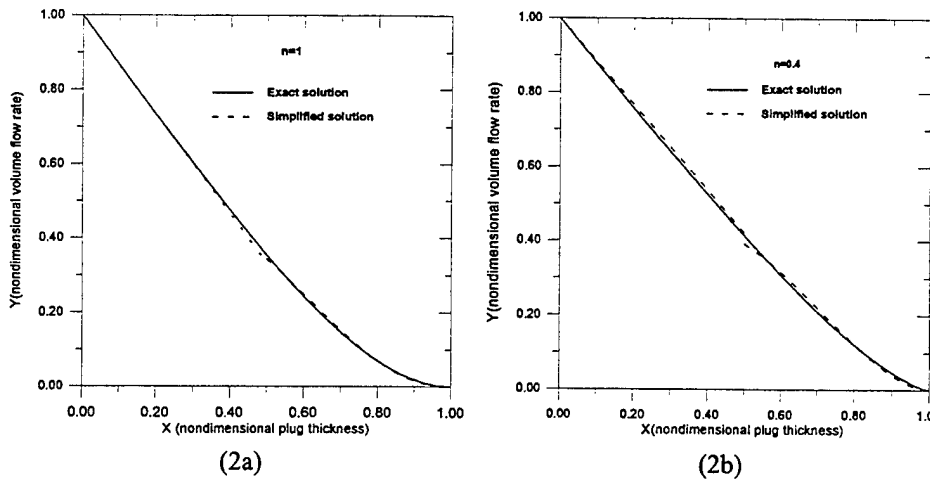


Figure 2. Comparison between the exact and simplified versions of Herschel-Bulkley pipe flow formulation for two different flow index, n .

Pb(Mg_{1/3}Nb_{2/3})O₃-PbTiO₃ Ceramics for High Power Transduction Applications

Yun-Han Chen¹, Senji Hirose², Dwight Viehland³ and Kenji Uchino¹

¹International Center for Actuators and Transducers, Material Research Laboratory

The Pennsylvania State University, University Park, PA 16802

²Yamagata University, Yonezawa-shi, Yamagata 992, Japan

³Code 2132; Naval Undersea Warfare Center, Newport, RI 02835

Piezoelectric ceramics are potential high-power electro-acoustic sources, and have been studied for many years. However, when these devices are driven under high level vibration, the electromechanical characteristics depart significantly due to the loss and nonlinear behavior in terms of elastic and dielectric properties. In this paper, we present results concerning the development of modified Pb(Mg_{1/3}Nb_{2/3})O₃-PbTiO₃ (PMN-PT) ceramics for high-power application. We have focused efforts on base PMN-PT compositions close to the morphotropic phase boundary. Different doping have been studied to understand the doping effects on the properties of PMN-PT ceramics and, moreover, to improve the properties for the high-power application. Investigations of the nonlinearity of the electromechanical properties on the vibrational amplitude were performed using a constant displacement method. The degradation of the mechanical quality factor with increasing drive amplitude also presents thermal stability problems for the usage of these materials in high power transducer applications. This work is supported by Office of Naval Research.

Active Tuning and Coupling Enhancement of Piezoelectric Vibration Absorbers for Variable Frequency Harmonic Excitations in MDOF Mechanical Systems

Ronald Morgan and K. W. Wang
Structural Dynamics and Controls Lab
The Pennsylvania State University
University Park, PA 16802

Piezoelectric materials have been shown to be useful for passive vibration damping by shunting them with electrical networks. An electro-mechanical vibration absorber can be created by coupling the piezo material with a circuit containing resistive and inductive elements. Researchers have further proposed semi-active piezoelectric vibration absorbers designed to track varying excitation frequencies. The implementation of these semi-active devices can be accomplished using either a variable inductor or a variable capacitor element, but both of these methods have some inherent limitations. For instance, the variable capacitor method limits the tuning of the piezo absorber to a relatively small frequency range. The variable inductor, which is usually accomplished using a synthetic inductor circuit, can add a significant parasitic resistance to the circuit, which is usually undesirable in narrow-band applications. In addition, the semi-active elements used in both of these approaches can be difficult to tune rapidly and accurately.

The design presented here is a high performance active-passive alternative to semi-active piezoelectric vibration absorbers. The intended application is any structure that is subject to harmonic excitations of varying frequency. One example of this type of excitation is a machine with a rotating unbalance. The frequency variation could be a slow drift due to changes in operating conditions or a ramping spin-up when the machine is turned on. The approach here is to use one part of the active control law to imitate a variable inductor so that the shunt circuit is always tuned to the correct frequency. In addition, a passive inductor can be tuned to the nominal or steady state excitation frequency in order to reduce the voltage requirement of the active inductor. The advantages of the active inductor include fast and accurate adjustment, no parasitic resistance, and easier implementation compared to a semi-active inductor. For a single mode structure the resonant frequency of the piezo absorber should be equal to the excitation frequency in order to completely attenuate the disturbance. The optimal tuning ratio for higher order (MDOF) structures is derived here in terms of the system modal parameters. This more accurate tuning law is necessary to obtain high performance when dealing with complex structures because the performance of the absorber is quite sensitive to the proper tuning. One way to make the absorber less sensitive to tuning errors would be to increase the electro-mechanical coupling of the system, however this coupling is limited by the piezoelectric material parameters. Therefore, the second part of the active control law presented here is used to actively increase the electro-mechanical coupling of the piezoelectric actuator using feedback. It is shown that this active coupling control can significantly increase the robustness of the system to frequency variations.

To demonstrate the effectiveness of this active control law, an LQR optimal control law is used as a baseline for the suppression of spin-up forces in a cantilever beam. The performance weightings of the optimal control law are chosen so that its RMS control voltages is equal to that of the system controlled by an active piezoelectric absorber. The analysis results show that the active piezo absorber can achieve a 92% reduction in RMS system response compared to the optimal control law. If a passive inductor is used, the active-passive piezo absorber can achieve this same increased performance while requiring 71% less control voltage than the optimal control law. These results clearly show the merit of the active-passive hybrid piezoelectric vibration absorber for systems with variable frequency harmonic excitations.

PENNSTATE



Active Tuning and Coupling Enhancement of Piezoelectric Vibration Absorbers for Variable Frequency Harmonic Excitations in MDOF Mechanical Systems

R. A. Morgan

K. W. Wang

Structural Dynamics and Controls Lab
Department of Mechanical Engineering
The Pennsylvania State University
University Park, PA 16802
USA

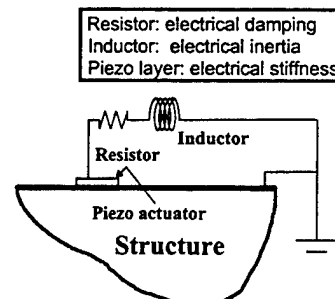
Structural Dynamics and Controls Lab

PENNSTATE



Background on Passive Piezoelectric Vibration Absorbers

- Piezoelectric materials can be used for passive damping if shunted with external circuits
 - Example: series R-L circuit
 - Piezo materials have capacitive electrical properties
 - A resonant RLC circuit that is coupled to the structure
 - Structure exchanges energy with piezo and electrical circuit
- => An electromechanical vibration absorber



Structural Dynamics and Controls Lab



Self-Tuning Piezo Vibration Absorbers

- **Can track changing excitation frequency using variable inductor or capacitor elements to tune circuit (Hollkamp and Starchville, 1994; Davis and Lesieutre, 1997)**
- **Limitations of these semi-active devices:**
 - Relatively slow and inaccurate tuning capabilities
 - Very limited frequency range (variable capacitor method)
 - Internal resistance of inductor element reduces performance (variable inductor method)

Structural Dynamics and Controls Lab



New Idea and Approach

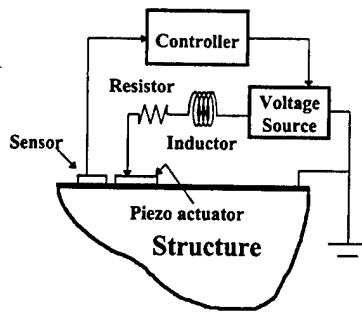
A High Performance Active-Passive Alternative

- Tune passive inductor to nominal excitation frequency
- Use active feedback to imitate variable inductor for frequency tracking
- Increase absorber performance and robustness using active feedback to enhance electro-mechanical coupling

Structural Dynamics and Controls Lab



Active-Passive Hybrid Piezoelectric Networks (APPN)



Piezoelectric Actuators
with Active Voltage
Source and RL Shunt
Circuit (Agnes, 1994;
Kahn and Wang, 1994;
Tsai and Wang, 1996)

**A Different and Innovative Approach Toward
Utilizing the APPN Configuration**

Structural Dynamics and Controls Lab



System Model

- Model of general continuous structure with single PZT patch and R-L circuit (in modal space):

$$M\ddot{\eta} + C\dot{\eta} + K\eta + K_C Q = \hat{F} * f(t)$$

$$L_p \ddot{Q} + R_p \dot{Q} + Q / C_p^S + K_C^T \eta = V_C$$

for linear spin-up disturbances

$$f(t) = \begin{cases} m * e * \omega^2 \sin(\frac{\omega t}{2}), & t < t_o \\ m * e * \omega_o^2 \sin(\omega_o(t - \frac{t_o}{2})), & t \geq t_o \end{cases}$$

M, C, K = modal mass, damping and stiffness matrices

K_C = piezo coupling vector

η = vector of modal coordinates

Q = charge on piezo actuator

L_p = circuit inductance

R_p = circuit resistance

C_p^S = capacitance of piezo at constant strain

m = unbalance mass

e = unbalance eccentricity

ω_o = steady-state frequency

t_o = spin-up time

Structural Dynamics and Controls Lab



Active Coupling Control Law

- Performance of piezo absorber is limited by electromechanical coupling of material
- Use feedback to increase this coupling

$$L_p \ddot{Q} + R_p \dot{Q} + Q / C_p^S + K_C^T \underline{\eta} = 0 \quad (\text{no active coupling})$$

↓ ↓

$$L_p \ddot{Q} + R_p \dot{Q} + Q / C_p^S + K_C^T \underline{\eta} = V_{AC} = -G_{AC} K_C^T \underline{\eta}$$

- Coupling in circuit equation is $(G_{AC}+1)$ times greater
- For structures with collocated piezo sensor and actuator:

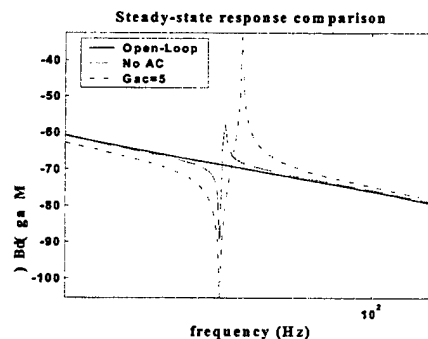
$$V_S = K_C^T \underline{\eta} \quad \text{sensor voltage}$$

$$\Rightarrow V_{AC} = -G_{AC} V_S \quad \text{simple proportional feedback}$$

Structural Dynamics and Controls Lab



Effect of Active Coupling Control Law



- Active coupling increases notch width and depth
 - improves steady-state performance
 - more robust with respect to uncertainty in excitation frequency
 - better performance for transient excitations

Structural Dynamics and Controls Lab



Optimal Tuning Law

- **Classical absorber theory - tune absorber to excitation frequency**
 - only optimal for SDOF undamped system
- **Need more accurate tuning law for MDOF structures**
 - For slowly-varying excitation frequencies, can use quasi-steady-state (QSS) assumption
 - Steady-state modal response (neglecting damping):

$$\left| \frac{\eta_j}{F}(\omega_{exc}) \right| = \frac{1}{k_j - m_j \omega_{exc}^2} \left[\frac{K_{Cj} \sum_{i=1}^N \frac{K_{Ci} \hat{F}_i}{k_i - m_i \omega_{exc}^2}}{\frac{1}{C_p^S} \left(1 - \frac{1}{\delta^2} \right) - \sum_{i=1}^N \frac{K_{Ci}^2}{k_i - m_i \omega_{exc}^2}} + \hat{F}_j \right]$$



Optimal Tuning Law

Solve for δ that minimizes the desired displacement w

$$w(x, t) = \sum_{i=1}^N W_i(x) \eta_i(t) \quad , W = \text{modal contribution vector}$$

$$\delta = \frac{\omega_a}{\omega_{exc}} \quad \text{where} \quad \omega_a = \frac{1}{\sqrt{L_{tot} C_p^S}} \quad , \quad L_{tot} = L_p + L_a$$

- **Two possible solutions:**

$$\delta_{opt} = \left\{ 1 + C_p^S \left[\frac{\sum_{j=1}^N W_j M_j (a_j - \hat{F}_j b)}{\sum_{j=1}^N W_j M_j \hat{F}_j} \right] \right\}^{-\frac{1}{2}}$$

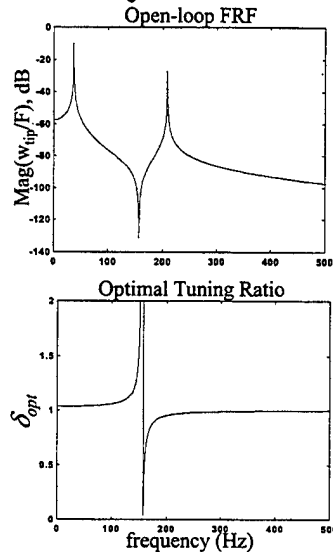
or

$$\delta_{opt} = \infty \quad (\text{short circuit})$$

$$\begin{aligned} M_j &= \frac{1}{k_j - m_j \omega_{exc}^2} \\ a_j &= K_{Cj} \sum_{i=1}^N \frac{K_{Ci} \hat{F}_i}{k_i - m_i \omega_{exc}^2} \\ b &= \sum_{i=1}^N \frac{K_{Ci}^2}{k_i - m_i \omega_{exc}^2} \end{aligned}$$



Optimal Tuning Law



- **Observations on optimal tuning ratio:**
 - close to unity near resonant frequencies
 - diverges from unity near anti-resonances
 - equal to unity at all frequencies for SDOF systems (classical result)
 - optimal tuning ratio is significantly affected by active coupling gain
- **Frequency dependent optimal tuning law is necessary to achieve best performance with MDOF systems**

Structural Dynamics and Controls Lab



Control Law Summary

$$L_p \ddot{\underline{Q}} + R_p \dot{\underline{Q}} + \underline{Q} / C_p^S + K_C^T \underline{\eta} = Vc$$

- **Active Inductor Control:**

$$V_{AI} = -L_a \ddot{\underline{Q}} \quad \text{where } L_a = L_{tot} - L_p$$

- **Active Coupling Control:**

$$V_{AC} = -G_{AC} K_C^T \underline{\eta}$$

- **Total Control Voltage:**

$$Vc = V_{AI} + V_{AC} = -L_a \ddot{\underline{Q}} - G_{AC} K_C^T \underline{\eta}$$

Structural Dynamics and Controls Lab



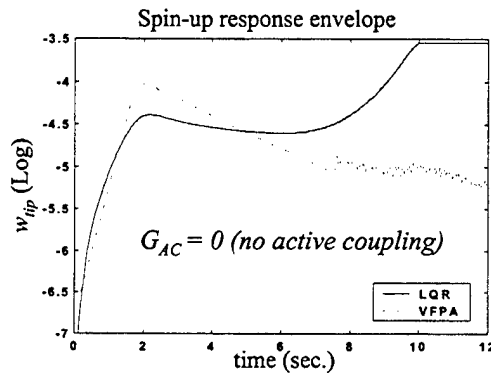
Analysis Results

- LQR optimal control law is used as baseline for comparison
- No passive inductor is used - allows a fair comparison of active control law performance
- LQR weightings are adjusted so that control effort is same for both control laws
- Two mode cantilever beam model is used

Spin-up Test Parameters:

$$\omega_o = 209 \text{ Hz (2nd resonance)}$$

$$t_o = 10 \text{ sec.}$$

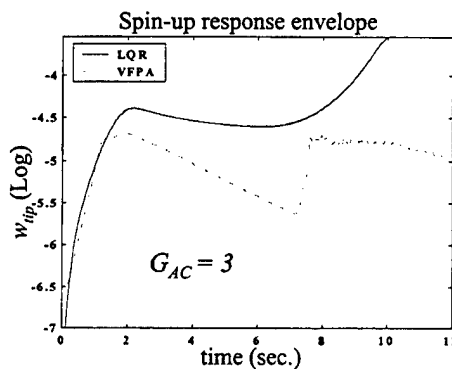


Structural Dynamics and Controls Lab



Analysis Results

- Performance compared to LQR optimal control (no active coupling):
 - 75.8% reduction in RMS response
 - 67.5% reduction in peak response



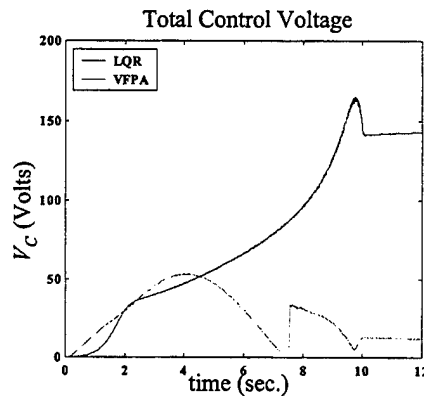
- With active coupling:
 - 91.6% reduction in RMS response
 - 92.8% reduction in peak response
- Can get much better performance than LQR using same control effort

Structural Dynamics and Controls Lab



Analysis Results

- If passive inductor is tuned to ω_o , can greatly reduce voltage requirements



- Can achieve same performance as previous case plus
 - 68.7% reduction in RMS control voltage
 - 67.9% reduction in peak control voltage

Structural Dynamics and Controls Lab



Conclusions

- Active-passive piezoelectric absorber appears promising for structures with variable frequency harmonic excitations
- An optimal tuning scheme for general MDOF structures has been derived
- A simple and effective control law, with both active tuning and active coupling, has been developed
- Analysis results for spin-up disturbances show much better performance using less control effort, compared to direct optimal control

Structural Dynamics and Controls Lab

Optimization of Enhanced Active Constrained Layer (EACL) Treatment on Helicopter Flexbeams for Aeromechanical Stability Augmentation

A. Badre-Alam, K. W. Wang, F. Gandhi

Rotorcraft Center of Excellence
The Pennsylvania State University
University Park, PA 16802

ABSTRACT

Over the last couple of decades, increasing effort has been devoted to the design and development of bearingless main rotors for helicopters. The main advantages of such rotor systems compared to the articulated ones are mechanical design simplification, reduced drag, lower weight, parts and maintenance cost, higher moment capability and hence better handling qualities. Bearingless main rotors are usually designed to be soft in-plane (fundamental in-plane frequency less than rotational frequency) to reduce the dynamic stresses. However such designs are known to be susceptible to aeromechanical instabilities such as ground- and air-resonance. To alleviate these instabilities, helicopters have traditionally been equipped with passive elastomeric or hydraulic lag dampers at the rotor hub. However, these dampers have a number of drawbacks. They result in hub complexity, weight, and aerodynamic drag. Additionally, passive damper performance in general could significantly degrade due to environmental changes and operating condition variations.

This research investigates the feasibility of employing Enhanced Active Constrained Layer (EACL) damping treatments on the flexbeams of soft in-plane bearingless main rotors (BMRs) for lag mode damping and aeromechanical stability augmentation. The EACL configuration was developed to improve the performance of the original active constrained layer (ACL) treatment. ACL in general consist of a viscoelastic material (VEM) layer sandwiched between the host structure (e.g., the flexbeam) and a piezoelectric (PZT) cover sheet (active constraining layer). As the host structure undergoes bending, the viscoelastic layers will undergo shear and hence provide passive damping while the PZT is used to provide the active damping. It has been demonstrated that by adding a pair of edge elements at the ends of the PZT layer and directly connect the active source (PZT) to the host structure, the transmissibility between the actuator electrical field input and the active control force output to the host structure can be greatly increased. It was found that the EACL could be designed to produce significant active control actions, while still maintaining a fair amount of passive damping

In this study, a finite element based mathematical model of the EACL damping treatment of flexbeam has been developed. The mathematical model is verified using a bench top experiment. A derivative controller based on the flexbeam tip transverse velocity is used in this investigation to provide active damping. It is demonstrated that high active damping in forward flight can only be achieved if a filter is used in the feedback loop to remove 1/rev component of the signal. Hence, a filter is designed and implemented to remove 1/rev component of velocity in the feedback signal. A thorough optimization/design study is conducted to understand the influence of various design parameters such as viscoelastic layer thickness, PZT actuator thickness, and edge element stiffness, on PZT actuator electrical field levels, induced axial stress levels and available lag damping. Based on the optimization study, an EACL treatment design chart is developed that relates the performance to the size of the treatment. The results of this study shows that the EACL treatments on the flexbeams has good potential for rotor stability augmentation

OBJECTIVE

PENNSTATE



Ensuring adequate lag-damping to alleviate rotor-fuselage ground-and air-resonance instability is crucial in the design & development of any helicopter

Usual Technique : Passive Lag Dampers

■ Draw Backs and Short Comings of Passive Dampers

- ☐ Sensitive to environmental changes (e.g., temperature)
- ☐ High damper/flexbeam loads (high damping not always required)
- ☐ Hub complexity

■ Objective/Goal

- ☐ Ensure sufficient damping by actively compensating for changes in environment and operating conditions
- ☐ Increase damper life by reducing damping if not required and increase when critical
- ☐ Reduced aerodynamic drag by designing aerodynamically cleaner hub

Solution : Adaptive Damping

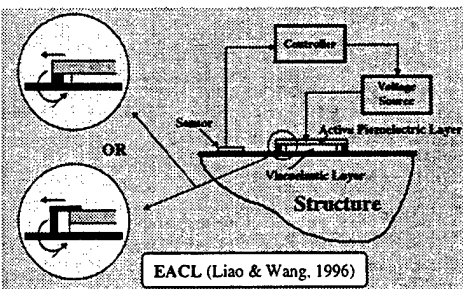
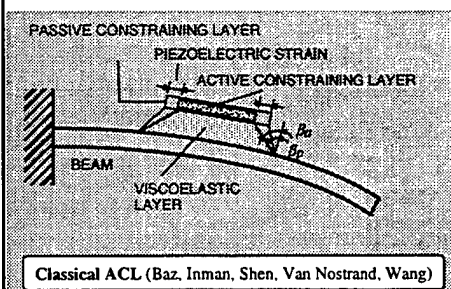
BACKGROUND

PENNSTATE



Enhanced Active Constrained Layer (EACL) Treatment

Integrating the merits of both active and passive damping

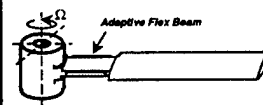


■ ENHANCED PASSIVE DAMPING

- ☐ PZT Active Constrained Layer increases the shear angle

■ ACTIVE CONTROL

- ☐ Edge element improves the active control authority



INTRODUCTION

PENNSTATE



Technical Challenges

■ Helicopter Flexbeams are Subjected to Very Large Aerodynamic and Inertial Forces

□ Can EACL treatment provide adequate **active** and **passive** damping under the physical design constraints ?

○ Stresses, Electric Field Limit, Size and weight

■ Controller Development

Approach

■ Developed Rotor-Flexbeam Model with EACL Treatment

■ Developed Control Law for Adaptive Damping

■ Experimentally Verified the Mathematical Model

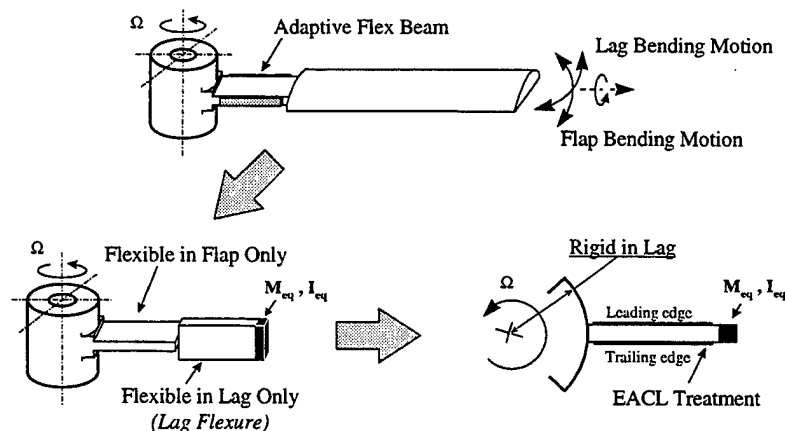
■ Performed Analysis & Setup Design Requirements

■ Optimized the EACL Design

■ Examined Performance

ROTOR MODEL DESCRIPTION

PENNSTATE



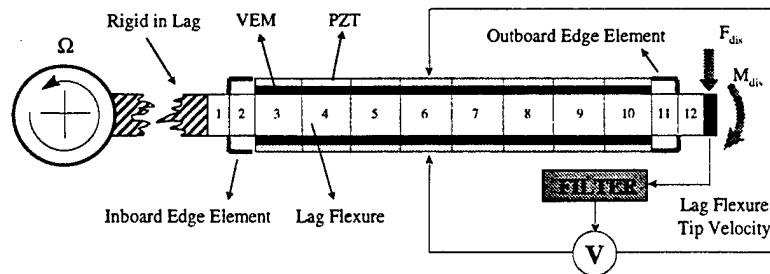
Reduces to a rotating beam with end mass & inertia having EACL treatment on two flat surfaces

MATHEMATICAL MODEL

PENNSTATE



Finite Element Model



Control Law

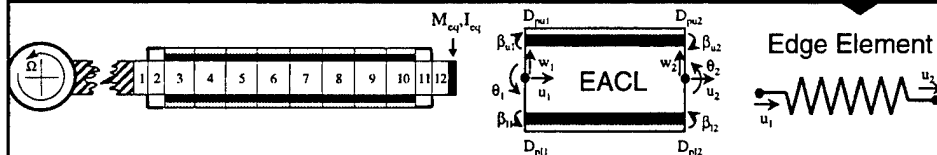
$$\text{Derivative Control : } V = -K\dot{w}|_{\text{Tip (Filtered)}}$$

- Based on Sikorsky S-76 bearingless main rotor

- Tip force & moment come from aerodynamic and inertial forces on the blade

MATHEMATICAL MODEL

PENNSTATE



$$\varepsilon = \frac{\partial u}{\partial x} - z \frac{\partial^2 w}{\partial x^2} + \frac{1}{2} \left(\frac{\partial w}{\partial x} \right)^2 \longrightarrow \text{Centrifugal Stiffening}$$

$$V = \frac{\partial R}{\partial t} + \Omega \times R \longrightarrow \text{Centrifugal Loads}$$

u : Linear shape function
 β : Linear shape function
 D : Linear shape function
 w : Cubic shape function

- GHM Method for VEM Modeling

- Energy Method (Hamilton's Principle)

$$[M]\{\ddot{x}\} + [C]\{\dot{x}\} + ([K]_E + [K]_G - \Omega^2[K]_R)\{x\} + [\Omega_D][D_p] = \{F\}_T + \{F\}_S + \{F\}_P$$

$$[\Phi]\{\dot{x}\} + [\alpha][D_p] + [\psi]V_p = 0$$

- State Space

$$\{\dot{z}\} = [A]\{z\} + [B]V_p + [E_1]\{F\}_T + [E_2]\{F\}_S + [E_3]\{F\}_P$$

$$\{y\} = [C]\{z\}$$

- Control Law $V_p = -K\{y\}$

ROTOR FORCES

PENNSTATE



DISTURBANCE FORCES & MOMENTS

Static Forces	Centrifugal force (<i>kinetic energy</i>) Drag in hover ($F=1900N$, $M = 4800 N\cdot m$)
Periodic Forces (<i>Steady State</i>)	Result of periodic motion in forward flight (<i>Very high</i>) <i>Produce 1° lag rotation at tip</i>
Perturbation Forces (<i>Transient</i>) (<i>Modeled as Step</i>)	Result of gust <i>A 5% Change in lift produces approx. inplane force and moment of:</i> $F = 95N$, $M = 190 N\cdot m$

FILTER DESIGN

PENNSTATE



A filter is required in the feedback loop to remove 1/rev component of the velocity in forward flight

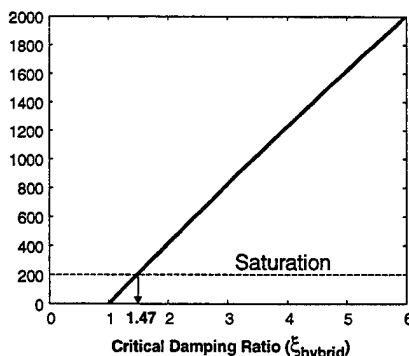
Control Law

$$V = -K\dot{x} = -\omega Kx$$

- The Current Control Law feeds back 1/rev motion
- Limits the maximum allowable damping in forward flight to be 1.47 % due to electrical field saturation
- Modify control law if extra damping is required in forward flight

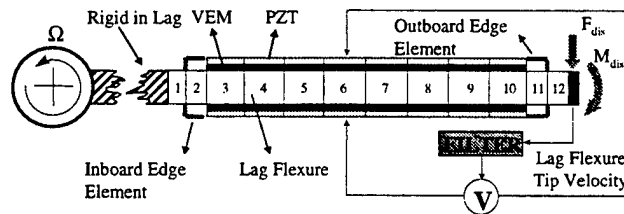
Electric Field < 200 V/mm

PZT Electrical Field (V/mm)



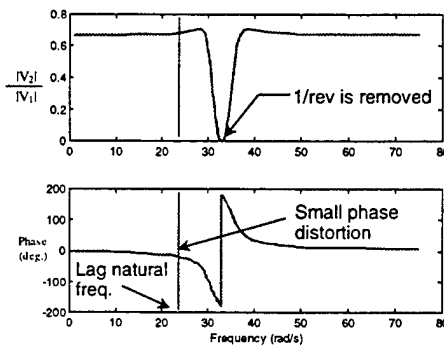
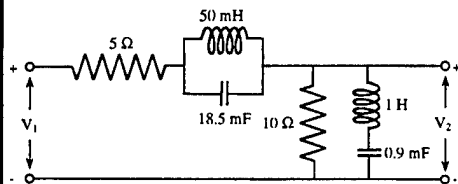
FILTER DESIGN

PENNSTATE



DESIGN GOAL

- Remove 1/rev velocity component in the feedback signal
- Signal at lag natural freq. unchanged



EXPERIMENTAL VERIFICATION

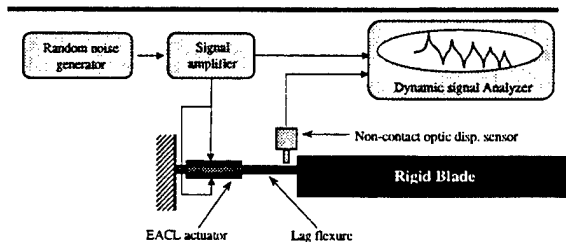
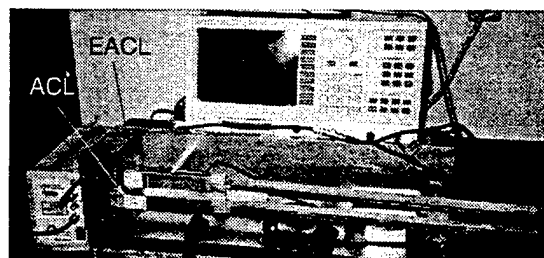
PENNSTATE



GOAL

Verify the mathematical model through a bench top experiment that captures the essential behavior of helicopter rotor flexbeams

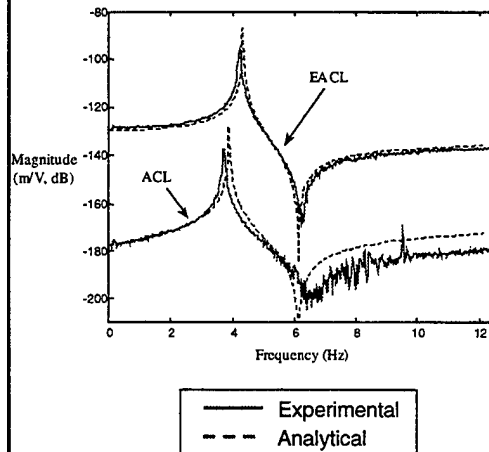
- ☐ Tip Inertia
- ☐ Natural Frequency



PENNSTATE

EXPERIMENTAL VERIFICATION

Frequency Response Function
(Tip disp./ Control Voltage)



OBSERVATIONS

- Good correlation between the experimental results and the analytical results
- EACL has significantly better active control authority than ACL

PENNSTATE

ANALYSIS / PROCEDURE

$$V = -K\dot{w}_{\text{Tip (Filtered)}}$$

Static Forces

- Centrifugal
- Drag in Hover

Periodic Forces

Perturbation Forces

Stresses

Electrical Field

- All three forces contribute to stresses
- Only perturbation forces generate electrical field

DESIGN GOAL

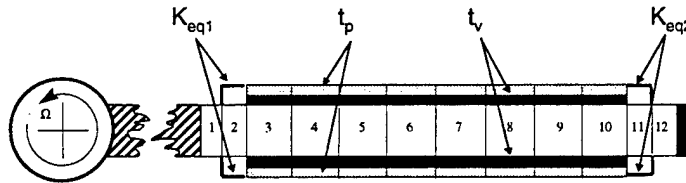
- Introduce damping in the first lag mode (*about 6 %*)
- Introduce passive damping to increase robustness
- Minimize weight of the treatment
- Keep the change in natural frequency small
- Low power requirements

DESIGN / IMPLEMENTATION CONSTRAINTS

- Electrical Field < 200 V/mm
- Stress < 80 MPa

OPTIMIZATION

PENNSTATE



SELECT POPULAR COMMERCIAL VEM AND PZT MATERIALS

- VEM : 3M ISD112
- PZT : Piezo Kinetics PK1502

DESIGN PARAMETERS (Four)

- Thickness of PZT (t_p)
- Thickness of VEM (t_v)
- Edge Element Stiffness (K_{eq1} , K_{eq2})

DESIGN SPACE

- $0.5 \text{ mm} < t_p < 4 \text{ mm}$
- $2 \text{ mm} < t_v < 4 \text{ mm}$
- $0 \text{ N-m} < K_{eq1,2} < 1 \times 10^9 \text{ N-m}$

CONSTRAINTS

- $EF < 200 \text{ V/mm}$
- $\sigma < 80 \text{ MPa}$
- $\Delta \omega_n < 10 \%$
- $t_p + t_v \leq x$ (treatment thickness)

OPTIMIZATION

PENNSTATE



OPTIMIZATION GOAL (3 CASES)

■ CASE 1: BEST PASSIVE DESIGN

- ☐ Maximize $\xi_{passive}$ for all values of x

■ CASE 2: BEST OVERALL PERFORMANCE

- ☐ Maximize total hybrid damping for all values of x

■ CASE 3: PERFORMANCE & FAIL SAFE

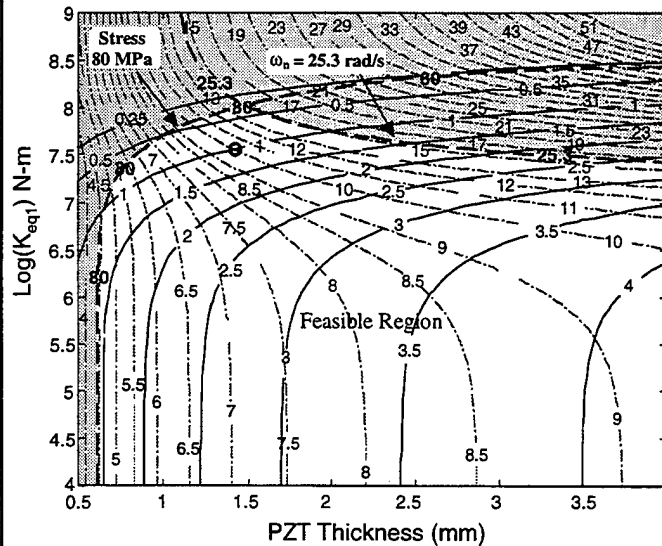
- ☐ Maximize hybrid damping such that $\xi_{passive}$ has a minimum prescribed limit for all values of x

OBSERVATIONS

- Two out of four parameters (t_v and K_{eq2}) always take the extreme values
- The optimum thickness of PZT is fixed if x is fixed thickness is fixed
- Optimization problem can be reduced to one variable only, K_{eq1}

DESIGN CHART

PENNSTATE



- t_v and K_{eq2} are known
- Can be used to design EACL treatment for any damping requirements
- Can be used to design thinnest EACL treatment with a certain combination of passive and total hybrid damping req.
- Instantaneous power requirement (Less than 100 watts)

RESULTS

PENNSTATE



Design	
$t_p = 1.45 \text{ mm}$	$K_{eq1} = 3.5 \times 10^7 \text{ N-m}$
$t_v = 2.00 \text{ mm}$	$K_{eq2} = 1 \times 10^7 \text{ N-m}$

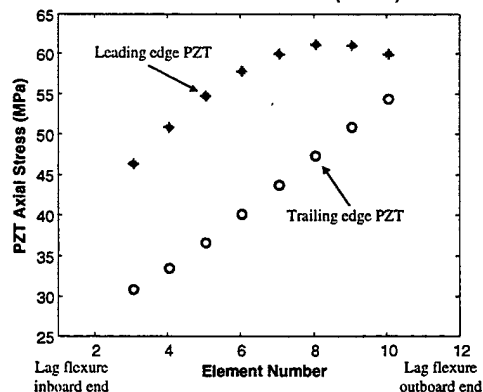
WORST CASE STRESS

Worst case is when the peaks of stresses of the three responses coincide

Max Stress = 61.5 MPa

Stress induced in PZT by all three forces together remains below the design limit of 80 MPa

PZT AXIAL STRESS (MPa)



RESULTS

PENNSTATE



Design

$t_p = 1.45 \text{ mm}$ $K_{eq1} = 3.5 \times 10^7 \text{ N-m}$
 $t_v = 2.00 \text{ mm}$ $K_{eq2} = 1 \times 10^7 \text{ N-m}$

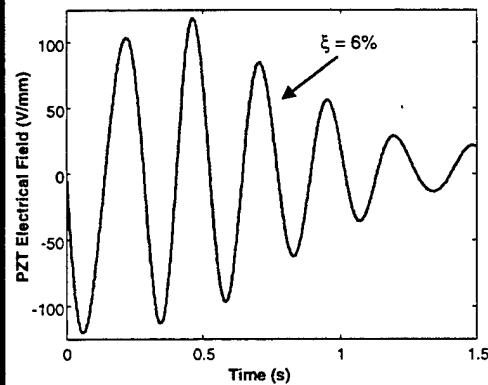
Elect. Field in Forward Flight

Max Electrical Field for 6%
damping is 120.5 V/mm

Electrical Field < 200 V/mm

Electrical field and stress levels remains within PZT allowable
limit of 200 V/mm

PZT Electrical Field (V/mm)



SUMMARY

PENNSTATE



Accomplishments

- Completed development of a mathematical model of rotating flex beam with EACL treatment on a full size rotor
- Developed a controller to provide adaptive damping
- Performed analysis and initial design study to demonstrate feasibility
- Conducted experimental verification of the mathematical model
- Completed an optimization study

Conclusion

- Study to date shows the potential of EACL treatment on flex beams for rotor stability augmentation
 - Sufficient damping can be achieved to alleviate ground and air resonance without exceeding the electrical field and stress levels of PZT
 - Passive damping can be introduced to improve robustness
 - Low power requirements



University of Maryland
Department of Aerospace Engineering



U N I V E R S I T Y O F M A R Y L A N D

**Modeling and Testing of a
Multifunctional Sensor**

Adrian Hood
Graduate Research Assistant

Darryll J. Pines
Associate Professor

Army Research Office
4th Workshop on Smart Structures
The Pennsylvania State University
University Park, PA
August 16-18, 1999



Objective



U N I V E R S I T Y O F M A R Y L A N D

- To develop adaptive multi-functional sensors to detect sources of acoustic and structure-borne noise. Sensor will be capable of detecting strain and acoustic pressure.
- Use sensor in active vibration/acoustic control of noise from transmission and main rotor blades.

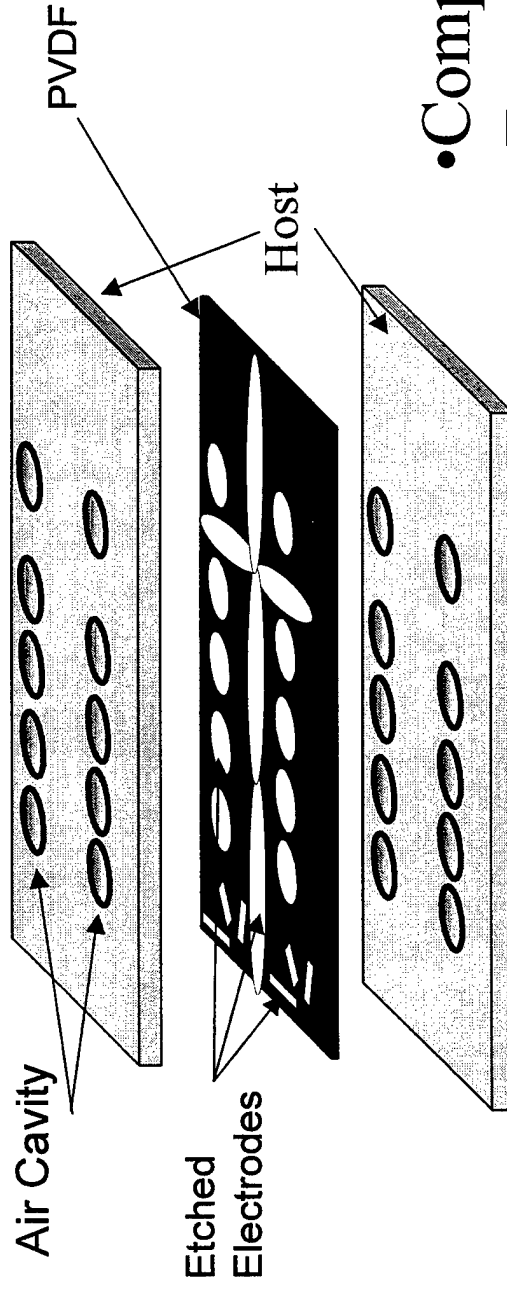




Technical Approach: Custom Etching



U N I V E R S I T Y O F M A R Y L A N D

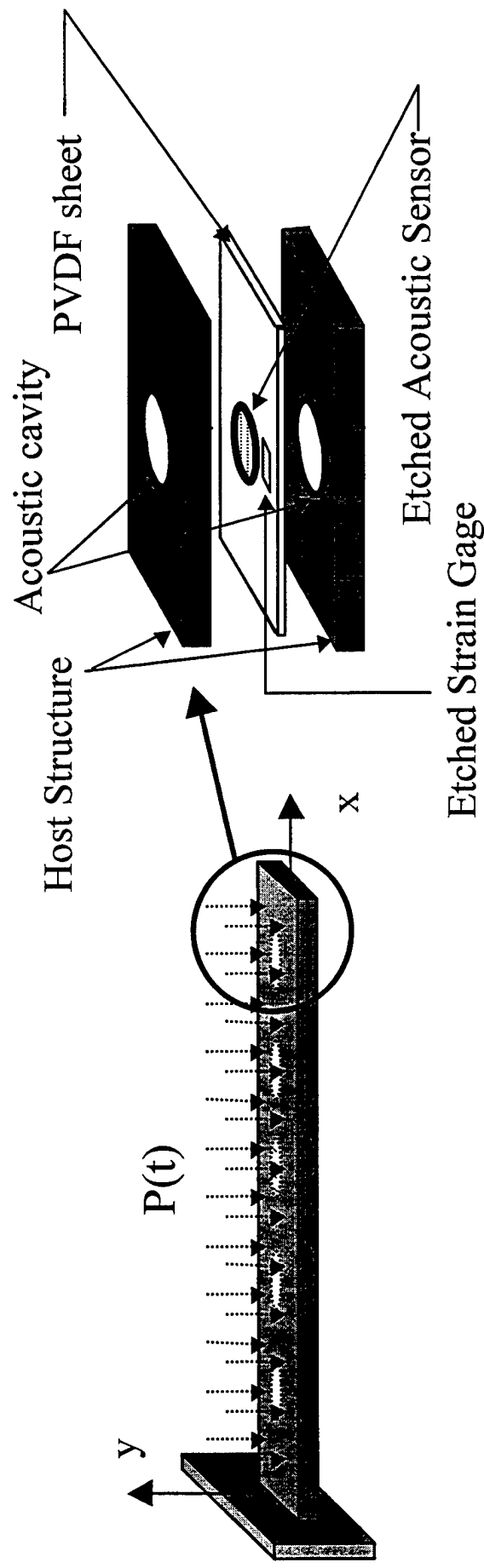


- Compliant
- Easy to use
- Custom electrode patterns
- Linear response

Multi-Functional Concept



UNIVERSITY OF MARYLAND



$$\epsilon_{total} = \epsilon_{mechanical} + \epsilon_{acoustic} \longrightarrow V_{acoustic} = V_{measured} - \frac{A_1}{A_2} V_{mechanical}$$

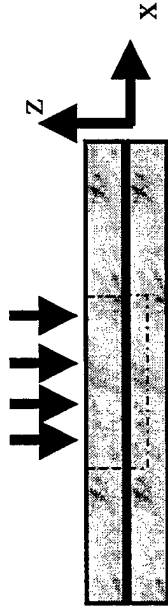
Thin Plate Analysis



UNIVERSITY OF MARYLAND

• Circular Transducer

$$P(r) = P_0 e^{i\alpha t}$$



$$D\nabla^2(\nabla^2 Y) + \frac{\partial^2 Y}{\partial t^2} + K_{cav} Y = P_0 e^{i\alpha t}$$

$$Y(r, \theta, t) = w(r, \theta) e^{i\alpha t}$$

$$\Psi(r, \omega) = \frac{w_0(r)}{P_0} = \bar{C}_0 \left\{ \frac{I_1(\lambda)}{J_1(\lambda)} J_0(\kappa r) + I_0(\kappa r) \right\} - \frac{1}{\rho h}$$

$$\text{where: } \bar{C}_0 = \frac{-J_1(\lambda)}{K_{cav} - \rho h \omega^2} \frac{I_1(\lambda) J_0(\lambda) + J_1(\lambda) I_0(\lambda)}{I_1(\lambda) J_0(\lambda) + J_1(\lambda) I_0(\lambda)}$$

$$\text{and } K^4 = \frac{\rho \omega^2 - K_{cav}}{D}$$

2-D Sensor Equation



UNIVERSITY OF MARYLAND

- Charge per unit pressure generated by piezoelectric material

$$\frac{q_3^\theta}{P_0} = S^* = \iint_A \{ d_{31} \quad d_{32} \quad d_{36} \} \left[\begin{array}{c} \frac{E_1^*}{1-\nu_{12}^* \nu_{21}^*} \quad \frac{E_1^* \nu_{21}^*}{1-\nu_{12}^* \nu_{21}^*} \\ \frac{E_1^* \nu_{21}^*}{1-\nu_{12}^* \nu_{21}^*} \quad \frac{E_2^*}{1-\nu_{12}^* \nu_{21}^*} \\ 0 \quad 0 \quad G_{LT}^* \end{array} \right] \left[\begin{array}{c} 0 \\ \frac{\partial u}{\partial x} \quad \frac{\partial v}{\partial x} \\ \frac{1}{2} \left(\frac{\partial u}{\partial y} + \frac{\partial v}{\partial x} \right) \end{array} \right] - z \left[\begin{array}{c} \frac{\partial^2 \Psi}{\partial x^2} \quad \frac{\partial^2 \Psi}{\partial y^2} \\ \frac{\partial^2 \Psi}{\partial x \partial y} \end{array} \right] F(x, y) dA$$

where

Ψ : Transverse displacement per unit pressure

d_{3i} $i=1,2,3$: Piezoelectric constants

z : Half the thickness of the film

q_3 : output charge in the (3-direction)

E : Elasticity Matrix

- No external electric field

Charge Sensitivity



UNIVERSITY OF MARYLAND

$$\frac{q_3}{P_0} = -z\pi\beta\bar{C}_0 \left\{ \frac{\kappa^2}{2} \left\{ \frac{I_1(\lambda)}{J_1(\lambda)} \Sigma_1 + \Sigma_2 \right\} + \Sigma_3 \right\}$$

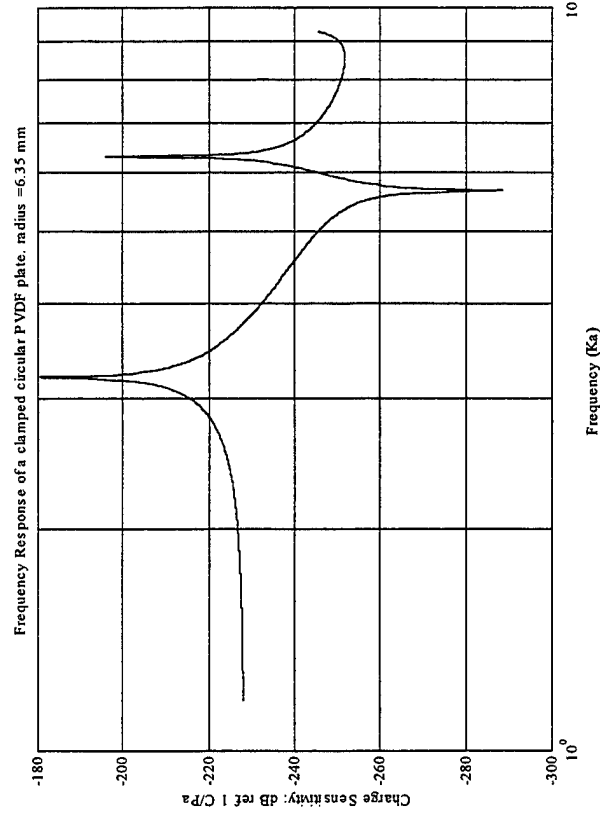
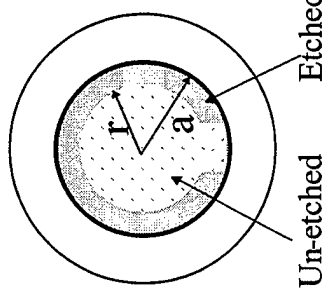
$$\beta = E_{111}d_{31} + E_{112}(d_{31} + d_{32}) + E_{222}d_{32}$$

$$\lambda = \kappa a \quad \zeta = \frac{r}{a}$$

$$\Sigma_1 = -\frac{2\zeta a}{\kappa} J_1(\zeta\lambda) + \frac{1}{\kappa^2} (1 - J_0(\zeta\lambda))$$

$$\Sigma_2 = \frac{2\zeta a}{\kappa} I_1(\zeta\lambda) + \frac{1}{\kappa^2} (1 - I_0(\zeta\lambda))$$

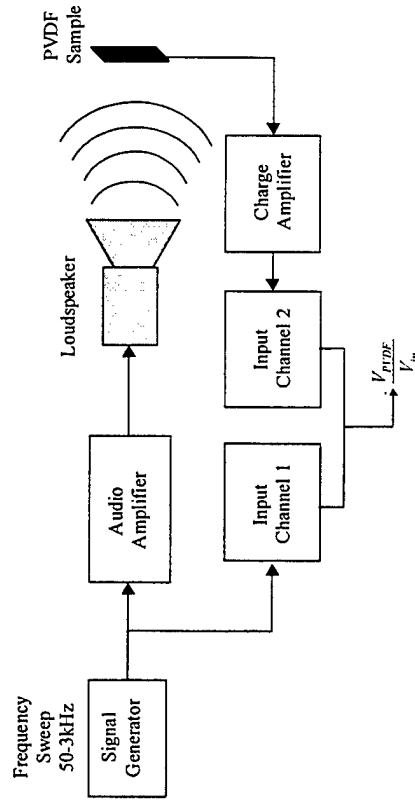
$$\Sigma_3 = \frac{I_1(\lambda)}{J_1(\lambda)} (J_0(\zeta\lambda) - 1) + (I_0(\zeta\lambda) - 1)$$



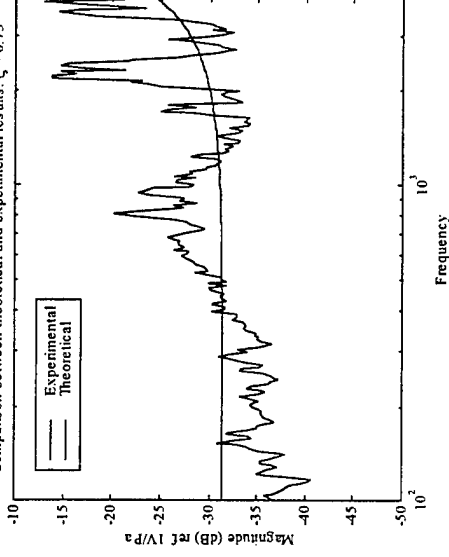
Experimental Results



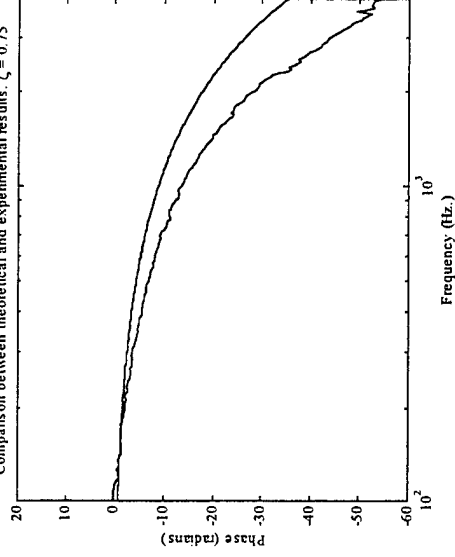
UNIVERSITY OF MARYLAND



Comparison between theoretical and experimental results. $\zeta = 0.75$



Comparison between theoretical and experimental results. $\zeta = 0.75$



$$\frac{V_0}{P_0} = \frac{\left(\frac{V_{pvd}}{V_{in}} \right)_{tf} \left(\frac{S_{mic}}{G_{mic}} \right)}{\left(\frac{V_{mic}}{V_{in}} \right)_{tf}}$$

SURFACE DAMPING TREATMENT WITH AN ACTIVE-PASSIVE HYBRID CONSTRAINING LAYER

Yanning Liu and K. W. Wang
Structural Dynamics and Controls Lab
Mechanical Engineering Department
The Pennsylvania State University
University Park, PA 16802
Phone: (814) 865-2183, Email: kwwang@psu.edu

Passive Constrained Layer (PCL) and Active Constrained Layer (ACL) treatments have been explored by various researchers in the past. These systems generally consist of a piece of viscoelastic material (VEM) sandwiched between a constraining layer (cover sheet) and a host structure. In ACL, the cover sheet is usually made of piezoelectric materials. The main purpose of using a piezoelectric coversheet in ACL is that its active action can enhance the viscoelastic layer damping ability by increasing the VEM shear angle during operation (the so-called *enhanced passive damping* action). When the active action fails, significant passive damping could still exist in ACL, which would be important for fail-safe reasons. On the other hand, since the soft VEM layer reduces the active authority of the piezoelectric layer, it has been recognized that the applications best suitable for ACL treatments are those that can utilize significant damping from deforming the VEM, rather than from direct piezoelectric-structure interactions.

Given the above observations, it would be important to optimize the open-loop characteristics (the so-called *baseline* structure without active action) of the ACL treatment, as well as the system's closed-loop behavior from the *enhanced passive damping action*. In both cases, the constraining layer material property plays an important role. In general, the selections of ACL constraining layer materials are limited (e.g., PZT, PVDF, etc.), and they might not provide good open-loop performance. On the other hand, for a purely PCL system, much larger selections of constraining layer materials are available. However, they cannot provide the active action and enhanced damping ability.

In this research, a new configuration of surface damping treatments, active-passive hybrid constrained layer damping, is proposed and analyzed. The purpose is to improve the performance of ACL and PCL treatments by mixing passive and active materials in the constraining layer. In this new configuration, the VEM is constrained by an active-passive hybrid constraining layer - the active part is made of PZT ceramics, and the passive part can be selected by the designer to meet different requirements. The active and passive constraining parts are mechanically connected such that the displacement and force are continuous at the connecting point, but are isolated electrically so the passive constraining layer will not affect the function of the active component.

Non-dimensional equations of motion of a generic treatment model are developed and closed form solutions are derived. Using the damping loss factors as indices, parametric studies are performed to investigate the effects of the relative stiffness and relative length between the passive constraining material and active constraining material on the system damping characteristics. It is shown that by selecting a stiffer passive constraining material and an optimal active-to-passive length ratio, the new proposed configuration can achieve better closed-loop and open-loop performances than the treatments with a pure PZT constraining layer. It is also illustrated that the inclusion of a passive material in the constraining layer would provide more flexibility for the treatment design to satisfy different requirements, such as weight penalty versus damping authority.

PENNSTATE



Surface Damping Treatment with an Active-Passive Hybrid Constraining Layer

Yanning Liu and K. W. Wang

Structural Dynamics and Controls Lab
Department of Mechanical Engineering
The Pennsylvania State University
University Park, PA 16802, USA

Structural Dynamics and Controls Lab

PENNSTATE



Background Information

Active constraining layer

- Can provide active action to enhance VEM deformation
- Limited selections in material property

Passive constraining layer

- More selections - materials property can be optimized through different selections
- Cannot provide active action

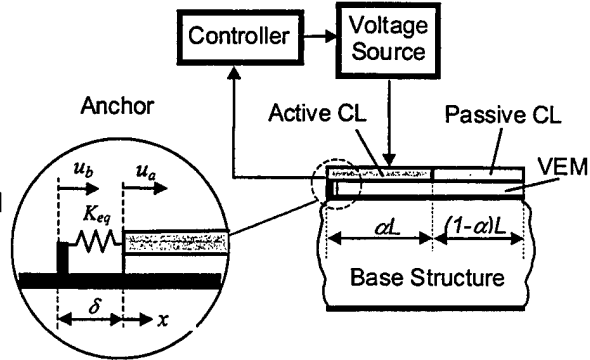
IDEA: Combine active materials (for active action) and passive materials (properties can be optimized for better baseline performance) into a hybrid constraining layer configuration

Structural Dynamics and Controls Lab



A New Hybrid Configuration

- Include both passive and active materials in the constraining layer
- Active and passive constraining parts are mechanically connected
- Active and passive constraining parts are isolated electrically



Objective

Design an active-passive constraining layer (material properties, active-to-passive length ratio) such that an active-passive Hybrid Constrained Layer (HCL) obtains more damping than the treatments with a purely passive or purely active cover sheet

Structural Dynamics and Controls Lab



System Description and Model

•Equilibrium equations

$$\frac{d^2 \bar{U}_a}{d\bar{x}^2} - \Gamma_a^2 \bar{U}_a = -\Gamma_a^2 \bar{U}_b$$

$$0 < \bar{x} < \alpha$$

$$\frac{d^2 \bar{U}_p}{d\bar{x}^2} - \Gamma_p^2 \bar{U}_p = -\Gamma_p^2 \bar{U}_b$$

$$\alpha < \bar{x} < 1$$

•Boundary conditions

$$\frac{d\bar{U}_a}{d\bar{x}} - \frac{\Lambda}{e^{i\alpha x}} = K(\bar{U}_a - \bar{U}_b) \quad \bar{x} = 0$$

$$\frac{d\bar{U}_a}{d\bar{x}} - \frac{\Lambda}{e^{i\alpha x}} = S_p \frac{d\bar{U}_p}{d\bar{x}}, \quad \bar{U}_p = \bar{U}_a \quad \bar{x} = \alpha$$

$$\frac{d\bar{U}_p}{d\bar{x}} = 0 \quad \bar{x} = 1$$

Structural Dynamics and Controls Lab



System Description and Model

General solutions to the equations of motion

$$\bar{U}_a = A \cosh(\Gamma_a \bar{x}) + B \sinh(\Gamma_a \bar{x}) + \sum_{j=0}^N \alpha_j \bar{x}^j$$

$$\bar{U}_p = C \cosh(\Gamma_p \bar{x}) + D \sinh(\Gamma_p \bar{x}) + \sum_{j=0}^N \beta_j \bar{x}^j$$

Self-sensing control algorithm

$$\Lambda = K_g \left[\frac{\partial u_a(0,t)}{\partial t} - \frac{\partial u_a(\alpha L,t)}{\partial t} \right] = iG [\bar{U}_a(0) - \bar{U}_a(\alpha)] e^{i\alpha x}$$

Constant strain field in the host beam

$$\bar{U}_b = c_0 + \varepsilon_0 \bar{x}$$

Structural Dynamics and Controls Lab



Definition of Loss Factors

- Energies dissipated per cycle by active control (w_a) and passive damping (w_p), respectively, are

$$W_a = \pi G E_a h_a b L |\bar{U}_a(0) - \bar{U}_a(\alpha)|^2$$

$$W_p = \pi \eta_p G_v h_v b L \int_0^1 |\gamma|^2 d\bar{x}$$

- Active loss factor η_a and passive loss factor η_p

$$\eta_a = \frac{W_a}{2\pi W_s}$$

$$\eta_p = \frac{W_p}{2\pi W_s}$$

where

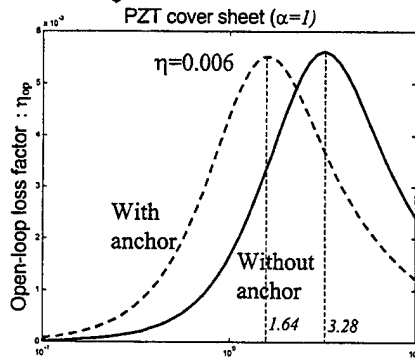
$$W_s = \frac{E_a h_a b L}{2} \left\{ S_b \varepsilon_0^2 + \int_0^1 \left| \frac{d\bar{U}_a}{d\bar{x}} \right|^2 d\bar{x} + S_p \int_0^1 \left| \frac{d\bar{U}_p}{d\bar{x}} \right|^2 d\bar{x} \right. \\ \left. + \operatorname{Re}[\Gamma_a^2] \theta_v^2 \int_0^1 |\gamma|^2 d\bar{x} + K |\bar{U}_a(0) - \bar{U}_b(0)|^2 \right\}$$

- Active-passive hybrid loss factor η_s : $\eta_s = \eta_a + \eta_p$

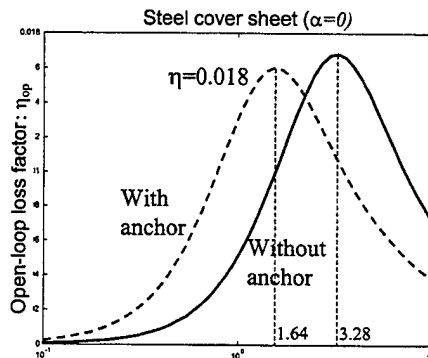
Structural Dynamics and Controls Lab



Damping of HCL: Open-Loop



Characteristic length: $\sqrt{\frac{G_v^* L^2}{E_c h_c h_v}}$



Characteristic length: $\sqrt{\frac{G_v^* L^2}{E_c h_c h_v}}$

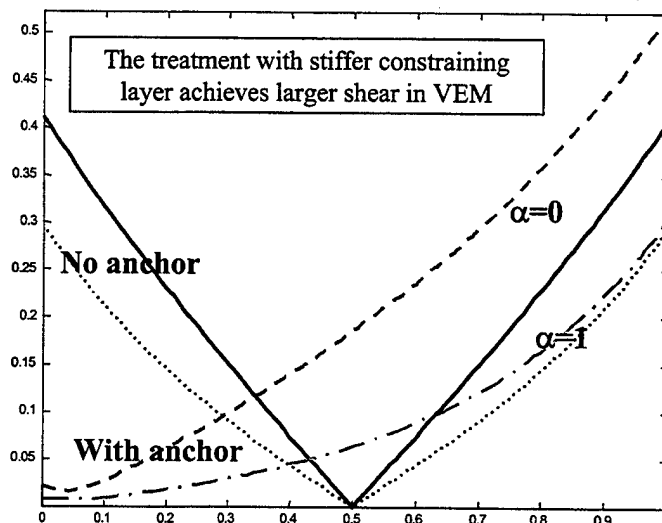
The treatment with stiffer passive cover sheet has more damping than the one with PZT cover sheet without active action

Structural Dynamics and Controls Lab



Damping of HCL: Open-Loop

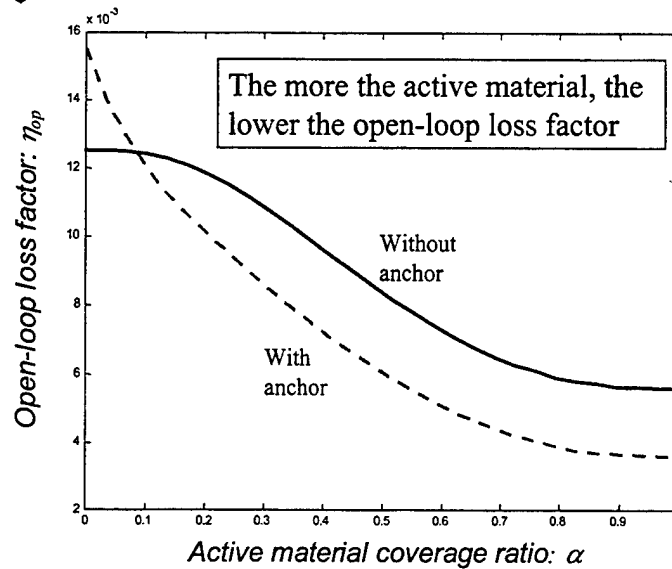
Non-dimensional shear distribution in VEM



Structural Dynamics and Controls Lab



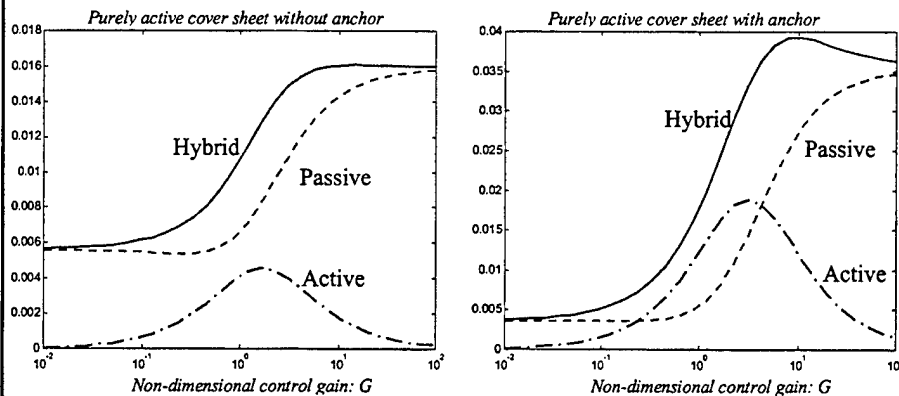
Damping of HCL: Open-Loop



Structural Dynamics and Controls Lab



Damping of HCL: Gain Effect



- Passive damping saturates at high control gain
- An optimal control gain for the active damping

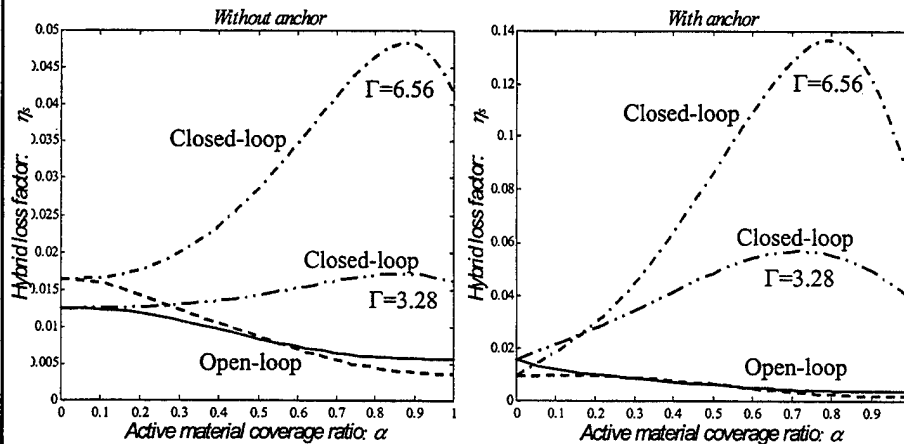


An optimal control gain for the hybrid damping

Structural Dynamics and Controls Lab



Damping of HCL

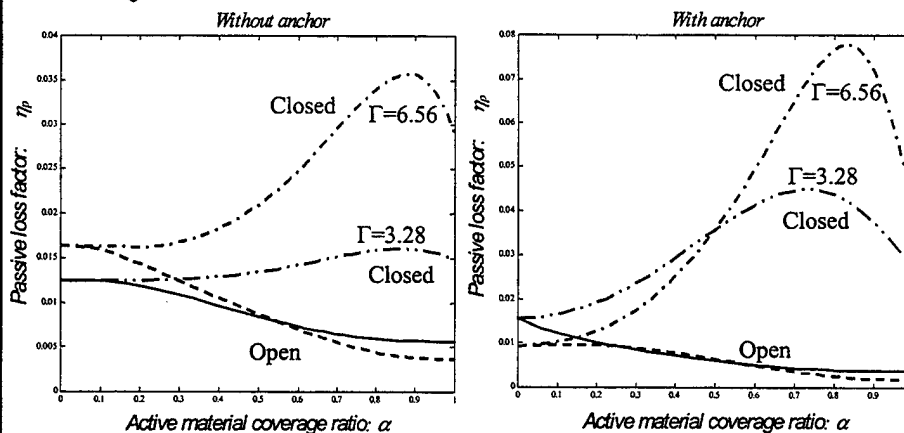


There is a range of α such that HCL outperforms the treatment with purely active cover sheet ($\alpha=1$) both in the open-loop and closed-loop damping

Lab



Enhanced Passive Damping



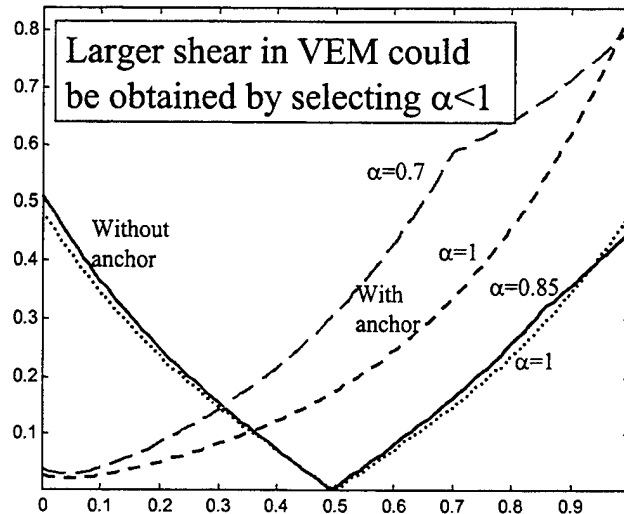
There is a range of α such that the enhanced passive damping from HCL is higher than the treatment with purely active cover sheet ($\alpha=1$)

Structural Dynamics and Controls Lab



Enhanced Shear in VEM

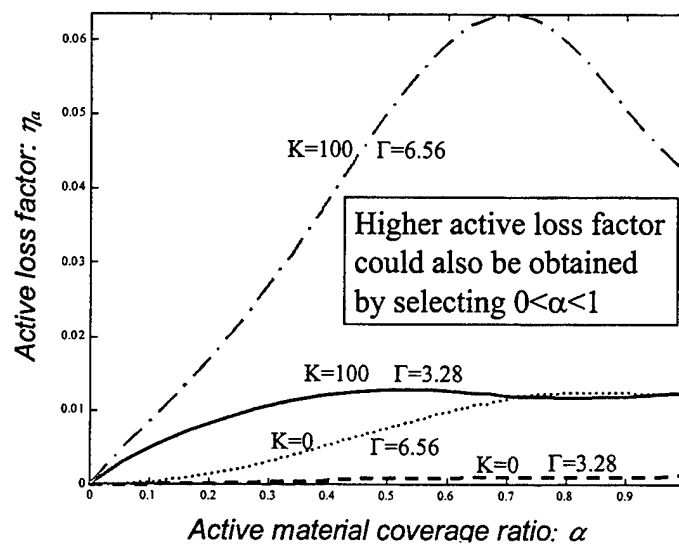
Shear distribution in VEM



Structural Dynamics and Controls Lab



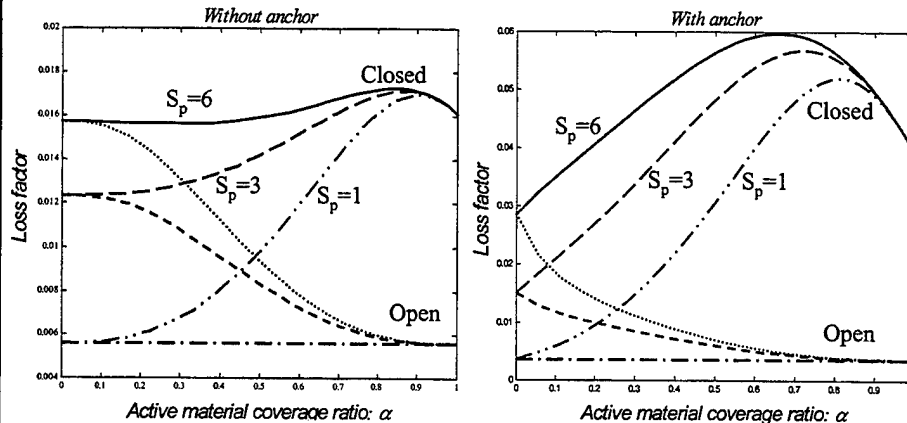
Damping from Direct Active Control



Structural Dynamics and Controls Lab



Effect of Passive-to-Active Stiffness Ratio



- HCL damping can be increased by designing larger passive-to-active extensional stiffness ratio S_p
- HCL provide more flexibility in the damping design

Structural Dynamics and Controls Lab



Conclusions

- With an appropriate selection of the active-to-passive length ratio, the treatment with an active-passive hybrid constraining layer could outperform the treatment with a purely active cover sheet both in the open-loop and closed-loop damping when a self-sensing control algorithm is applied.
- Exist optimal active material coverage ratio
- The stiffer the passive coversheet material relative to active coversheet material, the better the HCL treatment
- HCL provides more flexibility for damping design to satisfy different requirements, such as weight penalty versus damping authority

Structural Dynamics and Controls Lab



Alfred Gessow Rotorcraft Center

U N I V E R S I T Y O F M A R Y L A N D



Helicopter Transmission Diagnostics

Paul D. Samuel Darryll J. Pines
Graduate Fellow Associate Professor

Army Research Office
16-18 August 1999



Motivation



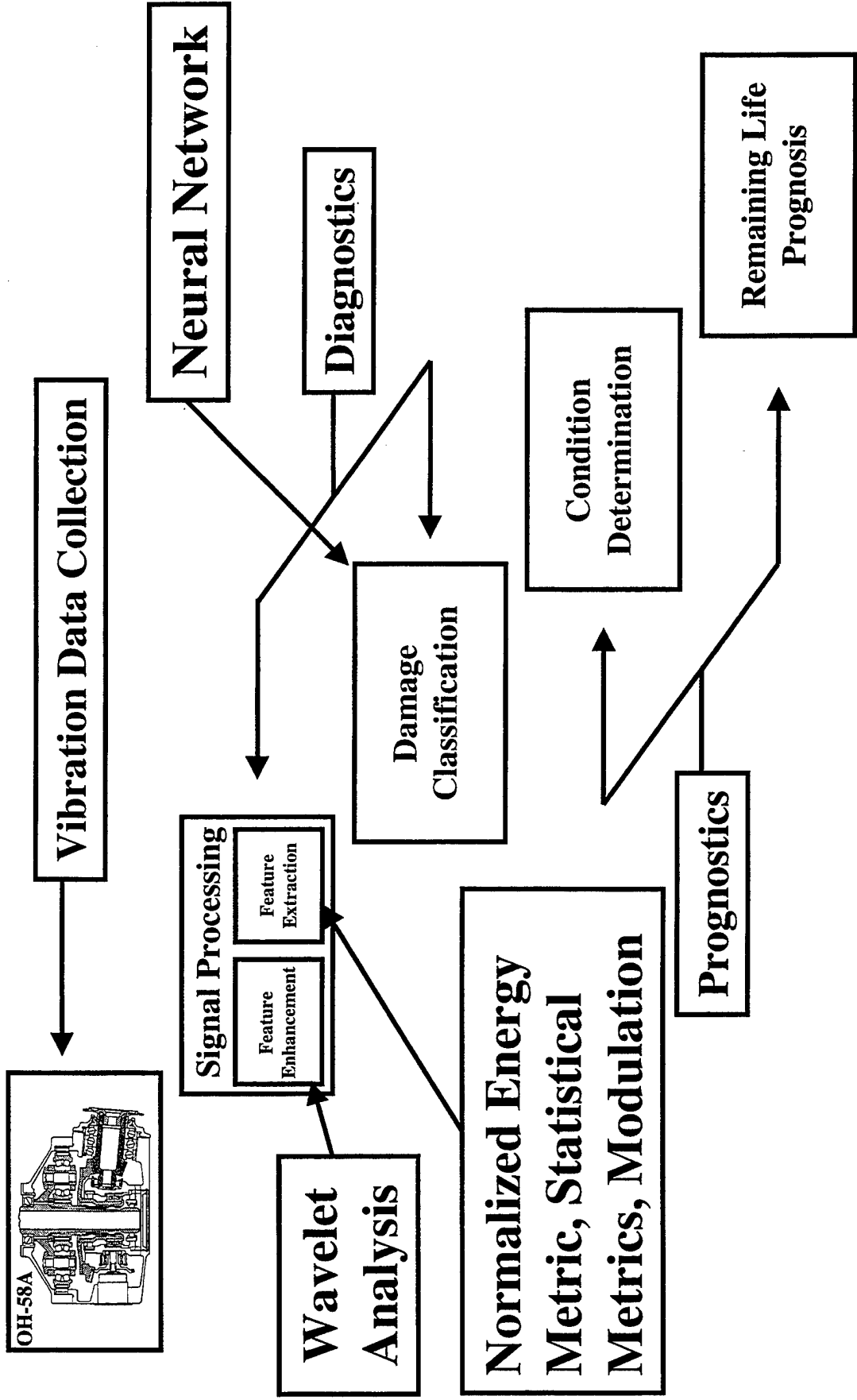
U N I V E R S I T Y O F M A R Y L A N D

- The main transmission is critical to rotorcraft performance, safety and reliability.
- Faults appearing in the main transmission can significantly affect the performance of the coupled vibratory response of the vehicle.
- These faults can lead to an increase in maintenance inspections and reduced component life of many flight critical parts.
- If undetected, certain faults are capable of causing catastrophic failures of the rotorcraft.
- Health and usage monitoring (HUM) of rotorcraft flight components has been proposed as an approach for detecting incipient damage in rotorcraft transmissions.



Comprehensive HUM System

UNIVERSITY OF MARYLAND

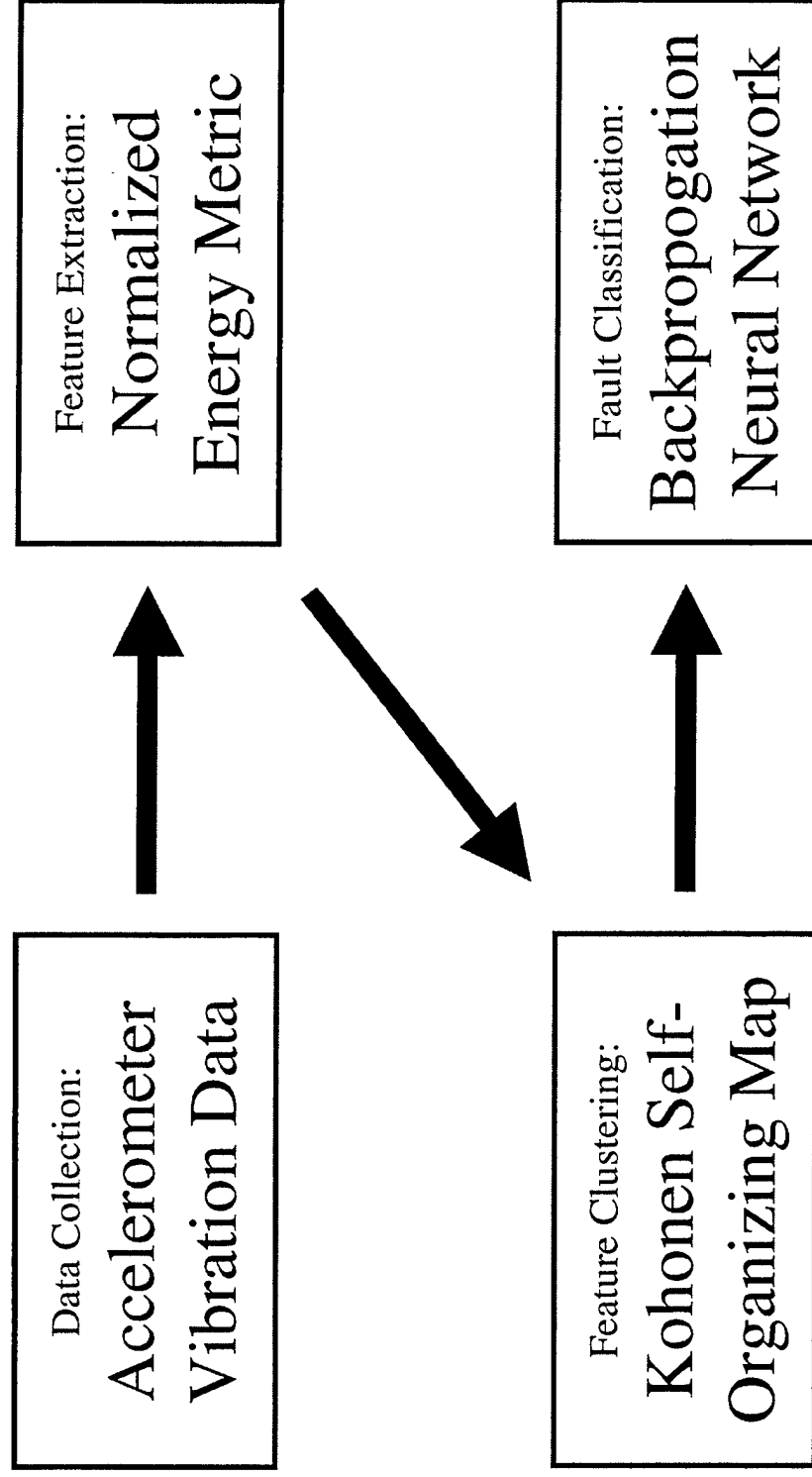




Complete Diagnostic Strategy



U N I V E R S I T Y O F M A R Y L A N D





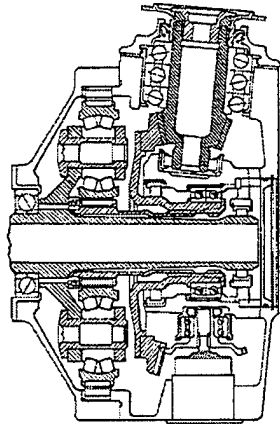
NASA Glenn OH-58A Transmission



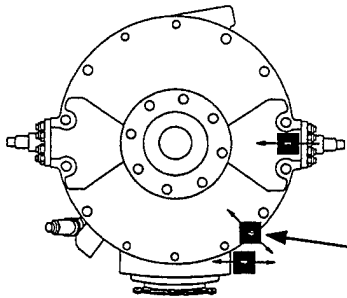
UNIVERSITY OF MARYLAND

OH-58A Main-Rotor Transmission

Side

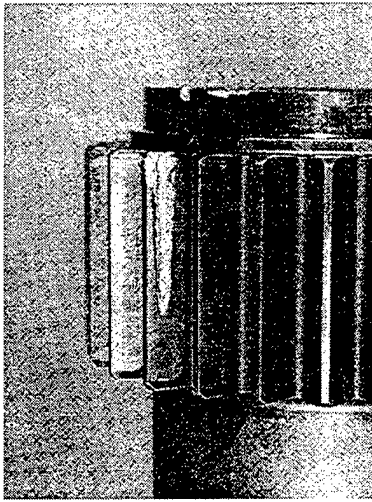


Top

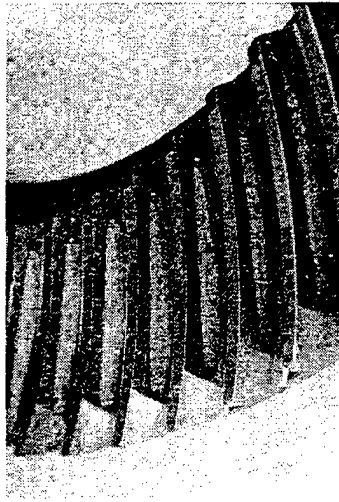


Accelerometer under consideration.

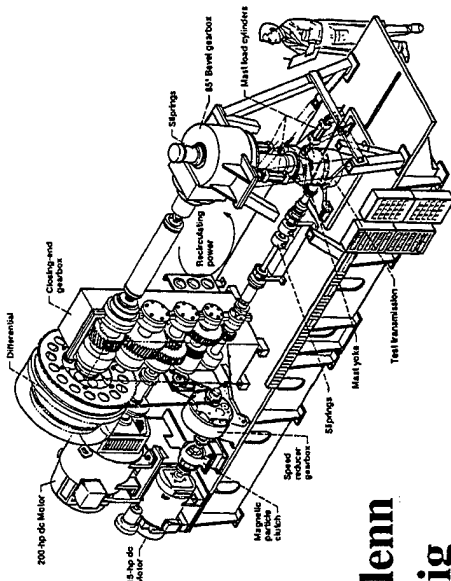
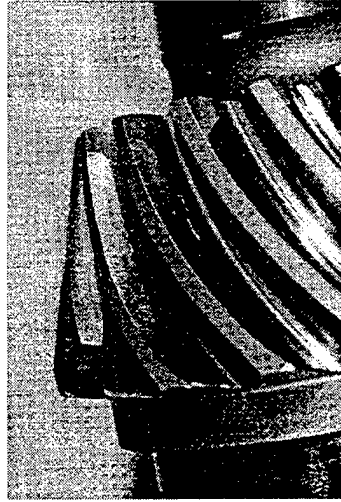
Spalled Sun Gear



Scored Spiral Bevel Face Gear



Scored Spiral Bevel Pinion



NASA Glenn
Test Rig



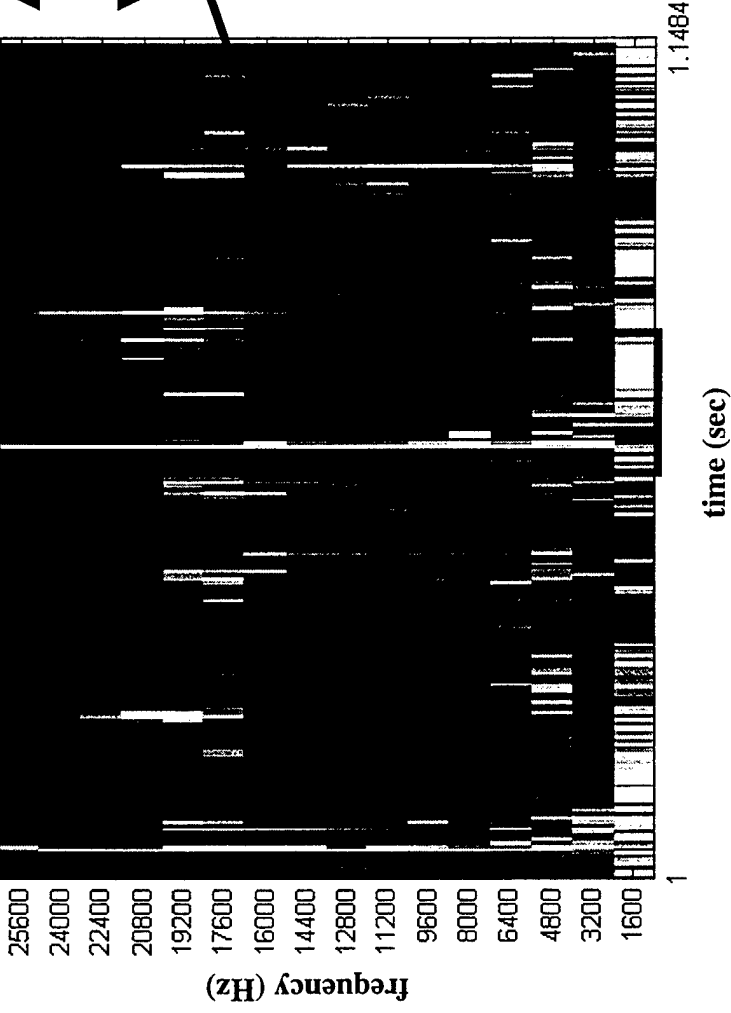
Normalized Energy Metric



UNIVERSITY OF MARYLAND

Mean Square Wavelet Map:
Harmonic Basis
Function

Window size and frequency range can be tuned
to optimize the performance of the index.



Compute the normalized
energy over a given range,
such as one cycle.

$$NE_{i,j} = \frac{E_{i,j}}{\sum_{j=1}^n E_{i,j}}$$

where:

i = time index

j = frequency band index

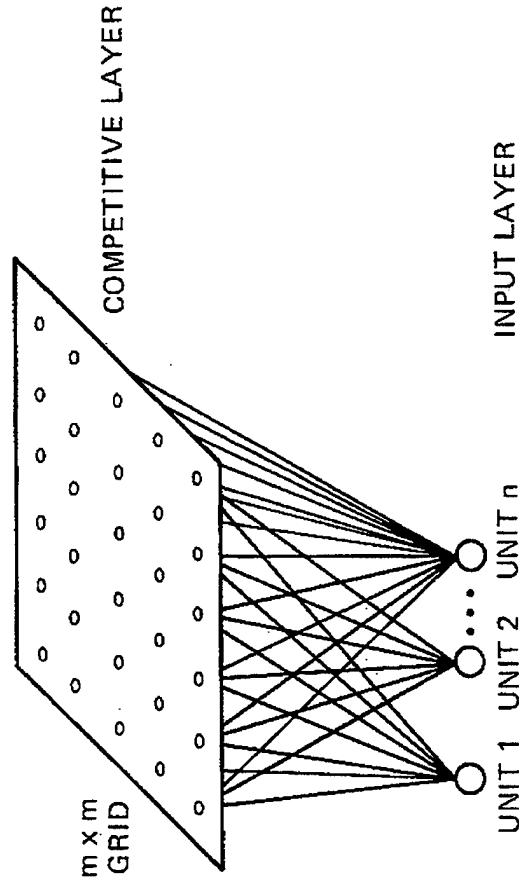
$E_{i,j}$ = the energy at time i and frequency j



Kohonen Self Organizing Map



U N I V E R S I T Y O F M A R Y L A N D

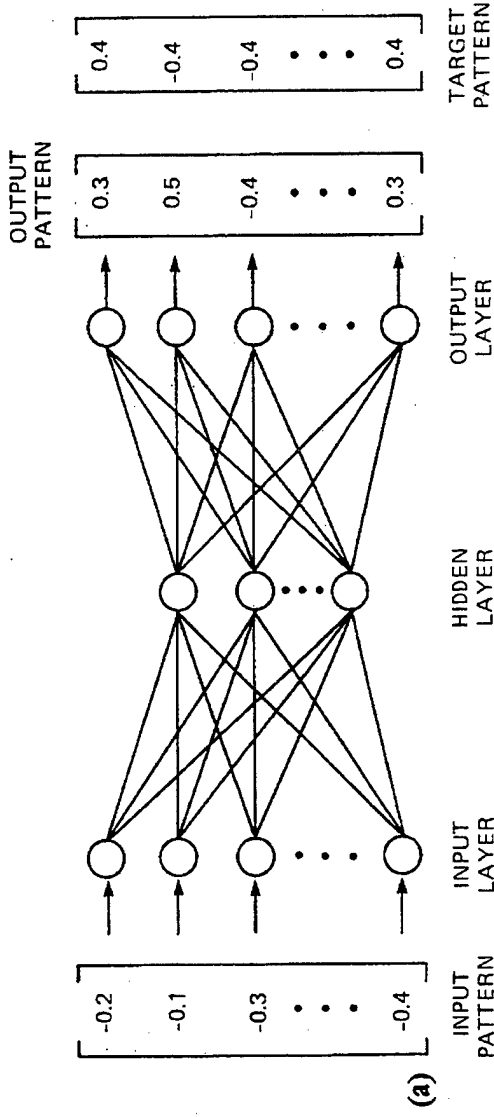


- A normalized energy feature vector served as input for the SOM.
- Only components of the feature vector corresponding to the sidebands of the planetary stage mesh frequency and its harmonics were used.
- An 8 X 8 grid was chosen for the output.



Backpropagation Network

UNIVERSITY OF MARYLAND



- The 8 X 8 grid from the SOM served as input for the backpropagation neural network.
- The input layer consisted of 64 neurons, the hidden layer consisted of 6 neurons, and the output layer consisted of 1 neuron.
- The chosen target pattern was 0 for no damage, 1 for spiral bevel damage, and -1 for planetary damage.

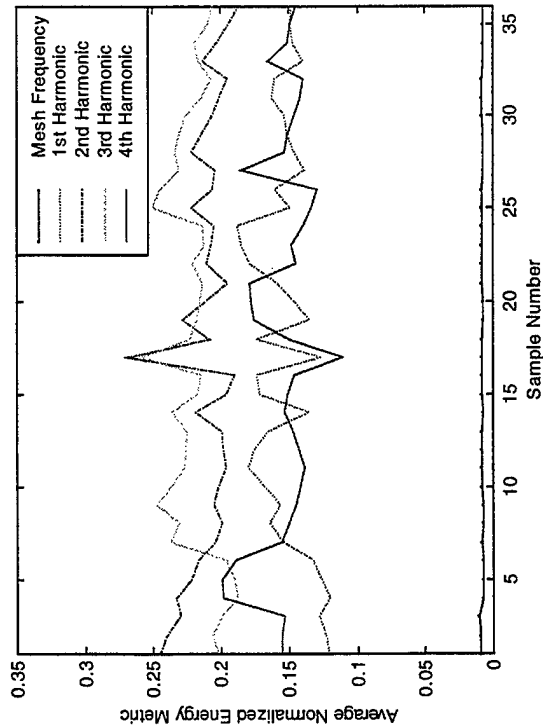


Results: Accelerometer 6

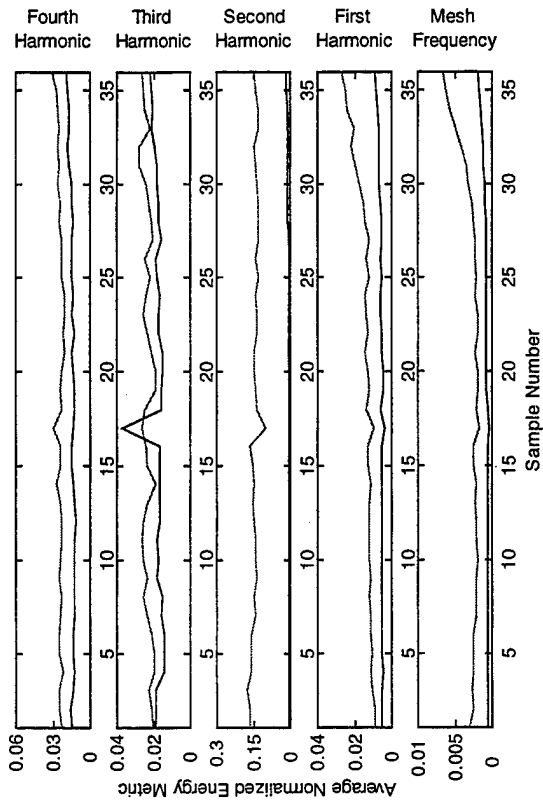
U N I V E R S I T Y O F M A R Y L A N D

Normalized Energy Metric

Regular Meshing Components



Sidebands





Results: Accelerometer 6

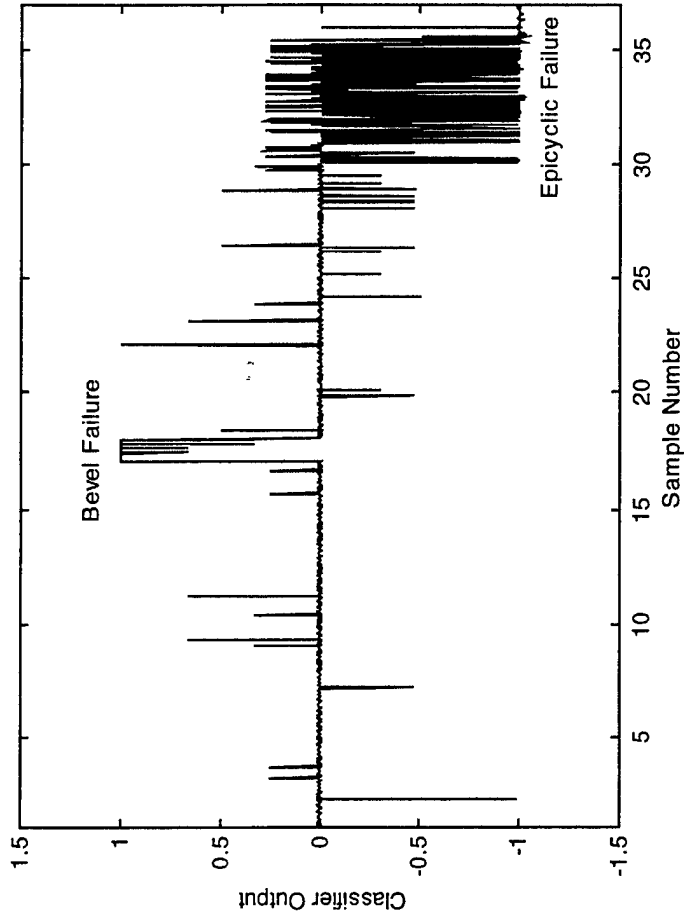
Neural Network Classification Strategy

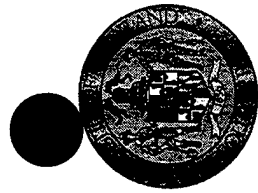
SOM Output

3	3	3	3	3	3	1,3	1
3	3	3	3		3		1
3	3	3	3	3	3	1	1
					3	1	1
2	2	2	2	2	1,2	1	1
2	2		2		1,2	1	1
2	2	2	2		1	1	1
2	2	2	2		1	1	1

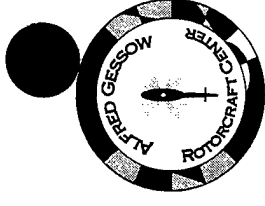
- 1 = No Damage
- 2 = Spiral Bevel Fault
- 3 = Planetary Fault

Complete Classifier Output





*Alfred Gessow
Rotorcraft Center*



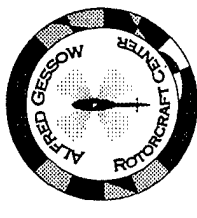
A Modal-Based Damage Detection Technique for Helicopter Rotor Blades

*Jason S. Kiddy
Dr. Darryll Pines*

**Army Research Office
4th Workshop on Smart Structures
Pennsylvania State University
University Park, PA
August 16-18, 1999**



Objectives



-
- Develop a real-time modal based damage detection algorithm to detect and characterize damage in main rotor blades while in operation.
 - Emphasis is placed on detecting damage that affects the global properties of the rotor blade, i.e. modal dynamics.
 - Damage can have an affect on the mass, stiffness or damping (aerodynamics) of the rotor blade.





Eigenstructure Assignment



- Advantages

- Eigenstructure Assignment has previously been used to accurately detect and characterize damage in non-rotating structures.
- Current extension incorporates the effects of centrifugal forces leading to an enhanced sensitivity of the eigenstructure to mass changes.
- By placing the eigenstructure assignment algorithm into a state-space formulation, aerodynamic damping can be considered

- Disadvantages

- A distributed array of sensors on the blade is required.
- Structural stiffness changes become harder to detect at higher rotation rates.
- Poor results when noise is added to the system

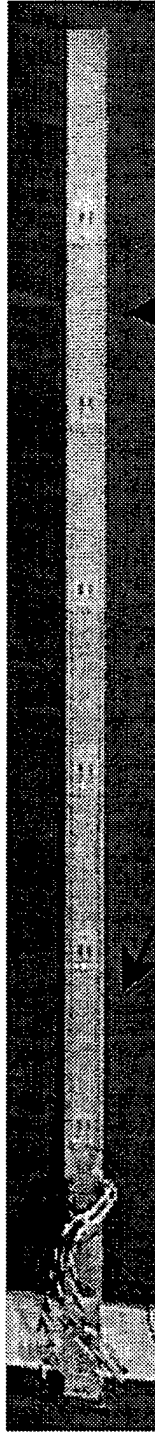


Experimental Validation - Vacuum Chamber



- Rotational testing performed in the U. of MD. Vacuum Chamber
- Undamaged blade was tested and then retested after simulated ballistic damage.

Length	.84 meters
Thickness	.00226 meters
Width	.02544 meters
Material	2024 Aluminum
Number of Strain Gage Bridges	7
Rotation Rate	0, 250, 500, 750 RPM

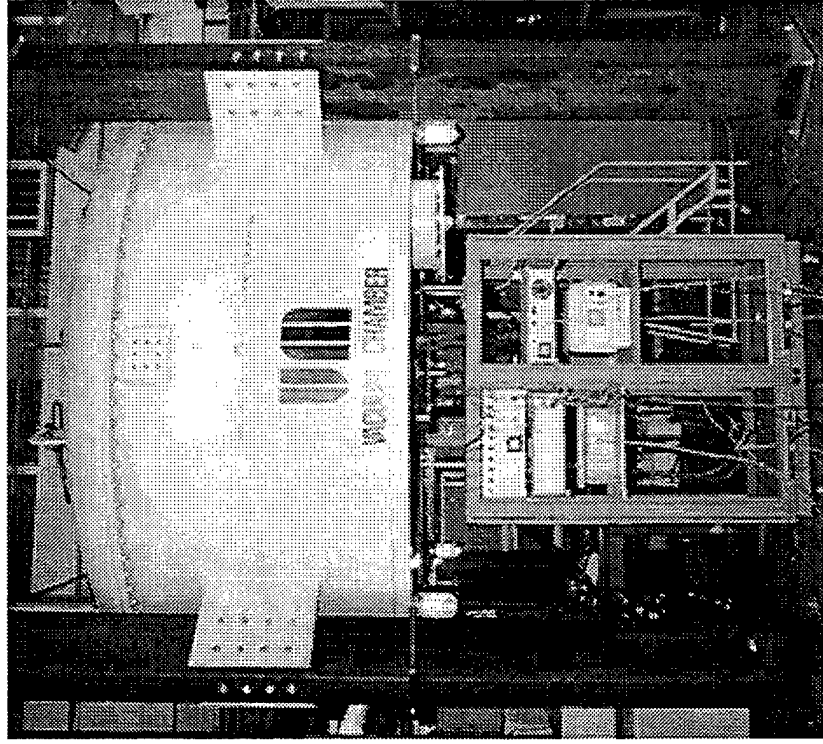


1/4" Hole	1.04% Loss of Mass
3/8" Hole	2.34% Loss of Mass
2 - 3/8" Holes	4.68% Loss of Mass
3 - 3/8" Holes	7.02% Loss of Mass

Locations of Simulated
Ballistic Damage
(Elements 2 and 6)



Vacuum Chamber



64 Channel Slip Ring

10 Full-Bridge Strain
Gage Channels

12 Power Channels

2 mbar pressure

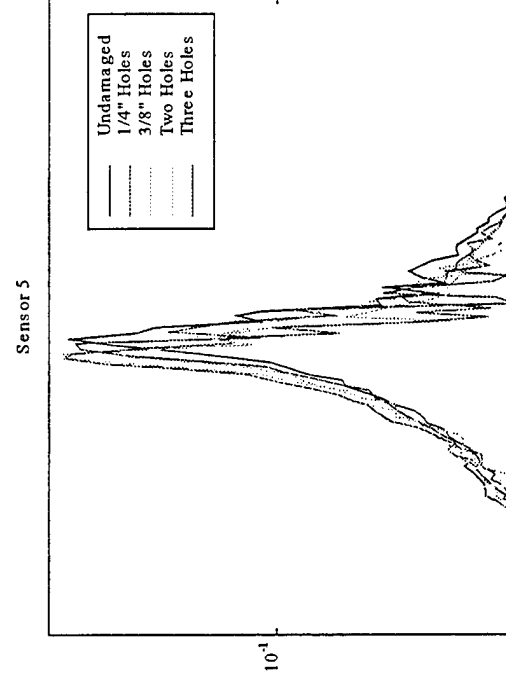
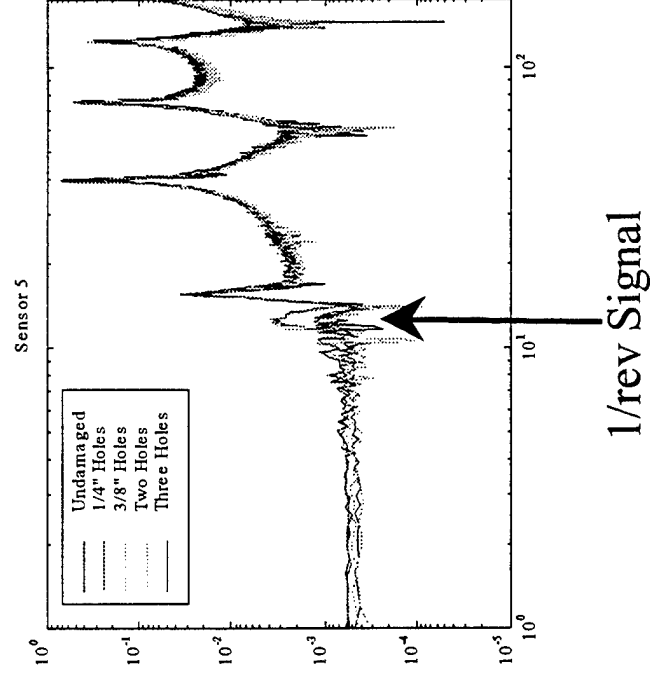
0-1000 RPM
Motor



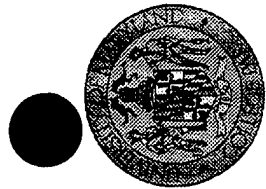
Experimental Transfer Functions (750 RPM) - Blade 1



<i>FEM</i>	<i>Undamaged</i>	<i>1/4" Hole</i>	<i>3/8" Hole</i>	<i>2 Holes</i>	<i>3 Holes</i>
15.3	15.44	15.44	15.43	15.46	15.5
39.9	39.7	39.6	39.44	39.34	39.3
75.9	75.11	74.81	74.07	74.71	74.38
125	123.93	123.61	122.48	122.94	122.94



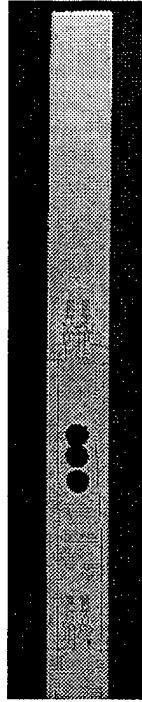
Mode 4



Experimental Damage Detection Results III



3-3/8" Holes



- 750 RPM
- Modes 2,3,4

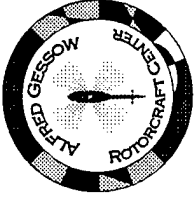
Element #	1	2	3	4	5	6	7
Standard Deviation Stiffness	0.0159	0.7905	0.4515	0.4927	0.0699	0.0489	1.0395
Average Stiffness Change	-0.374	3.3042	-0.1364	-0.6494	-0.4057	-0.2761	-0.8014
Standard Deviation Mass	0.0625	0.1291	0.0883	0.5067	0.1218	0.0244	0.3546
Average Mass Change	-0.3622	0.6257	0.1227	-0.3122	0.0344	-0.0577	0.1245

Actual Mass Loss : 7.02%

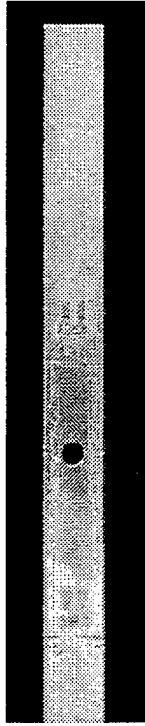


Experimental Damage Detection

Results IV



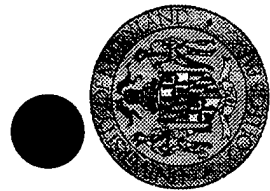
3/8" Hole



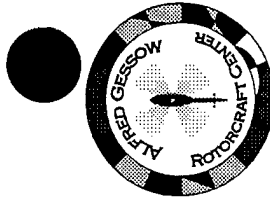
- 250 RPM
- Modes 2,3,4

Element #	1	2	3	4	5	6	7
Standard Deviation Stiffness	0.0456	0.2175	0.106	1.289	0.7807	0.4424	0.2501
Average Stiffness Change	0.04	2.3035	-0.6868	0.4166	-0.605	-0.3132	-0.7192
Standard Deviation Mass	0.3345	0.1217	0.0625	0.8274	1.4805	0.6871	0.1729
Average Mass Change	1.1396	1.2044	-0.3411	0.3506	-0.9324	-0.2065	-0.1656

Actual Mass Loss : 2.34%



Damage Detection Results - Blade 1

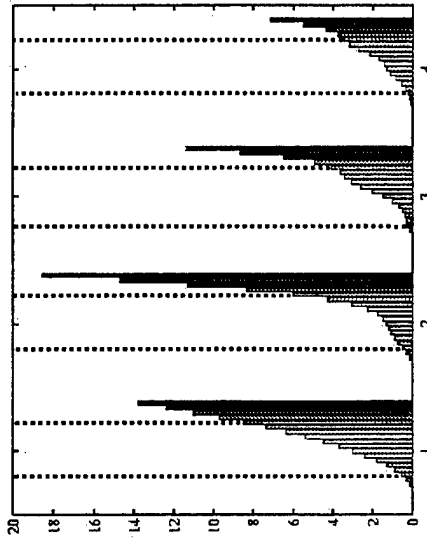
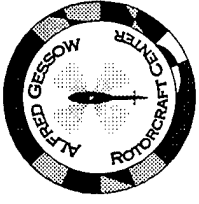


Was the damage properly detected?

	1/4" Hole	3/8" Hole	2 - 3/8" Holes	3 - 3/8" Holes
0 RPM	No	No	No	No
250 RPM	No	No	No	No
500 RPM	No	No	Yes	No
750 RPM	Yes	Yes	Yes	Yes

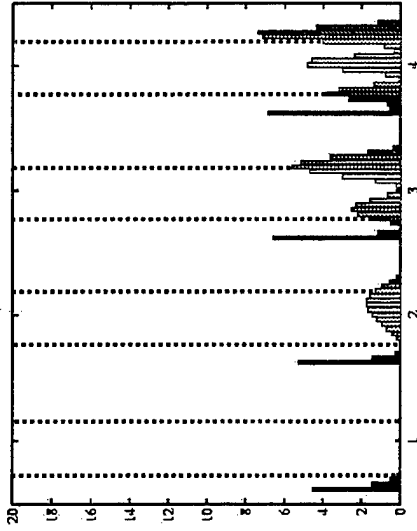


Potential Energy Vacuum Chamber Blades I



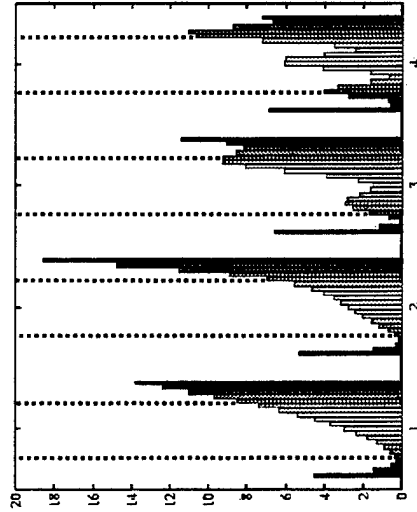
Energy due to CF Stiffness

+



Energy due to EI Stiffness

=



Total Potential Energy

750 RPM
Modes 1-4

PENNSTATE



High Force Piezoelectric Linear Stepping Motors

George A. Lesieutre
Gary H. Koopmann
Jeremy Frank
Weiching Chen

17 August 1999

ARO Smart Structures Workshop
State College, PA

Shape Control w/ Solid-State Devices

- **Actuation energy density**

- **by volume:**
$$\propto \frac{1}{2} \sigma_{\max} \epsilon_{\max} \approx \frac{1}{2} Y \epsilon_{\max}^2$$

- **by mass:**
$$\propto \frac{1}{2} \frac{Y}{\rho} \epsilon_{\max}^2 \approx \frac{1}{2} \left(c \epsilon_{\max} \right)^2$$

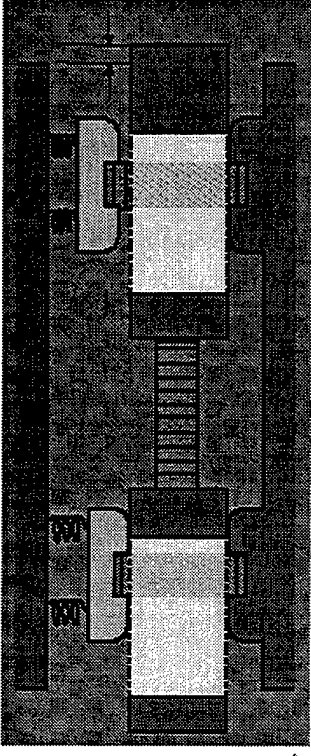
Material-based, no parasitic device effects

- **Max delivered to matched load:**
$$\propto \frac{1}{8} \sigma_{\max} \epsilon_{\max}$$

- **Solid state devices inadequate for some applications**

Non-Solid-State Device: Inchworm

- High force & stroke req'ts suggest inchworm
- Maximum force is smaller of:
 - pusher blocked force & clamp holding force
 - force ~ CS area
 - length depends on clearances
- Stroke can be large
 - High effective energy density



- Max rate independent of size
 - Max step size, rate inversely related
 - About 1.2 m/s for piezo pusher
neglecting parasitic effects
 - Reduced under load

$$\propto \frac{1}{4} c \epsilon_{\max}$$

Inchworm Power Density

- **Actuation power density**

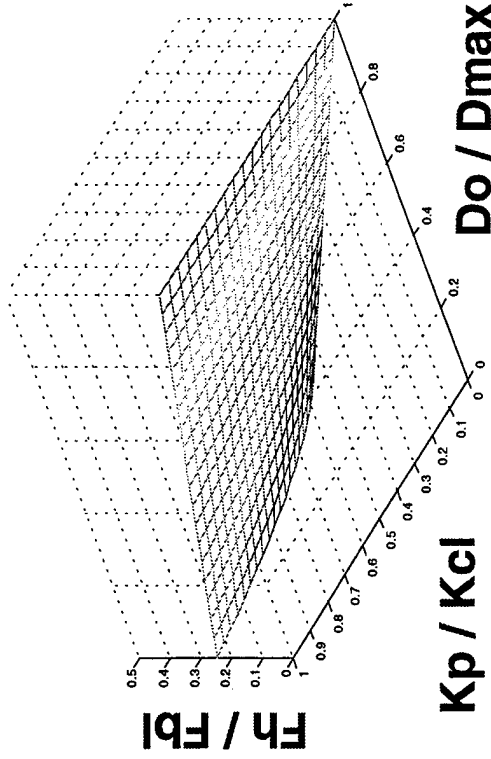
- by mass:
$$\propto \frac{1}{8} \left(\frac{Y}{\rho} \right)^{3/2} \varepsilon_{\max}^2 L_{\max}^{-1} \approx \frac{1}{8} c^3 \varepsilon_{\max}^2 L_{\max}^{-1}$$

- Pusher material-based only, no parasitic device effects
 - Sub-resonant drive
 - Highest power density obtained for small length scale (L)
- **Small size limited by tolerance issues**
- **Resonant drive**
 - A kind of gearing (increase disp, reduce force)
 - Low “dynamic stiffness”

Clamp Holding Force Sensitivity



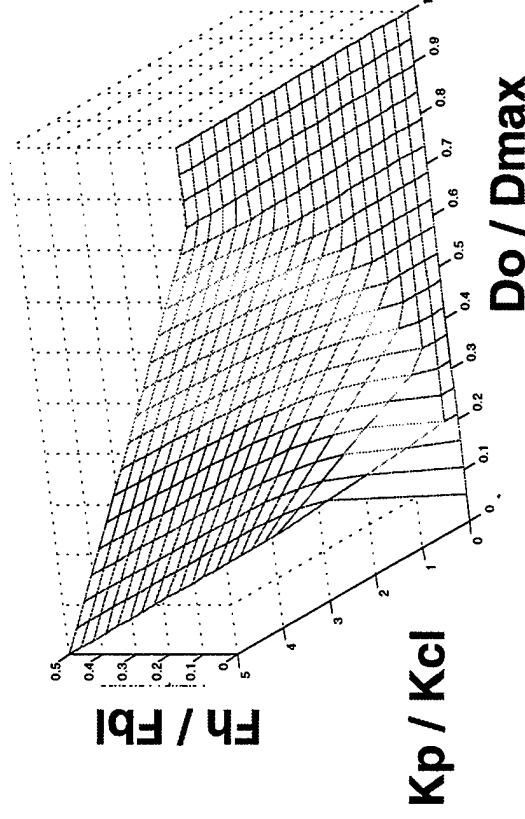
Clamp with initial clearance



small clearance
stiff clamp



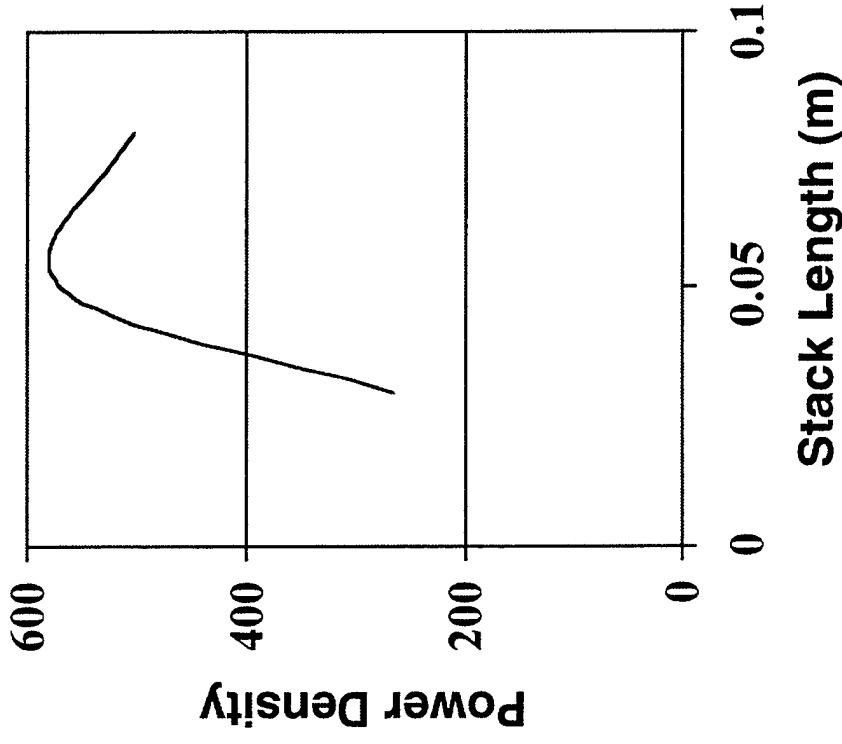
Clamp with initial preload



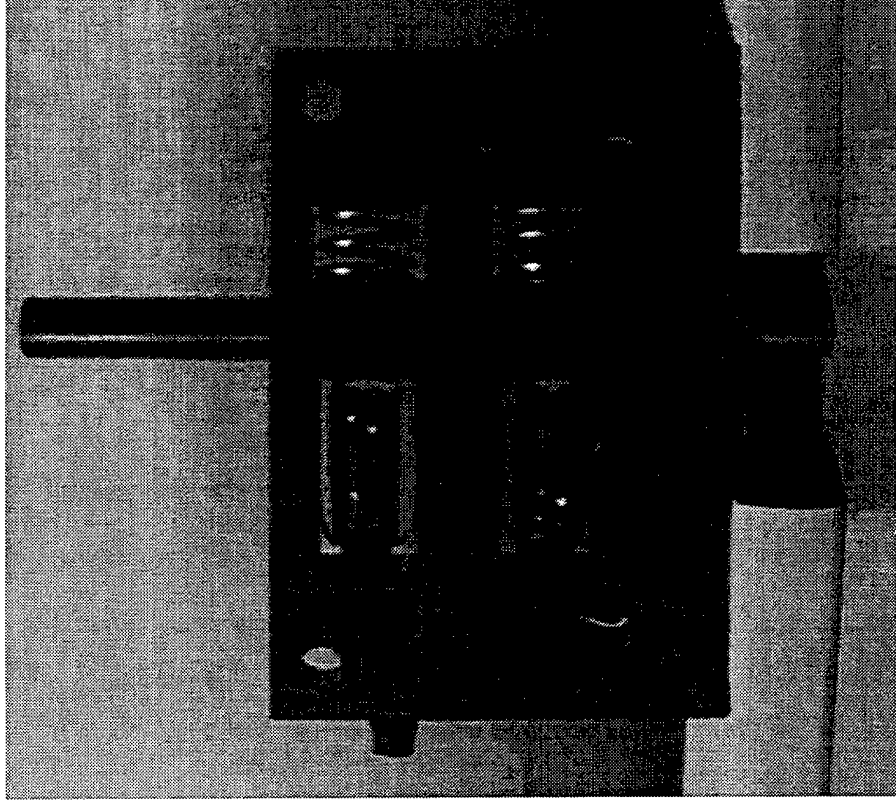
small clearance
soft clamp

Sample Scaling

- **Linear actuation**
 - Run at max freq for max power density
 - Optimize electronics for fixed-freq ops
- **Long stack => low max freq**
- **Short stack => step size vs. backlash**
- **CS area => high force, overcome friction**



H3DB (direct clamp)



Performance @ 120V

Max. Force = 140 N

Max. Disp. = Unlimited

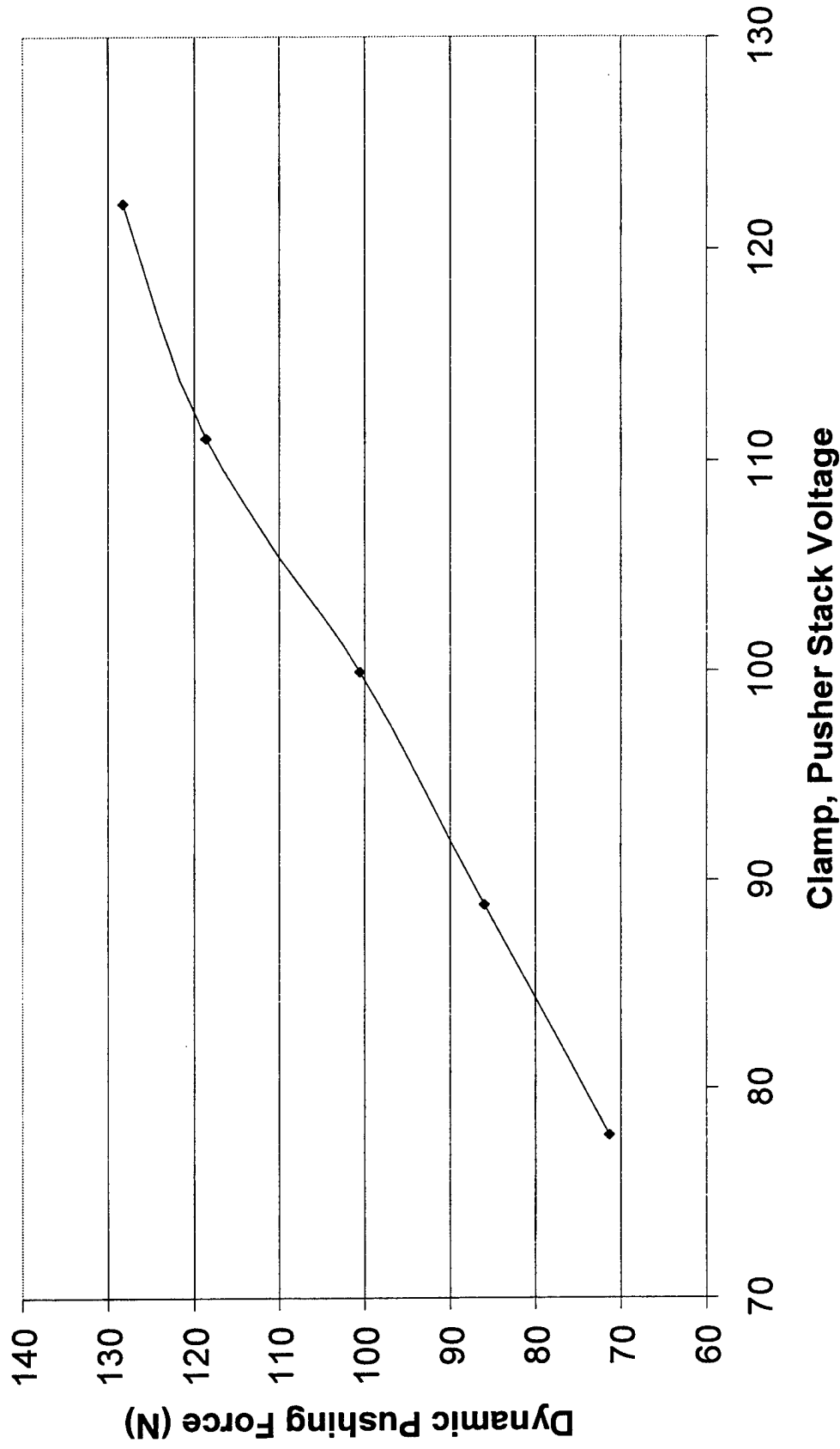
Max. Vel. = 1.5 mm/s

Stacks Req'd. = 4

Unlocked w/o power

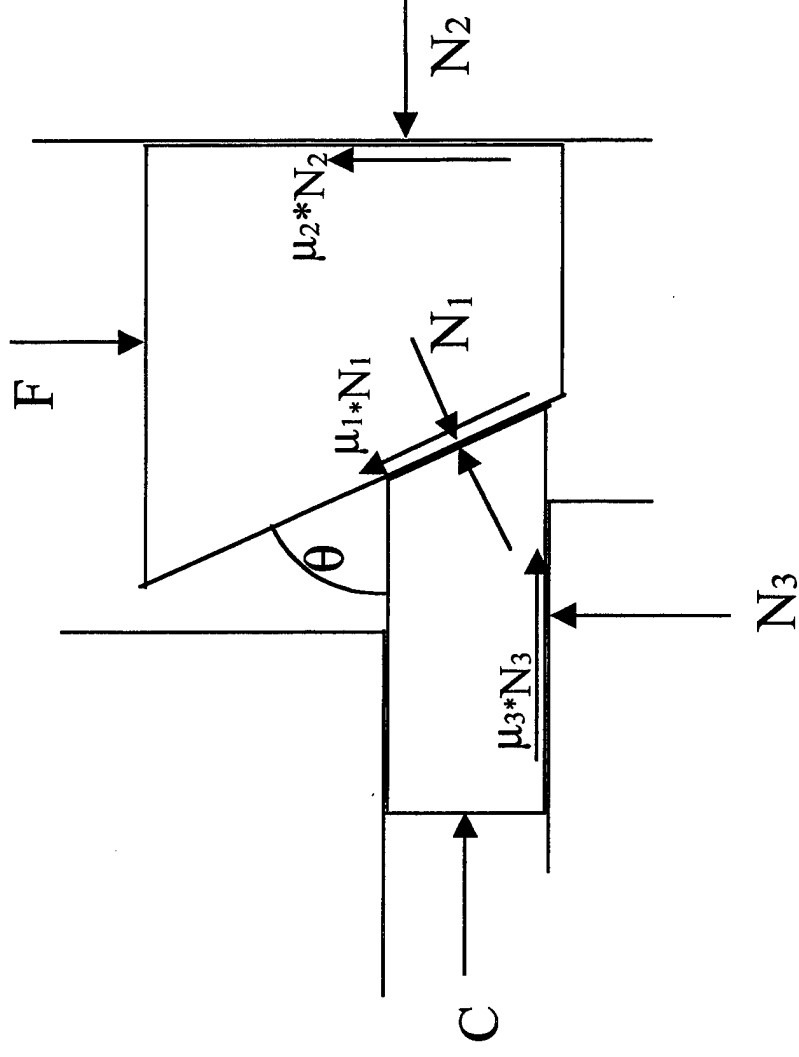
H3DB Dynamic Force

H3DB Maximum Dynamic Pushing Force vs. Stack Voltage



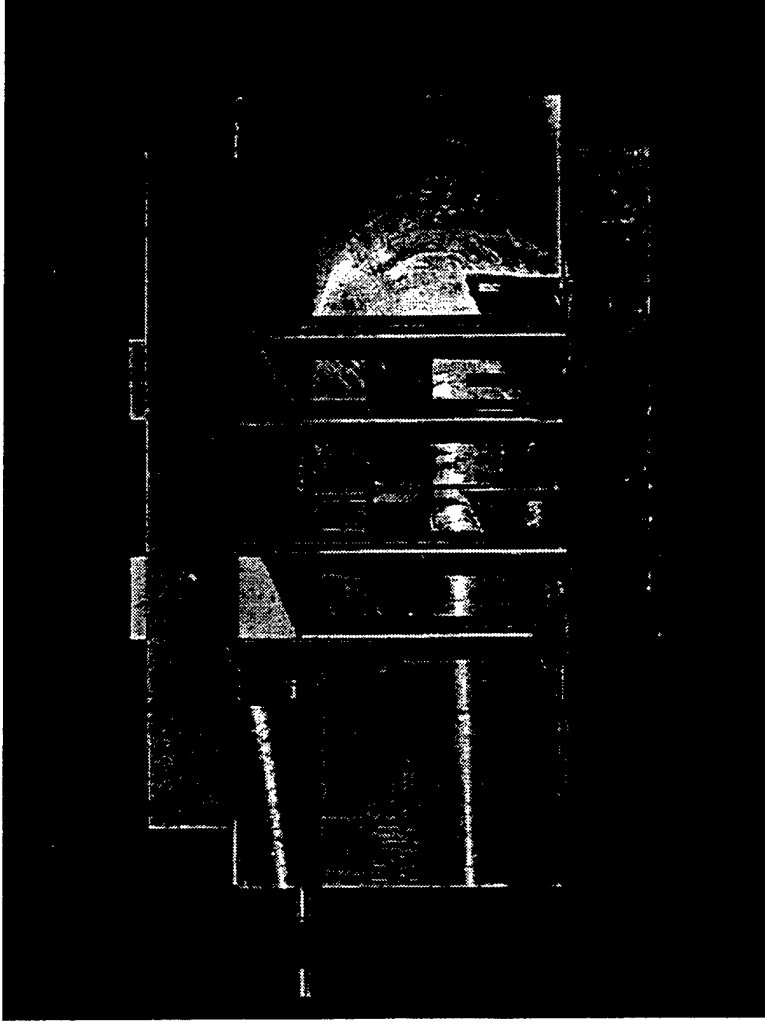
Alternative Clamp

- “Wedgeform” based on “self-locking taper”



For some wedge angle and friction coefficients, the wedges are self-locking: no force “C” needed

Wedge worm I



Performance

**Max. Force = 250 N
(1000 N goal)**

Max. Disp. = 25 mm

**Max. Vel. = 8 mm/s
@ 100V, 200 Hz**

Stacks Req'd. = 1

**Bi-directional motion possible;
Self locking not perfect**



Summary: High-Force Piezo Linear Stepping Motors

- Shape Control Actuation
 - Solid state devices have poor disp and energy density
 - Reduce structural stiffness
 - Use non-solid-state, load-bearing actuator
 - Electroceramic inchworms have potential advantages over hydraulics (integration)
electric motors (conformability)
SMA (faster response)
 - Potential for high power density
- Inchworms in development (H3C, H3DB, WW1, WW2)
 - Measured and modeled performance (rate, force)
 - Issues: high force (clamping), reliability, feedback
 - ◆ WEDGEWORM concept for high clamp holding force
 - Potential for compact drive electronics

Interior Noise Control Using Smart Materials

E. Luft and B. Balachandran
Department of Mechanical Engineering
University of Maryland
College Park, MD 20742-3035

Research Objective

The overall aim of this task is to help in the development of viable active materials based control schemes for reducing rotorcraft interior noise. Specific objectives include the following: a) development and validation of structural-acoustic models and b) investigations into non-model based and model based control schemes for creating multiple quiet zones.

Approach

A combined experimental and analytical investigation into the use of piezoelectric materials on a flexible panel to control transmission of multiple tones through this panel into three-dimensional enclosure is conducted. The multiple tones are considered in a bandwidth of 40 Hz to 1000 Hz. Lead Zirconate Titanate (PZT) patch pairs, which are bonded symmetrically on the flexible panel, are used as actuators and a combination of microphones and Polyvinylidene Fluoride (PVDF) films are used as sensors. Spatially local vibration control on the flexible panel and spatially local noise control inside the enclosure are experimentally attempted by using digital feedforward control schemes. A mechanics based state-space model is developed to model the structural-acoustic system and numerical simulations are conducted by using this model. Influences of nonlinearities are also examined.

Accomplishments

Extensive analytical and experimental studies of spatially local noise control of disturbances with multiple tones have been conducted and it has been demonstrated that actuator grouping can be beneficial for local noise control. Through the experiments, it has been demonstrated that nonlinearities associated with piezoelectric actuation can lead to higher harmonics in the response and pose problems for realizing local noise control. A mechanics based model inclusive of piezoelectric actuator nonlinearities and plate nonlinear elasticity effects has been developed. Through use of the model and through experiments, it has been demonstrated that actuator nonlinearities can be significant beyond certain electric field strength limits. A passive panel-spacer concept has also been explored experimentally, and the potential for reducing sound transmission has been shown.

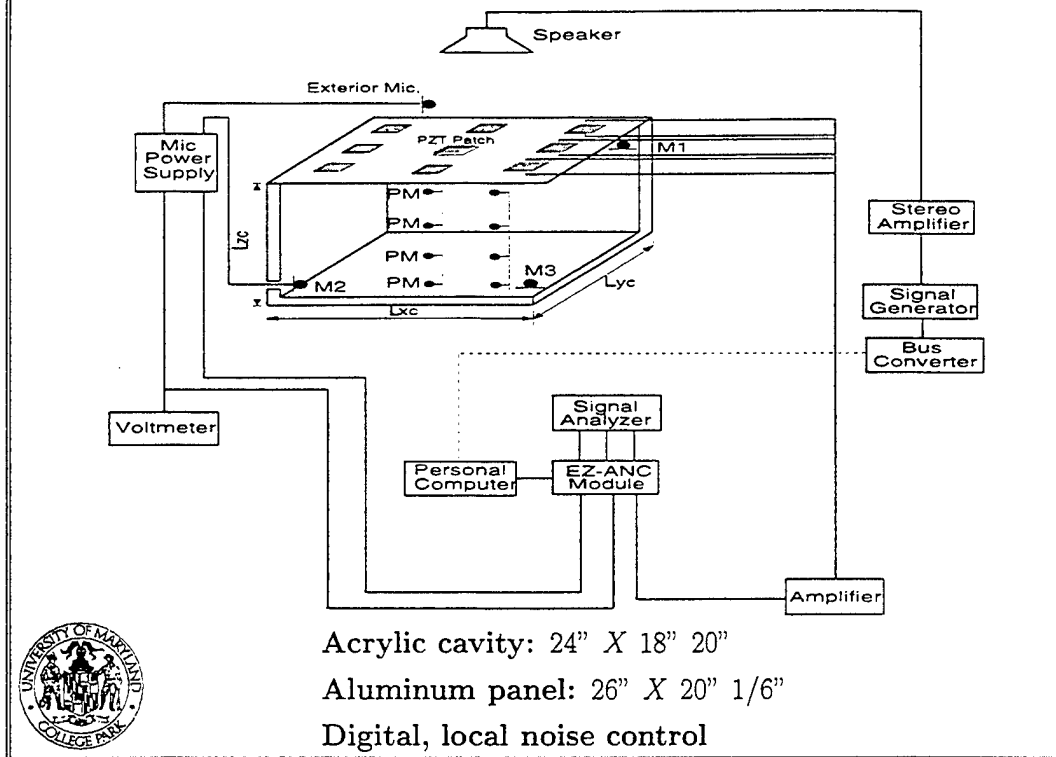
Future Work

Future work will include the following: a) investigations into obtaining further understanding of the influence of nonlinearities through experiments and analysis, b) exploration of the new active-passive panel spacer concept, and c) studies on actuator grouping and actuator/sensor pairing to realize zones of local noise control.

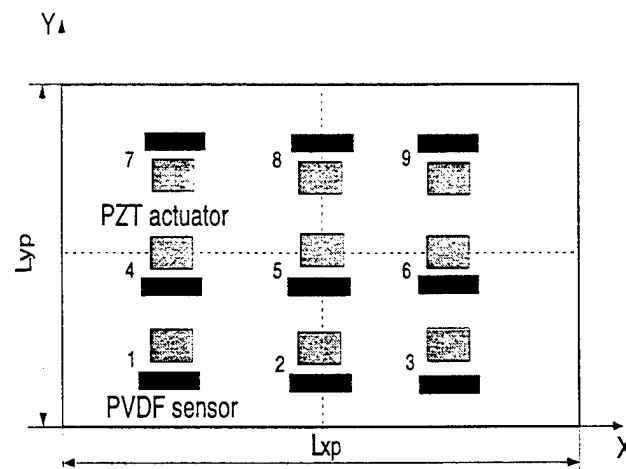
Significance

The outcome of this task will be useful for assessing the viability of active materials based schemes for controlling multiple tones in a three-dimensional enclosure such as a rotorcraft cabin.

Experimental Arrangement



Locations of Sensors and Actuators on Trim Panel

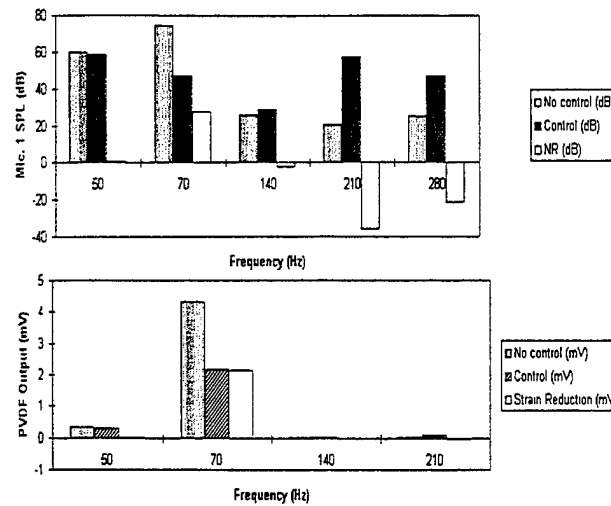


Group 1: Actuator pairs 1, 4, and 7

Group 2: Actuator pairs 3, 6, and 9

Group 3: Actuator pairs 2, 5, and 8

Experimental Result for Control of Tonal Disturbance

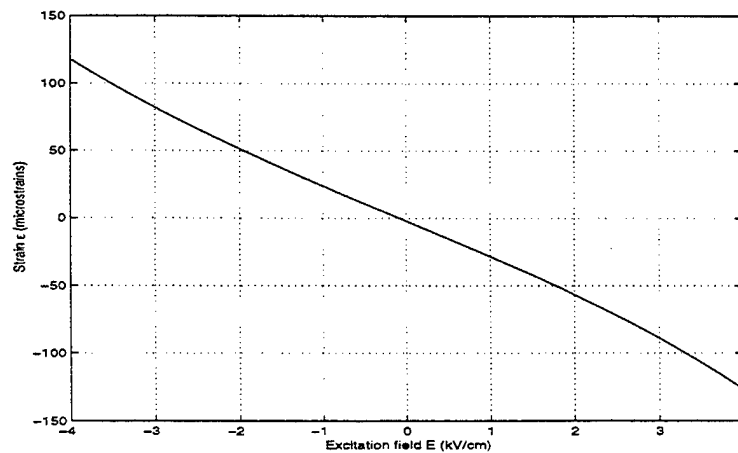


Responses observed at tonal disturbance of 70 Hz: actuator pairs 5 and 3 and error sensor Mic. 1 are used

Piezoelectric Actuator: Free Strain Behavior

$$\epsilon = a + bE + cE^2 + dE^3$$

$a = -1.9637, b = -25.82, c = -0.1535, \text{ and } d = -0.298.$



• Sirohi and Chopra (1998)

Analytical Development

- Sound pressure in the enclosure

$$\nabla^2 p - \frac{1}{c_0^2} \frac{\partial^2 p}{\partial t^2} - \gamma_a \frac{\partial p}{\partial t} = 0$$

- Displacement of the plate-piezo system

$$\begin{aligned} D \nabla^4 w + \rho_p h_p \ddot{w} + \gamma_p \dot{w} = & p_{in}(x, y, t) - p_{out}(x, y, t) \\ & - \sum_{i=1}^K \frac{(h_p + h_{pz})}{1-\nu} E_{pz} d_{31} \nabla^2 \chi_i V_i(t) \\ & + \text{nonlinear terms} \end{aligned}$$

- Nonlinear terms due to plate elasticity and piezoelectric actuator behavior



Analytical Development

- Interior pressure field:

$$p(x, y, z, t) = \sum_{i=1}^N \psi_i(x) \phi_i(y) \Gamma_i(z) q_i(t)$$

- Panel displacement field:

$$w(x, y, t) = \sum_{k=1}^M \alpha_k(x) \beta_k(y) \eta_k(t)$$

- Equation governing a panel mode:

$$\begin{aligned} \rho_p h_p \ddot{\eta} + \gamma_p \dot{\eta} + (K_1 + K_2) \eta + K_3 \eta^3 - \sum_{i=1}^N C_i q_i(t) = \\ - \frac{(h_p + h_{pz}) E_{pz} t h_{pz} t}{1-\nu} \sum_{i=1}^K \left(b \frac{V_i}{h_{pz} t} + d \frac{V_i^3}{h_{pz}^3 t} \right) \int_{A_f} \alpha \beta \nabla^2 \chi_i(x_i, y_i) dA_f \end{aligned}$$

Note: Coefficient K_2 is a function of V_i^2

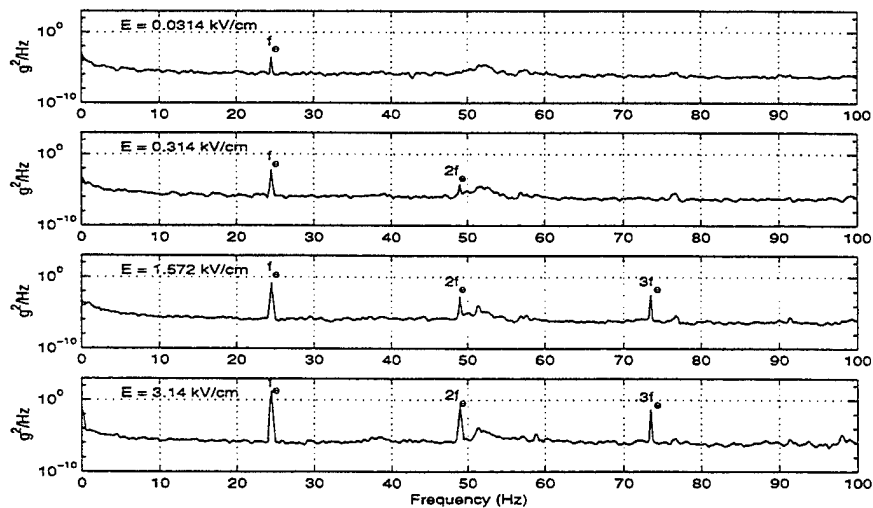


System Parameters

- Plate: $0.660\text{ m} \times 0.508\text{ m} \times 1.58\text{ mm}$
- Enclosure: $0.609\text{ m} \times 0.457\text{ m} \times 0.508\text{ m}$
- PZT patch pair 5 at center: $50.8\text{ mm} \times 25.4\text{ mm} \times 0.318\text{ mm}$
- System resonances: 48.5 Hz , 72.5 Hz , 98.0 Hz , 123.5 Hz , 130.0 Hz , 271 Hz , 324.3 Hz , 367.0 Hz , 424.8 Hz , and 448.3 Hz
- Accelerations close to location of patch pair 5 determined and compared with corresponding experimental measurements

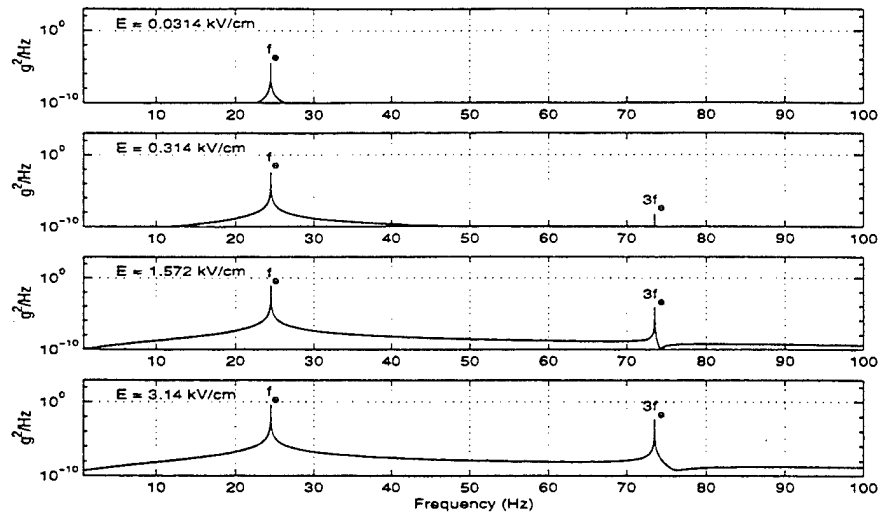


Experimental Measurements: Plate Accelerations



Response spectra to harmonic excitations at 24.5 Hz

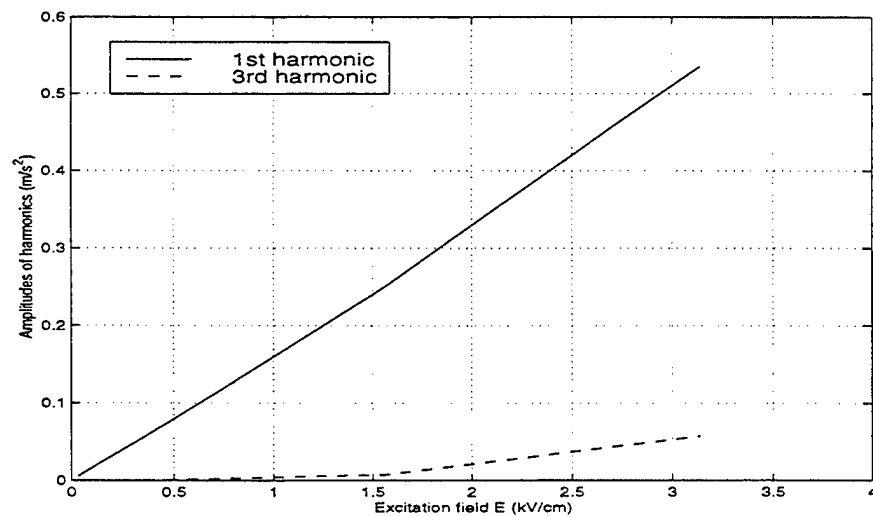
Numerical Predictions: Plate Accelerations



Response spectra to harmonic excitations at 24.5 Hz



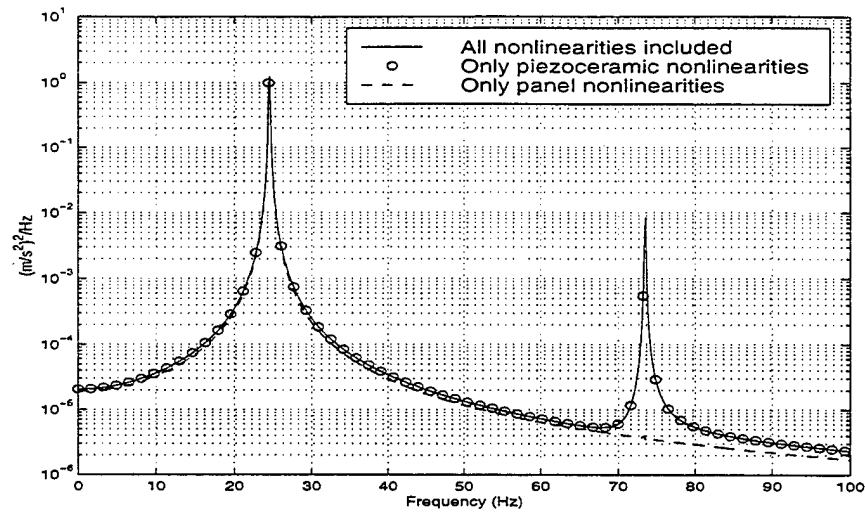
Plate Acceleration: Amplitudes of Harmonics



Harmonic input into piezoelectric patch pair 5 at 24.5 Hz

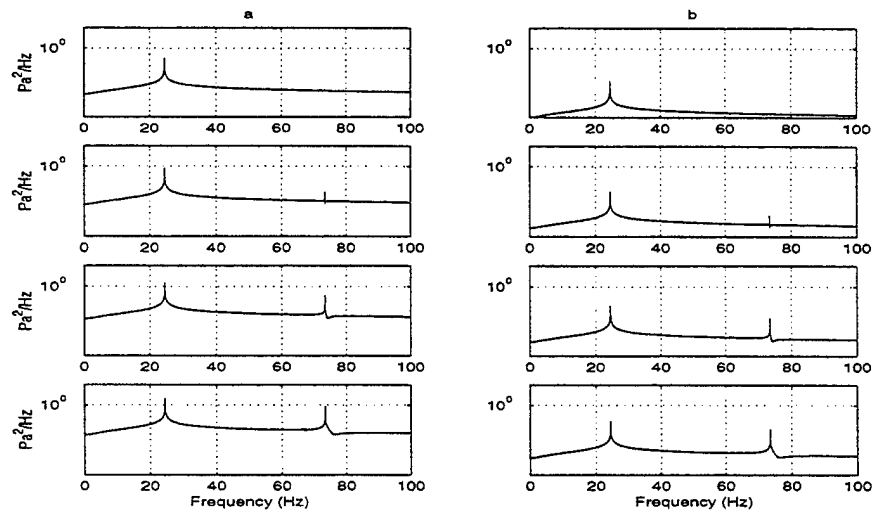


Numerical Predictions: Effects of Nonlinearities



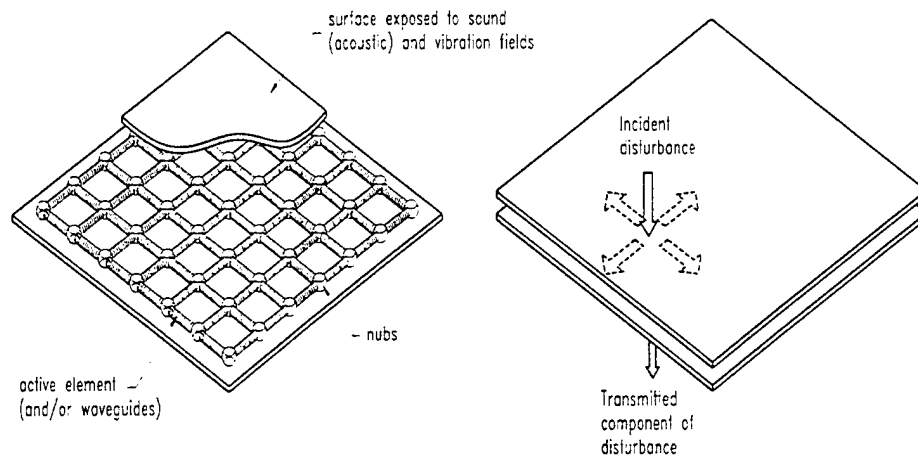
Responses to harmonic input into piezoelectric patch pair 5 at 24.5 Hz and $E = 2.83 \text{ kV/cm}$

Numerical Predictions: Enclosure Pressure

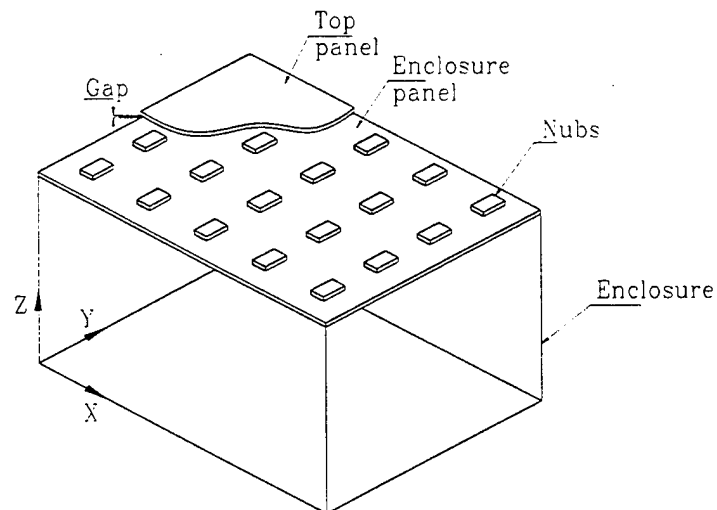


Response spectra to harmonic excitations at 24.5 Hz at two different microphone locations: (a) three inches below piezo patch pair 5 and (b) eight inches below piezo patch pair 5

Active-Passive Panel Spacer



Passive Panel Spacer



Nub material and dimensions:

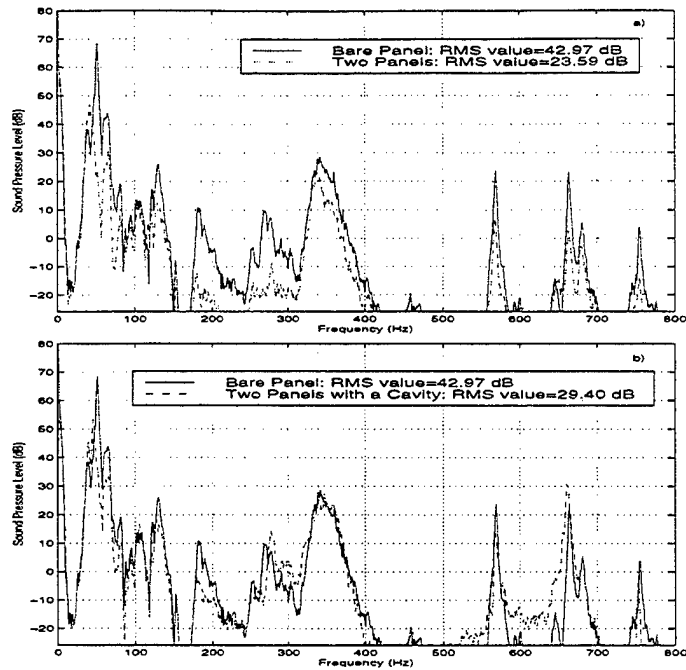
- AKTON, (0.9"x0.9"x0.35")
and (0.9"x1.8"x0.35)
- DYAD, (1"x1"x0.05")

Nub Spacing:

- 4.25" in X direction
- 4.5" in Y direction

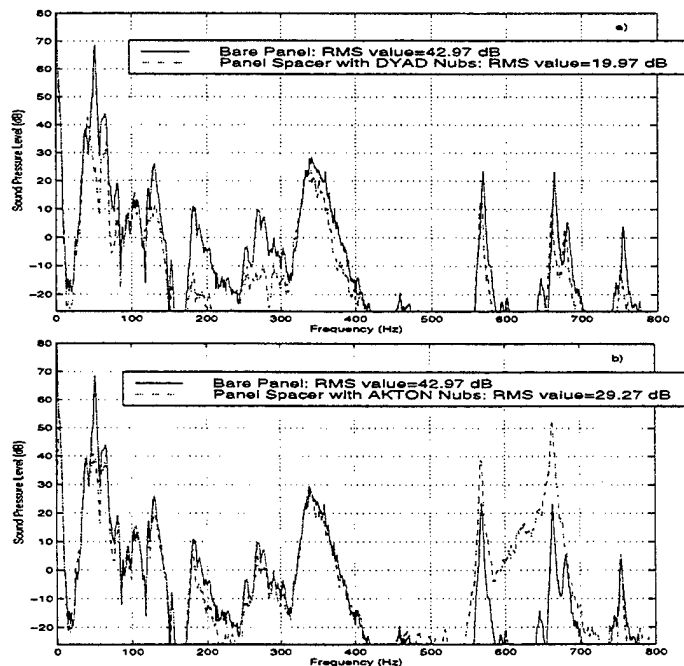


Experimental Results for Passive System



Sound pressure level at the microphone location (13", 10", 5"): a) two panels on top of each other and b) two panels separated by a 1.0" deep cavity

Experimental Results for Passive System



Sound pressure level at the microphone location (13", 10", 5") with panel spacer on top of enclosure: a) DYAD nubs (1", 1", 0.05") and b) AKTON polymer nubs (0.9", 0.9", 0.35")

Summary

- Active control of sound fields with energy in the bandwidth of 40 Hz to 1000 Hz considered
- Influence of actuator nonlinearities examined analytically and experimentally; model results in good agreement with experimental measurements of first and third harmonics of excitation frequency
- Model unable to predict the discernible second harmonics seen in the experiments
- Actuator nonlinearities dominant compared to nonlinearities due to plate elasticity
- Panel spacer concept promising for control of sound fields over a broad bandwidth



Future Work

- Conduct further investigations to obtain a more complete understanding of the influence of nonlinearities through experiments and analysis
- Explore active-passive panel spacer concept
- Studies on actuator grouping and actuator/sensor pairing to realize zones of local noise control: Experiments with helicopter fuselage



Thermomechanical Modeling of Elastomeric Lag Dampers

Ramkumar Krishnan
Graduate Research Assistant

Vijay Madhavan
Graduate Research Assistant

Norman M. Wereley
Associate Professor

Alfred Gessow Rotorcraft Center, Department of Aerospace Engineering
University of Maryland, College Park, Maryland

Helicopter rotors are subject to ground and air resonance which pose a crucial problem of vibration control. Elastomeric dampers are a class of lag dampers used extensively to provide stability and control this vibration problem of rotors by damping and dissipating the vibrational energy in form of heat through material hysteresis. The non-linear nature of these elastomeric dampers has given way to many unique analysis that attempt to explain their behavior. These dampers exhibit stiffness and damping properties that are complex functions of the frequency, strain amplitude and temperature. Since elastomeric dampers are used over a wide range of temperatures, one needs to study the hysteresis behavior of these dampers under varying frequencies, amplitude and temperatures to ascertain and predict their non-linear behavior and their dependence on the above mentioned parameters. A mechanisms based analysis would thus give a more definite explanation of the hysteresis characteristics of the damper compared to prevalent non-mechanisms based analysis.

The mechanisms based model calls for extensive testing of these dampers under varying temperature and frequencies and analysis of the hysteresis data. The results of tests conducted on a Silicone-rubber based elastomeric double lap shear specimen are presented. These materials typically have loss factors ranging from 0.7-1.1 as compared to the lower loss factors of existing lag dampers and hence provide better damping and rotor stability. The testing was carried out on a MTS servo-hydraulic machine that has multi-functional capabilities. The dampers were tested for a range of amplitudes (0-200 mils) and frequencies (2.5 Hz-7.5 Hz) at varying temperatures. The damper was mounted inside an ATS temperature chamber to achieve and maintain these different ambient temperature conditions. The specimen temperature was monitored using a thermocouple embedded in the material. The testing was done at single and dual frequency sinusoidal loading for different amplitudes to account for interference in real-time situations. The dampers were tested for two loading situations, with zero preload and 10% preloaded cases. Results for varying frequencies and amplitude at room temperature (25°C) and 50°C for both zero preloaded and 10% preloaded cases are presented.

It is observed that the preheating and higher ambient temperature loosens and reduces the stiffness while preloading increases the stiffness property of the material as expected. While the loss factor is higher at low amplitudes it reduces significantly at higher amplitudes stating that the stiffness is more predominant at low amplitudes and damping is more effective at higher amplitudes. Material self-heating is also observed which gives rise to increased material temperatures and hence higher strain. The force-displacement hysteresis cycle show the strong amplitude dependence exhibited by this material. A non-linear mechanisms based model to explain and capture these effects has been proposed and developed. The temperature dependence of the stiffness and damping properties is to be studied and incorporated into the model to account for thermal effects.

Research supported by Paulstra Vibrachoc and Army Young Investigator Program (Dr. Gary Anderson serving as technical monitor).

Dynamic Characterization and Analysis of Magnetorheological Damper Behavior

Rebecca Snyder
Graduate Research Asst.

Gopalakrishna M. Kamath
Research Scientist

Norman M. Wereley
Associate Professor

Department of Aerospace Engineering
University of Maryland, College Park, MD 20742

The steady state hysteresis behavior of a linear stroke magnetorheological (MR) damper is examined for varying magnetic fields and sinusoidal excitations. A truck seat damper, manufactured by the Lord Corporation, was used to create two data sets. The first set was used to identify and predict model parameters, while the second was used to validate the predictions. The identification data set was tested at a frequency range of 1.00 - 3.0 Hz in increments of 0.25 Hz, with applied current varying from 0.0 - 1.0 A in increments of 0.2 A. The second validation data set consisted of tested frequencies of 1.125 - 2.875 Hz, with increments of 0.25 Hz. The applied current varied from 0.1 - 0.9 A, in increments of 0.2 A.

Four different nonlinear modeling perspectives are discussed that characterize dynamic behavior including: (1) nonlinear Bingham plastic model, (2) nonlinear biviscous model, (3) nonlinear hysteretic biviscous model, and (4) nonlinear viscoelastic-plastic model. The first three nonlinear models are piecewise continuous in velocity. The fourth model is piecewise smooth in velocity. By adding progressively more model parameters with which to better represent preyield damper behavior, the force vs. velocity hysteresis model is substantially improved. Of the three nonlinear piecewise continuous models, the nonlinear hysteretic biviscous model provides the best representation of force vs. velocity hysteresis. The nonlinear viscoelastic plastic model is superior for purposes of simulation to the hysteretic biviscous model because it is piecewise smooth in velocity, with a smooth transition from preyield to postyield behaviors.

The parameters for each of the four models are determined from the experimental data using optimization routines. These identified parameters are used to reconstruct the force vs. displacement and the force vs. velocity hysteresis cycles. The performance of the models is evaluated using error in the equivalent viscous damping and force time histories. The errors are calculated from the reconstructed and experimental hysteresis cycles for the steady state behavior of the damper.

In addition to the model identification study, identified model parameters from the nonlinear hysteretic biviscous and the nonlinear viscoelastic-plastic models were used to predict damper behavior for the offset conditions of the validation data set. Each parameter was predicted from the identification data set using a two dimensional interpolation function in MATLAB. The predicted parameters were then used to reconstruct hysteresis cycles for both models. These cycles are compared with the experimental data collected in the validation set at the same current and frequency values. Errors were again calculated for the equivalent viscous damping and the force time histories between the experimental data and the predicted models. The hysteretic biviscous and viscoelastic plastic models are shown to be most and comparably accurate in predicting damping performance, although the viscoelastic plastic model is best when predicting steady state response of the damper to sinusoidal loading.

This research was supported under the Army Young Investigator program to NMW with Dr. Gary Anderson as the technical monitor.

Active System Solutions

Midé Technology Corporation

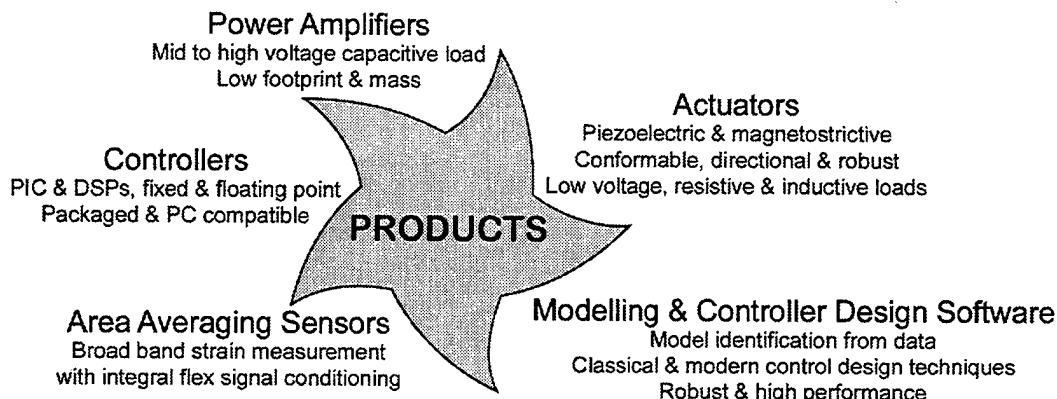
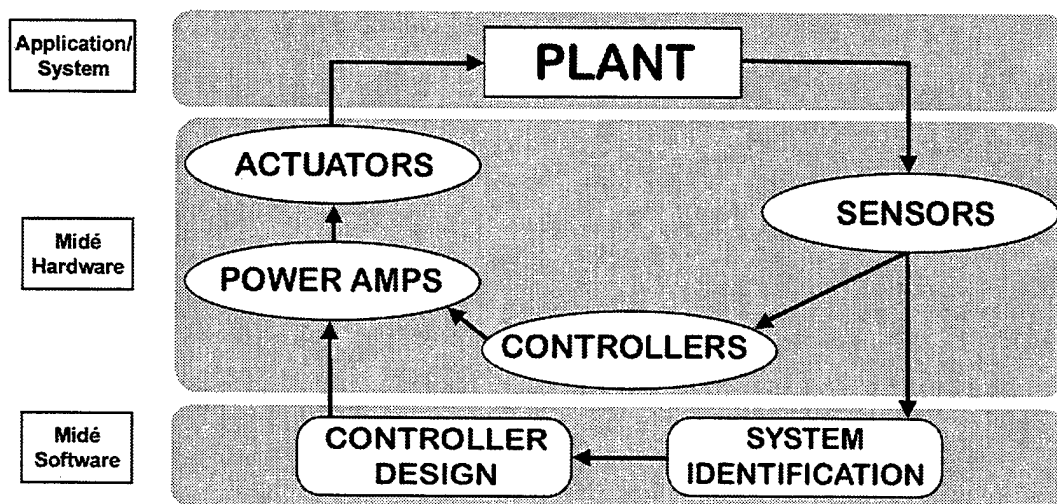
<http://www.mide.com>

56 Rogers Street, Cambridge, MA 02142

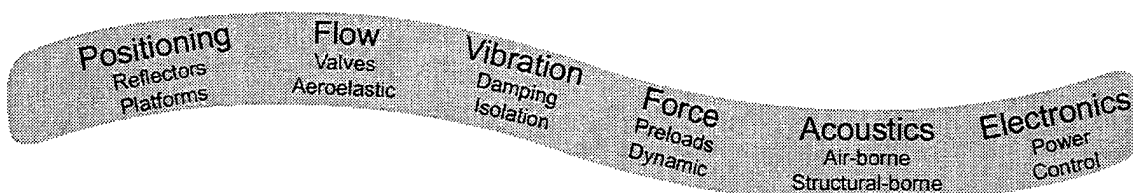
Tel: (617) 252-0660 x235, Fax: (617) 252-0770

Contact: Dr. John Rodgers (rodgers@mide.com)


Midé has recognized the need to provide a system solution for active vibration and noise control. In order to address this need Midé has developed hardware and software products (Figure below) that completes the set needed to implement an active solution. With the Midé's products, design engineers can integrate into their applications an end-to-end active system solution.

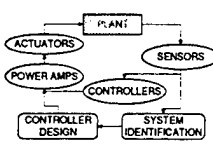


OPPORTUNITIES



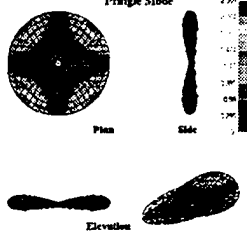
Plant Modeling





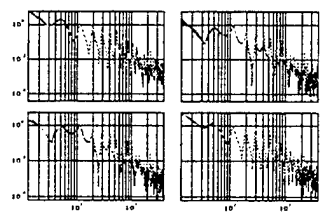
- Midé has experience in developing analytical models of complex linear and nonlinear dynamic systems and the use of these models to construct high fidelity state-space measurement based models.
 - Shown is a finite element model of a flexible membrane mirror and a state-space model fitted (green) to experimental data (blue).

Principle Mode




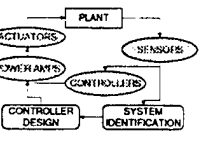
Plan

Elevation



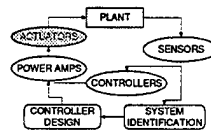
Midé's Hardware



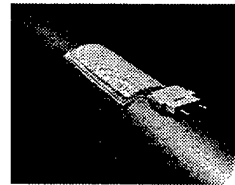
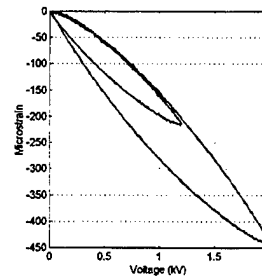


- Midé offers the following hardware products:
 - Area Averaging Strain Sensors (AAS)
 - A low-cost conformable, piezoelectric actuator (PowerAct)
 - High-voltage small-package capacitive load power amplifier
 - Packaged DSP Controller boards
- Midé can custom design:
 - Axial and surface piezoelectric, magnetostrictive and magnetically activated actuators
 - Self-sensing piezoelectric actuators/sensors
- Midé has extensive linear and nonlinear plant modeling experience

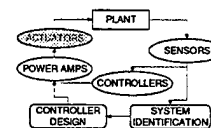
PowerAct™



- Midé sells a low-cost conformable piezoelectric actuator (PowerAct™) with performance comparable to Active Fiber Composites
- Custom PowerActs can be supplied in different shapes with complex directional actuation
- Shown are free strain performance and the PowerAct attached to a curved surface

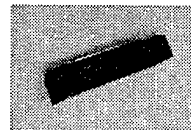
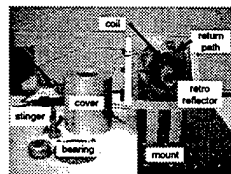


MASMA Actuator

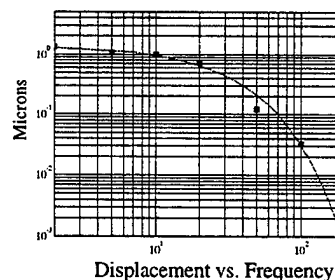


- Features - Magnetically activated shape memory alloy (MASMA) Actuator single crystal NiMnGa

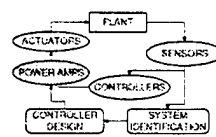
- Preloaded with coil centering and return path



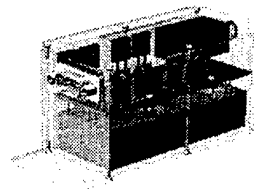
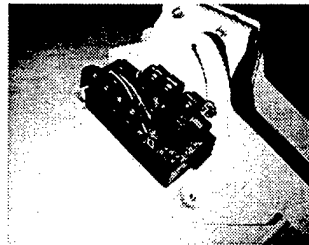
NiMnGa alloy developed at MIT



2 kV Power Amplifier

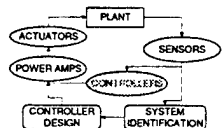


- 28 V/2A DC supply
- 0-2 kV output to 2 kHz
 - 200 V/V gain
 - 12 mA
- modular (range of output voltages)
- 2.00 x 2.25 x 3.75", 7.3 oz
- \$1000/unit in small quantities

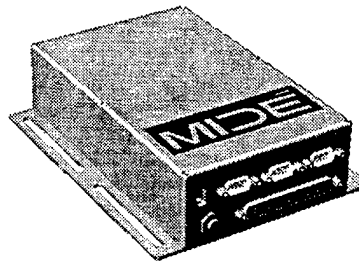


Advantages: Wiring, heat, safety

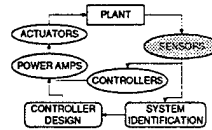
C32 DSPs



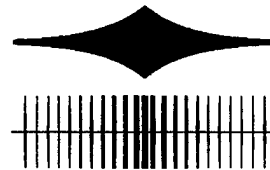
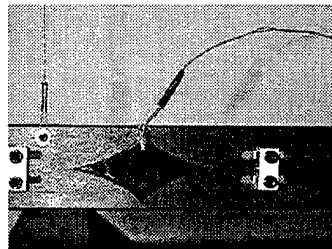
- Small form packaged C32 DSP boards
- 4 analog inputs/4 analog outputs
- 48 Digital I/O lines
- >40 states at 10kHz
- 512KW RAM
- RS-232 Interface
- Power: 28V/5W
- Volume: 5"x3"x2"



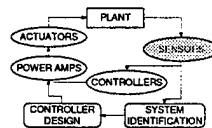
Area Averaging Sensors (AAS)



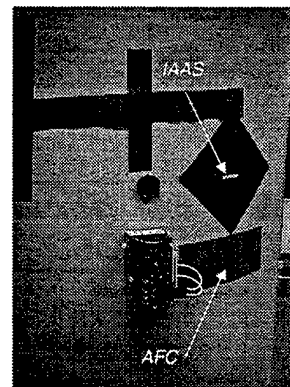
- Area Averaging Sensor - spatial filtering of dynamic strain
 - * low form
 - * simple signal conditioning
 - * tailored for good signal to noise
- Reduces risk of adapting to wrong modes & nonlinear harmonics



AAS Form and Packaging

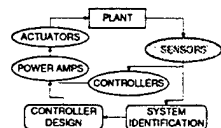


- PVDF area averaging shaped sensor developed with integrated electronics
 - * signal conditioning and external contacts
 - * flexible circuit technology
 - * surface mount components
- Midé's PowerAct actuator, AAS sensor and High-voltage power amplifier on a scaled payload shroud




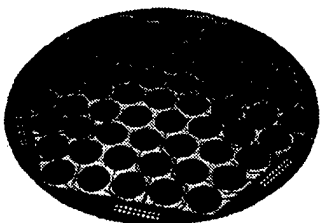
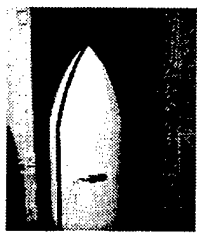
AAS Applications

- Modal sensing, frequency response shaping without phase fluctuations, vibro-acoustic sensing
- Improved sensors for acoustic application
- Delta shroud fiberglass test-bed



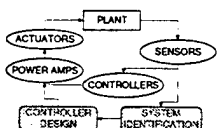
A block diagram showing the control loop: ACTUATORS → PLANT → SENSORS → CONTROLLERS → POWER AMPS → back to ACTUATORS. Below this, two boxes labeled 'CONTROLLER DESIGN' and 'SYSTEM IDENTIFICATION' are connected to the CONTROLLERS block.







Midé's Software

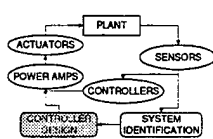

- Midé offers two software packages that significantly reduces controller design and implementation
- DynaMod is a MatLab based frequency domain model identification tool
 - Has a user friendly Graphical User Interface (GUI)
 - Menu driven and interactive process yields high fidelity measurement based control models
- DynaCon is an expert system, where a menu driven MatLab tool enables:
 - Design of robust LQG and H_∞ controllers
 - Rapid control prototyping



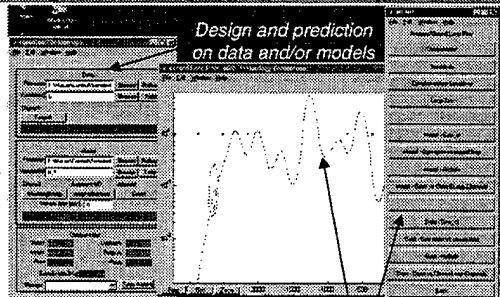
A block diagram showing the control loop: ACTUATORS → PLANT → SENSORS → CONTROLLERS → POWER AMPS → back to ACTUATORS. Below this, two boxes labeled 'CONTROLLER DESIGN' and 'SYSTEM IDENTIFICATION' are connected to the CONTROLLERS block.



DynaCon Control Design Tool

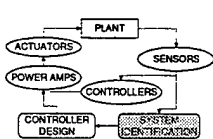




- Frequency domain robust control
- LQG, H_{∞} , etc
- Embedded expertise
- User friendly GUI
- Rapid control prototyping
 - * 4 hour design cycle (from system identification to DSP closed loop)
- Midé Product

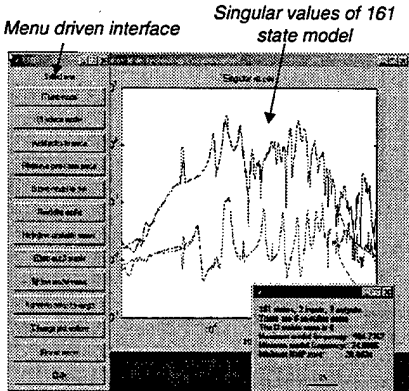


Frequency domain tuning functions

DynaMod System Identification Tool

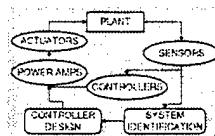
- Matlab frequency domain GUI identification tool
- Interactive fitting of pole-zero structures to frequency domain data to obtain a measurement based model
- User friendly GUI
- Shown is a 161 state structural/ acoustic model



Singular values of 161 state model

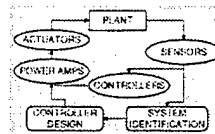
Midé Product (Royalties to MIT)

Integrated Active Solutions

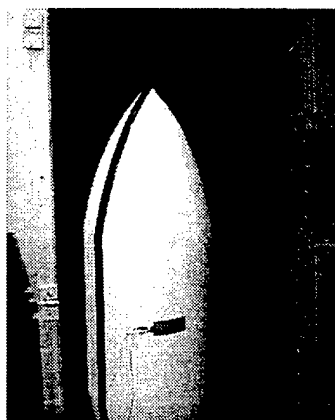


- Using its suite of hardware and software products Midé has solved several challenging problems:
 - The reduction of noise transmitted through launch shrouds
 - The development of a tunable vibration and noise absorber (SmartShunt)
 - Using SmartShunt to reduce the noise radiated by underwater systems
- Midé also innovates and develops in many engineering fields:
 - Smart gels
 - Positive pressure relief valves
 - Custom designed loadcells, sensors

Acoustic Transmissions

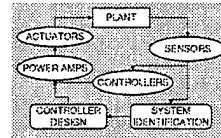


- Midé developed an integrated system for the reduction of acoustic noise transmission through structures
- For example: Acoustic noise transmission through payload fairing is major design constraint for satellites
- Scale Delta launch shroud testbed
 - AFC actuator pair
 - anechoic chamber
 - DSP based control system design



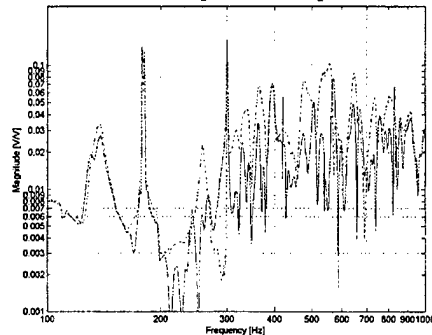
Acoustics Control Testbed

Broadband Active Acoustic Control

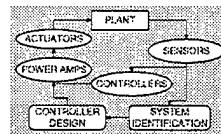


- Broadband interior noise reduction demonstrated
- 4.88 dB 100-1000Hz

Disturbance speaker to performance mic.
Closed (-) vs Open (--) Loop



SmartShunt Concept



- An integrated sensor, signal processing and actuation product that adapts to and passively quiets radiating modes of a mass/fluid loaded structure.

